Analysis of Compound Climate Indices across Europe: from Trends to Risk Zones

Doctoral Dissertation of

Smit Chetan Doshi







2026


PROBABILISTIC
EUROPE
HOTSPOT
COPULA
RISK
EXPOSURE
CMIP6
LAND USE
E-OBS
POPULATION
CLIMATE INDICES
PRECIPITATION
MACHINE LEARNING
SEN'S SLOPE
TREND ANALYSIS
COMPOUND EVENTS
BIAS CORRECTION
RISK EXPOSURE

Analysis of Compound Climate Indices across Europe: from Trends to Risk Zones

A dissertation submitted in fulfillment of the requirements for the ***double doctoral degree:***

Doctorate in natural sciences (Dr. rer. nat.) – Physics

Faculty 1 - Physics / Electrical Engineering of the Universität Bremen, Germany

and

Doctoral Degree in Environmental and Infrastructure Engineering

Department of Civil and Environmental Engineering, Politecnico di Milano, Italy

by

Smit Chetan Doshi
(Student ID: 10783521)

Bremen, Germany

First Supervisor: Prof. Dr. Gerrit Lohmann
Universität Bremen, Bremen, Germany

Second Supervisor: Prof. Dr. Carlo De Michele
Politecnico di Milano, Milan, Italy

Academic Year: 2025/26

Abstract

With climate change impacts increasing evident across European continent, understanding and accurately characterizing climatic events and their compound interactions is important for effective climate risk assessment and mitigation strategies. Climate indices is an important tool for monitoring changes in the frequency, intensity, and duration of climate events, yet detailed continental scale assessments remains limited. The focus of the dissertation (five interrelated studies) is to provide a comprehensive framework for analyzing climate trends, identifying compound risk patterns, and improvising precipitation data across Europe through advanced statistical techniques and high-resolution data analysis.

The first study determines the spatial and temporal trends of 74 climate indices from 1950 to 2021 at a high resolution of 0.1° on a monthly scale. Using Mann-Kendall and Sen's slope estimator, significant increase in growing degree days and decrease in heating degree days are identified, along with changes in other climate indices such as universal thermal climate index, relative humidity, wind chill index, global radiation, and potential evapotranspiration. Country-specific zoning reveals southeastern Europe experiences highest number of warmer days, while eastern Europe faces lower colder days.

The second part focuses on compound climate indices, employing 27 bivariate and 10 trivariate high correlated climate indices pairs of copula models to identify regions with risks. Northern and eastern Europe countries are vulnerable to compounded risks involving global radiation, temperature, evapotranspiration, and bioclimatic indices. The exposure of agricultural and coastal areas to these risks, need further integrated risk assessment approaches.

In the third study, probabilistic approach used to derive high exposure zones across Europe based on 56 climate indices. Precipitation and temperature based indices are important in identifying high-risk regions for southern and southeastern Europe, while northern and western Europe are more affected by precipitation indices. This study also tracks the exposure of dominant land use types and population density to these risks.

To improvise the accuracy of the precipitation based climate indices, the fourth study addresses the challenge of wet antenna attenuation in commercial microwave links used for rainfall estimations. By developing frequency dependent models calibrated with rain gauge data, the study improves reliability of rainfall intensity estimates, particularly for high-frequency bands.

The final study evaluates the bias-correction technique for downscaling precipitation data from CMIP6 models across Europe. The Empirical Quantile Mapping (EQM) technique outperforms other methods, and when combined with Random Forest machine learning models, provides more accurate regional precipitation predictions, especially for low rainfall intensities. The approach reduces the overestimation in central and eastern Europe and is also a part of enhancement technique of precipitation data.

Collectively the study advances the climate indices impacts in Europe and provides methodological framework for improving the accuracy of precipitation data. By integrating detailed trend analysis, compound event assessment, high-risk exposure zones, and advance downscaling techniques, this dissertation contributes to the field of climate science especially in developing effective strategies to mitigate the climate risks in Europe.

Zusammenfassung

Da die Auswirkungen des Klimawandels auf dem gesamten europäischen Kontinent immer deutlicher werden, ist es für eine wirksame Bewertung des Klimarisikos und für Strategien zur Eindämmung des Klimawandels wichtig, die Klimaereignisse und ihre Wechselwirkungen zu verstehen und genau zu beschreiben. Klimaindizes sind ein wichtiges Instrument zur Überwachung von Veränderungen in der Häufigkeit, Intensität und Dauer von Klimaereignissen, doch sind detaillierte Bewertungen auf kontinentaler Ebene nach wie vor begrenzt. Der Schwerpunkt der Dissertation (fünf zusammenhängende Studien) liegt auf der Bereitstellung eines umfassenden Rahmens für die Analyse von Klimatrends, die Ermittlung von zusammengesetzten Risikomustern und die Verbesserung von Niederschlagsdaten in ganz Europa durch fortschrittliche statistische Verfahren und hochauflösende Datenanalyse.

In der ersten Studie werden die räumlichen und zeitlichen Trends von 74 Klimaindizes von 1950 bis 2021 mit einer hohen Auflösung von 0,1° auf einer monatlichen Skala bestimmt. Unter Verwendung des Steigungsschätzers von Mann-Kendall und Sen werden ein signifikanter Anstieg der Wachstumsgradtage und ein Rückgang der Heizgradtage sowie Veränderungen bei anderen Klimaindizes wie dem universellen thermischen Klimaindex, der relativen Luftfeuchtigkeit, dem Windchill-Index, der Globalstrahlung und der potenziellen Evapotranspiration festgestellt. Die länderspezifische Zonierung zeigt, dass Südosteuropa die höchste Anzahl an wärmeren Tagen erfährt, während Osteuropa mit weniger kalten Tagen konfrontiert ist.

Der zweite Teil konzentriert sich auf zusammengesetzte Klimaindizes, wobei 27 bivariate und 10 trivariate hoch korrelierte Klimaindexpaare von Copula-Modellen verwendet werden, um Regionen mit Risiken zu identifizieren. Die nord- und osteuropäischen Länder sind anfällig für zusammengesetzte Risiken, die Globalstrahlung, Temperatur, Evapotranspiration und bioklimatische Indizes umfassen. Die Gefährdung von landwirtschaftlichen und küstennahen Gebieten durch diese Risiken erfordert weitere integrierte Risikobewertungsansätze.

In der dritten Studie wurde ein probabilistischer Ansatz verwendet, um auf der Grundlage von 56 Klimaindizes Hochrisikozonen in ganz Europa zu ermitteln. Niederschlags- und temperaturbasierte Indizes sind wichtig für die Ermittlung von Hochrisikoregionen in Süd- und Südosteuropa, während Nord- und Westeuropa stärker von Niederschlagsindizes betroffen sind. In dieser Studie wird auch die Exposition der vorherrschenden Landnutzungsarten und der Bevölkerungsdichte gegenüber diesen Risiken verfolgt.

Um die Genauigkeit der auf Niederschlag basierenden Klimaindizes zu verbessern, befasst sich die vierte Studie mit der Herausforderung der Dämpfung von nassen Antennen in kommerziellen Mikrowellenverbindungen, die für Niederschlagsschätzungen verwendet werden. Durch die Entwicklung frequenzabhängiger Modelle, die mit Regenmesserdaten kalibriert werden, verbessert die Studie die Zuverlässigkeit der Niederschlagsintensitätsschätzungen, insbesondere für Hochfrequenzbänder.

In der abschließenden Studie wird die Technik der Bias-Korrektur für das Downscaling von Niederschlagsdaten aus CMIP6-Modellen in Europa bewertet. Die Technik des Empirical Quantile Mapping (EQM) übertrifft andere Methoden und liefert in Kombination mit Random-Forest-Modellen des maschinellen Lernens genauere regionale Niederschlagsvorhersagen, insbesondere für niedrige Niederschlagsintensitäten. Der Ansatz reduziert die Überschätzung in Mittel- und Osteuropa und ist auch Teil der Anreicherungstechnik von Niederschlagsdaten.

Insgesamt bringt die Studie die Auswirkungen von Klimaindizes in Europa voran und bietet einen methodischen Rahmen für die Verbesserung der Genauigkeit von Niederschlagsdaten. Durch die Integration einer detaillierten Trendanalyse, der Bewertung zusammengesetzter Ereignisse, von Hochrisikogebieten und fortgeschrittenen Downscaling-Techniken leistet diese Dissertation einen Beitrag zur Klimawissenschaft, insbesondere zur Entwicklung wirksamer Strategien zur Minderung des Klimarisikos in Europa.

Inclusive Author's References

Parts of the dissertation have been published in several peer-reviewed journals. It is a cumulative dissertation based on total of five (5) manuscripts: three already published and two currently under review, with the author of the dissertation listed as the first author.

Publications as first author

Doshi, S.C., Lohmann, G., Rimbu, N., Ionita, M., (2023). Spatiotemporal trend analysis of climate indices for the European continent. J. Water Clim. Chang. 14, 3112–3130. https://doi.org/10.2166/wcc.2023.183 *(Included as Chapter 3 of the doctoral thesis)*

Doshi, S.C., Lohmann, G., Ionita, M., (2023). Hotspot movement of compound events on the Europe continent. Sci. Rep. 13, 18100. https://doi.org/10.1038/s41598-023-45067-6 *(Included as Chapter 4 of the doctoral thesis)*

Doshi, S.C., Gerrit, L., and Ionita, M., (2025). Probabilistic assessment of climate indices across Europe: analysing risk exposure in population density and land use types. Geomatics, Nat. Hazards Risk 16, 2484397. https://doi.org/10.1080/19475705.2025.2484397 *(Included as Chapter 5 of the doctoral thesis)*

Publications as first author (published after thesis submission)

Doshi, S.C., De Michele, C., Cazzaniga G., Nebuloni R., (2025). A framework for minimizing the impact of wet antenna attenuation on rainfall estimates provided by commercial microwave links. IEEE Journal of Selected Topics in Applied Earth Observations and Remote Sensing. (*Large part of manuscript is based on Chapter 6).* https://doi.org/10.1109/JSTARS.2025.3632933

Doshi, S.C., Lohmann, G., Ionita, M., De Michele, C., (2025). Continental-scale bias correction and random forest downscaling of CMIP6 precipitation across Europe. Geocarto International. *(Large part of manuscript is based on Chapter 7).* https://doi.org/10.1080/10106049.2026.2657618

Publications as co-author (not included in the dissertation)

Rimbu, N., Spiegl, T., Ionita, M., Doshi, S., Lohmann, G., 2024. A synoptic scale perspective of solar forcing on extreme precipitation and floods over Europe during summer. J. Geophys. Res. Atmos. 129, e2024JD041952. https://doi.org/10.1029/2024JD041952

Conference presentation:

Doshi, S.C., Lohmann, G., Ionita, M., (2022). Assessment of Artificial Neural Network with or without Bias Correction. 12th REKLIM Workshop[1] & Machine Learning Summer School[2] (best poster award), Germany.

1. https://www.reklim.de/fileadmin/user_upload/www.reklim.de/home/Aktuelles_und_Aktivitaeten/REKLIM_Veranstaltungen/2022_Workshop_Rhoen/List_of_posters-Workshop-2022.pdf
2. https://www.tuhh.de/mle/news-archive/mle-days-2022

Doshi, S.C. (2023). Where should we move with Climate Change? (Second prize awarded), Science Slam 2022, Germany. https://www.bremerhaven.de/de/aktuelles/presse-tourismus/science-slam-superman-brachte-den-sieg.133850.html / https://www.youtube.com/watch?v=7_6xehS9jkI&t=3s (time: 01:30)

Doshi, S.C., Lohmann, G., Ionita, M., (2024). Tracing hotspot dynamics of compound events in Europe. 14th REKLIM Workshop, Germany. https://www.reklim.de/fileadmin/user_upload/www.reklim.de/home/Aktuelles_und_Aktivitaeten/REKLIM_Veranstaltungen/2024/2024_workshop/Programm_REKLIM-workshop_2024_v20240312.pdf

Doshi, S.C., Lohmann, G., Ionita, M., (2024). Tracing compounded risks by radiation and temperature on the European continent. 3rd MeteoXchange ECS conference, Germany (best poster award). https://www.emetsoc.org/events/event/3rd-meteoxchange-ecs-conference-2024/

Doshi, S.C., De Michele C., Nebuloni R., (2025). Optimizing Wet Antenna Attenuation Models for Improved Rainfall Estimation Using Commercial Microwave Links. International Conference on Opportunistic Sensing of Precipitation – OpenSense, Germany. https://www.dwd.de/SharedDocs/termine/DE/klima/250625_opensense_conference_2025.html

Co-authorship network:

[1] Doshi, S.C. – Smit Chetan Doshi
[2] Lohmann G. – Gerrit Lohmann
[3] Ionita M. – Monica Ionita
[4] Rimbu N. – Norel Rimbu
[5] De Michele C. – Carlo De Michele
[6] Nebuloni R. – Roberto Nebuloni
[7] Cazzaniga G. – Great Cazzaniga

Index

Abstract ..... **v**

Zusammenfassung ..... **vii**

Inclusive Author's References ..... **ix**

Chapter 1: Introduction **1**

1.1 General Overview 1

1.2 IPCC and assessment reports on extremes and compound events 2

1.3 Key research questions 5

1.4 Outline of the dissertation 8

Chapter 2: Scientific Background: Methods and Data **10**

2.1 Climate indices and relevance 10

2.2 Review: compound events across Europe 11

2.3 Methodological advances: Probabilities and Copulas 15

2.4 Precipitation: measurement to prediction using advanced techniques 18

2.4.1 Enhancing precipitation utilization with Commercial Microwave Links (CMLs) 19

2.4.2 Precipitation prediction using random forest: with and without bias correction 21

2.5 Previous work from our research group relevant to this dissertation 23

Chapter 3: Spatiotemporal trend analysis of climate indices for the European continent **25**

Chapter 4: Hotspot movement of compound events on the Europe continent **46**

Chapter 5: Probabilistic assessment of climate indices across Europe: analysing risk exposure in population density and land use types **66**

Chapter 6: A framework for minimizing the impact of wet antenna attenuation on rainfall estimates provided by commercial microwave links **95**

6.1 Rainfall estimation and the challenge of wet antenna attenuation (WAA) 96

6.2 Empirical framework: study area, data sources, rainfall retrieval methodology 98

6.2.1 Study area description 98

6.2.2 CML based rainfall estimation methodology 100

6.3 Review of WAA models for CML rainfall estimation 102

6.4 Data insights and strategy for assessment 108

6.5 Model performance assessment: results 111

6.5.1 Parameter calibration for WAA estimation using VFB-model 111

6.5.2 Comparison of rainfall intensity derived using various empirical WAA models 112
6.6 Implications for CML-based rainfall estimation and future directions 115
Chapter 7: Continental-scale bias correction and random forest downscaling of CMIP6 precipitation across Europe 118
7.1 Advances in bias correction and ML downscaling of precipitation in Europe 119
7.2 Information on CMIP6 models, observed data and preprocessing 122
7.2.1 Selection and characteristics of CMIP6 models 122
7.2.2 Observational reference data: E-OBS 123
7.3 Bias correction and Random Forest (RF) downscaling methodology 125
7.3.1 Bias correction methods 126
7.3.2 Random Forest (RF) model development and implementation 127
7.4 Comparative assessment of bias correction methods and ML downscaling performance: results 128
7.4.1 Comparison of bias correction (BC) methods across various CMIP6 models 128
7.4.2 Statistical analysis of Random Forest (RF) with or without bias correction (BC) method 130
7.4.3 Comparison of observed and statistical downscaling of precipitation: predicted and future scenarios 133
7.5 Key findings on continental-scale precipitation downscaling and prediction 137
Chapter 8: Conclusions 139
8.1 Summary 139
8.2 Addressing research questions 141
8.3 Outlook 144
Appendix 146
A. Supplementary materials for chapter 3 (including common figures from chapter 4 & 5) 146
B. Supplementary materials for chapter 4 184
C. Supplementary materials for chapter 5 230
D. Supplementary materials for chapter 7 234
References 237
Acknowledgments 259

Chapter 1

Introduction

1.1 General Overview

A region's climate refers to a mean weather conditions, specified by detailed long-term statistical analysis of meteorological components (WMO, 2002). It is commonly stated "weather is what you get, and climate is what you expect" (Heinlein, 1973). Climate change refers to change in area's climate, resulting from persistent anthropogenic (human activities) changes, or due to natural internal process / external forcing (Pachauri and Reisinger, 2007). Climate change is an inter-governmental global complex challenge, posing range of threats to humans and environment, with influence on multiple components including ecological (Leal Filho et al., 2021), environmental (Adger et al., 2005), socio-political (Tyfield et al., 2022), and socio-economic (Gasper et al., 2011) aspects. The latest Intergovernmental Panel on Climate Change (IPCC) reports highlights that ~3.3 - 3.6 billion people globally reside in regions highly susceptible to climate change (IPCC, 2023). Extreme weather events in recent decades across the world has witnessed increase in frequency, intensity, and duration (Clarke et al., 2022; Seneviratne et al., 2021) due to population and climate change (Dell et al., 2014; Field et al., 2012). Extreme weather and climate related events caused the European Union an estimated loss of EUR 738 billion between 1980 and 2023, with approximately EUR 162 billion occurring between 2021 and 2023 (EEA, 2024). Extreme weather and climate events, represents climate variability (Ebi et al., 2021). As climate change intensifies the frequency and severity of extreme events, building robust societies resilience become critical (Ritchie et al., 2022). Strengthening societal resilience and reducing vulnerability are important strategy for achieving the sustainable development goals (Z. Li et al., 2021).

A naturally occurring extreme event transforms into a natural hazard that has negative effect on human populations, societal systems, or environmental ecosystems (Rutgersson et al., 2021). Natural hazards may persist for extended periods or emerge as compound event, amplifying their destructive impacts for human activities to prevail. These hazards become significantly more devastating when they occur in densely populated regions (Bull-Kamanga et al., 2003). A natural hazard represents the potential or likelihood of human encountering extreme natural events, rather than the actual event occurrence (Montz et al., 2017). It becomes natural disaster only after the event has taken place and resulted in loss of life or property damage (Montz et al., 2017). Further, the unpredictable nature and devastating effects of natural disasters highlights the urgent need for advanced methods of early detection and mitigation strategies (Venkadesh et al., 2024). Before implementing mitigation strategies for natural disasters, it

is crucial to address the key question: how disaster events are changing, what type of natural disaster are likely to affect a given area, how vulnerable is the zone to different type of disasters (Ritchie et al., 2022).

1.2 IPCC and assessment reports on extremes and compound events

IPCC established in 1988, to inform policymakers about scientific assessments regarding climate change, its consequences, potential future risks, and to present adaptation and mitigation strategies (IPCC, 2025). IPCC has completed six assessment cycles and released six assessment reports, with comprehensive scientific, methodology, special, and technical reports about climate change available globally (IPCC, 2025). We will focus on the key information presented in Chapter 11: Weather and Climate Extreme Events in a Changing Climate of the IPCC report, specifically related to the extreme and compound events across Europe (Seneviratne et al., 2021).

Extreme weather and climate events – include temperature extremes, intense precipitation and floods, droughts, and storms are a key focus of the IPCC's assessment reports. Robust evidence supporting likely increase in maximum temperatures and frequency of heatwaves across Europe (Seneviratne et al., 2021). Increase in magnitude and frequency of extreme high maximum temperature recorded especially at central, southern, and northern (winter warming) Europe (Lorenz et al., 2019; Vikhamar-Schuler et al., 2016). Furthermore, extreme summer events of 2003 and 2010 in Europe were warmer leading out as some of the hottest year in the past 500 years or more (Barriopedro et al., 2011). A significant portion of warming observed in hottest days of western Europe since mid-1990s is attributed to decrease in aerosol concentrations (Dong et al., 2017). Based on observed trends, regions in Europe experience a very likely increase in intensity and frequency of hot extremes and decrease in cold extremes, with very likely human influence contributing to the observed changes (Hu et al., 2020). Southern Europe regions are projected to experience maximum increase in number of heatwave days, whereas central Europe is expected to see largest rise in heatwave temperatures (Guerreiro et al., 2018). Frequency and intensity of heavy precipitation events have likely increased in Europe since 1950s (Seneviratne et al., 2021). Between 1950 and 2018, Europe has experienced significant increase in both annual maximum daily precipitation and annual maximum consecutive 5-day precipitation (Sun et al., 2021). Evidence of increasing extreme precipitation in Europe is more frequently observed during summer and winter season, trend not consistent in other seasons (Madsen et al., 2014). Increase in precipitation extremes observed in central Europe, whereas in Netherlands total precipitation from extreme events exceeding 99th percentile is observed to double for each 1°C rise in temperature (Myhre et al., 2019; Seneviratne et al., 2021).

Future climate projections for Europe suggest amplified shifts in temperature and precipitation extremes (Seneviratne et al., 2021). These regional climate changes including various extreme events will scale quasi-linearly with changes in global warming (IPCC, 2013). Climate models indicate a rise in frequency and intensity of extremes such as warm days, warm nights, and heatwaves alongside a decline in cold extremes such as cold days and nights, across Europe (Dunn et al., 2020). Increased trend projection for western, central, eastern, and northern Europe at global warming levels of 1.5°C, 2°C, and 4°C related to the 1995-2014 historical period (Seneviratne et al., 2021). Extreme precipitation events are likely to become more frequent and intense across Europe, specifically at the global warming levels of 2°C or lower (higher confidence). Median increases in 10- and 50-year return period for annual maximum daily precipitation and annual maximum consecutive 5-day precipitation events across most of Europe at 2°C (C. Li et al., 2021). With each additional 1°C of global warming, the severe precipitation events seen today would double in frequency (Myhre et al., 2019). Increases are anticipated in both winter and summer season across Europe, although regional variations exist: southern Europe may experience decrease or no significant change, central Europe shows uncertain trends, while Alps (in winter) and northern Europe are projected to see an increase (Seneviratne et al., 2021). In a 3°C warmer world, over 80% of northern Europe's land areas are expected to experience a significant rise in extreme precipitation (Cardell et al., 2020; Donnelly et al., 2017; Madsen et al., 2014).

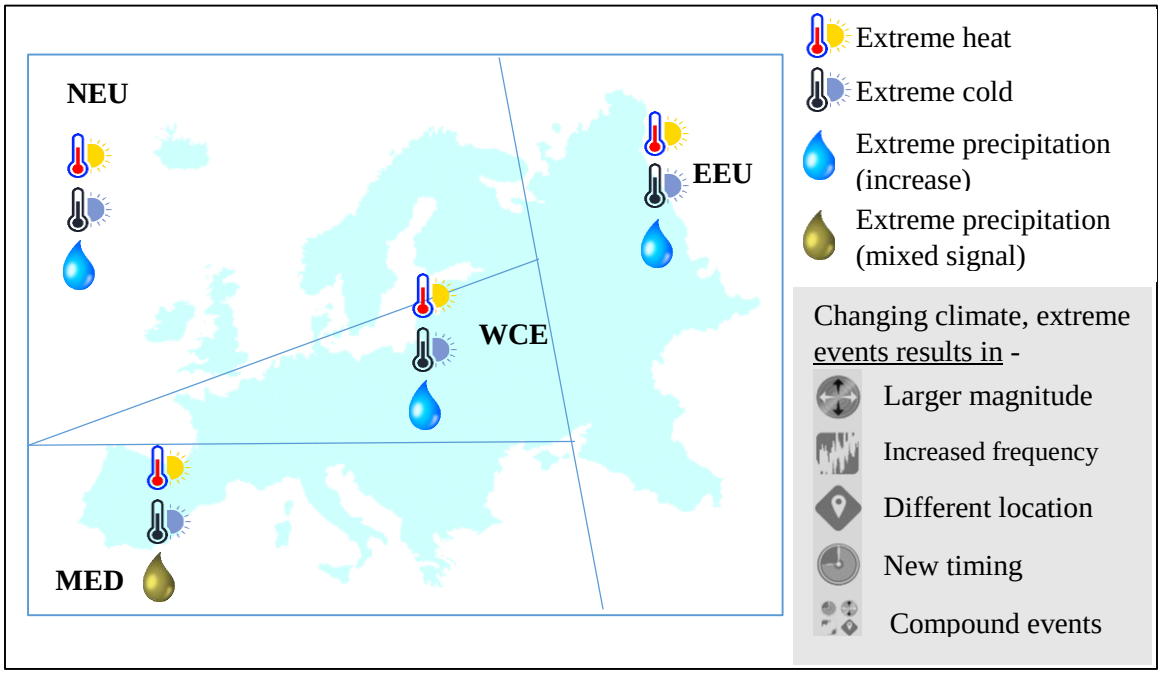

Figure 1.1: Overview of observed changes in climate extremes across Europe. NEU – northern Europe, EEU- eastern Europe, WCE – western and central Europe, MED – Mediterranean. Results in the figure are based on IPCC (Seneviratne et al., 2021).

Figure 1.1 provides the concluding overview of the observed changes in climate extremes across various zones of the Europe. Furthermore, as the climate change continues, the multiple climate extremes results in new combinations termed as compound events. Compound events are important because they can lead to greater impacts than the same extreme events occurring individually (Seneviratne et al., 2021). Probability of occurrences of compound events increases with increasing global warming levels (Vogel et al., 2020). Compound events in Europe include dry/hot conditions resulting to wildfires, storm surges resulted due to sea level rise and intense precipitation, concurrent heatwaves and drought, and multiple extreme events occurring simultaneously (Seneviratne et al., 2021). In Netherlands, a compound surge and precipitation event was recorded (van den Hurk et al., 2015). During 2018 boreal spring-summer season discussed extreme heat and intensified droughts across large regions of the mid-latitudes in northern hemisphere including Europe, resulted in severe crop loss (Kornhuber et al., 2019). In 2019, European heatwave is another such example for concurrent extreme event (Vautard et al., 2020). Compound hot and dry growing season in Germany in 2018 (Zscheischler and Fischer, 2020). Studies have also investigated compound summer temperature and precipitation extremes over central Europe (Sedlmeier et al., 2018). Simultaneous heatwaves and hot extremes are projected to increase with global warming (Seneviratne et al., 2021). The occurrences of concurrent extremes in various regions, poses a significant challenges to adaptation and risk management capacities (Seneviratne et al., 2021). To understand the risk of severe consequences from extreme events, it is essential to consider the spatial extent of the events and the possibility of compound events happening together leading to extremes (Seneviratne et al., 2021). Only few studies have examined the combination of extreme events that might occur with emerge of global warming intensification (Seneviratne et al., 2021).

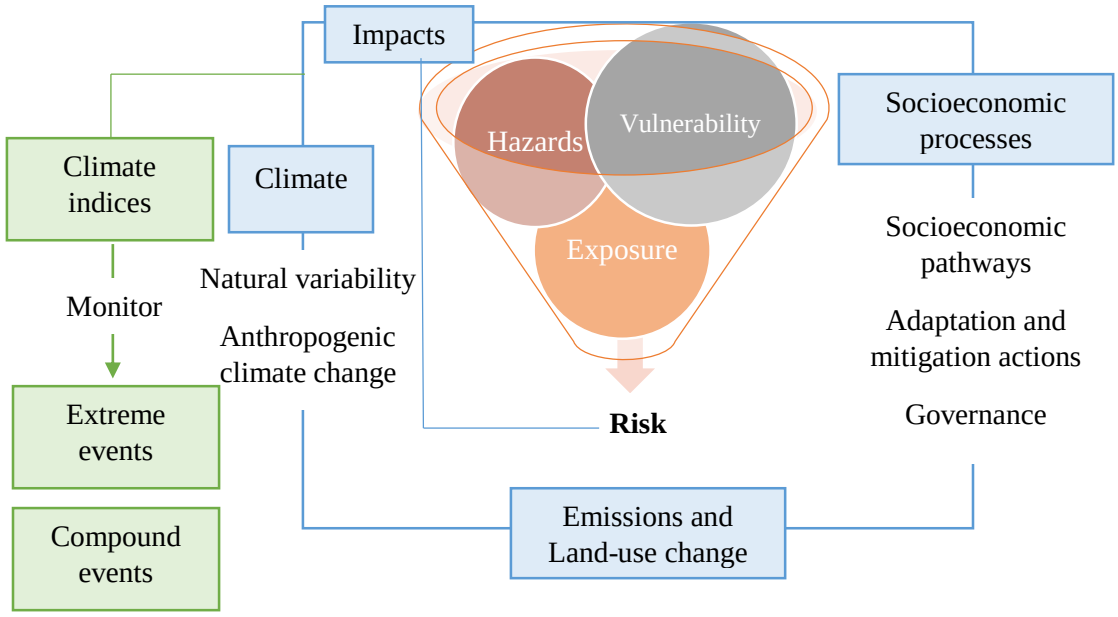

Figure 1.2: Framework for climate risk assessment. Risk figure based on IPCC (Field and Barros, 2014).

Figure 1.2 shows that estimating risk (as shown in equation 1.1), requires incorporating climate indices, and focusing on probability / joint probability associated with the hazard P(H), alongside exposure (based on population and land use data) (E), and vulnerability (V).

$$R = P(H) * E * V \tag{1.1}$$

To account for co-occurrences (compound) events in risk assessment, equation 1.1 can be modified by multiplying a co-occurrence factor, which reflects simultaneous occurrence of multiple climate indices.

1.3 Key research questions

- *"How have the spatiotemporal patterns of a wide range of climate indices evolved across Europe over the past seven decades, and what are the direction, magnitude, and statistical significance of these trends at a high spatial resolution and temporal scale?"*

  This study focuses on the European continent and conducts a comprehensive assessment of the spatiotemporal trends of 74 climate indices from 1950 to 2021 period. These climate indices computed through a wide range of climatic variables, including global radiation, precipitation, relative humidity, sea level pressure, temperature, and wind speed, which collectively provide a multifaceted view of the region's climate dynamics. Using solely observed data the analysis

conducted at a monthly timescale and a high spatial resolution of 0.1° (~11 km), allowing a detailed picture of how these climate indices have shifted across varied European landscapes. With the use of robust state-of-the-art statistical technique such as Mann-Kendall test and Sen's slope estimator, these research quantifies the direction (increasing/decreasing), magnitude (amount of change), and statistical significance of these climate indices trends. A key insight from this approach is the potential for identifying compound effects, which are interactions of multiple climate indices such as rising temperature-derived indices alongside decreasing precipitation-derived indices – which can be spatially mapped across the European continent. This method increases our understanding of the complex patterns and variability in climate indices across country-specific regions of Europe. Further, the observed trends (nature and magnitude) point to future trajectories, which plays an important role in highlighting the high-risk zones and require monitoring to address emerging climate vulnerabilities across Europe. These findings are important for policymakers and stakeholders such as agriculture, water management, and disaster reduction, for developing adaptation strategies and mitigate the impacts of the climate indices analyzed in this study.

- *"How do the spatial and temporal dynamics of compound climate events across Europe, identified through high correlated pairs of climate indices with high spatial resolution and temporal scale, reveal the hotspot movements, high-risk zones, and their impacts on land cover and population over the past seven decades?"*

  This study addresses these gaps by analyzing the hotspot movement of compound climate events across European continent from 1950 to 2021, using 74 climate indices from the ENSEMBLES daily gridded observational dataset (E-OBS) dataset. A hotspot refers to a spatial location where the occurrences of compound climate events – two or more climate related phenomena (different nature) occur concurrently or consecutively which are usually of high-risk. These hotspots identification are through advance statistical analysis of climate indices, initially identifying high correlated pairs of climate indices (such as temperature-derived indices and global radiation-derived indices), and then using copula models to develop joint probability risk maps. This method provides critical information about high-risk zones, hotspot clusters, monthly shifts in hotspot locations, and trends in joint probabilities of compound events, with a particular focus on their exposure to land cover (such as agriculture and coastal area), and population density. These findings offer significant value to stakeholders by providing a comprehensive framework for understanding the interconnected impacts of compound climate events, as analyzed through climate indices across European continent.

1.3 Key research questions

- *"How do the probabilistic assessment of climate indices derived from high-resolution E-OBS data over the past seven decades, identify high-risk zones, co-occurrences, and persistence of climate events across Europe, and what are their implications for land use and population density exposure at a monthly temporal scale?"*

  This study addresses the inadequacies by using a probabilistic approach to analyze 74 climate indices from the high-resolution E-OBS dataset during the period 1950 – 2021. Multiple variables are used to compute various climate indices at a monthly temporal scale and a spatial resolution of 0.1° (~11 km). Using 26 marginal probability distribution function and the Kolmogorov-Smirnov (K-S) test, we identify high-risk zones with probabilities exceeding 90%, along with co-occurrences (compound events), and persistence (consecutive high-probability events) of these climate indices across the European continent. This analysis will reveal distinct regional patterns; with elevated risk of specific climate indices based hazards. By integrating these findings with population density and land use maps, we may quantify the risks to compound climate events across Europe. Further, a detailed analysis of country-by-country of how specific climate indices poses high-probability risk to different land use types and population densities each month can be quantified. These insights would also enhance the stakeholder's decision through climate monitoring and planning mitigation strategies.

- *"How can the impact of wet antenna attenuation (WAA) be minimized to improve the accuracy of rainfall intensity estimates, and what are the statistical improvements when applying such an optimization framework?"*

  This study address the limitation by proposing a methodological framework to minimize the impacts of WAA on commercial microwave links (CMLs) derived rainfall estimates. With total path attenuation including precipitation-induced effects, WAA a time-variant factor affects the transmitted signal level (TSL) while being logged as the received signal level (RSL) of CML network raw data. In this study, we apply various WAA models to a dataset of TSL and RSL measurements from CML networks, and assess them against the observed rainfall data. To minimize the errors, these WAA models require optimization by calibrating the parameters. Further, the optimization needs to test for extreme precipitation events to check whether the WAA models improves the accuracy of precipitation retrievals. The derived precipitation estimates enable the integration of precipitation-derived climate indices for monitoring particularly in data-scarce regions.

- *"How does bias correction of CMIP6 data using observed data affects the predictive performance of a random forest (RF) model for precipitation climate variable, and what are the difference in assessment outcomes comparing with or without bias corrected CMIP6 data across Europe?"*

  This study investigates the efficacy of bias correction in improving CMIP6 data utility for predictive climate modeling across Europe. Considering the precipitation's high unpredictability and uncertainty, we employ E-OBS data to correct biases in CMIP6 data output, with a focus on this climate variable. We compute and assess predictions from both bias corrected and uncorrected CMIP6 data using a RF model, a robust machine learning (ML) algorithm. RF model training is with hyperparameters optimized using Bayesian optimization technique. The model is trained with historical CMIP6 data (with and without bias correction) and then compare its prediction performance to E-OBS observation as a raw data. Further, we examine future scenarios across using CMIP6 projections under various shared socioeconomic pathway (SSP), to check how bias correction improves prediction accuracy across shifting climate conditions. Assessments are based on statistical indicators, with the aim to quantify the bias correction impacts on prediction accuracy and regional climate assessments. This work refines understanding of bias correction models in ML based climate modeling, providing insights into enhancing projections across European continent.

1.4 Outline of the dissertation

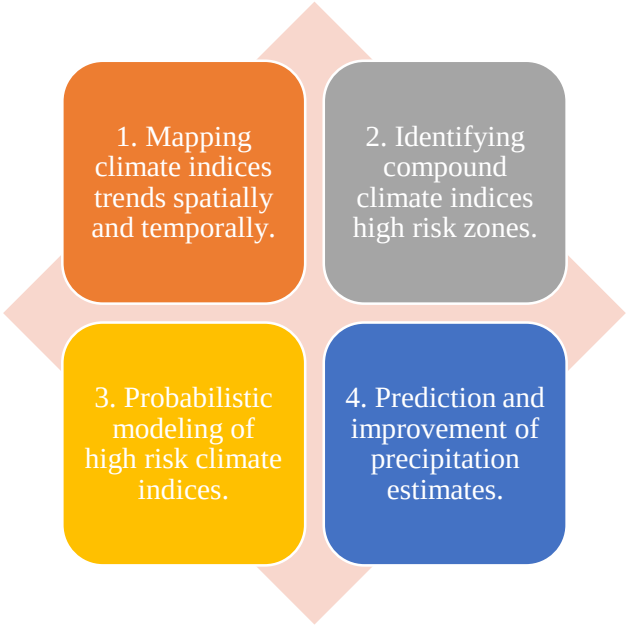

Figure 1.3: Research objectives addressed within the dissertation.

Several chapters of this dissertation have been published in peer-reviewed publications, as detailed on page ix. Chapters based on these publications include description of author's contribution to those works.

The structure of the dissertation is as follows: Chapter 1 introduces an overview of the study and review of IPCC assessment report related to extreme events and compound events. Chapter 2 discusses about the literature review on climate indices, compound events, methodologies for modeling compound events, and techniques to enhance precipitation estimates, which forms the base for the studies in subsequent chapters. Chapter 3 presents the spatiotemporal trend analysis of 74 climate indices across Europe from 1950 to 2021 at a monthly scale, based on Doshi et al., 2023b, mapping the nature, magnitude, and significance using E-OBS data. Chapter 4 investigates the movement and risks of compound climate event hotspots across Europe, based on Doshi et al. 2023a, identifying the high-risk zones and their exposure to population and land cover types using copula models. Chapter 5 is the probabilistic assessment of varied climate indices to derive high-risk zones across Europe, based on Doshi et al. 2025, analyzing their co-occurrences, persistence, and risk exposure to population density and land use types using probability distribution functions. Chapter 6 and 7 shifts the emphasis from compound event using climate indices to advancements in precipitation component. Chapter 6 specifically focuses on precipitation estimation using CMLs, with a particular concentration on WAA models to enhance the accuracy of precipitation data. Chapter 7 focuses on precipitation prediction using RF technique, comparing outcomes with and without bias correction applied to CMIP6 historical data. Finally, Chapter 8 summarizes the findings of the thesis and presents future directions of the research in an outlook.

Chapter 2

Scientific Background: Methods and Data

2.1 Climate indices and relevance

There is an increasing need for weather and climate extremes information services as a result the focus of this doctoral research is primarily on utilizing the climate indices for multi-decadal assessment of compound events across European continent. Climate indices are monitoring tools for climate change (especially climate shifts) as they provide important information about the frequency, intensity, and duration of extreme weather events over time and space (Peña-Angulo et al., 2020; Williams and Eggleston, 2017). Even though climate observations typically translate into quantitative variables with physical meaning, the effects on different sector such as environment, society, and economy depends on particular climatic event characteristics (Crockett and Westerling, 2018; Van Dijk et al., 2013). Climate indices are quantitative indicators of climate extremes that are statistically consistent (Chervenkov and Slavov, 2021). An assessment of climate variability and change processes under present and future climate change scenarios can also be obtained with the use of these indices (Sillmann et al., 2013; Zhou et al., 2014). Depending on the measurable climatic data and its combination, a range of different climate indices analysis can assist researchers and policymakers in assessing climate change impacts and developing adaptation strategies (Deen et al., 2021). For example, a combination of weather variables can affect some industries. For instance, in human health monitoring, a bioclimatic index utilizes combination of air temperature, relative humidity, wind and solar radiation (Di Napoli et al., 2018). Understanding the complex impacts of climate change on different regions and sectors requires the integration of high-resolution climate data and indices, especially in Europe where regional patterns of climate variability and extremes are distinct (Domínguez-Castro et al., 2020). Climate extremes and societal impacts do not always correlate directly; some rare climatic events have minimal societal effects, while events that are more frequent can cause significant disruptions (Persson et al., 2007). Climate extremes characteristics vary both spatial and temporal scale: short-duration events have localized impacts and persistent nature covers broader geographical areas (Persson et al., 2007). Cumulative impact of persistent climate events can be more significant than individual daily climate extremes. To understand the complex climate systems numerous specialized climate indices have been developed from the raw climate variables (Easterling et al., 2000; Peña-Angulo et al., 2020). The Expert Team on Climate Change Detection and Indices (ETCCDI) has developed a set of core extreme climate indices, endorsed jointly by commission for climatology of the World Meteorological Organization

(WMO), Joint Commission for Oceanography and Marine Meteorology (JCOMM), and by the Climate Variability and Predictability (CLIVAR) project (Tank et al., 2009). ETCCDI has developed core set of 27 climate indices focused on temperature and precipitation extremes (Tank et al., 2009). Understanding the resilience threshold of society and environment to various climate extremes is crucial for effective risk assessment and adaptation planning.

Examples of different climate indices that can help understand the climate extremes include:

- Extreme value indices – maximum and minimum of the weather variable.
- Threshold exceedance indices – number/count of days exceeding X value or percentile.
- Duration indices – longest period of consecutive days exceeding a specific high/low value.
- Timing indices – earliest date of occurrence of minimum/maximum weather variable, which is above/below in specific season.

Over past two to three decades, there has been growing interest in defining and analyzing trends in meteorology (Güçlü, 2020). There are two approaches to identify the significant trends in climatologic time series: parametric and non-parametric (Gocic and Trajkovic, 2013). Non-parametric trend tests need data be independent, whereas parametric trend tests require data to be independent and normally distributed (Gocic and Trajkovic, 2013). Mann-Kendall (MK) test (Kendall, 1975; Mann, 1945) and Sen's Slope (Sen, 1968) estimator are one of the prominent approach for trend identification in climate data. These techniques can quantify nature and magnitude of trends. Hence, in this study, these two non-parametric methods were employed to detect the trends in climate indices. Extensive trend analysis research has been conducted on climate indices to better understand the impact of extreme weather occurrences (Razavi et al., 2016).

2.2 Review: compound events across Europe

Even if the extreme events are important, we still need to improve our overview and understand in-depth what happens when two or more of the extreme events occurs concurrently or consecutively, creating what is known as a compound extreme event (Zscheischler et al., 2018). The term "compound event", referring to the combination of multiple processes, was first introduced in the IPCC special reports on climate extremes (Seneviratne et al., 2012). The compound events can be defined as: i) two or more extreme events occurring simultaneously or in succession, ii) combination of extreme events with underlying conditions that intensify their impacts, or iii) a combination of non-extreme events that, when combined resulted in extreme event (Seneviratne et al., 2012). Compound events would increase the impacts and cause major extreme consequences that might not necessarily be extreme occurrences independently (AghaKouchak et al., 2020). Understanding the interaction of climate variability,

densely populated areas, and complex topography features in Europe highlights the importance of understanding of compound events. Figure 2.1 illustrates the framework for assessing compound events related risk across Europe using climate indices.

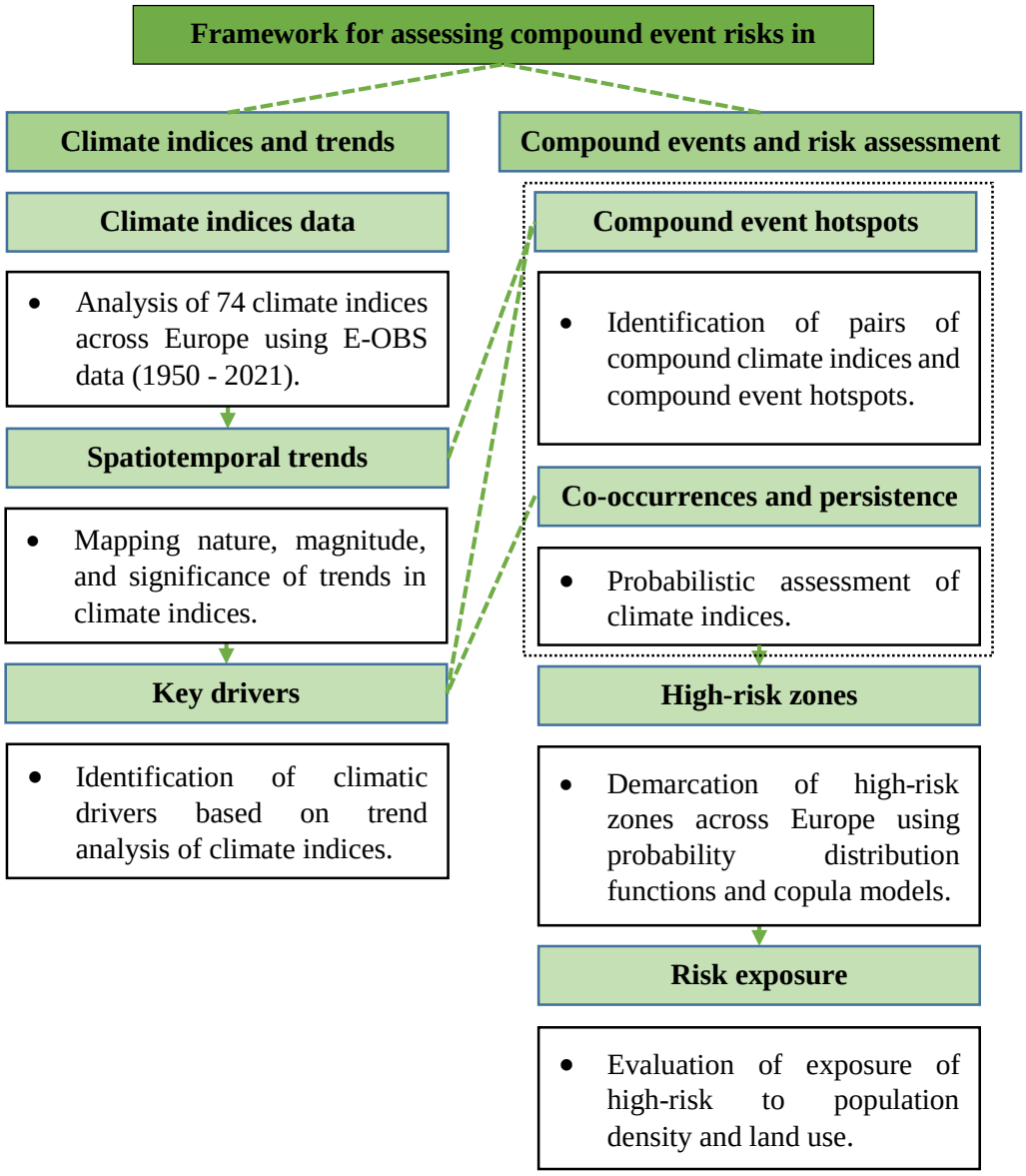

Figure 2.1: Framework for assessing climate indices based compound event risks in Europe.

One example of compound event is a compound drought and heatwave (CDHW) which has received growing attention due to impacts on agriculture, water resources, ecosystem, and energy, with central Europe showing the greatest increase in frequency through the late 21st century (Tripathy et al., 2023). Shifts in hot and dry extremes in central Europe has linkage to atmospheric circulation anomalies and

land-atmosphere interactions (such as soil water deficiency) (Tian et al., 2024). Between 1979 and 2020, impacts of temperature on dry soil increased by 67%, while atmospheric drivers effect on soil moisture increased by 50% during compound hot-dry extremes (Tian et al., 2024). Projection showcases that southern hemisphere experiences a greater increase in CDHW occurrence, while northern hemisphere sees a greater rise in CDHW severity, with regional warming playing a significant role (Tripathy et al., 2023). Treating such extremes as independent events may lead to underestimation of the probability of their co-occurrence (Zscheischler and Seneviratne, 2017). CDHW events include 2003 European and 2010 Russian heat waves in accompanied by droughts (Miralles et al., 2014), causing significant societal and ecological loss – 55,000 deaths, a 25% drop in annual crop production, and > 1 million hectares of burned areas in Russia. Another record-breaking CDHW event was year 2018 in Germany, where the return period assessed emphasize the significant large uncertainties in such estimates due to event's extreme nature (Zscheischler and Fischer, 2020). In 2022, CDHW event hits the areas of Iberian Peninsula, France, and Italy, with temperatures exceeds > 2.5°C above average and persistence of severe drought lasting from May to August (Tripathy and Mishra, 2023). Severity of droughts were contribution of reduction in soil moisture due to precipitation deficits and high temperatures (Tripathy and Mishra, 2023). In southern and eastern Europe, tree mortality was found to be linked to CDHWs, worsened by increasing summer temperature and vapor pressure deficit (Gazol and Camarero, 2022). A study in Mediterranean basin examined compound warm spells and droughts, identifying two types of events – warm season compound events (May to October) and year round compound events, which led to conclusion that the rise in number of compound events is due to change in temperature rather than lack of precipitation (Vogel et al., 2021). Several studies examines the frequency and spatial extent of CDHW extremes and have highlighted their growing risk under global warming (Mazdiyasni and AghaKouchak, 2015; Sharma and Mujumdar, 2017). A study found that average precipitation trends could affect future CDHWs, strong local warming increases the chances of droughts alongside extreme heat, making CDHWs intensified (Bevacqua et al., 2022).

Another category of compound events is compound floods (CF), which is flooding due to combination of precipitation with storm surges, high river discharge, or saturated soils. In the study focused on CF events due to extreme river discharge and storm surges in northern and central Europe, found that rivers along Europe's west-facing coasts experienced a higher frequency of CF events driven by cyclonic westerly general weather pattern (Heinrich et al., 2023). The likelihood of CF, resulting from simultaneous occurrences of elevated sea levels, and heavy precipitation is projected to significantly increase (40% – 80%) by 21st Century, particularly in northern Europe. Areas under exposure are west coast of United Kingdom, northern France, east and south shores of North Sea, and coastlines of eastern portion of Black Sea (Bevacqua et al., 2019; van de Wal et al., 2023). A study on the Rhine delta

(Netherlands) found that the likelihood of extreme storm surge conditions after prolonged heavy precipitation is ~3 times higher than assumption of independent events, potentially leading to catastrophic events in low-lying areas (Kew et al., 2013). The devastating flood in July 2021 across western Germany, along with parts of Netherlands, Belgium, and Luxembourg, resulted in significant loss of life and economic damages, which were due to heavy precipitation combined with elevated soil moisture levels hindering infiltration (Roggenkamp and Herget, 2024). In urban areas with impervious surfaces reduced water absorption increases runoff both its speed and volume, which further increases the risk of floods and the probability of CF events (Kaur et al., 2019). Climate change and urbanization significantly contributes to future CF risk due to precipitation changes and sea level rise (Pariartha et al., 2023).

Rain-on-snow (ROS) events, where precipitation and snow coincides, occurs in winter (summer) months at lower (higher) elevations, as observed in a study focused on Switzerland (Morán-Tejeda et al., 2016). In Europe, many floods have triggered by snowmelt and the combination of heavy precipitation with high saturated soil (Berghuijs et al., 2019). A warmer climate could make ROS events more frequent (Guthrie et al., 2010), a factor which is important in hydrological slope-stability assessments that can prevent landslides (Gariano and Guzzetti, 2016). ROS events effect include floods and landslides, with rainfall freezing within the snowpack or on bare ground, impacting permafrost, vegetation, and wildlife (Pall et al., 2019). Future shifts from snowfall to rain may alter ROS events, affecting runoff patterns (3 – 32%) (Hotovy et al., 2023). Central European 40 mountain catchments showcases spatial and temporal variations in ROS trends, with increase at higher elevations and decreases at lower elevations in spring (Hotovy et al., 2023). A study examines two Swiss Alps catchments, and the projection show a 4°C temperature rise (RCP8.5), shifting snowfall to rainfall, reducing snowmelt by 50%, and increasing evapotranspiration by 10% (Moraga et al., 2021). Due to this streamflow is expected to rise (drop) by 40% (20-40%) in winter (summer), outcome will be increased winter floods (Moraga et al., 2021). In Greece, monitoring wet-cold (WC) compound events from November to April reveals a projected decline in their likelihood under the RCP8.5 scenario, especially in high-latitude areas (Markantonis et al., 2022). Another significant type of compound event that can have severe impacts involves extreme precipitation and strong winds (Martius et al., 2016). A systematic statistical analysis reveals that the location of European extremes (wet and windy) depends on the North American region affected by cold air outbreaks (CAOs) (Leeding et al., 2023). CAOs over eastern and central USA co-occur with frequent wind extremes in Iberia, while CAOs in eastern Canada followed by wind extremes in northern Europe and British Isles (Leeding et al., 2023). Further, precipitation extremes often occur before the CAOs peak (Leeding et al., 2023). Extreme precipitations and wind events often co-occur in coastal and tropical cyclone prone regions (Martius et al., 2016).

There is a strong regional variation globally, influenced by weather-topography interactions and cyclone tracks, highlighting their significance for risk assessment and insurance (Martius et al., 2016). The dependence between precipitation and wind extremes in Europe reveals that 70% of these co-occurrence occurs within 1,110 km of cyclone (Owen et al., 2021).

The occurrences of compound events across Europe varies due to geographic and climatic variability. Overall, compound event-related risks in Europe include heatwave-wildfire occurrences in southern region (Fink et al., 2004; Leone et al., 2023), CF events along west and north facing coasts (Bevacqua et al., 2019; Heinrich et al., 2023), compound hoy-dry conditions in southern and eastern areas (Gazol and Camarero, 2022), and compound temperature-precipitation extremes over central Europe during summer (Sedlmeier et al., 2018). These compound event pairs indicate the multidimensional nature of climate risk in Europe. Most studies in literature review focus on univariate or multivariate events, but the set of compound events is much broader with various co-occurrences. Compound events are highly complex, involving multiple interaction processes across different temporal and spatial scales, making probabilistic methods challenging to apply (Zscheischler et al., 2022). The impacts of compound events results from interactions between physical drivers (e.g. temperature, precipitation, wind) and preconditioned factors (e.g. soil moisture), often amplified by different land cover types. This regional variability and complexity emphasize the need for reliable, robust, and tailored research framework strategies to access the impacts of compound events. We provide new insights into various climate indices to analyze the spatial and temporal characteristics of compound events and their impacts on different land-cover types and population density. Extending our understanding of compound events can enhance the forecasting accuracy, mitigate future damages, and play a critical role in advancing climate resilience across the European continent.

2.3 Methodological advances: Probabilities and Copulas

This dissertation advances with the analysis of compound events across Europe by developing methodological framework using probabilistic techniques and copula-based modeling. The probabilistic technique involves modeling a probabilistic fit based on distributions that follows either parametric or non-parametric approaches. A total of 27 different probability distribution functions were used to fit the climate indices including Beta, Binomial, Birnbaum-Saunders, Burr, Exponential, Extreme Value, Gamma, Generalized Extreme Value, Generalized Pareto, Half-Normal, Inverse Gaussian, Kernel (normal, box, triangle, Epanechnikov), Logistic, Log-Logistic, Log-Normal, Nakagami, Negative Binomial, Normal, Poisson, Rayleigh, Rician, Stable, T–Location Scale, and Weibull (Bowman and Azzalini, 1997; Johnson et al., 1995). The marginal distribution for each variable initially modeled by identifying the best-fit probability distribution function at each grid across all

climate indices. From this, two key insights can be derived: first, towards the development of copula independent of marginal distributions (Miao et al., 2016) and second the identification of pairs of persistent and co-occurring climatic events (Pradhan et al., 2022). A climatic event can occur at same location in consecutive years, which can be referred as persistence (Beniston and Goyette, 2007).

Copulas are commonly utilized to compute the joint probability of climatic indices, serving as a key factor in evaluating compound events. A copula is a multivariate distribution that standardizes the marginal distribution to a uniform range between 0 and 1, to derive the joint distribution (figure 2.2) for multiple variables which is independent of their original marginal distributions (Hao and AghaKouchak, 2013; Leonard et al., 2008). Copulas are classified into several families, example Clayton, Gumbel, Frank (Archimedean copulas), and Gaussian, Student's t (elliptical copula) are the most commonly used (Miao et al., 2016).

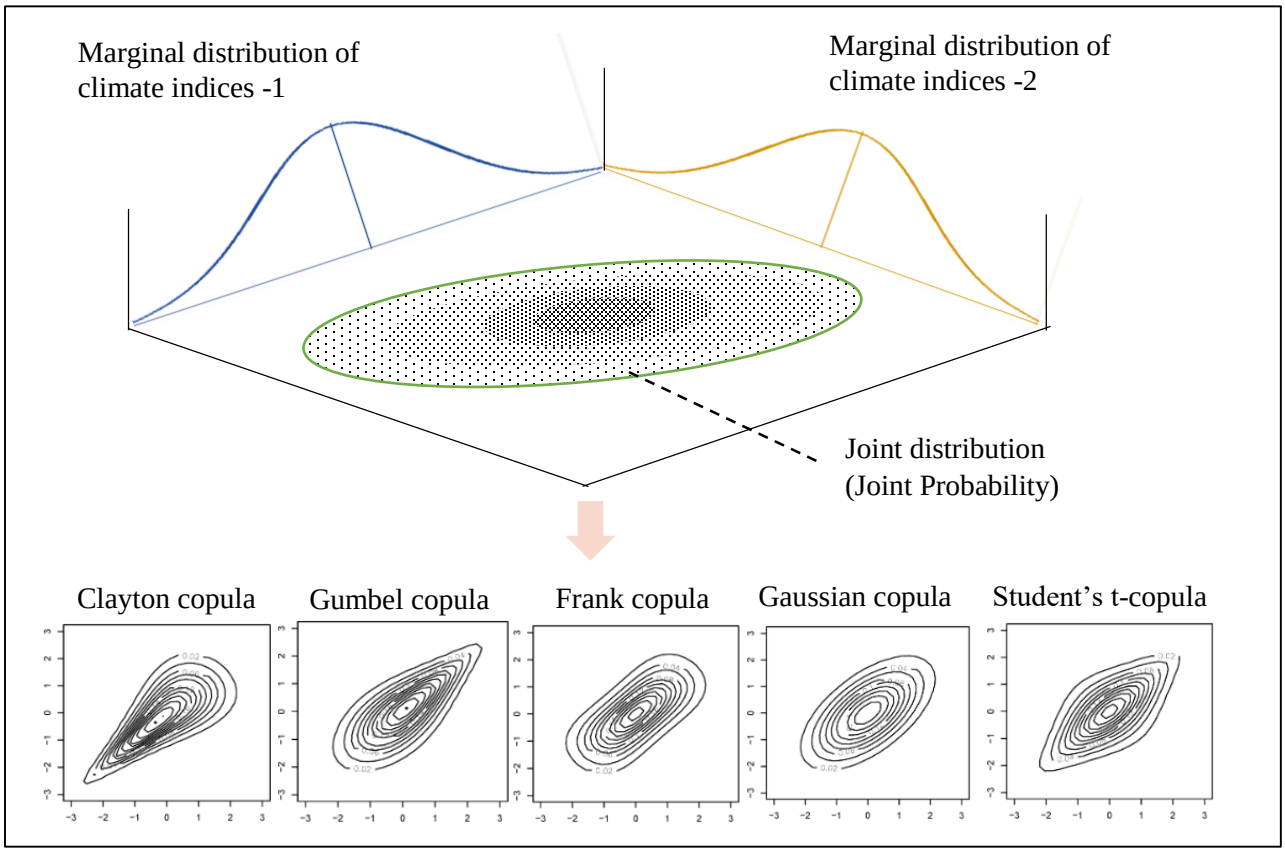

Figure 2.2: Joint distribution of Climate Indices using Copula Models. Bivariate copula densities visualized through contour plots for various copula models (Stenšin and Bloznelis, 2022).

An n-dimensional copula (C) is the joint probability of univariate marginal distribution Z1, Z2,…,Z_n as follows:

$$H(x_1, x_2, \dots, x_n) = C[Z_1(x_1), Z_2(x_2), \dots, Z_n(x_n)] = C(r_1, r_2, \dots, r_n) \quad (2.1)$$

where $r_1,r_2,\dots,r_n$ is the cumulative distribution functions of $x_1,x_2,\dots,x_n$ (Joe, 2014). While applying a copula, certain checkpoints need to be considered in order to avoid misconceptions. The steps involved in the analysis of two variables are: pre-processing of data, copula selection and parameter estimation, and selection of copula method based on goodness–of–fit (Tootoonchi et al., 2022). A recent study by (Tootoonchi et al., 2022) conducted a literature review on the use of copulas for hydroclimatic analysis. After reviewing many articles, the author found that only a few incorporated all these steps, which affects the accuracy of fitted copulas and consequently the assessment of compound event impacts. These research gaps, pertaining to the application of copulas for compound events were further explored in subsequent studies. A study conducted in the Loess Plateau region (Miao et al., 2016) analyzed changes in temperature and precipitation using various extreme climate indices. Based on copula theory, the study utilized a joint probabilistic approach, with results analyzed on a yearly timescale and a 0.5° x 0.5° grid. The climate indices were aligned with those by the ETCCDI. During, the analysis, multiple copulas were evaluated and one was ultimately selected as the most suitable for the entire study area. The characterization of extreme events was limited to precipitation and temperature as climatic weather variables. Additionally, when computing the copula, the joint probability was assessed without a statistical analysis of the strength of relationships among the climate indices. This approach way lead to underestimating or overestimating the copula fit for gridded data, particularly if the fit varies adjacent grids capturing extreme / compound extreme events. This represents a significant gap, compounded by the lack of physical understanding or a relationship matrix for the selected compound event pairs. Another study (Ridder et al., 2020), explored hotspots of compound events through spatial estimates on a global scales. In this study, the focus was on a multivariable approach, specifically targeting compound events driven by precipitation and temperature. This emphasis reveals a notable gap, as these drivers are not the sole contributors to the compound events. Additionally, challenges such as sparse data coverage and the need for high-resolution outcomes were evident for robust and reliable findings was discussed in the results and discussion section (Ridder et al., 2020).

Table 2.1 outlines the methodological advancements in using probabilities and copulas to assess compound events across Europe, addressing specific research gaps identified based on prior studies. These gaps include coarse data resolution, limited climate indices, broad temporal scales, inadequate copula and probability distribution fits. The table 2.1 below details how the study bridges these research gaps, enhancing understanding and application of compound events.

Table 2.1: Comparison of previous and advanced methodologies for analyzing compound climate events in Europe.

Aspect	Previous Methodology	Advanced Methodology
Data Resolution	Coarse resolution limiting the ability to capture regional variability.	High spatial resolution available from E-OBS data, enabling detailed mapping of regional variability.
Climate Indices	Focused on climate indices derived typically from precipitation and temperature, overlooking other factors like bioclimatic indices.	Incorporates 74 climate indices, including drought, radiation, and bioclimatic indices, providing integrative view.
Temporal Scale	Analyzed compound events on broad timescales, often yearly.	Conduct analysis on monthly temporal scale across 7 decades, capturing monthly shifts and trends over time.
Relationship Analysis	Computed joint probabilities without assessing the strength of relationships between climate indices.	Performs detailed correlation analysis to identify high correlated and statistically significant pairs of compound events.
Probability Distributions	Modeled for limited set of probability distribution functions.	Fits with 27 different probability distribution functions.
Copula Application	Relied on single probability/copula fits applied uniformly across region, without grid-specific optimization.	Optimized grid-by-grid probability/copula based modeling using weighted statistical indicators as goodness-of-fit.
Physical Context	Provided limited integration with physical or societal impacts, missing links to exposure or risk.	Links compound event to different land cover and population exposure.
Outcome Application	Identifying compound events that have no physical meaning, with missing detailed risk exposure and dynamics.	Provided detailed risk exposure maps, high-probability zone identification, monthly shifts including persistence, and trends.

2.4 Precipitation: measurement to prediction using advanced techniques

One of the main components of the energy and water cycle influencing the Earth's climate system is precipitation (Kidd et al., 2017). Precipitation is an important aspect of research not just in atmospheric science but also in hydrology, oceanography, cryosphere studies, environmental science, ecology, and

biology (Kidd et al., 2017). (Stephens et al., 2010) demonstrated that climate models do not accurately represent precipitation. Determining the current state of distribution and intensity of precipitation that influences our climate and monitoring changes in it depends on its measurement (Kidd et al., 2017). Precipitation makes it one of the most difficult geophysical indicators to measure and monitor due to its spatial and temporal variability (Roversi et al., 2020). Precipitation measurements primarily rely on rain gauges, weather radars, and satellites (Zhang et al., 2023). Rain gauges give direct surface precipitation data but have low spatial resolution and are impacted by wind and splash effects, causing measurement uncertainties (Nešpor and Sevruk, 1999). Weather radars allows for large-scale quantitative precipitation estimation (QPE), but accuracy is limited by the sensitivity of the Z-R (reflectivity (Z) and rain rate (R)) relationship to raindrop size distribution, precipitation type, and climatic conditions (Ulbrich and Lee, 1999). Satellites provide near-global precipitation measurements, important for areas where radar and rain gauge are missing; however, their low spatial and temporal resolution makes them unsuitable for small-scale monitoring, and their precipitation estimation algorithms require further accuracy improvements (Hou et al., 2014; Stephens et al., 2022). The average precipitation observed over Europe has been stable since 1960, according to E-OBS dataset (Osso et al., 2023). However, at the subcontinental scale, winter precipitation has decreased in southern Europe while increasing by up to 70 mm/decade in northern Europe (Maraun, 2013a). During summer, precipitation has decreased in southern Europe while increasing in northern Europe (Van den Besselaar et al., 2013).

2.4.1 Enhancing precipitation utilization with Commercial Microwave Links (CMLs)

A viable alternative option for ground based precipitation estimation is Commercial Microwave Links (CMLs), which make use of signal attenuation data from telecommunication networks (Messer et al., 2006). CMLs provide a cost-effective solution to enhance the precipitation monitoring based on the extensive CMLs networks established and maintained by mobile network operators as opportunistic sensors (Fencl et al., 2015). CMLs in addition of observations in locations without rain sensors improves the spatial and temporal resolution and accuracy of precipitation products (De Vos et al., 2020; Gosset et al., 2016). In areas with few or no ground-based observation tools, CMLs can be used in integration to weather radar and rain gauge networks. The principle behind precipitation retrieval is the relation between microwave single attenuation and rainfall intensity. Rainfall along a CMLs path attenuates the transmitted signal, and through power-law relationships, the degree of attenuation varies with the rate of rainfall (Atlas and Ulbrich, 1977; Olsen et al., 1978). Figure 2.3 represents the CMLs and the behavior of signal attenuation during precipitation. Rainfall estimation from signal attenuation data of CMLs, however presents a set of challenges. The primary challenge include signal drop in

CMLs data during dry spells and errors from antenna wetness during rain, which can lead to an overestimation of precipitation (Leijnse et al., 2008; Messer and Sendik, 2015; Overeem et al., 2016).

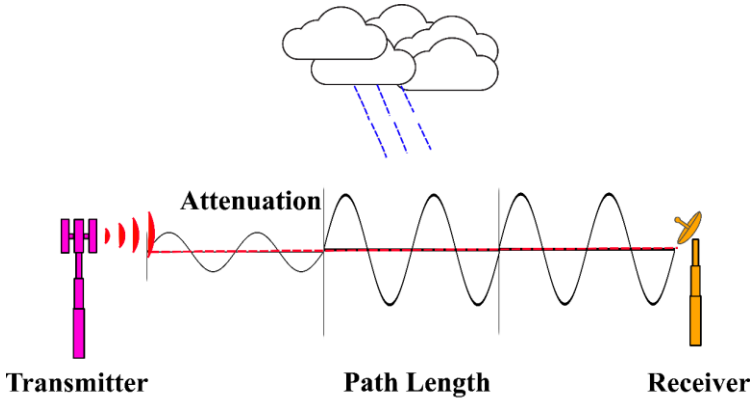

Figure 2.3: Schematic view of CMLs during precipitation.

In order to solve this challenge associated to wetness of antenna for precipitation estimation, the doctoral dissertation advances to develop a framework for calibrating wet antenna attenuation (WAA) models utilizing ground truth data from rain gauge. Empirical equations derived from field tests and long-term observation studies are approaches for WAA estimation. There is a significant gap of no unified approach for WAA estimations, as WAA models do not take into account wetting dynamics, antenna characteristics, or environmental conditions like wind, temperature, humidity, and solar radiation (Schleiss et al., 2013; Valtr et al., 2019). Some WAA models assume constant WAA level through rain period (Overeem et al., 2013); others adopt a dynamic approach, as an exponential increase and decrease to a constant level during rainfall (Schleiss et al., 2013). Certain models are dependent on measured attenuation (Kharadly and Ross, 2001), while others impose maximum threshold limits (Kharadly and Ross, 2001; Schleiss et al., 2013). Additionally, some models compute WAA directly using parameters and precipitation data without applying such limits (Valtr et al., 2019). Despite these variations, a common conjecture among all the WAA models in the possibility of universal application requires optimization as they were derived based on defined frequency ranges. We have identified the following research gaps based on the processes outlined in the previous studies (Moroder et al., 2019; Pastorek et al., 2021) that we examined in this study.

I) Parameter determination for empirical WAA models:
   a) Parameters derived from literature review may not be reliably applied to different regional studies, leading to inaccuracies.

b) Rainfall intensity comparison rely on "good" CML links (those without erratic behavior), but this approach becomes questionable when rain gauges are located far from CMLs.

c) Optimization methods require an initial guess to solve equations with multiple parameters as unknowns, which can significantly influence convergence and accuracy. Even when literature derived values are used as initial estimate, WAA model parameters are forced to converge based on system biases rather than actual WAA effects.

II) Lack of comprehensive assessment and analysis:

a) There is no integrated evaluation considering rain gauge distance, CMLs link length, and rainfall intensity peaks as key optimization factors or statistical indicators for comparing different WAA models and improving precipitation estimation.

These advancements show how CMLs can offer high-resolution precipitation estimates, particularly in areas that are high-probability risk zones or experiences extreme weather events. In the future, compound event assessments for climate indices based on precipitation estimates from CMLs, integrated with other precipitation data sources, could be computed and utilized.

2.4.2 Precipitation prediction using random forest: with and without bias correction

To understand the global environmental system, extensive long-term precipitation dataset is necessary (Sheffield et al., 2006). Climate patterns and weather extremes, such as periods of heavy rainfall, are simulated using global climate models (GCMs) (Ridder et al., 2021). A variety of emission scenarios are used by GCMs to model future climate conditions (Abdelmoaty et al., 2025). Due to restrictions in parametrization and mathematical computations based on thermodynamic and physical laws used in development, GCMs by nature produces biased output (Kesavavarthini et al., 2023). Coupled Model Intercomparison Project Phase 6 (CMIP6), provides largest set of simulations with the highest spatial resolution, in comparison to previous phases CMIP5 (Bourdeau-Goulet and Hassanzadeh, 2021; Eyring et al., 2016). GCMs have coarse resolutions for local applications and exhibits biases at regional scales (Li et al., 2019). Regional Climate Models (RCMs), which are finer resolution, are employed more and more to overcome this scale gap, however they show significant errors, passes down from the GCMs (Hall, 2014; Rummukainen, 2010). GCM precipitation projection includes significant biases, which reduce their reliability and effectiveness in climate adaptation and mitigation strategies (Li et al., 2020; Tian and Dong, 2020). Statistical bias correction has become an important method for improving climate model outputs (Huang et al., 2024). Therefore, a part of doctoral dissertation focuses on downscaling and bias correction techniques, which are necessary for analyzing compound events studies at regional scales when utilizing CMIP6 data. This study models various bias correction

techniques to adjust key distribution characteristics of precipitation through mean, variance and quantiles approach.

Overall, CMIP6 models have minimal agreement on precipitation trends, with some models indicating a contrasting regional pattern (Osso et al., 2023). A study found that, in most regions CMIP6 model errors in asymmetry are associated with biases in skewness of regional precipitation variability (Sengupta et al., 2025). To better, depict the asymmetry in teleconnections with El Niño-Southern Oscillation (ENSO), improvements needed in the simulation of heavy-tailed precipitation distribution, intensity and location of precipitation (Sengupta et al., 2025). Several research have evaluated and compared various bias correction approaches for improving CMIP6 (GCMs) precipitation estimates (Salman et al., 2022; Shiru and Park, 2020; Wada et al., 2023). Research shows that for GCMs performance of distribution-based (such as quantile mapping) bias correction outperforms in comparison to only mean or variance based bias correction for precipitation dataset (Bennett et al., 2011; Chen et al., 2013a). Other approaches from sophisticated distribution mapping include simple scaling and delta method (Teutschbein and Seibert, 2012). However, the performance varies depending on the time of year, location, and section of distribution considered, it is impossible to identify a single best performing bias correction technique (Räty et al., 2014). Bias correction significantly enhances the spatial correlation of model and observed seasonal and annual precipitation (Bennett et al., 2011). However, the effectiveness of bias correction technique varies when projecting climate change scenarios and assessing climate change impacts (Teutschbein and Seibert, 2012). Furthermore, it is well known that any bias correction technique can introduce additional uncertainty (Chen et al., 2011). Most bias correction methods do not account for circulation biases or uncertainty in internal variability but can correct biases associated with parameterization and model resolution (Maraun and Widmann, 2015).

In recent years, several studies have used machine learning (ML) methods to integrate CMIP data for predicting precipitation (Dey et al., 2022; Wang et al., 2018). ML provides an advantage for extracting information from climate system through pattern recognition and feature extraction approach (Tanimu et al., 2024). As a result, ML-based bias correction has received a considerable attention in recent years (Cho et al., 2020; Kim et al., 2021; Ling et al., 2022). Overfitting during training can cause inaccurate estimation of precipitation while using ML algorithms (Seo and Ahn, 2023). Thus, the improvement of bias correction using ML algorithms is not assured. Random forest (RF) is an advancement in ML that has found significant application in variety of prediction applications, including weather and climate forecasting (Tong et al., 2019). RF is a ML algorithm that combines output of many decision trees to extend the prediction (Shiru et al., 2019). RF algorithm uses both bagging and feature randomization

to develop an uncorrelated forest of decision trees (Breiman, 2001). Yang et al. 2022 evaluated the performance of RF algorithm for multi-model precipitation data and revealed that the RF had produces the smallest error in comparison to decision tree and adaptive boosting algorithm. Recent study highlighted the research gap that the application of ML methods for multi-model integration faces various challenges, including limited number of GCMs and lack of integrated bias correction techniques (T. Liu et al., 2024). A comparative assessment must be conducted to evaluate the ML models (in this case RF) with and without bias correction of CMIP6 data within the context to predict precipitation data.

2.5 Previous work from our research group relevant to this dissertation

The paleoclimate dynamics section (climate sciences) of the Alfred Wegner Institute, Helmholtz Centre for Polar and Marine Research under the leadership of Prof. Dr. Gerrit Lohmann, has made extensive contribution specifically in climate dynamics, earth system modeling, and climate risk analysis. Group's interdisciplinary and multidisciplinary work provides critical foundation for the current dissertation.

Some of the research work includes analysis of spatiotemporal variability of climate indices and atmospheric circulation patterns. A study by Ionita et al., 2012, examined the interannual to decadal variability of European summer drought using self-calibrated Palmer drought severity index (a drought based climate indices), in relation with global sea surface temperature (SST). The study highlighted that this variability is influenced by large-scale ocean-atmosphere patterns and indicated a lag relationship between winter SST and summer droughts. This study indicates the importance of climate indices and its usability a key focus of this dissertation.

Another study where in the multi-variables (precipitation, soil moisture, and sea level pressure) were utilized to predict the major flooding event – June,2013 in Europe (Ionita et al., 2015). 55% of the Elbe river extreme discharge could be predicted with the multi-variable selection (Ionita et al., 2015). An approach, which justifies the alignment and importance of compound event detection and high-risk zones. Spatial and temporal pattern analysis of compound hot and dry events in Europe can be related to the large-scale atmospheric circulation, which can help understand the driving mechanism and frequency of such events (Ionita et al., 2021). These findings showcases the need for advanced statistical techniques to identify and analyze more such pairs, in order to better understand compound events.

Previous study already demonstrates that utilizing probabilistic models in extreme value theory (fitting generalized extreme value distribution) and copula theory offers a robust approach for validating the

performance of climate models, particularly related to the intensity and spatial co-occurrence of climate extremes (Contzen et al., 2022). These methods within the dissertation supports the advance statistical technique copula and probabilistic modeling for demarcation of high-risk zones of the climate extremes.

A large part of the group focuses on the model-data integration and model development, especially for paleoclimate and future scenarios. A model-data comparison of the Holocene global SST with marine proxies indicated that, although the model captures the direction of SST changes, but the magnitude is weaker in comparison to the proxy data; this highlights an ongoing challenge in model evaluation (Lohmann et al., 2013). These indicates a need to adjust the biases of the model based on the output for better analytical assessment. Although opportunistic sensing based precipitation estimates is new to the groups portfolio, however studies have already been done within the group to showcase the importance of precipitation estimates in prediction and forecasting of streamflow for various modeling studies (Khozani et al., 2024).

Overall, the dissertation integrates and advances multiple research areas by combining high-resolution observational analysis, compound event risk modeling, probabilistic assessment approaches, and machine learning-based climate model bias corrections and prediction. These contribute to the group's broader goal of deepening our understanding to the regional and continental-scale climate processes, risks, and their socio-environmental impacts.

Chapter 3

Spatiotemporal trend analysis of climate indices for the European continent

Research Question: *"How have the spatiotemporal patterns of a wide range of climate indices evolved across Europe over the past seven decades, and what are the direction, magnitude, and statistical significance of these trends at a high spatial resolution and temporal scale?"*

Synthesis:

The objective of this study is to analyze and visualize the spatial distribution of trends for 74 climate indices on a monthly time-scale in direction,magnitude, and significance level at a resolution of 0.1° during the period of 1950–2021 over the European region. The Mann–Kendall and Sen's slope estimators reveal that growing degree days with mean air temperature .4 °C (gd4) and heating degree days with mean air temperature ,17 °C (hd17) show the largest increase (0.93 °C August) and decrease (1.03 °C July), respectively. The universal thermal climate index (utci), relative humidity (rh), wind chill index (wci), global radiation (bio20), and potential evapotranspiration (pet) are of significant importance due to higher correlation and magnitude of change. Country-specific zoning shows the highest warmer days during August experienced by Bosnia and Herzegovina (southeastern Europe) and lower colder days during January by Belarus (eastern Europe). High wind and high utci were experienced by Liechtenstein (southeastern Europe) region during July. The highest wci was experienced by San Marino (southern Europe) in June and Portugal (southern Europe) in March. Bio20 and rh decline were experienced by Russia (eastern Europe) and Moldova (southeastern Europe) in May and September, respectively. Results are useful to mitigate the risk associated with each of the climate indices for specific European regions.

Authors contributions:

Smit Chetan Doshi (S.C.D.), Gerrit Lohmann (G.L.), Norel Rimbu (N.R.), and Monica Ionita (M.I.) conceptualized the study. S.C.D. and M.I. acquired data; S.C.D. and M.I. prepared the methodology. S.C.D. did analysis; S.C.D. did programming. G.L., N.R., M.I. did project administration; G.L., N.R., and M.I. supervised the study, S.C.D. wrote the original draft; S.C.D., G.L., N.R., and M.I. reviewed the article.

This chapter is based on already published study in the Journal of Water & Climate Change, International Water Association (Doshi et al., 2023b). Appendix A includes the supplementary information for this paper. Download input data (steps), code used for the statistical analysis (R and matlab) and output data generated from: https://zenodo.org/record/8250835.

Journal of
Water & Climate Change

Check for updates

IWA PUBLISHING

© 2023 The Authors

Journal of Water and Climate Change Vol 14 No 9, 3112 doi: 10.2166/wcc.2023.183

Spatiotemporal trend analysis of climate indices for the European continent

Smit Chetan Doshi [a,b,*], Gerrit Lohmann [a,b], Norel Rimbu [a] and Monica Ionita [a]

[a] Alfred Wegener Institute Helmholtz Center for Polar and Marine Research, Bremerhaven, Germany
[b] University of Bremen, Bremen, Germany
*Corresponding author. E-mail: smitdoshi5@gmail.com

SCD, 0000-0001-5358-5477; GL, 0000-0003-2089-733X; NR, 0000-0003-2832-9396; MI, 0000-0001-8240-4380

ABSTRACT

The objective of this study is to analyze and visualize the spatial distribution of trends for 74 climate indices on a monthly time-scale in direction, magnitude, and significance level at a resolution of 0.1° during the period of 1950–2021 over the European region. The Mann–Kendall and Sen's slope estimators reveal that growing degree days with mean air temperature >4 °C (gd4) and heating degree days with mean air temperature <17 °C (hd17) show the largest increase (0.93 °C August) and decrease (1.03 °C July), respectively. The universal thermal climate index (utci), relative humidity (rh), wind chill index (wci), global radiation (bio20), and potential evapotranspiration (pet) are of significant importance due to higher correlation and magnitude of change. Country-specific zoning shows the highest warmer days during August experienced by Bosnia and Herzegovina (southeastern Europe) and lower colder days during January by Belarus (eastern Europe). High wind and high utci were experienced by Liechtenstein (southeastern Europe) region during July. The highest wci was experienced by San Marino (southern Europe) in June and Portugal (southern Europe) in March. Bio20 and rh decline were experienced by Russia (eastern Europe) and Moldova (southeastern Europe) in May and September, respectively. Results are useful to mitigate the risk associated with each of the climate indices for specific European regions.

Key words: climate indices, Europe, Mann–Kendall, Sen's slope, trend analysis

HIGHLIGHTS

- Trend analysis of 74 climate indices in Europe using Mann–Kendall and Sen's slope.
- Correlation value of climate indices reveals patterns of annual, seasonal, and monthly tie-ups.
- Increase shifts in average temperature and warmer conditions in European regions.
- Analysis indicates small European regions are also impacted.
- Climate indices trend assessment of the most susceptible country of Europe.

This is an Open Access article distributed under the terms of the Creative Commons Attribution Licence (CC BY 4.0), which permits copying, adaptation and redistribution, provided the original work is properly cited (http://creativecommons.org/licenses/by/4.0/).

Downloaded from http://iwaponline.com/jwcc/article-pdf/14/9/3112/1301084/jwc0143112.pdf
by guest

GRAPHICAL ABSTRACT

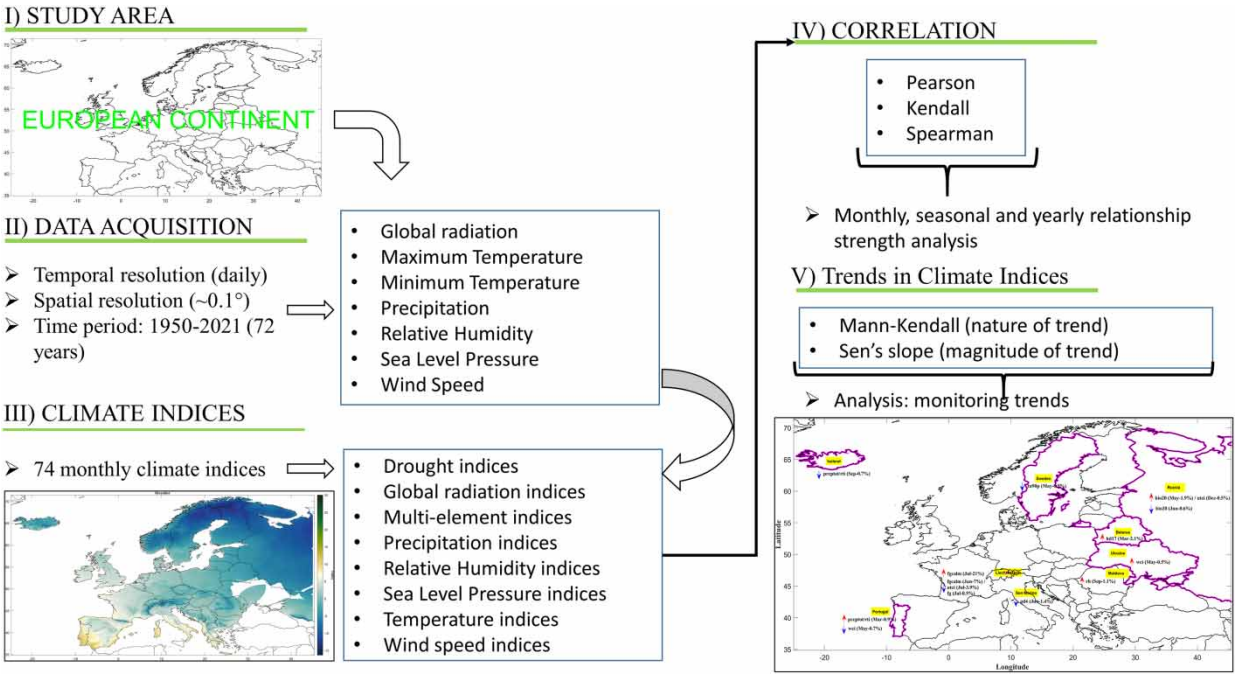

1. INTRODUCTION

The occurrence of unanticipated catastrophic extreme weather events as a result of an uncertain climate causes human fatalities, devastation, ecosystem impacts, and economic losses in all areas of the world (Eyshi Rezaei *et al.* 2015; Sergio *et al.* 2018). Understanding such extreme events has become increasingly important in the last two decades because of their consequences (Sillmann *et al.* 2013). Climate data are needed for monitoring and management and can be summarized using a set of standardized useful climate metrics. Trends in past and future climate data have been extensively researched to better understand how a climate influences the frequency and intensity of extreme weather occurrences (Razavi *et al.* 2016). Analysis of future climate trends is necessary for future climate risk assessments, and the analysis of historical observational data is critical for understanding the current consequences of global warming in comparison to the past (Rimbu *et al.* 2014, 2017; Felix *et al.* 2021). Long-term monthly or seasonal averages, such as gridded global temperature or precipitation datasets are often used in climate change research (Brohan *et al.* 2006; Smith & Reynolds 2005). The assessment of not only the features of the mean climate but also extreme climate and weather occurrences is an essential aspect in modern climatology. Climate change, variability, and extreme events are important aspects of society (Ruiz-Alvarez *et al.* 2020).

The fifth assessment report (AR5) of the Intergovernmental Panel on Climate Change (IPCC) particularly in the chapter titled 'Observations: Atmosphere and Surface' evaluated the research on regional and global changes in climate extremes (Hartmann *et al.* 2013). The summary stated that there is limited evidence of changes in extremes associated with other climate variables since the mid-20th century (Hartmann *et al.* 2013). One of the most serious challenges to humanity is the rise in global temperature and its consequences (Outten & Sobolowski 2021). From 1880 to 2012, global land and ocean surface temperature increased by 0.65–1.06 °C, resulting in the warming of Earth and exhibits substantial inter-annual to decadal fluctuations (Hartmann *et al.* 2013). Observed global climate changes are unprecedented, such as the warming of atmosphere, decreased ice and snow, and increasing sea level (IPCC 2014). Understanding temperature extremes is crucial for assessing the impacts of climate change (Almazroui *et al.* 2014). The most important effects of global warming would be an increase in the size of occurrence of severe precipitation events caused by higher atmospheric moisture levels, thunderstorms, or large-scale storm activity (Roy & Balling 2004). Average global precipitation is expected to grow by 2–3% for every 1 °C in temperature (Schneider *et al.* 2010). The fraction of severe precipitation in relation to total yearly precipitation is increasing (Alexander *et al.* 2006). Droughts are becoming more common worldwide because precipitation in areas is too low in the expected mean for a given period (Dai 2011; Trenberth *et al.* 2014). One of the findings indicates a high level of uncertainty

Downloaded from http://iwaponline.com/jwcc/article-pdf/14/9/3112/1301084/jwc0143112.pdf
by guest

in global scale drought patterns during the last 60 years, with no indication of a rise in the overall area impacted by droughts (Seneviratne 2012). The IPCC assessment identified significant uncertainty in drought data, and conflicting results from research on several regional drought patterns (Seneviratne *et al.* 2012).

Agro-climatic zones – weather extremes that occurred in historical scenarios of the selected weather data; significant seasonal variations in global radiation were also potential crucial criteria for future climate forecasts (Kahiluoto *et al.* 2014; Mäkinen *et al.* 2018). Heat stress, with a combined effect of temperature and relative humidity, is likely to rise as the global climate warms. Studies on the relative humidity relevance to the death rates are less common, but resulting in poor health has already been discovered (Callan *et al.* 1993). A link of fatalities between total relative humidity and excess winter mortality across Europe with a strong significance has already been showcased (Healy 2003). The observed rise in the impacts of weather related hazards was attributed due to the increase in population exposure, with a potential contribution from global warming (Forzieri *et al.* 2017). One of the findings showcased that the disaster could affect two-thirds of the European population by the year 2100 compared with 5% during the year 1981–2010 (Forzieri *et al.* 2017). Additionally, the most vulnerable people that are the ones with precarious physical environment living conditions or in environments where there are dramatic physical modifications (Liverman 2013).

The objective of this work is to perform a detailed analysis of the climatology and temporal evolution of 74 climate indices for the European continent from 1950 to 2021 at a monthly scale. The patterns of variation and temporal-spatial distribution characteristics of global radiation, maximum and minimum temperature, precipitation, relative humidity, and sea level pressure extreme events are quantified. The special feature is that the climate indices for each individual country in Europe were evaluated with high spatial resolution and up-to-date data. The main objectives are: For each climate indices covering Europe at a monthly frequency from 1950 to 2021, three statistics are obtained: (i) correlation coefficient using Pearson, Kendall, and Spearman; (ii) trend nature and significance using the Mann–Kendall test, and (iii) magnitude of trend using Sen's slope estimator.

2. DATA AND METHODS

2.1. Climate indices

The European Climate Assessment and Dataset (ECA&D) Ensembles daily gridded observational dataset (E-OBS) v25.0e (Cornes *et al.* 2018) were used to create a gridded database of 74 climate indices listed in Figure 1. The European National Meteorological and Hydrological Services (NMHSs) entities provide all the station data. E-OBS remains a significant dataset for model validation, also utilized broadly for climate monitoring across Europe, notably for assessing the magnitude and frequency of extremes. The monthly spatial extent of various climate indices is computed based on the daily gridded E-OBS dataset with a horizontal resolution of $0.1° \times 0.1°$ (highest resolution dataset of about 11 km) and cover an area of 25°N-71.5°N × 25°W-45°E (entire European land surface). The global radiation is measured at the Earth's surface, the maximum and minimum temperature at 2-m height, precipitation recorded with a total daily amount of rain, snow and hail, relative humidity at 2-m height, sea level pressure at sea level, and wind speed at 10-m height. Based on the gridded observational dataset of E-OBS the computed climate indices and abbreviation of each of them are shown in supplementary table S2.

This study used the R platform's 'ClimInd' (https://cran.r-project.org/web/packages/ClimInd/index.html) and 'scPDSI' (https://cran.r-project.org/web/packages/scPDSI/index.html) package to compute 74 climate indices at monthly temporal frequencies for Europe. Figure 1 shows the list of climate indices selected. The selection is based on the possible monthly scale climate indices from available input weather data (global radiation, maximum and minimum temperature, precipitation, relative humidity, sea level pressure, and wind speed), literature review discussed in the introduction section and important priority sectors such as agriculture, health, water, disaster risk reductions, and tourism. The climate indices were divided into eight categories: drought (15), global radiation (1), multi-element (5), precipitation (16), relative humidity (1), sea level pressure (1), temperature (32), and wind speed (3).

Figure 2 indicates the monthly spatial distribution of heat index, one of the multiple-element climate indices for the Europe region from year 1950 to 2021 (72 years). To have a visualization of each of the 74 climate indices Supplementary Information, Figure S1 has been attached. The visualization of wind speed linked indices (fg, fg6bft, fgcalm, utci, and wci) indicates a lesser known observational dataset leading to fewer regions covered in terms of spatial variability as other resources such as ERA5-reanalysis dataset have been avoided due to spatial resolution difference and different data sources.

Downloaded from http://iwaponline.com/jwcc/article-pdf/14/9/3112/1301084/jwc0143112.pdf
by guest

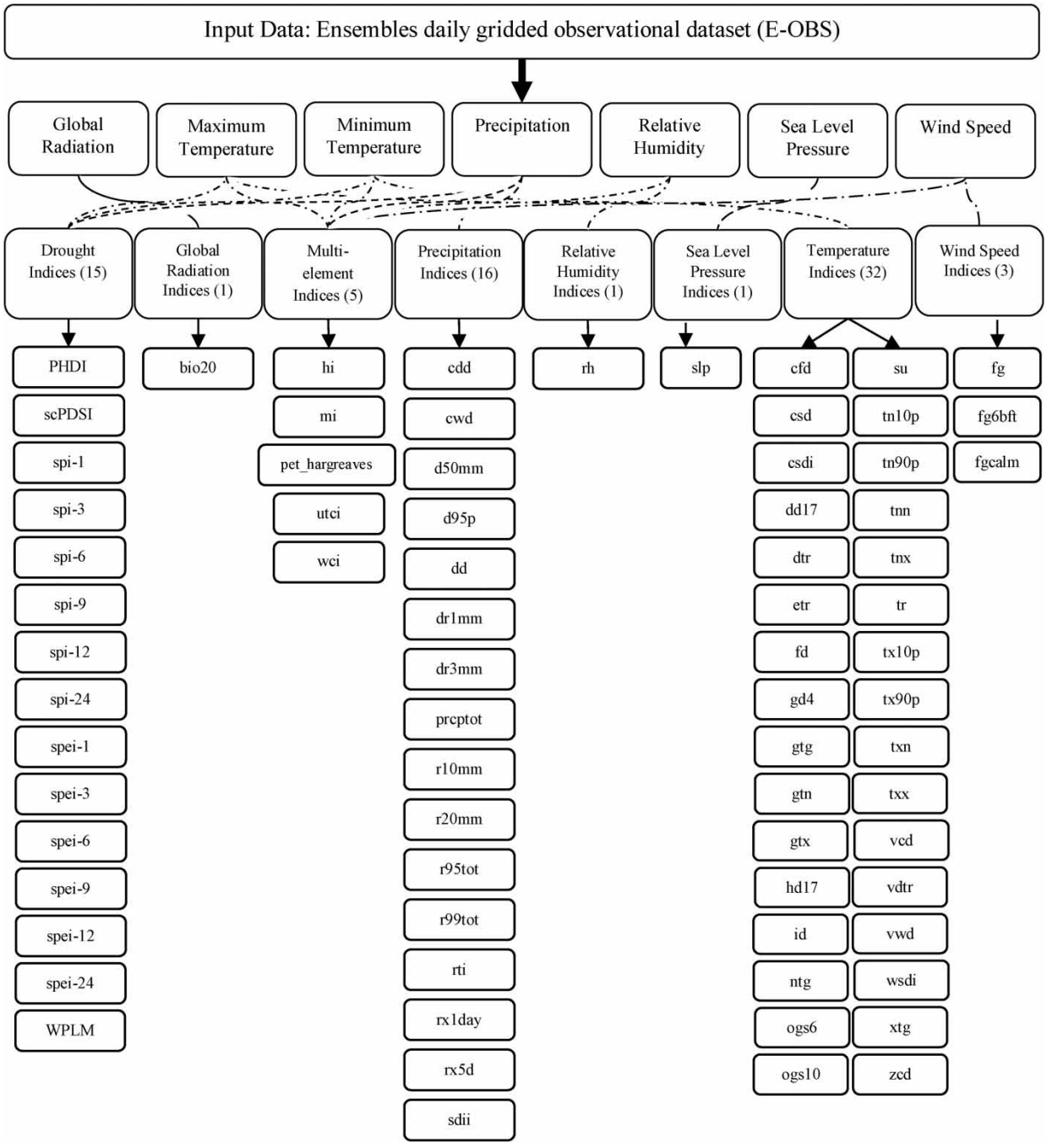

Figure 1 | List of climate indices (the lines above each of the grouped climate indices indicate which weather data from E-OBS are utilized).

However, the global radiation is not only computed from *in situ* observations but CERS global radiation satellite; the dataset is taken into account due to the resources not allowing users to take into account the analysis of only *in situ* observations. The indices linked with the global radiation (bio20) for computation must take into account the variability associated due to this combination of two different sources.

2.2. Statistical analysis

For each climate index covering Europe at a monthly frequency from 1950 to 2021, the study obtained three statistics (Section 1 explained as main objectives). The correlation coefficient between different possible combinations of climate indices was

Downloaded from http://iwaponline.com/jwcc/article-pdf/14/9/3112/1301084/jwc0143112.pdf
by guest

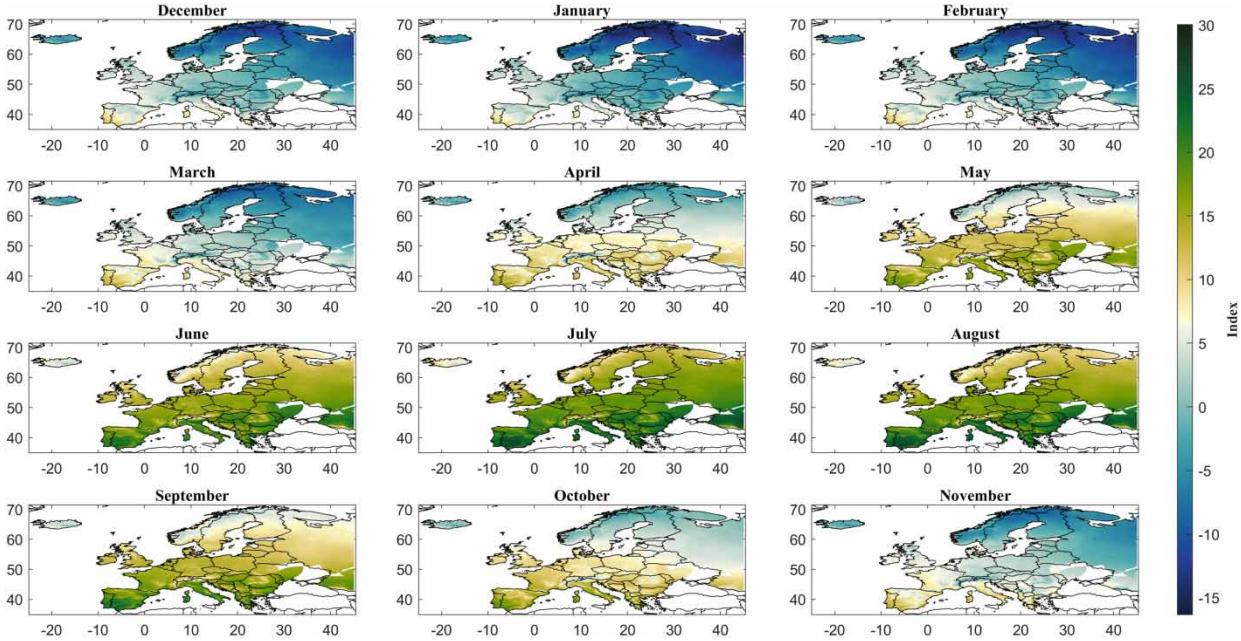

Figure 2 | Monthly spatial distribution of heat index (hi) climate indices – 1950–2021.

computed using each of the Pearson, Kendall, and Spearman methods. Pearson is widely used to measure linear relationships whereas Kendall and Spearman are non-parametric measures. Considering the nature of different climate indices being analysed we employed all three correlation techniques, finally, the resultant value was selected based on the maximum of three methods to avoid any missing crucial information for future assessments based on thresholds of the correlation value. There are two types of tests for detecting the significant trends in climatological time series: parametric (data are independent and normally distributed) and non-parametric (data is independent). Mann–Kendall and Sen's slope estimator are both non-parametric approaches which are employed in this study to detect variability and long-term monotonic trends in climate indices. The Mann–Kendall test was used to assess whether the climate indices nature is increasing (positive) or decreasing (negative) over time, and trend direction is statistically significant or not. A p-level of < 0.05 (statistically significant) and >0.05 in both the increasing (positive) and decreasing (negative) trend was represented spatially taking serial correlation into consideration. The Sen's slope estimator was used to compute the climate indices percentage of change over each year for the 72 year period (1950–2021). The value would indicate for instance how much on average it has modified each year either positively or negatively (indicating direction and size of trend) by overcoming the gross data time series errors and outliers if any.

Statistically, the Mann–Kendall test (Henry 1945; Kendall 1975) is calculated as:

$$S = \sum_{i=1}^{n=1} \sum_{j=i+1}^{n} \mathrm{sgn}(x_j - x_i),\ \mathrm{sgn}(x_j - x_i) = \begin{cases} +1 & (x_j - x_i) > 0 \\ 0 & (x_j - x_i) = 0 \\ -1 & (x_j - x_i) < 0 \end{cases} \tag{1}$$

where n is the number of data points, x_i and x_j are the data values in time series i and j, $\mathrm{sgn}(x_j – x_i)$ is the sign function.

The variance is calculated as:

$$Var(S) = \frac{n(n-1)(2n+5) - \sum_{i-1}^{m} t_i(t_i-1)(2t_i+5)}{18} \tag{2}$$

where m is the number of tied groups and t_i is the number of ties of extent i.

Downloaded from http://iwaponline.com/jwcc/article-pdf/14/9/3112/1301084/jwc0143112.pdf
by guest

The standard normal test statistic Z is calculated as:

$$Z = \begin{cases} \dfrac{S-1}{Var(S)^{1/2}}, & S > 0 \\ 0, & S = 0 \\ \dfrac{S+1}{Var(S)^{1/2}}, & S < 0 \end{cases} \tag{3}$$

Z-value positive indicates increasing trend and negative indicates decreasing trend. Testing of the trends is done at the 0.05 significance level. $|Z| > Z_{1-0.05/2}$, the null hypothesis of no trend is rejected, a significant trend exists in the dataset. The value of $Z_{1-0.05/2}$ is obtained from the standard normal distribution table which is 1.96 (5% significance level).

Sen's slope equation (Sen 1968) for a set of sample data pairs is calculated as:

$$Q_i = \frac{(x_j - x_i)}{j - i}, \ i = 1, 2, 3, \ \ldots, \ N \tag{4}$$

where x_i and x_j are data values in time series i and j. n values of x_j will be $N = n(n-1)/2$ slope estimates; N value is sorted for Q_i from small to large and then Sen's slope is obtained based on the two-tailed estimate for the Q_{med} (median Q_i), which is calculated as:

$$Q_{med} = \begin{cases} Q_{(N+1)/2}, & N = \text{odd} \\ \dfrac{Q_{N/2} + Q_{(N+1)/2}}{2}, & N = \text{even} \end{cases} \tag{5}$$

The analysis was further disintegrated into each of the European countries specifically to analyze the nature and magnitude of the trend. The statistical output of this study is showcased in the Results section. The study highlights how each of the climate indices of high spatial resolution varies across monthly frequency for European countries and regions as a whole extent.

3. RESULTS AND ANALYSIS

3.1. Monthly spatial distribution of climate indices

Based on the visualization attached as a part of Supplementary information figure S1, the results indicate the following: PHDI, scPDSI, and WPLM are within the normal range except regions of Croatia and Slovenia which indicate a low to moderate drought, certain parts of southern Russia close to Black sea which indicates moderate to severe drought, more moist region across the Eastern and Northern Europe. spi-1 indicates that the southern part of Spain, Portugal, and Italy is moderately wet during June, July, and August as a progression of bell shape curve. Mild drought has been observed in the southern part of Greece, Spain, and Portugal mostly prevailing in August through spi-3, 6 indices. The eastern part of Russia indicates an increase of mild wetness from spi-1,3,6,9,12, and 24 months. Similar conditions are confirmed with the SPEI related indices for various frequencies. bio20 reveals that the southern part of Europe receives more global radiation in comparison to the northern part with the highest in June and July. Combined indices hi indicates that the experience would be cold ~−10 °C in the northern part of Europe, ~0 °C at central Europe, and warm ~10 °C in Southern Europe during the winter season. There are increases in temperature during spring from Southern Europe to Central Europe, spreading across the western and eastern parts, and further increasing to reach the maximum in Northern Europe in July ~30 °C. The temperature descends in autumn. The 'mi' index is ~10 days during the summer and autumn seasons, with the highest in Western France, Eastern Ukraine, Northern Ireland, and Northern and Central United Kingdom. Hargreaves method was used to obtain the PET (Pet Evapotransportation) indices, which increase gradually from Southern Europe towards Western Europe and then cover Eastern and Northern Europe. The highest could be visualized in July and the Southern and Southern Eastern Europe Spain, Portugal, Monaco, Italy, San Marino, Southern Russia, Southern Ukraine, Serbia, Greece, Bulgaria, Bosnia and Herzegovina, Moldova, Romania. The maximum it can go is up to 200 mm/month during that period. Due to limited spatial availability of wind data the UTCI cannot be computed and spatially visualized for the whole European region. The northern part of Sweden and Finland experiences a feel of −80 °C during winter, and Germany, Netherlands,

Downloaded from http://iwaponline.com/jwcc/article-pdf/14/9/3112/1301084/jwc0143112.pdf
by guest

France, and some region of Spain experiences a feel of 20 °C during summer. WCI on the other hand indicates a similar experience during summer but for winter it is −20 °C maximum. Spatial spreading across the regions is similar to that of UTCI. Southern Europe especially Spain, Portugal, Italy and Greece has dry periods as long as one month during summer and approximately half for the month during other seasons and the other half as wet days. The probability is more than 95% for this occurrence of the event. During autumn southern France, some regions of Italy, Slovenia, northern Norway, and San Marino experience precipitation of more than 50 mm for as long as 1.5 days. Each of the European countries receives more than 1 and 3 mm of precipitation for all the seasons with highest during the December (winter) and July (spring) ~20 days, respectively. The maximum amount of precipitation received in any given month for the European region at a recorded location is 400 mm. Europe receives >10 days of 10 mm and >6 days of 20 mm precipitation mostly Italy, San Marino, Southern France, Slovenia, Croatia, northern banks of Norway, and Southern Russia. The highest recorded average precipitation for any given day is ~80 mm in the month of November (summer) and cumulative of 5 days is ~150 mm along the similar regions where Europe receives most 10 and 20 mm precipitation. The relative humidity indices are in the range of 40–90% with the maximum during winter and lowest during the summer season. Spatially Northern, Eastern and Western Europe receives more relative humidity in comparison to central and Southern Europe. Sea level pressure does not vary much across the European region but reduces by ~200 hPa in Southern Russia (eastern Europe) near the Black Sea, Ukraine, and Moldova for all the seasons except winter. During winter Northern, Central and Eastern Europe receive a minimum air temperature <0 °C for a full month which further reduces in the succeeding months. Maximum consecutive summer days are visualized during the summer season in Southern and Southern Eastern Europe. Cold spell duration of >1.5 days is observed in central, eastern and southern eastern Europe during winter. During summer months there has been a maximum difference of ~21 days for maximum temperatures above/below 17 °C across Europe. The difference between the mean and maximum daily maximum and minimum air temperature during that period is >15 and >35 °C, respectively. During the summer season Southern and South Eastern Europe have mean air temperatures > 4 °C for >600 sum of degree days. The highest mean of minimum, maximum and mean air temperature during summer is ~20, ~30, ~25 °C and in winter is ~–20, ~–10, ~–15 °C, respectively. Mean air temperature >5 °C during spring where the first span of 6 days and 10 days moves from Southern Europe (March) to Central and Eastern Europe (April), to Northern Europe (May). Tropical nights could be observed during July and August in the southern part of Spain, Russia and France, Ukraine and Italy. The number of days when maximum temperature >0 °C and minimum temperature <0 °C is >20 during winter and spring shifts from Southern and Eastern Europe to Northern Europe; maximum during April in Sweden, Norway, Finland, and Northern Russia. fg indicate average wind speeds are higher during the winter season also the southern part of Norway, Finland, the central and northern part of Germany and Netherlands experiences relatively higher wind speed ~10 m/s prevailing for >10 days.

3.2. Correlation of climate indices for Europe

74 climate indices would result in 2,701 correlation coefficient values considering the respective month and the method used (Pearson, Kendall, and Spearman). The calculated bivariate analysis would indicate the strength and direction between the climate indices. Based on the values obtained, grouping into very high correlation (±0.80 to ±1.00), high correlation (±0.60 to ±0.80), medium correlation (±0.40 to ±0.60), low correlation (±0.20 to ±0.40), and very low correlation (±0.00 to ±0.20) is done. Here, ± indicates the direction of the correlation: positive or negative. The results are further analyzed, not considering the correlation when the input data source is the same, as the value would be misleading. The interest of the study is to determine the highly correlated climate indices. Figure 3 shows the average annual correlation value obtained from the monthly climate indices.

There has been a very high positive correlation between gtx, txn with gtn, tnn, tnx with gtx, wci, pet_hargreaves with hi, txn, txx with tnn and tnx, wci, utci with pet_hargreaves for all the months throughout the 72 year time series of climate indices. This indicates that the following indices have no/less impact on seasonality in their correlation. Both the compared variables of climate indices have a perfect linear/non-linear relationship and modification of one variable would consistently change another (upward slope). In other terms, throughout the year mean, minimum, maximum of minimum and maximum daily air temperature, heat index which is a combination of air temperature and relative humidity and wind chill index which is the lowering of body temperature linked with the passing flow of lower-temperature air, potential evapotranspiration computed by Hargreaves method and heat index, wind chill index and universal thermal climate index which is the reference condition of air temperature causing the same model response as actual condition across Europe is positively correlated with >0.8 value. The indices which show positive very high correlation seasonality connections for winter (DJF) are pet_hargreaves, gtx, txn, txx, wci with slp, gd4, gtx, gtg, hi, ntg, tnn, txn, txx, utci, wci, pet_hargreaves, slp, xtg with bio20, cfd, fd with id,

Downloaded from http://iwaponline.com/jwcc/article-pdf/14/9/3112/1301084/jwc0143112.pdf
by guest

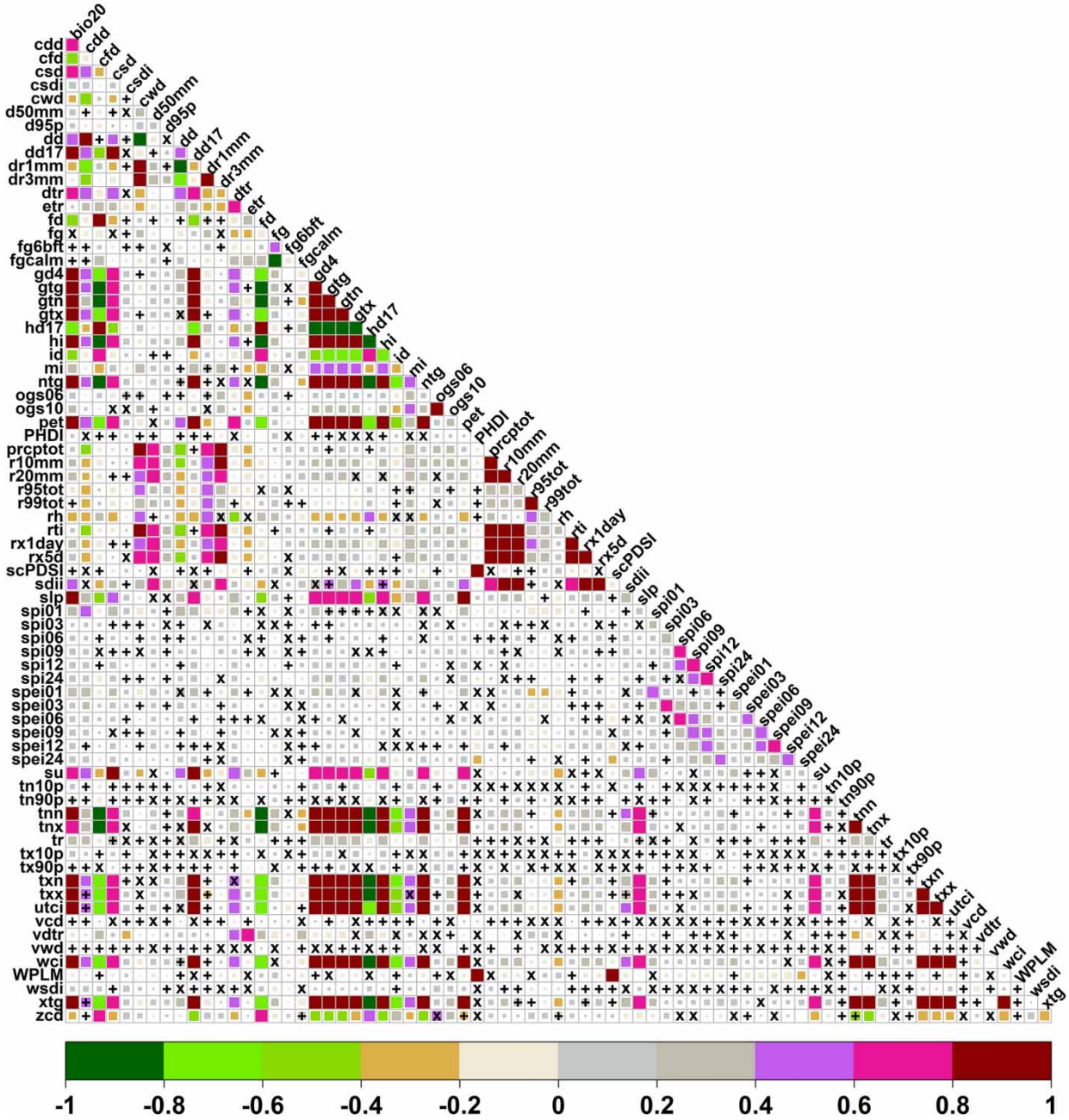

Figure 3 | Correlation of climate indices (maximum value of Pearson, Kendall, and Spearman). 'x' and '+' indicate significance level less (p-value) > 0.05 and < 0.01, respectively. Colour bar indicates correlation value (highest positive is maroon and highest negative is dark green). Please refer to the online version of this paper to see this figure in colour: http://dx.doi.org/10.2166/wcc.2023.183.

mi with wci; for spring (MAM) are gtn, tnn, tnx with dd17; for summer (JJA) are csd, dd17, gd4, gtg, gtx, hi, pet_hargreaves, su, txn, wci with bio20, gtn, tnn, tnx with dd17, gtn, tnn, tnx with su, gtn, tnn, tnx with csd; for autumn (SON) are gd4, gtg, gtn, gtx, hi, ntg, pet_hargreaves, slp, tnn, tnx, txn, txx, utci, wci, xtg with bio20, gtx, pet_hargreaves, txx, utci, wci, xtg with slp. During the winter season changes in average sea level pressure impact the minimum daily air temperature indices, wind chill index, and potential evapotranspiration, changes in average global radiation impact the mean, maximum and minimum daily air temperature indices as well as the sum of degree days over 4 °C, heat index, wind chill index, potential evapotranspiration, universal thermal climate index, changes in wind chill index and number of days with daily maximum temperature < 0 °C have a direct impact on the number of days and consecutive days with minimum daily temperature < 0 °C. During the

Downloaded from http://iwaponline.com/jwcc/article-pdf/14/9/3112/1301084/jwc0143112.pdf
by guest

spring season changes in the difference between the days with maximum temperature >17 and <17 °C have a direct impact on the minimum daily air temperature indices. During the summer the changes in average global radiation impact the number of consecutive days with maximum temperature >25 °C, the difference between days with maximum temperature >17 and <17 °C, the sum of days with mean temperature >4 °C, the number of days with maximum temperature >25 °C, mean of daily mean and maximum temperature, heat index, potential evapotranspiration, minimum of maximum temperature, wind chill index, maximum number of days and consecutive summer days with maximum temperature >25 °C and difference days with maximum temperature >17 and <17 °C is impacted by change in minimum temperature indices. During the autumn season changes in average global radiation impact the sum of days with mean temperature >4 °C, mean of maximum, minimum, and mean daily temperature, heat index, minimum of daily mean temperature, potential evapotranspiration, average sea level pressure, minimum and maximum of minimum and maximum daily air temperature, universal thermal climate index, wind chill index, maximum of daily mean air temperature, change in average sea level pressure impacts the mean and maximum of maximum daily air temperature, potential evapotranspiration, universal thermal climate index, wind chill index, and maximum of daily mean air temperature. The very high positive correlation monthly climate indices which do not fall into the seasonality or yearly brackets are listed in Table 1. For different months most of the indices are a part of global radiation, multi-element, temperature, and sea level pressure indices except for the months of July and August which includes precipitation indices whereas August includes relative humidity indices. However, none of the drought related or wind speed related indices is part of the highly positively correlated indices for Europe.

The indices which show a negative very high correlation seasonality connections for winter (DJF) are hd17, id with bio20, gtx, txn, txx with cfd and fd, gtn, tnn, tnx with id; for spring (MAM) are dd17, gtx, txn, txx with cfd and fd; for autumn (SON) are fd, hd17 with bio20, gtx, txn, txx with cfd, gtx, txn, txx with fd. During the winter season, the change in global radiation will impact inversely to the daily mean air temperature <17 °C and the number of days with daily maximum air temperature <0 °C, changes in the maximum number of days and consecutive days with daily minimum air temperature <0 °C impacts inversely to the mean, minimum and maximum of maximum daily air temperature, changes in number of days with daily maximum temperature <0 °C impacts inversely to the mean, minimum and maximum of minimum daily air temperature. During spring season changes in the maximum number of days and consecutive days with daily minimum air temperature <0 °C will impact inversely the difference between the daily maximum air temperature >17 and <17 °C, mean, minimum and maximum daily maximum air temperature. During the autumn season, the average global radiation will impact inversely the number of days with a daily minimum temperature <0 °C and daily mean air temperature <17 °C, changes in the number of days and consecutive number of days with daily minimum temperature <0 °C impacts inversely the mean, minimum, and maximum of daily maximum air temperature. The very high negative correlation monthly climate indices which do not fall into the seasonality or yearly brackets are listed in Table 2. For different months most of the indices are a part of global radiation, multi-element, temperature, and sea level pressure indices except for the months of July and August which include precipitation indices whereas July, August, and September includes relative humidity indices. However, none of the drought related or wind speed related indices is part of the highly negatively correlated indices for Europe.

3.3. Trend analysis of climate indices throughout Europe

In climate studies, the variability of trends in monthly calculated climate indices is an important aspect. The spatial behaviour can be classified into four categories using the Mann–Kendall test: (i) climate indices with a positive trend and significance level less than 0.05 (highly significant); (ii) climate indices with a positive trend and significance level more than 0.05; (iii) climate indices with negative trend and significance level less than 0.05 (highly significant); and (iv) climate indices with negative trend and significance level more than 0.05 and using Sen's slope estimator test to determine the magnitude of annual change for each of the four categories. Figure 4 shows the overall monthly trend analysis in the form of a radial plot for the entire European region. A country-specific visualization can be found in Supplementary Information Figure S2-A and S2-B.

Based on the results of the radial chart, gd4 and hd17 show the highest direction (increasing and decreasing trend, respectively), significance level, and magnitude of change with respect to spatial distribution. Figures 5 and 6 show important months where indices have changed >0.10%. The remaining climate indices for Europe are included as part of Supplementary Information Figures S3 and S4.

Analysis of the Mann–Kendall and Sen's slope estimator tests over 72 years of E-OBS data shows that for the European region there is an increasing trend in spi-3, spi-6, spi-9, spi-12 and spi-24 (drought indices), hi and pet (multi-element indices), d50mm, d95p, r10mm, r20mm, r95tot, r99tot, rx1day and sdii (precipitation indices), dd17, gd4, gtg, gtn, gtx, ntg, tn90p, tnn,

Downloaded from http://iwaponline.com/jwcc/article-pdf/14/9/3112/1301084/jwc0143112.pdf
by guest

Table 1 | Very high positive correlation (>0.8) monthly climate indices

Jan	Feb	Mar	Apr	May	Jun	Jul	Aug	Sep	Oct	Nov	Dec
gtg, hi, ntg with slp	gd4, gtg, hi, ntg, utci, xtg with slp	cfd, fd with id	cfd, fd with id	gtn, tnn, tnx with csd		cdd, dd, ntg, txx, utci, xtg with bio20	csd, dd17 gtx, su with dd	cdd, gtn, tnn, tnx with dd17	cfd, fd with id	cfd, fd with id	utci with slp
gtn with bio20	dd17, gtn with bio20	dd17, gd4, gtg, gtn, gtx, hi, ntg, pet, slp, tnn, tnx, txn, txx, utci, wci, xtg with bio20	dd17, gd4, gtg, gtn, gtx, hi, ntg, pet, tnn, tnx, txn, txx, utci, wci, xtg with bio20	gtn, tnn, tnx, with su		csd, su with cdd	csd, su with cdd	csd, dd17, dtr, su with bio20	csd, dd17, dtr, su with bio20	pet, wci with mi	
	gtn, slp, tnn, tnx with dd17	dd17, gd4, gtg, gtn, gtx, hi, ntg, pet, tnn, tnx, txn, txx, utci, wci, xtg with slp	gtn, tnn, tnx with su			csd, dd17 gd4, gtg, gtx, ntg, su, txn, wci with dd	cwd, dr1mm with rh	csd, gtx, txx, su with cdd	gtn, tnn, tnx with dd17		
		mi with wci	mi with wci			dr1mm with hd17	dd, dtr, gtn, ntg, slp, tnn, tnx, txx, utci, xtg with bio20	csd, dd17, gd4, gtg1 hi, ntg, su with slp	dd17, dtr, gtg, hi with slp		
							dd17, gtx, txn, txx with tr	gtn, tnn, tnx with csd	gtn, tnn, tnx with csd		
								gtn, tnn, tnx with su	gtn, tnn, tnx with su		

Downloaded from http://iwaponline.com/jwcc/article-pdf/14/9/3112/1301084/jwc0143112.pdf
by guest

Table 2 | Very high negative correlation (<–0.8) monthly climate indices

Jan	Feb	Mar	Apr	May	Jun	Jul	Aug	Sep	Oct	Nov	Dec
hd17, id with slp	cfd, fd with dd17	cfd, fd, hd17, id with bio20	cfd, fd, hd17 with bio20	cfd, fd with csd	dd17, gtx, txn, txx with cfd	cwd, dr1mm, dr3mm, hd17, rh with bio20	cwd, dr1mm, hd17, rh with bio20	cfd, rh, zcd with bio20	cfd, id, zcd with bio20	bio20, gtn, tnn, tnx with id	
	hd17, id with slp	cfd, hd17, id with slp	cfd, fd with csd	cfd, fd with su	dd17, gtx, txn, txx with fd	cdd with rh	cdd with rh	cdd with rh	csd, dd17, su with cfd		
		gtn, tnn, tnx with id	cfd, fd with su			cwd, dr1mm, dr3mm, rh with csd	cwd, dr1mm, dr3mm, rh with csd	csd, dd17, su with cfd	csd, dd17, su with fd		
			gtn, tnn, tnx with id			dd17, gtx, su, txn, wci with cwd	gtx, su with cwd	csd, pet, su with rh	gtn, tnn, tnx with id		
						dd with hd17	dd, dtr, gtx, pet, su, txx, xtg with rh	csd, dd17, su with fd	hd17 with slp		
						dd17, gd4, gtg, gtx, ntg, su, txn, wci with dr1mm	dd17, gtx, su with dr1mm	hd17 with slp			
						dd17, gd4, gtg, gtx, ntg, su, txn, wci with dr3mm	su with dr3mm				
						dtr, pet, su with rh					

tnx, tx90p, txn, txx, vwd, wsdi and xtg (temperature indices), whereas a decreasing trend in spei-12 and spei-24 (drought indices), rh (relative humidity indices), cfd, csdi, fd, hd17, id, tn10p, tx10p, vcd, and zcd (temperature indices), fg and fg6bft (wind speed indices) throughout all the months. The magnitude of change is per month for all the climate indices. The highest magnitude of change in increasing trend was recorded for gd4 which is in the range of 0.14–0.93 °C, lowest in January and highest in August with an average increase of 0.49 °C/month, followed by pet which is in the range of 0.01 to 0.15 mm/day, lowest in December and highest in July with an average increase of 0.07 mm/day, followed by tn90p which is in the range of 0.04–0.14%, lowest in February and highest in August with an average increase of 0.08%, followed by tx90p which is in the range of 0.02–0.10%, with lowest in September and highest in June with an an average increase of 0.06%, followed by dd17 which is in the range of 0 to 0.09 days, with lowest in January and highest in April with an average increase of 0.04 days, followed by rx1day which is in the range of 0.01–0.05 mm, with lowest in August and highest in October with an average increase of 0.02 mm, followed by ntg which is in the range of 0.01–0.05 °C, with lowest in September and highest in March with an average increase of 0.03 °C. The highest magnitude of change in decreasing trend was recorded for hd17 which is in the range of 0.29–1.03 °C, lowest in January and highest in July with an average decrease of 0.64 °C, followed by rh which is in the range of 0–0.11%, lowest in October and highest in April with an average decrease of 0.05%, followed by tn10p which is in the range of 0.01–0.10%, lowest in February and highest in July with an average decrease of 0.05%. The percentage of change in the trend of climate indices is close to 0 in the rest of the indices throughout all the months for both the increasing and decreasing trends.

Downloaded from http://iwaponline.com/jwcc/article-pdf/14/9/3112/1301084/jwc0143112.pdf
by guest

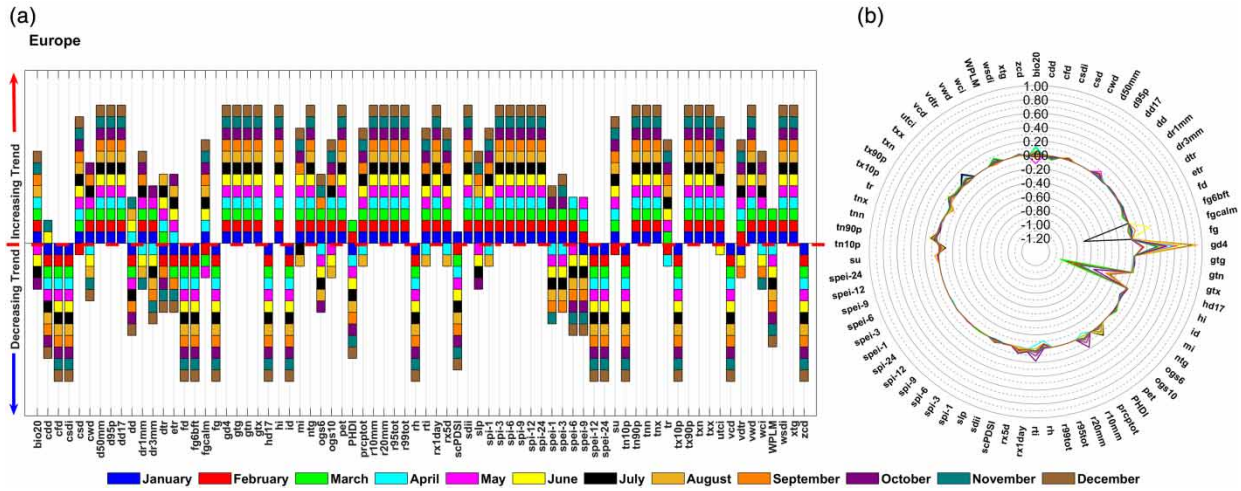

Figure 4 | Monthly trend analysis across Europe (a) increasing and decreasing trend and (b) % of change for each of the climate indices (units for each of the indices can be referred to in supplementary table S1.

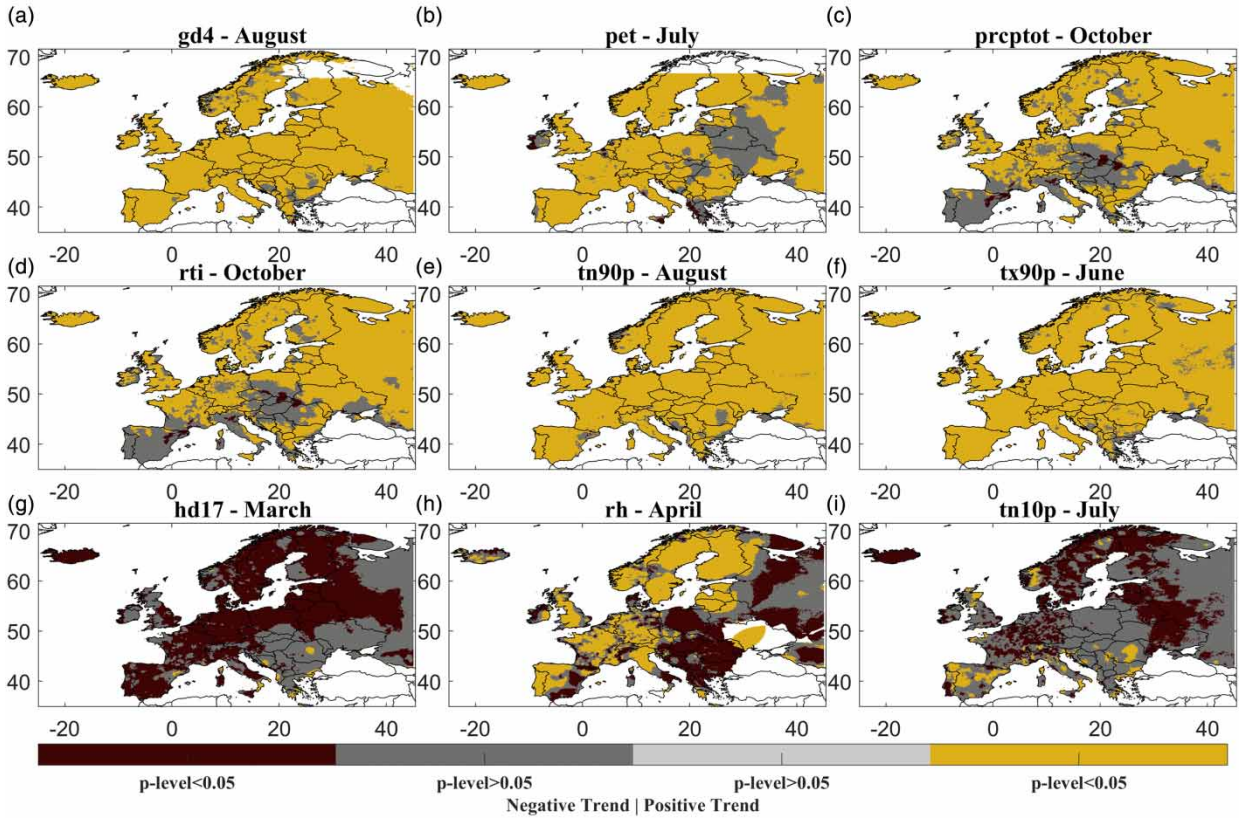

Figure 5 | Spatial trend using Mann–Kendall test across Europe (some of the important climate indices behaviour in particular month – dark red is a negative trend with significance level <–0.05 and dark yellow is a positive trend with significance level <–0.05, dark and light shades of grey are negative and positive trend with a significance level >0.05). Please refer to the online version of this paper to see this figure in colour: http://dx.doi.org/10.2166/wcc.2023.183.

In terms of seasonality for the European region during winter (DJF) there is an increasing trend in spi-1, spei-1, spei-1 and spei-3 (drought indices), bio20 (global radiation indices), mi, utci and wci (multi-element indices), dr1mm, prcptot, rti and rx5d (precipitation indices), slp (sea level pressure indices), ogs6 and ogs10 (temperature indices) and decreasing trend in

Downloaded from http://iwaponline.com/jwcc/article-pdf/14/9/3112/1301084/jwc0143112.pdf
by guest

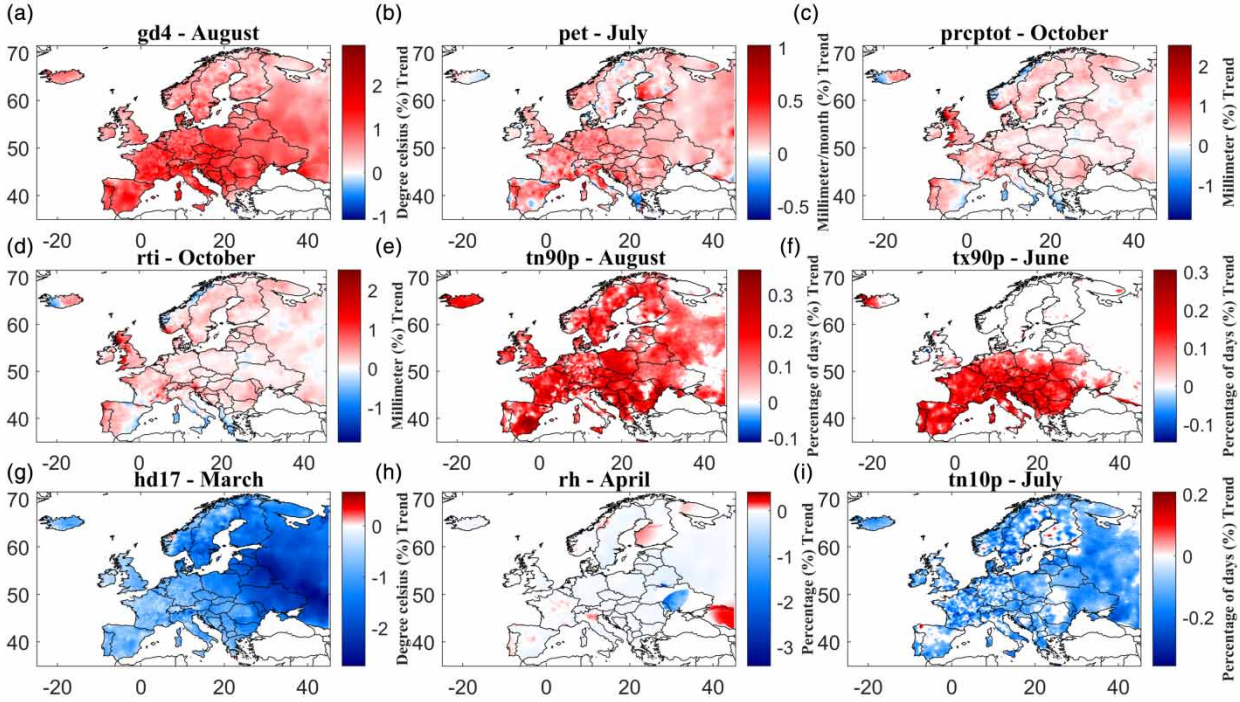

Figure 6 | Spatial trend using Sen's slope estimator across Europe (some of the important climate indices behaviour in particular month – red represents a positive change in the magnitude of the trend, white represents zero, and blue represents a negative change in the magnitude of the trend). Please refer to the online version of this paper to see this figure in colour: http://dx.doi.org/10.2166/wcc.2023.183.

cdd and dd (precipitation indices), dtr and etr (temperature indices), spring (MAM) there is an increasing trend in spei-9 (drought indices), mi and utci (multi-element indices), csd, dtr, su and vdtr (temperature indices) and decreasing trend in scPDSI (drought indices), cdd (precipitation indices), summer (JJA) there is an increasing trend in csd, dtr, etr, su, and tr (temperature indices), fgcalm (wind speed indices) and decreasing trend in PHDI, scPDSI, spei-1, spei-3, spei-6, spei-9, and WPLM (drought indices), dr3mm (precipitation indices), ogs6 (temperature indices), autumn (SON) there is an increasing trend in spi-1 (drought indices), mi and utci (multi-element indices), prcptot, rti and rx5d (precipitation indices), csd, ogs10, su and tr (temperature indices), fgcalm (wind speed indices) and decreasing trend in PHDI, scPDSI, spei-6, spei-9 and WPLM (drought indices), dtr (temperature indices). The one which does not follow an annual cycle but is season based with the highest magnitude of change during winter (DJF) with an increasing trend was recorded for utci which has a 0.13 indice value in January and decreasing trend for etr which is 0.02 °C value in December, spring (MAM) with an increasing trend recorded for utci which is 0.07 indice value in March and decreasing trend for cdd which is 0.01 days in March and May, summer (JJA) with an increasing trend recorded for fgcalm which is 0.28 days in June and decreasing trend for dr3mm which is 0.01 days in June, autumn (SON) with an increasing trend recorded for rti and prcptot which is 0.18 mm in October. The highest monthly recorded decreasing trend is bio20 which is 0.13 W/m^2 in May. One of the climate indices fgcalm shows an increasing trend in the Mann–Kendall test however Sen's slope indicates a negative magnitude of change which is 0.69 days in July. Country-specific trend analysis from Supplementary Table S2 indicates regions from Europe highly influenced by various climate indices inclusive of experiencing increasing or decreasing trends over the month. Figure 7 is the visualization of Supplementary Table S2 but for climate indices with magnitude >0.5%.

4. DISCUSSION

Climate indices are essential for analyzing the change and influence of climate on various sectors of society to provide stakeholders with information on the state of the climate. The seasonal trends of climate indices indicated a considerable change across seasons, indicating the necessity to undertake climate research at diverse time scales in order to understand the causes and implications of climate change (Peña-Angulo *et al.* 2020). In this study, efforts are made to calculate a series of monthly

Downloaded from http://iwaponline.com/jwcc/article-pdf/14/9/3112/1301084/jwc0143112.pdf
by guest

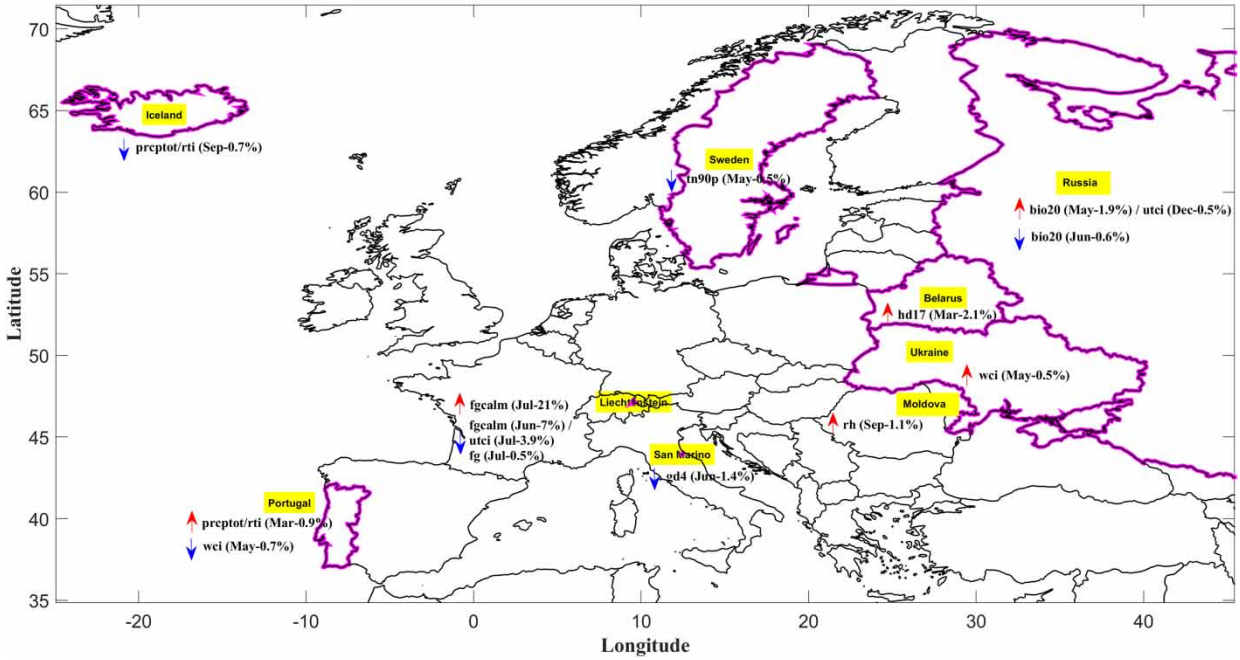

Figure 7 | Monitoring climate indices nature and magnitude of trend (red (blue) arrow pointing upwards (downwards) shows the nature of trend is increasing (decreasing). Countries are highlighted in yellow for the specific climate indices that had magnitude of change per month >0.5%). Please refer to the online version of this paper to see this figure in colour: http://dx.doi.org/10.2166/wcc.2023.183.

climate indices by using long-term weather datasets with high resolution and European regional coverage with information of real-world representation; direction and magnitude are also analyzed. Most studies have been conducted with the objective of quantifying the extremes through studies of temperature and precipitation climate indices or focusing on the 27 core extreme climate indices (Peterson *et al.* 2001). Other, less common climate indices have a significant impact on agriculture, environmental/ecological, hydrology, health, tourism and recreation.

The result and analysis of the study related to the monthly correlation of 74 climate indices in Europe during the period of 1950–2021 indicate that using Pearson, Kendall, and Spearman techniques for various climate indices showcases that Pearson had a marginal higher difference followed by Kendall and Spearman in comparison. The high positive (>0.80) and negative correlation (<–0.80) throughout the year, various seasons and months indicate the significance of each of the indices (not derived from similar weather datasets). Other indices than temperature and precipitation which are repetitive for most of the seasons and months include global radiation, heat index, mould index, potential evapotranspiration, sea level pressure and wind chill index. Potential Evapotranspiration has importance not only during the summer months but also during winter as it has a high correlation with global radiation and sea level pressure. Hence, computation and selection of potential evapotranspiration method plays a significant role. For summer months temperature difference below and above 17 °C is of major relevance to the minimum and maximum temperature derived temperature indices. Some of the temperature derived indices and precipitation indices are highly negatively correlated for the summer months which is quite obvious. Temperature indices computed based on temperature <0 °C (cold) are also highly negatively correlated with the global radiation and temperature derived indices using minimum and maximum air temperature for winter, spring and autumn. None of the drought based indices shows a strong correlation with any of the other climate indices. The importance of the correlation as a strength of the association between climatic variables is a key to confirming that not all climate indices follow the annuity or seasonality (monthly patterns of winter (DJF), spring (MAM), summer (JJA), autumn (SON)). So usage in climate research with an assumption and division based on seasonality and annual computation of the following indices might hide the ground reality.

It is essential to realise that the long-term climate history has inherent uncertainties that exhibit a rapid trend reversal. However, previous research has indicated a similar conclusion based on various indices such as in winter, significant rising precipitation trends during the 20th century dominate both average precipitation intensity and moderately intense occurrences, length of dry spells grew insignificantly, summer precipitation indices show few significant changes, negligible

Downloaded from http://iwaponline.com/jwcc/article-pdf/14/9/3112/1301084/jwc0143112.pdf
by guest

drying trends over Scandinavia, wetting trends over Central and Western Europe from 1921 to 1999, length of summer dry periods rose insignificantly, temperature distribution warm and cold tails warmed, significantly low cold tail values for maximum and minimum temperature in early 1940, winter warming from 1946 to 1999, summer warming is more in the first half of the century (Moberg & Jones 2005). In the European region from 1979 to 2017, temperature indices demonstrate that cold days and nights had negative trends, whereas warm days and nights had a positive trend, the precipitation indices showed a positive trend in Northern and Central Europe, whereas negative trend in Western Europe (Peña-Angulo *et al.* 2020). For European regions in the future significant rise in the summer heat, Mediterranean regions were vulnerable, positive trend in spring and fall, cold evenings will be less common, the frequency of warm days decrease, cold periods will be less frequent and intense with a significant fall in Northern Europe, heavy precipitation days to rise in central and northern Europe, a decrease in Mediterranean locations, increase in midsummer heavy precipitation days, summer and autumn with fewer wet days but higher rainfall volumes, Baltic nations and northern regions with increase in number of rainy days, changes in drought patterns, dryness over the Mediterranean, droughts will become less common in Europe (Cardell *et al.* 2020). Because the 1950s were a relatively dry decade in Central Europe, drought trends estimated for 1951–2015 are similar in direction but less in magnitude in comparison to 10 years shorter period 1961–2015, drying tendencies were seen in spring but were less prominent in summer, whereas wetting trends were observed in fall and winter, drought and high precipitation increase occurred concurrently at multiple locations in spring (Hänsel *et al.* 2019). For Western Europe from 1851 to 2018, spi-3 with a negative trend in summer, a decrease in severe drought during winter, spi-12 magnitude trends showed spatial differences with a positive trend in North France, Germany, British and Irish Isles, negative trends in Southeast of Iberian Peninsula, Balkans, and Italy, long-term drought patterns over Western Europe are statistically non-significant (Vicente-Serrano *et al.* 2021). For the European region trend analysis indicates spei-12 and scPDSI, most nations in Mediterranean and Central Europe show a substantial decreasing trend from 1902–2019, whereas countries in Northern Europe show positive trends, spi-12 follow the precipitation trend decrease in frequency from 2001–2019, frequency of drought has increased in Central Europe and Mediterranean in 2001–2019 (Ionita & Nagavciuc 2021). Wind indices displayed a negative trend in the north not statistically significant in the majority of the European region and a positive trend in the south particularly in spring and summer (Peña-Angulo *et al.* 2020). Since 1979, bioclimatic indices such as utci have increased by 1 °C indicating an increase in heat stress for Europe (Di Napoli *et al.* 2018). Bioclimatic indices indicate a cold-related stress decline compared to 1970 in colder European cities and Northern Europe with more decline, heat stress indicates an upward trend from 1976 to 2018 in all cities (Founda *et al.* 2019).

The visualization indicates that the standard precipitation index (spi) and standard precipitation evapotranspiration index (spei) are mostly of similar types of drought categories and can be used as an alternative during the unavailability of data to indicate the drought or wet conditions for Europe. However, drought values of spei are lower than spi. Combined indices – mi indicates it is not just temperature or relative humidity but the combined effect of temperature and relative humidity which is prevalent in the European region. utci indicates a colder experience than the minimum air temperature during winter and for summer it feels less warm than the maximum air temperature. wci indicates an approximately similar minimum and maximum air temperature. This indicates that the relative humidity and global radiation are prevailing in Europe which makes it significant to have a warmer or colder body experience than the normal temperature. Not much variation is observed among seasonality in drought indices PHDI, scPDSI and WPLM, the significant change is relatively low in Northern, Eastern, and Southeastern Europe with increasing trend and Southern, Western Europe with decreasing trend. A similar trend is observed in spi and spei with various frequencies of months 1, 3, 6, 9, 12, and 24. The drought indices with an increase in the frequency of months indicate a more increasing trend in the European regions discussed above. The heat index across Eastern Europe is increasing across all the months but for Ukraine from January to May, July and November it is decreasing, ice days decrease over the period of winter and spring in Northern, Eastern, Southeastern Europe. Increasing precipitation (prcptot, rx1day, rx5d, sdii) direction and magnitude in Northern Europe during winter however longer drier periods were observed resulting in a focus on compound analysis for such effects. Ukraine shows maximum variance along the seasons for relative humidity and southern Russia for sea level pressure. Cold days (cfd, fd) tend to decrease for the winter season whereas warmer days tend to increase for the summer season in Central and Eastern Europe. Mean, minimum and maximum air temperature increases, whereas mean temperature <17 °C decreases significantly across most zones of the European region spatially. Difference between maximum and minimum air temperature (dtr,etr,vdtr) during winter shows decreasing trend with ~0.1 °C magnitude of change negatively for Northern, Central (some regions) and Eastern Europe, but positively for Southern and Western Europe.

Downloaded from http://iwaponline.com/jwcc/article-pdf/14/9/3112/1301084/jwc0143112.pdf
by guest

Mann–Kendall and Sen's slope test indicates there has been an increasing trend in standard precipitation index at 3, 6, 9, 12, and 24 months, potential evapotranspiration, heat index, precipitation derived indices such as days more than 1 mm/total days, 10 mm, 20 mm, 50 mm, 95 percentile, total, 95 percentile/total, 99 percentile/total of precipitation. Warm, very warm days, warm spell duration and nights are of increasing nature. The increasing trend of warmer temperatures is counterbalanced by the decreasing trend in frost days, very cold days, zero crossing days, and cold spell duration. Standard precipitation evapotranspiration indices 12 and 24 show a decreasing trend which contradicts the spi behaviour. Wind speed and days with wind speed >10.8 m/s, relative humidity shows a decreasing trend. Global radiation, sea level pressure, universal thermal climate index, wind chill index, wet days of >1 mm, spi and spei for time-scale of 1 month show an increasing trend; whereas dry days, longest dry periods, diurnal temperature range, and extreme temperature range show a decreasing trend in the winter season. Summer days, diurnal temperature range, tropical nights, extreme temperature range, calm days show an increasing trend; whereas precipitation ≥3 mm, growing season 6 days with >5 °C, drought indices such as PHDI, scPDSI, WPLM, spei 1,3,6,9 months shows a decreasing trend in the summer season. Maximum percentage change of magnitude increasing trend has been observed in the sum of days with mean air temperature >4 °C at 0.93 °C (August), calm days with average wind speed ≤ 2 m/s at 0.28 days (June), total precipitation and days of total precipitation ≥1 mm at 0.18 mm (October), universal thermal climate index at 0.15 indice value (July), potential evapotranspiration at 0.14 mm/day (July), global radiation at 0.12 W/m^2 (April) and decreasing trend has been observed in heating degree days with mean air temperature <17 at 1.03 °C (January), calm days with average wind speed ≤ 2 m/s at 0.69 days (July), global radiation at 0.13 W/m^2 (May), relative humidity at 0.11% (December) across Europe.

European countries which would experience the highest possible change of climate indices increasing trend with >1% change and p-value < 0.05 of gd4 during August are Bosnia and Herzegovina (1.28 °C), Slovakia, San Marino, Croatia, Czechia, Montenegro, Slovenia, Republic of Serbia, Italy, Austria, Hungary, France, Malta, Andorra, Moldova, Poland, Luxembourg, Belgium, Portugal, Spain, Romania and Albania (1 °C), decreasing trend with >1% change and p-value < 0.05 of hd17 during January are Belarus (1.60 °C), Latvia, Estonia, Ukraine, San Marino, Slovenia, Croatia, Hungary, Poland, Montenegro, Slovakia, Republic of Serbia, Denmark, Czechia, Andorra, Iceland, Germany, Belgium, and Netherlands (1 °C). These countries experienced more warmer days during August and fewer colder days during January. Liechtenstein undergoes lower wind speed by 7 days during June and higher wind speed by 21 days during July. The universal thermal climate index of Liechtenstein increased by 3.88 indices value during July. High wind and high thermal climate indices were experienced by the Liechtenstein region during July. San Marino experienced warmer days during June by 1.39 °C. Portugal experienced more wind chill index of 0.72 indice value during May. Belarus experienced warmer days by 2.13 °C during March, Russia with a radiation decline of 1.92 W/m^2 during May, and Moldova with relative humidity by 1.07% during September. The indices which show a high percentage of change in both direction and magnitude are bio20, fgcalm, gd4, hd17, and utci. The indices which show a significant increase but a relatively low decrease in direction and magnitude of change are gd4, tn90p, and utci whereas the indices which show a significant decrease but relatively low increase in direction and magnitude of change are hd17 and rh.

5. CONCLUSION

To summarize, climate indices must be distinguished for each region according to whether they follow annual, seasonal, or monthly trends. Spatial patterns of climate indices indicate differences between annual, seasons and months for some of the analyzed climate indices. Furthermore, indices which follow a trend require a significance level check. If there is an increase or decrease in trend or magnitude of change for Europe overall it would still undergo bisection of country by country to add more relevant information for the performance of the indices. Various correlations would also add information about the inter-dependability of the various climate indices which might highlight if further multivariate analysis needs to be carried out. We already acknowledged the importance of potential evapotranspiration (pet) and in future, spatiotemporal trend analysis of climate indices that requires potential evapotranspiration for computation could be assessed with different evapotranspiration methods. Wind speed related indices are also of high importance but due to limited spatial data availability at higher resolution, it creates a void of trend assessment. The study can be utilized to define the recent climatic conditions of Europe and also the specific countries could focus on their climate relevant framework based on the trend of the climate indices. In future, multivariate techniques like EOFs could be used to identify the spatial patterns of climate variability and dominant patterns of variability in a dataset for the highly correlated positive and negative climate indices.

Downloaded from http://iwaponline.com/jwcc/article-pdf/14/9/3112/1301084/jwc0143112.pdf
by guest

Further investigations would be required to understand how true it is to the ground reality based on the stakeholder experiences.

The most important findings from this study are summarized as follows:

- Climate indices indicate a monthly variability and the selection of any studies based on seasonality or annually leads to more uncertainty in assessments.
- Climate indices correlation values could be useful for determining the month, seasonal and annual compound event pairs that are highly correlated either positively or negatively.
- Climate index showing the highest increasing (decreasing) trend during all months is gd4 (hd17) across Europe. Maximum increase of +0.93 °C in August (gd4) and decrease of −1.03 °C in July (hd17).
- Country-specific data reveals more information such as climate indices abrupt magnitude of change/month and experiences due to increasing or decreasing trends over a specific European region.
  (a) Increasing trend results in fewer windy days (fgcalm – 7 days, June) and experience warmer (utci – 3.88 indice value, July) in Liechtenstein, warmer (gd4 – 1.39 °C, June) in San Marino, high wind speed and temperature (wci – 0.72 indice value, May) in Portugal.
  (b) Decreasing trend results in high windy days (fgcalm – 21 days, July) in Liechtenstein, more warmer days (hd17 – 2.13 °C, March) in Belarus, less radiation (bio20 – 1.92 W/m^2, May) in Russia, lower relative humidity (rh – 1.07%, September), Moldova.
- The analysis is not limited to the hotspot regions but also the visualization of nearby countries that can result in abrupt change over 72 years through various climate indices, which could be important for the stakeholder from a decision-making and hazard control perspective in response to shifting trends.

ACKNOWLEDGEMENTS

We acknowledge the E-OBS dataset from the EU-FP6 project UERRA (https://www.uerra.eu) and the Copernicus Climate Change Service, and the data providers in the ECA&D project (https://www.ecad.eu).

AUTHORS CONTRIBUTION

S.C.D., G.L., N.R., and M.I. conceptualized the study. S.C.D. and M.I. acquired data; S.C.D. and M.I. prepared the methodology. S.C.D. did analysis; S.C.D. did programming. G.L., N.R., M.I. did project administration; G.L., N.R., and M.I. supervised the study,S.C.D. wrote the original draft;S.C.D., G.L., N.R., and M.I. reviewed the article.

DATA AVAILABILITY STATEMENT

All relevant data are included in the paper or its Supplementary Information. Download input data (steps), code used for the statistical analysis (R and matlab) and output data generated from: https://zenodo.org/record/8250835.

CONFLICT OF INTEREST

The authors declare there is no conflict.

REFERENCES

Alexander, L. V., Zhang, X., Peterson, T. C., Caesar, J., Gleason, B., Klein Tank, A. M. G., Haylock, M., Collins, D., Trewin, B. & Rahimzadeh, F. 2006 Global observed changes in daily climate extremes of temperature and precipitation. *J. Geophys. Res. Atmos* **111**, D05109.

Almazroui, M., Islam, M. N., Dambul, R. & Jones, P. D. 2014 Trends of temperature extremes in Saudi Arabia. *Int. J. Climatol.* **34**, 808–826. https://doi.org/10.1002/joc.3722.

Brohan, P., Kennedy, J. J., Harris, I., Tett, S. F. B. & Jones, P. D. 2006 Uncertainty estimates in regional and global observed temperature changes: a new data set from 1850. *J. Geophys. Res. Atmos.* **111**, 1–21. https://doi.org/10.1029/2005JD006548.

Callan, T., Nolan, B. & Whelan, C. T. 1993 Resources, deprivation and the measurement of poverty. *J. Soc. Policy* **22**, 141–172. https://doi.org/DOI: 10.1017/S0047279400019280.

Cardell, M. F., Amengual, A., Romero, R. & Ramis, C. 2020 Future extremes of temperature and precipitation in Europe derived from a combination of dynamical and statistical approaches. *Int. J. Climatol.* **40**, 4800–4827. https://doi.org/10.1002/joc.6490.

Cornes, R. C., van der Schrier, G., van den Besselaar, E. J. M. & Jones, P. D. 2018 An ensemble version of the E-OBS temperature and precipitation data sets. *J. Geophys. Res. Atmos* **123**, 9391–9409. https://doi.org/10.1029/2017JD028200.

Downloaded from http://iwaponline.com/jwcc/article-pdf/14/9/3112/1301084/jwc0143112.pdf
by guest

Dai, A. 2011 Drought under global warming: a review. *Wiley Interdiscip. Rev. Clim. Change* **2**, 45–65.
Di Napoli, C., Pappenberger, F. & Cloke, H. L. 2018 Assessing heat-related health risk in Europe via the Universal Thermal Climate Index (UTCI). *Int. J. Biometeorol.* **62**, 1155–1165. https://doi.org/10.1007/s00484-018-1518-2.
Eyshi Rezaei, E., Webber, H., Gaiser, T., Naab, J. & Ewert, F. 2015 Heat stress in cereals: mechanisms and modelling. *Eur. J. Agron.* **64**, 98–113. https://doi.org/10.1016/j.eja.2014.10.003.
Felix, M. L., Kim, Y. K., Choi, M., Kim, J. C., Do, X. K., Nguyen, T. H. & Jung, K. 2021 Detailed trend analysis of extreme climate indices in the Upper Geum River Basin. *Water (Switzerland)* **13**. https://doi.org/10.3390/w13223171.
Forzieri, G., Cescatti, A., e Silva, F. B. & Feyen, L. 2017 Increasing risk over time of weather-related hazards to the European population: a data-driven prognostic study. *Lancet Planet. Health* **1**, e200–e208.
Founda, D., Pierros, F., Katavoutas, G. & Keramitsoglou, I. 2019 Observed trends in thermal stress at European cities with different background climates. *Atmosphere (Basel)* **10**. https://doi.org/10.3390/atmos10080436.
Hänsel, S., Ustrnul, Z., Łupikasza, E. & Skalak, P. 2019 Assessing seasonal drought variations and trends over Central Europe. *Adv. Water Resour.* **127**, 53–75. https://doi.org/10.1016/j.advwatres.2019.03.005.
Hartmann, D. L., Tank, A. M. G. K., Rusticucci, M., Alexander, L. V., Brönnimann, S., Charabi, Y. A. R., Dentener, F. J., Dlugokencky, E. J., Easterling, D. R. & Kaplan, A. 2013 Observations: atmosphere and surface. In: *Climate Change 2013 the Physical Science Basis: Working Group I Contribution to the Fifth Assessment Report of the Intergovernmental Panel on Climate Change*. (T. F. Stocker, D. Qin, G. -K. Plattner, M. Tignor, S. K. Allen, J. Boschung, A. Nauels, Y. Xia, V. Bex & P. M. Midgley, eds.) Cambridge University Press, Cambridge, pp. 159–254.
Healy, J. D. 2003 Excess winter mortality in Europe: a cross country analysis identifying key risk factors. *J. Epidemiol. Community Health* **57**, 784–789. https://doi.org/10.1136/jech.57.10.784.
Henry, M. 1945 Nonparametric tests against trend. *Econometrica* **13**, 245–259.
Ionita, M. & Nagavciuc, V. 2021 Changes in drought features at the European level over the last 120 ~ years. *Nat. Hazards Earth Syst. Sci.* **21**, 1685–1701. https://doi.org/10.5194/nhess-21-1685-2021.
IPCC, I. 2014 Fifth assessment synthesis report. *Clim. Change* 1–15.
Kahiluoto, H., Kaseva, J., Hakala, K., Himanen, S. J., Jauhiainen, L., Rötter, R. P., Salo, T. & Trnka, M. 2014 Cultivating resilience by empirically revealing response diversity. *Global Environ. Change* **25**, 186–193. https://doi.org/10.1016/j.gloenvcha.2014.02.002.
Kendall, M. G. 1975 *Rank Correlation Methods*.
Liverman, D. M. 2013 Vulnerability to global environmental change. In: *Global Environmental Risk*. Routledge, pp. 201–216.
Mäkinen, H., Kaseva, J., Trnka, M., Balek, J., Kersebaum, K. C., Nendel, C., Gobin, A., Olesen, J. E., Bindi, M., Ferrise, R., Moriondo, M., Rodríguez, A., Ruiz-Ramos, M., Takáč, J., Bezák, P., Ventrella, D., Ruget, F., Capellades, G. & Kahiluoto, H. 2018 Sensitivity of European wheat to extreme weather. *F. Crop. Res.* **222**, 209–217. https://doi.org/10.1016/j.fcr.2017.11.008.
Moberg, A. & Jones, P. D. 2005 Trends in indices for extremes in daily temperature and precipitation in central and Western Europe, 1901-99. *Int. J. Climatol.* **25**, 1149–1171. https://doi.org/10.1002/joc.1163.
Outten, S. & Sobolowski, S. 2021 Extreme wind projections over Europe from the Euro-CORDEX regional climate models. *Weather Clim. Extremes* **33**, 100363. https://doi.org/10.1016/j.wace.2021.100363.
Peña-Angulo, D., Reig-Gracia, F., Domínguez-Castro, F., Revuelto, J., Aguilar, E., van der Schrier, G. & Vicente-Serrano, S. M. 2020 ECTACI: European climatology and trend atlas of climate indices (1979–2017). *J. Geophys. Res. Atmos.* **125**, 1–17. https://doi.org/10.1029/2020JD032798.
Peterson, T. C., Folland, C. C., Gruza, G., Hogg, W., Mokssit, A. & Plummer, N. 2001 *Report on the Activities of the Working Group on Climate Change Detection and Related Rapporteurs 1998–2001. Rep. WCDMP-47, WMO-TD 1071 143*.
Razavi, T., Switzman, H., Arain, A. & Coulibaly, P. 2016 Regional climate change trends and uncertainty analysis using extreme indices: a case study of Hamilton, Canada. *Clim. Risk Manage.* **13**, 43–63. https://doi.org/10.1016/j.crm.2016.06.002.
Rimbu, N., Lohmann, G. & Ionita, M. 2014 Interannual to multidecadal Euro-Atlantic blocking variability during winter and its relationship with extreme low temperatures in Europe. *J. Geophys. Res. Atmos* **119**, 13–621.
Rimbu, N., Lohmann, G., Werner, M. & Ionita, M. 2017 Links between central Greenland stable isotopes, blocking and extreme climate variability over Europe at decadal to multidecadal time scales. *Clim. Dyn.* **49**, 649–663.
Roy, S. S. & Balling, R. C. 2004 Trends in extreme daily precipitation indices in India. *Int. J. Climatol.* **24**, 457–466. https://doi.org/10.1002/joc.995.
Ruiz-Alvarez, O., Singh, V. P., Enciso-Medina, J., Ontiveros-Capurata, R. E. & dos Santos, C. A. C. 2020 Observed trends in daily extreme precipitation indices in Aguascalientes. *Mexico. Meteorol. Appl.* **27**, 1–20. https://doi.org/10.1002/met.1838.
Schneider, T., O'Gorman, P. A. & Levine, X. J. 2010 Water vapor and the dynamics of climate changes. *Rev. Geophys.* **48**, 1–22. https://doi.org/10.1029/2009RG000302.
Sen, P. K. 1968 Estimates of the regression coefficient based on Kendall's tau. *J. Am. Stat. Assoc.* **63**, 1379–1389. https://doi.org/10.1080/01621459.1968.10480934.
Seneviratne, S. I. 2012 Historical drought trends revisited. *Nature* **491**, 338–339. https://doi.org/10.1038/491338a.
Seneviratne, S. I., Nicholls, N., Easterling, D., Goodess, C. M., Kanae, S., Kossin, J., Luo, Y., Marengo, J., Mc Innes, K., Rahimi, M., Reichstein, M., Sorteberg, A., Vera, C., Zhang, X., Rusticucci, M., Semenov, V., Alexander, L. V., Allen, S., Benito, G., Cavazos, T., Clague, J., Conway, D., Della-Marta, P. M., Gerber, M., Gong, S., Goswami, B. N., Hemer, M., Huggel, C., Van den Hurk, B., Kharin, V. V., Kitoh,

Downloaded from http://iwaponline.com/jwcc/article-pdf/14/9/3112/1301084/jwc0143112.pdf
by guest

A., Klein Tank, A. M. G., Li, G., Mason, S., Mc Guire, W., Van Oldenborgh, G. J., Orlowsky, B., Smith, S., Thiaw, W., Velegrakis, A., Yiou, P., Zhang, T., Zhou, T. & Zwiers, F. W. 2012 Changes in climate extremes and their impacts on the natural physical environment. *Manag. Risks Extrem. Events Disasters to Adv. Clim. Chang. Adapt. Spec. Rep. Intergov. Panel Clim. Chang.* **9781107025**, 109–230. https://doi.org/10.1017/CBO9781139177245.006.

Sergio, F., Blas, J. & Hiraldo, F. 2018 Animal responses to natural disturbance and climate extremes: a review. *Glob. Planet. Change* **161**, 28–40.

Sillmann, J., Kharin, V. V., Zhang, X., Zwiers, F. W. & Bronaugh, D. 2013 Climate extremes indices in the CMIP5 multimodel ensemble: part 1. Model evaluation in the present climate. *J. Geophys. Res. Atmos* **118**, 1716–1733. https://doi.org/10.1002/jgrd.50203.

Smith, T. M. & Reynolds, R. W. 2005 A global merged land–air–sea surface temperature reconstruction based on historical observations (1880–1997). *J. Clim.* 18, 2021–2036. https://doi.org/10.1175/JCLI3362.1.

Trenberth, K. E., Dai, A., Van Der Schrier, G., Jones, P. D., Barichivich, J., Briffa, K. R. & Sheffield, J. 2014 Global warming and changes in drought. *Nat. Clim. Change* **4**, 17–22.

Vicente-Serrano, S. M., Domínguez-Castro, F., Murphy, C., Hannaford, J., Reig, F., Peña-Angulo, D., Tramblay, Y., Trigo, R. M., Mac Donald, N., Luna, M. Y., Mc Carthy, M., Van der Schrier, G., Turco, M., Camuffo, D., Noguera, I., García-Herrera, R., Becherini, F., Della Valle, A., Tomas-Burguera, M. & El Kenawy, A. 2021 Long-term variability and trends in meteorological droughts in Western Europe (1851–2018). *Int. J. Climatol.* **41**, E690–E717. https://doi.org/10.1002/joc.6719.

First received 15 March 2023; accepted in revised form 25 July 2023. Available online 8 August 2023

Downloaded from http://iwaponline.com/jwcc/article-pdf/14/9/3112/1301084/jwc0143112.pdf
by guest

Chapter 4

Hotspot movement of compound events on the Europe continent

Research Question: *"How do the spatial and temporal dynamics of compound climate events across Europe, identified through high correlated pairs of climate indices with high spatial resolution and temporal scale, reveal the hotspot movements, high-risk zones, and their impacts on land cover and population over the past seven decades?"*

Synthesis:

Climate indices are often used as a climate monitoring tool, allowing us to understand how the frequency, intensity, and duration of extreme weather events are changing over time. Here, based on complex statistical analysis we identify highly correlated significant pairs of compound events at the highest spatial resolution, on a monthly temporal scale across Europe. Continental-scale monthly analysis unleashes information on compound events such as high-risk zones, hotspots, monthly shifts of hotspots and trends, risk exposure to land cover and population, and identification of maximum increasing trends. While there are many studies on single or compound climate extremes there are only a few studies that addresses the relationship between pairs of hazards, the incorporation of bioclimatic indices, the determination of a grid best-fit copula approach, and the outlining relevance of this work of compound event risks with exposures. In this respect, here, using 27-bivariate and 10-trivariate copula models, we show that the different hazard pairs have high combined risks of indices related to radiation, temperature, evapotranspiration, bioclimatic-based indices, such as the universal thermal climate index, wind chill index, and heat index, mainly over the northern and
eastern European countries. Furthermore, we show that over the last 7 decades, agricultural and coastal areas are highly exposed to the risks of defined hotspots of compound events. In some of the hotspots of compound events-identified by clusters, there is no monthly shifts of hotspots, leading to higher impacts when compounded. Future work needs to integrate the framework and process to identify other compound pairs.

Authors contributions:

Conceptualization: Smit Chetan Doshi (S.C.D.), Gerrit Lohmann (G.L.), Monica Ionita (M.I.). Data Acquisition: S.C.D., M.I. Methodology: S.C.D, M.I. Analysis: S.C.D. Programming: S.C.D. Funding

acquisition: M.I. Project administration: G.L., M.I. Supervision: G.L., M.I. Writing- original draft: S.C.D. Review: S.C.D., G.L., M.I..

This chapter is based on already published study in the Scientific Reports, Nature Portfolio (Doshi et al., 2023a). Appendix B includes the supplementary information for this paper. Please note that the supplementary figures and tables in common can be found in Appendix A. Processed data and code to produce the results are available at: https://doi.org/10.5281/zenodo.10014462.

scientific reports

Check for updates

OPEN

Hotspot movement of compound events on the Europe continent

Smit Chetan Doshi[1,2]✉, Gerrit Lohmann[1,2] & Monica Ionita[1,3]

Climate indices are often used as a climate monitoring tool, allowing us to understand how the frequency, intensity, and duration of extreme weather events are changing over time. Here, based on complex statistical analysis we identify highly correlated significant pairs of compound events at the highest spatial resolution, on a monthly temporal scale across Europe. Continental-scale monthly analysis unleashes information on compound events such as high-risk zones, hotspots, monthly shifts of hotspots and trends, risk exposure to land cover and population, and identification of maximum increasing trends. While there are many studies on single or compound climate extremes there are only a few studies that addresses the relationship between pairs of hazards, the incorporation of bioclimatic indices, the determination of a grid best-fit copula approach, and the outlining relevance of this work of compound event risks with exposures. In this respect, here, using 27-bivariate and 10-trivariate copula models, we show that the different hazard pairs have high combined risks of indices related to radiation, temperature, evapotranspiration, bioclimatic-based indices, such as the universal thermal climate index, wind chill index, and heat index, mainly over the northern and eastern European countries. Furthermore, we show that over the last 7 decades, agricultural and coastal areas are highly exposed to the risks of defined hotspots of compound events. In some of the hotspots of compound events-identified by clusters, there is no monthly shifts of hotspots, leading to higher impacts when compounded. Future work needs to integrate the framework and process to identify other compound pairs.

Extreme weather events, such as heatwaves, droughts, floods and storms (including cyclones) have become more frequent and severe in recent years due to the impact of climate change (IPCC, 2021 and the references therein). Extreme events are of major interest due to their potential to produce significant harm and repercussions on people, infrastructure, and environment[1]. However, we still need a better overview and an in-depth understanding of what happens when two or more of these extreme events occur simultaneously, creating what's known as a compound extreme event. Compound extreme events can result in devastating consequences for human and natural systems, and understanding their likelihood and impact is crucial for effective risk management and decision-making[2]. Compound events which are two or more events occurring concurrently or consecutively would increase the impacts and cause major extreme consequences that may not necessarily be extreme occurrences independently[3–6]. For example, in central Europe and western Russia during 2003 and 2010, severe drought conditions concurrent with extreme heat waves produce more damage than either excessive heat or extreme dryness would have alone[7]. Other compound event examples includes April 2021 and 2022, with Central Europe experiencing consecutive frost days following warm spring which highly impacted the crop yield[8]. Experience of compound floods due to coincidence of storm surges, waves, tides, precipitation and discharges of river are already identified in many locations of Europe (e.f. over the period 1870–2016, 23 compound flood events were recorded[9]). Extratropical cyclones were identified due to co-occurrences of precipitation and wind across northwestern central Europe during winter season[10], where events in Great Britain showcased a time difference of 0 to 13 days between peak discharge and extreme wind[11]. Further, the latest IPCC report about "weather and climate extreme events in changing climate" has mentioned that the likelihood of compound events has probably grown in past and will continue to rise with further climate change[12]. It has been suggested that heatwaves and droughts are occurring more often, with hot, dry, and windy events leading to long-lasting fire hazards. Moreover, the number of compound flooding due to extreme rainfall, storm surge, and river discharges also increased[12]. Hazards warnings can be evaluated by climate and weather variables[13]. Numerous societally significant extremes are not well represented by a single climatic variable at a defined location and time, which leads us to focus our

[1]Alfred Wegener Institute Helmholtz Center for Polar and Marine Research, Bremerhaven, Germany. [2]Physics Department, University of Bremen, 28359 Bremen, Germany. [3]Forest Biometrics Laboratory—Faculty of Forestry, "Ștefan cel Mare" University of Suceava, Universității Street, no. 13, 720229 Suceava, Romania. ✉email: smitdoshi5@gmail.com

study to account for multiple climate variables and links between extremes of similar or different types in time and space[14]. An effort is required to comprehend the dependence structure among multiple climate variables through multivariate techniques[15–20]. Copula-based multivariate techniques have garnered the most attention to study the interplay between various climatic variables due to the process of creating joint distribution for different marginal distribution of random variables[21,22]. Nevertheless, is challenging to apply the strategy to a highly multivariate situation due to the fact that the majority of copula dependence models are bivariate with higher dimensions produced by nested bivariate copulas[23].

The probabilistic behaviour of extreme events has been investigated in previous research works either through univariate[24–26] or multivariate[13,22,27] approach. Previous studies had lacked in one or several aspects such as considering climate extreme indices to determine compound events through multivariate approach by undergoing straightforward application of copula for development of joint distribution, but this might not hold true and may change regionally at different spatial and temporal scales. Defining correlation coefficient only using one technique to indicate the climate indices dependence strengths between one another can diverge too far from reality in evaluation. There are families of copula and selection of copula methods based on the goodness-of-fit, which is commonly considered the best approach in previous published papers[27,28], but whole study region considering each grid needs to be verified for a proper selection of copula. Recent literature review[29] had highlighted the missing information gaps of covering all the aspects such as dependence of multiple climatic variables, pre-treatment of data, copula selection and statistical examination of fits of the selected copula. It is essential to define the ties (data with similar rank) or autocorrelation and stationarity between the climate extreme indices but smaller temporal scales such as monthly analysis using daily data overcomes the essential requirement as it is less likely to be observed[29]. Most of the compound events are linked with joint probabilities of precipitation and temperature based climate indices but it must be acknowledged there are indices which are physiologically relevant and needs to be assessed in these combination[30–33]. Comparing multiple climate indices, gains added understanding of the climate system and connection through different sectors. With the available daily weather data and known possible indices—74 monthly spatial climate indices are computed which covers multidisciplinary range of indices with integration of bioclimatic indices that is often neglected. Bioclimatic indices, which indicate how the climate affects human physiology, need also to be considered as they vary both seasonally and regionally in Europe[34]. For the temporally compounding of clusters, an identified gap based on persistence of co-occurrences of compound events requires further study[35]. Persistence refers to climatic events that occur in same location for a consecutive time span[36]. This hotspot identification is important from two reasons: first, the identified hotspot have an increased vulnerability even though not extreme in nature, and second if there are co-occurrences at one specific zone than there will be more limited time to make mitigation decision due to similar or different type of compound event.

Here, we depict the first high resolution European hotspot monthly movement of compound events through bivariate and trivariate copula analysis. Hotspot refers to the high joint probability of the identified compound events. Movement is referred to the path followed by these shifts of hotspots across each month. To understand which could be the new hotspots in future and track its movement, trend analysis with maximum increasing trend was identified along with computing the magnitude of change. Monitoring these hotspots movement can help the stakeholders to allocate the resources effectively and if any strategical planning or management is required than, they could prioritize those areas understanding its impact joint probabilities. For warning systems, hotspot movement acts as a predicted path for the evacuation, mitigation or preparation purposes. If previous mitigated regions underlying causes are unidentified, it can relate to the hotspot compound events. Initially hotspots and later on movement through patterns for various compound events are determined by applying a joint copula distribution and evaluation of the joint probabilities are based on the combination of these 74 climate indices. Climate indices are downscaled based on the dependence strength determined by the correlation coefficient from three different techniques and determining the best-fit copula for each of the grid individually from the families of copula for further analysis. This research analyses gaps of missing information[29] such as consideration of climate indices, ties, best-fit copula selection, secondly the computation possible in terms of climate indices from available daily data over a longer period (72 years) and thirdly representation of hotspots plus movements of compound event for Europe at a monthly scale. The compound pairs we would discuss check three criteria (i) high correlation value > 0.6 and < -0.6 for each month (ii) significance value < 0.05 (iii) climate indices computed from different variables (e.g. precipitation, minimum and maximum temperature, radiation, etc.). The graphical representation and analysis would involve best-fit copulas, hazard maps, patterns of hotspots, and risk analysis in conjunction with population density and landuse maps for highly dependent combination of climate indices responsible for compound events, which will be of high importance to many stakeholders across the European region. Based on the interest of the stakeholder these relationships would be useful for estimating the risk of an impact[13].

Results and discussion

Determining compound events

To determine the compound event pairs for bivariate and trivariate analysis it is necessary to first evaluate the correlation and significance values of various combinations of the 74 climate indices (abbreviation elaboration in Table 1) using Pearson, Kendall and Spearman correlation methods. On the basis of climate indices computed, 5402 pairs of combination could be produced, with a wide range of computed values. The correlation and significance values for each method and each month can be visualized in Supplementary Fig. S1. Out of all potential combinations of climate indices and based on the 3 criteria defined above, we look for further analysis of 27 combinations of bivariate analysis and 10 combinations of trivariate analysis. The hazard pairs for each month that have a positive correlation of greater than 0.80 are gtn and gtx, gtn and txn, gtx and tnn, gtx and tnx,

ID	Indices name	Definitions	Units
Drought indices			
PHDI	Palmer hydrological drought index	Time series of palmer hydrological drought index	
scPDSI	Self-calibrated palmer drought severity index	Time series of self-calibrated palmer drought severity index	
spi-1	Standardized precipitation index 1	Standardized precipitation index calculated at 1-month time scale	
spi-3	Standardized precipitation index 3	Standardized precipitation index calculated at 3-month time scale	
spi-6	Standardized precipitation index 6	Standardized precipitation index calculated at 6-month time scale	
spi-9	Standardized precipitation index 9	Standardized precipitation index calculated at 9-month time scale	
spi-12	Standardized precipitation index 12	Standardized precipitation index calculated at 12-month time scale	
spi-24	Standardized precipitation index 24	Standardized precipitation index calculated at 24-month time scale	
spei-1	Standardized precipitation-evapotranspiration index 1	Standardized precipitation-evapotranspiration index calculated at 1-month time scale	
spei-3	Standardized precipitation-evapotranspiration index 3	Standardized precipitation-evapotranspiration index calculated at 3-month time scale	
spei-6	Standardized precipitation-evapotranspiration index 6	Standardized precipitation-evapotranspiration index calculated at 6-month time scale	
spei-9	Standardized precipitation-evapotranspiration index 9	Standardized precipitation-evapotranspiration index calculated at 9-month time scale	
spei-12	Standardized precipitation-evapotranspiration index 12	Standardized precipitation-evapotranspiration index calculated at 12-month time scale	
spei-24	Standardized precipitation-evapotranspiration index 24	Standardized precipitation-evapotranspiration index calculated at 24-month time scale	
WPLM	Weighted palmer drought severity index	Time series of weighted palmer drought severity index	
Global radiation			
bio20	Mean radiation	Average daily global radiation	W/m^2
Multi-element indices			
hi	Heat index	Combines air temperature and relative humidity to determine the human-perceived equivalent temperature	
mi	Mould index	Combined air temperature and relative humidity affecting growth rate of mould. Number of days with a relative humidity over 90% and temperature falls over 10 °C	
pet	Reference evapotranspiration	Using Hargreaves method	mm/day
utci	Universal thermal climate index	Air temperature of reference condition causing the same model response as actual conditions	
wci	Wind chill index	Combines air temperature and wind speed; lowering of body temperature due to the passing-flow of lower-temperature air	
Precipitation indices			
cdd	Longest dry period	Maximum length of consecutive dry days	days
cwd	Longest wet period	Maximum length of consecutive wet days	days
d50mm	Heavy precipitation days	Number of days with precipitation above 50 mm	days
d95p	Very wet days	Days with precipitation > 95th percentile	days
dd	Dry days	Number of days with precipitation less than 1 mm	days
dr1mm	Wet days 1 mm	Total number of wet days ≥ 1 mm	days
dr3mm	Wet days 3 mm	Total number of Wet days ≥ 3 mm	days
prcptot	Total precipitation wet days	Precipitation amount on days ≥ 1 mm	mm
r10mm	Days precipitation ≥ 10mm	Days with daily precipitation amount ≥ 10 mm	days
r20mm	Days precipitation ≥ 20mm	Days with daily precipitation amount ≥ 20 mm	days
r95tot	Percentage precipitation of very wet days	Precipitation at days exceeding the 95th percentile divided by total precipitation	%
r99tot	Precipitation fraction extremely wet days	Precipitation at days exceeding the 99th percentile divided by total precipitation	%
rti	Total precipitation	Total amounts of precipitation	mm
rx1day	Maximum precipitation	Highest amount of daily precipitation	mm
rx5d	Maximum 5 days precipitation	Maximum consecutive 5-day precipitation	mm
sdii	Simple precipitation intensity index	Sum of precipitation in wet days (> 1 mm) divided by number of wet days in the period	mm/day
Relative humidity indices			
rh	Mean relative humidity	Average daily relative humidity	%
Sea level pressure indices			
slp	Mean sea level pressure	Average daily sea level pressure	hPa
Temperature indices			
cfd	Maximum consecutive frost days	Maximum number of consecutive days with TN < 0 °C	days
csd	Maximum consecutive summer days	Maximum number of consecutive summer days with TX > 25 °C	days
csdi	Cold spell duration	Count of days with at least 6 consecutive days when daily minimum temperature < 10th percentile	days
dd17	Difference days above/below TX-17 °C	days TX > 17 °C–days TX < 17 °C	days
dtr	Diurnal temperature range	Mean difference between TX and TN	°C
etr	Extreme temperature range	Difference between the maximum TX and the minimum TN	°C
fd	Frost days	Number of days with TN < 0 °C	days
gd4	Growing degree days	Sum of degree days of TG over 4 °C	°C
Continued			

ID	Indices name	Definitions	Units
gtg	Mean TG	Mean of daily mean air temperature (TG)	°C
gtn	Mean TN	Mean of daily minimum air temperature (TN)	°C
gtx	Mean TX	Mean of daily maximum air temperature (TX)	°C
hd17	Heating degree days	Accumulated degree when TG is below 17 °C	°C
id	Ice days	Number of days with TX < 0 °C	days
ntg	Minimum TG	Minimum value of daily mean air temperature	°C
ogs6	Onset of growing season 6 days	Date of the start of the first span with at least 6 days with TG > 5 °C	days
ogs10	Onset of growing season 10 days	Date of the start of the first span with at least 10 days with TG > 5 °C	days
su	Summer days	Number of days with daily maximum temperature > 25 °C	days
tn10p	Percentage of cold nights	Percentages of days with TN < 10th percentile	%
tn90p	Percentage of warm nights	Percentages of days with TN > 90th percentile	%
tnn	Minimum TN	Minimum of daily minimum air temperature	°C
tnx	Maximum TN	Maximum of daily minimum air temperature	°C
tr	Tropical nights	Number of days with TN > 20 °C	days
tx10p	Percentage of cold days	Percentages of days with TX < 10th percentile	%
tx90p	Percentage of warm days	Percentages of days with TX > 90th percentile	%
txn	Minimum TX	Minimum of daily maximum air temperature	°C
txx	Maximum TX	Maximum of daily maximum air temperature	°C
vcd	Very cold days	Days with TN < 1st percentile	days
vdtr	Mean daily difference dtr	Mean absolute day-to-day difference in dtr	°C
vwd	Very warm days	Days with TX > 99th percentile	days
wsdi	Warm spell duration	Number of days which are part of groups of at least 6 consecutive days when TX > 90th percentile	days
xtg	Maximum TG	Maximum of daily mean air temperature	°C
zcd	Zero crossing days	Number of days with TX > 0 °C and TN < 0 °C	days
Wind speed indices			
fg	Mean of daily FG	Mean of daily mean wind strength	m/s
fg6bft	Number of days with FG ≥ 10.8m/s	Number of days with averaged wind ≥ 10.8m/s	days
fgcalm	Calm days	Number of days with averaged wind ≤ 2m/s	days

Table 1. List of climate indices computed for Europe (1950–2021).

hi and wci, tnn and txn, tnn and txx, tnx and txn, tnx and txx, gtn and txx, hi and pet, pet and wci, pet and utci; pairs with correlation greater than 0.60 are bio20 and gd4, bio20 and gtg, bio20 and gtn, bio20 and hi, bio20 and ntg, bio20 and tnn, bio20 and txn, bio20 and utci, bio20 and wci, bio20 and xtg, bio20 and tnx; and the pairs of bio20 and hd17, cfd and txx, fd and txx (see Data and method for the definition of each index) have correlation less than 0.60. All the aforementioned pairs of climate indices have significance level less than 0.05. These pairs act as a base step for further bivariate analysis and for trivariate analysis. The similar pairs are correlated resulting in a combination of hi, pet and wci for correlation greater than 0.80; bio20, txn and gtn, bio20, wci and hi, bio20, txn and tnn, bio20, tnx, and txn, bio20, gtn and txx, bio20, tnn and txx, bio20, tnx and txx for correlation greater than 0.60; and correlation less than 0.60 results in cfd, txx and bio20, fd, txx and bio20. Figure 1 depicts the maximum correlation value of climate indices pairs using three different techniques. There are compound event pairs which are identified that could be opposite in nature such as hi and wci. Statistically it makes a pass but the physical meaning retains to the rare event, which occurs during transition of winter to summer or vice versa perceived by humans. The winter events perceived in Europe were linked to winter cold spells in North America; the wind related indices bivariate pairs might have relevance with the compound extreme pan-Atlantic[37]. Compound pairs of low radiation and high temperature indices can be a major limiting factor for the crop yield[38]. Linkages between heat and human health has raised awareness, thus the pairs of utci, wci, and hi in relation to temperature and radiation that compounds would help to estimate humans feel with varietal climatic conditions[39]. Interdependence of variables of compound events can result from a number of interacting physical processes such as regional sensitivity to global warming, circulation patterns (high or low pressure system)[40] or natural cycles (El Nino – Southern Oscillation, ENSO)[41].

Overall, from the hazard monthly pairs global radiation indices such as bio20, combined indices such as pet, hi, utci, wci, and some of the temperature indices (cfd, fd, gd4, gtn, gtg, gtx, hd17, ntg, tnn, tnx, txn, txx, xtg) indicates high correlation and significance level less than 0.05 using all three-correlation measures. There are climate indices related to drought, precipitation, relative humidity, sea-level pressure and wind speed which have strong correlation across the list of indices computed but they do not follow throughout annual strong positive or negative correlation hence have been eliminated. However if seasonal or specific month is to be focused then further analysis could be carried out[42]. Supplementary Table S1 indicates those pairs of very high and statistically significant positive (negative) correlation of seasonal and monthly climate indices, which do not fall in the annual cycles. Further, climate indices derived from similar weather data might reveal strong correlation values that must also be eliminated. The strength of correlation values however varies slightly, with Pearson being largest,

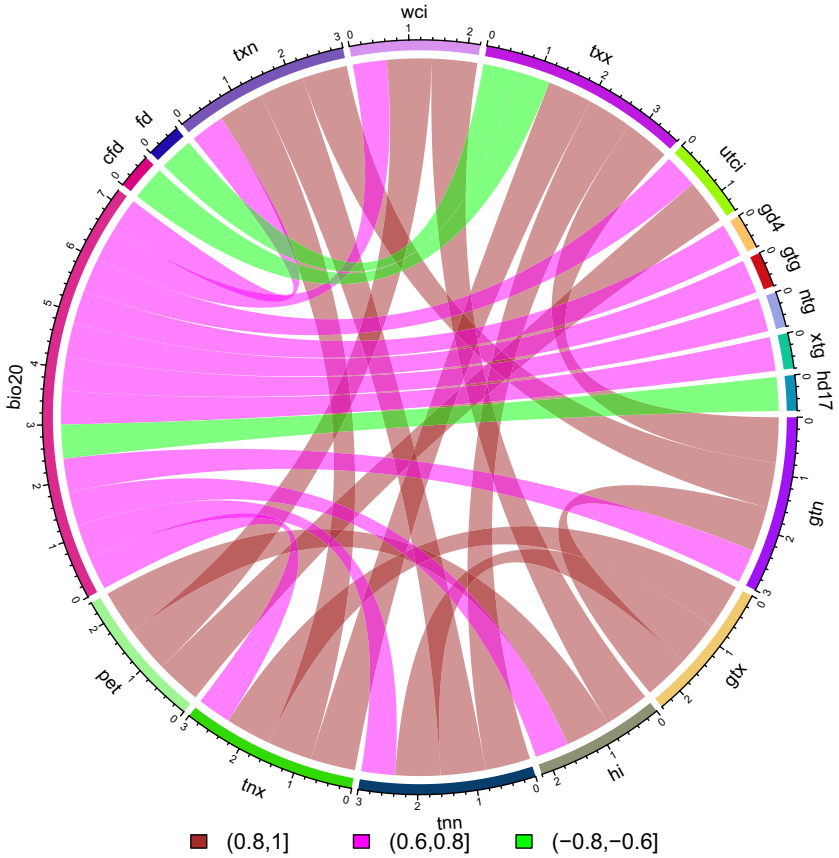

Figure 1. Compound event pairs using correlation coefficient values. Indicating compound event pairs with strong positive (maroon and pink), negative (green) correlation coefficient values, and significance level < 0.05 obtained from 74 climate indices, Pearson, Kendall, and Spearman analysis.

followed by Kendall and Spearman where the difference are smaller. Characteristics of each correlation technique creates these differences as Pearson assumes that the relationship is parametric between variables and highly sensitive to outliers whereas Kendall and Spearman are non-parametric and robust to extreme values. Our results, depicts that Kendall (tau), Pearson (r), and Spearman (rho) are useful measures for selection of hazard pairs for compound events giving further insights of relationship between climate indices variables under significance value of 0.05. Based on the correlation strength (threshold > 0.60 & < − 0.60) and significance values < 0.05; 27 bivariate and 10 trivariate pairs are highly possible compound events for the European region. The bivariate and trivariate pairs that include wind speed computed indices that is wci and utci, results in less spatial coverage due to the missing observed gridded data (~ 31%), limitation of the risk map coverage related to entire European continent for those indices based compound pairs must be acknowledged in this analysis.

Risk maps of compound event

Compound event hazard pairs are identified based on the correlation coefficient and using various copulas; (see "Methodology"—"Hazard maps of compound events"). The joint probabilities are computed at a monthly scale for a spatial resolution of 0.1°. In multivariate analysis (bivariate and trivariate) joint probabilities for each grid are based on selection of best-fit copula from the combined statistical indicators Akaike information criterion (AIC), Bayesian information criterion (BIC), Maximum likelihood (MAXL), Nash–Sutcliffe model efficiency coefficient (NSE) and root mean square error (RMSE). Statistical significance (p-value) of the selected copula was tested using Cramér-von-Mises (CvM) hypothesis. Previous research study shows the application of the goodness-of-fit requires at least one performance measure with CvM being utilized often in comparison to Kolmogorov–Smirnov (K-S) statistics[27]. However, CvM tends to be more powerful than K-S test taken with similar approach[43]. To include as a tool for elimination before application of statistical indicators depends on several factor, as the significance value is highly inaccurate for smaller sample size as it plays a significant role in the parametric bootstrap procedure to determine the statistics null distribution[43]. All the monthly risk maps related to bivariate and trivariate compound event pairs are shown in Supplementary Fig. S2. The hotspot analysis leads to the assumption that we are targeting only the highest value (joint probability). However, the next best value could be a region near the hotspot or another area in Europe. Defining the threshold for a hotspot could be a difficult decision if one does not understand the regional functioning, as lower probabilities sometimes lead to high risks and vulnerabilities due to lack of resources and timely decisive management[44,45]. Figure 2 shows a conclusive

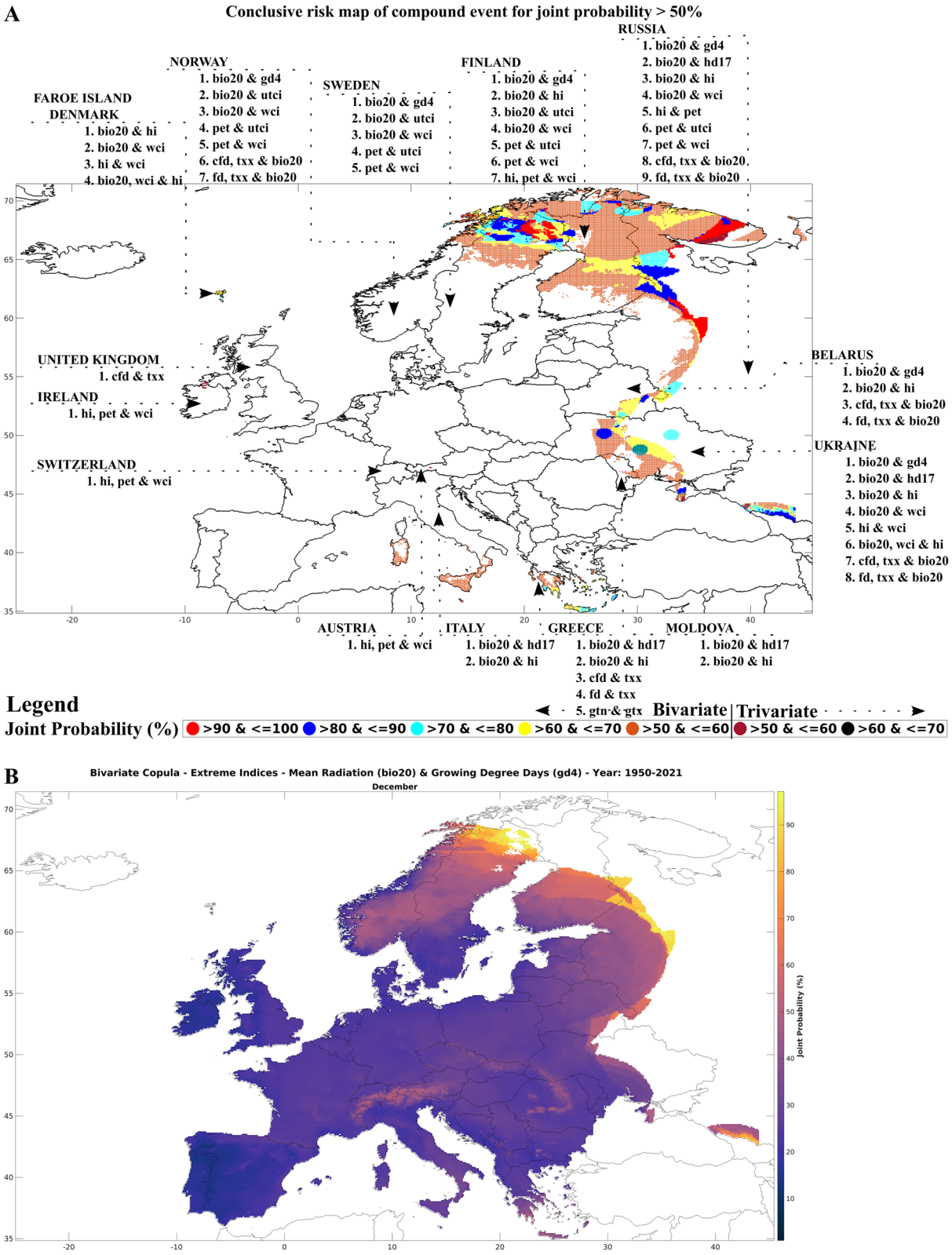

Figure 2. Highlighting Europe's high risk zone: compound event analysis with joint probability exceeding 50%. (**A**) Identifying the zones, which are of high risk. Red (maroon) colour indicates maximum joint probability for bivariate (trivariate) pair. (**B**) Highest joint probability of 97% for bivariate pair bio20 and gd4 during December to analyse the risks.

risk map of compound events occurring in various countries with a joint probabilities > 50%. Once the country and the compound event identified, the specific risk maps can be examined in detail from Supplementary Fig. S2.

Prior research studies[8,42,46,47] estimated copula selection using one best fit for entire study area; however each grid could represent a different copula fit; this misconception leads to errors which have been highlighted in a recent study[29]. Furthermore, steps of methodology failed to demonstrate best copula method opted was on which statistical indicators as their integration with combining performance of multiple indicators were missing. In our study, we have identified the proper copula, through ranking statistical indicators on a scale of 0 to 1, and assigning this scales based on their performance and cumulating it at the end for each grid. The findings indicate that the copula method at each grid for defined pairs of compound event varies. If the values are averaged, for each of the compound event across Europe than Gumbel method is best fit for capturing maximum number of outliers and Student-t can capture both the minimum and maximum outliers. Gaussian copula has outperformed in comparison with all the copula methods and can fit maximum values of joint probability based on the quartile range. Supplementary Fig. S3 indicates comparison of various copula approaches through visualization of box plots for all the determined monthly joint probability of compound event pairs. The above statements of using averaged best-fit copula method on whole Europe would be misleading and add uncertainty if every grid is not tested separately to determine joint probability. Figure 3 hotspots for compound events are shown in Supplementary Table S2, along with the month in which they had high joint probabilities, the best-fit copula technique for that particular grid at that time, and the value of joint probability for bivariate and trivariate pairs.

Based on the aforementioned findings, it is evident that the northern and eastern regions of Europe face the highest risk for the derived compound events. Hotspot regions with compound events of high correlation value for each month where the climate monitoring is required are Sweden, Finland, Russia, Ukraine, Greece, United Kingdom and Ireland. Specifically, the combinations of various hazard pairs, such as temperature, radiation, potential evapotranspiration, and bioclimatic indices, pose significant threats to Norway, Sweden, Finland, and Russia. Belarus and Ukraine are at risk of similar combination of compound event pairs except potential evapotranspiration. Southern Europe is also vulnerable, with temperature and radiation based extremes, posing the

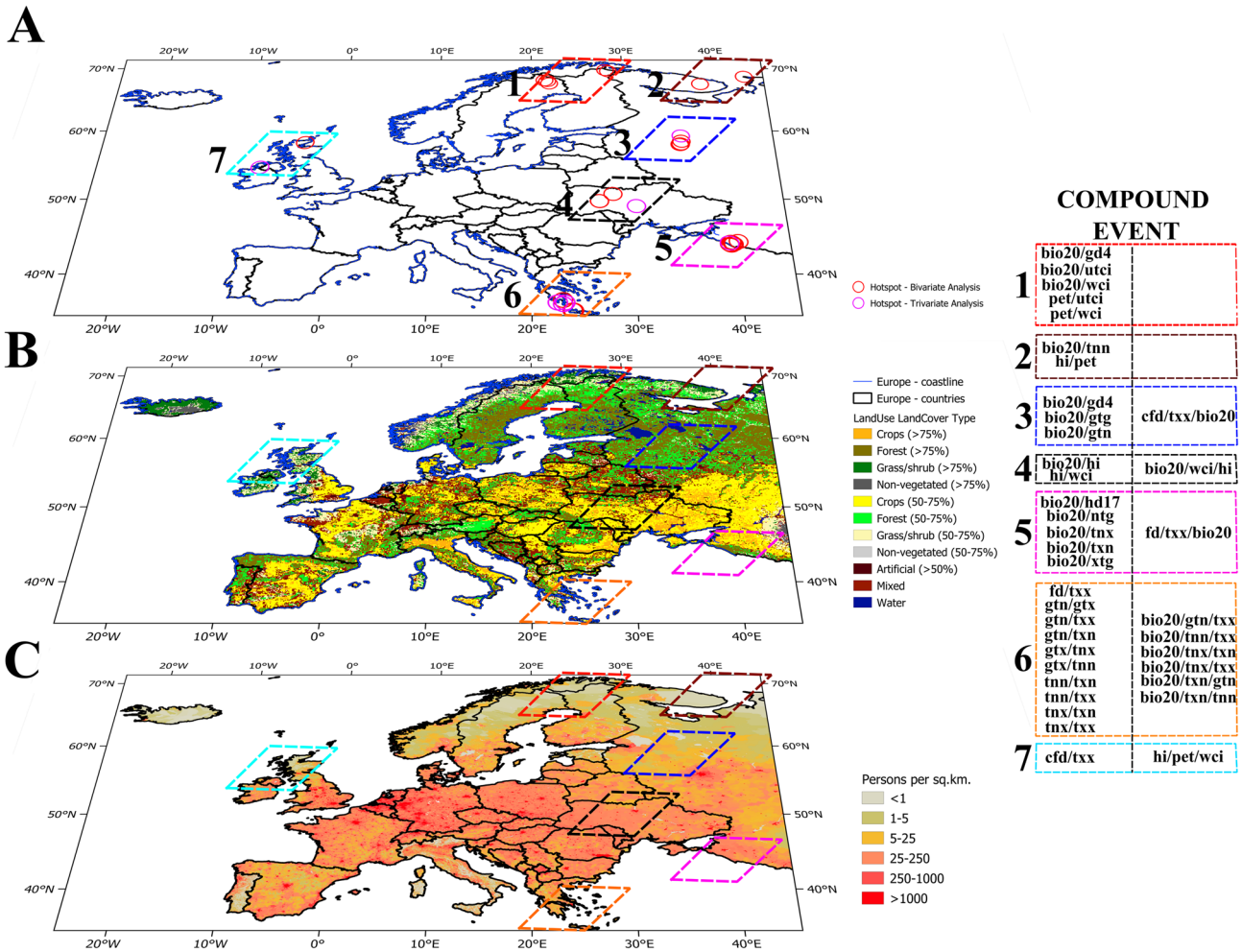

Figure 3. Hotspot of high risks compound events. (**A**) Hotspots of compound events highlighting bivariate and trivariate pairs (**B**) LandUse/LandCover map of Europe (resolution ~ 1 km) (reference: European Environment Agency for coastline demarcation[48]; Food and Agriculture Organization for landcover map[49]) (**C**) Population density map (resolution ~ 1 km) (reference: socioeconomic data and application center[50]).

higher risk. In Italy, additional threats from radiation and bioclimatic indices – heat index occur. In the western part of Europe, the Faroe island are affected by radiation, bioclimatic indices such as heat and wind chill index, while the United Kingdom faces risks associated with temperature and radiation indices. For bivariate pair bio20 and gd4 (hd17), pet and utci (wci) indicates a likelihood of occurrence of > 90%. The upper bound for trivariate pairs is 64% for bio20, wci and hi compound event. Ireland, Switzerland and Austria are at risk from trivariate pairs of potential evapotranspiration, heat index, and wind chill index. The joint probability increases in extent along the adjoining zones as the threshold of joint probability decreases. However, the assumption of considering the threshold > 50% should not be misinterpreted as the impact of lower joint probabilities being ignorable. This is because the compounding effect with other pairs or unidentified pairs could lead to more vulnerability[51]. Therefore, it is crucial to consider all possible combinations of hazards to fully assess the risk posed by compound events in different regions of Europe. Figure 3 displays the countries of European regions where compound events are producing high risks based on the visualization and copula analysis of joint probability.

According to the zonal analysis of hotspot, combined effects of radiation with growing degree days > 4 °C, thermal stress and prevailing wind effects on environment experienced by Kiruna-Sweden. The landuse map reveals that the agricultural sectors of mixed forest and grass in that zone are affected by this phenomenon. Even though there is no significant trend over past 100 years, the ongoing climate change leads to flooding in Sweden, primarily due to temperature acting as a strongest climatic driver resulting in high flows due to snowmelt[52]. Potential evapotranspiration with thermal stress and prevailing wind effects is influencing Northern Lapland and Finland coastal zones of similar landcover type. Various zones of western Russia experience a higher likelihood of extreme events due to radiation, with minimum of daily minimum, mean and maximum temperature, maximum of daily minimum and maximum temperature, mean of daily minimum and mean temperature, growing degree days > 4 °C and heating degree days < 17 °C, heat index and potential evapotranspiration. Western Russia also experiences a higher likelihood of events due to radiation, maximum of daily maximum temperature and frost days. The landcover type for most of the hotspot zone in western Russia is a mixture offorest and grass, with some regions in proximity to the coastline. Frost days and maximum of daily maximum temperature combined effects are prevailing in Inverness-United Kingdom as well whereas Donegal-Ireland experiences trivariate effect of potential evapotranspiration, heat and wind chill index. Landcover for both the event pairs is grass zone and near coastal zone. Zhytomyr (Cherkasy) Oblast located in northern (central) Ukraine are likely to be impacted by combined effect of radiation with heat index and wind chill index. Various locations in the Greece are likely to be influenced by bivariate and trivariate pairs of minimum, mean and maximum of daily minimum, mean and maximum temperature, radiation and frost days. The areas of Ukraine and Greece impacted are urban and crop areas. Population density map indicates that most of the regions where hotspots are marked lies under a low-density class. However, regions in proximity to the hotspots especially the southern Europe could lead to more distress condition as that zone is under high population density class. There are different seasonal or monthly compound event pairs (Supplementary Table S1) but the focus was on pairs that have a high correlation value (i.e. > 0.8 and < − 0.8) and is statistically significant (p-value < 0.05) throughout the annual period for this hotspot zones of high priority as monthly shifts could be tracked.

To outline the relevance of this work, we need to further access the compound events defined hotspot in connection to ground reality. The combined effect of bio20 and gd4 on the agricultural sector influences crop growth development, which in turn affects landuse strategies. For instance, stakeholders in Kiruna, Sweden, have declared a need for a change in the landuse plans through animal footprints of reindeer herding across the Northern Sweden affected by rough weather change[53]. Urban designs proposals for the region must also consider thermal comfort[54] that could be altered by the combined effect of bio20 with utci and wci. Changes in the dynamics of the treeline ecotone for various species has been discussed with underlying cause mentioned as global warming[55], but the combination of pet with utci and wci could have influenced the scenario. Western Russia has combined effects of temperature, heat, radiation and potential evapotranspiration, which could be responsible for hot and dry compound events[56]. Further, these effects could also be underlying reason for a drop of more than 70% in wheat producing at oblasts affecting food security and agricultural impacts[57]. It has already proven that the drought event of Western Russia had developed due to combination of heat and increased evaporative demand[58]. Zhytomyr Oblast, Ukraine recently has experienced wildfire events where air quality change and episodes of dust storm were major reason for this extreme event[59] and the hazard linked with it suspects towards combination of radiation, heat index and wind chill index. In Greece similar extreme events took place risking infrastructure which compounded by ecological responses through increased crop growth leading to more vulnerable situation than expected[60]. Inverness, United Kingdom experiences increased ticks with warmer climate[61] from ecological perspective and vulnerable conditions for population due to coastal erosion[62] with underlying cause unidentified other than mentioning climate change. Landslides[63] and wildfires[64] for last 12 decade has been impacting Donegal, Ireland county and the underlying causes are identified but combined effects identified in this study is still missing to be addressed as a part of the issue. Outlining the relevance of this work signifies the results would have added benefit in the previous researches for identifying the other drivers responsible for hazards. The identified compound event along with joint probability could further mitigate the risk by re-designing the framework plans. Land-use and population density maps would be a key to focus on dividing the sector responsible and the prioritizing the key compound events. The further assessment is based on arbitrary threshold; that is focusing on pairs only where the frequency of occurrence for compound event is > 50%. Further, once hotspot has been analysed a monthly shifts indicates how does the movement of the hotspot occurs across the European region.

Monthly shifts of compound event hotspot

Supplementary Table S3 presents the statistical performance using various statistical indicators and statistical significance (p-value) for the derived compound event pairs of the selected copula method. From statistical

performance highlighted in Supplementary Table S3 it could be stated that AIC, BIC, MAXL, RMSE and NSE for all the selected copula methods outperforms from statistical standards indicating a best fit. Statistical significance was computed for the stakeholders to make a final decision based on the best possible selection of the model with a similar approach to previous study[27,29]. AIC and BIC value are similar for the compound events across all the months, while the copula method varies across each month for same compound event. Some copula families are best to capture extreme joint probabilities due to number of times it repeats for entire study area but an analysis of grid-by-grid is required as it could vary especially if hotspots are to be identified. The goodness of fit misses the study for consideration of p-value to check the statistical significance of theoretical copula fits to empirical copula as an elimination step for selection of copula[43,65]. However, the underlined statistical significance of the hotspots determined was tested through nature of trends where the statistical threshold p-value is < 0.05, indicating the selection of copula fit is correct. A detailed Supplementary Table S4 indicates the monthly movement of hotspots of identified compound event pairs along with direction and magnitude of trend using Mann–Kendall and Sen's slope approach respectively. Statistical estimation always leads to uncertainties and rather sizeable uncertainties exists in multivariate analysis. Previous studies have addressed this uncertainty based on copula fits and developed procedures to estimate based on parametric or non-parametric bootstrapping[66,67]. This study also misses the uncertainty of the copula model selection, parameter and input data, which needs further investigation to acknowledge the stakeholders how uncertain the hotspot estimates are. In previous studies, it was estimated that with decreasing probabilities, the uncertainty range of the copula parameter estimation and input data for copula are increasing[68]. Further, stronger the heavy tailed marginal distribution such as extreme events, the greater is the uncertainty of the joint distribution leading higher uncertainty in joint probabilities[69].

Figure 4 provides an overview of the movement of hotspot for each month and clusters for similar compound events occurring and timeline for how frequently they repeat each month. This information may be helpful for mitigation purpose and as a deciding factor for stakeholders. The marker sizes on the map indicate the intensity of joint probability, whether there is an influence of this compound event over the region and underlying cause for any potential hazards. Figure 4 shows only the pairs where the highest monthly threshold limit of joint probability $> 50\%$. Spatial distribution of identified compound event after application of Mann–Kendall and Sen's slope is shown in Supplementary Fig. S4 and based on that Supplementary Table S4 is produced at each identified hotspot grids displaying the direction and magnitude of change of the compound events. In addition, it depicts the location where there is maximum increasing trend and warning signs of potential future hazards. This could be considered as a monthly shift of hotspots in future from the previously shown in Figs. 2, 3A and 4. The magnitude of change is expressed as a percentage increase/decrease per month. The hotspot movements for bio20 and gd4 are observed in Russia and Sweden, with Russia showing increasing trend in risks during summer months, and Greece at the similar time has the maximum % increasing trend. In winter, the risk is $> 90\%$ for the compound event to occur over Russia, however the warning zone could be Greece in future. Spring season in Russia indicates a decreasing trend of risks due to bio20 and hd17, but Greece during June and September shows an increasing trend. Greece would experience the maximum risk in future due to joint probability increasing each month at least at a rate of more than 0.70%/month for bio20 and hd17 compound events. Ukraine shows a cluster of bio20 and hi compound event with increasing trend but no significant movement across months except during December where Iceland is influenced. For future, Belarus shows highest increasing risk trend of $> 1\%$/month for the compound event pair. Winter, spring, and summer season of Finland (Ukraine) experience a decreasing (increasing) trend of ~ 0.9–1.1%/month joint probability for bio20 and utci (bio20 and wci). Clusters across Finland (Ukraine) indicates prolonged impact but the movement in future could modify. Highest increasing trend ~ 0.9–1.1%/month occurs in France, United Kingdom, Netherlands, Germany, Spain for bio20 and utci whereas for bio20 and wci similar countries along with Hungary and Sweden movement could be possible. Greece for all seasons would experience a risk of compound event related to frost days and maximum temperature. Hotspot shows a minimum increasing risk trend $> 0.6\%$/month in Greece but in future, for some season France could also influence the clusters as it is increasing at a rate ~ 0.9–1.1%/month. Gtn and gtx combined events across Greece is prevalent for each of the months with an increasing trend of risks ranging from ~ 0.6–1.1%/month and this cluster could change for some months to Sweden and France where the risk has been increasing at rate $> 0.9\%$/month. Hi and pet movement varies a lot across the region without following any seasonality of cluster but highest joint probability 50–55% is in Russia with increasing trend of $\sim 0.84\%$/month during December however maximum trend is observed in France $\sim 0.89\%$/month. Countries that are currently encountering the influence of these compound events are Norway, Sweden, Ukraine, Greece, Moldova and Russia whereas in future warnings could appear in Italy and France. Hi and wci cluster at Ukraine with no movement throughout the year has high probability ~ 80–90% could be replaced by France in future as the trend is increasing at an alarming rate of $> 1\%$/month. Pet with combination of wci and utci follows similar movement across European countries influencing Finland, Norway, Switzerland, Austria, Belarus and Spain with highest risk in December of $> 90\%$ probability. Maximum increasing trend with a magnitude of $> 1.20\%$/month is observed in France during summer season. For trivariate pairs clusters forms at Ukraine region for compound event bio20, wci and hi and for various months, the maximum increasing trend is variable across various regions such as Sweden, Spain, France, Ireland, Belarus and Norway with the highest increasing trend at Ireland of $\sim 1\%$/month during August. Cfd (fd), txx and bio20 hotspot movements are within the eastern Europe within Russia and Ukraine. However, in future Greece and Italy could also be under surveillance for the effects due to this compound event as the rates are increasing at ~ 0.7–1.0%/month. Hi, pet and wci is highly variable in movement as the hotspot lies in Spain, Belarus, Norway Luxembourg, Finland, Ireland, Sweden, and Austria that is covering all zones of Europe. With the maximum trend, also, it is variable and the rates are high enough to replace the movements in future with Latvia, Croatia and Hungary. The analysis helps in identifying how the hotspot movement is taking place and which regions are susceptible to the compound event hazard. Stakeholders can make decision based on the compound event pairs which months are under scrutiny, mitigation decision and developing country framework

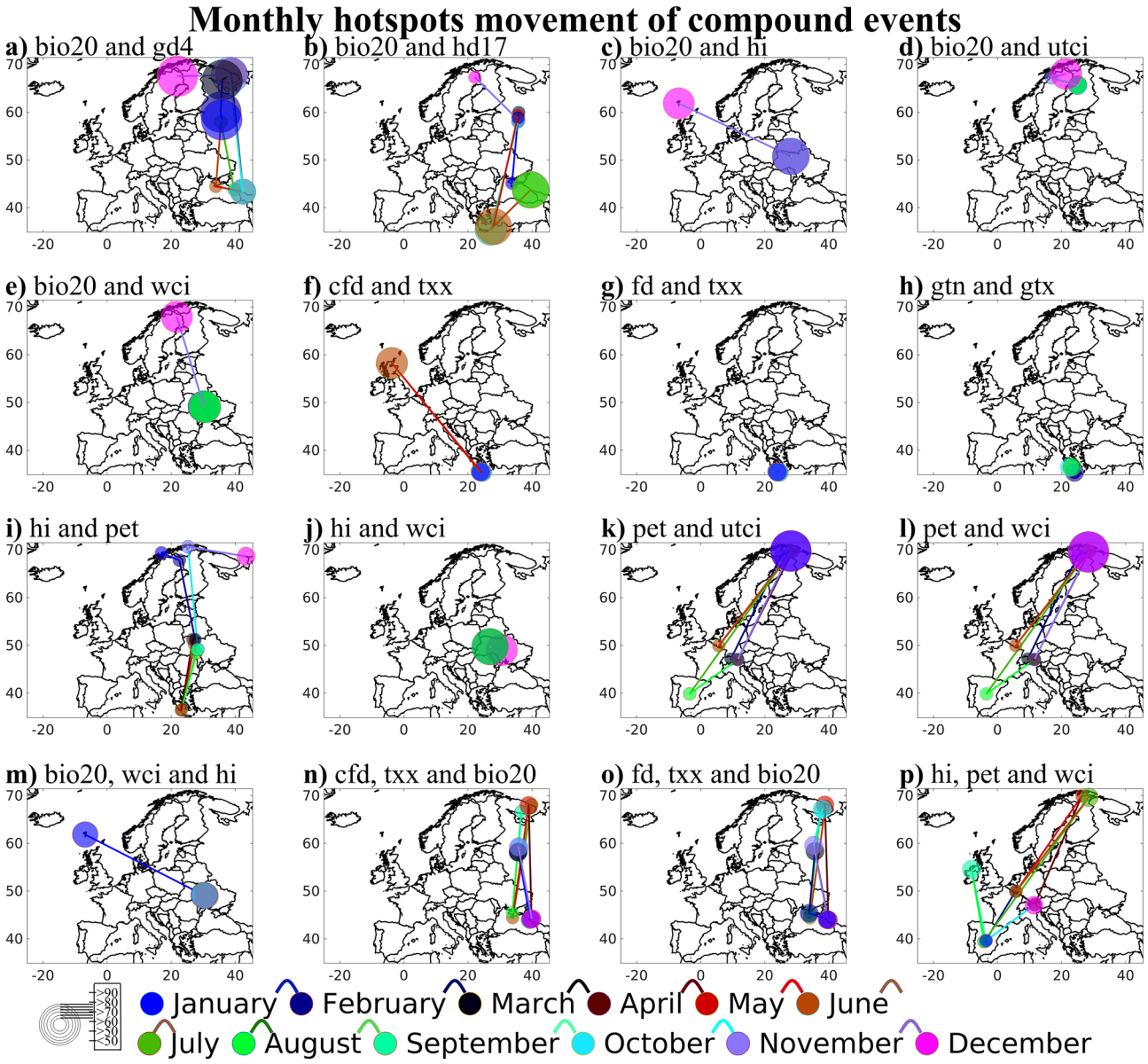

Figure 4. Monthly shifts of hotspots of compound events for joint probabilities > 50%. Movement of hotspot through combination of various bivariate (**a**–**l**) and trivariate analysis (**m**–**p**) where any of the month has threshold of joint probability > 50%. Legends include the circles where the size indicates the joint probability and the color depicts the specific month for the hotspot identified. The connecting line indicates the path of monthly hotspot shifts.

to reduce the risk. Figure 5 is the visualization of Supplementary Table S4 but for compound events that exhibits maximum increasing trend that would replace in future the hotspots of Fig. 2 demarcated.

Conclusions

In this study We identified 27-bivariate and 10-trivariate pairs of compound events derived from 74 climate indices that exhibit a high correlation ($r > 0.6$) and statistical significance (p-value < 0.05) at the continental scale. The methodology for determining the joint probability of these hazard pairs using copula covers all the misconception identified in the recent study[29]. The compound events include bioclimatic indices that influence the living organism such as hi, utci and wci, potential evapotranspiration, radiation (bio20) and temperature based indices. The pairs depict correlation strength and significance marker for each month. Due to the fact that they only follow seasonal relationships, the pairs of indices relating to precipitation or drought were not discussed in the current study. Other correlation pairs could be examined in future with similar approach to determine the hotspots and movements within the season of interest. The average best-fit copula method is student-t copula to capture outliers. Considering the values of statistical indicators and the computation time, this approach could be utilized, but to avoid uncertainties, each grid must be tested similar to this study.

Based on the analysis of the compound event pairs derived we conclude:

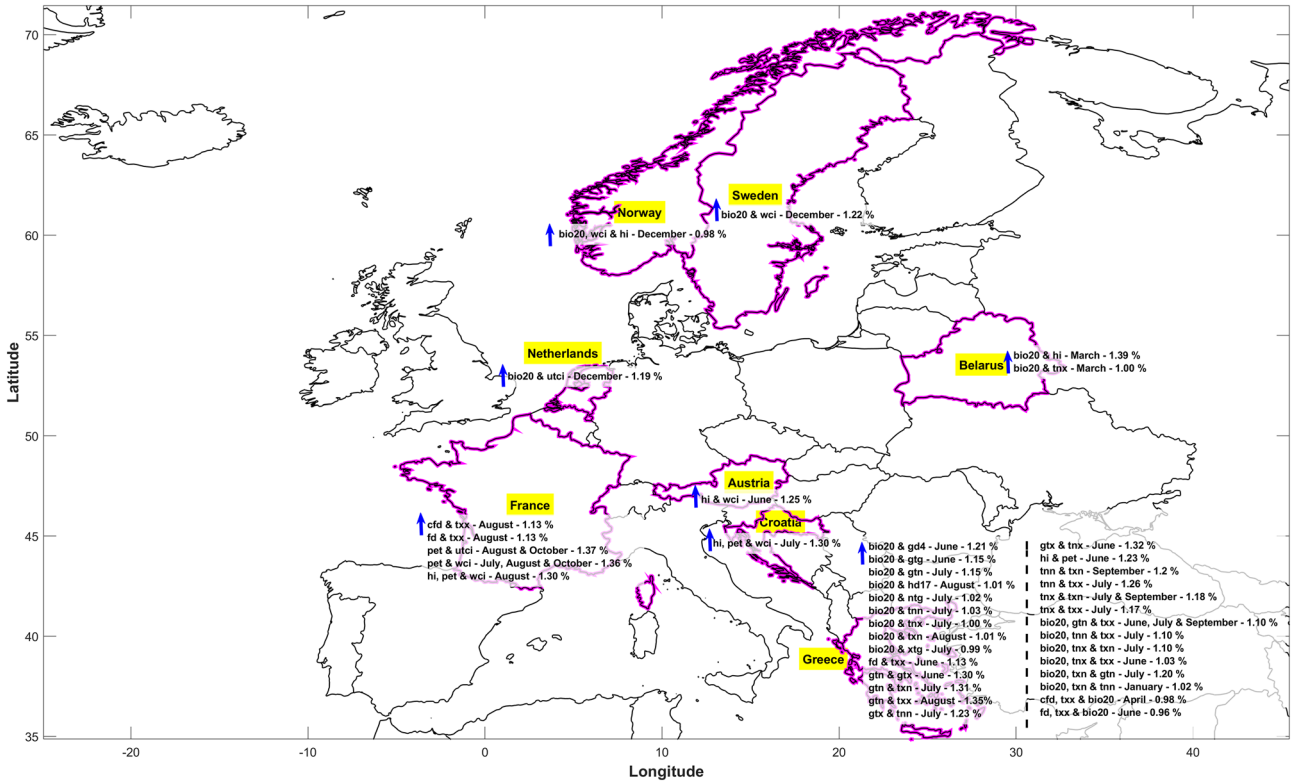

Figure 5. Footprints of future hotspots of compound events. Monitoring the compound events nature and magnitude of trend, (blue) arrow pointing upwards shows maximum future increasing nature and magnitude of trend. Countries are highlighted in yellow with the magnitude of change per month expressed in %.

- Northern and Eastern Europe are highly influenced by the risks due to hazard pairs of indices related to radiation, temperature, evapotranspiration and bioclimatic-based indices, such as the universal thermal climate index, wind chill index, and heat index.
- Agricultural and coastal zones highlighted higher vulnerability compared to urban infrastructure.
- Outlining the relevance of this work, results indicate that the climate change is affecting certain regions but most of the studies fail to indicate the influencing factors for such modification.
- Monthly shifts of hotspots for compound events are clustered for pairs related to bioclimatic indices – hi, utci, and wci, which leads to more risk on living organisms due to compounded effect.
- The trend analysis showcase that the increasing trend might affect the movement and the shifts of hotspot patterns could lead to risk other European countries.

For the future it is advisable to identify a list of compound event pairs that are of high risks and adhere to specific countries to include them as a part of a potential warning system, similar to how ETCCDI has determined a set of 27 core climate indices[70,71] to monitor occurrence of climate extremes. As an illustration, Sweden and Russia could integrate bio20 and gd4 due to high risk of joint probability and during that period Ukraine and Greece should be closely monitored as it is showing hotspot interference by higher increasing trend during that period. Overall, this study is still challenging in answering the unresolved question of why these compound events pose a high risk to this zone and what mitigation measures are in place to reduce vulnerability to these events when they increase many times over. By understanding the dependence between different variables/climate extreme indices, we can better predict the likelihood of extreme events occurring and develop strategies to mitigate their impact. Moreover, the use of copulas is an important tool for improving our understanding of the complex and interdependent nature of extreme climate events.

Methods

Data

The study region focused here is Europe which is the westernmost part of Eurasia and whose climatic data covering the entire European land surface (25° N–71.5° N × 25° W–45° E) is obtained through European Climate Assessment and Dataset (ECA&D) Ensembles daily gridded observation dataset (E-OBS) v25.0e[72]. These data source provides daily gridded observation dataset from 1950 to 2021 (72 years) with resolution ~ 11 km (0.1°) of global radiation, maximum air temperature, minimum air temperature, precipitation, relative humidity, sea level pressure and wind speed which is further utilized to obtain the monthly gridded climate indices. The data source was opted due to the high resolution gridded observational data, requisite frequency of weather data, European area coverage, and significant model validation for climate monitoring[73–75]. The European National

Meteorological and Hydrological Services (NMHSs) entity provides the station data; weather data such as wind speed is covered less spatially and global radiation is derived based on in-situ and satellite data—Clouds and the Earth's Radiant Energy System (CERES). Other sources, such as ERA-5 reanalysis, could be used to obtain complete spatial coverage of wind speed related weather data, but it has been avoided due to different spatial resolution and data source that can further lead to uncertainties and lacking consistencies[76–78]. However, for global radiation users do not have the option to utilize only in-situ observations. 74 climate indices diversified into drought indices, global radiation indices, multi-element indices, precipitation indices, relative humidity indices, sea level pressure indices, temperature indices and wind speed indices which are computed is showcased in Table 1 along with the description of each of them. The computation of climate indices is carried out using R platform "ClimInd" (https://cran.r-project.org/web/packages/ClimInd/index.html) and "scPDSI" (https://cran.r-project.org/web/packages/scPDSI/index.html) package[79,80]. The decision of selection of climate indices were based on potential monthly time-scale from the input weather data. The spatial visualization of all the climate indices across Europe is showcased in Supplementary Fig. S5. Further, the climate indices used in this study cover also all the 27 core extreme climate indices defined by Expert Team on Climate Change Detection and Indices (ETCCDI)[70,71].

Methodology

This study's workflow along with strategies used are detailed below and depicted in Fig. 6.

Data processing

The majority of data acquisition has been covered in the data section, with an important note to consider the uncertainty associated with the global radiation as well as the spatial variability coverage across Europe in relation to wind speed data for the computed climate indices. The daily gridded weather data from E-OBS, when used an input for the requisite R-package results in 74 different monthly climate indices. Mean wind speed (fg), number of days with wind speed ≥ 10.8m/s (fg6bft), and calm days (fgcalm) are climate indices that only use wind speed as input weather data, while universal thermal climate index (utci) and wind chill index (wci) combine it with other weather data. Mean radiation (bio20) is a climate index that only used global radiation as input weather data. Climate indices reference evapotranspiration (pet) further impacting computation of drought indices requires attention through proper selection of empirical method. By using the Hargreaves method which requires only minimum and maximum air temperature as climatological data for the calculation, instead of the Penman–Monteith method in this case, we are able to achieve the full coverage of Europe over uncertain global radiation data and lower spatial coverage due to wind speed data. The Hargreaves method is a recommended approach because the simulations are continuous, the approach is straightforward and produces acceptable results with readily available input data[81].

Analysis

Correlation of climate indices

Number of correlation coefficients are available based on various statistical hypothesis which are popular to quantify the degree of two variables in relation. There are three of them Kendall, Pearson and Spearman rank correlation coefficient commonly used[82–84]. Pearson is parametric test[85] and Kendall and Spearman are non-parametric test[86] to measure the degree of strength and association between climate indices variables. Pearson is utilized with an assumption that data is normally distributed about regression line[85] whereas Kendall and Spearman are rank-based computation illustrating monotonic relationships[86]. In our situation where there are climate

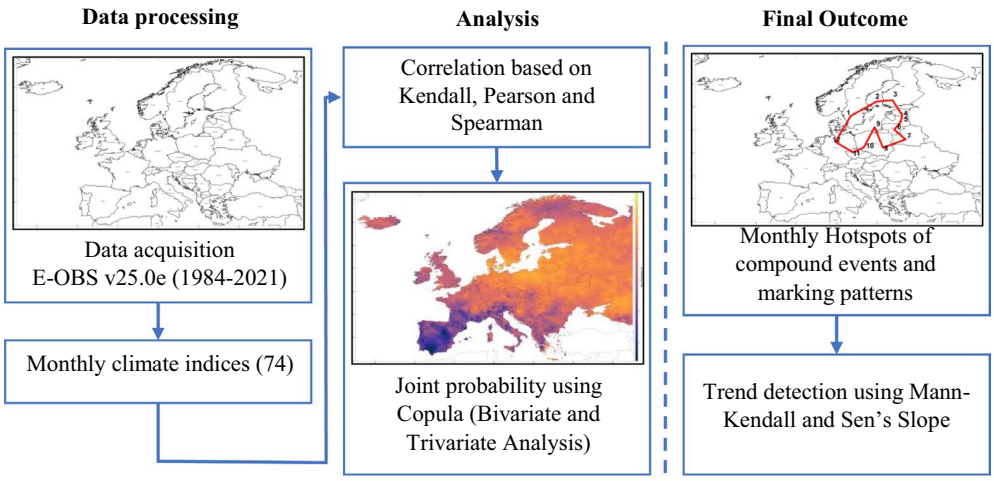

Figure 6. Schematic representation of the methodological framework. The steps taken to determine the monthly hotspots and patterns of the compound events.

indices which are numerically equal such as zeros, the values are given an arithmetic mean rank numbers related to the ties. Kendall and Spearman have different correlation procedures to handle ties[87]. For 74 climate indices, the correlation values based on each technique were computed using the built-in "corr" function of Matlab. In the documentation for the Matlab function, the formulas for each of the technique have been described[88–91]. The next phase involved choosing the climate indices that had a strong correlation value and were statistically significant. The correlation coefficient value ranges between ± 1; ± shows the correlation's direction. Climate indices are divided into groups of ± 0.80 to ± 1.00 (very high correlation), ± 0.60 to ± 0.80 (high correlation), ± 0.40 to ± 0.60 (medium correlation), ± 0.20 to ± 0.40 (low correlation), ± 0.00 to ± 0.20 (very low correlation). The statistical significance level (p-value) is set at < 0.05; this means that the null hypothesis is rejected if the targeted statistical correlation reaches statistical significance. With this boundary points framework, the question of correlation strength cannot be justified[92]; however, for further multivariate analysis we are interested in the climate indices with correlation > 0.60, < − 0.60 and significance level (p-value) < 0.05. The correlation and significance values of each methodology would be different, but the combination is based on the union of a subset of the Penman, Kendall, and Spearman methods.

Hazard maps of compound events

"Hazard" maps is a visualization of the probability of occurrence that a given natural phenomenon of a given magnitude will occur within a given time frame and given location[93]. In our study, multivariate analysis (bivariate and trivariate) through joint probability is used to visualize the hazard maps of compound events. Joint probabilities are computed statistically through copula function. Early works by Sklar[94] introduced copula which is a joint multivariate distribution in which the marginal distribution is uniform over range (0, 1) and from which the joint distribution of two or more variables may be derived[95,96], assuming variables are continuous and time-independent[29]. If R is an n-dimensional cumulative distribution function (CDF) with 1-dimenisonal marginal distribution $F_i(x_i)$, then n-dimensional copula (C) exists such that:

$$R(x_1, x_2, \ldots, x_n) = C(F_1(x_1), F_2(x_2), \ldots, F_n(x_n)) = C\left(u_1, u_2, \ldots, u_n\right), \tag{1}$$

where $(x_1,x_2,\ldots,x_n)$ are random variables, and $(F_1(x_1),F_2(x_2),\ldots,F_n(x_n))$-denoted by $(u_1,u_2,\ldots,u_n)$ are marginal distribution for which dependence structure is to be modelled by copula C[97]. Copula distribution is diversified into empirical and theoretical copula. The two types of copulas most frequently used in theoretical work are Elliptical (Gaussian and Student-t) and Archimedean (Clayton, Frank, Gumbel). In this study the joint probability distribution of bivariate and trivariate combinations of climate indices were analysed using Gumbel, Clayton, Frank, Gaussian and Student-t copula. General formula for Elliptical and Archimedean copula are defined below[29,98,99]:

Elliptical copula:

$$C(u_1, u_2) = \phi\left[\phi^{-1}(u_1), \phi^{-1}(u_2)\right] \in [0, 1]^2, \tag{2}$$

where, ϕ^{-1} is inverse of univariate marginal distribution, ϕ is multivariate distribution.

Archimedean copula:

$$C(u_1, u_2) = \psi\left[\psi^{-1}(u_1), \psi^{-1}(u_2)\right] \in [0, 1]^2, \tag{3}$$

where, ψ^{-1} is pseudo-inverse of generator function, ψ is generator function which is continuous strictly decreasing convex function.

The computation of multivariate joint distribution was carried out using the Statistics and Machine Learning Toolbox of Matlab with 'copula' package[100]. Various aspects of the dependence structure are captured differently by various theoretical copula families, with some copulas being better suited to model the overall dependence while others are suited to represent the dependence at the tails of the distribution[101–103]. Main features of probability concentration of various copula such as Clayton in lower tail, Frank in symmetry, Gaussian in symmetry, Gumbel in upper tail, and Student-t in symmetry, upper tail, and lower tail[29]. Assessment of the best-fitted copula based on goodness-of-fit is determined. To identify performance from the families of copula analytical tests such as Cramér-von-Mises (CvM) hypothesis test is one such viable approach[29]. The CvM test[43,104] was used to evaluate the goodness of fit of theoretical copulas with a lower p-value means we accept the null hypothesis that both samples are drawn from the same underlying distribution and have confidence in the theoretical distribution fit[27]. The p-values for each copula of families for each grid of climate indices compound pair computed joint probability are obtained using Eq. (4)[104].

$$T_c = \frac{mn}{N}\int_{\infty}^{-\infty}[A_m(x) - B_n(x)]^2 dH_N(x), \tag{4}$$

where criterion of testing to obtain p-value is based on A_m and B_n which are empirical and theoretical distribution of copula based on compound pairs. H_N is empirical distribution function of combined sample, with $N = m + n$. Different statistical indicators such as AIC, BIC, MAXL, NSE and RMSE are used to determine the best fit from families of theoretical copula in comparison to empirical copula. The formula to compute each of the statistical indicators: AIC[105,106], BIC[107], MAXL, RMSE and NSE are defined below.

$$AIC = 2D - 2l = 2D + n\ln\left\{\frac{\sum_{i=1}^{n}[\tilde{y}_i - y_i(\theta)]^2}{n}\right\} - 2CS, \tag{5}$$

$$\mathrm{BIC} = \mathrm{Dln(n)} - 2\mathrm{l} = \mathrm{Dln(n)} + \mathrm{nln}\left\{\frac{\sum_{i=1}^{n}[\widetilde{y}_i - y_i(\theta)]^2}{n}\right\} - 2\mathrm{CS}, \tag{6}$$

$$\mathrm{MAXL} = -\frac{n}{2}\ln\left\{\frac{\sum_{i=1}^{n}[\widetilde{y}_i - y_i(\theta)]^2}{n}\right\}, \tag{7}$$

$$\mathrm{RMSE} = \sqrt{\frac{\sum_{i=1}^{n}[\widetilde{y}_i - y_i(\theta)]^2}{n}}, \tag{8}$$

$$\mathrm{NSE} = 1 - \frac{\sum_{i=1}^{n}[\widetilde{y}_i - y_i(\theta)]^2}{\sum_{i=1}^{n}\left[\widetilde{y}_i - \widetilde{\overline{y}_i}\right]^2}, \tag{9}$$

where D is the number of parameters of statistical model, l is the log-likelihood value of best parameter set, $\widetilde{\sigma}^2 = \frac{\sum_{i=1}^{n}[\widetilde{y}_i - y_i(\theta)]^2}{n}$ is gaussian assumption of error residuals, θ is the copula parameter, and cs is a constant. AIC estimates are based on the residual sum of squares instead of maximizing the likelihood function of distribution; the minimum the AIC value the better is the fit of the copula. Similarly, in order to determine the copula of families, it is preferred that BIC have a smaller value, AIC have a higher value, NSE have a higher value near to 1, and RMSE have a lower value near to 0. The method is repeated for each grid in order to calculate the joint probability using each family of copulas and then compare the results with empirical copulas. Based on a variety of statistical indicators, related to each copula family the finalized theoretical copula is the one with the highest total towards goodness of fit. Values from the theoretical copula are close to those from the empirical copulas, they performed well based on statistical indicators used for various climate indices combinations. For various combinations of climate indices that have a correlation > 0.60 and < − 0.60 and significance level (p-value) < 0.05, the joint probability for each grid indicating the best matched copula, is calculated and displayed as a hazard map. Different combinations of the 74 possible climate indices are discussed in the result section within correlation of climate indices para. Best fit copula for the each of the combination using bivariate and trivariate analysis and the joint probability visualization has been discussed in the result section within hotspots and patterns of compound events para.

Final outcome

Defining hotspots and patterns

Copula-based derived joint probabilities of various combined climate indices surpassing the threshold of correlation and significance level for each grid help a stakeholder to determine the frequency of occurrence of that particular compound event for each month. Each grid value of hazard pairs is sorted based on highest to lowest order and a rank is assigned. Further the hotspots are defined based on highest possible frequency of occurrence (rank with number 1 is assigned) across Europe. This process is repeated for each month and for each of the compound events shortlisted from the bivariate and trivariate analysis. Patterns are formed by linking the tagged month of the defined hotspot and additional analyses are based on those patterns, answering the question in the result section: which zones are more vulnerable? For which kind of compound event? And for which month?

Trend detection

There are parametric and nonparametric approaches for detecting significant trends in time-series of climate. Non-parametric trend tests need that the data be independent whereas parametric trend test demands data is independent as well as normally distributed[108]. Non-parametric approach Mann–Kendall and Sen's slope estimator at each grid point was used to assess the trends in the joint probabilities of bivariate and trivariate analysis derived climate indices combinations. Assumption that while computation of trends of the joint probabilities, we assume the stationarity of the climate. Statistical significance of trends estimated using nonparametric Mann-Kendall[109] method and magnitude of trends were derived using Sen's slope estimator[110]. The trend analysis that is Kendall's tau significance and Sen's slope estimate is computed using R platform "wql" (https://cran.r-project.org/web/packages/wql/index.html) package with function "mannKen". The formula to determine the trend using Mann-Kendall[90,111] and Sen's slope[110] is defined below:

Mann–Kendall:

$$\mathrm{S} = \sum_{i=1}^{n-1}\sum_{j=i+1}^{n}\mathrm{sgn}\left(x_j - x_i\right), \tag{10}$$

where, n is number of data points, x_i and x_j are data values in time series and sign function-sgn is given by:

$$\mathrm{sgn}\left(x_j - x_i\right) = \begin{cases} +1, x_j - x_i > 0 \\ 0, x_j - x_i = 0 \\ -1, x_j - x_i < 0 \end{cases}. \tag{11}$$

Increasing and decreasing trend is determined by Z_s based on positive and negative values obtained respectively. Z_s is computed using:

$$Z_s = \begin{cases} \frac{S-1}{\sqrt{Var(S)}}, S > 0 \\ 0, S = 0 \\ \frac{S+1}{\sqrt{Var(S)}}, S < 0. \end{cases} \quad (12)$$

Sen's Slope:

$$Q_i = \frac{(x_j - x_i)}{j - i}, i = 1, 2, 3, \ldots, N, \quad (13)$$

where N value is sorted for Qi from small to large and then Sen's slope is obtained based on the two-tailed estimate for the median Qi (Q_{med}), which is determined by:

$$Q_{med} = \begin{cases} Q_{\frac{N+1}{2}}, N = odd \\ \frac{Q_{\frac{N}{2}} + Q_{\frac{N+1}{2}}}{2}, N = even \end{cases}. \quad (14)$$

The outcome from Mann–Kendall would capture the direction of trend that is percentage increasing (positive value) or decreasing (negative value) and Sen's slope would capture the magnitude of trend that is percentage change in year for the joint probabilities of climate indices resulting compound event over each month for European regions.

Data availability

All data are from E-OBS (Version 25.0e) used in our analysis are freely available. (https://surfobs.climate.copernicus.eu/dataaccess/)[72]. LandUse/LandCover map of Europe freely available at Food and Agriculture Organization for landcover map (https://data.apps.fao.org/)[49]. Data for coastline demarcation freely available at European Environment Agency (https://www.eea.europa.eu/)[48]. Population density map freely available at socioeconomic data and application center (https://sedac.ciesin.columbia.edu/)[50]. Processed data and code to produce the results are available at: https://doi.org/10.5281/zenodo.10014462.

Received: 25 May 2023; Accepted: 15 October 2023
Published online: 23 October 2023

References

1. McPhillips, L. E. *et al.* Defining extreme events: A cross-disciplinary review. *Earth's Future* **6**, 441–455 (2018).
2. Zscheischler, J. *et al.* Future climate risk from compound events. *Nat. Clim. Change* **8**, 469–477 (2018).
3. Zscheischler, J. *et al.* A typology of compound weather and climate events. *Nat. Rev. Earth Environ.* **1**, 333–347 (2020).
4. Zscheischler, J. *et al.* Future climate risk from compound events. *Nat. Clim. Change* **8**, 469–477 (2018).
5. Raymond, C. *et al.* Understanding and managing connected extreme events. *Nat. Clim. Change* **10**, 611–621 (2020).
6. AghaKouchak, A. *et al.* Climate extremes and compound hazards in a warming world. *Annu. Rev. Earth Planet. Sci.* **48**, 519–548 (2020).
7. Hauser, M., Orth, R. & Seneviratne, S. I. Role of soil moisture versus recent climate change for the 2010 heat wave in western Russia. *Geophys. Res. Lett.* **43**, 2819–2826 (2016).
8. François, B. & Vrac, M. Time of emergence of compound events: Contribution of univariate and dependence properties. *Nat. Hazards Earth Syst. Sci.* **23**, 21–44 (2023).
9. Paprotny, D., Morales-Nápoles, O., Vousdoukas, M. I., Jonkman, S. N. & Nikulin, G. Accuracy of pan-European coastal flood mapping. *J. Flood Risk Manag.* **12**, e12459 (2019).
10. Owen, L. E., Catto, J. L., Stephenson, D. B. & Dunstone, N. J. Compound precipitation and wind extremes over Europe and their relationship to extratropical cyclones. *Weather Clim. Extrem.* **33**, 100342 (2021).
11. De Luca, P., Hillier, J. K., Wilby, R. L., Quinn, N. W. & Harrigan, S. Extreme multi-basin flooding linked with extra-tropical cyclones. *Environ. Res. Lett.* **12**, 114009 (2017).
12. Seneviratne, S. I. et al. 11 Chapter 11: Weather and climate extreme events in a changing climate (2021).
13. Leonard, M. *et al.* A compound event framework for understanding extreme impacts. *Wiley Interdiscip. Rev. Clim. Change* **5**, 113–128 (2014).
14. Horton, R. M., Mankin, J. S., Lesk, C., Coffel, E. & Raymond, C. A review of recent advances in research on extreme heat events. *Curr. Clim. Change Rep.* **2**, 242–259 (2016).
15. De Michele, C., Salvadori, G., Canossi, M., Petaccia, A. & Rosso, R. Bivariate statistical approach to check adequacy of dam spillway. *J. Hydrol. Eng.* **10**, 50–57 (2005).
16. De Michele, C. & Salvadori, G. A generalized Pareto intensity-duration model of storm rainfall exploiting 2-copulas. *J. Geophys. Res. Atmos.* https://doi.org/10.1029/2002JD002534 (2003).
17. Favre, A., El Adlouni, S., Perreault, L., Thiémonge, N. & Bobée, B. Multivariate hydrological frequency analysis using copulas. *Water Resour. Res.* https://doi.org/10.1029/2003WR002456 (2004).
18. Gräler, B. *et al.* Multivariate return periods in hydrology: A critical and practical review focusing on synthetic design hydrograph estimation. *Hydrol. Earth Syst. Sci.* **17**, 1281–1296 (2013).
19. Salvadori, G., Tomasicchio, G. R. & D'Alessandro, F. Practical guidelines for multivariate analysis and design in coastal and off-shore engineering. *Coast. Eng.* **88**, 1–14 (2014).
20. Salvadori, G. & De Michele, C. Frequency analysis via copulas: Theoretical aspects and applications to hydrological events. *Water Resour. Res.* https://doi.org/10.1029/2004WR003133 (2004).
21. AghaKouchak, A., Bárdossy, A. & Habib, E. Copula-based uncertainty modelling: Application to multisensor precipitation estimates. *Hydrol. Process.* **24**, 2111–2124 (2010).
22. Kumar, N. *et al.* Joint behaviour of climate extremes across India: Past and future. *J. Hydrol.* **597**, 126185 (2021).
23. Zhang, L. & Singh, V. P. Trivariate flood frequency analysis using the Gumbel-Hougaard copula. *J. Hydrol. Eng.* **12**, 431–439 (2007).
24. Kharin, V. V., Zwiers, F. W., Zhang, X. & Wehner, M. Changes in temperature and precipitation extremes in the CMIP5 ensemble. *Clim. Change* **119**, 345–357 (2013).

25. Gomes, M. I. & Guillou, A. Extreme value theory and statistics of univariate extremes: A review. *Int. Stat. Rev.* **83**, 263–292 (2015).
26. Oliver, E. C. J. *et al.* Longer and more frequent marine heatwaves over the past century. *Nat. Commun.* **9**, 1–12 (2018).
27. Miao, C., Sun, Q., Duan, Q. & Wang, Y. Joint analysis of changes in temperature and precipitation on the Loess Plateau during the period 1961–2011. *Clim. Dyn.* **47**, 3221–3234 (2016).
28. Zscheischler, J. & Seneviratne, S. I. Dependence of drivers affects risks associated with compound events. *Sci. Adv.* **3**, e1700263 (2017).
29. Tootoonchi, F. *et al.* Copulas for hydroclimatic analysis: A practice-oriented overview. *Wiley Interdiscip. Rev. Water* **9**, e1579 (2022).
30. Jendritzky, G., de Dear, R. & Havenith, G. UTCI-why another thermal index?. *Int. J. Biometeorol.* **56**, 421–428 (2012).
31. Lankford, H. V. & Fox, L. R. The wind-chill index. *Wilderness Environ. Med.* **32**, 392–399 (2021).
32. Persson, G., Bärring, L., Kjellström, E., Strandberg, G. & Rummukainen, M. *Climate Indices for Vulnerability Assessments* (SMHI, 2007).
33. Michelozzi, P. *et al.* High temperature and hospitalizations for cardiovascular and respiratory causes in 12 European cities. *Am. J. Respir. Crit. Care Med.* **179**, 383–389 (2009).
34. Vinogradova, V. Using the universal thermal climate index (UTCI) for the assessment of bioclimatic conditions in Russia. *Int. J. Biometeorol.* **65**, 1473–1483 (2021).
35. Chen, Y., Moufouma-Okia, W., Masson-Delmotte, V., Zhai, P. & Pirani, A. Recent progress and emerging topics on weather and climate extremes since the fifth assessment report of the intergovernmental panel on climate change. *Annu. Rev. Environ. Resour.* **43**, 35–59 (2018).
36. Beniston, M. & Goyette, S. Changes in variability and persistence of climate in Switzerland: Exploring 20th century observations and 21st century simulations. *Glob. Planet. Change* **57**, 1–15 (2007).
37. Riboldi, J., Leeding, R., Segalini, A. & Messori, G. Multiple large-scale dynamical pathways for Pan-Atlantic compound cold and windy extremes. *Geophys. Res. Lett.* **50**, e2022GL102528 (2023).
38. Wu, D., Yu, Q., Lu, C. & Hengsdijk, H. Quantifying production potentials of winter wheat in the North China Plain. *Eur. J. Agron.* **24**, 226–235 (2006).
39. Di Napoli, C., Allen, T., Méndez-Lázaro, P. A. & Pappenberger, F. Heat stress in the Caribbean: Climatology, drivers, and trends of human biometeorology indices. *Int. J. Climatol.* **43**, 405–425 (2023).
40. Ionita, M., Nagavciuc, V., Scholz, P. & Dima, M. Long-term drought intensification over Europe driven by the weakening trend of the Atlantic Meridional Overturning Circulation. *J. Hydrol. Reg. Stud.* **42**, 101176 (2022).
41. Kopp, R. et al. Potential surprises–compound extremes and tipping elements (2017).
42. Tootoonchi, F. *et al.* Uni-and multivariate bias adjustment methods in Nordic catchments: Complexity and performance in a changing climate. *Sci. Total Environ.* **853**, 158615 (2022).
43. Genest, C., Rémillard, B. & Beaudoin, D. Goodness-of-fit tests for copulas: A review and a power study. *Insur. Math. Econ.* **44**, 199–213 (2009).
44. Kliem, R. L. & Ludin, I. S. *Reducing Project Risk* (Routledge, 2019).
45. Perera, D., Agnihotri, J., Seidou, O. & Djalante, R. Identifying societal challenges in flood early warning systems. *Int. J. Disaster Risk Reduct.* **51**, 101794 (2020).
46. François, B., Vrac, M., Cannon, A. J., Robin, Y. & Allard, D. Multivariate bias corrections of climate simulations: Which benefits for which losses?. *Earth Syst. Dyn.* **11**, 537–562 (2020).
47. Robin, Y., Vrac, M., Naveau, P. & Yiou, P. Multivariate stochastic bias corrections with optimal transport. *Hydrol. Earth Syst. Sci.* **23**, 773–786 (2019).
48. European Environment Agency. https://www.eea.europa.eu/.
49. Dominant Land Cover and Use—Food and Agriculture Organization of the United Nations. https://data.apps.fao.org/.
50. Center for International Earth Science Information Network - CIESIN - Columbia University. Gridded Population of the World, Version 4 (GPWv4): Population Density, Revision 11. https://doi.org/10.7927/H49C6VHW (2018).
51. Brunner, M. I., Furrer, R. & Favre, A.-C. Modeling the spatial dependence of floods using the Fisher copula. *Hydrol. Earth Syst. Sci.* **23**, 107–124 (2019).
52. Arheimer, B. & Lindström, G. Climate impact on floods: Changes in high flows in Sweden in the past and the future (1911–2100). *Hydrol. Earth Syst. Sci.* **19**, 771–784 (2015).
53. Rosqvist, G. C., Inga, N. & Eriksson, P. Impacts of climate warming on reindeer herding require new land-use strategies. *Ambio* **51**, 1247–1262 (2022).
54. Ebrahimabadi, S., Johansson, C., Rizzo, A. & Nilsson, K. Microclimate assessment method for urban design–A case study in subarctic climate. *Urban Des. Int.* **23**, 116–131 (2018).
55. Kullman, L. A review of Abisko case study: Recent and past trees and climates at the Arctic/Alpine margin in Swedish Lapland. *Chall. Issues Environ. Earth Sci.* **2**, 1–25 (2021).
56. Hao, Z., Hao, F., Xia, Y., Singh, V. P. & Zhang, X. A monitoring and prediction system for compound dry and hot events. *Environ. Res. Lett.* **14**, 114034 (2019).
57. Hunt, E. *et al.* Agricultural and food security impacts from the 2010 Russia flash drought. *Weather Clim. Extrem.* **34**, 100383 (2021).
58. Christian, J. I., Basara, J. B., Hunt, E. D., Otkin, J. A. & Xiao, X. Flash drought development and cascading impacts associated with the 2010 Russian heatwave. *Environ. Res. Lett.* **15**, 94078 (2020).
59. Savenets, M., Osadchyi, V., Oreshchenko, A. & Pysarenko, L. Air quality changes in Ukraine during the April 2020 wildfire event. *Geogr. Pannon.* **24**, 271–284 (2020).
60. Simpson, N. P. *et al.* A framework for complex climate change risk assessment. *One Earth* **4**, 489–501 (2021).
61. Li, S., Gilbert, L., Harrison, P. A. & Rounsevell, M. D. A. Modelling the seasonality of Lyme disease risk and the potential impacts of a warming climate within the heterogeneous landscapes of Scotland. *J. R. Soc. Interface* **13**, 20160140 (2016).
62. Fitton, J. M., Hansom, J. D. & Rennie, A. F. A method for modelling coastal erosion risk: The example of Scotland. *Nat. Hazards* **91**, 931–961 (2018).
63. Holmes, R., Long, D. & Dodd, L. R. Large-scale debrites and submarine landslides on the Barra Fan, west of Britain. *Geol. Soc. Lond. Spec. Publ.* **129**, 67–79 (1998).
64. Jeffers, J. M. Particularizing adaptation to non-predominant hazards: A history of wildfires in County Donegal, Ireland from 1903 to 2019. *Int. J. Disaster Risk Reduct.* **58**, 102211 (2021).
65. Brunner, M. I., Seibert, J. & Favre, A. Bivariate return periods and their importance for flood peak and volume estimation. *Wiley Interdiscip. Rev. Water* **3**, 819–833 (2016).
66. Dodangeh, E., Shahedi, K., Solaimani, K., Shiau, J.-T. & Abraham, J. Data-based bivariate uncertainty assessment of extreme rainfall-runoff using copulas: Comparison between annual maximum series (AMS) and peaks over threshold (POT). *Environ. Monit. Assess.* **191**, 1–18 (2019).
67. Villarini, G., Serinaldi, F. & Krajewski, W. F. Modeling radar-rainfall estimation uncertainties using parametric and non-parametric approaches. *Adv. Water Resour.* **31**, 1674–1686 (2008).

68. Li, Z., Shao, Q., Tian, Q. & Zhang, L. Copula-based drought severity-area-frequency curve and its uncertainty, a case study of Heihe River basin. *China. Hydrol. Res.* **51**, 867–881 (2020).
69. Zhang, Q., Xiao, M. & Singh, V. P. Uncertainty evaluation of copula analysis of hydrological droughts in the East River basin, China. *Glob. Planet. Change* **129**, 1–9 (2015).
70. Karl, T. R., Nicholls, N. & Ghazi, A. Clivar/GCOS/WMO workshop on indices and indicators for climate extremes workshop summary. In *Weather and Climate Extremes* (eds Karl, T. R. *et al.*) 3–7 (Springer, 1999).
71. Peterson, T. *et al. Report on the Activities of the Working Group on Climate Change Detection and Related Rapporteurs* (World Meteorological Organization Geneva, 2001).
72. Cornes, R. C., van der Schrier, G., van den Besselaar, E. J. M. & Jones, P. D. An ensemble version of the E-OBS temperature and precipitation data sets. *J. Geophys. Res. Atmos.* **123**, 9391–9409 (2018).
73. Cardoso Pereira, S., Marta-Almeida, M., Carvalho, A. C. & Rocha, A. Extreme precipitation events under climate change in the Iberian Peninsula. *Int. J. Climatol.* **40**, 1255–1278 (2020).
74. Tramblay, Y., Feki, H., Quintana-Seguí, P. & Guijarro, J. A. The SAFRAN daily gridded precipitation product in Tunisia (1979–2015). *Int. J. Climatol.* **39**, 5830–5838 (2019).
75. Brocca, L. *et al.* River flow prediction in data scarce regions: Soil moisture integrated satellite rainfall products outperform rain gauge observations in West Africa. *Sci. Rep.* **10**, 1–14 (2020).
76. Albergel, C. *et al.* ERA-5 and ERA-interim driven ISBA land surface model simulations: Which one performs better?. *Hydrol. Earth Syst. Sci.* **22**, 3515–3532 (2018).
77. Abdalla, S. & Yilmaz, N. Suitability of ECMWF ERA-20C for wind and wave climate in the Black Sea (2015).
78. Liu, L., Gu, H., Xie, J. & Xu, Y. How well do the ERA-Interim, ERA-5, GLDAS-2.1 and NCEP-R2 reanalysis datasets represent daily air temperature over the Tibetan Plateau?. *Int. J. Climatol.* **41**, 1484–1505 (2021).
79. Wells, N., Goddard, S. & Hayes, M. J. A self-calibrating Palmer drought severity index. *J. Clim.* **17**, 2335–2351 (2004).
80. Palmer, W. C. *Meteorological Drought* Vol. 30 (US Department of Commerce, Weather Bureau, 1965).
81. Ebrahimian, A., Wadzuk, B. & Traver, R. Evapotranspiration in green stormwater infrastructure systems. *Sci. Total Environ.* **688**, 797–810 (2019).
82. Göktaş, A. & İşçi, Ö. A comparison of the most commonly used measures of association for doubly ordered square contingency tables via simulation. *Adv. Methodol. Stat.* **8**, 17–37 (2011).
83. Rasmussen, J. L. Data transformation, type I error rate and power. *Br. J. Math. Stat. Psychol.* **42**, 203–213 (1989).
84. Good, P. Robustness of Pearson correlation. *Interstat* **15**, 1–6 (2009).
85. Hauke, J. & Kossowski, T. Comparison of values of Pearson's and Spearman's correlation coefficients on the same sets of data. *Quaest. Geogr.* **30**, 87–93 (2011).
86. Murray, J. Likert data: What to use, parametric or non-parametric?. *Int. J. Bus. Soc. Sci.* **4**, 258–264 (2013).
87. Hamadeh, N., Karouni, A., Daya, B. & Chauvet, P. Using correlative data analysis to develop weather index that estimates the risk of forest fires in Lebanon & Mediterranean: Assessment versus prevalent meteorological indices. *Case Stud. Fire Saf.* **7**, 8–22 (2017).
88. Gibbons, J. D. & Chakraborti, S. *Nonparametric Statistical Inference* (CRC Press, 2014).
89. Hollander, M., Wolfe, D. A. & Chicken, E. *Nonparametric Statistical Methods* (Wiley, 2013).
90. Kendall, M. G. *Rank Correlation Methods* (1975).
91. Best, D. J. & Roberts, D. E. Algorithm AS 89: The upper tail probabilities of Spearman's rho. *J. R. Stat. Soc. Ser. C Appl. Stat.* **24**, 377–379 (1975).
92. Kozak, M. What is strong correlation?. *Teach. Stat.* **31**, 85–86 (2009).
93. Marker, B. R. Hazard and risk mapping BT. In *Encyclopedia of Natural Hazards* (ed. Bobrowsky, P. T.) 426–435 (Springer Netherlands, 2013). https://doi.org/10.1007/978-1-4020-4399-4_165.
94. Sklar, M. Fonctions de repartition an dimensions et leurs marges. *Publ. Inst. Stat. Univ. Paris* **8**, 229–231 (1959).
95. Hao, Z. & AghaKouchak, A. Multivariate standardized drought index: A parametric multi-index model. *Adv. Water Resour.* **57**, 12–18 (2013).
96. Leonard, M., Metcalfe, A. & Lambert, M. Frequency analysis of rainfall and streamflow extremes accounting for seasonal and climatic partitions. *J. Hydrol.* **348**, 135–147 (2008).
97. Joe, H. *Dependence modeling with copulas*. (CRC press, 2014).
98. Nelsen, R. B. *An Introduction to Copulas* (Springer Science & Business Media, 2007).
99. McNeil, A. J. & Nešlehová, J. Multivariate Archimedean copulas, d-monotone functions and ℓ1-norm symmetric distributions. *Ann. Stat.* **37**, 3059–3097 (2009).
100. Bouyé, E., Durrleman, V., Nikeghbali, A., Riboulet, G. & Roncalli, T. Copulas for finance-a reading guide and some applications. *SSRN J.* https://doi.org/10.2139/ssrn.1032533 (2000).
101. Vandenberghe, S., Verhoest, N. E. C. & De Baets, B. Fitting bivariate copulas to the dependence structure between storm characteristics: A detailed analysis based on 105 year 10 min rainfall. *Water Resour. Res.* https://doi.org/10.1029/2009WR007857 (2010).
102. Zscheischler, J., Van Den Hurk, B., Ward, P. J. & Westra, S. Multivariate extremes and compound events. In *Climate Extremes and their Implications for Impact and Risk Assessment* (eds Zscheischler, J. *et al.*) 59–76 (Elsevier, 2020).
103. Vogl, S., Laux, P., Qiu, W., Mao, G. & Kunstmann, H. Copula-based assimilation of radar and gauge information to derive bias-corrected precipitation fields. *Hydrol. Earth Syst. Sci.* **16**, 2311–2328 (2012).
104. Anderson, T. W. On the distribution of the two-sample Cramer-von Mises criterion. *Ann. Math. Stat.* **33**, 1148–1159 (1962).
105. Akaike, H. A new look at the statistical model identification. *IEEE Trans. Autom. Control* **19**, 716–723 (1974).
106. Akaike, H. A Bayesian analysis of the minimum AIC procedure. In *Selected Papers of Hirotugu Akaike* (eds Parzen, E. *et al.*) 275–280 (Springer, 1998).
107. Schwarz, G. Estimating the dimension of a model. *Ann. Stat.* **6**, 461–464 (1978).
108. Gocic, M. & Trajkovic, S. Analysis of changes in meteorological variables using Mann-Kendall and Sen's slope estimator statistical tests in Serbia. *Glob. Planet. Change* **100**, 172–182 (2013).
109. Mann, H. B. Nonparametric tests against trend. *Econom. J. Econom. Soc.* **13**, 245–259 (1945).
110. Sen, P. K. Estimates of the regression coefficient based on Kendall's Tau. *J. Am. Stat. Assoc.* **63**, 1379–1389 (1968).
111. Kendall, M. G. Rank correlation methods (1948).

Acknowledgements

Funding by the AWI Inspires Project—"Compound extreme events: a long-term perspective (LongCEX)" (S.C.D.) and by the Helmholtz Climate Initiative—REKLIM (M.I.) is gratefully acknowledged. M.I. and G.L. are supported by Helmholtz Association through the joint program 'Changing Earth—Sustaining our Future' (PoF IV) program of the AWI. We acknowledge support by the Open Access Publication Funds of Alfred-Wegener-Institute for Polar and Marine Research. We acknowledge the E-OBS dataset from the EU-FP6 project UERRA (https://www.uerra.eu) and the Copernicus Climate Change Service, and the data providers in the ECA&D project (https://

www.ecad.eu). MI was partially supported by a grant of the Ministry of Research, Innovation and Digitization, under the "Romania's National Recovery and Resilience Plan - Founded by EU –NextGenerationEU" program, project"Compound extreme events from a long-term perspective and their impact on forest growth dynamics (CExForD)" number 760074/23.05.2023, code 287/30.11.2022, within Pillar III, Component C9, Investment 8.

Author contributions

Conceptualization: S.C.D., G.L., M.I. Data Acquisition: S.C.D., M.I. Methodology: S.C.D, M.I. Analysis: S.C.D. Programming: S.C.D. Funding acquisition: M.I. Project administration: G.L., M.I. Supervision: G.L., M.I. Writing-original draft: S.C.D. Review: S.C.D., G.L., M.I.

Funding

Open Access funding enabled and organized by Projekt DEAL.

Competing interests

The authors declare no competing interests.

Additional information

Supplementary Information The online version contains supplementary material available at https://doi.org/10.1038/s41598-023-45067-6.

Correspondence and requests for materials should be addressed to S.C.D.

Reprints and permissions information is available at www.nature.com/reprints.

Publisher's note Springer Nature remains neutral with regard to jurisdictional claims in published maps and institutional affiliations.

Open Access This article is licensed under a Creative Commons Attribution 4.0 International License, which permits use, sharing, adaptation, distribution and reproduction in any medium or format, as long as you give appropriate credit to the original author(s) and the source, provide a link to the Creative Commons licence, and indicate if changes were made. The images or other third party material in this article are included in the article's Creative Commons licence, unless indicated otherwise in a credit line to the material. If material is not included in the article's Creative Commons licence and your intended use is not permitted by statutory regulation or exceeds the permitted use, you will need to obtain permission directly from the copyright holder. To view a copy of this licence, visit http://creativecommons.org/licenses/by/4.0/.

© The Author(s) 2023

Chapter 5

Probabilistic assessment of climate indices across Europe: analysing risk exposure in population density and land use types

Research Question: *"How do the probabilistic assessment of climate indices derived from high-resolution E-OBS data over the past seven decades, identify high-risk zones, co-occurrences, and persistence of climate events across Europe, and what are their implications for land use and population density exposure at a monthly temporal scale?"*

Synthesis:

We present a probabilistic approach to climate indices to derive high exposure zones across the European continent, utilizing high-resolution observed data over the last 70 years. 56 distinct climate indices related to drought, global radiation, precipitation, relative humidity, sea level pressure, and temperature are identified, shedding light on the complexity and multifaceted nature of risks encountered by European regions during co-occurrences of the different climatic events. Our findings suggest that precipitation and temperature-based indices are particularly useful in identifying high-risk regions in southern and southeastern Europe, whereas precipitation-based indices are for Northern and Western Europe. Temperature indices and potential evapotranspiration account for most risk exposure to Europe's dominant land use type. The highest exposure percentage of the population occurs with differences in days above and below the maximum temperature of 17 °C. About 17 climate indices with high-risk magnitudes are present regionally and in specific months, emphasizing diverse risk exposure. Russia, Norway, Iceland, and Sweden experience diverse high-risk co-occurrences, with multiple climate indices related to precipitation and temperature. The findings expand the range of climate indices and demarcate hotspots and risk zones, allowing for more effective climate monitoring and risk mitigation strategies.

Authors contributions:

Smit Chetan Doshi: Conceptualization, Data curation, Formal analysis, Investigation, Methodology, Software, Validation, Visualization, Writing – original draft, Writing – review & editing; Gerrit Lohmann: Project administration, Resources, Supervision, Writing – review & editing; Monica Ionita: Funding acquisition, Project administration, Resources, Supervision, Writing – review & editing.

This chapter is based on already published study in the Geomatics, Natural Hazards and Risk, Taylor & Francis (Doshi et al., 2025). Appendix C includes the supplementary information for this paper. Please note that the supplementary figures and tables in common can be found in Appendix A. Download input data (steps), code used for the statistical analysis (R and matlab) and output data generated from: https://zenodo.org/records/14993468.

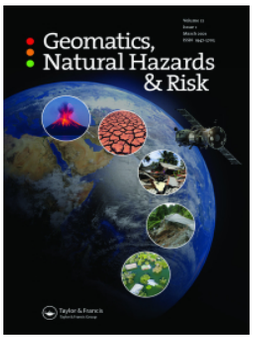

Geomatics, Natural Hazards and Risk

ISSN: (Print) (Online) Journal homepage: www.tandfonline.com/journals/tgnh20

Probabilistic assessment of climate indices across Europe: analysing risk exposure in population density and land use types

Smit Chetan Doshi, Gerrit Lohmann & Monica Ionita

To cite this article: Smit Chetan Doshi, Gerrit Lohmann & Monica Ionita (2025) Probabilistic assessment of climate indices across Europe: analysing risk exposure in population density and land use types, Geomatics, Natural Hazards and Risk, 16:1, 2484397, DOI: 10.1080/19475705.2025.2484397

To link to this article: https://doi.org/10.1080/19475705.2025.2484397

© 2025 The Author(s). Published by Informa UK Limited, trading as Taylor & Francis Group.

View supplementary material

Published online: 04 Apr 2025.

Submit your article to this journal

View related articles

View Crossmark data

Full Terms & Conditions of access and use can be found at
https://www.tandfonline.com/action/journalInformation?journalCode=tgnh20

GEOMATICS, NATURAL HAZARDS AND RISK
2025, VOL. 16, NO. 1, 2484397
https://doi.org/10.1080/19475705.2025.2484397

Taylor & Francis
Taylor & Francis Group

OPEN ACCESS Check for updates

Probabilistic assessment of climate indices across Europe: analysing risk exposure in population density and land use types

Smit Chetan Doshi[a,b], Gerrit Lohmann[a,b] and Monica Ionita[a,c]

[a]Alfred Wegener Institute Helmholtz Center for Polar and Marine Research, Bremerhaven, Germany; [b]University of Bremen, Bremen, Germany; [c]Faculty of Forestry, 'Ștefan cel Mare', University of Suceava, Suceava, Romania

ABSTRACT

We present a probabilistic approach to climate indices to derive high exposure zones across the European continent, utilizing high-resolution observed data over the last 70 years. 56 distinct climate indices related to drought, global radiation, precipitation, relative humidity, sea level pressure, and temperature are identified, shedding light on the complexity and multifaceted nature of risks encountered by European regions during co-occurrences of the different climatic events. Our findings suggest that precipitation and temperature-based indices are particularly useful in identifying high-risk regions in southern and southeastern Europe, whereas precipitation-based indices are for Northern and Western Europe. Temperature indices and potential evapotranspiration account for most risk exposure to Europe's dominant land use type. The highest exposure percentage of the population occurs with differences in days above and below the maximum temperature of 17 °C. About 17 climate indices with high-risk magnitudes are present regionally and in specific months, emphasizing diverse risk exposure. Russia, Norway, Iceland, and Sweden experience diverse high-risk co-occurrences, with multiple climate indices related to precipitation and temperature. The findings expand the range of climate indices and demarcate hotspots and risk zones, allowing for more effective climate monitoring and risk mitigation strategies.

ARTICLE HISTORY
Received 7 July 2024
Accepted 19 March 2025

KEYWORDS
Climate indices; risk analysis; probability distribution; population density and land use

1. Introduction

Over the last decades, Europe has faced devastating natural hazards such as floods, droughts, heatwaves, storms, landslides, and wildfires, impacting various societal, demographic and economic aspects (Bakke et al. 2020; Feng et al. 2020; Ionita et al.

CONTACT Smit Chetan Doshi smitdoshi5@gmail.com

Supplemental data for this article can be accessed online at https://doi.org/10.1080/19475705.2025.2484397.

© 2025 The Author(s). Published by Informa UK Limited, trading as Taylor & Francis Group.
This is an Open Access article distributed under the terms of the Creative Commons Attribution License (http://creativecommons.org/licenses/by/4.0/), which permits unrestricted use, distribution, and reproduction in any medium, provided the original work is properly cited. The terms on which this article has been published allow the posting of the Accepted Manuscript in a repository by the author(s) or with their consent.

2021; Merz et al. 2021; Kreibich et al. 2022; Rentschler et al. 2022; Laino and Iglesias 2023). Globally, the occurrence of natural hazards affecting humans (and/or several socio-economic sectors) is increasing (Fuchs et al. 2015) and the risks associated with natural hazards are also increasing (Ward et al. 2020). The development and implementation of disaster management strategies heavily depend on accurately assessing natural hazard risks, which includes identifying regions prone to hazards and their frequency of occurrence (Silva et al. 2022). Sendai framework incorporates risk as the combination of hazard, exposure and vulnerability (UNISDR 2015). Hazard refers to the identification and likelihood of occurrence of various natural hazards; exposure refers to the location of infrastructure or people in hazard-prone area; and vulnerability refers to the assessment of potential damage and loss caused by different types of hazards (Ward et al. 2020). Therefore, there has been rising recognition of the importance of analyzing the impacts of climate variability and change on natural hazards in recent years.

Climate processes (interactions and mechanisms in Earth's climate system) are difficult to monitor and quantify, given their significant socioeconomic and environmental impacts accurate assessment is important (Rezaei et al. 2015; Bachmair et al. 2018; Sergio et al. 2018). If the impacts are caused by the 'fusion' of several climate variables, the difficulty is further increased (Domínguez-Castro et al. 2020). Climate indices provide valuable information for monitoring and assessing natural hazards, as they are quantitative indicators of the climate conditions, including both extremes and mean values (Chervenkov and Slavov 2021). These climate indices are helpful for giving an assessment of climate variability and change under the current and future scenarios (Zhou et al. 2014; Dosio 2016; Campozano et al. 2017). To monitor climate extremes, the expert team on climate change detection and indices (ETCCDI) identified 27 core climate indices (Klein Tank et al. 2009), based on precipitation and temperature indices. These climate indices are essential for assessing variability and trends in climate extremes. Climate indices are widely used in Europe (Van den Besselaar et al. 2013; Riediger and Gratzki 2014; Pradhan et al. 2022) with a wide range of applications, but the majority of them are focused on precipitation or temperature, to capture extreme events such as flood or droughts. Previous studies in Europe have focused on computing climate indices derived from weather data by utilizing various data sources and integrating future change scenarios through climate models (Moberg et al. 2006; Riediger and Gratzki 2014). Further studies are required to extend the use of climate indices beyond merely precipitation and temperature and to incorporate other factors like radiation, wind, humidity and sea-level pressure. Europe has been witnessing destructive extreme events that have disastrous effects and extremely high death tolls, such as heat waves of 2003 (2017) in Central (Southern) Europe (Russo et al. 2015; Kew et al. 2019) and 2010 severe cold waves in Northern and Western Europe (Cattiaux et al. 2010). Unseasonably warm weather and extended drought periods in Central and Northern Europe during 2018 resulted in recorded unprecedented wildfires, mortality and severe decrease of crop yield (Bakke et al. 2020; Schuldt et al. 2020). Very few studies incorporate different types of climate indices within one study and this concern has already been addressed in previous studies (Peña-Angulo et al. 2020). Combining different weather variables

could lead to bioclimatic or drought indices, which would be comprehensive to understand the climate system and its impacts on various socio-economic sectors. For example, the Universal Thermal Climate Index (UTCI), as a bioclimatic index, has already been used to validate the results with mortality rates from 17 European countries along with the 2003 European heatwave, demonstrating its effects on human health (Di Napoli et al. 2018) and its usage where high-quality station data is not available (Urban et al. 2021). On the other hand, a study reveals that tree mortality has increased in Europe due to exposure to droughts (Senf et al. 2020). Monitoring various climate indices trends has revealed that Europe has experienced decreasing trends in cold days (nights), wind indices, and precipitation indices in the western part, whereas increasing trends in warm days (nights) and precipitation-related indices for northern and central regions (Seneviratne et al. 2012; Peña-Angulo et al. 2020).

The frequency of climate extremes is projected to increase in a warming world leading to heavy precipitation, droughts, or heat waves (Rahmstorf and Coumou 2011; Seneviratne et al. 2012; Dai 2013; Kirtman et al. 2013; Myhre et al. 2019). Anthropogenic-induced warming increases the risk of not only individual climate extremes but also compound (co-occurring) and cascading hazards (AghaKouchak et al. 2020; Zscheischler et al. 2020). These co-occurrences of climate extremes at the same place and time is a crucial aspect of compound events, that are expected to become more frequent due to climate change across Europe, resulting in compound hazard (Forzieri et al. 2016). However, defining a compound event requires considering it as the combination of multiple drivers and/or hazards, that results in societal and environmental risk (Zscheischler et al. 2018). For example, during the years 1990–2018, few places in Europe experienced droughts, wildfires, and heatwaves all at once (Sutanto et al. 2020). However, the analysis of whether the co-occurrence is increasing or decreasing at same location in the same year is missing and this research gap has been highlighted in the previous study (Chen et al. 2018). The frequency and intensity of occurrences of climatic events can be determined using probability distribution fits to climate indices. For example, many researchers found that either Gamma or generalized extreme value (GEV) are the best fit for the probability distribution of precipitation indices (Alexander et al. 2006; Wang et al. 2013a, 2013b). However, one of the studies suggests that each station needs analysis individually as GEV is not always the best probability distribution approach to fit the precipitation indices (Fischer et al. 2012). In this study, the analysis includes identifying hotspots (probability threshold $>$ 90%) of occurrences and co-occurrences at various spatial and temporal scale by using best-fit probability distribution. Further analysis defines the persistence of climate extremes, which is using co-occurrences of extreme events that occurs consecutively for years at same location (Beniston and Goyette 2007). No studies have exclusively discussed about the best fit of probability density function at the hotspots of occurrences and co-occurrences of climate indices across Europe. By identifying and analyzing these events, stakeholders can improve their understanding of the underlying drivers that cause these occurrences and develop prediction that is more robust for their future occurrences. As a result, the observations lead to the following general gaps in previous studies:

i. Lack of focus (only a few studies) on climate indices other than temperature and precipitation in most of the studies for assessment.
ii. A generalized best fit of probability distribution for the entire study area and selected climate indices; overlooking the specific probability distribution suitable for hotspot.
iii. Neglecting the assessment of hotspots of occurrences, co-occurrences, and persistence of climate events at the monthly temporal scale.
iv. Risk exposure of population density and land use for the identified monthly high probability climate indices events.

This paper aims to bridge the above-highlighted gaps for the European continent by computing 74 climate indices at a monthly temporal scale using high-resolution observed daily weather data, considering the last 72 years (i.e. 1950–2021). The primary research objective is to identify the hotspots of high-risk zones (that is probability exceeding 90%), co-occurrences of hotspots (that is combination of various climate indices), and persistence (that is hotspots co-occurrences at the same location for consecutive months). The detailed analysis includes best-probability distribution fit for climate indices at hotspot locations for each month and includes a graphical representation of conclusive risk maps together with the integration of population density and land use maps to determine the risk exposure. Further, the results are validated through a literature review to demarcate its implications on that region.

2. Data and methods

2.1. Data and climate indices

European Climate Assessment and Dataset (ECA&D) Ensembles daily gridded observational dataset (E-OBS) remains a significant data source for climate monitoring across Europe, specifically to assess the magnitude and frequency of extreme events (Lavaysse et al. 2018; Manning et al. 2019; Cardoso Pereira et al. 2020). The European National Meteorological and Hydrological Services (NMHSs) provides quality controlled meteorological data through observed stations which is the source for E-OBS (Cornes et al. 2018). The dataset provides high-quality gridded daily air temperature (maximum and minimum), global radiation, precipitation, relative humidity, sea level pressure, wind speed, and elevation data from January 1950 to December 2021 (v25.0e). We employed data from E-OBS to estimate 74 different climate indices of the European continent. Herein, the gridded climate indices were computed with a spatial resolution of 0.1° (∼11 km horizontal resolution) and temporal resolution of monthly time scale. The available spatial extent of data (European land surface) covers an area of 25°N-71.5°N × 25°W-45°E. Smaller number of observation stations for acquiring wind speed records in the east of the European continent leads to missing values in terms of spatial variability. Another data source related highlights to global radiation data that incorporates both in-situ observations and satellite data - Clouds and the Earth's radiant energy system (CERES).

'ClimInd' and 'scPDSI', which are developed packages within R (https://cran.r-project.org/web/packages/ClimInd/index.html and https://cran.r-hub.io/web/packages/scPDSI/),

are used to calculate set of 74 climate indices. The climate indices are classified into eight broad categories: drought ($n = 15$), global radiation based ($n = 1$), multi-element ($n = 5$), precipitation based ($n = 16$), relative humidity based ($n = 1$), sea level pressure based ($n = 1$), temperature based ($n = 32$), and wind speed based ($n = 3$). Supplementary table S1 lists these indices and their description in detail. The computation of these indices is explained in R-packages; however, the weather data required to compute individual indices is showcased in Figure 1. The climate indices are calculated on a monthly time scale with the usage of daily weather data acquired from E-OBS for a continuous period of 72 years (1950–2021). For climate indices that can span multiple months, the values are assigned based on the calendar month in which it occurs. For example, cdd is calculated on a monthly basis by separating daily data at the end of the month. This means the cdd value for January is based on the daily data from 1st January to 31st January. Similar reference period is considered for analysis of percentile and threshold based climate indices.

In addition, next part of the methodology involves analysing risk exposure by incorporating data of population density and different types of land use. Gridded data on population density (GPWv4) for 2020 are provided by the Socioeconomic

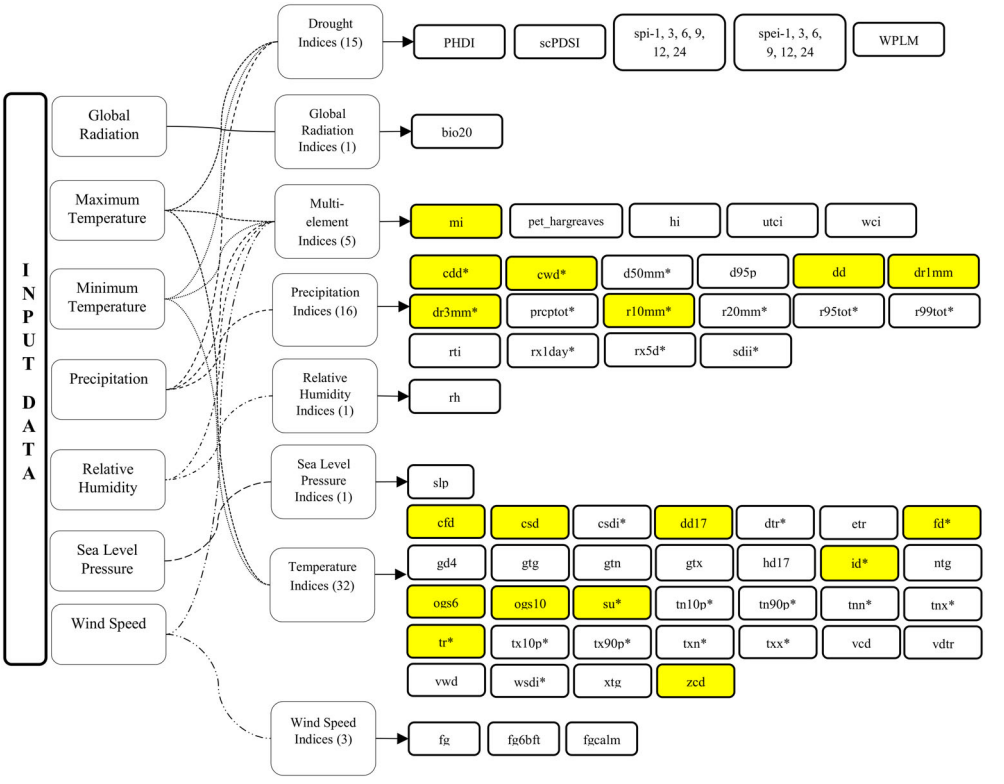

Figure 1. Climate indices derived from E-OBS weather data. Figure represents the weather data input used for climate indices computation over 1950–2021. Refer to supplementary table S1 for abbreviations and detailed descriptions of 74 climate indices. Yellow highlights indicate 17 climate indices with high probabilities (>90%) in the specific European zones for particular months, while asterisks (*) mark the 27 core climate indices from the ETCCDI (Klein Tank et al. 2009).

Data and Application Center (SEDAC) (open source data: http://sedac.ciesin.columbia.edu/). The global population density map extraction is based on the spatial extent of the European continent and upscaled from ~1 km to ~11 km resolution using simple averaging techniques carried in geographic information systems. The 2020 population density map for the European continent shows that ~64% of the population resides in areas with a density of 5–250 people/sq.km. A similar statistical process is carried out for land use data having a 10 m resolution for 2021 derived from the European Space Agency (ESA) Sentinel-2 imagery (Karra et al. 2021). The resolution and spatial extent are identical to the computed climate indices through the E-OBS data set. In general, the land use cover during 2021 for the European continent includes rangeland (~45%), crops (~29%), trees (~17%), built area (~6%), and bare grounds, snow/ice, clouds and water each ~<1%.

2.2. Probabilistic assessment

To identify hotspot zones, with a high probability of occurrence for the monthly climate indices, it is first necessary to develop the marginal distribution for each of the climate indices in each grid cell. 26 different marginal distributions were used to fit the climate indices which includes beta, binomial, Birnbaum-Saunders, burr, exponential, extreme value, gamma, generalized extreme value, generalized Pareto, half-normal, inverse Gaussian, kernel-box, kernel-triangle, kernel-Epanechnikov, logistic, log-logistic, log-normal, Nakagami, negative binomial, normal, Poisson, Rayleigh, Rician, stable, t-location scale, and Weibull. Binomial, negative binomial, and Poisson are among the well-known discrete probability functions and the rest are continuous probability functions, with applications in a wide range of fields (Ohemeng and Kozubowski 2023). The statistics and machine learning toolbox of MATLAB (v2023b) offers the generic probability density distribution listed above along with an equation and the statistical indicator to determine the performance of each of them based on the Kolmogorov-Smirnov (K-S) test.

To determine which probability distribution type was most appropriate for each of the climate indices at each of the grid, the K-S test (Massey Jr 1951) is used to evaluate the goodness-of-fit of each theoretical and empirical distribution. The K-S test is a non-parametric statistic that uses the largest maximum difference between empirical and theoretical cumulative distribution functions to determine disagreement (Massey Jr 1951). Finally, it returns a *p*-value inversely proportional to the level of confidence at which the two samples fail the hypothesis. Greater the *p*-value, the greater the confidence in the theoretical distribution fit. The null hypothesis assumes that there is no difference between the empirical and theoretical probability distributions, and the test statistic D is computed as follows:

$$D = \text{maximum}|F_o(X) - F_r(X)| \tag{1}$$

where $F_o(X)$ and $F_r(X)$ is the cumulative distribution function (cdf) of two samples constructed from empirical (observed values) and theoretical (probability distribution fitted values) models, respectively. D is the test statistic, which indicates the maximum absolute difference between two cdf ($F_o(X)$ and $F_r(X)$). Because of the

distortion of the distributions introduced by random sampling of a large group of samples, applying the K-S test requires a relatively large sample size to accurately reject the null hypothesis (Saylor and Sundell 2016). This above condition is sufficient for applying the K-S test, as the computed climate indices are based on a large sample size from a continuous time series. The output produced would be each grid of climate indices indicating the best fit of probability distribution along with probability values. We calculate the average non-exceedance probabilities for each grid point by averaging the probability values from the fitted distributions over the entire 72-year period for each climate indices. Additionally, for grid points with no variability in probability values across each month over the 72-year period, such scenarios were excluded from high-probability regions because fitted distribution yields a zero value.

2.3. Risk exposure

The risk map, which indicates the probability value based on the best-fit probability distribution function at each grid cell, is the marker for defining the hotspots across the European continent. Further, the high probability that is modelled fitted probability distribution exceeding the threshold is considered to be greater 90% for all the climate indices. Here, the 90% defined high probability zones are visualized using spatial maps, highlighting their distribution and months in which they occur. Some regions however, exhibit maximum values of the climate indices for specific month but due to their lack of climate variability the probability values result in a 0-value outcome. Therefore, results related to those grids does not contradict the likelihood of occurrence but rather highlights the behaviour of the fitted probability distribution under 0-variance. Such regions can be characterized for stability and extreme conditions, due to this constant pattern. Now, there are climate indices, which display 90% high probability in the entire European continent for all or specific months. However, it also possible that only certain regions in the European continent highlight a high probability for specific climate indices. These regions are analysed in detail, as a specific interest of this study. Co-occurrences and persistence both are identified through spatial maps. Visualization also includes the number of co-occurrences for each month that are compound events of all high-probability climate indices derived from different weather variables. It must be understood that the high probability doesnot necessarily mean that the values are extreme. Instead, it indicates a high likelihood of occurrence, prompting the need for specific monitoring of these climate indices to further assess their potential impacts and consequences.

High probability zones for the European continent from the risk maps act as a layer, which are superimposed on the population density and land use maps (Figure 2C,D). Using simple averaging of statistical analysis values for all overlapping grids, a specific month analysis is made on the population density and each land use type exposed to those high risks. The statistical values are displayed in terms of the percentage of exposure to the population density and land use of different types. Land use can be grouped into 9 different classes: Water, trees, flooded vegetation, crops, built trees, bare ground, snow/ice, clouds, and rangeland. High exposure for each of them is computed separately whereas population density is collectively computed.

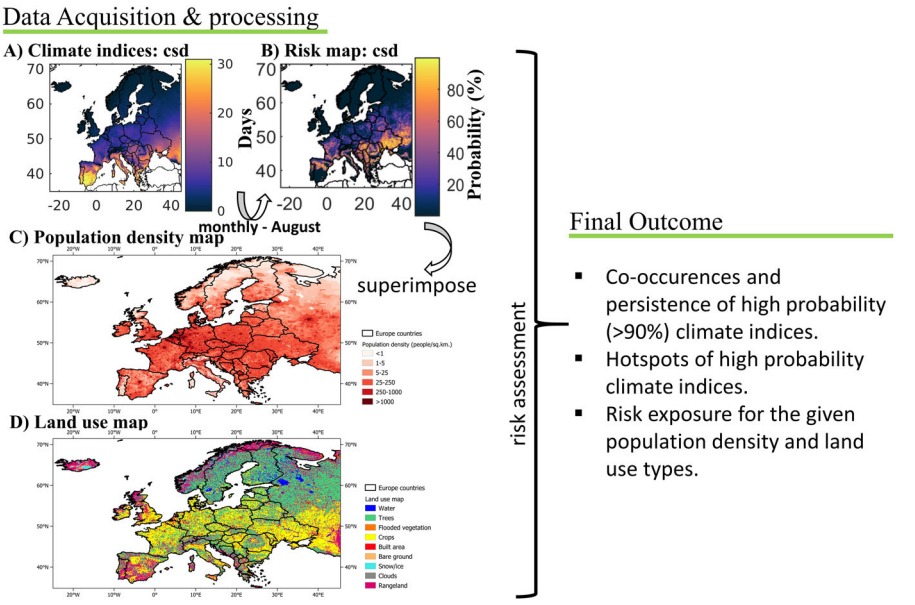

Figure 2. Schematic view of the methodology. Overview of methodology for assessment of risk exposure of the population density and land use types across European continent. (A) Mean monthly values of the climate indices computed over entire 72-year period (1950–2021) using E-OBS daily data. (B) Risk map showing probability values based on best-fit probability distribution for each grid cell. (C) Population density map for 2020, derived from GPWv4 data (∼11 km resolution). (D) Land use map for 2021, based on ESA Sentinel-2 imagery (∼ 11 km resolution). The figure integrates climate indices with socioeconomic data to identify high-risk zones.

To analyse the co-occurrences (compound event) of climate indices computed from different weather variables, we use the same visualization tool to map their compound impact on population density and land use types. The use of various climate indices, each providing unique and valuable information, offers detailed insights into monitoring risk regions. However, it must be understood that these climate indices might not have direct implication with landuse types or population density, but their role in informing decisions will always be critical for effectively assessing risk. This study focuses on evaluating the current exposure of population density and land use to the high-probability climate indices, with potential for future exploration into their variability over decades.

3. Results and discussion

3.1. Identifying risk zones on the European continent

Probability values at each grid are calculated based on the best marginal distribution fit for each of the climate indices (see methods - probabilistic assessment (2.2)). In the section, there are two ways to visualize the risk zones: (1) all zones with climate indices that had high probability (>90%) and (2) the highest probability from the high probability value derived for climate indices (termed here as hotspot). Out of 74

different climate indices, 56 climate indices depicts more than 90% high probabilities for any one of the specific months across Europe, of which 17 climate indices (Figure 1 and supplementary table S1—yellow highlights) have high probabilities for the specific month at certain zones of Europe. The remaining 39 climate indices have higher probability (> 90%) almost across entire European continent (supplementary table S1—green highlights). Figure 3 shows conclusive risk zones across various European countries where probability for the 17 climate indices >90%, based on different probabilistic models developed for each month using a comprehensive 72 years of daily climate data.

Previous studies estimated probability distribution function selection using a single best fit for the entire study region, which may not be accurate in reality, particularly for identifying high-risk zones (Mandal and Choudhury 2015; Miao et al. 2016). A higher p-value in K-S test indicates a higher likelihood that the difference between theoretical and empirical distribution is by random chance. The finding suggests that the probability density function at each grid varies significantly, meaning that different grids have different probability functions for various climate indices. Based on analysis of the probability distribution averaged for various climate indices across Europe, the conclusion can be drawn:

i. Distribution with smaller interquartile range while capturing higher probability values with consistent data - burr, generalized extreme value, Kernel (box, triangle, Epanechnikov), log-logistic, log-normal, Nakagami, Normal, and Rician.
ii. Distribution capturing high variability and outliers: Extreme value, Kernel-normal, logistic, stable, and t-location scale.
iii. Skewed distribution with larger interquartile ranges: Birnbaum-Saunders, half-normal, inverse-Gaussian, and Rayleigh.

The skewed distribution with large interquartile ranges signifies skewness with data points and their influence is substantial in extreme event analysis and representation. Discrete probability functions such as Poisson, negative-binomial, and binomial are not suitable for the selection of distribution fit especially for high-risk zone determination due to interquartile range fitting mostly for lower probability values. Supplementary figure 1 displays the comparison of various probability distribution functions through a box plot for all determined monthly probabilities of climate indices.

Based on the aforementioned analysis (Figure 3), we find that the southern and southeastern parts of Europe experience the highest risk for precipitation (temperature) indices like cdd (csd, su) for the majority of the months. Further, it depicts that precipitation indices like dd, dr1mm, and dr3mm pose a concern to northern, northeastern and western Europe. The risk indicators cwd, r10mm, ogs6, ogs10, tr, and mi have concentrations in limited zones of Europe. For each month, the rest of the high probability categorized indices such as fd, dd17, fd, id, and zcd are widely scattered across Europe. The majority of the regions are at high risk due to the longest dry period for Italy, Moldova, Portugal, Spain, and Ukraine, particularly during April. During December, regions along the Norwegian coast have a high risk of dry days <

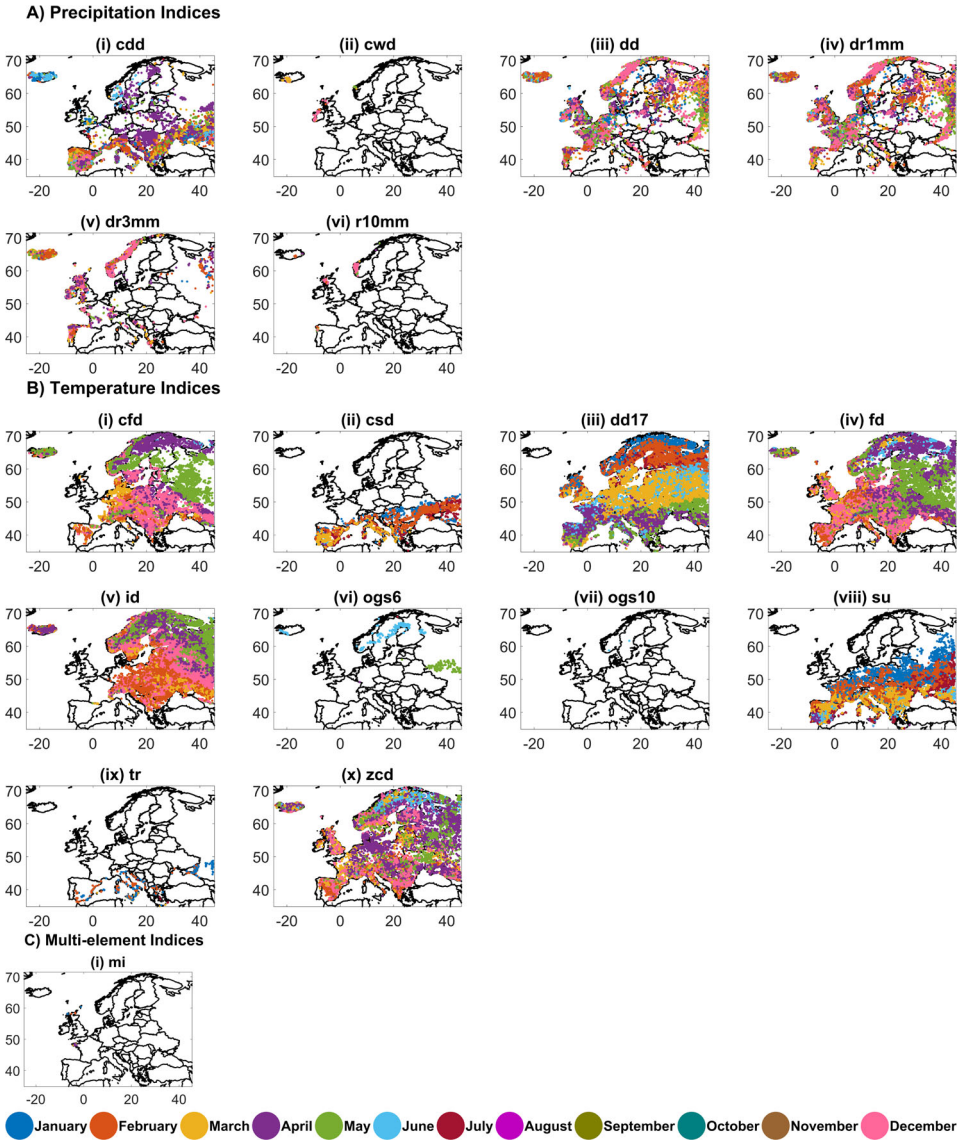

Figure 3. Identifying high-risk zones in Europe. Spatial distribution of high-risk zones (>90% probability) for 17 climate indices across Europe. Coloured legends indicate monthly risks mapping of climate indices influenced zones in Europe. See supplementary table S1 for climate indices detailed description.

1 mm and wet days $\geq$ 1/3/10 mm. Iceland, on the other hand, poses a high risk due to the longest dry (wet) period during January and June (March). Furthermore, dry days are scattered around Iceland during the months of February, March, April, and December. In March, Iceland has a risk due to a combination of two opposite occurrences of events (wet and dry days). Maximum consecutive frost days related risks are observed in northern Norway, Finland, Russia, and Sweden during April, Iceland and western Russia during May, and the majority of countries in southern, southeastern, central and western Europe zones for the rest of the months. Frost days have a

greater number of regions with a higher probability of risk, although the zones demarcated for the specific months are identical to consecutive frost days. Southern Ukraine and Russia (Italy, Portugal, and Spain) experience high risk due to consecutive summer days during February (March). In January, February, and July, the difference days above/below the maximum temperature 17 °C begins with Finland, Ireland, Norway, Russia, Sweden, and the United Kingdom and moves to the majority of central and eastern European countries such as Austria, Belarus, Belgium, Czechia, Denmark, Germany, Netherlands, Poland, Russia, and Ukraine during March and June. Furthermore, throughout April and May, Bulgaria, France, Italy, Romania, Serbia, and Spain are affected. Ice days based risk is observed in the central-eastern, northern-eastern, northern-eastern and northern, central-eastern Europe zones in March, April, May and December, respectively. The onset of the growing season with a base of 6 days is specific to southern Norway, central Sweden and Finland, western Iceland during June and central-western Russia during May. Belarus, Czechia, France, Germany, Italy, Poland, Portugal, Romania, Slovakia, Spain, and Ukraine are at high risk due to summer days during January, February, and March. During January and February, the number of days with minimum temperature $> 20\,^{\circ}C$ (tropical nights) is depicted in several locations in Italy and Spain. The number of days with minimum (maximum) temperature $<$ ($>$) $0\,^{\circ}C$ (zero crossing days) based risk varies across multiple zones during the same month, such as during April in Belarus, Belgium, Denmark, Germany, Hungary, Moldova, Netherlands, Norway, Poland, Romania, Russia, southern Finland, Sweden, and Ukraine. During January and February, the number of days with relative humidity $> 90\%$ (mould index) is concentrated in the northern area of the United Kingdom. The countries discussed specific to the high probability risk do not imply that entire country is at risk, but rather that the majority of the country is at risk. Stakeholders could utilise the information as a climate monitoring system to decrease hazard risks in Europe by integrating climate indices, at specific months, and regions. The assumption here is to demarcate high-risk zones of varied climate indices with a probability threshold of $> 90\%$; this should not be misinterpreted that zones with lesser probabilities are not at risk. The reason for this lies in the complexity of disaster risks (de Ruiter and Van Loon 2022), as there could be higher impact owing to a compound hazard (Leonard et al. 2014; Zscheischler et al. 2018), which is not identified for the present list of climate indices.

Supplementary figure 2 (A) highlights the number of compound occurrences that could occur on a monthly time scale in a specific zone of Europe with a high-risk probability ($>90\%$). For each grid, it displays in numbers the various types (climate indices derived from different weather data as an input) of climate indices that can potentially compound from the list of climate indices. It can be stated that using the given list of climate indices there at most two co-occurrences of climate indices (derived from different weather variables) across the European continent for a specific month. In addition, the supplementary figure 2 (B) depicts the variability of climate indices co-occurrences across different countries in Europe. According to insights, Russia, Norway, Iceland and Sweden are the European countries with highest possible co-occurrences of events (>10) from the given list of climate indices across each month. Russia experiences the highest number of co-occurrences of events in months

March, October, and November, requiring monitoring of multiple climate indices, including wet/dry days, heavy precipitation of 1, 3, and 10 mm, cold frost/ice days, difference of maximum temperature, onset of growing season, and diurnal temperature. In October, Iceland also shows a high number of co-occurrences, while Norway and Sweden exhibits significant co-occurrences in December for the indices related to precipitation of 3 and 10 mm, frost days, and temperature extreme indices. In, February, Italy and France have the highest co-occurrences (7 co-occurrences), whereas in June, Spain records the highest (5 co-occurrences). These co-occurrences are primarily linked to precipitation and temperature based extreme indices. These regions and specific months require monitoring for compound related risks, which could be either bivariate or trivariate in nature. The type of indices that cause the co-occurrences are drawn from the previous list of 17 climate indices (Section 3.1—'Identifying risk zones on the European continent').

3.2. Hotspots of identified risk zones

High-risk zones need a crucial consideration of further downscaling with the highest risk exposure based on hotspots of high probability climate indices at different zones of Europe. Hotspots are the 17 climate indices with the highest monthly probability value, which identifies spatially the risk zones that require monitoring and will have the least time to make mitigation decisions during an unprecedented event. Figure 4 displays the countries of the European region where the climate indices provide the maximum number of high risks based on probability values.

Locations for each of the hotspots were identified based on the Figure 4. Wherever high-risk climate indices intersected with the world map, these locations were highlighted. According to the hotspots (Figure 4), the effects of the longest dry periods due to precipitation are evident in August and September in Krasnodar Krai, Russia. Tver Oblast, Russia and Stavropol Krai, Russia, have a high risk for consecutive frost days as a result of low temperatures in November and December, respectively. Odessa Oblast, Ukraine, and Toldeo, Spain have the maximum consecutive summer days due to the highest temperature in August and September. The longest wet period in Ireland affects Knockrour East and Galway owing to precipitation in December. Due to low precipitation in May, Grímsnes- og Grafningshreppur, Iceland has dry days. Difference days above/below 17 °C due to maximum temperature in February, April, and July affect Granada, Spain, Stavropol Krai, Russia, and Murmansk Oblast, Russia, respectively. In January Eyjafjarðarsveit (Skaftárhreppur), Iceland is at risk due to wet days with 1 (3) mm of precipitation. Frost days occur in Krasnodata Krai, Russia, and Odesa Oblast, Ukraine, in March as well as Teruel, Spain, in November. In March, ice days occur in various regions of Iceland, including Skaftárhreppur, Eyjafjarðarsveit, Múlaþing, Vesturbyggð, and Súðavíkurhreppur. In August, the mould index was noticed in Highland Council, UK, as a result of mean temperature and relative humidity. In April, Oryol Oblast, Russia, and Valle Municipality, Norway observe at least 6 days with mean temperature >5 °C (ogs6). Several regions in Sweden, Finland, and Norway, are at risk by ogs6 in May, including Lillehammer Municipality, Orsa Municipality, Kalajoki, Älvsbyn Municipality,

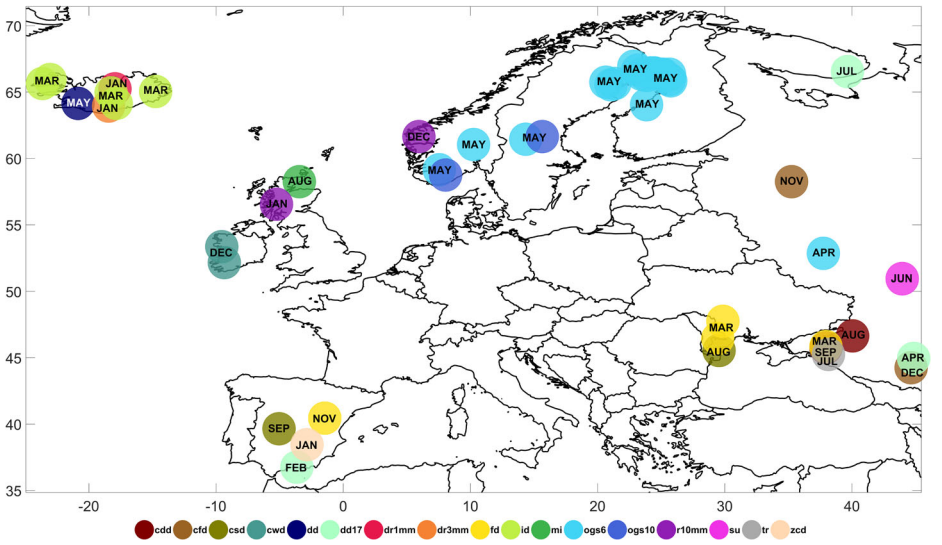

Figure 4. Hotspot of high-risk climate indices based events. Hotspot of 17 different high-risk climate indices with the highest monthly probability values (>90%), across Europe. Locations and specific months highlights where maximum high probability risk occurs. The findings interprets that during may, fennoscandia exhibits a high probability of the onset of the growing season (a condition favourable for plant growth during this month). Supplementary table S2 provides details on climate indices, locations, months, and best-fit probability distributions. The figure points out critical areas requiring monitoring for specific climate indices.

Piteå Municipality, Simo, Tervola, Ylitornio, Övertorneå Municipality, Rovaniemi, and Korpilombolo. In May, Risdal, Norway, and Färila, Sweden, see at least 10 days with mean temperature $> 5\,^{\circ}C$. Daily precipitation ≥ 10 mm affects Inner Seas off the West Coast of Scotland and Hyen, Norway in January. Summer days in Volgograd Oblast, Russia, with maximum temperature $> 25\,^{\circ}C$ in June. Krasnodar Krai, Russia, is influenced by days with minimum temperature $> 20\,^{\circ}C$ in July. Jaén, Spain, observes number of days with maximum temperature $> 0\,^{\circ}C$ and minimum temperature $< 0\,^{\circ}C$ in January. The 39 hotspots from the climate indices specified in (Section 3.1—'Identifying risk zones on European continent') will be included in the visualization of hotspots of climate indices. To highlight the co-occurrences and persistence of zonal hotspots, the following are some further analysis to demonstrate the necessity of the visualization during risk exposure assessment. In Russia, Krasnodar Krai exhibits the persistence of high risks climate indices cdd in August and September with fd (high risk in March) and tr (high risk in July) co-occurrence. Similarly, cfd and dd17 co-occur in in Russia, Stavropol Krai. Other co-occurrences include csd and fd in Odesa Oblast, Ukraine and dr1mm (dr3mm) and id at Eyjafjarðarsveit (Skaftárhreppur), Iceland.

The validation based on past references for the exposed environment's ground reality is essential to delineate the importance of the hotspots demarcated. For instance, an increase in sea surface temperature near the coast (Lebedev et al. 2017) and temporal flooding of riverside areas (Alekseevskii et al. 2016) are typical in Krasnodar Krai. Based on observed records, Russia has seen severe atmospheric

drought dynamics, as well as a 6.8% increase in the number of days with warm period (Cherenkova 2007). The importance of Krasnodar territory in agriculture and tourism has been noted as being vulnerable to the occurrences of extreme weather events (Kostianoy et al. 2017). The number of shrews in Tver oblast varies greatly and mortality is associated with the preceding summer and the severity of winters in that zone (Kalinin 2008). Observed data from Stavropol Krai region demonstrates increased air temperature, which leads to warmer spells during vegetative period and further leading to precipitation (not intense) which contributes to erosion (Savinova et al. 2020). Odessa experiences a more intense winter with a combined increase in precipitation however; a decrease in precipitation during warm period was highlighted in the previous study; shifts in precipitation with cold and warm periods has been showcased (Karamushka et al. 2022). Pre-and post-impact of heat waves had been studied for Toledo indicating increase of mortality in the region for specific period (Linares et al. 2015). West-coast sites in Ireland, especially during wet hours, results in rain depths for months have already been identified due to precipitation with an increasing trend (Kiely 1999). Temperature rise in Iceland, with minimum temperature rise greater than maximum temperature rise, leading in enhanced warming in Iceland's north and northwest (Gosseling 2017). However, precipitation trends were unclear, but total precipitation was predicted to rise with a positive trend in all parts of Iceland (Gosseling 2017). Furthermore, Iceland has a strong influence in winter due to sea ice cover and wind direction in warming; nevertheless; estimating sea ice cover through models has proved difficult (Gosseling 2017). In the Scottish Highlands, UK, the variability of winter humidity has increased 8-fold, affecting calluna (shrubs) (Hancock 2008). Fennoscandia has a large degree of climatic diversity; an analysis of the start of the growing season in these zones indicates an increase of 1 °C in spring temperatures results in 5–6 day advance in the start of the growing season (Karlsen et al. 2007). Outlining the significance of this work indicates that the results would also be relevant to past studies (referenced for validation) for identifying additional drivers responsible for hazards that were acting concurrently with the already identified ones. The identified high-risk probability climate indices could further mitigate the risk by re-designing the framework plans. Further assessment includes population density and land use map categorized risk exposure for the varied high-risk climate indices.

3.3. Risk exposure of population density and land use type

During October-March, the European continent population is at a high risk due to climate indices dd17 (difference days above/below maximum temperature 17 °C). These climate indices (dd17) higher probability and positive (negative) value suggest warmer (colder) weather condition. While dd17 has no direct implications to the population density similar to many other climate indices, it serves as an important indicator of temperature variability where shifts can influence the entire ecosystem. During January and February, gd4, fd, cdd, and cfd based risks are exposed to 100–165 people/km^2 of the European population. In March, a greater proportion of the population is exposed to gd4 and ogs6, whereas in April, it is ogs6, dr1mm, dd, and

dd17. csd, su, dr1mm tops during the month of May and in June except dr1mm exposure continues for the population of Europe. Climate indices tr and cdd are prevalent in July, and tr during August. Exposure to csd repeats in September, su, cdd in October, gd4 in November, and gd4, cdd, fd in December poses a substantial risk to the European continent's population. In all of the previously described climate indices, the population density at risk for the continent is >100 people/km^2. However, there are a majority of the population, which are at risk due to different climate indices, as visualized in Figure 5(A). These methodological study act as a diversity of risks based on high likelihood of occurrences faced by Europe due to complexity of various climate indices. From temperature indices such as dd17 to precipitation indices such as dr1mm and other climate indices, the population is exposed to variety of challenges. Prolonged exposure to dd17, cdd, gd4, fd, and dr1mm, indicates the importance of long-term planning as the risks persists beyond single month and importance in community resilience, disaster preparedness and infrastructure development this is required (Koliou et al. 2018). Different regions and different population within it face different risks at different times of the year, understanding the variation is crucial for the development of region specific adaptation plans (Field and Barros 2014).

Rangelands, crops and built areas dominate the land use map of Europe. Rangeland land use is at risk to temperature based climate indices gtg, gtn, and hd17 during winter season (DJF). Further in March and summer season (JJA) drought indices such as spi-24 and spi-6 contribute the most. During April and May, gtg and gtn whereas September and November it is gtx has maximum risk exposure for the rangeland land use. Potential evapotranspiration is critical throughout the month of October for risk exposure in rangeland land use. The risk exposure for the rangeland land use can pose problems for grazing animals, affecting agricultural and communities (Thornton et al. 2007). Challenges related to rangeland soil quality, which is the reliable indicator still needs to be addressed which aligns along this study (Herrick and Whitford 1995). Crops as a land use type are under risk exposure due to potential evapotranspiration and temperature based indices such as hd17, gtn, gtg, gd4, gtx, and ntg. The vulnerability of the crop land use owing to potential evapotranspiration suggests the need for agricultural practices modification, more water-efficient irrigation system or drought-resistant crop varieties (Zahoor et al. 2019). Temperature based crop indices may influence planting seasons or crop varieties cultivated in specific regions (Sacks et al. 2010). Built areas are also under similar risk exposure due to potential evapotranspiration and temperature based indices like ntg, gtg, hd17, and gtn. For different type of climate indices and the land cover percentage under risk could be visualized in Figure 5(B). It is evident that the different climate indices influence various land use types in Europe.

To outline actionable steps for stakeholders based on findings (Figure 6), the risk assessment framework first involves identifying climate indices and their associated probabilities. The figure then highlights the population and land use areas that are at high exposure. This framework indicates to the stakeholders to prioritize areas with high exposure, particularly with precipitation and temperature in southern and southeastern Europe, while northern, northeastern, and western with precipitation

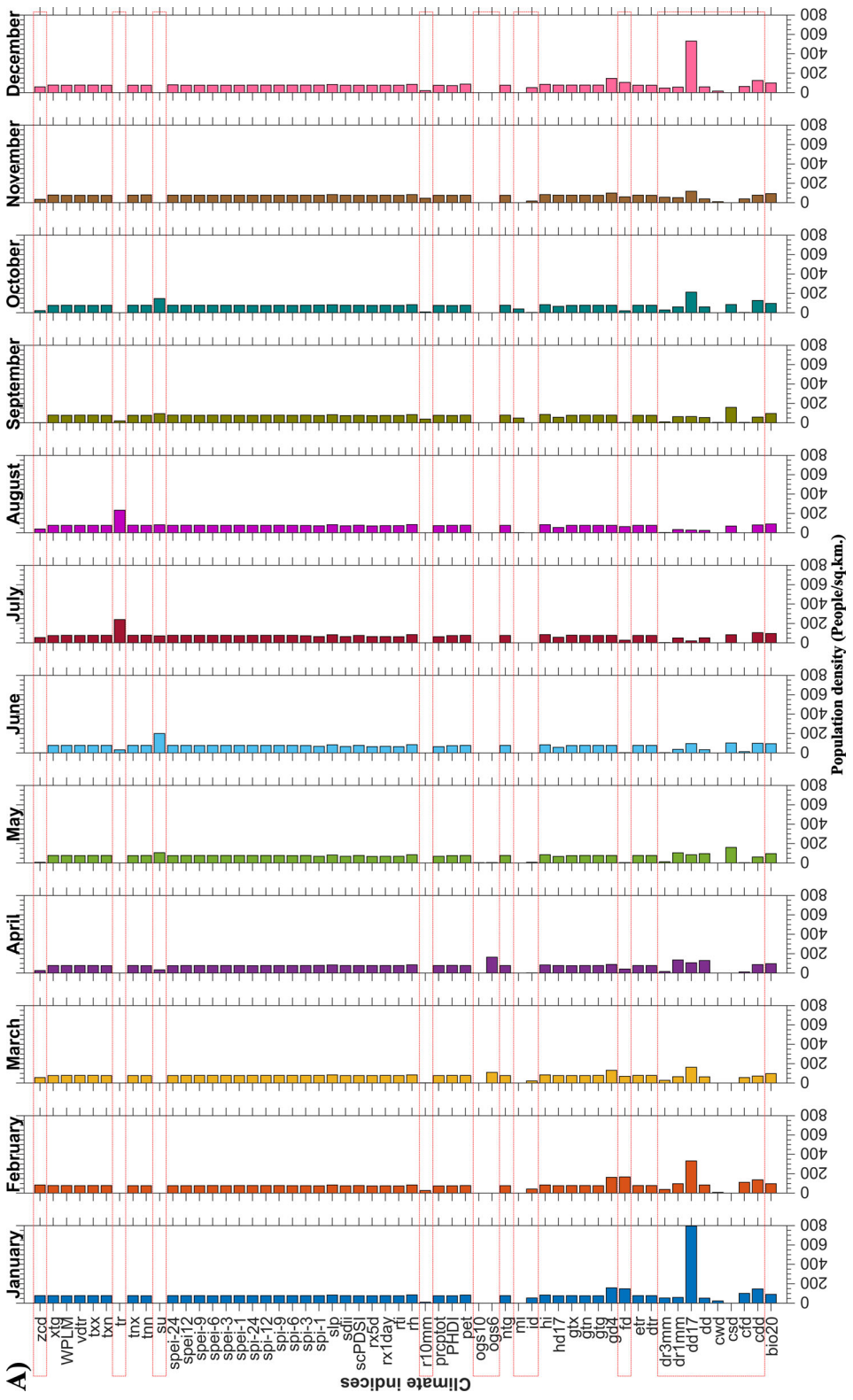

Figure 5. Population density and land use risk exposure. Risk exposure to 74 climate indices for (A) population density and (B) land use types across Europe. The red-boxes in (A) and (B) denote 17 categorized region specific high-risk climate indices.

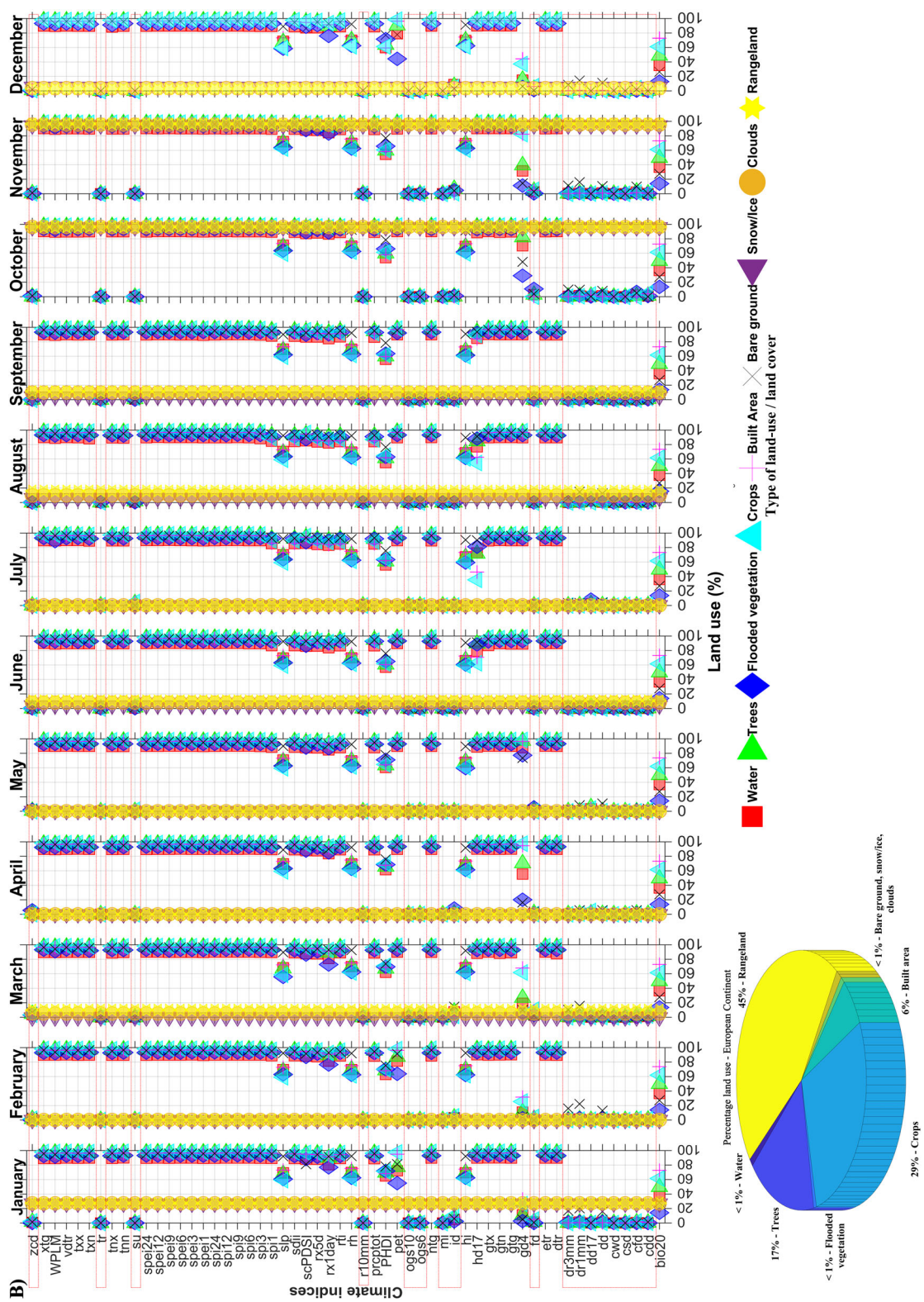

Figure 5. Continued.

exposure. The high risk zone exposure for the built areas due to climate indices might require changes in urban planning and infrastructure (Wamsler et al. 2013). Temperature indices based risk exposure requires counteract through better insulation in infrastructure (Dover 2015) or the provision of urban green spaces to improve the overall liveability of the cities (Bilgili and Gökyer 2012). The regions demarcated, as a hotspot based on high-probabilities requires stakeholder to initiate public awareness campaigns to educate communities about risks associated with climate indices occurrences and co-occurrences, which further would promote the disaster preparedness and community resilience (Petal 2009; Vicari et al. 2019). This risk assessments framework requires continuous monitoring and tuning to account for changes in climate indices. High exposure zones should be updated and communicated to the relevant warning system authorities. Additionally, the study should be integrated with predictive models to enable timely interventions. Further, integrating land use planning can help prevent disasters as well as protect valuable assets from related risks (Bajracharya et al. 2011). For example, land use areas primarily dedicated to crops are particularly exposed to the effects of evapotranspiration. Implementing restrictions on such land use in these regions maybe a necessary step in mitigating climate impacts.

3.4. Limitations and future studies

Policymaker or stakeholders must recognize the limitations and uncertainties associated in the study before applying it for future use, as this is essential for making accurate assessments. The E-OBS dataset suffers from sparse station coverage in southeastern Europe and northern Africa. While northern Africa was excluded from our study due to the focus on the European continent, southeastern Europe was included. However, the sparse station coverage in southeastern Europe introduces higher uncertainty, particularly impacting precipitation data more than temperature

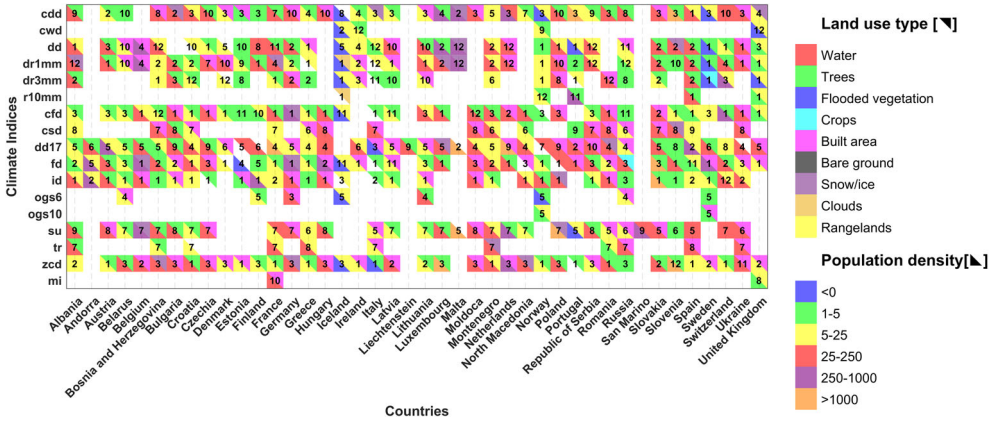

Figure 6. Country specific monthly high exposure of climate indices for various land use and population density. The figure integrates risk maps (Figure 3) with population and land use data, highlighting dominant climate indices. Region specific adaptation strategies could be tailored to address these climate risks identified.

data (Cornes et al. 2018). With a limiting effect on the results discussed, the grid interpolation process may cause boundary effects in parts of southern and eastern most part of Europe. Insufficient station density in certain southeastern regions can result to biased precipitation based input climate indices (Figure 1). As the study is grid based, the data may not adequately capture the spatial variability of precipitation patterns, potentially leading to overestimation or underestimation of probability values, which could influence our high-risk zone identification. Previous studies (Hofstra et al. 2009) have highlighted the weakness of E-OBS dense station network as inhomogeneity that underestimate extremes in comparison to regional climate model output; potential solution suggested is collation of data. Therefore, if high-probability zone from southeastern Europe coincides with high-risk areas identified in the study, especially for precipitation based indices, and wherever the precipitation data was used as input, further validation with additional datasets and accountability of uncertainty due to limited data coverage are necessary. Further, ERA5-reanalysis data could have be opted but it was restricted here due to different data source and different spatial resolution.

The current framework can be utilized to estimate the total risk (Equation 2), by incorporating climate indices, and emphasize on the function of probability associated to the hazard P(H) (based on Figure 3), exposure (quantified using population and land use data) (E) (based on Figure 5), and vulnerability (V).

$$R = P(H)\ x\ E\ x\ V \tag{2}$$

To include co-occurrences and persistence into the risk assessment, Equation (2) can be adjusted by multiplying it with a co-occurrence factor, which accounts for multiple climate indices occurring simultaneously, and a persistence factor, dependent on the duration of high-probability exposure conditions. In order to map the risks in the twenty first century, climate indices related hazards for the exposed population density and land use should be supplemented with vulnerability components such as infrastructure conditions, availability of emergency services, and socioeconomic conditions of the country. However, vulnerability assessment challenges are associated with such studies due to scale implications: different working conditions regional and national level, varied components of vulnerability, different disciplines uses different approaches, and multimodal target dimensions of vulnerability assessment (Fekete et al. 2010; Fuchs et al. 2011). Another supplementation required is climate change assessments that could address the potential impacts of climate change on the frequency of the hotspots demarcated and assessed with the risk maps. In future studies, risk maps and exposure could be combined for various climate indices with the vulnerability and climatic projection scenarios. Further studies could explore the historical variability of population density and land use maps at decadal scale to understand how climate indices probability risk zones interact with these maps over time. Additionally, future studies can analyse the co-occurrences and persistence of both low-probability and high probability climate indices to better understand their risk exposure in specific regions, aspects not addressed in our current analysis. To improvise the understanding of the compound extreme events, it is essential to focus

on quantifying the risks and impacts associated with the co-occurrences and persistence of climate indices at different spatial and temporal scales.

4. Conclusion

The study provides a detailed analysis and visualization of climate risk zones across the European continent based on 74 different climate indices and probabilistic assessment of high temporal and spatial resolution observed data. Further, it identifies the high-risk zones using a probability threshold of >90%, indicating 56 climate indices that are significant in specific regions across Europe. These climate indices are derived from various meteorological data and they indicate the challenges faced by different regions of the European continent. The study introduces an approach wherein the focus is on co-occurrences and persistence from the analysis of singular climate indices, disclosing the complex interaction between different indices. Insights drawn by the identification of 17 from 56 climate indices which are high risk at specific regions and time scales of Europe both through zonal and hotspot have been discussed. The analysis of the study goes beyond by integrating population density and land use maps into the exposure of high-risk climate indices through a risk assessment framework.

Based on the analysis of the best-fit probability distribution derived risk assessment we conclude:

- Southern and southeastern Europe face the highest risk for precipitation (cdd) and temperature (csd, su) based indices across most of the months, while northern, northeastern, and western Europe are concerned about precipitation indices like dd, dr1mm, and dr3mm.
- Climate indices need categorization for high exposure based on regional specific (such as cwd, r10mm, ogs6, ogs10, tr, and mi) or continental scattered (such as fd, dd17, id, and zcd).
- Co-occurrences of climate indices across Europe are widely diverse varying significantly each month. Specific zones in Russia, Norway, Iceland, and Sweden face multiple high-risk events simultaneously, primarily driven by precipitation and temperature based climate indices.
- The optimum probability fit distribution for most of the hotspot detection is the kernel distribution with a normal type function. The hotspot indicates that Russia is at a risk due to dry and frost days, Ukraine to frost and summer days, Fennoscandia to the onset of the growing season, the UK to precipitation and mould index and Iceland to precipitation and ice days.
- The European population faces the highest risk due to exposure of climate indices – dd17 (difference days above/below maximum temperature 17 °C). Rangelands, crops, and built areas face major risks related to temperature–based indices and potential evapotranspiration.

The findings suggest that the climate indices are significantly distinct, and that monthly computation is required for accurate risk assessment based on probability

rather than seasonal or annual spatial maps of hotspots. The nature of climate indices varies spatially across the European continent, and sometimes it has risk due to two opposing occurrences of events within the same month, such as wet and dry days. In future, climate research should focus on more such climate indices to determine co-occurrences and persistence. Furthermore, application to future scenarios with finer temporal and spatial scales can boost the climate monitoring system for high-risk zone identification.

Acknowledgments

Funding by the AWI Inspires Project - 'Compound extreme events: a long-term perspective (LongCEX)' (S.C.D.) and by the Helmholtz Climate Initiative - REKLIM (M.I.) is gratefully acknowledged. M.I. and G.L. are supported by Helmholtz Association through the joint program 'Changing Earth - Sustaining our Future' (PoF IV) program of the AWI. We acknowledge support by the Open Access Publication Funds of Alfred-Wegener-Institute for Polar and Marine Research. We acknowledge the E-OBS dataset from the EU-FP6 project UERRA (http://www.uerra.eu) and the Copernicus Climate Change Service, and the data providers in the ECA&D project (https://www.ecad.eu).

Authors' contributions

CRediT: **Smit Chetan Doshi**: Conceptualization, Data curation, Formal analysis, Investigation, Methodology, Software, Validation, Visualization, Writing – original draft, Writing – review & editing; **Gerrit Lohmann**: Project administration, Resources, Supervision, Writing – review & editing; **Monica Ionita**: Funding acquisition, Project administration, Resources, Supervision, Writing – review & editing.

Disclosure statement

No potential conflict of interest was reported by the author(s).

Funding

The authors declare that no funds, grants, or other support were received during the preparation of this manuscript.

ORCID

Smit Chetan Doshi http://orcid.org/0000-0001-5358-5477
Gerrit Lohmann http://orcid.org/0000-0003-2089-733X
Monica Ionita http://orcid.org/0000-0001-8240-4380

Data availability statement

All data are from E-OBS (Version 25.0e) used in our analysis are freely available: https://surfobs.climate.copernicus.eu/dataaccess/. Global landUse/landCover map of Europe freely available at: https://livingatlas.arcgis.com/landcover/. Population density map freely available at socioeconomic data and application center: https://sedac.ciesin.columbia.edu/. All relevant data are included in the paper or its Supplementary Information. Download input data (steps),

code used for the statistical analysis (R and matlab) and output data generated from: https://zenodo.org/records/14993468.

References

AghaKouchak A, Chiang F, Huning LS, Love CA, Mallakpour I, Mazdiyasni O, Moftakhari H, Papalexiou SM, Ragno E, Sadegh M. 2020. Climate extremes and compound hazards in a warming world. Annu Rev Earth Planet Sci. 48(1):519–548. doi: 10.1146/annurev-earth-071719-055228.

Alekseevskii NI, Magritskii DV, Koltermann PK, Toropov PA, Shkol'nyi DI, Belyakova PA. 2016. Inundatios on the Black Sea coast of Krasnodar Krai. Water Resour. 43(1):1–14. doi: 10.1134/S0097807816010036.

Alexander LV, Zhang X, Peterson TC, Caesar J, Gleason B, Klein Tank AMG, Haylock M, Collins D, Trewin B, Rahimzadeh F, et al. 2006. Global observed changes in daily climate extremes of temperature and precipitation. J Geophys Res. 111(D5):D05109. doi: 10.1029/2005JD006290.

Bachmair S, Tanguy M, Hannaford J, Stahl K. 2018. How well do meteorological indicators represent agricultural and forest drought across Europe? Environ Res Lett. 13(3):034042. doi: 10.1088/1748-9326/aaafda.

Bajracharya B, Childs I, Hastings P. 2011. Climate change adaptation through land use planning and disaster management: local government perspectives from Queensland. In: 17th Pacific Rim Real Estate Soc Conf. p. 16–19.

Bakke SJ, Ionita M, Tallaksen LM. 2020. The 2018 northern European hydrological drought and its drivers in a historical perspective. Hydrol Earth Syst Sci. 24(11):5621–5653. doi: 10.5194/hess-24-5621-2020.

Beniston M, Goyette S. 2007. Changes in variability and persistence of climate in Switzerland: exploring 20th century observations and 21st century simulations. Glob Planet Change. 57(1–2):1–15.

Van den Besselaar EJM, Klein Tank AMG, Buishand TA. 2013. Trends in European precipitation extremes over 1951–2010. Int J Climatol. 33(12):2682–2689.

Bilgili BC, Gökyer E. 2012. Urban green space system planning. Landsc Plan. 360.

Campozano L, Vázquez-Patiño A, Tenelanda D, Feyen J, Samaniego E, Sánchez E. 2017. Evaluating extreme climate indices from CMIP3&5 global climate models and reanalysis data sets: a case study for present climate in the Andes of Ecuador. Intl J Climat. 37(S1):363–379. doi: 10.1002/joc.5008.

Cardoso Pereira S, Marta-Almeida M, Carvalho AC, Rocha A. 2020. Extreme precipitation events under climate change in the Iberian Peninsula. Intl Journal of Climatology. 40(2):1255–1278. doi: 10.1002/joc.6269.

Cattiaux J, Vautard R, Cassou C, Yiou P, Masson-Delmotte V, Codron F. 2010. Winter 2010 in Europe: a cold extreme in a warming climate. Geophys Res Lett. 37(20).

Chen Y, Moufouma-Okia W, Masson-Delmotte V, Zhai P, Pirani A. 2018. Recent progress and emerging topics on weather and climate extremes since the fifth assessment report of the intergovernmental panel on climate change. Annu Rev Environ Resour. 43:35–59.

Cherenkova EA. 2007. Dynamics of severe atmospheric droughts in European Russia. Russ Meteorol Hydrol. 32(11):675–682. doi: 10.3103/S1068373907110027.

Chervenkov H, Slavov K. 2021. ETCCDI climate indices for assessment of the recent climate over southeast Europe. In: Adv High Perform Comput Results Int Conf 'High Perform Comput Borovets, Bulg 2019'. Berlin: Springer; p. 398–412.

Cornes RC, van der Schrier G, van den Besselaar EJM, Jones PD. 2018. An ensemble version of the E-OBS temperature and precipitation data sets. JGR Atmospheres. 123(17):9391–9409. doi: 10.1029/2017JD028200.

Dai A. 2013. Increasing drought under global warming in observations and models. Nature Clim Change. 3(1):52–58. doi: 10.1038/nclimate1633.

de Ruiter MC, Van Loon AF. 2022. The challenges of dynamic vulnerability and how to assess it. IScience. 25(8):104720. doi: 10.1016/j.isci.2022.104720.
Di Napoli C, Pappenberger F, Cloke HL. 2018. Assessing heat-related health risk in Europe via the Universal Thermal Climate Index (UTCI). Int J Biometeorol. 62(7):1155–1165. doi: 10.1007/s00484-018-1518-2.
Domínguez-Castro F, Reig F, Vicente-Serrano SM, Aguilar E, Peña-Angulo D, Noguera I, Revuelto J, van der Schrier G, El Kenawy AM. 2020. A multidecadal assessment of climate indices over Europe. Sci Data. 7(1):125. doi: 10.1038/s41597-020-0464-0.
Dosio A. 2016. Projections of climate change indices of temperature and precipitation from an ensemble of bias-adjusted high-resolution EURO-CORDEX regional climate models. JGR Atmospheres. 121(10):5488–5511. doi: 10.1002/2015JD024411.
Dover JW. 2015. Green infrastructure: incorporating plants and enhancing biodiversity in buildings and urban environments. Abingdon: Routledge.
Fekete A, Damm M, Birkmann J. 2010. Scales as a challenge for vulnerability assessment. Nat Hazards. 55(3):729–747. doi: 10.1007/s11069-009-9445-5.
Feng S, Wu X, Hao Z, Hao Y, Zhang X, Hao F. 2020. A database for characteristics and variations of global compound dry and hot events. Weather Clim Extrem. 30:100299. doi: 10.1016/j.wace.2020.100299.
Field CB, Barros VR. 2014. Climate change 2014–Impacts, adaptation and vulnerability: regional aspects. Cambridge: Cambridge University Press.
Fischer T, Su B, Luo Y, Scholten T. 2012. Probability distribution of precipitation extremes for weather index–based insurance in the Zhujiang River basin, South China. J Hydrometeorol. 13(3):1023–1037. doi: 10.1175/JHM-D-11-041.1.
Forzieri G, Feyen L, Russo S, Vousdoukas M, Alfieri L, Outten S, Migliavacca M, Bianchi A, Rojas R, Cid A. 2016. Multi-hazard assessment in Europe under climate change. Clim Change. 137(1–2):105–119. doi: 10.1007/s10584-016-1661-x.
Fuchs S, Keiler M, Zischg A. 2015. A spatiotemporal multi-hazard exposure assessment based on property data. Nat Hazards Earth Syst Sci. 15(9):2127–2142. doi: 10.5194/nhess-15-2127-2015.
Fuchs S, Kuhlicke C, Meyer V. 2011. Editorial for the special issue: vulnerability to natural hazards—the challenge of integration. Nat Hazards. 58(2):609–619. doi: 10.1007/s11069-011-9825-5.
Gosseling M. 2017. CORDEX climate trends for Iceland in the 21st century. Iceland: Icelandic Meteorol Off.
Hancock MH. 2008. An exceptional Calluna vulgaris winter die-back event, Abernethy Forest, Scottish Highlands. Plant Ecol Divers. 1(1):89–103. doi: 10.1080/17550870802260772.
Herrick JE, Whitford WG. 1995. Assessing the quality of rangeland soils: challenges and opportunities. J Soil Water Conserv. 50(3):237–242.
Hofstra N, Haylock M, New M, Jones PD. 2009. Testing E-OBS European high-resolution gridded data set of daily precipitation and surface temperature. J Geophys Res. 114(D21). doi: 10.1029/2009JD011799.
Ionita M, Dima M, Nagavciuc V, Scholz P, Lohmann G. 2021. Past megadroughts in central Europe were longer, more severe and less warm than modern droughts. Commun Earth Environ. 2(1):1–9. doi: 10.1038/s43247-021-00130-w.
Kalinin AA. 2008. Quantitative estimation of population numbers of shrews (mammalia, insectivora) after wintering. Contemp Probl Ecol. 1(5):619–623. doi: 10.1134/S1995425508050184.
Karamushka V, Boychenko S, Kuchma T, Zabarna O. 2022. Trends in the environmental conditions, climate change and human health in the Southern region of Ukraine. Sustainability. 14(9):5664. doi: 10.3390/su14095664.
Karlsen SR, Solheim I, Beck PSA, Høgda KA, Wielgolaski FE, Tømmervik H. 2007. Variability of the start of the growing season in Fennoscandia, 1982–2002. Int J Biometeorol. 51(6):513–524. doi: 10.1007/s00484-007-0091-x.
Karra K, Kontgis C, Statman-Weil Z, Mazzariello JC, Mathis M, Brumby SP. 2021. Global land use/land cover with Sentinel 2 and deep learning. In 2021 IEEE Int Geosci Remote Sens Symp IGARSS. Piscataway, New Jersey: IEEE; p. 4704–4707.

Kew SF, Philip SY, Jan van Oldenborgh G, van der Schrier G, Otto FEL, Vautard R. 2019. The exceptional summer heat wave in southern Europe 2017. Bull Am Meteorol Soc. 100(1): S49–S53. doi: 10.1175/BAMS-D-18-0109.1.

Kiely G. 1999. Climate change in Ireland from precipitation and streamflow observations. Adv Water Resour. 23(2):141–151. doi: 10.1016/S0309-1708(99)00018-4.

Kirtman B, Power SB, Adedoyin AJ, Boer GJ, Bojariu R, Camilloni I, Doblas-Reyes F, Fiore AM, Kimoto M, Meehl G. 2013. Near-term climate change: projections and predictability. Clim Chang 2013 Phys Sci Basis IPCC Work Gr I Contrib to AR5.:953–1028.

Klein Tank A, Zwiers F, Zhang X. 2009. Guidelines on analysis of extremes in a changing climate in support of informed decisions for adaptation. World Meteorol Organ.

Koliou M, van de Lindt JW, McAllister TP, Ellingwood BR, Dillard M, Cutler H. 2018. State of the research in community resilience: progress and challenges. Sustain Resilient Infrastruct. (3):131–151. doi: 10.1080/23789689.2017.1418547.

Kostianoy AG, Serykh IV, Ekba YA, Kravchenko PN. 2017. Climate variability of extreme air temperature events in the Eastern Black Sea. Ecol Mont. 14:21–29. doi: 10.37828/em.2017.14.3.

Kreibich H, Van Loon AF, Schröter K, Ward PJ, Mazzoleni M, Sairam N, Abeshu GW, Agafonova S, AghaKouchak A, Aksoy H, et al. 2022. The challenge of unprecedented floods and droughts in risk management. Nature. 608(7921):80–86. doi: 10.1038/s41586-022-04917-5.

Laino E, Iglesias G. 2023. Extreme climate change hazards and impacts on European coastal cities: a review. Renew Sustain Energy Rev. 184:113587. doi: 10.1016/j.rser.2023.113587.

Lavaysse C, Cammalleri C, Dosio A, van der Schrier G, Toreti A, Vogt J. 2018. Towards a monitoring system of temperature extremes in Europe. Nat Hazards Earth Syst Sci. 18(1): 91–104. doi: 10.5194/nhess-18-91-2018.

Lebedev SA, Kostianoy AG, Bedanokov MK, Akhsalba AK, Berzegova RB, Kravchenko PN. 2017. Climate changes of the temperature of the surface and level of the Black Sea by the data of remote sensing at the coast of the Krasnodar krai and the Republic of Abkhazia. Ecol Mont. 14:14–20. doi: 10.37828/em.2017.14.2.

Leonard M, Westra S, Phatak A, Lambert M, van den Hurk B, McInnes K, Risbey J, Schuster S, Jakob D, Stafford-Smith M. 2014. A compound event framework for understanding extreme impacts. Wiley Interdiscip Rev Clim Chang. 5(1):113–128. doi: 10.1002/wcc.252.

Linares C, Sánchez R, Mirón IJ, Díaz J. 2015. Has there been a decrease in mortality due to heat waves in Spain? Findings from a multicity case study. J Integr Environ Sci. 12(2):153–163. doi: 10.1080/1943815X.2015.1062032.

Mandal S, Choudhury BU. 2015. Estimation and prediction of maximum daily rainfall at Sagar Island using best fit probability models. Theor Appl Climatol. 121(1–2):87–97. doi: 10.1007/s00704-014-1212-1.

Manning C, Widmann M, Bevacqua E, Van Loon AF, Maraun D, Vrac M. 2019. Increased probability of compound long-duration dry and hot events in Europe during summer (1950–2013). Environ Res Lett. 14(9):094006. doi: 10.1088/1748-9326/ab23bf.

Massey Jr FJ. 1951. The Kolmogorov-Smirnov test for goodness of fit. J Am Stat Assoc. 46(253):68–78. doi: 10.1080/01621459.1951.10500769.

Merz B, Blöschl G, Vorogushyn S, Dottori F, Aerts JCJH, Bates P, Bertola M, Kemter M, Kreibich H, Lall U, et al. 2021. Causes, impacts and patterns of disastrous river floods. Nat Rev Earth Environ. 2(9):592–609. doi: 10.1038/s43017-021-00195-3.

Miao C, Sun Q, Duan Q, Wang Y. 2016. Joint analysis of changes in temperature and precipitation on the Loess Plateau during the period 1961–2011. Clim Dyn. 47(9–10):3221–3234. doi: 10.1007/s00382-016-3022-x.

Moberg A, Jones PD, Lister D, Walther A, Brunet M, Jacobeit J, Alexander LV, Della-Marta PM, Luterbacher J, Yiou P, et al. 2006. Indices for daily temperature and precipitation extremes in Europe analyzed for the period 1901–2000. J Geophys Res. 111(D22). doi: 10.1029/2006JD007103.

Myhre G, Alterskjær K, Stjern CW, Hodnebrog Ø, Marelle L, Samset BH, Sillmann J, Schaller N, Fischer E, Schulz M, et al. 2019. Frequency of extreme precipitation increases extensively

with event rareness under global warming. Sci Rep. 9(1):16063. doi: 10.1038/s41598-019-52277-4.
Ohemeng MA, Kozubowski TJ. 2023. A triptych on three continuous analogs of the Poisson, binomial, and negative binomial distributions. J Comput Appl Math. 432:115275. doi: 10.1016/j.cam.2023.115275.
Peña-Angulo D, Reig-Gracia F, Domínguez-Castro F, Revuelto J, Aguilar E, van der Schrier G, Vicente-Serrano, SM. 2020. ECTACI: European climatology and trend atlas of climate indices (1979–2017). J Geophys Res Atmos. 125(16):e2020JD032798.
Petal M. 2009. Education in disaster risk reduction. Disaster Manag Glob challenges local Solut Univ Press India. p. 285–301.
Pradhan P, Seydewitz T, Zhou B, Lüdeke MKB, Kropp JP. 2022. Climate extremes are becoming more frequent, co-occurring, and persistent in Europe. Anthr Sci. 1(2):264–277. doi: 10.1007/s44177-022-00022-4.
Rahmstorf S, Coumou D. 2011. Increase of extreme events in a warming world. Proc Natl Acad Sci U S A. 108(44):17905–17909. doi: 10.1073/pnas.1101766108.
Rentschler J, Salhab M, Jafino BA. 2022. Flood exposure and poverty in 188 countries. Nat Commun. 13(1):3527. doi: 10.1038/s41467-022-30727-4.
Rezaei EE, Webber H, Gaiser T, Naab J, Ewert F. 2015. Heat stress in cereals: mechanisms and modelling. Eur J Agron. 64:98–113.
Riediger U, Gratzki A. 2014. Future weather types and their influence on mean and extreme climate indices for precipitation and temperature in Central Europe. metz. 23(3):231–252. doi: 10.1127/0941-2948/2014/0519.
Russo S, Sillmann J, Fischer EM. 2015. Top ten European heatwaves since 1950 and their occurrence in the coming decades. Environ Res Lett. 10(12):124003. doi: 10.1088/1748-9326/10/12/124003.
Sacks WJ, Deryng D, Foley JA, Ramankutty N. 2010. Crop planting dates: an analysis of global patterns. Glob Ecol Biogeogr. 19(5):607–620. doi: 10.1111/j.1466-8238.2010.00551.x.
Savinova SV, Loshakov AV, Bratkov VV, Lomakin GV, Ivanova NA. 2020. Current climate conditions and their impact on agricultural production in Stavropol Krai. In: IOP Conf Ser Earth Environ Sci. Vol. 579. Bristol: IOP Publishing; p. 12010.
Saylor JE, Sundell KE. 2016. Quantifying comparison of large detrital geochronology data sets. Geosphere. 12(1):203–220. doi: 10.1130/GES01237.1.
Schuldt B, Buras A, Arend M, Vitasse Y, Beierkuhnlein C, Damm A, Gharun M, Grams TEE, Hauck M, Hajek P, et al. 2020. A first assessment of the impact of the extreme 2018 summer drought on Central European forests. Basic Appl Ecol [Internet]. 45:86–103. doi: 10.1016/j.baae.2020.04.003.
Seneviratne S, Nicholls N, Easterling D, Goodess C, Kanae S, Kossin J, Luo Y, Marengo J, McInnes K, Rahimi M. 2012. Changes in climate extremes and their impacts on the natural physical environment.
Senf C, Buras A, Zang CS, Rammig A, Seidl R. 2020. Excess forest mortality is consistently linked to drought across Europe. Nat Commun. 11(1):6200. doi: 10.1038/s41467-020-19924-1.
Sergio F, Blas J, Hiraldo F. 2018. Animal responses to natural disturbance and climate extremes: a review. Glob Planet Change. 161:28–40. doi: 10.1016/j.gloplacha.2017.10.009.
Silva V, Brzev S, Scawthorn C, Yepes C, Dabbeek J, Crowley H. 2022. A building classification system for multi-hazard risk assessment. Int J Disaster Risk Sci. 13(2):161–177. doi: 10.1007/s13753-022-00400-x.
Sutanto SJ, Vitolo C, Di Napoli C, D'Andrea M, Van Lanen HAJ. 2020. Heatwaves, droughts, and fires: exploring compound and cascading dry hazards at the pan-European scale. Environ Int. 134:105276. doi: 10.1016/j.envint.2019.105276.
Thornton PK, Herrero MT, Freeman HA, Okeyo Mwai A, Rege JEO, Jones PG, McDermott JJ. 2007. Vulnerability, climate change and livestock-opportunities and challenges for the poor. J Semi-Arid Trop Agric Res.
UNISDR. 2015. Sendai framework for disaster risk reduction 2015–2030. United Nations Off Disaster Risk Reduct Geneva, Switz.

Urban A, Di Napoli C, Cloke HL, Kyselý J, Pappenberger F, Sera F, Schneider R, Vicedo-Cabrera AM, Acquaotta F, Ragettli MS, et al. 2021. Evaluation of the ERA5 reanalysis-based Universal Thermal Climate Index on mortality data in Europe. Environ Res. 198:111227. doi: 10.1016/j.envres.2021.111227.

Vicari R, Tchiguirinskaia I, Tisserand B, Schertzer D. 2019. Climate risks, digital media, and big data: following communication trails to investigate urban communities' resilience. Nat Hazards Earth Syst Sci. 19(7):1485–1498. doi: 10.5194/nhess-19-1485-2019.

Wamsler C, Brink E, Rivera C. 2013. Planning for climate change in urban areas: from theory to practice. J Clean Prod. 50:68–81. doi: 10.1016/j.jclepro.2012.12.008.

Wang W, Shao Q, Yang T, Peng S, Yu Z, Taylor J, Xing W, Zhao C, Sun F. 2013a. Changes in daily temperature and precipitation extremes in the Yellow River Basin, China. Stoch Environ Res Risk Assess. 27(2):401–421. doi: 10.1007/s00477-012-0615-8.

Wang B, Zhang M, Wei J, Wang S, Li S, Ma Q, Li X, Pan S. 2013b. Changes in extreme events of temperature and precipitation over Xinjiang, northwest China, during 1960–2009. Quat Int. 298:141–151. doi: 10.1016/j.quaint.2012.09.010.

Ward PJ, Blauhut V, Bloemendaal N, Daniell JE, de Ruiter MC, Duncan MJ, Emberson R, Jenkins SF, Kirschbaum D, Kunz M, et al. 2020. Natural hazard risk assessments at the global scale. Nat Hazards Earth Syst Sci. 20(4):1069–1096. doi: 10.5194/nhess-20-1069-2020.

Zahoor SA, Ahmad S, Ahmad A, Wajid A, Khaliq T, Mubeen M, Hussain S, Din MSU, Amin A, Awais M. 2019. Improving water use efficiency in agronomic crop production. Agron Crop Vol 2 Manag Pract. 13–29.

Zhou B, Wen QH, Xu Y, Song L, Zhang X. 2014. Projected changes in temperature and precipitation extremes in China by the CMIP5 multimodel ensembles. J Clim. 27(17):6591–6611. doi: 10.1175/JCLI-D-13-00761.1.

Zscheischler J, Martius O, Westra S, Bevacqua E, Raymond C, Horton RM, van den Hurk B, AghaKouchak A, Jézéquel A, Mahecha MD, et al. 2020. A typology of compound weather and climate events. Nat Rev Earth Environ. 1(7):333–347. doi: 10.1038/s43017-020-0060-z.

Zscheischler J, Westra S, Van Den Hurk BJJM, Seneviratne SI, Ward PJ, Pitman A, Aghakouchak A, Bresch DN, Leonard M, Wahl T, et al. 2018. Future climate risk from compound events. Nature Clim Change. 8(6):469–477. doi: 10.1038/s41558-018-0156-3.

Chapter 6

A framework for minimizing the impact of wet antenna attenuation on rainfall estimates provided by commercial microwave links

Research Question: *"How can the impact of wet antenna attenuation (WAA) be minimized to improve the accuracy of rainfall intensity estimates, and what are the statistical improvements when applying such an optimization framework?"*

Synthesis:

This study explores the comparison of empirical wet antenna attenuation (WAA) models and the calibration of parameters for estimating rainfall intensity with commercial microwave links (CMLs). A new framework for optimizing the parameters of Valtr-Fencl-Bareš model (VFB) was designed based on link length, rain gauge distance, weighted factor of extreme events, and different statistical indicators such as biases (BIAS), root mean square error (RMSE), and Spearman correlation coefficient (SCC). The framework was applied to Seveso River basin. The study suggests that SCC can be utilized to remove erratic signals that show low positive or negative correlation values. Standard WAA models show similar attenuation at higher rainfall intensity. The results highlight that CMLs-rainfall intensity estimates using the VFBm-model with calibrated parameters' values retrieved from observed precipitation values enhances the outcome. Compared to other WAA models, VFBm-model outperforms through lower biases and errors using as reference rain gauges (RGs) data. The issue of shorter link length does not affect the model's performance, suggesting the potential use for smaller link lengths to estimate rainfall intensity. Possibilities of no rain detection through CMLs highlight the future research gap to move forward with this framework and assessment.

6.1 Rainfall estimation and the challenge of wet antenna attenuation (WAA)

Rainfall is a key variable in hydrological analysis and environmental monitoring and has high temporal and spatial variability. For hydrological research, water resource management and analysis of global change, the quantity and quality of rainfall data are essential (Sun et al., 2018). To accurately model, the hydrological conditions of natural systems, rainfall observations with high spatial and temporal precision are essential (Mahmoud et al., 2020). Planning, managing, and mitigating water resource management effectively depends on the accurate estimation of rainfall especially for regions with continued population growth, frequent natural hazards, increased rainfall variability or water stress regions (Berg et al., 2013; Vörösmarty et al., 2000). For the estimation of rainfall, rain gauge (RGs) networks and weather radars are common and well used tools (De Vos et al., 2019). The main issue related to a RGs network is that it consists in point observations, which leads to spatially sparse data especially in mountainous or urban areas, resulting in missing accuracy with spatial variability of rainfall (Kidd et al., 2017). Further, these rainfall data have uncertainties due to errors induced by other climatic factors such as wind exposure (Nešpor and Sevruk, 1999). Weather radar provides indirect measurements few 10s' or 100s' kilometer above ground, which further require bias correction (Bhatti et al., 2016) or calibration and validation with ground based rainfall data (Michaelides et al., 2009). Other choices include sensors such as disdrometers that are challenging to install widely due to the high costs. The retrieval of rainfall data remotely using satellite data is also a viable option however, the challenge of quantification of uncertainty related to individual product needs to be tested beforehand and might require further calibration and validation with ground based rainfall data (Sorooshian et al., 2011). The development of low cost and high spatial-temporal resolution sensors for monitoring ground-level rainfall is needed (Jiang et al., 2019).

"Opportunistic sensors" is a term used to refer to sensors (e.g. CMLs, or broadband satellite terminals) developed for other purposes (e.g. telecommunications) and used in this case for the investigation of precipitation phenomenon (McCabe et al., 2017) – is another emerging and viable option. Attenuation, due to absorption and scattering through a transmission, results in decrease of signal strength. During the rainfall, this attenuation is further interfered and rainfall estimates could be derived from commercial microwave link (CMLs) signals, with frequencies above 10 GHz (Fencl et al., 2017; Graf et al., 2020; Imhoff et al., 2020; Zheng et al., 2022). CMLs set up is a point-to-point line provided by backhaul of cell phone network. A significant possibility exists in environmental studies in general and precipitation monitoring in particular for the use of CMLs, as cellular networks, or fixed microwave radio networks, which are both growing quickly (Goldshtein et al., 2009). Signals propagating from transmitter to receiver antennas of CMLs attenuate during rainfall. Studies related to CMLs data have

shown their applicability for rainfall estimates in country wide (Overeem et al., 2013), or regional contexts (Song et al., 2021), their use in places where rainfall observations from RGs or weather radars were unavailable (Doumounia et al., 2014), or applications in real-time operations (Chwala et al., 2016). The wide availability of CMLs due to terrestrial network coverage following near ground is a great advantage (Moroder et al., 2019). Another advantage over conventional RGs is the higher temporal resolution measurements (Minda and Nakamura, 2005). However, rainfall estimates obtained through CMLs exhibit uncertainties and inaccuracies, including:

i) erratic signals – sources of attenuation other than rainfall (example water vapor or oxygen), refraction, reflection, or multipath propagation of beam (Graf et al., 2020; Upton et al., 2005; Van Leth et al., 2018).

ii) instrumental field error – wet antenna contribution, rainfall spatial inhomogeneity along the CMLs path, variation of drop size distribution or link downtime (Leijnse et al., 2008; Nebuloni et al., 2022). To overcome these issues, one option is to identify and eliminate the problematic links or pre-process the CMLs data by applying statistical techniques to reduce the errors.

Pre-processed CMLs data might reduce the biases and uncertainty if the temporal sampling is increased, the value of received signal (RSL) is segmented, the baseline is identified accurately and wet antenna attenuation (WAA) effect is computed precisely - especially for the identified rainfall events (Leijnse et al., 2010; Zinevich et al., 2010). WAA is the major and challenging component in accurately computing rainfall intensity estimates using CMLs (Moroder et al., 2019; Uijlenhoet et al., 2018), during the wet-period (rain event). The WAA is due to a thin layer of water that forms on the randome cover of the antenna during rain event. WAA depends on material, direction, and wetting conditions of antenna, randome thickness, frequency, elevation angle, dish size, rainfall rate, and reflector surface (Cheah, 1993; Mandeep, 2009). The estimation of WAA is addressed using empirical equations derived through field experiments and long observation studies. There is a gap represented by the absence of a unified approach for the estimation of WAA, such as some models do not take into account wetting dynamics (Schleiss et al., 2013), antenna characteristics nor environmental conditions such as wind, temperature, humidity or solar radiation (Valtr et al., 2019). To determine the rain attenuation, various models are used such as International Telecommunication Union (ITU)-R P.350 model. However, this model does not consider WAA effects (Recommendation, 2017). Generalized WAA model also has limitations such as equations derived for specific radar dataset for a model by Leijnse et al. (Leijnse et al., 2008; Overeem et al., 2013) computed WAA effects as constant level over course of wet period, however the limitation is that it provides reasonable result with that approach, but contradictory to the

statement of (Pastorek et al., 2021). There is a WAA model, which is dynamic in nature, and considers an exponential increase-decrease to a constant level during the rain events (Schleiss et al., 2013), and there are WAA models, where WAA effects are dependent on the measured attenuation at rain events (Kharadly and Ross, 2001). Some WAA models are bounded within the maximum threshold limits (Kharadly and Ross, 2001; Schleiss et al., 2013), whereas some are computed directly with parameters and rainfall without considering the limits (Valtr et al., 2019). Irrespective of the WAA models, a common conjecture was the possibilities of universal application as there were defined frequencies on which the models were fitted to derive the equation.

Although the WAA importance has been acknowledged in literature review, additional attention is required before microwave link can be utilized accurately to estimate rainfall intensities (Leijnse et al., 2008). This clearly shows a need for a study, wherein various WAA models are compared, and a firm statement is needed for the selection of the best model to estimate the rainfall intensity. However, recently a regional study (Prague, Czech Republic) on the comparison of various empirical WAA model is done (Pastorek et al., 2021) and the selection of best model statement is concluded to be diverging with different case studies (Moroder et al., 2019). In this study, a fundamental framework of estimation of rainfall intensity using various WAA models is presented. The framework was on the research gaps identified and sensible approaches carried out to account WAA. Results highlight a general insight into the variability of the parameters of WAA model for various extreme rain events indicating its reliability and selection of WAA model for the rainfall intensity estimation for the application to future scenarios.

6.2 Empirical framework: study area, data sources, rainfall retrieval methodology

6.2.1 Study area description

The study area is Seveso peri-urban basin, located in the provinces of Como and Milano, Lombardy region, Northern Italy (Bocchi et al., 2012). This area is urbanized and industrialized, with severe hydraulic-environmental issues due to intense land use (Bocchi et al., 2012; Masseroni et al., 2017). The identified critical situations in this catchment are related to the risk of flooding urban areas due to inadequate discharge capacity of watercourses (Masseroni et al., 2017) and increased frequency and intensity of flooding events (Masseroni and Cislaghi, 2016). Seveso basin boundary is determined using a Digital Terrain Model (DTM) with 5 m resolution. Operational RGs data were made available by the Environmental Protection Agency of Lombardy region. The data of CMLs network were made available by Vodafone Italia S.p.A (Sec. 6.2.1.(2)). Figure 6.1 shows the Seveso basin, the CMLs network and the location of RGs.

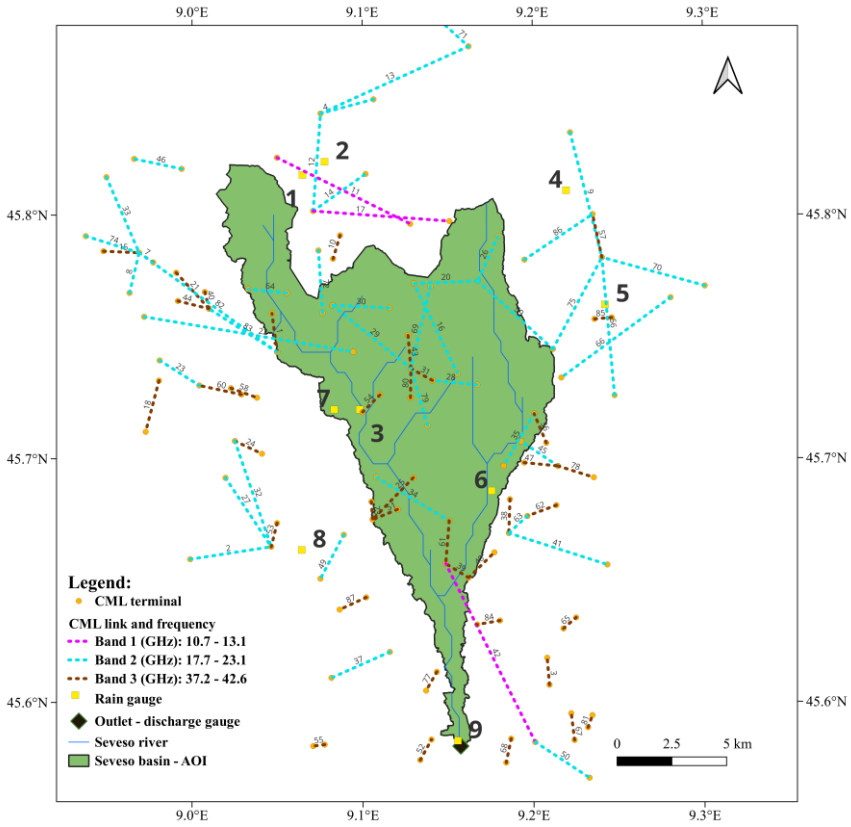

Figure 6.1: Catchment area of Seveso river, Northern Italy (green), CML deployment (dashed lines), and location of the nine RGs (yellow squares). Different line colors correspond to CMLs operating in different frequency bands.

1) Rain gauges (RGs)

According to the Köppen climate classification system, the Seveso basin has a humid subtropical climate (Masseroni et al., 2017). 10 minutes temporal scale tipping-bucket RGs data with a 0.2 mm tip sensitivity, for the study area, are freely available at the website (https://www.arpalombardia.it/) of ARPA Lombardia (Environmental Protection Agency of Lombardy Region). It is important to remember that since the sensors are not heated, they could potentially freeze if temperature falls below 0°C, hence a crucial check is required whether the temperature is above the freezing level. Nine RGs were selected for the Seveso basin according to the Thiessen polygon approach. The 10-minute raw data of RGs were resampled to hourly timescale.

2) Commercial Microwave Links (CMLs)

CMLs were selected based on the transmitter or receiver terminal falling under the Thiessen polygons

of each sub-basin. Figure 6.1 shows the location of CMLs selected within the study area. CMLs data was provided by the mobile network operator Vodafone Italia S.p.A. A total of 77 CMLs are available over the given study area. The key characteristics of the CMLs are the link length (distance between transmitter and receiver) and the frequency. The majority of CMLs are in the range of 1-3 km, the average link length being 3.3 km. Most CMLs work in three frequency bands: 18-19 GHz, 22-23 GHz and 38-39 GHz. Longer links usually work at lower frequency, as lower frequencies are less impacted by rain attenuation (Overeem et al., 2021). Minimum and maximum transmitted and received signals over 15 minutes interval are available for the 45 rainfall events. The raw data of CMLs were scaled into rainfall intensity and subsequently resampled to the hourly timescale for comparison against RGs.

6.2.2 CML based rainfall estimation methodology

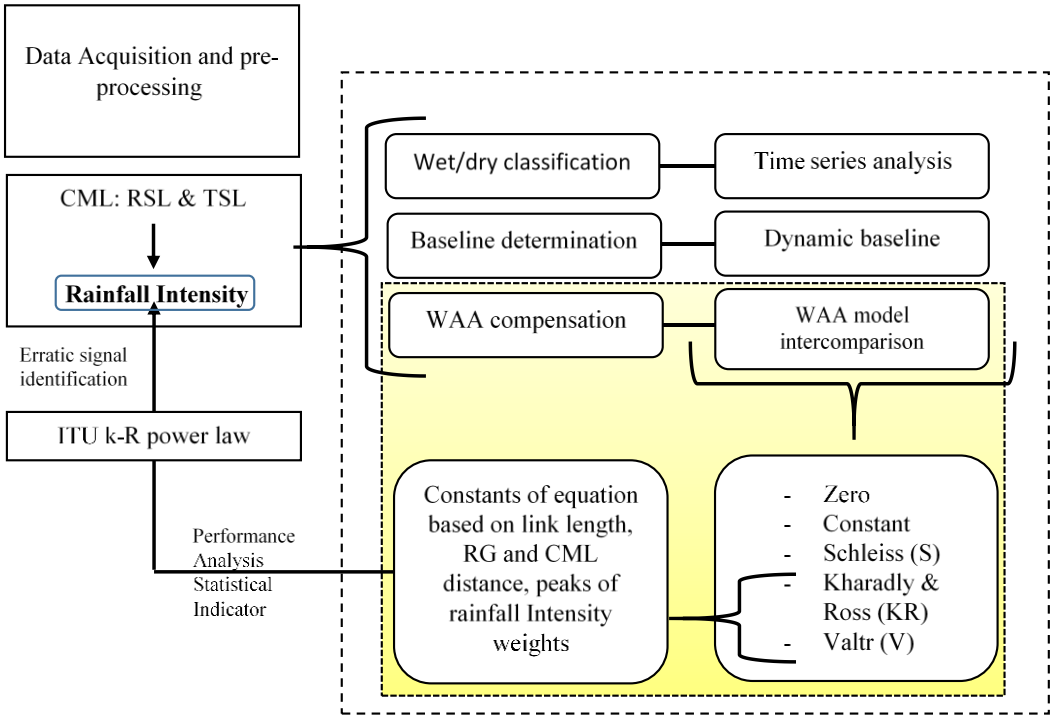

Figure 6.2: Framework followed to estimate the rainfall intensity using CML data.

Direct conversion of CML data using only received signal (RSL) and transmitted signal (TSL) to rainfall intensity estimates is not possible. Before analyzing there was, firstly an assumption that rainfall intensity remains uniform throughout the link length. The attenuation rate in decibel (dB) requires several processing step for conversion to rainfall intensity as showcased in Figure 6.2. CMLs can be used as opportunistic rainfall sensors once the contribution due to rainfall across the path is extracted from the transmitted signal level (TSL) and the received signal level (RSL). First, rainfall attenuation (A_r) is usually computed by the following link budget equation (6.1):

$$A_r = A - A_b - A_w \quad (6.1)$$

where A is total path attenuation (dB), calculated as the difference between TSL and RSL, A_b (dB) is the baseline level, which basically accounts for all the sources of signal attenuation present anytime, and finally A_w (dB) is the Wet Antenna Attenuation (WAA). The available raw data logged by CMLs networks are usually TSL and RSL. Path attenuation includes components that are constant and dependent on link parameters only (e.g., free space attenuation), some others that are slowly dependent on time such as attenuation due to the ever-present atmospheric gasses and, finally, the deep and fast signal oscillations due to rainfall. The baseline attenuation Ab captures all the time-invariant and the weakly time-variant contributions to the received signal, so that the difference A - A_b - basically quantifies signal variations during rainfall. There are several methods for calculating A_b from the raw data (Fenicia et al., 2012; Jiang et al., 2019; Ostrometzky and Messer, 2017). In this work, a dynamic value of A_b was calculated as detailed in (Nebuloni et al., 2022), based on a preliminary classification of the 15-min time slots into wet and dry. Attenuation due to falling raindrops is not the only source of signal loss while it is raining. It has been shown that an extra attenuation contribution, namely Wet Antenna Attenuation (WAA), is produced by the process of antenna wetting, which results into a thin layer of water over the antenna (or radome) surface, which absorbs part of the incident electromagnetic radiation.

Once A_r has been derived from (6.1), an average value of rainfall intensity across the path is obtained moving from the well-known power-law relationship between rainfall intensity (mm/h) and attenuation per unit path length γ (dB/km):

$$\gamma = \kappa R^{\alpha} \quad (6.2)$$

where the coefficients κ and α are usually taken from the values tabulated in ITU-R P. 838 (ITU-R, 2005) as a function of frequency and polarization. However, in principle κ and α depend also on the Drop-Size Distribution (DSD) of rainfall. Due to regional and microclimatic variations in the microphysics of precipitation, site-specific values for κ and α are sometimes estimated from DSD data collected by disdrometers through a theoretical calculation of γ by electromagnetic theory and a best fit of the power law formula in the γ – R plane. Finally, the relationship between A_r and γ is approximated by

$$A_r = L\,\gamma \quad (6.3)$$

where L is the path length. Strictly Eqn. (6.3) holds only if the rainfall intensity is assumed constant along the path. Eqn. (6.3) is assumed by many authors to be valid for “short” links, even though it is clear that this assumption maybe not realistic for highly localized precipitation. No missing data of CMLs occurred, but if they occur then they could be interpolated using some statistics. Erratic signals

could be removed at the initial stages using filtering based on monthly statistics of CMLs raw data similar to previous studies (Graf et al., 2021). Here, we highlighted and eliminated at the end stage by the comparison with the rainfall intensity of the associated RGs based on applying threshold to outliers (assumption that depends on allowable uncertainty and accuracy required). The threshold based on the standard deviation of RGs was considered for the whole time series. The CMLs showcasing standard deviation of more than 10 with respect to RGs derived rainfall intensity were eliminated. There are models for the path reduction factor, i.e., the decrease in path attenuation due to the spatial inhomogeneity of rainfall, but they hold on to a statistical basis, i.e., they can be used to correct the first order statistics of rain attenuation rather than the time series (da Silva Mello and Pontes, 2007; Lin, 1977; Series, 2015).

6.3 Review of WAA models for CML rainfall estimation

There are two different approaches for WAA estimation.

- Physically-based approach: A_w is directly measured with ad-hoc experiments featuring, for instance, simulated rain. It is predicted by electromagnetic theory.
- Data driven approach: First, A_r is estimated from independent measurements usually based on disdrometers, rain gauges or, again, radar data, and A_w is obtained subtracting A_r from A-A_b.

Even though WAA is usually considered the dominant element in the last term of Eqn. (6.1), in principle, the data driven approach can compensate for any impairment present during rainfall not due to falling raindrops and not accounted by A_b. Models are in general validated considering first order statistics of rainfall attenuation or of rainfall depth integrated over suitable time intervals, which allows to assess whether there are biases left. However, this procedure does not prevent large discrepancies from occurring when examining time series. The rainfall intensity (as a time-series) retrieved by CMLs is directly compared to the one observed by RGs, through indicators such as the Bias (BIAS), Root Mean Square Error (RMSE), and Spearman Correlation Coefficient (SCC).

In principle, WAA depends on several factors - rainfall intensity (including its spatial distribution along the path), signal frequency, antenna type and size and radome properties (if a radome is present), antenna elevation angle, weather conditions (wind, temperature, humidity, and solar radiation). However, most of the available WAA models are simple and rely on a single input and a few parameters that are trained according to the data driven approach. Table 6.1 gives an overview of several WAA models alongside their parameters (the values are the ones provided in the original papers and, information about links and antennas used to train each model).

Table 6.1: Overview of WAA models considered in this study

No.	Model	Analytical expression	Parameters	Links and antennas
1.	Schleiss, Rieckermann and Berne (SRB) (Schleiss et al., 2013)	$A_{w,i} = \begin{cases} min\left(A_i, W, W_{i-1} + (W - W_{i-1})\frac{3T}{\tau_w}\right), \\ if\ i\ wet \\ min(A_i, W), if\ i\ dry \end{cases}$ (i=discrete time index, T=time step)	τ_w=15 min, W=2.3 dB (38 GHz)	1.85 km link; 30 cm antennas
2.	Kharadly and Ross (KR) (Kharadly and Ross, 2001)	$A_w = C(1 - e^{-dA})$	C=6 dB, d=0.167 dB^{-1} C=8 dB, d=0.125 dB^{-1}	Satellite link; Parabolic dish, 30° elevation, unspecified size
			C=5 dB, d=0.125 dB^{-1}	820 m link, 30 cm antennas (Minda and Nakamura, 2005)
3.	Garcia-Rubia, Riera, Benarroch and Garcia-del-Pino (GRBG) (Garcia-Rubia et al., 2011)	$A_w = C(1 - e^{-dA_r})$	C=2 dB, d=2.41 dB^{-1} (38 GHz)	840 m link, 30 cm parabolic dish
4.	Valtr, Fencl and Bareš (VFB) (Valtr et al., 2019)	$A_w = k'R^{\alpha'}$	k'=0.68, α'=0.34 (32 GHz)	820 m and 611 m links; 30 cm antennas with a radome
5.	Valtr, Fencl and Bareš modified (VFBm) (this paper)	$A_w = k'R^{\alpha'}$	k'=0.82, α'=0.38	Calibration over 24 links in two different bandwidths

Basic WAA models as the ones in (Overeem et al., 2011) and (Ostrometzky et al., 2017) assume that WAA is constant as far as it is raining. The resulting WAA values obtained from data of 70 rainfall events collected by two E-band links (73 GHz) of slightly different length are rather scattered even though they do not depend on the average rainfall intensity during an event. The SRB model (Schleiss et al., 2013) is based on a rigorous estimate of rain attenuation obtained through electromagnetic theory from the DSD data collected by an array of disdrometers deployed along the path of a 1.85 km link operating at 38 GHz, with 30 cm antennas. The major features of SRB model are as follows: a) when

it starts raining, Aw exponentially increases up to a maximum value W, with a time constant τ_w, b) Aw remains constant and equal to W as far as it is raining, regardless of rain intensity, and, c) it exponentially decreases after rain has stopped. The antenna drying process is much slower (from 0 min to 5 h, with an average of 2 h) than the wetting stage (from 6 to 36 min, with an average of 15 min). The model parameters are τ_w and W only, as the Aw profile during the wet-dry transient is fully determined by the recursive algorithm proposed by the authors. A limitation of the SRB model is that the authors obtained the optimum parameters (in their Table 6.1) during light to moderate rainfall conditions (the maximum path-averaged rainfall intensity was about 7.5 mm/h). Hence, the authors did not verify that Aw remains constant at the large rainfall intensity values typical of convective events. The advantage of the SRB model is that the authors provide a method to calibrate the model parameters τ_w and W, as well as a recursive method to estimate Aw from CMLs data only, provided each time slot has been previously classified as dry or wet. Hence, in principle, this method can be applied to estimate τ_w and W of each of the CMLs in the network. A similar procedure as SRB recursive method and based on the long short-term memory neural networks has been proposed in (Pu et al., 2020). The W was corrected to 2 dB for the given study area based on the approach similar to a previous study (Nebuloni et al., 2022).

An electromagnetic model for WAA was developed in (Leijnse et al., 2008). WAA is due to a uniform thin film of water on the material covering the antenna. The thickness of the water layer, l, depends on rainfall intensity at the antenna location as follows

$$l = \gamma R^{\delta} \tag{6.4}$$

where the coefficients of the power-law relationship are dependent on the frequency and the characteristics of the antenna cover. WAA can be calculated through the standard theory of wave propagation across layers of different materials and its expression is reported in Appendix B of (Leijnse et al., 2008). The model is validated with a similar method as in (Schleiss et al., 2013) over a 27 GHz link, using an array of rain gages deployed across the link and calibrating Eqn. (2) with a disdrometer. The comparison between WAA values estimated from measurements and those from the model highlights a large scatter.

KR (Kharadly and Ross, 2001) proposed a WAA model based on the comparison between attenuation measurements under rainy conditions across a satellite link at 20 and 27 GHz and measurements simulating rain on the antenna by a system of four elevated sprinklers. KR is one of the few experiments (another one is in (Hong et al., 2017)), where WAA was directly measured. The authors formulated both a dual-frequency model of WAA and a simpler single frequency model. The latter moves from a heuristic expression, which calculates Aw from the measured path attenuation A as follows:

$$A_w = C(1 - \mathrm{e}^{-dA}) \tag{6.5}$$

where, C and d are model parameters. The authors provided values for C and d for their case study (Table 6.1). In practice, the above parameters should be determined by the aforementioned best-fit procedure based on an independent prediction of rain attenuation. KR got some remarkable findings: 1) as far as the antenna is wet, there is a bulk WAA level, and 2) WAA produces signal oscillations that become faster as the (simulated) rainfall intensity increases (their Figure 4(a) and(b)), which the authors ascribe to water build-up and run-off on the antenna surfaces. GRBG (Garcia-Rubia et al., 2011) proposed a modified version of (5), where rainfall attenuation across the path A_r replaces total path attenuation:

$$A_w = C\left(1 - e^{-dA_r}\right) \tag{6.6}$$

Please note that in both (5) and (6) the value of A_w depends on the path length, as both A and A_r are quantities integrated across the line-of-sight propagation path. In order to get consistent results, i.e., the same value of A_w across links, with the same hardware and frequency but with different lengths, when rain is uniform, the parameter d should be inversely proportional to the path length L in (6), by virtue of (3), while in (5) the dependence of d on L is more complex. Some other authors suggested to modify the KR model to feature γ or R, as input, as shown later. Finally, some used the KR model to describe WAA, while it is raining together with a model based on the exponential decrease observed by SRB to describe WAA soon after the rain event (Leijnse et al., 2007; Minda and Nakamura, 2005).

VFB model (Valtr et al., 2019) is based on the aforementioned best fit procedure between measured attenuation across two short links (816 and 611 m) at 32 GHz and predicted rain attenuation across the path from RGs placed nearby link terminals, assuming a linear variation of the rainfall intensity along the path. The authors calculated the κ and α coefficients in advance from local DSD data. Differently from KR, the WAA model input is the rainfall intensity measured close to each terminal, i.e.

$$A_w = \kappa R^{\alpha} \tag{6.7}$$

Please note that in VFB and GRBG models WAA is zero, if R=0, which is not the case at least during the decreasing attenuation transient after rain has ceased, as observed by SRB and others (Nešpor and Sevruk, 1999). Moreover, VFB model predicts an unbound increase of Aw as precipitation intensity increases. The results of the above models cannot be easily cross-checked as the links used for calibration are different. However, if we compare SRB, GRBG and VFB models (same antennas), the maximum WAA returned by SRB and GRBG models is 2.3 dB and 2 dB, respectively at 38 GHz (both antennas), while it is about 3 dB at 32 GHz (assuming a maximum rainfall intensity of 100 mm/h), according to VFB model for one antenna only, hence 6 dB for two antennas. As WAA is expected to increase with the frequency, this discrepancy may be due to the relatively low rainfall rates observed

by SRB. In GRBG (Garcia-Rubia et al., 2011), the authors state that model calibration was done in a two-month period, but they do not provide statistics of the rainfall rate. From the CCDF of rainfall attenuation in their Figure 4, gathered from disdrometer data, and using ITU-R coefficients, we argue a maximum rainfall intensity of about 40 mm/h. VFB model predicts 2.6 dB at 7.5 mm/h and 4.8 dB at 40 mm/h at 32 GHz (both antennas). These conclusions are also confirmed by the results of the comparison in (Pastorek et al., 2021) where KRm (modified KR) and VFB model performs basically the same.

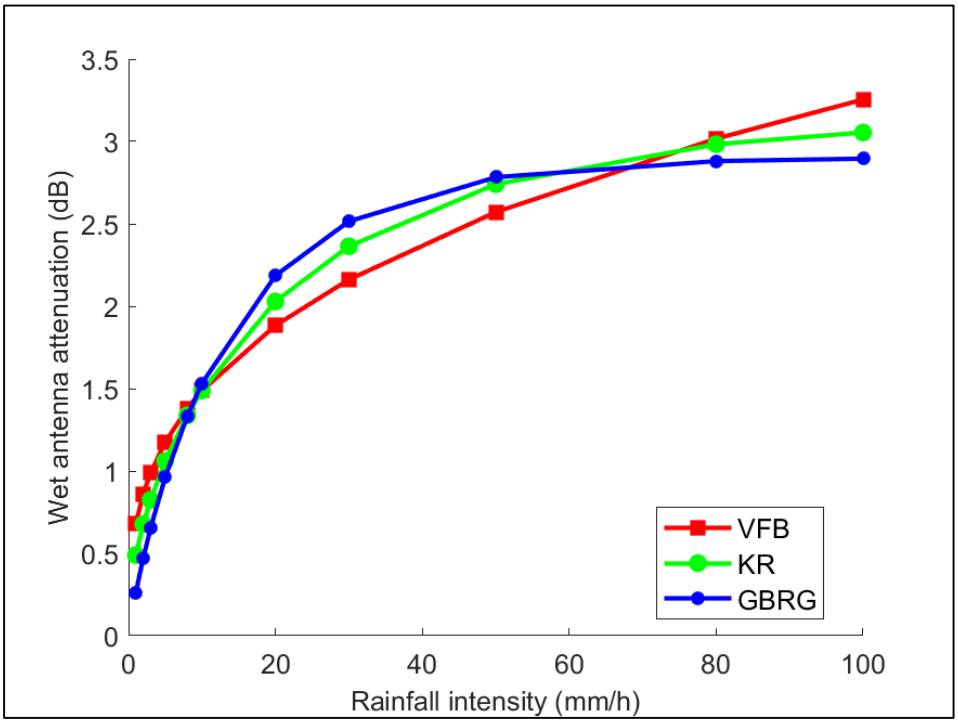

Figure 6.3: Comparison among different WAA models, assuming a 1 km path length at 32 GHz.

We investigate the difference between the above models (exponential and the power-law expressions for WAA), by the following simple test: calculate WAA from VFB model with model parameters as in Table 6.1 over a rainfall intensity axis R, then calculate the corresponding path attenuation A and rainfall attenuation Ar over a link of a certain length L and find the KR and GRBG parameters that fit the value of WAA returned by VFB over R. Finally, calculate the difference between WAA from KR and GRBG models and the reference, i.e., VFB. In practice, KR, VFB and GRBG expressions are rather similar. The results of this simple exercise for L = 1 km in Figure 6.3 indicates that the percent difference is within 20% (on dB values) if $R \geq 5$ mm/h, and within 0.4 dB at lower rain rates.

The above models can be applied once the model parameters have been estimated, in principle, for each CMLs. To this aim, ad-hoc setups are needed, which, in general, is possible only with experimental

links. In the case of operational CMLs networks, only links in strategic positions can be individually calibrated, e.g. where nearby RGs are available not only to provide a single-point rainfall intensity, hence attenuation per unit length estimate, but also to detect the spatial variations of the rainfall field across CMLs. Radar data could be used as well, at least to get basic inputs as wet/dry classification or spatial distribution of rainfall. When radar data are available, it is possible to state whether both or only one antenna are wet at a certain time. Using radar data for calibrating the WAA model parameters looks more difficult though. Whatever the accuracy of QPE by radars, the problem of the spatial resolution of radar data remains unsolved. Available radar products provide resolutions as high as 1 x 1 km on a cartesian grid. However, these products are based on raw data collected on a radial grid, which angular size increases linearly moving away from the radar. Several PPIs (i.e. azimuthal scans of space at a fixed elevation angle) are usually combined to generate a Cartesian grid aloft and then projected down to the ground. Finally, (Pastorek et al., 2021) has a thorough comparison between 6 different methods: constant WAA, SRB, KR, VFB, and modified versions of KR and VFB.

In previous study (Pastorek et al., 2021), CMLs data are taken from a network of 16 links located in a suburb of the city of Prague (Czech Republic). Most of them are positioned in a network star-topology. The models are calibrated and assessed against three local RGs in a very simple way, comparing the average of the rainfall accumulated over 15-min slots by the three RGs with CMLs estimates, after WAA subtraction. Hence, the ground truth is the same for all the CMLs, no matter their position and length. The results show that the 15-min rainfall depth estimates obtained using WAA models dependent on rainfall intensity provide a better agreement with RGs measurements than the ones assuming a constant WAA value between the dry/wet and wet/dry transients. In addition, the whole system biases were considered in WAA resulting in way above threshold limits of model parameters for certain CMLs. Assumption of comparison is true but weightage of all the errors in WAA estimation through model parameters is not true practically. If WAA models perform in a similar way, the choice about whether it is more convenient is based on practical considerations that include model calibration and operation. When a network of operational rain gauges is available, a model based on R or on γ would be convenient, even though the underlying assumption that the rainfall measurement collected by the rain gauge is representative of the rain across the link. As the models are equivalent, one may calibrate the WAA parameters using a model based on R or γ and a RGs set-up for calibration, then convert into a model based on attenuation (VFB) and use the latter for quantifying WAA during operation with no need for RGs. To avoid initial guesses for solving numerical equations, iteration and optimization algorithms we focused on the original equations to determine the WAA estimation for VFB model. However, the calibration was required for the model parameters to estimate WAA, because the values of literature studies were for different study areas, CMLs length and frequency.

6.4 Data insights and strategy for assessment

The purpose of this analysis is to evaluate the performance of various WAA models in the context of rainfall estimation by CMLs, with a particular focus on heavy rain. Moreover, we carry out a sensitivity analysis of the WAA methods with respect to path length and frequency. Specifically, we compare CML generated rainfall data after WAA compensation with observed RGs data through a set of statistical indicators. CML and RG data are available (with interruptions) in the period from 22 June 2019 to 13 June 2020. An overall 45 rain days, hereinafter referred to as events were identified in the study area. A rainfall event is intended here as a day when at least one of the six RG in the study area detected rain (> 0 mm/h). The events were grouped in classes based on the peak rainfall intensity (mm/h) detected by the RGs, according to the rationale discussed in a previous study in Italy (Beritelli et al., 2018). Out of 45 rainfall events, 12 are WR (weak rain: <2.5 mm/h), 10 are MR (moderate rain: 2.5 – 5 mm/h), 4 are HR (heavy rain: 6 – 10 mm/h), 15 are VHR (very heavy rain: 11 – 30 mm/h) and, finally, 4 are CB (cloud burst: > 30 mm/h). Some RGs may detect NR (No rain) even during CB recorded by other RGs due to the highly localized distribution of extreme events or to the motion of rain cells, which produces differences in timing of the events.

Then, CMLs were associated with RG, according to a minimum distance rationale, as follows. First, the CMLs-RG distance has been calculated dividing the link length into segments and averaging the distance d* between the RG and each segment of the CML, following (Nebuloni et al., 2022). This approach takes considers the effect of CML length and of its deployment with respect to a simpler approach where the CML-RG distance is calculated from the RG to an individual point of the CMLs path (e.g., the midway point or the closest point of the path to the RG). Finally, the CML with the minimum value of d^* was associated to a certain RG. The detailed location of CMLs and RGs along the catchment can be visualized in Figure 6.1. Table 6.2 lists the CMLs associated with each RGs. The dense RGs network available is an advantage as the majority of the CMLs are located within 5 km from the associated RG. Moreover, each RGs has at least 6 CMLs associated in different frequency bands.

Table 6.2: List of RGs and associated CMLs (B1 – frequency band 10.7 – 13.2 GHz, B2 – frequency band 17.7 – 23.1 GHz, B3 – frequency band 37.2 – 42.6 GHz)

RG	No. of CML links	Frequency	Link length (km)			Distance (km)		
			Min	Max	Mean	Min	Max	Mean
1	6	5 (B3), 35 (B2), 50 (B3), 57 (B2), 62 (B2), 66 (B3)	1.12	2.85	1.94	3.06	6.79	4.99
2	6	3 (B2), 6 (B1), 7 (B2), 8 (B2), 9 (B2), 11 (B1)	2.49	7.41	5.05	1.38	5.12	2.81

3	11	10 (B2), 15 (B3), 19 (B2), 20 (B2), 21 (B2), 22 (B3), 33 (B3), 43 (B3), 60 (B2), 71 (B2), 72 (B3)	1.11	4.59	2.56	0.59	5.27	3.64
4	6	4 (B2), 12 (B2), 17 (B2), 45 (B2), 51 (B3), 76 (B2)	2.01	5.89	3.46	1.83	6.96	3.58
5	9	16 (B2), 46 (B2), 53 (B2), 58 (B2), 61 (B2), 64 (B2), 65 (B2), 68 (B3), 75 (B3)	0.79	6.32	4.06	0.60	5.48	2.93
6	15	24 (B2), 25 (B2), 26 (B2), 27 (B3), 28 (B3), 29 (B3), 31 (B2), 34 (B2), 36 (B3), 37 (B3), 39 (B1), 54 (B3), 55 (B3), 56 (B2), 69 (B3)	1.15	29.01	3.97	1.19	8.41	3.23
7	6	1 (B3), 13 (B2), 14 (B3), 49 (B3), 52 (B3), 73 (B2)	1.16	9.66	3.15	4.38	5.74	5.09
8	11	2 (B2), 18 (B2), 23 (B2), 30 (B2), 38 (B2), 40 (B3), 42 (B3), 47 (B2), 48 (B2), 63 (B3), 77 (B3)	0.83	5.10	2.86	1.40	4.03	2.84
9	7	32 (B1), 41 (B3), 44 (B3), 59 (B3), 67 (B3), 70 (B2), 74 (B3)	0.98	9.11	2.46	1.68	5.66	3.39

One of the WAA models considered, namely VFB, was calibrated over the above dataset of CML and RG measurements by optimizing its parameters to minimize the difference and biases between RG measurements (assumed as ground truth) and the associated CML measurements. Indeed, VFB model has the advantage that the model input is rainfall intensity, i.e., the quantity measured by RGs. The calibration was done considering only the 28 CMLs with d*<2 km. The VFB model calibrated with Seveso catchment data is hereinafter referred to as VFBm, where m stands for modified. VFBm parameters were obtained by an iterative procedure starting from VFB parameter values and changing these values in discrete 1.5% step up to ±20%. WAA attenuation obtained with every pair of VFBm coefficients is subtracted from total attenuation to get rain attenuation and converted it into rainfall intensity, which is compared to the one provided by the associated RG.

The calibration is crucial for empirical WAA models like VFB, however it is important to calibrate the model parameters in a way that does not introduce bias correction by modifying them beyond the actual physical ranges. The evaluation of the WAA output from the optimized calibrated parameters of VFBm model indicates that during the low rainfall intensity (< 2 mm/h) the WAA accounts for about 2 dB, whole during extreme rainfall intensity (>100 mm/h) it reaches 6 – 10 dB. This demonstrates that the

model parameters maintain the physical meaning, as the WAA is similar to discussion of previous study (Fencl et al., 2018). For a broader range of parameter value (± 40%), it would lead to better estimation of WAA especially if the rainfall intensity through CMLs is overestimating in comparison to RGs. As higher parameter, value leads to higher WAA component which results in higher reduction of RSL. Technically complete physical value of the model parameter covers as a bias correction of the system for deriving rainfall intensity, leading to inaccurate meaning of the model parameters just to attain model accuracy. In previous study (Pastorek et al., 2021), similar approach was carried out but with a wide range of selection of the optimizing parameters of WAA model. The integration of the importance of extreme events is crucial for assessment of statistical performance during selection of optimized calibration parameter of the VFB model for various CMLs derived rainfall intensity. This importance has not been highlighted in any past study to derive rainfall intensity using CMLs (Blettner et al., 2022; Lian et al., 2022; Zheng et al., 2022). The approach is to apply different weights to the RGs data and CML data based on the RG data. This approach will ensure that the extreme values are given more importance, which are of greater interest in many applications. Firstly, fitting an empirical cumulative distribution curve to the RG data. Further, intercepting different percentiles at increment of 5 to the fitted curve, resulting in computation of underlying areas based on trapezoidal numerical integration approach to determine probability weights associated with each percentiles. These weights are then multiplied to the RG and CML derived rainfall intensity to further compute the statistical indicators, which provides a more comprehensive assessment (ability to capture extreme events over no rain events) of VFBm model performance.

The performance of CML-based rainfall estimates were assessed based on the three different statistical indicators: Bias (BIAS), Root Mean Square Error (RMSE), and Spearman Correlation Coefficient (SCC) for various types of WAA models and rainfall intensity, as defined in the following relationships:

$$\mathrm{BIAS} = \frac{\sum_{i=1}^{n}\left(Y_i^{mod} - Y_i^{obs}\right)}{\sum_{i=1}^{n}\left(Y_i^{obs}\right)};$$

$$\mathrm{RMSE} = \sqrt{\frac{\sum_{i=1}^{n}(Y_i^{mod} - Y_i^{obs})^2}{n}}; \tag{6.8}$$

$$\mathrm{SCC} = 1 - \frac{6\sum d_i^2}{n(n^2-1)}$$

where Y_i^{mod} is model data (hourly WAA models rainfall intensity) Y_i^{obs} is the observed data (hourly RGs rainfall intensity), n is the number of samples and di is the difference between the ranks of Y_i^{mod}

and of Y_i^{obs} (i.e. the labels of the sorted versions of Y_i^{mod} and of Y_i^{obs}). The comparison between model and observations will be showcased for each RGs i) for all CMLs; ii) against CMLs frequency; iii) against link length; iv) against the class of rain.

6.5 Model performance assessment: results

In this section, we present the results of VFB calibration as well as the comparison of CML-based rainfall estimates using three different WAA models with the rainfall measurements provided by RGs.

6.5.1 Parameter calibration for WAA estimation using VFB-model

The calibration of the VFBm model was performed using data from 34 rainfall events (Supplementary Table ST1 No. 1 to 34), while the model performance was tested on the remaining 11 rainfall events (Supplementary Table ST1 No. 35 to 45) with the obtained calibrated parameters. The outliers' values of CMLs were eliminated considering the standard deviation > 10 with respect to RGs, and further as we compute one pair of WAA model parameter for all the links, it is important to study the statistical indicator performance over all the CMLs in the area while calibrating over a subset of CML within 2 km distance from RGs. In contrast, if link-specific parameters are computed, this analysis would not make any importance.

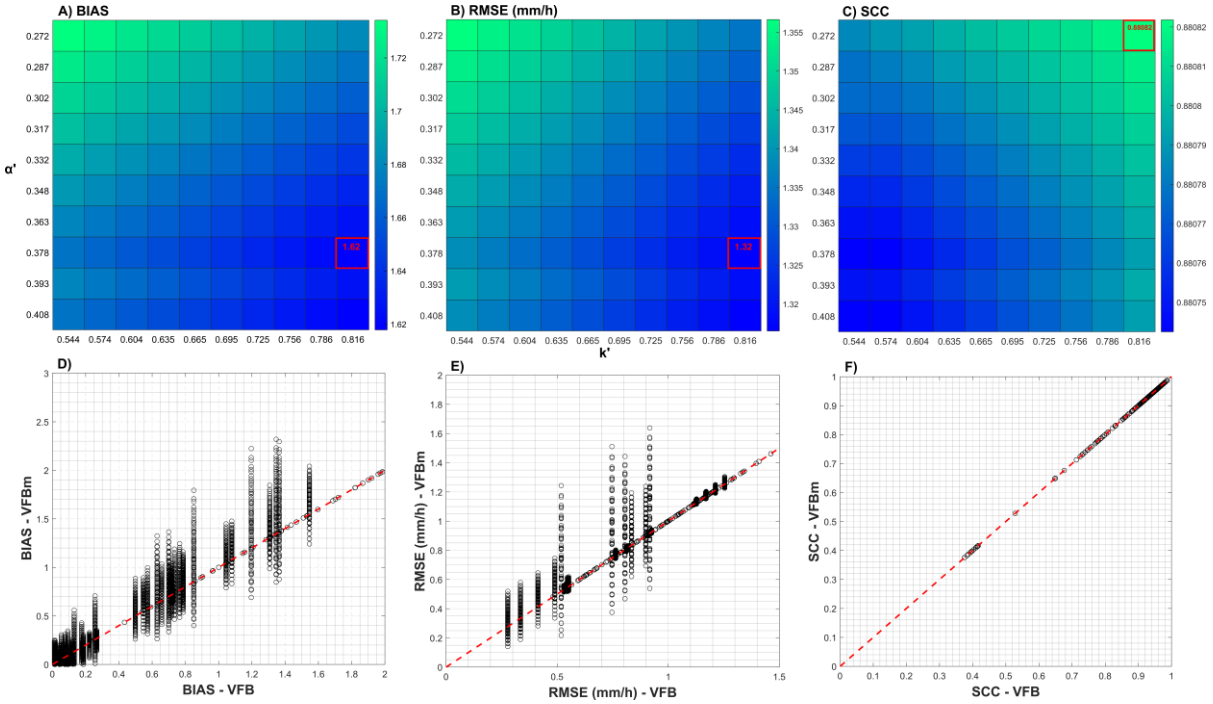

Figure 6.4: Performance of calibrated VFBm-model parameters. Panels A), B) and C) show three different statistical indicators, i.e. Relative BIAS, RMSE (mm/h) and SCC. The red circle indicates the

optimum value of the parameter. D), E) and F) are scatter plots of statistical performance for various iterated k and α (VFBm-model) and fixed literature review-based k and α (VFB-model), indicating behavior of iterated values for each CMLs link of VFBm-model in comparison to V-model. The blue dotted line indicates the uncertainty of the VFB-model and VFBm-model for the estimation of WAA.

Figure 6.4 shows the performance of the VFBm-model according to the indicators defined in Sec. 6.4. Panels A-C show the values of BIAS, RMSE and SCC, as a function of the two model parameters. The pair k= 0.82 and α= 0.38 (red circle in Figure 6.4(A) and (B)) returns the minimum values of BIAS and RMSE. On the other hand, the maximum SCC is obtained with k=0.82 and α= 0.27 (red box in Figure 6.4(C)). When the calibrated parameter values of VFBm are applied to the validation dataset of 11 rainfall events (02-June-2020 to 13-June-2020), the BIAS is 1.618, the RMSE is 1.317 mm/h, and the SCC is 0.88082. These validation performances of statistical indicators are close to the ones obtained in calibration (Figures 6.4(A), (B), and (C)). The performances are rather insensitive the values of the model parameters, at least in the range of values explored by our analysis. In this scenario incidentally the model parameters of VFBm model has optimal value for BIAS and RMSE, however if they were different then a joint statistical indicator that considers all the statistical metrics need to be determined to select the most appropriate parameter value.

To understand the improvement provided by VFBm over VFB, i.e. using parameter values calibrated on our CMLs network rather than the original ones, we scatterplot the three statistical indicators in Figure 6.4(D-F). The vertical stripes in each plot represent individual CMLs. The individual circles correspond to k and pairs in the range ±20% from the VFB model. The dashed red lines pass through the points corresponding to the values of the indicators achieved by the VFB model. Please note that CMLs with high values of BIAS and RMSE are not affected by the actual values of k and α. SCC showcases an uncertainty close to 0 (Figure 6.4(F)), as this indicator only assess if there is a monotonic relationship between CMLs and RGs data. The reason for this behavior is an overestimation produced by some CMLs, which is not at all compensated by letting the model parameters range within the ±20% bounds. The maximum uncertainties in VFBm model were obtained from Figure 6.4(D) and (E), where we identified the highest value of BIAS and RMSE. The maximum uncertainty in VFBm-model is 1.02 and 0.76 mm/h for BIAS and RMSE respectively.

6.5.2 Comparison of rainfall intensity derived using various empirical WAA models

Rainfall intensity values measured by RGs and estimated by CMLs after WAA compensation through four different models are compared here: SRB, VFB and VFBm, plus the “zero model” (Z), i.e. no WAA compensation, taken as a worst-case benchmark, to assess the amount of errors introduced in rainfall intensity estimates when WAA is ignored.

6.5.2 Comparison of rainfall intensity derived using various empirical WAA models

The results are in Figure 6.5, which shows box-plots of the three statistical indicators (BIAS, RMSE and SCC) for the four WAA models, clustering the links according to frequency band (panels C-E), class of path length (F-H) and class of rainfall intensity (I-J), respectively. Figure 6.5(A) represents statistical indicator obtained by considering individual links and frequencies rather than averaging values for entire catchment presented in box plot. Figure 6.5(B), based on the methodology described in Sec. 6.2.2 is applied to eliminate erratic signals.

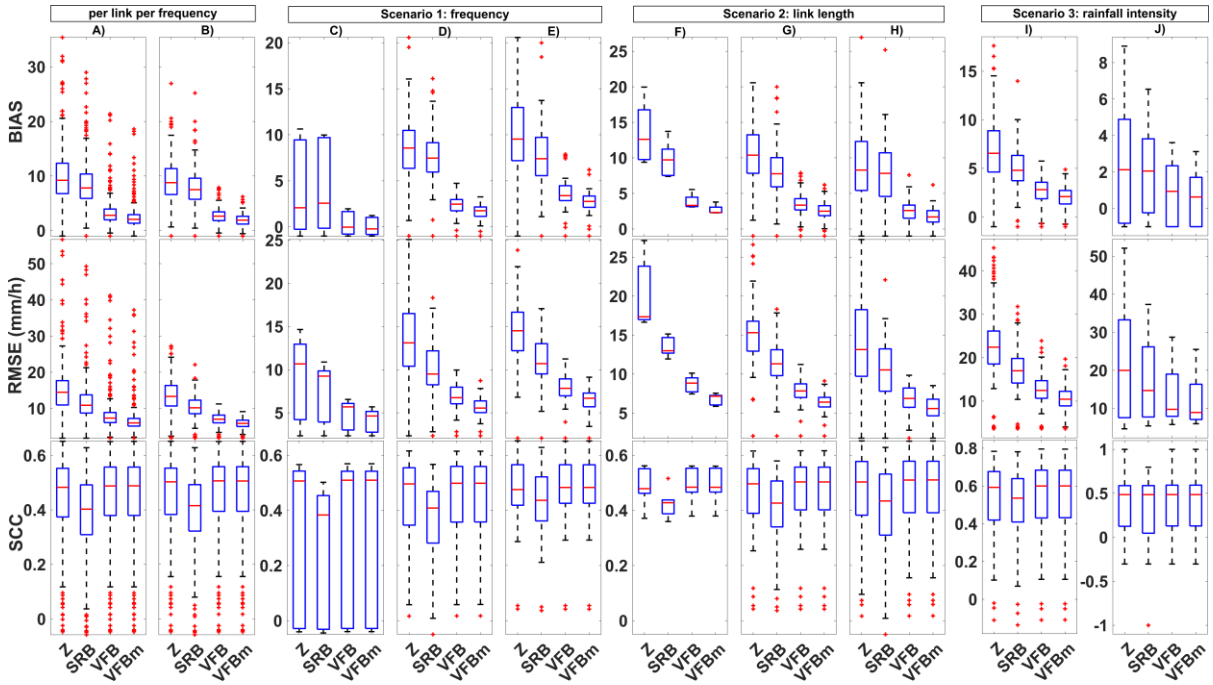

Figure 6.5: Hourly rainfall accumulation: CML estimates against RG measurements. Comparison of RGs and CMLs derived rainfall intensity using various WAA models (Z, SRB, VFB, VFBm (optimized model parameters) based on statistical indicators BIAS, RMSE and SCC. (A) all links including the ones showing erratic signal, B) all links except the ones showing erratic signal. Scenario 1: based on frequency classes C) B1 – frequency band 11.32 GHz – 12.95 GHz, D) B2 – frequency band 18.26 GHz – 22.54 GHz, E) B3 – frequency band 38.04 GHz – 41.85 GHz. Scenario 2: based on link length F) 0 km – 1 km G) 1 km – 2 km H) 2 km – 3 km. Scenario 3: based on rainfall intensity (type of rain) I) 11 mm/h – 30 mm/h (very heavy rain), J) > 30 mm/h (cloud burst).

CMLs tend to overestimate rainfall with respect to RGs measurements. However, rainfall intensity derived using VFBm has the lower outliers and lower median values of BIAS and RMSE, followed by VFB, SRB and Z, respectively. WAA compensation by VFBm reduces BIAS by almost 80% and RMSE by almost 60% with respect to Z-model. With VFB, the percent reduction is 70% and 50%, respectively. Additionally, the interquartile range of VFBm is the minimum. The reason for the better

performance of VFBm and VFB is that the model input is the rainfall intensity, hence the model parameter values include all the factors, that is frequency, polarization, drop size distribution and path length that may affect the attenuation-to- rainfall conversion (Valtr et al., 2019). This study confirms previous results (Lian et al., 2022), that is, the WAA model derived from the rainfall intensity is better than constant and wet-dry classification models. Some studies suggest that if enough data is not available the constant could also be used as a coarse estimate of WAA effects (Overeem et al., 2013), as WAA is almost constant for high rainfall intensities (Fencl et al., 2018). Links with lower frequencies (B3 – Figure 6.5(C)) highlight a negative correlation with the rainfall intensity, which requires a further investigation. The removal of erratic signals (Figure 6.5(B)) shows similar model performance to that observed without erratic signals performance (Figure 6.5(A)), based on similar WAA models. The reason holds due to the removing outliers exceeding based on standard deviation threshold from the observed values.

If we divide CMLs per frequency band, VFBm still outperforms all the other WAA models over each of the three frequency classes: RMSE is 4.6 mm/h, 5.54 mm/h, 6.68 mm/h, while BIAS is -0.21, 1.75 and 2.76, respectively (moving from the lower frequency to the higher frequency class). The SCC is similar to the one of VFB. In the lower frequency class – B1 (Figure 6.5(C)), the differences between the rainfall estimates (median) of different WAA models, are relatively smaller compared to higher frequency classes. However, all the WAA models still produce higher rainfall intensity estimates. As for Z-model, the values are significantly lower, and the differences are lower for lower frequency class in comparison with other frequency. Underestimation were visualized in some of the CMLs for all the WAA models in lower frequency class. Spearman correlation coefficient indicates a wide range of values for all the WAA models indicating the data has low relationship with the RGs data for the lower frequency class. For the frequency class - B1 and B2, SRB performs similar as Z in overestimation of rainfall intensity, while it is better in the higher frequency class. The general visualization (Figure 6.5 (C, D, E)) for various WAA models indicates is that SRB performs not so much better than Z model and clearly worse than VFB and VFBm model all the way. The key findings would be to recalibrate the frequency of the lower classes as the interquartile range is wide (SCC) and some CMLs have negative correlation with RGs rainfall intensity.

It has been reported that short link paths (< 2 km) have higher errors in comparison to observed rainfall intensity (De Vos et al., 2019). In our study, the majority of CMLs fall into this category. For short CMLs (48 - 128 m) another study stated that the WAA component was minimal in comparison to longer ones (296 – 497 m) (Fencl et al., 2018). The shorter (longer) ones in that study showcases the effect due to raindrop attenuation of about 0.2 dB (2.9 dB) during 20 mm/h rainfall intensity and 0.9 dB (12

dB) for 100 mm/h extreme rainfall intensity. Further, at lower frequencies of CMLs the statistical performance indicator shows a large scatter (Figure 6.5(C)). VFBm performs better than Z and SRB, while the difference with VFB is minimal. The performance of the population of short links is similar, while it gets more scattered for longer links. However, at the same time, the median biases and median RMSE decrease. The time series of Short CMLs shows a much earlier deviation from the rainfall peak and a longer duration of deviation after the peak compared to RGs observations, adding more uncertainty to the retrieval of the rainfall intensity from CMLs data. For zero and SRB dependent models it would not be ideal to have smaller link lengths to estimate rainfall intensity as the mean error (~>10 mm/h) and biases (~5) were higher.

The performance of WAA models as a function of rainfall intensity permits to understand which models are able to capture both cloud burst and very heavy rain intensity events. The ranges of interquartile were very high for CB events (> 30 mm/h) with some of the CMLs having negative correlation (< 0), RMSE also increased for VFBm to 10 mm/h and the overestimation is still prevalent. VFB and VFBm are more or less equivalent for the CB class. For events in the 11-30 mm/h class, the overestimation increases drastically by 2 folds, but this could be due to majority of the 45 storm events falling under this category. This clearly indicates that WAA compensation is important but there could be other parameters that are influencing the CMLs signal transmission that needs to be further evaluated on field. Finally, if the calibration is a challenge than the use of VFB-model, is desirable for WAA analysis as they can cover wide range of scenarios and provide the best performance across short CMLs links, different frequencies and rain event types. Even with WAA compensation, an overestimation of rainfall intensity is apparent in the majority of the CMLs, which may push to think that there are other factors biasing rainfall intensity estimates performed by CMLs. A pure data-drive strategies based on neural network could be developed as done in a few recent study a resulting in better accuracies (Daher et al., 2022; Pudashine et al., 2020).

6.6 Implications for CML-based rainfall estimation and future directions

Here, we have investigated the performance of various empirical wet antenna attenuation (WAA) models to estimate the rainfall intensity from commercial microwave links (CMLs). The results show that Valtr-Fencl-Bareš modified (VFBm) model improved accuracy in comparison to VFB model, for short CMLs (< 3 km), frequency of different classes ranging from 11 GHz to 42 GHz, and type of storm events. The calibration of the parameters is a must and an important framework requirement for empirical models such as VFB or Kharadly & Ross model (KR). However, for higher rainfall events the attenuation reached by VFB, KR and Garcia-Rubia et al. model (GBRG) are approximately similar for unit length of CMLs. The optimum value of the parameters should be determined using the

uncertainty range, the RGs proximity distance, the CMLs length and the extreme event integration through weights. This has not been highlighted in the past studies to derive the rainfall intensity using CMLs. This framework provides valuable insights of the behavior of model's parameters across each link highlighting that with higher error and biases there is not much significant impact on the whatever values are chosen for model's parameters, however for lower error and biases the uncertainty does play an important role in WAA estimation using both VFB and KR models. Thus, for different study areas, the optimum value of the model's parameters needs to be defined before the comparison with other WAA models. SCC for some of the CMLs is negative which acts as another indicator for the elimination of erratic signal including choices of standard deviation or threshold-based approach for negative relationship strength with RGs. The performance assessment through SCC did not vary much significantly between the various WAA empirical models. Thus, there is a need of joint weighted statistical indicator, which combines all the individual statistical indicators, to be developed for CMLs-derived estimation of rainfall intensity. The overall estimation of rainfall intensity was reduced by 78% (on average) and the error decreased by 58% when VFBm-model was incorporated, in comparison to Z-model. The VFBm-model exhibited lower biases and errors in rainfall intensity estimation. Short links (0-3 km) did impact the performance of the WAA models, with 0–1 km being the most affected. Capturing no rain or low rain events remains a challenge for deriving rainfall intensity from CMLs data, necessitating further studies and statistical analysis, particularly for applications in drought studies. Additionally, future detailed investigations are needed to determine the optimal link length of CMLs and the behavior of such links at various distances from rain gauges.

This study has several implications for the operation of systems that are affected by WAA; hence, the limitation also should be highlighted. Some of the limitations are:

i) The procedure proposed here requires a comparison with RGs data for calibration. The limitation of the procedure is that we need a dense network of RGs to cover the area of the CMLs network according to a minimum reciprocal distance.

ii) The dataset is limited to 45 rainfall events of ~ 1080 hrs of different types of rainfall events. In principle, to understand the behavior of the parameter values requires a dataset large enough, but also uniform data for different classes of severity of rain events.

The findings are important to setup a similar framework for accurate estimation of rainfall intensity using WAA models with CMLs data. Based on the above framework, the future recommendation would be a further assessment on:

- A mixture of Schleiss et al. (SRB) model and VFB taking advantage of the recursive procedure of SRB during the transients. SRB recursive application accounts for the transients and does not need for operational estimate of WAA.

- Application of machine learning techniques on all the links together (not individually!) for all the stages of the processing chain. Using all links would permit also to determine whether both antennas, or only one are under rain. Then we could add the RGs network and update in case required using calibration with a similar framework at a certain rate (e.g., daily or monthly). This system could be used for cross-calibration as well in a sensor fusion perspective.

Chapter 7

Continental-scale bias correction and random forest downscaling of CMIP6 precipitation across Europe

Research Question: *"How does bias correction of CMIP6 data using observed data affects the predictive performance of a random forest (RF) model for precipitation climate variable, and what are the difference in assessment outcomes comparing with or without bias corrected CMIP6 data across Europe?"*

Synthesis:

High-resolution precipitation data is important for climate risk assessments, specifically in regions with diverse topography like Europe. This study presents a comprehensive assessment of bias correction based downscaling approaches for precipitation data from 11-high resolution Coupled Model Intercomparison Project Phase 6 (CMIP6) models across Europe, using Ensembles daily gridded observation (E-OBS) dataset as reference. Among all the bias correction approaches, the non-parametric Empirical Quantile Mapping (EQM) method demonstrated better performance in aligning model outputs with observed precipitation data. Subsequently, Random Forest (RF) models, with and without EQM-based bias correction (RF-EQM), were modeled to predict the precipitation, using Bayesian optimization for hyperparameter tuning. The RF-EQM outperformed RF especially for low-rainfall intensity (0-5 mm/day) and with residual errors closer to zero across most European regions. Overestimation by CMIP6 models in central and eastern Europe was significantly bias corrected through the application of EQM, RF, and RF-EQM approaches. Seasonal analysis reveals lower residual errors in summer than winter for the current approaches. Future projections provides insights into the reduced overestimation of high quantiles, resulting in a more reliable precipitation estimates. The methodological framework suggests an integrated BC with machine learning (ML) enhances the accuracy of regional precipitation downscaling predictions, offering an important insight for developing early warning systems and risk management strategies across Europe

7.1 Advances in bias correction and ML downscaling of precipitation in Europe

Climate scenarios from 21st-century general circulation models (GCMs) are important for evaluating how ecological, physical, and cultural systems may respond to climate change (Tabor and Williams, 2010). Further, GCMs are important tools in climate change research, valued for their ability to use mathematical models to simulate historical climate patterns and project future climate scenarios (Hartmann, 2016; Shrestha and Pradhanang, 2022). Coupled Model Intercomparison Project (CMIP), initiated in 1995 under the World Climate Research Program, in order to compare GCMs, has evolved through several phases: CMIP (1995), CMIP2 (1997), CMIP3 (2004), CMIP4 (2005), CMIP5 (2013), and CMIP6 (2020 - (Eyring et al., 2016)). Many climate studies have utilized CMIP6 GCMs simulation data (Thrasher et al., 2022; Wang et al., 2021). The coarse resolution of GCMs limit their capacity to assess land surface processes and climate change impacts at local to regional scales, particularly in areas with complex topography and varied land cover (Giorgi and Gutowski Jr, 2015; Wilby et al., 2004). Furthermore, GCMs exhibit limitations in temporal and spatial resolutions, leading to intrinsic uncertainties and biases (Zhang et al., 2022), making their simulations unsuitable for regional-level climate impact studies (Jose et al., 2022). This limitation is especially evident for precipitation, a key climate variable that drives ecological and socioeconomic impacts due to changes in amount, frequency, and spatial distribution (Hess et al., 2023).

Precipitation is a critical component in wide-range of studies such as hydrological and soil erosion modelling, water balances and climate change projections (Talchabhadel et al., 2021). As global warming projected to persist in the future, assessing the impacts of changes in precipitation patterns is an urgent challenge (Masson-Delmotte et al., 2021). Precipitation in Europe varies significantly, reaching up to ~2000 mm/year or more in regions like Dinaric Alps, Pindus, Taurus, Caucasus and Alborz mountains, while areas just a few degrees latitude south may receive far less precipitation in magnitude (Francis et al., 2021). Precipitation based extreme climate indices shows significant increase in simple daily intensity index (intensification of precipitation) across Europe (Berényi et al., 2023). European climate studies show that northern Europe has become wetter and southern Europe drier, with seasonal changes varying by regions but the significant trends observed in winter (Berényi et al., 2023). Current state-of-the-art Earth System Models (ESMs) have a resolution order of ~100 km (occasionally ~50 km), but smaller-scale processes critical for precipitation, below the grid cell size cannot be explicitly resolved (Hess et al., 2023). Smaller-scale processes important in precipitation like droplet interactions, turbulence, and cloud phase transitions (Hess et al., 2023). It is widely known that the GCMs simulation often displays biases compared to observational references, such as observed or reanalysis data (Vrac et al., 2022). A recent study conducted indicates the GCMs compared with ERA5

reanalysis precipitation data across Europe found to overestimate the winter precipitation probability, while underestimating in summer (Plavcová et al., 2025). Correcting GCMs biases is a crucial step for accurate climate projections (Beyer et al., 2020).

Downscaling and bias correction (BC) methods are approaches to bridge the spatial gap between GCMs output and the fine-scale data requirements (Maraun and Widmann, 2018). BC transforms the historical data from the GCMs to align their statistical properties (such as mean, standard deviation, or probability distribution) with those of the observed data. The transformation derived from this is assumed to remain valid for future climate projections, where it is applied to the period of interest (Vrac et al., 2023). To reduce the biases from the GCMs many methods have been developed, broadly statistical downscaling and dynamical downscaling. Most researchers prefers statistical downscaling for GCMs due to advantage of low computational requirements and minimal maintenance cost (Fan et al., 2021; Rhymee et al., 2022). The Quantile Mapping (QM) approach is widely used statistical bias correction technique (Volosciuk et al., 2017; Vrac et al., 2016), reason lies in its easy implementation, computational efficient, and preserving simulation trends (Cannon et al., 2015). There are several other statistical downscaling approaches such as Empirical Quantile Mapping (EQM), Gamma Quantile Mapping (GQM), Gamma-Generalized Pareto Quantile Mapping (GPQM), scaling and many more (Daniel, 2023; Mendez et al., 2020).

Homsi et al. 2020 evaluated multiple bias correction methods for precipitation data in Syria, finding that the scaling method is the most effective approach for downscaling of GCMs. The gamma distribution based statistical bias correction method, improves the mean, intensity distribution, droughts, and heavy precipitation indices across Europe (Piani et al., 2010a). Another study compares downscaled data in Rhine basin, applying BC by fitting mean and coefficient of variation, which reduces precipitation biases significantly in summer (Terink et al., 2009). Further, it also improves the correlation of wet-dry fractions and lag-1 autocorrelation (Terink et al., 2009). In a central northern Germany study site, QM based downscaling of daily precipitation when applied to higher-resolution observations, overcorrects due to drizzle effect, leading to overestimates area-mean extremes (Maraun, 2013b). A recent review of bias correction approaches highlighted that the EQM is among the well performing bias correction methods for precipitation (Menapace et al., 2025). Luo et al. 2018 showed that no single BC method is universally applicable in all regions. To address the spatial and temporal variability, a comparative analysis of multiple BC approaches is required (Worako et al., 2022).

Recent progress in machine learning (ML) driven approaches, such as regression based techniques like Decision Trees, Artificial Neural Networks, Support Vector Machine, and Random Forests (RF), has showcased an effective bias correction in GCMs, improving accuracy of precipitation by capturing

nonlinear relationships and enhancing spatial-temporal patterns in comparison to conventional statistical approaches (Nourani et al., 2019; Zarei et al., 2021). RF as a ML technique has a widespread use in various predictive applications including climate and weather forecasting (Tong et al., 2019). The application of ML in BC has gained considerable focus in recent years; however, ML algorithms can sometimes result in inaccurate estimates due to overfitting (Seo and Ahn, 2023). The review indicates that various ML algorithm performance differently across different spatial datasets, with some limitation in effectively managing complex datasets (Shanmugam and Lakshmanan, 2025).

This study focuses on CMIP6 models with spatial resolution finer than ~100 km to better depict the climate dynamics across Europe's diverse topography. Considering the literature review despite the high-resolution data of historical and future climate projections these CMIP6-GCMs still requires BC to account for difference in precipitation outputs. We use highest resolution gridded data to adjust the CMIP6 precipitation data. The bias corrected data utilized as an input for RF model to generate a predictive model for future precipitation data. By comparing the performance of RF prediction with or without BC as input, we aim to check whether BC improves model ability to reproduce observed precipitation quantiles. The application of bias corrected data and CMIP6 data in development of RF model is important, as it can influence the prediction accuracy by potentially introducing errors that can alter the precipitation data. We then assess the implication of these methods for future climate projections using shared socioeconomic pathways (SSPs). Such a comprehensive study of quantiles performance that compares the various bias correction and the application of bias correction in prediction using ML at a continental scale is still underexplored. The objective of the study is to:

- Apply and compare BC to CMIP6 precipitation data from models with resolution finer than ~100 km to align with observed data.
- Model the RF with or without using the bias corrected CMIP6 data to analyze the prediction performance.
- Assess the effects of these approaches on future climate projections (ssp126, ssp245, ssp370, ssp585).

The research tackles the urgent demand for precise high-resolution precipitation downscale data in Europe, where varying precipitation patterns has significant societal and environmental consequences. By applying the framework to future SSP scenarios, it offers insights into the precipitation changes within a climate change context.

7.2 Information on CMIP6 models, observed data and preprocessing

7.2.1 Selection and characteristics of CMIP6 models

This study focuses on downscaling the precipitation data from the CMIP6 to evaluate the performance of bias correction and random forest (with or without bias correction) prediction across Europe. To achieve adequate spatial detail for regional climate studies, we chose CMIP6 models with nominal resolution ~100 km, as the individual grids of size larger than this are less capable to represent Europe's diverse topography and climate variability (Giorgi and Gutowski Jr, 2015; Soares et al., 2024). Table 7.1 lists various high-resolution CMIP6 models including the horizontal resolution, which provides daily precipitation data for the historical period (1950-2014) and future climate projections (2015-2100) under SSPs (ssp126, ssp245, ssp370, ssp585). These SSPs covers range of future scenarios from sustainability (ssp126) focused to high-emission pathways (ssp585), allowing assessments of precipitation variability across different climate projections.

Table 7.1: High-resolution CMIP6 models used in this study.

No.	**Model**	**Institution**	**~ resolution (°)**
M1	AWI-CM-1-1-MR	Alfred Wegner Institute, Helmholtz Centre for Polar and Marine Research (Germany)	0.94° x 0.94°
M2	BCC-CSM2-MR	Beijing Climate Center (China)	1.125° x 1.125°
M3	CESM2-WACCM	Climate and Global Dynamics Laboratory, National Center for Atmospheric Research (USA)	1.25° x 0.94°
M4	CMCC-ESM2	Euro-Mediterranean Center on Climate Change (Italy)	0.94° x 1.25°
M5	EC-Earth3-Veg	European EC-Earth Consortium (Europe)	0.70° x 0.70°
M6	GFDL-ESM4	Geophysical Fluid Dynamics Laboratory (United States)	1° x 1.25°
M7	INM-CM5-0	Institute for Numerical Mathematics, Russian Academy of Science (Russia)	1.25° x 2°

M8	MPI-ESM1-2-HR	Max Planck Institute for Meteorology (Germany)	0.94° x 0.94°
M9	MRI-ESM2-0	Meteorological Research Institute, Japan Meteorological Agency (Japan)	1.125° x 1.125°
M10	NorESM2-MM	Norwegian Climate Center (Norway)	0.94° x 1.25°
M11	TaiESM1	Research Center for Environmental Changes (Taiwan)	0.94° x 1.25°

CMIP6 data were retrieved from the Earth System Grid Federation (ESGF) data nodes (Eyring et al., 2016), with the resolution (Table 7.1) of each model derived from the metadata within corresponding NetCDF files. The r1i1p1f1 member selected for each of the CMIP6 model. We obtained precipitation daily data (variable 'pr') for each CMIP6 models and regridded it to a uniform 0.25° x 0.25° resolution through linear interpolation to enable comparison with the observed precipitation data. The historical period (1950-2014) is used as the reference for BC (RF) – model training and testing (prediction), while future climate projections (2015-2100) to evaluate long-term precipitation change. The individual model output were evaluated to test (predict) quantile changes in precipitation across Europe.

7.2.2 Observational reference data: E-OBS

To assess BC CMIP6 precipitation outputs, we used high-quality gridded observation datasets as reference data (Figure 7.1). The observed precipitation data is for the Europe, which is westernmost part of Eurasia (25° N – 71.5° N x 25° W – 45° E) is acquired through European Climate Assessment and Dataset (ECA&D) Ensembles daily gridded observation dataset (E-OBS) v29.0e (Cornes et al., 2018). The dataset offers daily gridded precipitation data from 1950 to 2023 at a resolution of 0.25° x 0.25°. Figure 7.1 provides a comprehensive assessment of European precipitation, highlighting spatial and temporal dynamics (trends, seasonality, anomalies, variability, and persistence).

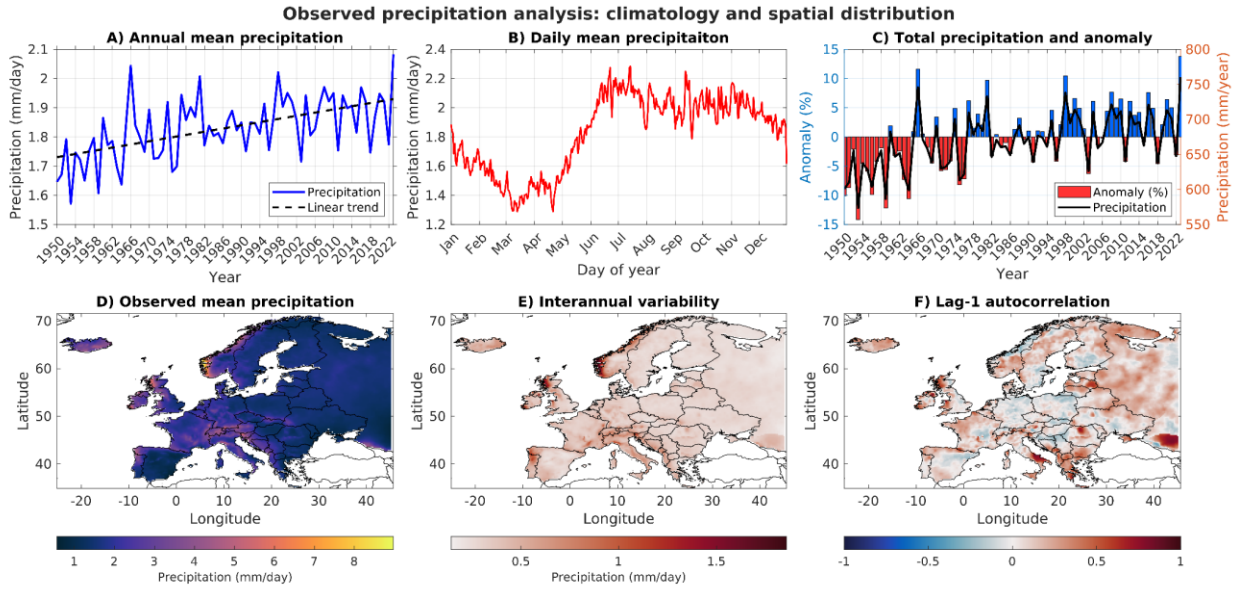

Figure 7.1: Observed precipitation analysis: climatology and spatial distribution across Europe (1950 – 2023). A) annual mean precipitation, B) daily mean precipitation, C) total annual precipitation and anomaly (%), D) observed mean precipitation, E) interannual variability (spatial distribution), F) lag-1 autocorrelation (correlation of precipitation by one time step (annual)).

The annual mean precipitation over the observed period indicates an increasing trend (Figure 7.1 (A)). The increase suggests long-term rise in precipitation across Europe, potentially driven by climate change (Furtak and Wolińska, 2023). The seasonal cycle (Figure 7.1 (B)) indicates elevated average precipitation in summer (peaking around July), with reduction during spring. This precipitation rate aligns with the North Atlantic Oscillation influence (Trigo et al., 2002). Annual total precipitation (Figure 7.1 (C)) shows significant variability, with mostly negative anomalies in the 1950s and 2000s, and mostly positive anomalies after 2000s. The spatial map shows the regional differences of average precipitation across Europe (Figure 7.1 (D)) – high precipitation (7-8 mm/day) recorded in Alps and western Norway, and lower precipitation in eastern Europe (1-2 mm/day). Figure 7.1 (E) shows regions with high interannual variability, i.e. northern Europe, mountain regions of Alps, and northern Spain, Portugal, and United Kingdom with variability up to 1.5 mm/day. Lag-1 autocorrelation (Figure 7.1 (F)) shows positive values in eastern and southern Europe indicating persistence in annual precipitation (i.e. wetter (or drier) year likely followed by another wetter (or drier) year), negative values in central Europe, suggesting less persistence.

There are limitations associated to the E-OBS data: such as limited coverage in southeastern Europe. The sparse station coverage in this region, leads to uncertainty specifically affecting precipitation data (Cornes et al., 2018). As the downscaling is grid based with the comparison of CMIP6 models with the

E-OBS (observed data), the regions in southeastern Europe might have a potentially misleading estimates. E-OBS dataset is the reference for BC and as a predictand (output) for the training the RF model.

7.3 Bias correction and Random Forest (RF) downscaling methodology

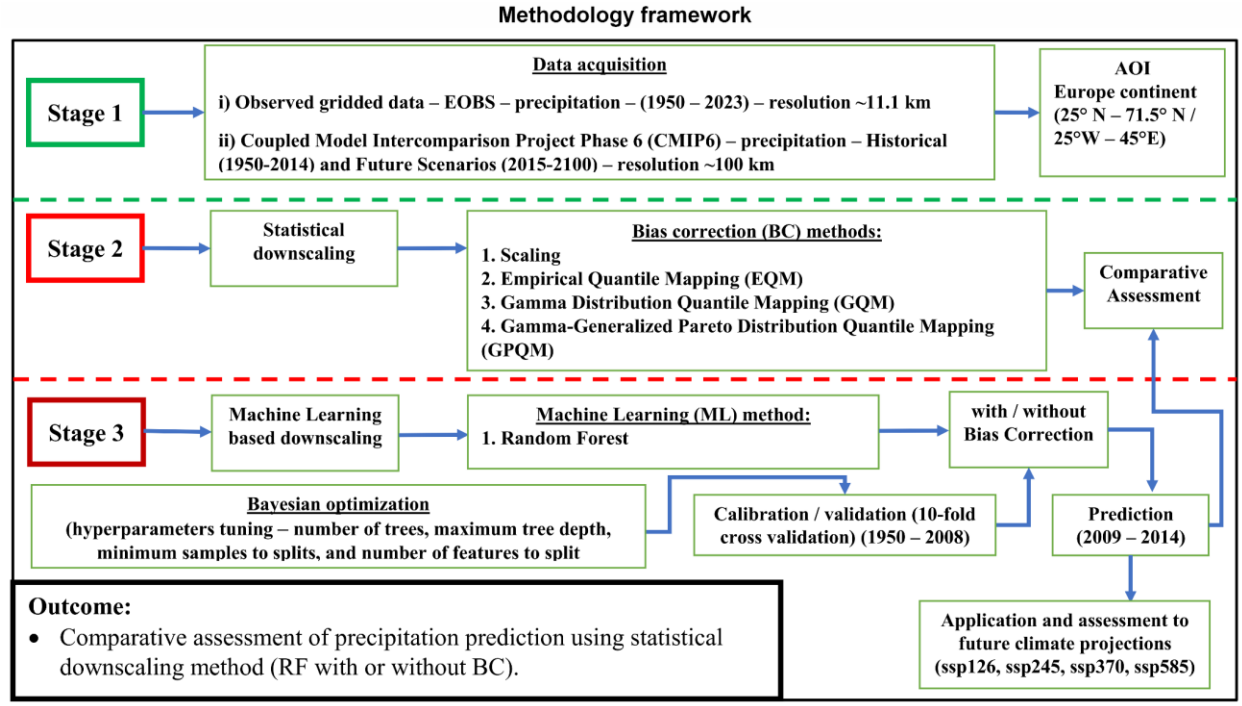

Figure 7.2: Methodology framework.

The methodology framework (Figure 7.2) outlines three-stage process for the entire study done for downscaling the CMIP6 data over the entire European continent. Initially as discussed, (see "data and methodology – data acquisition and observed precipitation data"), observed gridded precipitation data and CMIP6 models precipitation data is acquired. The second stage undergoes statistical downscaling, using various bias correction methods like scaling and QM techniques such as EQM, GQM, and GPQM, further followed by a comparative assessment such as box plots and quantiles. Subsequently stage 3 is a ML approach, specifically RF algorithm with Bayesian optimization for hyperparameters tuning, developed for prediction modelling. Either this predictive model will have predictor as a CMIP6 data (data acquired from stage 1) or bias corrected CMIP6 data from stage 2. This predictive model further applied to the future climate projections under different SSP scenarios.

7.3.1 Bias correction methods

Bias correction modifies CMIP6 precipitation data to align with observed data, correcting systematic errors in frequency, magnitude, and distribution (Teutschbein and Seibert, 2012). Implemented four bias correction techniques in this study, based on different assumption about precipitation distribution to assess the impacts on downscaling.

i) Scaling:

The scaling method aims to adjust the CMIP6 precipitation data using a multiplier factor to align the long-term monthly mean of the corrected values with observed data (E-OBS) (Fang et al., 2015; Lenderink et al., 2007). This method is mathematically expresses as follows (Jaiswal et al., 2022):

$$P_{corrected,m,d} = P_{raw,m,d} x \frac{\mu(P_{observed,m})}{\mu(P_{raw,m})} \quad (7.1)$$

where $P_{corrected,m,d}$ is the corrected precipitation (m and d is the month and day), $P_{raw,m,d}$ is the raw precipitation (CMIP6 data). Further multiplying factor to the mean (μ) of ratio of amount of observed and CMIP6 precipitation for the specified month.

ii) Empirical Quantile Mapping (EQM):

The EQM method employs a transfer function to adjust the distribution of CMIP6 precipitation data to match the observed data (Piani et al., 2010b), and mathematically represented as:

$$P_{BC} = F^{-1}_{observed}(F_{raw}(x)) \quad (7.2)$$

where P_{BC} is bias corrected precipitation data of CMIP6, F_{raw} is the cumulative distribution function (CDF) of the CMIP6 data, $F^{-1}_{observed}$ is inverse of CDF for the observed data, and x is the raw precipitation data by the model. EQM is a non-parametric method suitable for various type of precipitation distributions (Fang et al., 2015). EQM adjust biases in mean, standard deviation, wet-day frequencies, across range of quantiles (Themeßl et al., 2012). EQM calibrates the CMIP6 CDF by incorporating both mean and quantile specific range of observed precipitation distribution, blending the model and observation CDFs to construct the transfer function (Cannon et al., 2015; Piani et al., 2010b).

iii) Gamma Quantile Mapping (GQM):

QM can correct biases in CMIP6 models by applying parametric distributions instead of empirical CDFs. Similar to EQM this approach considers that both observed and model output follows a specific statistical distribution. Widely used option for modeling precipitation CDFs is gamma distribution referred as GQM, defined by two parameters: shape (k) and scale (b) (Piani et al., 2010a).

$$f\gamma(x|k,b) = x^{k-1}.\frac{1}{b^k.\Gamma(k)} \cdot e^{\frac{-x}{b}}; x \geq 0; k, b > 0 \quad (7.3)$$

The shape (k) influences the gamma distribution overall profile, whereas scale (b) determines its variability.

iv) Gamma-Generalized Pareto Quantile Mapping (GPQM)

The use of combined gamma distribution (core) and generalized Pareto distribution (tail end) within quantile mapping is termed as GPQM (Gutjahr and Heinemann, 2013; Yang et al., 2010). The core part is the central range of data between 5th and 95th percentiles where fitting is with gamma distribution while the upper and lower 5% tails are modelled with generalized Pareto distribution. This method expected to provide improved corrections for the higher percentiles of precipitation accurately by modeling the distribution tails.

BC performed on a daily basis for the historical period of (1950-2014) using E-OBS as the observed dataset for calibration and testing. Each BC method applied to daily precipitation time series at individual grid cell, with methods calibrated and tested using train-test split (1950-2008 for training, 2009-2014 for testing). The performance of each methods tested using mean quantiles and performance at the outliers before applying to the future climate projections.

7.3.2 Random Forest (RF) model development and implementation

RF a robust ensemble tree-based algorithm that models non-linear relationships between predictand (target variable – observed precipitation (E-OBS)) and predictor (input variable like precipitation data from CMIP6 models) (Breiman, 2001). RF algorithm builds an ensemble by averaging predictions of multiple decision trees, each trained on a bootstrap sample of the training dataset. Each split (or node) of trees, a random subset of predictor variable is assessed, creating model diversity and reduce correlation among decision trees. RF tends to avoid the risk of overfitting on the training dataset and delivers better performance in comparison to the standard decision tree model (He et al., 2016). To enhance the accuracy of RF model, hyperparameters tuning was conducted using Bayesian Optimization (R. Liu et al., 2024). The tuning of RF algorithm depends on two key hyperparameters: i) number of trees in forest, and ii) number of predictor samples required to split (Dey et al., 2022). In this study, we considered minimum samples to split and maximum tree depth additionally along with the two key hyperparameters for tuning. Bayesian optimization explores the hyperparameter range, maximizing the model performance using mean square error 10-fold cross validation. The RF model was trained/validated on both bias-corrected and non-bias corrected CMIP6 precipitation data from 1950-2008, prediction was done for 2009-2014 where the performance was assessed using quantile

based metrics. Metrics include mean absolute error (MAE) to evaluate the magnitude change in comparison to BC method and raw CMIP6 data, and percent bias (PBIAS) to compute the underestimation or overestimation of the models. The quantiles and intercomparison of the model performance will give insights into the ability of each approach to capture the average and extreme precipitation events. These predicted models at each grid applied to downscale the future climate projections of CMIP6 for 2014-2100 under the various SSPs.

7.4 Comparative assessment of bias correction methods and ML downscaling performance: results

7.4.1 Comparison of bias correction (BC) methods across various CMIP6 models

BC methods (Scaling, EQM, GQM, and GPQM) applied to CMIP6 precipitation data over Europe is showcased in Figure 7.3, which provides comprehensive comparison across multiple high-resolution CMIP6 models and BC techniques. The assessment has two main parts for visualization: boxplot comparison during calibration and testing, and mean quantile plots of the difference between observed and model precipitation for each BC method.

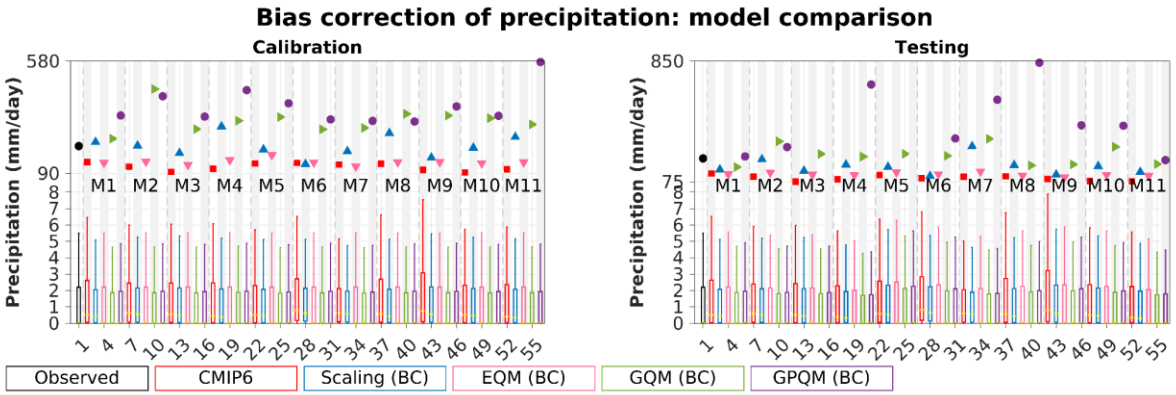

Figure 7.3: Comprehensive assessment of bias correction methods. BC of precipitation: model comparison (box plot) (notations similar to Table 7.1).

Figure 7.3 shows the box plot of precipitation distribution and outliers for 11 CMIP6 high-resolution models (M1 to M11 similar to (Table 7.1)) during the calibration (1950-2008) and testing (2009-2014) period. The box plot shows the median, interquartile range (middle 50%), upper and lower whisker, and outliers of daily precipitation (mm/day) for observed (E-OBS), historical CMIP6 and various bias corrected approaches data. During calibration, the CMIP6 models interquartile range (IQR) is ~ 2.5 mm/day for all the models and the median range varies from 0.40 to 0.80 mm/day across models. INM-CM-5-0 (M7) is the only model, which is showing underestimation in terms of IQR and upper whisker; however, the median values of all the models are higher than the observed E-OBS data. The

performance of the INM-CM model underestimation and largest errors discussed in the previous studies, which reasoned specific to JJA wind vectors and representing inadequately JJA blocking and annual precipitation in central Europe (Palmer et al., 2023). Finally, the maximum value of outliers of daily precipitation is in underestimation for all CMIP6 models when compared to the observed E-OBS data. CESM2-WACCM (M3) and NorESM2-MM (M10) highest difference in outliers value in comparison to the observed E-OBS dataset. During testing, all CMIP6 models have similar behavior (except range change), such as calibration in terms of IQR, median, upper and lower whisker, and outliers.

Comparison between calibration and testing reveals insights into the robustness of various bias correction methods. Based on testing data it can be stated that CMIP6 models have IQR higher for MRI-ESM2-0 (M9) (~3.11 mm/day) model while M7 (~2.05 mm/day) is the closest to the observed data. The precipitation data of all the models divided in calibration and testing for uncorrected CMIP6 data is stable except M9, which has a high variability of IQR and upper whisker due to extreme deviations. After bias correction, the medians of CMIP6 models aligns closely with observed E-OBS data, indicating decrease in errors. The performance of each of the BC method is different for each of the CMIP6 models considering IQR, and outliers. Scaling performance for outliers has reduced more than 100% for CMCC-ESM2 (M4) and M10 models during calibration and testing. Among the models, BCC-CSM2-MR (M2) under scaling approach downscales the most from the observed data (~2%) for outlier value. As a reference, it shows that for linear scaling the median are consistent across the models but limited improvement in variability (narrowing IQR). EQM approach exhibits strong performance, with IQR values closely matching observed E-OBS – for calibration it is ~ similar to observed (~2.20 mm/day), whereas for testing it is in the range of (~2.00 – 2.50 mm/day), but lower outliers in comparison to the observed data. GQM and GPQM tends to underestimate IQR, (e.g. M4 – 1.7 mm/day) and produce large outliers, suggesting instability particularly in testing. The distribution based parametric methods (GQM and GPQM) shows higher biases compared to non-parametric approach (EQM), likely due to assumption that both GCM (CMIP6) and observed data (E-OBS) follow theoretical distribution (this assumption is not true especially for temporal and spatial variability of precipitation patterns particularly during dry season (Chen et al., 2013b; Mendez et al., 2020).

Supplementary Figure S1 provided insights into the quantiles, compared with mean differences of observed and modeled precipitation (uncorrected CMIP6 and bias corrected CMIP6) data. The plot is of the differenced daily precipitation (mm/day) at quantiles from 0.01 to 0.99, with positive (negative) values indicating underestimation (overestimation) of CMIP6 (uncorrected/corrected model. The historical CMIP6 data show overestimation at lower quantiles (0.25-0.75) and underestimation at higher

quantiles (>0.95), depicting the inability to capture the Europe's precipitation distribution accurately. Scaling reduces the difference at the lower quantiles but further increases the underestimation of higher quantiles in comparison to the historical CMIP6 data. EQM is stable and improves the biases (difference of ±0.05 mm/day (calibration) and 1 mm/day (testing)) for entire range of quantiles. GQM and GPQM both shows high overestimation of the higher quantiles (heavy-tailed model) and even for quantiles >0.75. All the CMIP6 models with BC technique exhibits variability across quantiles, indicating unique characteristics; however, EQM remains stable in handling both underestimation and overestimation for the maximum number of models.

These findings suggests that EQM is the robust approach (in both calibration and testing) across most of the models, with minimizing the systematic errors (biases) and comparable distribution to observed (E-OBS) data (Gutjahr and Heinemann, 2013; Obada et al., 2016). The important consideration is that BC approaches performance during calibration is not similar to testing data or any future data (Cannon et al., 2015). As per previous findings, all BC methods effectively correct the mean values, but lacks the ability to capture the statistical characteristics such as percentiles (Teutschbein and Seibert, 2012). Future studies should aim to enhance the GQM and GPQM BC methods by focusing on medians and improving the strategies for overestimation of outliers in CMIP6 precipitation modeling. Additionally, sensitivity of models to changing climates, as non-stationarity remains a challenge (Hertig et al., 2015).

7.4.2 Statistical analysis of Random Forest (RF) with or without bias correction (BC) method

Figure 7.4 shows the results of RF model with (EQM) or without BC applied to 11 CMIP6 models (Table 7.1) over Europe. Similar to BC method the data split into calibration & validation (1950-2008), and prediction (2009-2014). The box plot compares the observed precipitation (E-OBS), CMIP6 data (historical period), bias corrected data using EQM (similar to results from section 3.1), RF downscaling without BC (RF), and RF downscaling with EQM bias correction (RF-EQM). The results will show the benefit of BC in enhancing prediction of RF performance for various quantiles, aiming to improve high-resolution precipitation estimates.

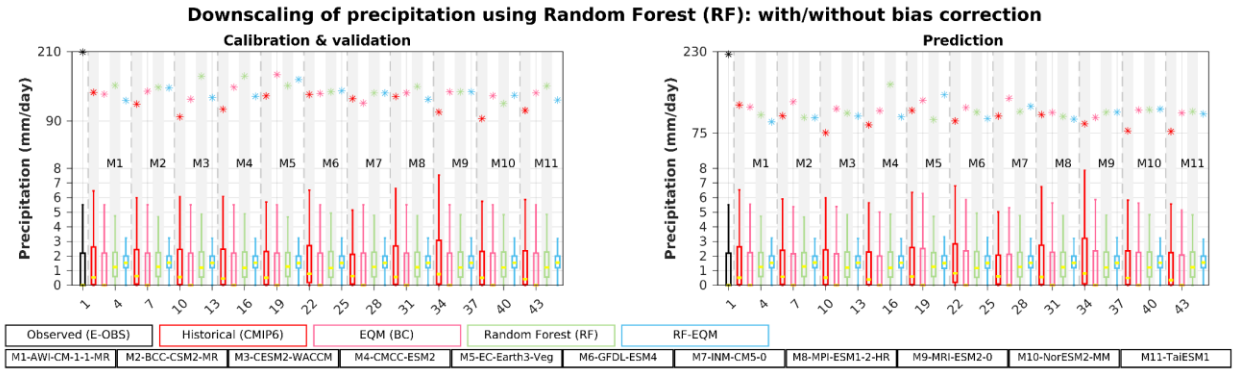

Figure 7.4: Downscaling of precipitation using RF, with and without BC. (Calibration and validation (left panel), and prediction (right panel)). M1 to M11 are CMIP6 models (notations similar to Table 7.1).

Based on the comparison of the BC methods (section 3.1), EQM demonstrates robustness in comparison to scaling, GPM, and GQM. Further, the comparison between RF and RF-EQM is focus here, while inclusion of observed (E-OBS), historical (CMIP6), and EQM (BC) precipitation data serves primarily for reference. RF downscaling without BC and with EQM shows reduction for IQR range and outlier in the CMIP6 models when compared to observed (E-OBS) precipitation data. The lower quartile values (lower 25%) have a noticeable shift in the RF model, and this shift increases with application of RF-EQM, results in a narrower IQR range. In addition, the upper whisker shows a substantial reduction in both RF and RF-EQM (more decrease in RF-EQM). Further, both RF and RF-EQM reduces variability; however, they continue to overestimates the median values, with RF-EQM showing a comparatively higher median. In RF and RF-EQM, the CMIP6 models downscaling perform similar during calibration/validation and prediction in terms of IQR, lower and upper whisker, indicating overall stability across models. However, the outliers extreme vary across different models. For calibration and prediction, RF without BC produces higher outliers, except for EC-Earth3-Veg (M5) and M10 CMIP6 models. The comparison also reveals model-specific response, overestimating CMIP6 models (example M9) shows improved correction in predicting outliers.

Figure 7.5 evaluates the statistical performance of the training/validation (1950-2008) and prediction (2009-2014) data for CMIP6, bias corrected EQM, RF and RF-EQM for 11 CMIP6 models over Europe in comparison to the observed data. The evaluation based on two assessment: percentage bias (PBIAS) as an indicator to determine overestimation and underestimation of each models, and absolute error in mm/day to assess the magnitude of the models. This will ascertain the outcome whether the downscaling approach is effective with or without BC for RF model during prediction.

7.4.2 Statistical analysis of Random Forest (RF) with or without bias correction (BC) method

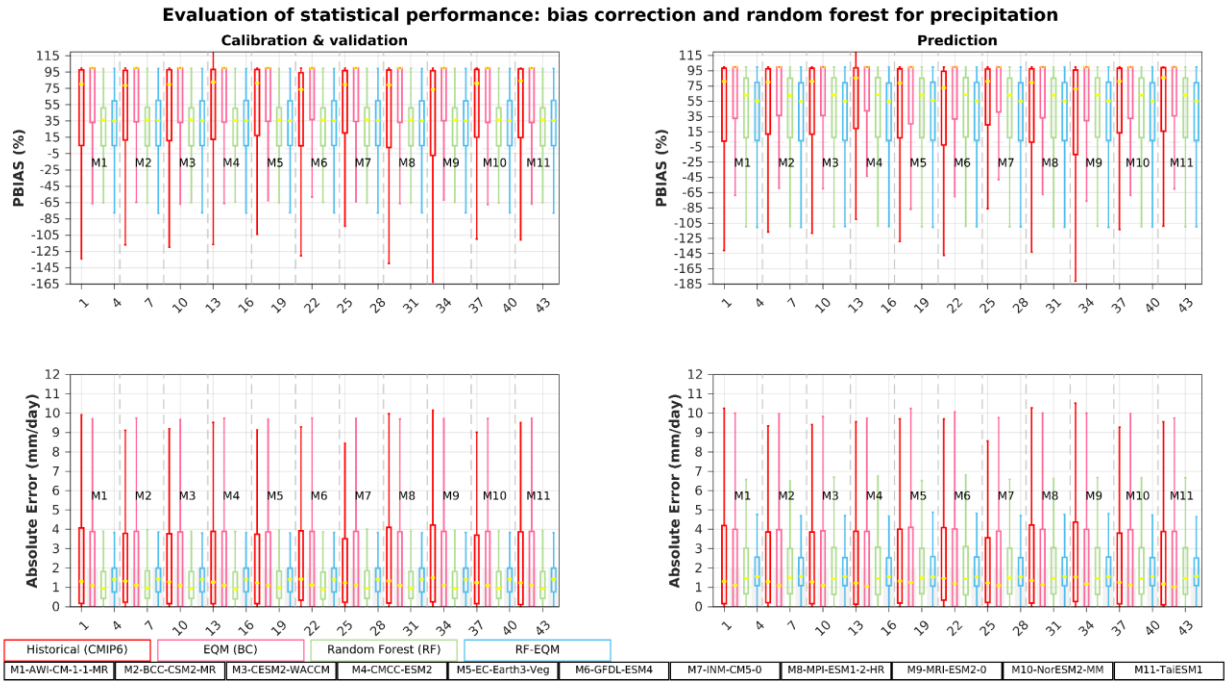

Figure 7.5: Evaluation of statistical performance: BC and RF for downscaling of precipitation. (Calibration and validation (left panel) and prediction (right panel)), statistical performance assessed with PBIAS (upper panel) and absolute error (lower panel). M1 to M11 are CMIP6 models (notations similar to Table 7.1).

During the prediction the PBIAS (MAE) value of CMIP6 ranges from -185% to 115% (0 to 10.5 mm/day) across all the uncorrected CMIP6 models in comparison to observed precipitation data. With PBIAS (MAE) often exceeding ±85% (8.5 mm/day) for all the models. M9 shows the highest negative biases and magnitude (e.g. ~-185% and ~10.5 mm/day) in uncorrected CMIP6 data indicating overestimation for lower precipitation data (that is <25% data). Indeed most of the models have overestimation in that range of precipitation data (<25% data). The median values of most of the models are in the range of 70-90% indicating an underestimation whereas absolute error shows a magnitude of ~1.3 mm/day when averaged across Europe for entire prediction time-period (2009-2014). The issue with CMIP6 models to exhibit high dry biases and their ability to capture the seasonal pattern, magnitude, and frequency of precipitation is already known (Tiku et al., 2025). After application of BC and RF (with or without BC), the PBIAS and absolute error significantly reduced. For instance, M9 model has reduced its overestimation (error) from ~-185% (~10.5 mm/day) in CMIP6 uncorrected to ~-70% (~10 mm/day) in EQM, ~-110% (~6.7 mm/day) in RF and (~4.8 mm/day) RF-EQM. For IQR and median values the RF prediction is shifting towards zero biases and lower magnitude errors (slightly better in RF-EQM) indicating a positive outlook with the variability of the data. A

recommendation to apply QM with RF to obtain better performance in comparison to observed model outputs, as well as suggestion on using BC methods that preserves trends (Raeesi et al., 2024) .

This study results is based on observed data (E-OBS) as output for predictive model like RF and RF-EQM, uncertainties in observational data affects the results in data-sparse regions (Cornes et al., 2018). In future, generative adversarial networks based machine learning approach - with or without bias corrected data could be tested, as they preserve large scale features while effectively correcting small scale precipitation biases (spatiotemporal and frequency) in the climate models (Hess et al., 2023).

7.4.3 Comparison of observed and statistical downscaling of precipitation: predicted and future scenarios

Figure 7.6 is a comprehensive comparison of observed and statistical downscaled precipitation (prediction time-period 2009-2014) for AWI -CM-1-1-MR (M1) – CMIP6 model focused on annual (Figure 7.6), winter (DJF) (Figure 7.7), and summer (JJA) (Figure 7.8) seasons over Europe. The figure includes spatial maps of difference between E-OBS (observed dataset), and various downscaled outputs (CMIP6 uncorrected data, EQM (BC method), RF, RF-EQM) and a histogram of residual error. This comparison would reveal significant annual and seasonal variations in downscaling accuracy and methodology framework performance.

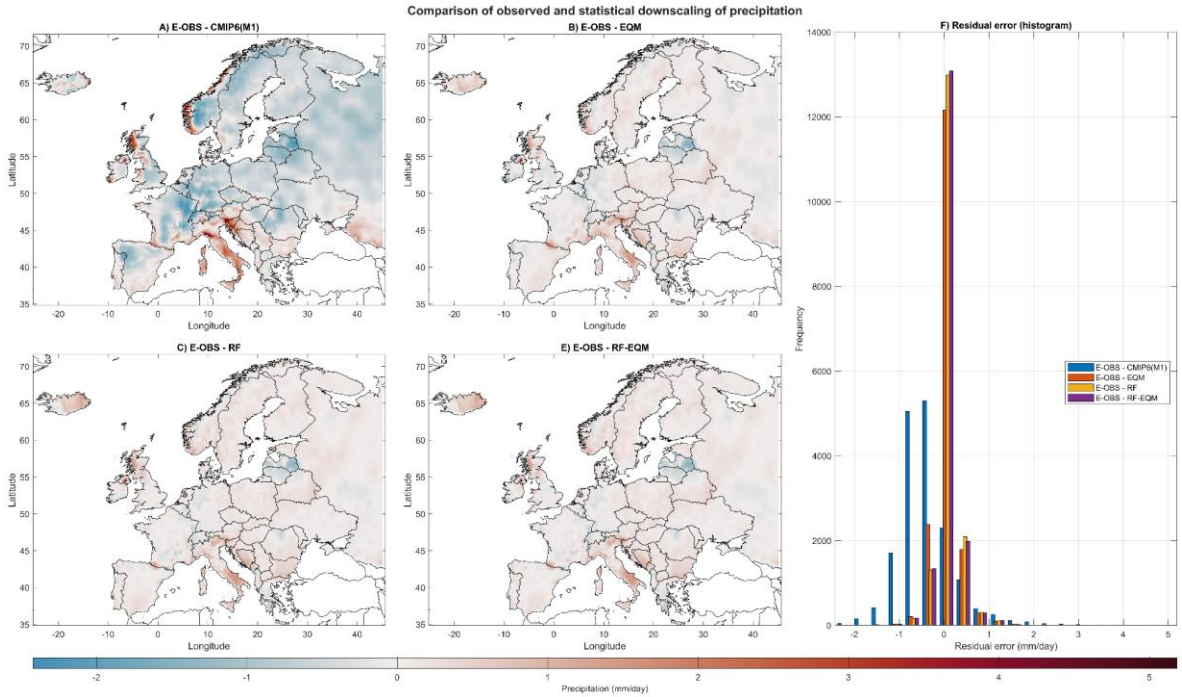

Figure 7.6: Comparison of observed and statistical downscaled precipitation, considering the annual scale. Difference between observed precipitation data (E-OBS) and A) historical data of CMIP6

model (AWI -CM-1-1-MR (M1)), B) BC technique (EQM), C) RF, and D) RF-EQM (prediction period: 2009 – 2014). Additionally, E) provides residual error histogram of statistically downscaled precipitation in comparison to E-OBS.

The uncorrected CMIP6 data (Figure 7.6 (A)) shows a wide spread negative biases compared to observed data (E-OBS), particularly enhanced overestimation in central and eastern European regions and underestimation in Scandinavia and southern Europe. These indicates a challenge in M1 – GCM model for representation of European precipitation, where the biases are large-scale in the central and eastern part of Europe. The EQM BC method improves the biases reducing the magnitude of errors ±1 mm/day for most of the European regions (Figure 7.6 (B)). The performance of EQM is effective in downscaling precipitation dataset due to its non-parametric approach and this findings support to previous studies (Chen et al., 2022; Tavares et al., 2025). The RF (Figure 7.6 (C)) and RF-EQM (Figure 7.6 (D)) both shows a similar spatial variability performance with areas substantial improvement like EQM BC data. However, the histogram of residual errors (Figure 7.6 (E)) for RF-EQM demonstrates superior performance among all marginally better by RF. The errors approaching to zero are more in comparison across most of the Europe, suggesting combining multiple statistical methods that is machine learning algorithm and BC method (RF-EQM) may provide a better alternative for prediction of regional precipitation downscaling.

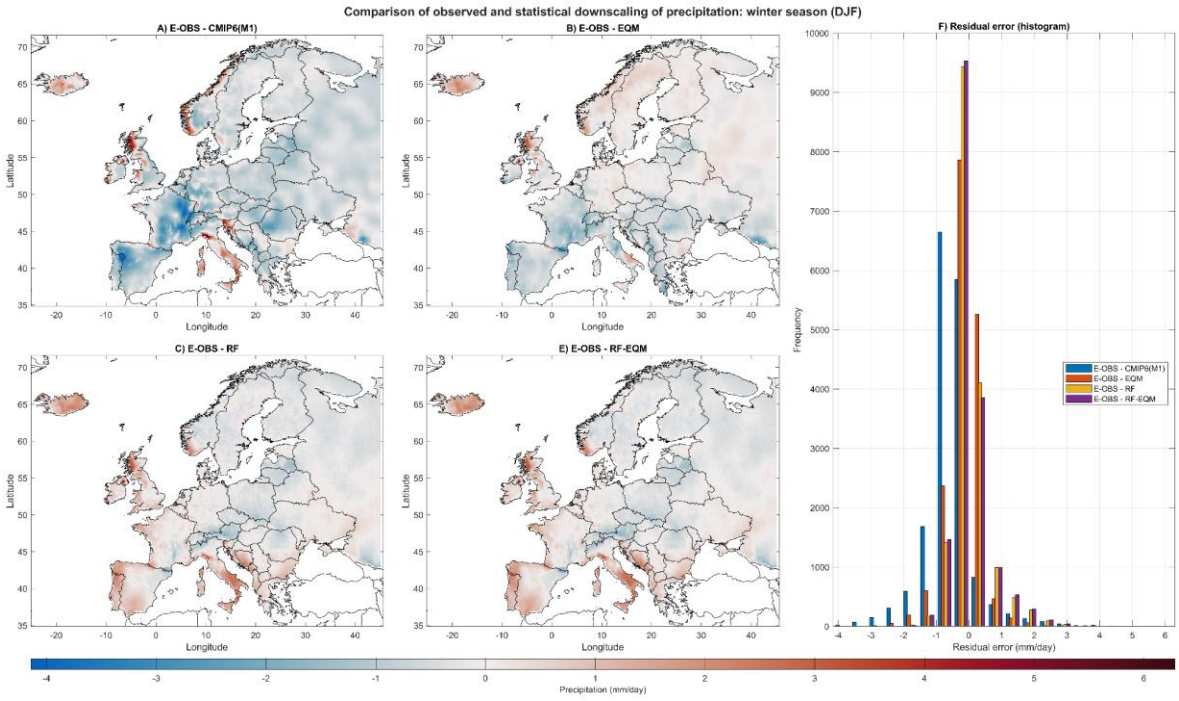

Figure 7.7: Comparison of observed and statistical downscaled precipitation in the winter season (DJF). Difference between observed precipitation data (E-OBS) and A) historical data of CMIP6 model

(AWI -CM-1-1-MR (M1)), B) BC technique (EQM), C) RF, and D) RF-EQM during the winter season (prediction period: 2009 – 2014). Additionally, E) provides residual error histogram of statistically downscaled precipitation in comparison to E-OBS.

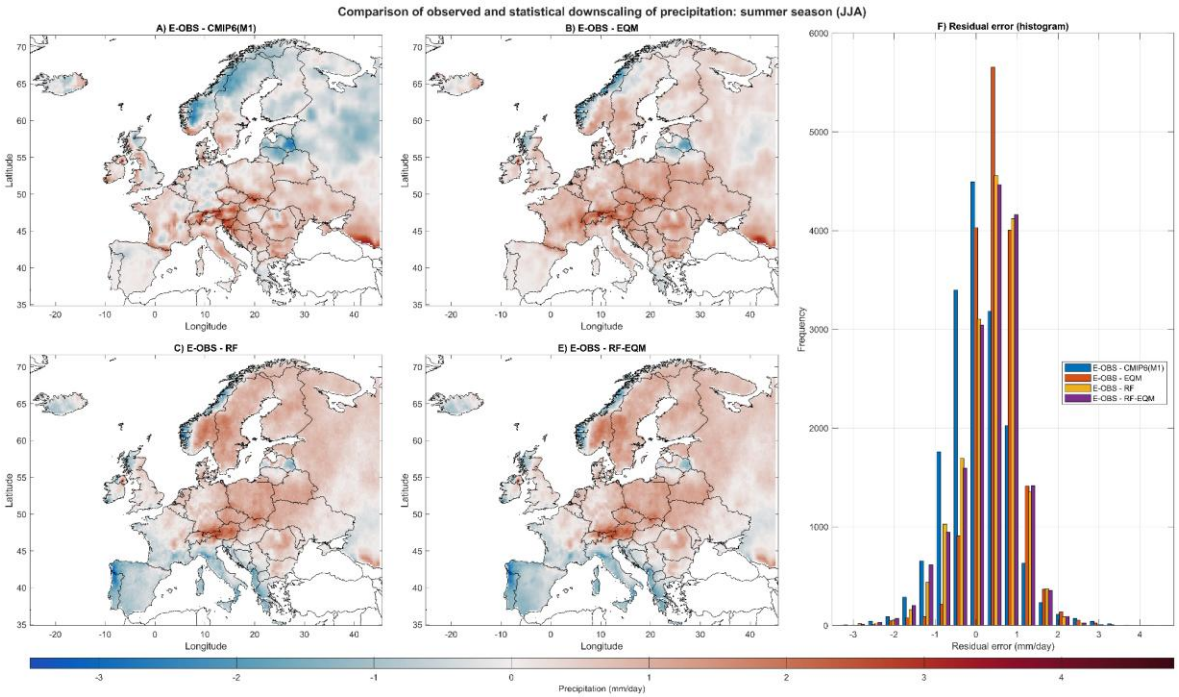

Figure 7.8: Comparison of observed and statistical downscaled precipitation in the summer season (JJA). Difference between observed precipitation data (E-OBS) and A) historical data of CMIP6 model (AWI -CM-1-1-MR (M1)), B) BC technique (EQM), C) RF, and D) RF-EQM during the summer season (prediction period: 2009 – 2014). Additionally, E) provides residual error histogram of statistically downscaled precipitation in comparison to E-OBS.

The winter season (Figure 7.7) precipitation downscaling is similar to annual precipitation outcomes in performance for the downscaling. That is overestimation with CMIP6 data in central and eastern Europe, underestimation in Scandinavia and southern Europe and the BC method EQM reduces the biases to ±1 mm/day for most of the European regions. Similar performance observed in RF and RF-EQM. RF-EQM superior performance with residuals approaching to zero. These overall indicates that the winter season abrupt changes in mean precipitation will have a huge influence on the annual precipitation outcome. Studies did show that inter-annual variability of seasonal precipitation across Europe is largely driven by fluctuations in large-scale circulation patterns especially North Atlantic Oscillation (NAO) (Hurrell, 1995). Specific to Scandinavian, central, and eastern Europe patterns many studies have related it to the extreme precipitation and other atmospheric circulation oscillations (Haylock and Goodess, 2004; Marshall et al., 2020).

7.4.3 Comparison of observed and statistical downscaling of precipitation: predicted and future scenarios

For the summer season (Figure 7.8), the CMIP6 models faces challenges to represent the warm season precipitation spatially. Underestimation in central and southern Europe and overestimation in northern Europe. These patterns are known limitations in CMIP6 models – that is maximum precipitation increase in summer at northern Europe and warming in southern Europe regions due to precipitation decrease (Coppola et al., 2021). The EQM shows better effectiveness during summer than winter and annual time scales, as more number of residual errors close to zero persist in several regions across Europe. However, for uncorrected CMIP6 data shows more zero residual errors specifically to summer in comparison to downscaling approaches. RF in this season rather has a marginal improvement in comparison with RF-EQM. The winter residual histogram shows the broadest distribution in comparison to summer season, indicating biases remain uncorrected for that specific season more. Previous research has already indicated that the BC methods struggle with non-stationarity of climate variables in Europe, particularly during seasons (Christensen et al., 2008) and may introduce another level of uncertainty (Nahar et al., 2017). The reduction in performance during summer, emphasize the need for season-specific evaluation and different methodological approach. However, the approach of RF-EQM combination suggest combining statistical technique with ML algorithm as a future direction for regional climate downscaling. Further, downscaled model approaches analyzed for future climate projections (SSPs) using quantiles comparison from a period of 2014-2100 for a M1 CMIP6 model over Europe depicted in Figure 7.9.

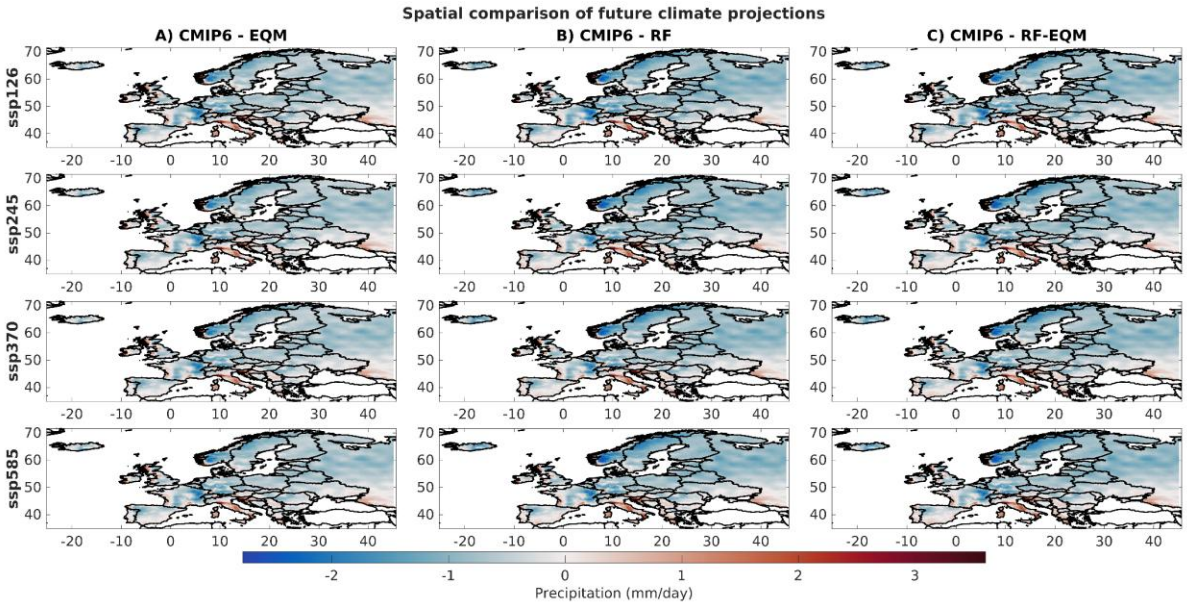

Figure 7.9: Spatial comparison for future climate projections: CMIP6 vs EQM vs RF vs RF-EQM. Differences in precipitation (mm/day) between A) CMIP6 and EQM, B) CMIP6 and RF, and C) CMIP6 and RF-EQM, across SSP scenarios (ssp126, ssp245, ssp370, ssp585).

On average, all the three BC approaches (EQM, RF, and RF-EQM) reduce the biases in future scenarios (ssp126, ssp245, ssp370, and ssp585) similarly, as shown in Figure 7.9A, B, and C. However, regional insights shows that bias remains relatively high for CMIP6 model (M1) in the northernmost part of Scandinavia and southern Europe after application of BC methods. Indeed, both the RF and RF-EQM approaches substantially reduce the biases in regions of northern Europe compared to EQM for future climate projections. The quantile comparison for various future scenarios shows that differences appear after the 0.95 quantile (95th percentile), as the outcomes are approximately similar across different downscaling approaches below this threshold in comparison to the CMIP6 data. ssp126 (Supplementary Figure S2), raw M1-CMIP6 data shows maximum quantiles to 160 mm/day. EQM further increases the range, indicating further increase in overestimation of the current ssp126 outcome. RF and RF-EQM downscale and narrow the high quantile range close to ~120mm/day, indicating a correction in extreme biases. For SSP245 scenario, similar trends for RF and RF-EQM are observed, however, EQM also corrects the biases from ~165 mm/day to 160 mm/day. RF reduces to ~145 mm/day and RF-EQM to ~120 mm/day. Under scenario ssp370 the precipitation data exhibit, even larger extremes for EQM model (~180 mm/day); with the ssp370 and ssp585, the performance of the downscaling approaches is similar to ssp126. Future research should explore other adaptive BC methods or multi-model ensembles, to further refine the future climate projections building similar methodology framework.

7.5 Key findings on continental-scale precipitation downscaling and prediction

The study evaluates the performance of BC methods and RF modeling – with or without BC, for downscaling CMIP6 (high-resolution models with nominal resolution ~100 km) precipitation data across European continent, to address the requirement of accurate precipitation estimates. Four BC methods were applied – scaling, EQM, GQM, and GPQM, with EQM consistently outperforming in comparison with others. This performance was on basis of the mean, variability, and quantiles during calibration (1950-2008) and testing (2009-2014) of models during historical scenario. EQM's non-parametric approach is robust in bias correction of CMIP6 precipitation data when compared to E-OBS data, particularly capturing spatial and temporal variability.

The RF and RF-EQM both reduces biases between CMIP6 and observed E-OBS, indicating ability to capture non-linear relationships through an ensemble of decision trees. RF-EQM had a marginal improvement over RF, more number of residual errors close to zero. However, both the approaches RF and RF-EQM had similar results for the median and IQR range, as RF's algorithm stabilizes predictions across precipitation ranges whether using raw or bias corrected CMIP6 data. RF-EQM outperformed in the residual errors because of the EQM based CMIP6 data aligns its quantiles with E-OBS, correcting biases in most of the values. The pre-process ensures RF-EQM starts the input data closer to error

defined by EQM in comparison to the observed data, resulting in precipitation of a specific range (similar to IQR) prediction more accurate. RF and RF-EQM performance was evident in central and eastern Europe, where uncorrected CMIP6 models had significant overestimation.

Seasonal analysis shows that the EQM and RF / RF-EQM performed better in summer than winter, decrease in residual error distribution. However, challenges remain with non-stationarity and seasonal variability. RF-EQM approach excelled for low-intensity rainfall (0-5 mm/day), while RF was more effective in rainfall with range of 5-20 mm/day. Both RF and RF-EQM reduces overestimation in high-quantiles of future scenarios (ssp126, ssp245, ssp370, ssp585), indicating a reliable projections of precipitation estimates.

In conclusion, these major key aspects of this study are:

- Empirical Quantile Mapping (EQM) outperforms other bias correct (BC) methods for CMIP6 precipitation data.
- Random Forest (RF) model improves the accuracy to downscale precipitation estimates, with further refinement achieved when EQM-based bias-corrected predictors are incorporated.
- RF-EQM combined approach improves the representation of rainfall intensities especially to low precipitation data (0-5 mm/day).
- The framework provides robust scenario analysis for future climate projections by integration of BC and ML downscaling technique.

Improvements are critical for capturing the rainfall distributions by reducing the biases associated to CMIP6 models, which will support towards informed decision-making for many stakeholders, specifically in climate risk assessments. As GCMs continue to advance, integrated approaches combining statistical BC and ML algorithm will become important to bridge the gap for accurate monitoring and acquiring actionable information at regional scales. These approaches is an important aspect for enhancing climate resilience and support effective adaptation planning.

Chapter 8

Conclusions

4.1 Summary

Chapter 3 discusses about high-resolution assessment of spatiotemporal trends of 74 climate indices across Europe from 1950 to 2021, based on peer reviewed studies (Doshi et al., 2023b). Utilizing daily observed data aggregated at a climate indices with monthly timescale and a spatial resolution of 0.1° (~11 km), the study offers an unprecedented level of detail in mapping climate indices based variability and trends across the European continent. The climate indices uses a diverse range of climate variables – global radiation, precipitation, relative humidity, sea level pressure, temperature, and wind speed – enabling a comprehensive view of Europe's climate system and its multifaceted complex variability over the past seven decades. The study uses non-parametric statistical technique – Mann-Kendall test to identify the nature of trends and Sen's slope approach to determine their magnitude ensuring that the results are statistically significant. The key findings highlight significant regional and seasonal differences in the spatial trends of various climate indices. Climate indices such as growing degree days and heating degree days exhibits the largest increase and decrease, indicating shifts in temperature based indices with implications for various sectors like agriculture and energy demands. The universal thermal climate index, relative humidity, wind chill index, global radiation, and potential evapotranspiration are of significant importance due to strong correlation and magnitude of change. Country-specific analysis pointed towards regions experiencing greatest warming, cooling, or change in wind such as Bosnia and Herzegovina for warmer days, Belarus for colder days, and southeastern/southern Europe for high wind. The study detailed trend analysis makes it possible to understand the impact of climate indices in small European countries as well, highlighting which indices are most relevant to monitor in specific regions.

Chapter 4 advances the understanding of compound climate events across Europe by analyzing the spatial and temporal dynamics of climate indices over a seven-decade period (1950-2021) (peer reviewed findings (Doshi et al., 2023a)). Using 74 climate indices derived from E-OBS dataset, the research identifies the hotspot regions where concurrent or consecutive (bivariate and trivariate pairs) climate indices exhibit high joint probabilities through advanced statistical methods like copula modeling. Evaluating correlation and significance across combinations of climate indices, reveals high-risk zones for the joint probabilities particularly for northern and eastern Europe. Compound events

involving global radiation, temperature, evapotranspiration, and bioclimatic indices like universal thermal climate index, wind chill index, heat index are most prevalent in these regions. The analysis reveals monthly shifts in hotspot location, persistence of climate indices clusters in specific regions (such as agriculture and coastal areas), and increasing trends in joint probabilities, highlighting increase risks exposure for population and different land cover types. These findings is important as the framework could justify the stakeholders to prioritize the mitigation efforts, resource allocation, and adaptive strategies in vulnerable regions demarcated.

Chapter 5 employs a probabilistic framework to assess 74 climate indices derived from high-resolution E-OBS dataset (1950-2021), identifying high-risk zones, co-occurrences, and persistence of climate indices across Europe at a monthly temporal scale (peer reviewed studies (Doshi et al., 2025)). A robust 26 different marginal probability distributions determine best fit for each climate indices at every grid cell, using Kolmogorov-Smirnov (K-S) test. Further, high-risk zones are identified (high probability > 90%) for various climate indices. Additionally, individual indices investigated with the co-occurrences and persistence of these high-probability risk zones. The analysis reveals diverse patterns regionally for these hazards across European continent. High-risk zones exhibit distinct spatial and seasonal patterns: southern and southeastern Europe shows temperature/precipitation based indices risks, while northern, northeastern, and western regions of Europe are prone to precipitation based indices. This study further integrates these identified high-risk zones with population density and land use maps to quantify the risk exposure. This enables a detailed assessment of which population density and land cover categories are most exposed to specific climate indices during a particular month. The insights gained are important for effective climate monitoring and for designing targeted strategies for risk reduction and adaptation across Europe.

Wet antenna attenuation (WAA) creates a source of error in rainfall intensity estimates derived from commercial microwave links (CMLs). Chapter 6 addresses these limitations by proposing and testing an optimization framework that calibrates WAA models using measurements from CML networks and rain gauges. Various WAA models, including Valtr-Fencl-Bareš (VFB) model were evaluated with particular detail to their parameters optimization and performance assessment across different frequency bands, link lengths, and rainfall intensity classes. Calibration was performed using 87 CMLs and 9 rain gauges within the Seveso river basin, in northern Italy. Results showcases that optimized WAA model, that is VFBm (parameter optimization of VFB model) reduce the bias and error in rainfall estimates compared to not taking into account WAA or generically parameterized model (like VFB). The optimized model performs consistently better in various link lengths, higher frequencies (37.2 -

42.6 GHz), and rainfall events. This methodology is important for climate studies in regions where rainfall data is sparse or not available.

Chapter 7 explores the prediction of random forest (RF) model using CMIP6 data with or without bias correction (BC). The motivation of this study was to enhance the utility of CMIP6 precipitation data for climate risk assessments in Europe. CMIP6 operates at a coarse resolution and exhibits biases, limiting their ability to capture regional small-scale processes important for precipitation. Initial test of determining the best BC method from four different methods showcased that Empirical Quantile Mapping (EQM) consistently performs better in alignment with the observed data across quantiles. Subsequently, RF models developed with raw CMIP6 data and EQM-corrected CMIP6 data (RF-EQM) as input both significantly reduces biases and absolute error in comparison to observed data. However, RF-RQM showed marginally better performance in reducing residual error across most of the European regions, due to the better alignment provided by EQM based CMIP6 input data. This integrated approach enhances downscaling accuracy by reducing overestimation biases in central and eastern Europe, further improvising reliability of future scenarios. Prediction accuracy can be improve with this strategy of combining statistical bias correction with machine learning (BC-ML) approach for regional precipitation in Europe.

4.2 Addressing research questions

The research question related to the spatiotemporal patterns of various climate indices in terms of direction, magnitude, and statistical significance is addressed through detailed analysis of 74 climate indices at monthly timescale from 1950 to 2021 (Doshi et al., 2023b). The study shows that the spatiotemporal variability in these climate indices vary greatly across different regions and seasons, highlighting complex interactions with the climate processes throughout Europe. Trend analysis identifies statistically significant positive and negative trends across several climate indices, with both the direction and magnitude of these changes varying by region and indices type. For instance, growing degree days (mean air temperature above 4°C) showed the highest positive trend up to 0.96°C in August, while heating degree days (mean air temperature below 17°C) recorded the largest native trend down to -1.03°C in July. Strong spatial clusters observed in indices related to universal thermal climate index, relative humidity, wind chill index, global radiation, and potential evapotranspiration. The magnitude of these trends using the estimator highlights that the regions in southeastern and eastern Europe were impacted mostly by intense warming and humidity declines respectively. The study also enables to identify the localized climate indices hotspots, providing a detailed view of vulnerability and risk at the continental and regional monthly scales. The statistical significance indicates that the trend detection and mapping across the continent, confirms that there is a shift in the European climate

system. Compound climate risks can be monitored for example rising temperature related indices occurring alongside declining precipitation indices, which might poses serious challenges for various stakeholders.

Further, the research addresses the question related to the spatial and temporal dynamics of the compound climate events across Europe from 1950-2021, focusing on hotspot movements, high-risk zones, and their impacts on the land cover and population using high-resolution climate indices (Doshi et al., 2023a). Firstly, high-correlation bivariate and trivariate pairs of climate indices (example temperature based indices paired with global radiation or bioclimatic indices) are having correlations >|0.60| and significance of <0.05. Copula models then quantify joint probabilities mapping hotspots where compound events are most likely for such different nature of climate indices pairs. Spatial analysis reveals high-risk zones (hotspots), primarily located in northern and eastern European countries. Southern Europe faces risks and requires monitoring for the temperature and radiation based indices. For instance Russia and Sweden experiences global radiation and growing degree days hotspots, however Greece showcases increasing trend for this climate indices pair, suggestion a monitoring in future could be this region. Clusters of the bioclimatic indices universal thermal climate index and global radiation pair show future shifts to countries like France, United Kingdom, Netherlands, Germany, and Spain. For some hotspots the clusters where there is no monthly shift leads to potentially higher impacts when events are compounded. Further, the study shows that over the last seven decades, agriculture and coastal areas are highly exposed to the risks of defined hotspots of compound events. Identified compound event (pairs of climate indices) can help reduce risk by informing the redesign of framework plans tailored to the specific sectors affected.

The research question addressing about the probabilistic assessment of climate indices identifies high-risk zones, co-occurrences, and persistence of climate events across Europe, and their implications for land use and population density exposure (Doshi et al., 2025). 56 out of 74 such climate indices showed high-probabilities in specific regions, with 17 consistently highlighting high-risk zones for particular months. The analysis reveals regional variations, southern and southeastern Europe are most vulnerable to temperature based indices (consecutive summer days, summer days), and precipitation indices (longest dry period) for most of the months. In contrast, northern, northeastern, and western Europe require more monitoring for the precipitation based indices such as dry days, wet days 1 mm and 3mm. Co-occurrences or compound events, identified by mapping simultaneous occurrence of high-probability multiple climate indices of different nature reveals that Russia, Norway, Iceland, and Sweden experiences highest number of co-occurrences mainly driven by temperature and precipitation based climate indices. Persistence is identifying the co-occurrences of climate indices with high-

probability (> 90%) that occurs consecutively for months at same region. For example, Russia experiences persistence of consecutive dry days during months of August and September. Finally, the European population are exposed to high risk from temperature differences above and below 17°C, while land cover types (rangelands, crops, and built areas) are exposed to potential evapotranspiration and temperature based indices.

For precipitation estimates related to WAA and CMLs, a data-driven methodological framework is applied to minimize the impact of WAA on rainfall estimates derived from CMLs. The main framework involves applying empirical WAA models, to raw CML data with measured data from rain gauges. To reduce errors WAA models optimized by calibrating their parameters using rain gauge data. A key finding from applying this methodology is that WAA models such as VFB is frequency dependent, with higher values observed in frequency of 37-43 GHz than in 17-23 GHz. The optimization process specifically targeted reducing errors linked to moderate to heavy precipitation events, which are the main source for biases in higher frequency band when WAA was not corrected. For all 87 CMLs within the study area, VFBm model achieved median relative bias (RB) of -0.13 and a median normalized root mean square error (NRMSE) of 1.18. VFBm model reduces RB by ~90% and NRMSE by ~70% in comparison to when WAA was not accounted for. This improvement in accuracy was evident across all CML categories – distance to rain gauge, frequency, link length, and various rainfall intensity levels: achieving lowest RB and NRMSE.

Another approach for precipitation estimation enhancement involves downscaling of CMIP6 data using bias correction and machine learning techniques. Non-parametric EQM approach indicates superior performance in comparison to scaling, Generalized Quantile Mapping (GQM), Gamma-Generalized Pareto Quantile Mapping (GPQM) BC techniques. EQM is robust for both calibration and testing period, with IQR values closely matching observed data (~2.00-2.50 mm/day). Across the entire range of quantiles, the EQM BC approach shows reduced biases, with differences up to 1 mm/day lower than observed data. Independent of the BC technique RF and RF-EQM reduces biases compared to CMIP6 data. Raw CMIP6 data shows biases from -185% to 115% (reduced to ~110% in RF and RF-EQM) and absolute error up to ~10.5 mm/day (reduced to ~6.7 mm/day in RF and ~4.8 mm/day RF-EQM) in prediction (MR1-ESM2-0 worst performing CMIP6 model for precipitation data). RF-EQM outperforms RF model, especially low rainfall intensities exhibiting residual errors closer to zero for most of the regions across Europe. Overestimations by CMIP6 models in central and eastern Europe significantly reduced by EQM, RF, and RF-EQM. Further, seasonal analysis reveals that the method produces lower residual errors during summer in comparison to winter, indicating better performance in warm-season precipitation patterns.

4.3 Outlook

Based on the findings of the spatiotemporal trend analysis of climate indices for the European continent, future research should integrate high-resolution climate projections to assess the trends for these climate indices under various high emission scenarios. Additionally, there is also a need to link the climate indices with more such climate indices from different sectors. Further, assess the impacts of such climate indices and develop a better adaptation strategies tailored to local vulnerabilities, which will eventually mitigate the associated risk and translate into effective climate resilience actions across Europe. Building on the identification of compound event hotspots (pairs of climate indices) the analysis can extend to identify additional climate indices pairs. An identified gap is the need to further study the persistence of co-occurrences of compound events in the same location at a smaller time-scale. Enhanced temporal resolution (example sub-monthly scales) could improve the early-warning systems for short-term compound events. Statistical estimation especially multivariate analysis involves uncertainties. Future investigation needed to address the uncertainty associated with copula model outcomes. A warning system could be developed to predict the list of such compound event pairs in advance that poses high risks to specific countries across Europe. Validation of the identified climate indices pairs with real-world observations is essential to assess the impacts of high-risk compound events. A need for integrating socio-economic datasets (example crop yield) would relate risks beyond population density and land cover types. Considering the probabilistic modeling the future research show explore on land management practices (example afforestation or urbanization) interacts with probabilistic hazard variability – and check whether it increases or decreases the risk associated to the regional vulnerability. To overcome the data limitations such as sparse observational regions an integrated hybrid probabilistic modelling (Bayesian for example) with the marginal probability distribution fitting can quantify uncertainties in hotspot identification. Another part, which could be important, is to acknowledge the system dynamics of the probabilistic framework such as shifts in crop growth and its impact on risk over time. Future work should focus on developing operational system such as real time probabilistic forecasting that estimates joint probability using data assimilation from various sensor or satellite data. This can support the development of a probabilistic early warning system; enabling actuarial scientists to design climate indices based insurance products from the risk maps. Precipitation estimates using CML has a wide application however; future research could focus on extending the WAA model framework to diverse climate regions and longer CML networks to test its generalized applicability. Machine learning techniques and real-time data assimilation may further enhance the model adaptability and performance. In addition, seasonal evaluation in WAA effects could provide deeper insights into optimization strategies. CML derived rainfall estimates could be further

improved by integration with satellite or radar based precipitation data. Implementation of this framework with monitoring system is essential to assess its accuracy and timely rainfall estimates for effective disaster management. Precipitation prediction using CMIP6 data requires downscaling using combine BC-ML approach but focus should be integrating this with other additional predictors such as soil moisture, temperature, and atmospheric circulation patterns to enhance the accuracy. Incorporating different ML models, further offers an additional advantage to capture non-linear relationships and improving predictions for extreme precipitation events. Further, this data coupled with hydrological models, to test the model behavior with the downscaled data. The development of digital twin models incorporating regionally downscaled precipitation data offers an informative approach for monitoring and predicting hydrological extremes, especially for future climate projections where enhanced reliability is important for effective risk management.

Appendix A

Supplementary materials for Chapter 3 (including common figures from chapter 4 & 5)

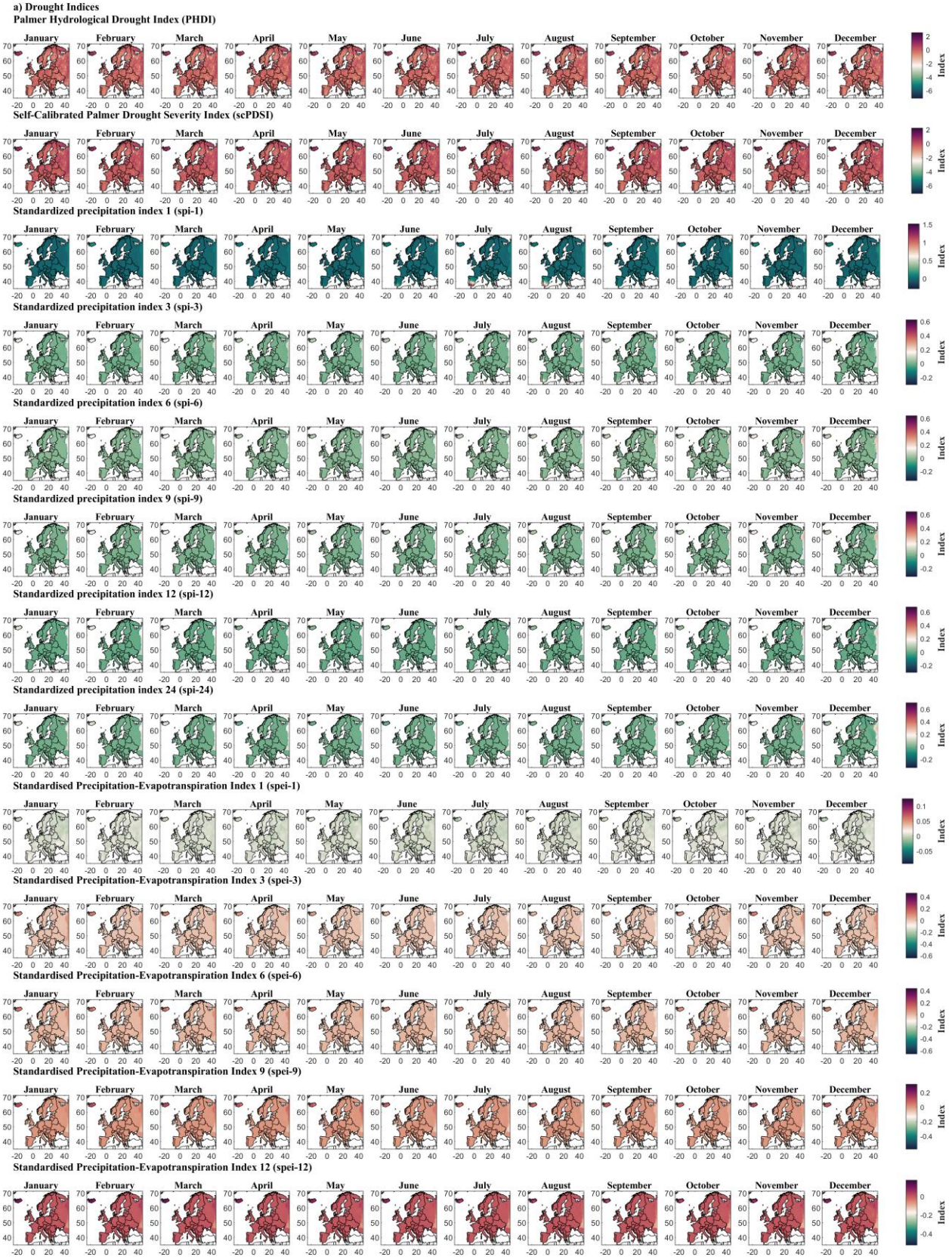
a) Drought Indices
Palmer Hydrological Drought Index (PHDI)
Self-Calibrated Palmer Drought Severity Index (scPDSI)
Standardized precipitation index 1 (spi-1)
Standardized precipitation index 3 (spi-3)
Standardized precipitation index 6 (spi-6)
Standardized precipitation index 9 (spi-9)
Standardized precipitation index 12 (spi-12)
Standardized precipitation index 24 (spi-24)
Standardised Precipitation-Evapotranspiration Index 1 (spei-1)
Standardised Precipitation-Evapotranspiration Index 3 (spei-3)
Standardised Precipitation-Evapotranspiration Index 6 (spei-6)
Standardised Precipitation-Evapotranspiration Index 9 (spei-9)
Standardised Precipitation-Evapotranspiration Index 12 (spei-12)
January
February
March
April
May
June
July
August
September
October
November
December
Index

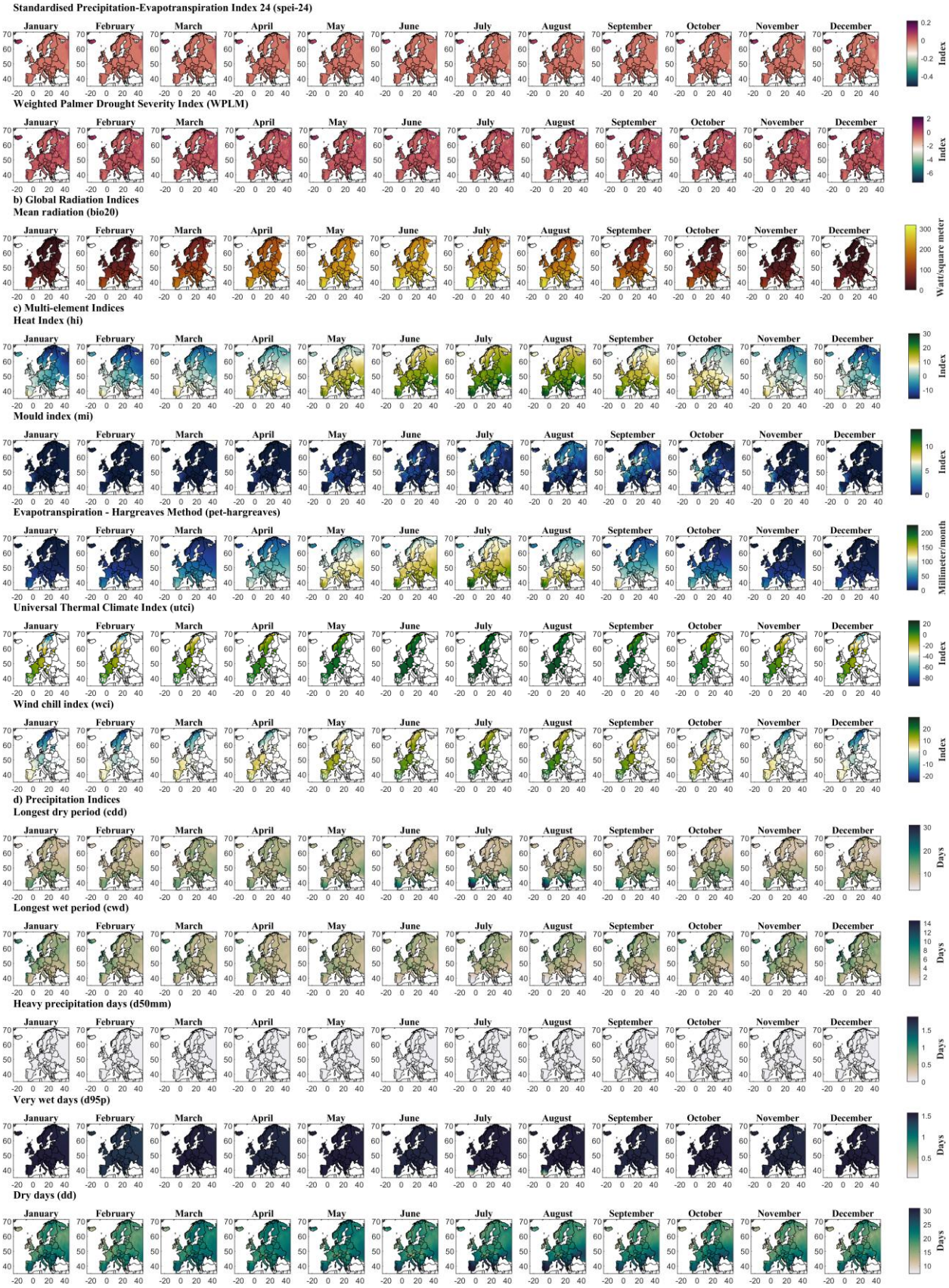
Standardised Precipitation-Evapotranspiration Index 24 (spei-24)
January February March April May June July August September October November December
Index
Weighted Palmer Drought Severity Index (WPLM)
Index
b) Global Radiation Indices
Mean radiation (bio20)
Watt/square meter
c) Multi-element Indices
Heat Index (hi)
Index
Mould index (mi)
Index
Evapotranspiration - Hargreaves Method (pet-hargreaves)
Millimeter/month
Universal Thermal Climate Index (utci)
Index
Wind chill index (wci)
Index
d) Precipitation Indices
Longest dry period (cdd)
Days
Longest wet period (cwd)
Days
Heavy precipitation days (d50mm)
Days
Very wet days (d95p)
Days
Dry days (dd)
Days


Wet days 1mm (dr1mm)
January February March April May June July August September October November December
Days
Wet days 3mm (dr3mm)
Total precipitation wet days (prcptot)
Millimeter
Days precipitation >= R10mm (r10mm)
Days precipitation >= R20mm (r20mm)
Percentage precipitation of very wet days (r95tot)
Percentage
Precipitation fraction extremely wet days (r99tot)
Total precipitation (rti)
Maximum precipitation (rx1day)
Maximum 5 days R (rx5d)
Simple precipitation intensity index (sdii)
Millimeter/day
e) Relative Humidity Indices
Mean Relative Humidity (rh)
f) Sea Level Pressure Indices
Mean Sea Level Pressure (slp)
Hecto pascals

g) Temperature Indices

Maximum consecutive frost days (cfd)

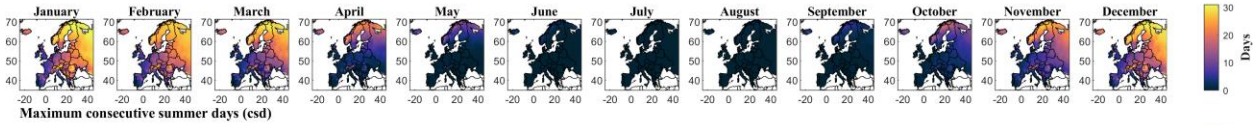

Maximum consecutive summer days (csd)

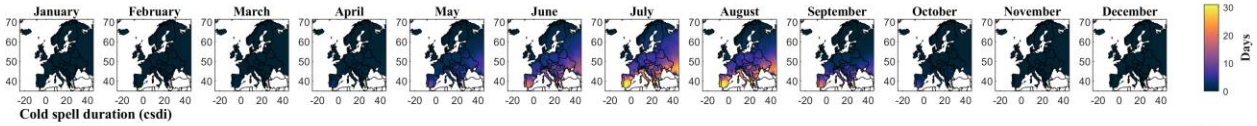

Cold spell duration (esdi)

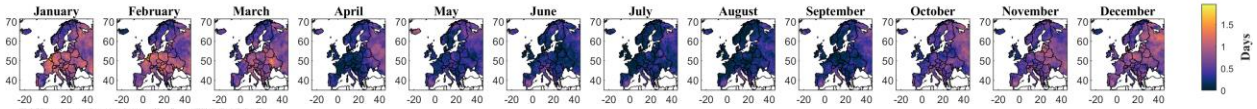

Difference days above/below Tx17 (dd17)

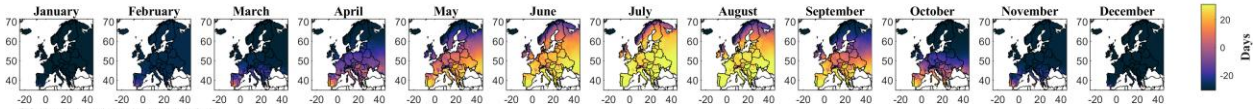

Diurnal temperature range (dtr)

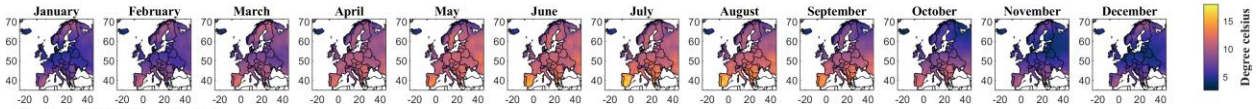

Extreme temperature range (etr)

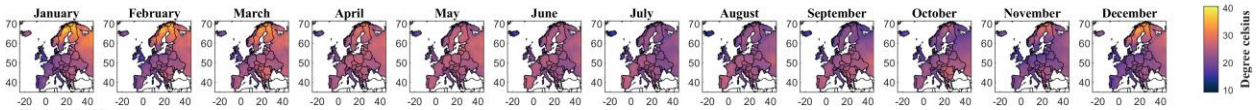

Frost days (fd)

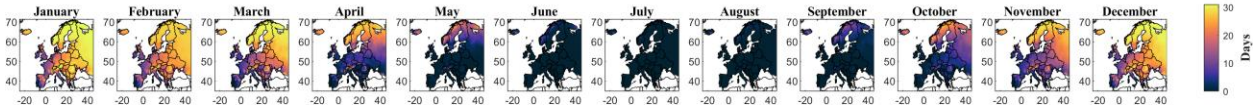

Growing degree days (gd4)

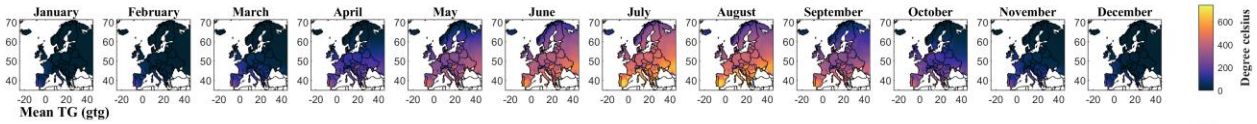

Mean TG (gtg)

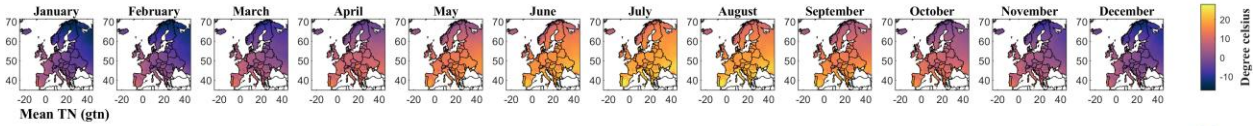

Mean TN (gtn)

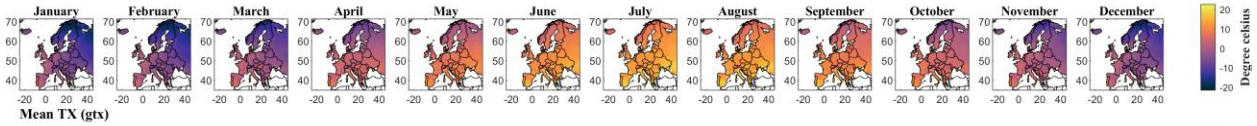

Mean TX (gtx)

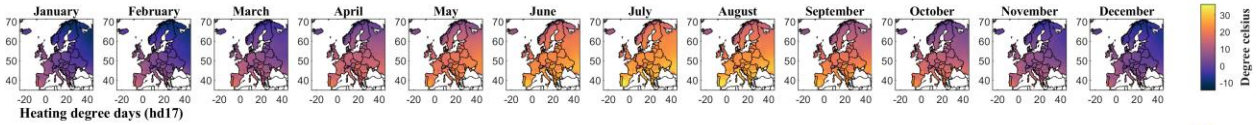

Heating degree days (hd17)

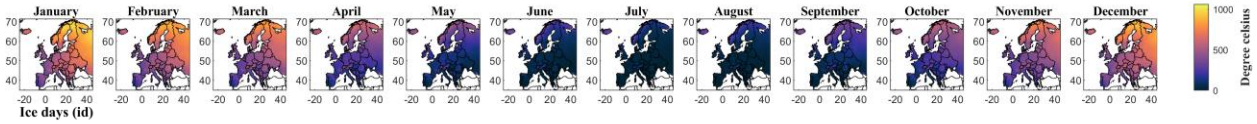

Ice days (id)

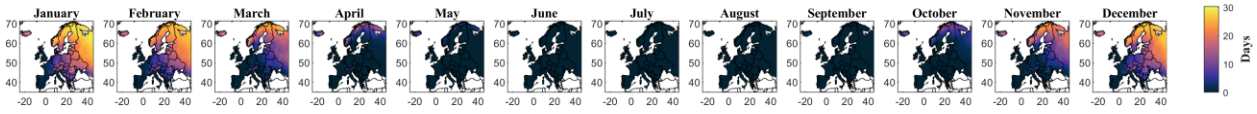

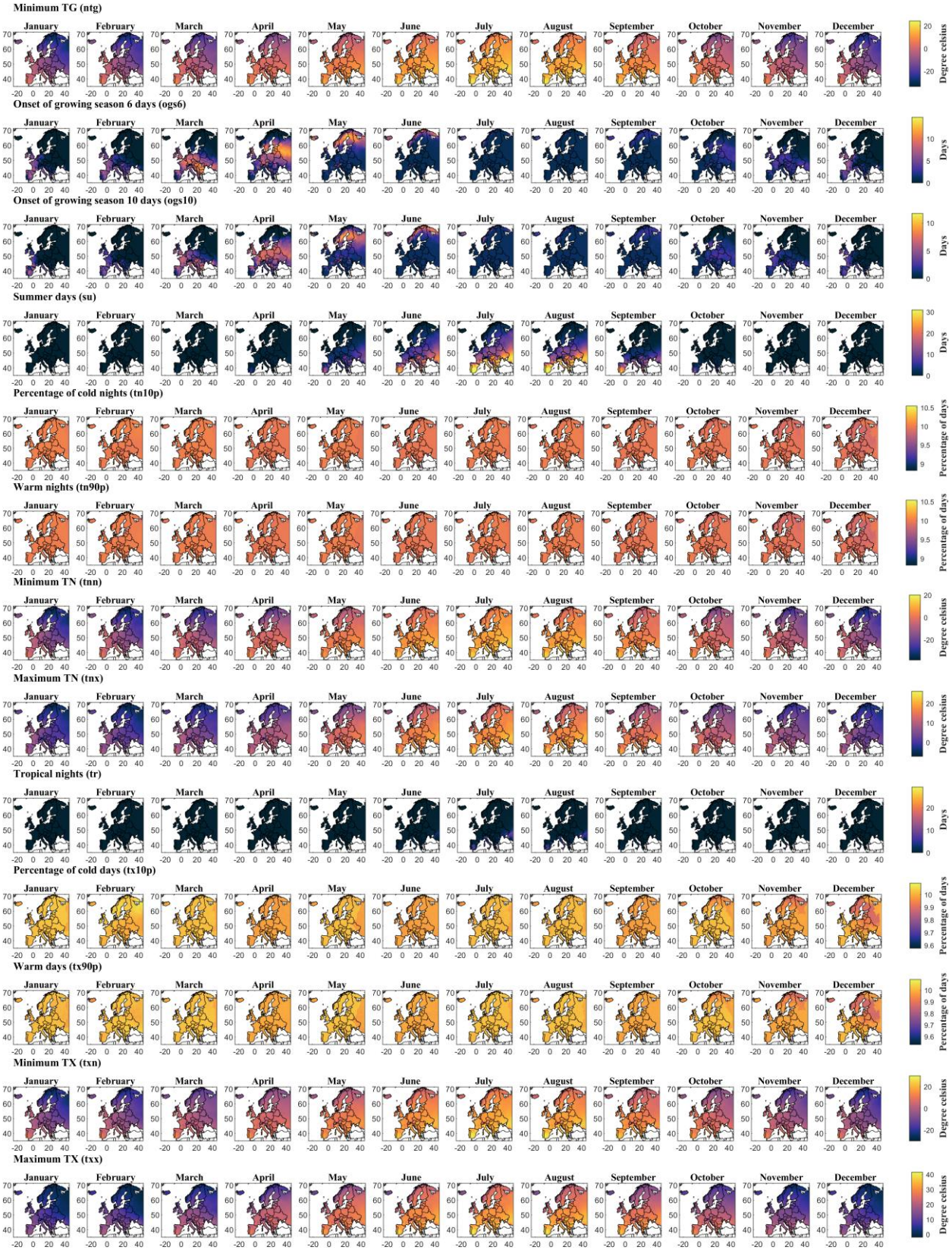
Minimum TG (ntg)
January February March April May June July August September October November December
Degree celsius
Onset of growing season 6 days (ogs6)
Days
Onset of growing season 10 days (ogs10)
Days
Summer days (su)
Days
Percentage of cold nights (tn10p)
Percentage of days
Warm nights (tn90p)
Percentage of days
Minimum TN (tnn)
Degree celsius
Maximum TN (tnx)
Degree celsius
Tropical nights (tr)
Days
Percentage of cold days (tx10p)
Percentage of days
Warm days (tx90p)
Percentage of days
Minimum TX (txn)
Degree celsius
Maximum TX (txx)
Degree celsius

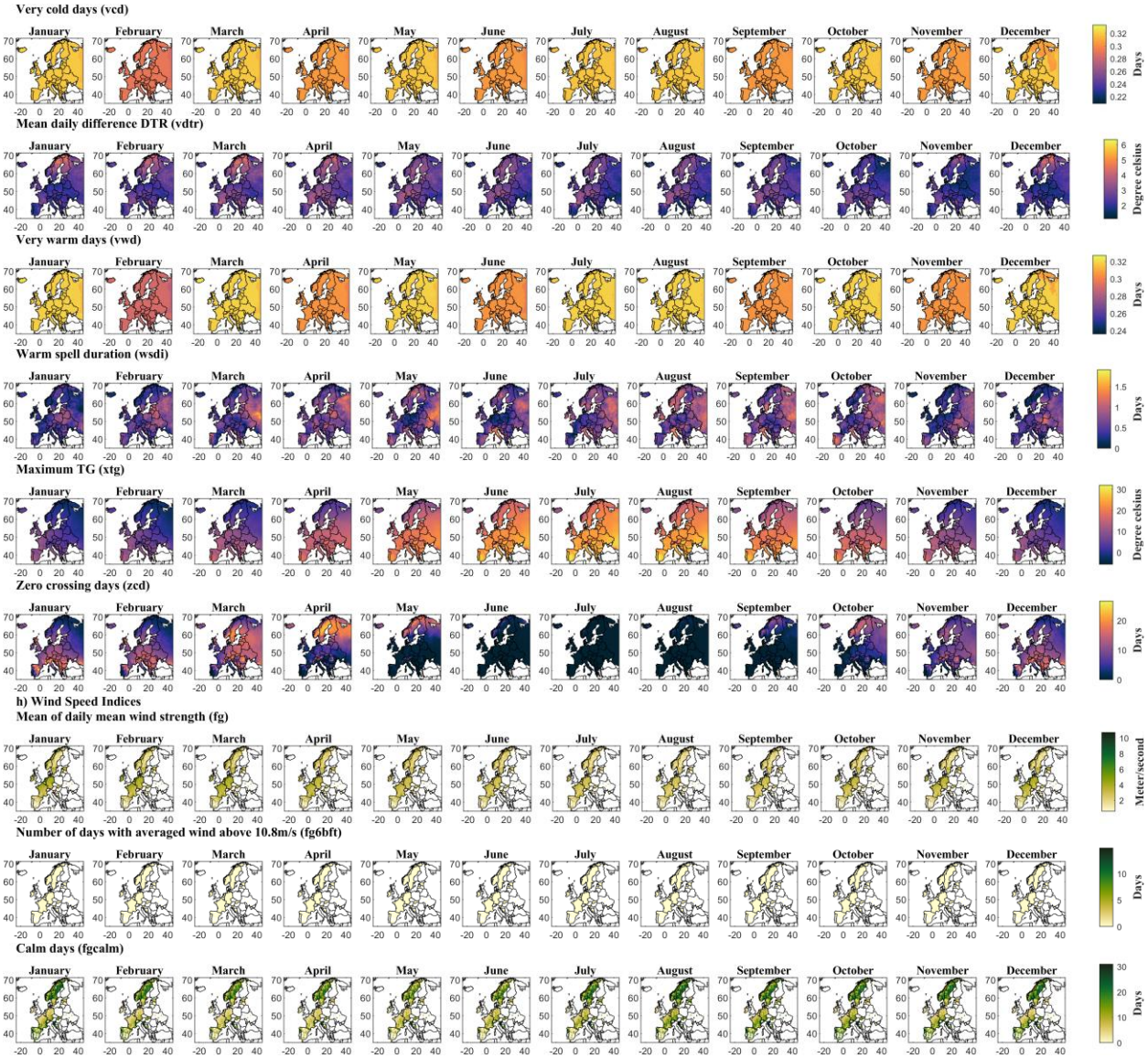

Figure S1: Monthly Spatial Distribution of Extreme Climate Indices – 1950-2021 (Chapter 4 – Figure S5).

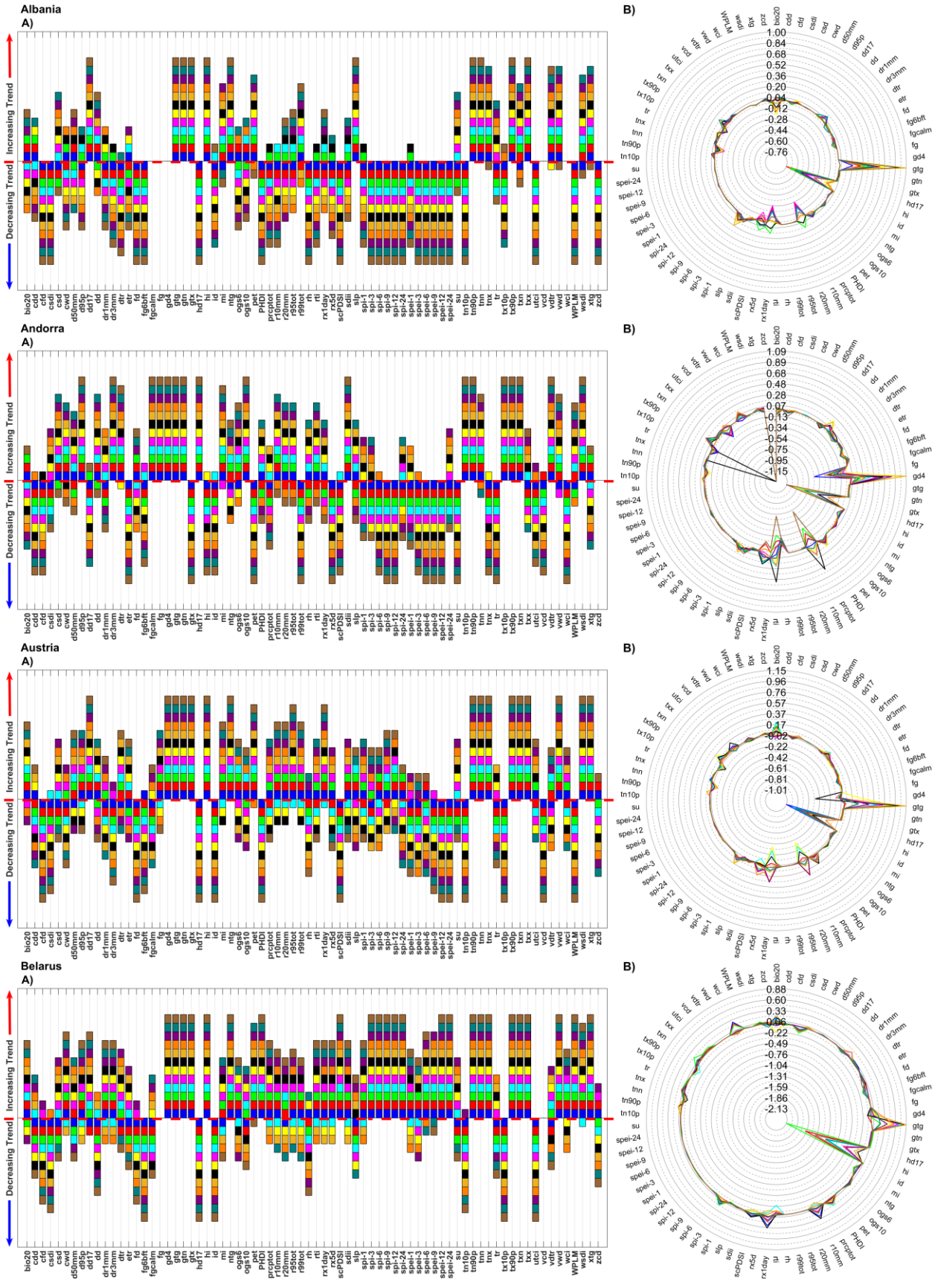
Albania
A)
B)
Andorra
A)
B)
Austria
A)
B)
Belarus
A)
B)
Increasing Trend
Decreasing Trend

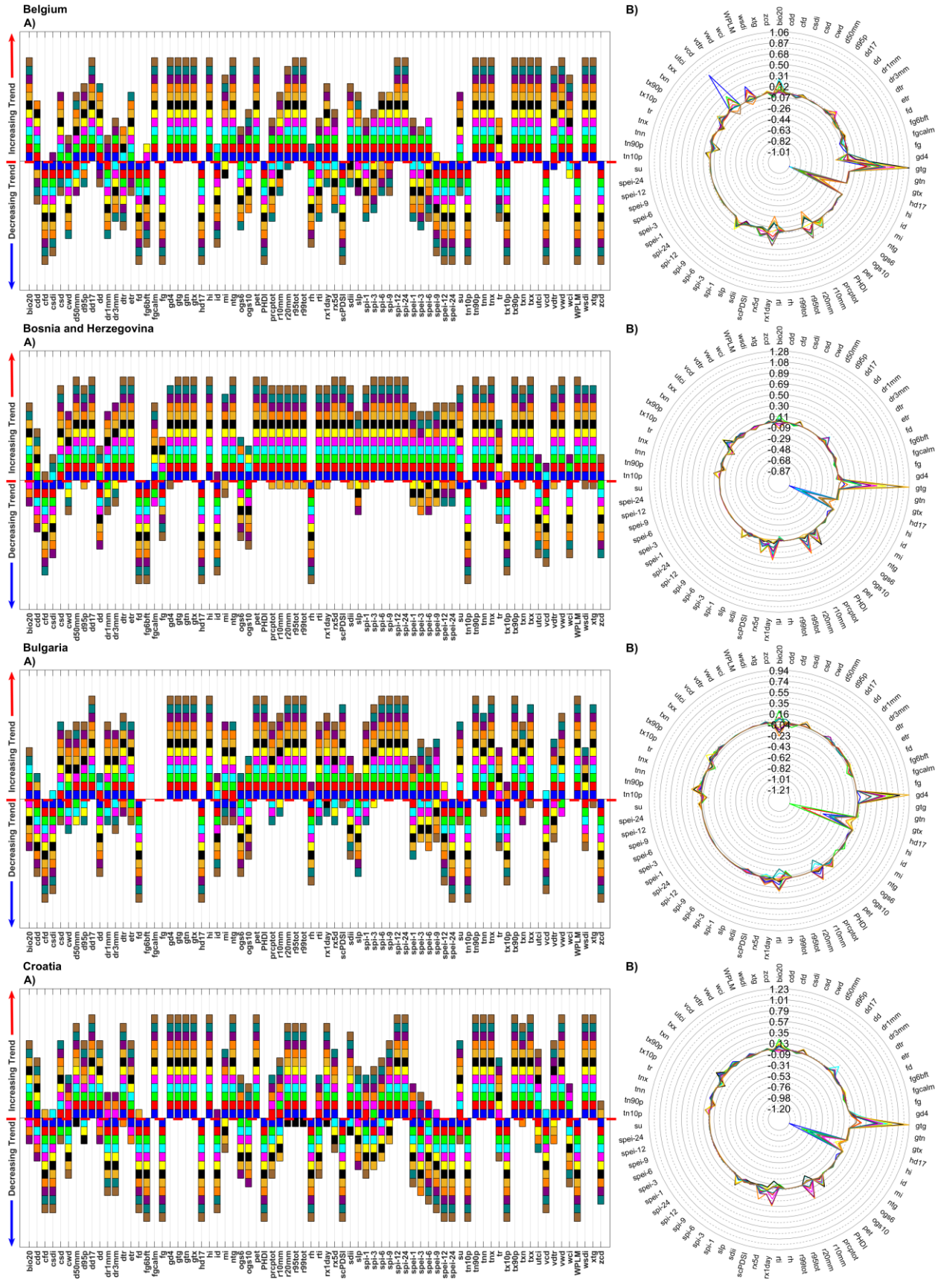
Belgium
A)
B)
Bosnia and Herzegovina
A)
B)
Bulgaria
A)
B)
Croatia
A)
B)
Increasing Trend
Decreasing Trend

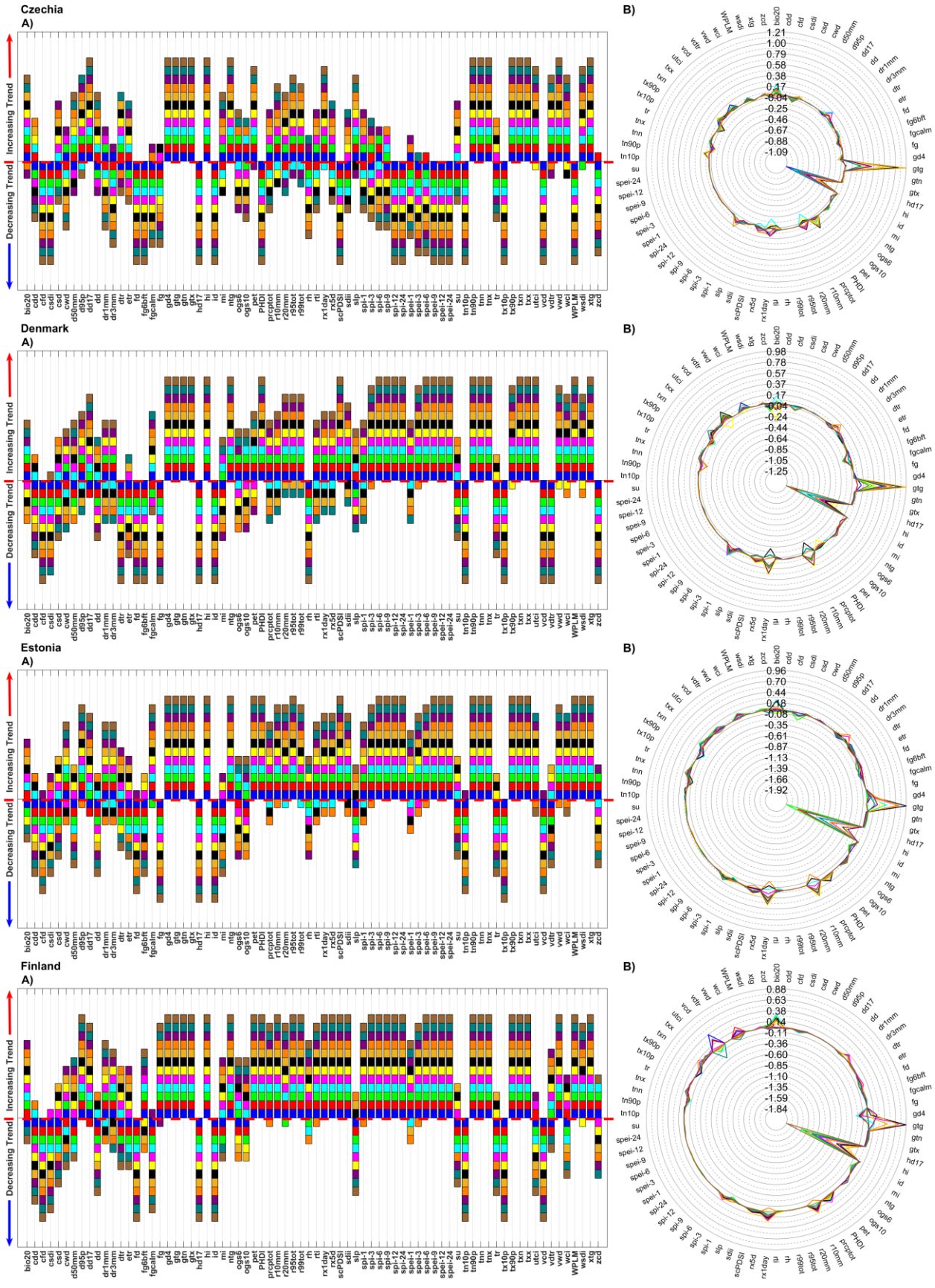
Czechia
A)
B)
Denmark
A)
B)
Estonia
A)
B)
Finland
A)
B)
Increasing Trend
Decreasing Trend

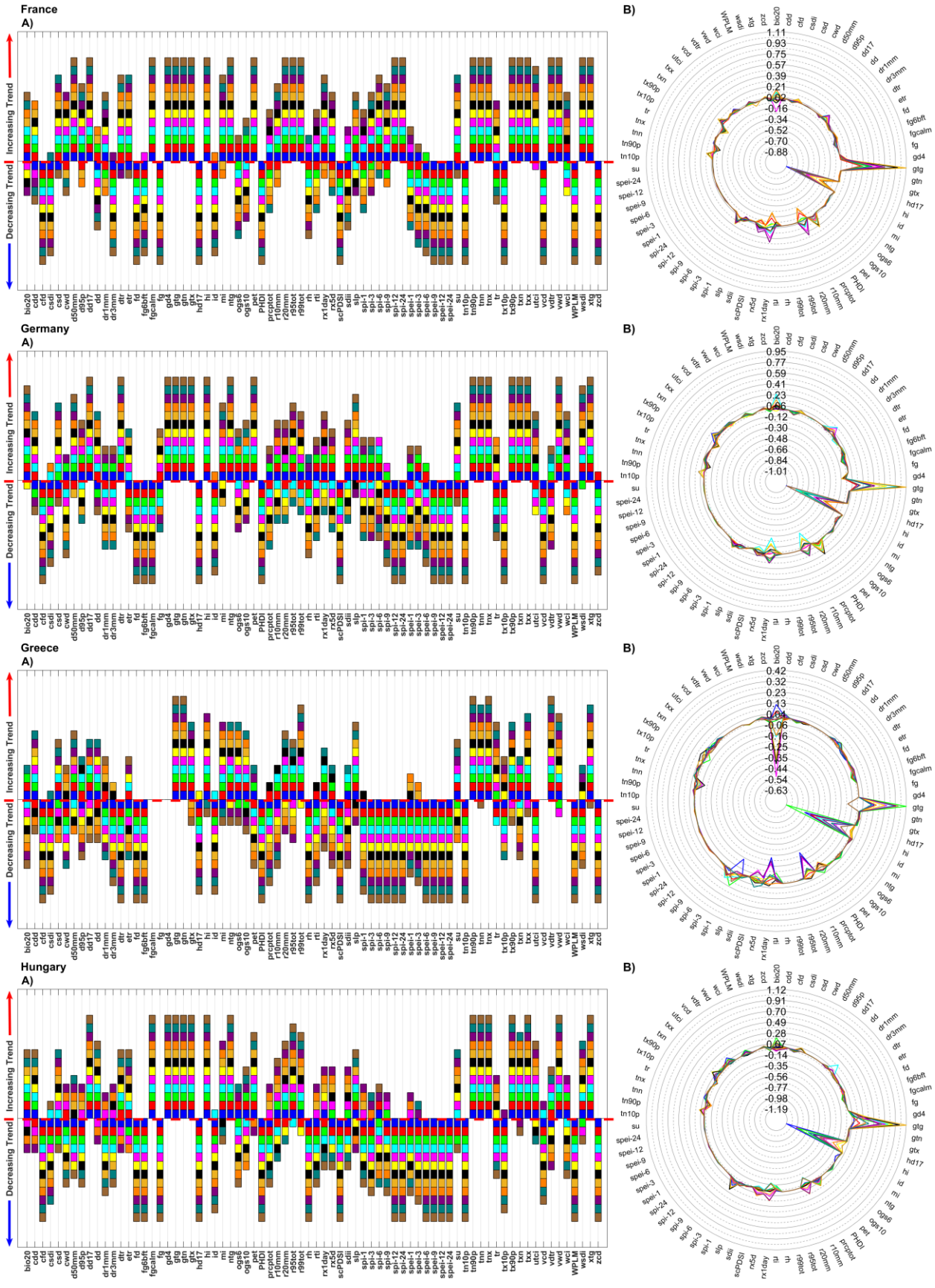
France
A)
B)
Germany
A)
B)
Greece
A)
B)
Hungary
A)
B)
Increasing Trend
Decreasing Trend

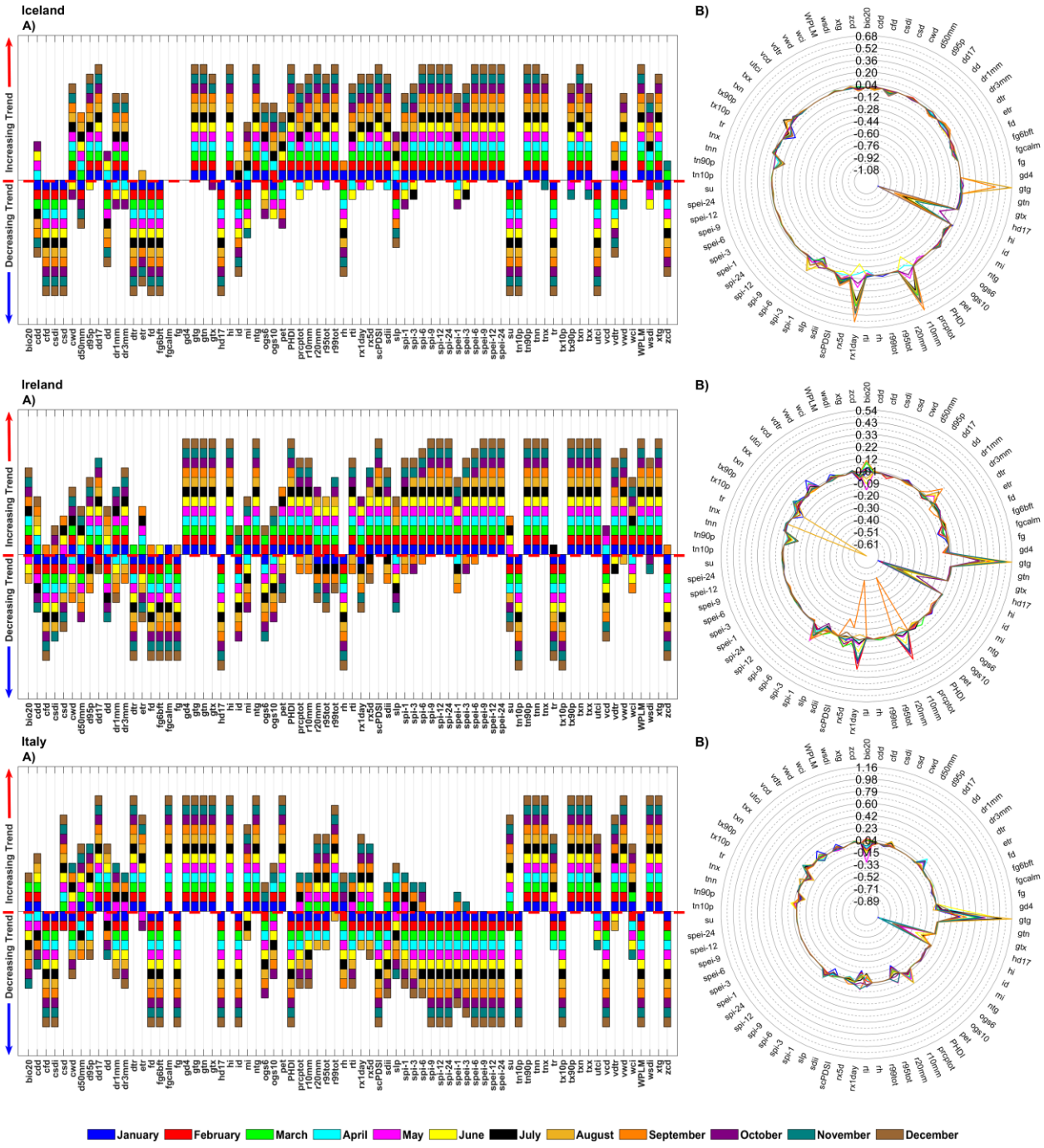

Figure S2: Monthly trend analysis across European countries (A-I) (A) nature of trend using Mann-Kendall B) magnitude of trend using Sen's slope for 74 climate indices).

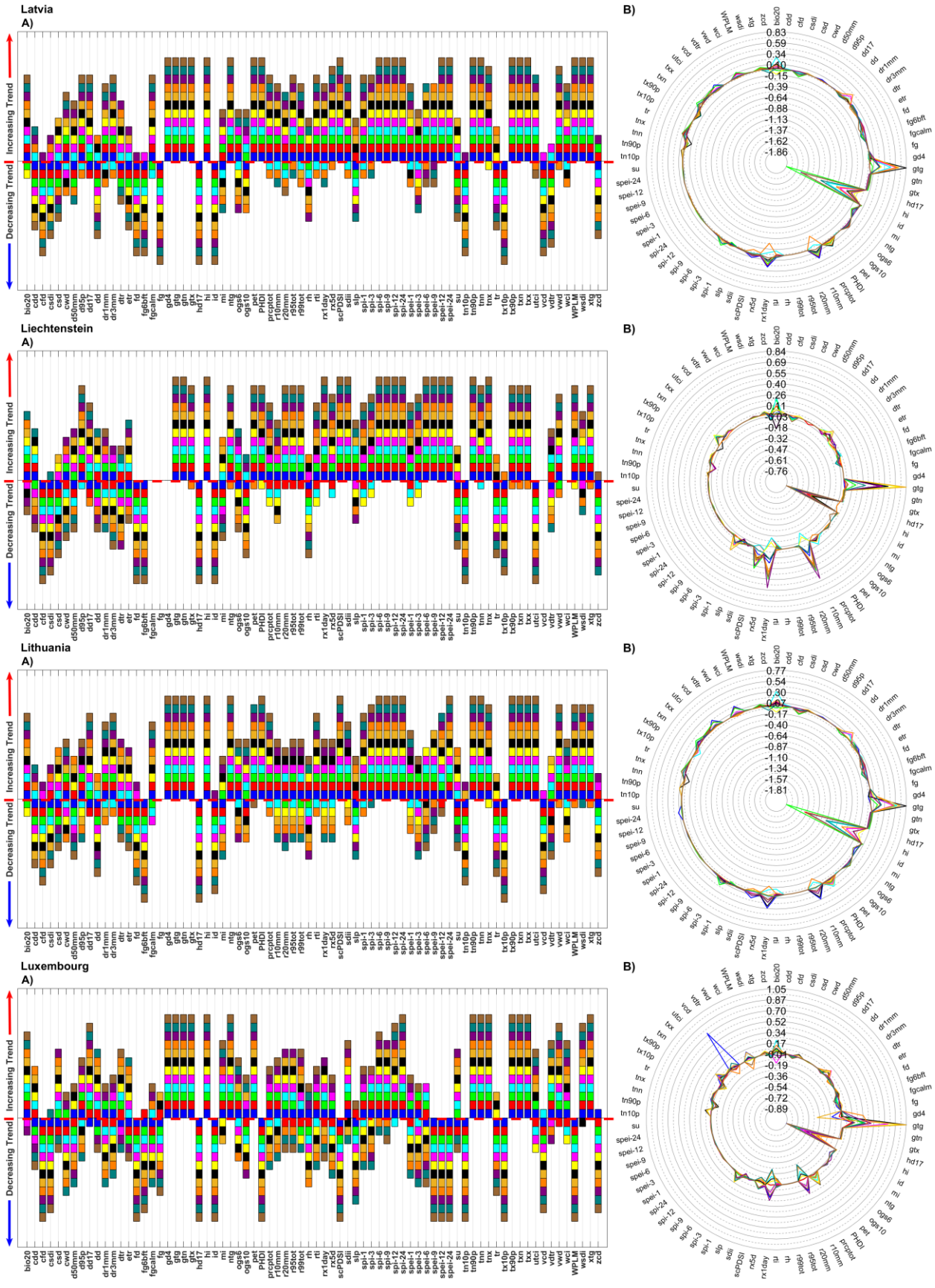
Latvia
A)
B)
Liechtenstein
A)
B)
Lithuania
A)
B)
Luxembourg
A)
B)
Increasing Trend
Decreasing Trend

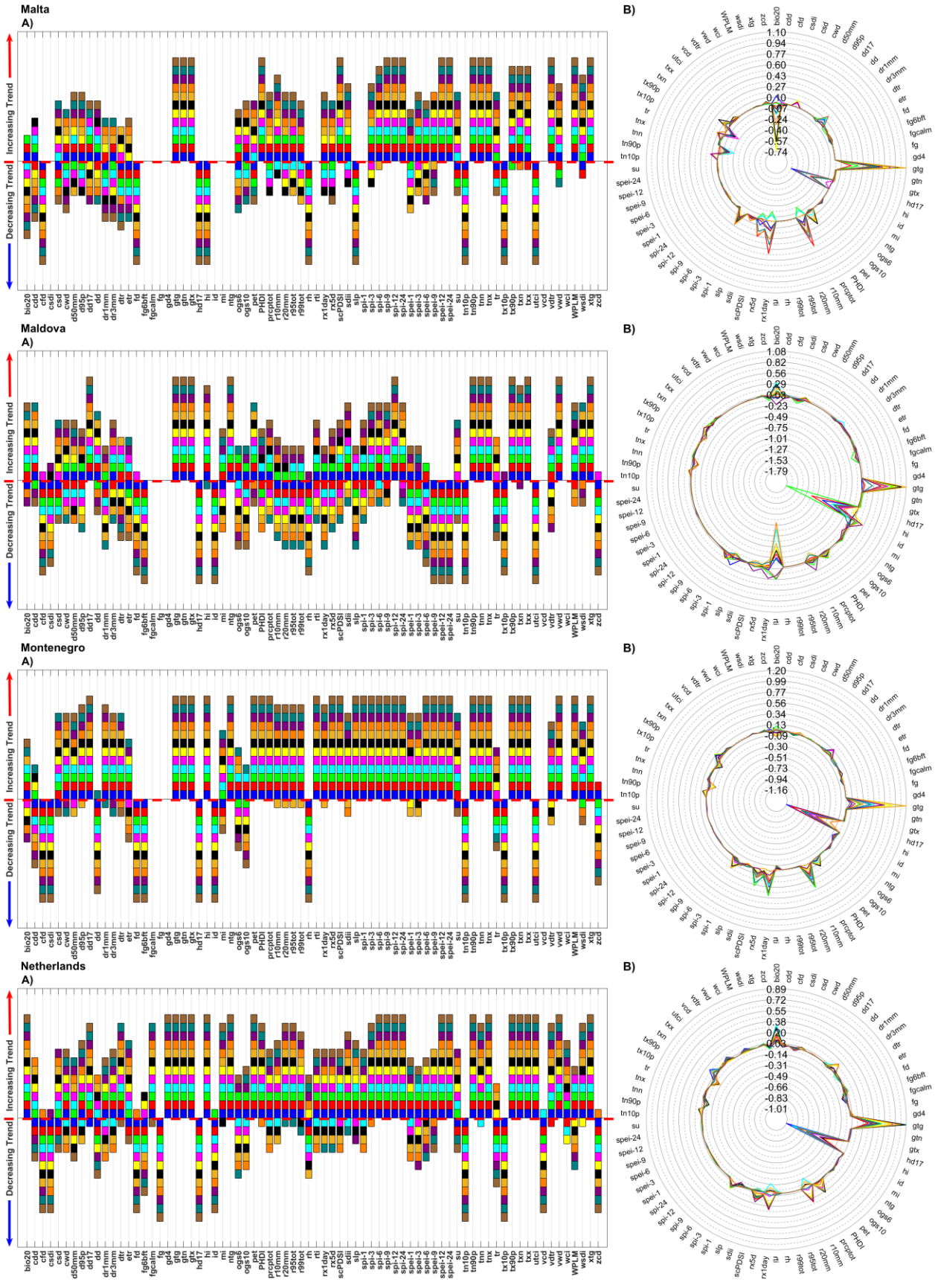
Malta
A)
B)
Maldova
A)
B)
Montenegro
A)
B)
Netherlands
A)
B)
Increasing Trend
Decreasing Trend

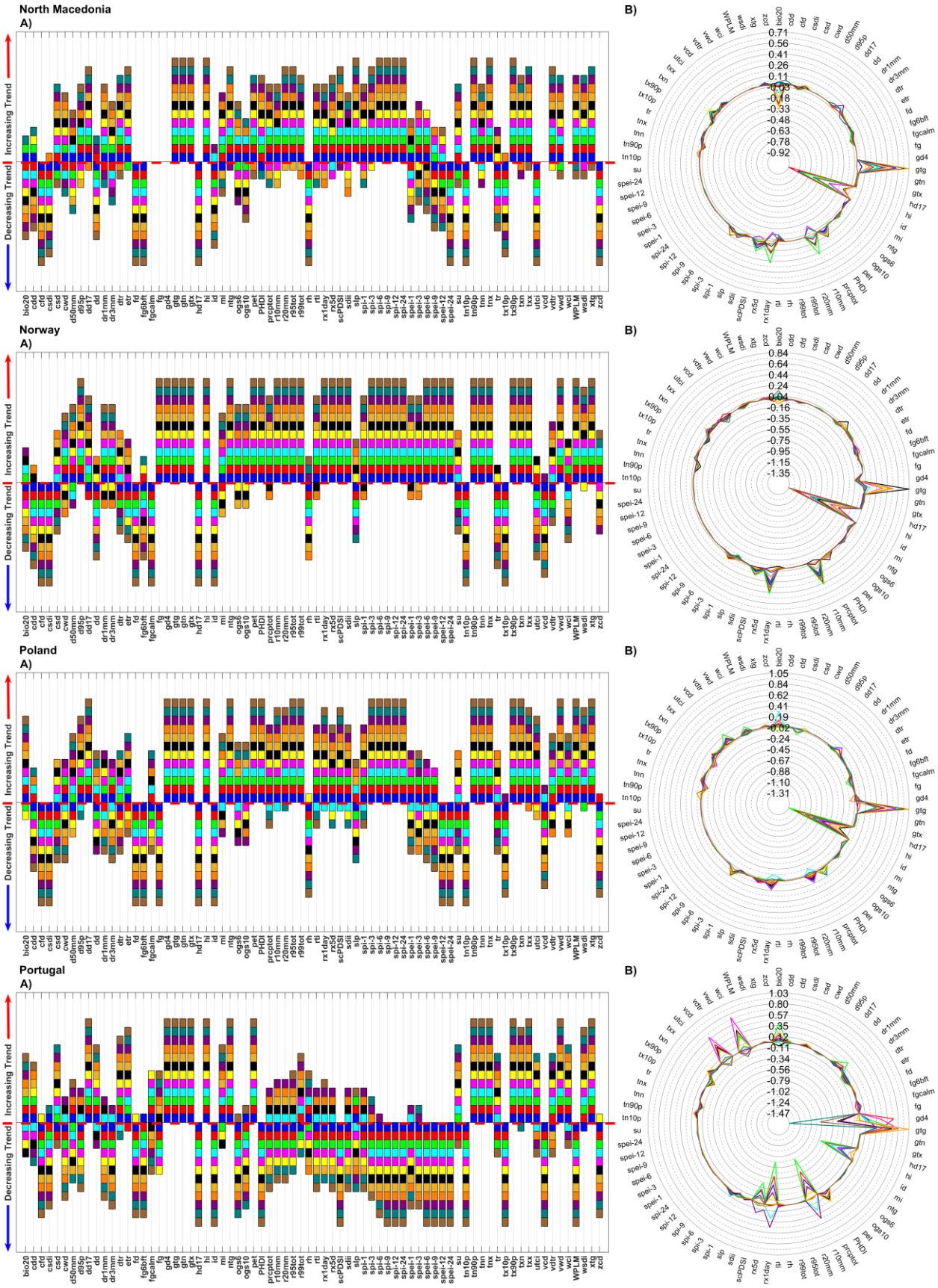
North Macedonia
A)
B)
Norway
A)
B)
Poland
A)
B)
Portugal
A)
B)
Increasing Trend
Decreasing Trend

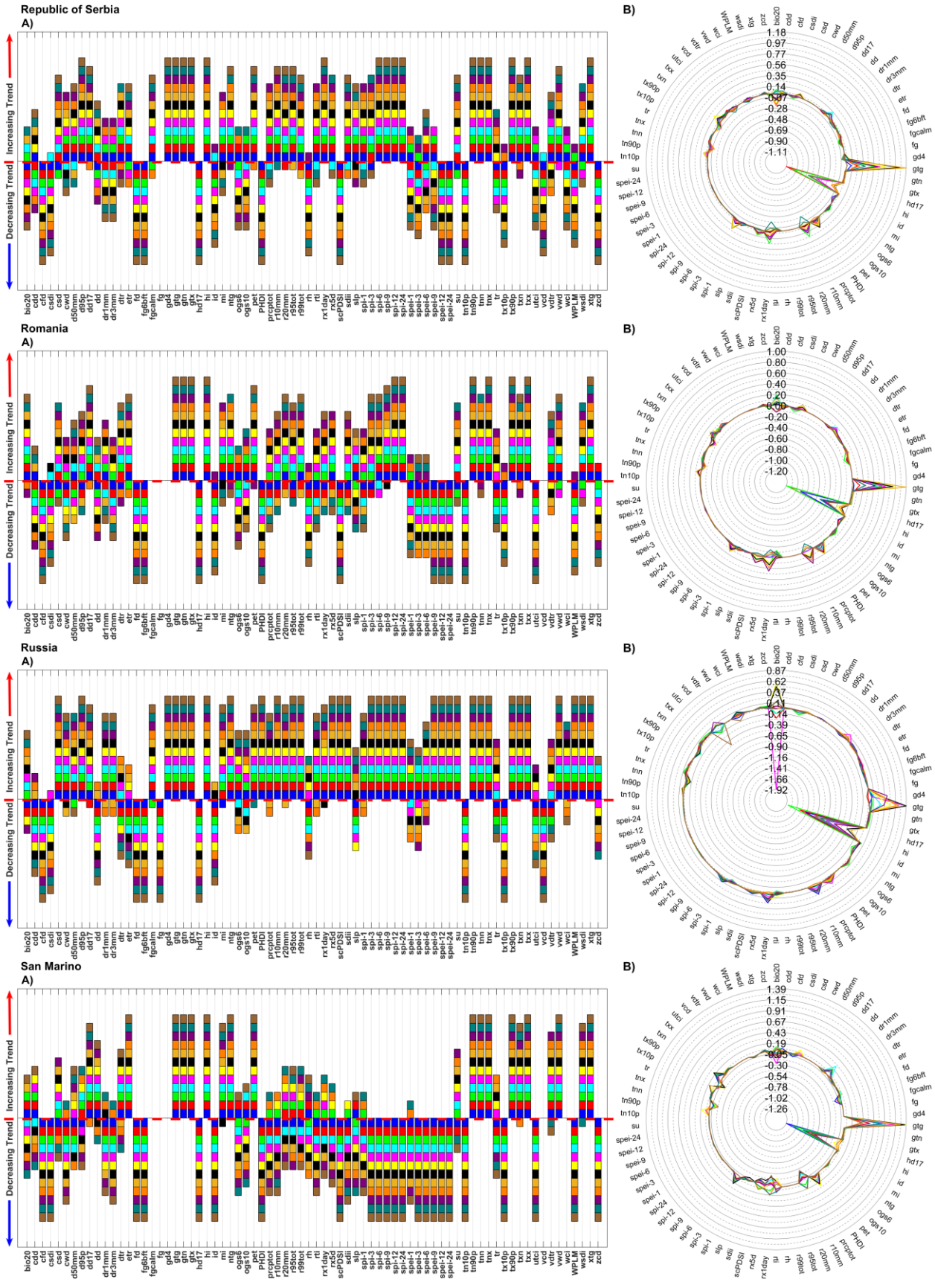
Republic of Serbia
A)
B)
Romania
A)
B)
Russia
A)
B)
San Marino
A)
B)
Increasing Trend
Decreasing Trend

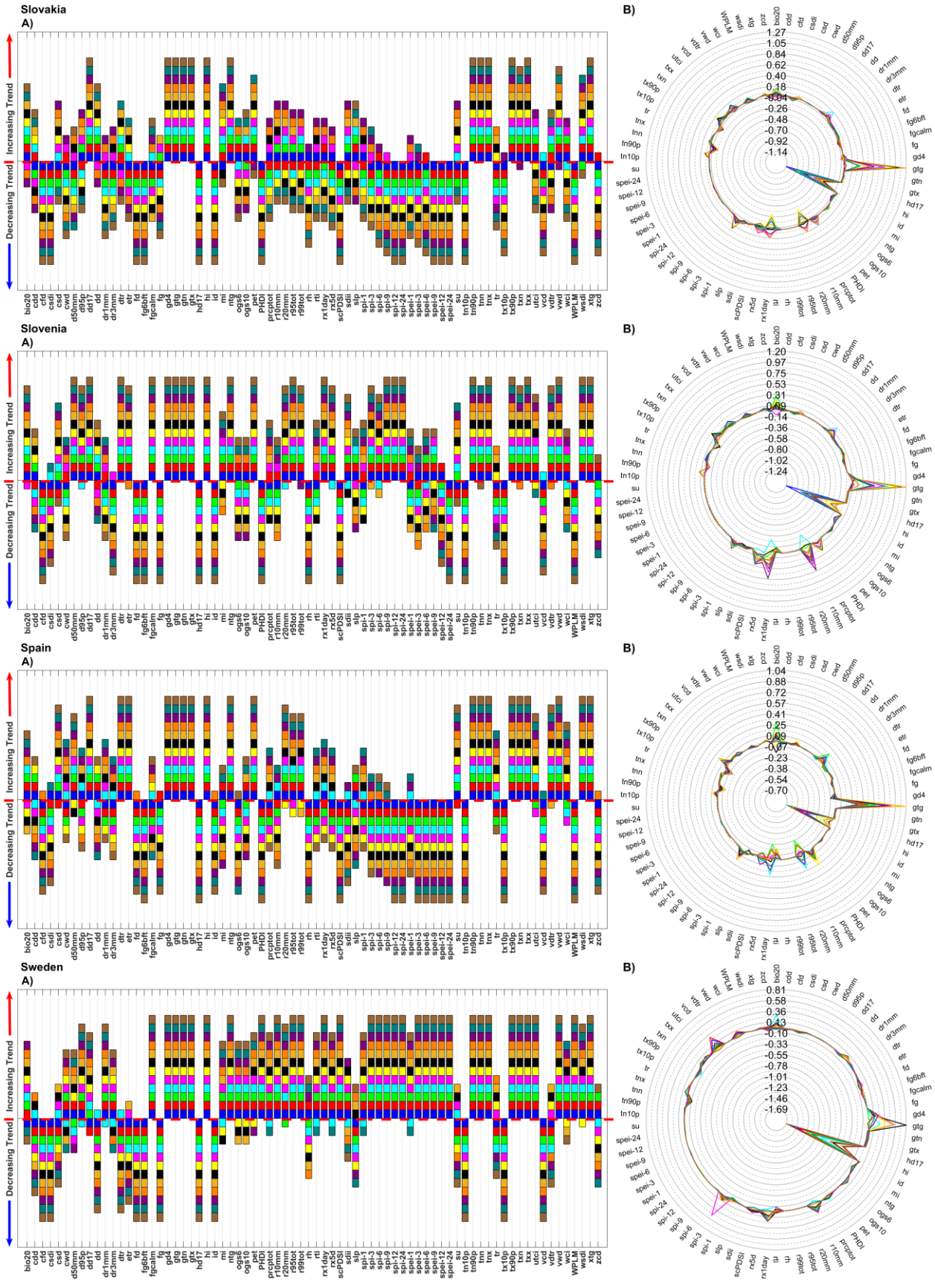
Slovakia
A)
B)
Slovenia
A)
B)
Spain
A)
B)
Sweden
A)
B)
Increasing Trend
Decreasing Trend

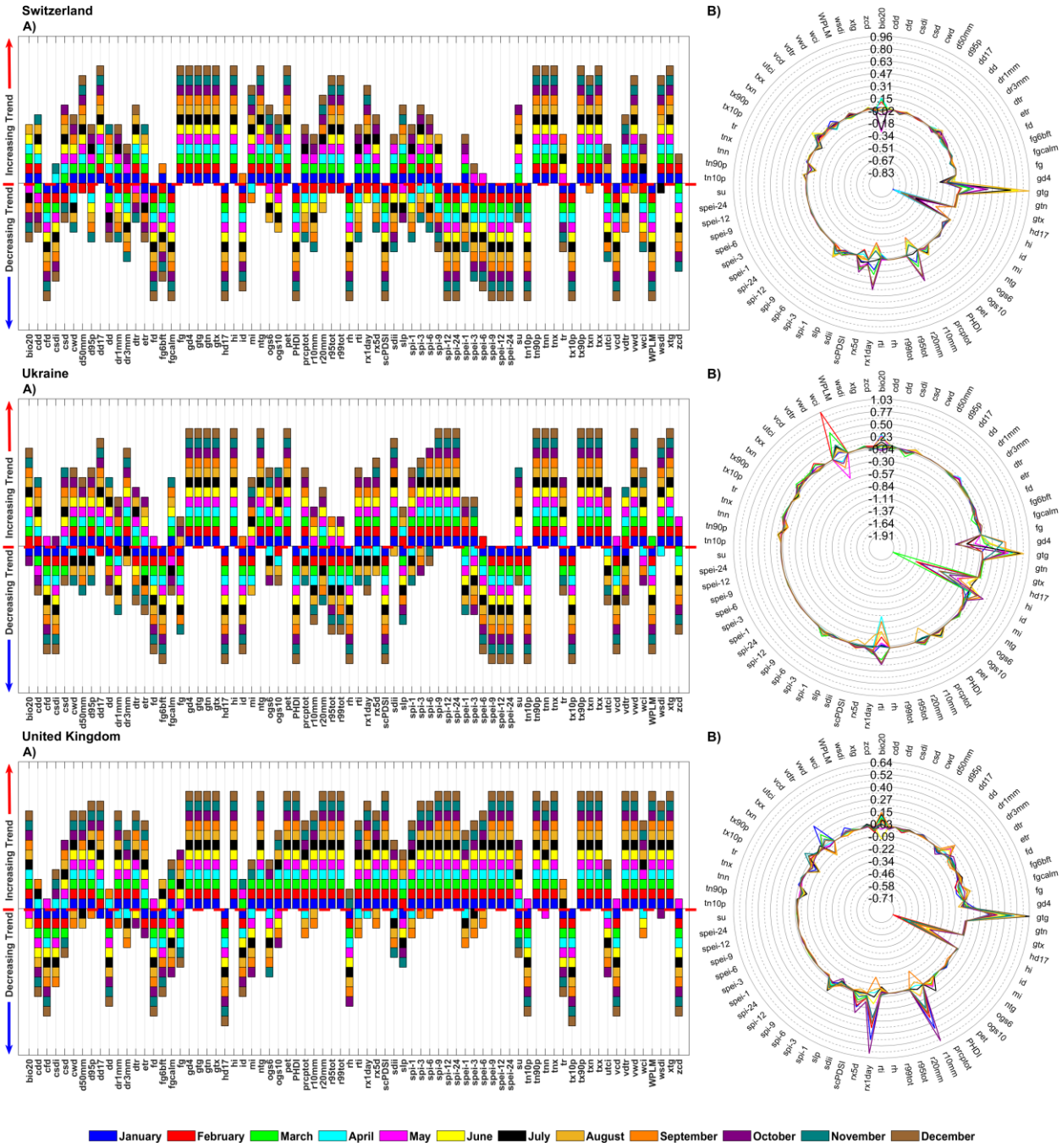

Figure S2: Monthly trend analysis across European countries (J-Z) (A) nature of trend using Mann-Kendall B) magnitude of trend using Sen's slope for 74 climate indices).

a) Drought Indices

Palmer Hydrological Drought Index (PHDI)

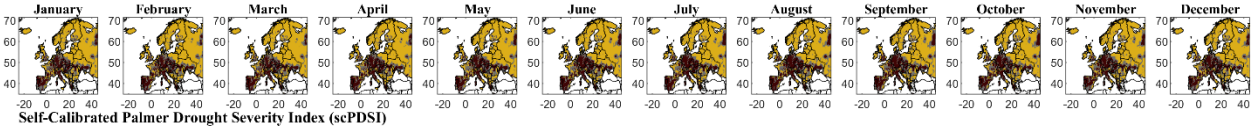

Self-Calibrated Palmer Drought Severity Index (scPDSI)

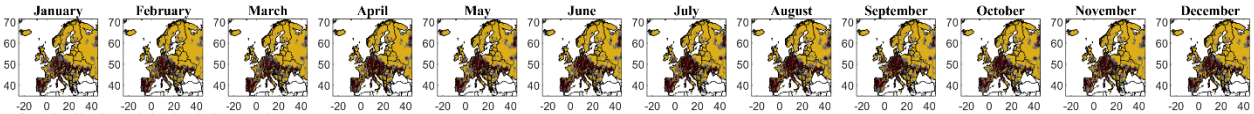

Standardized precipitation index 1 (spi-1)

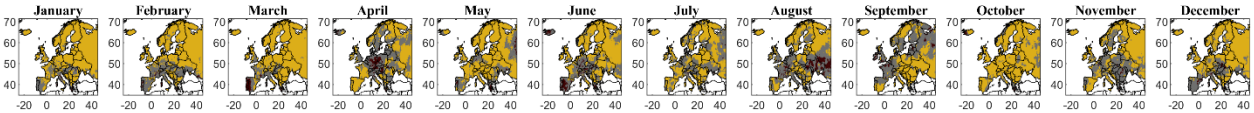

Standardized precipitation index 3 (spi-3)

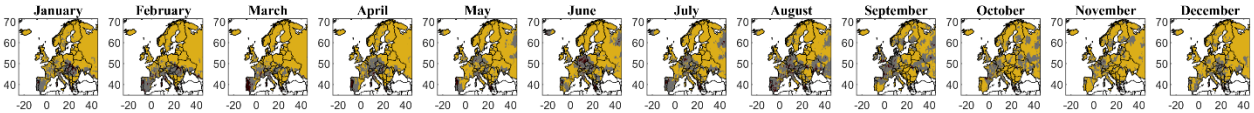

Standardized precipitation index 6 (spi-6)

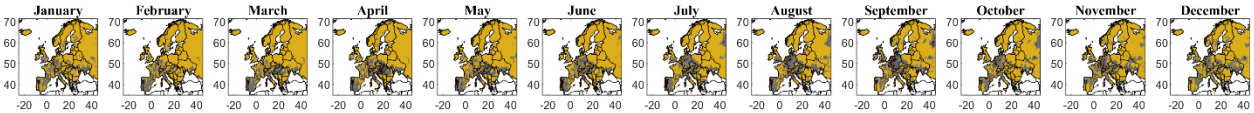

Standardized precipitation index 9 (spi-9)

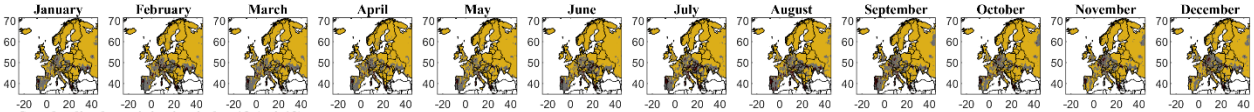

Standardized precipitation index 12 (spi-12)

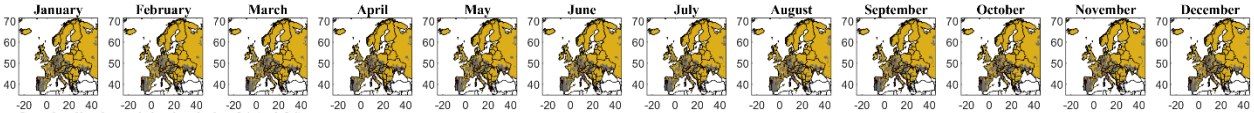

Standardized precipitation index 24 (spi-24)

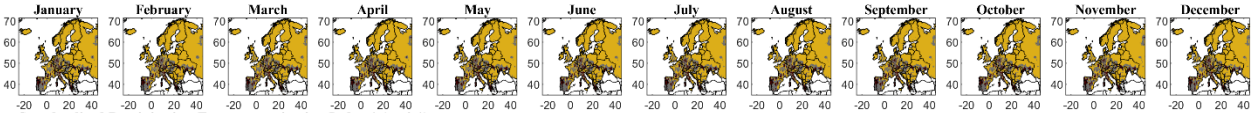

Standardised Precipitation-Evapotranspiration Index 1 (spei-1)

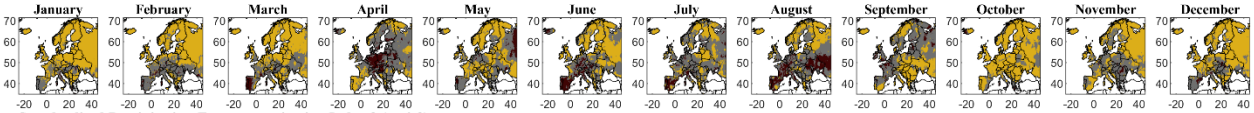

Standardised Precipitation-Evapotranspiration Index 3 (spei-3)

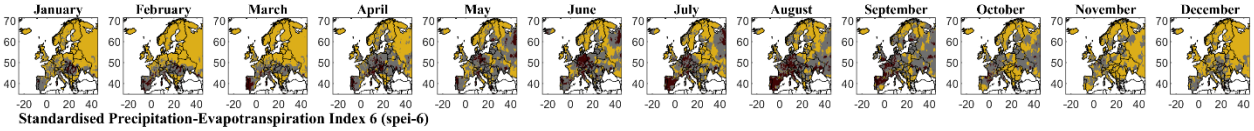

Standardised Precipitation-Evapotranspiration Index 6 (spei-6)

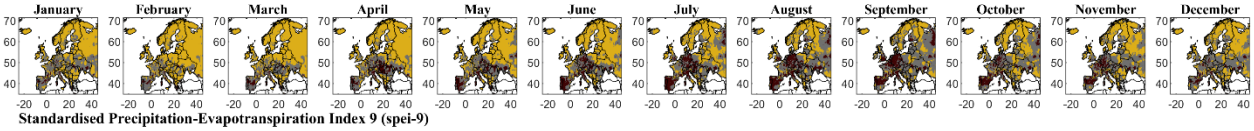

Standardised Precipitation-Evapotranspiration Index 9 (spei-9)

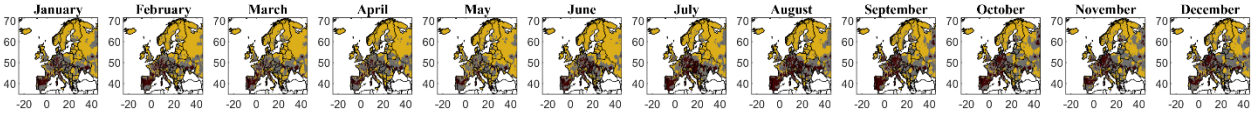

Standardised Precipitation-Evapotranspiration Index 12 (spei-12)

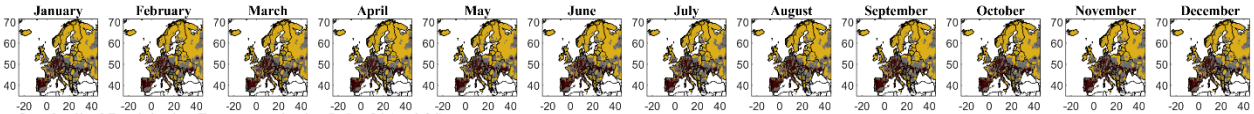

Standardised Precipitation-Evapotranspiration Index 24 (spei-24)

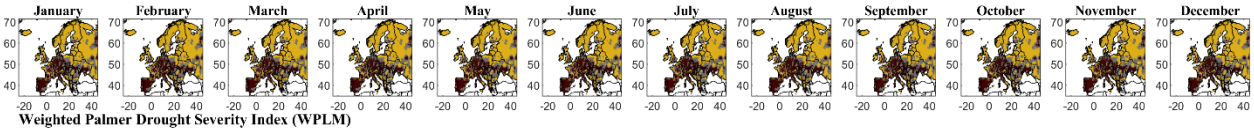

Weighted Palmer Drought Severity Index (WPLM)

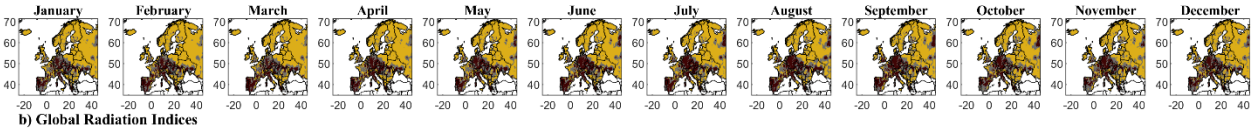

b) Global Radiation Indices

Mean radiation (bio20)

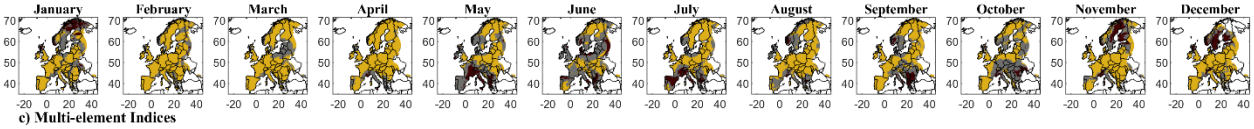

c) Multi-element Indices

Heat Index (hi)

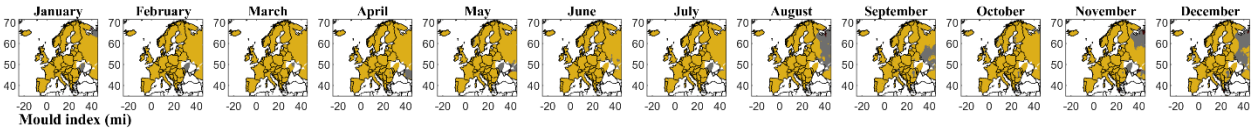

Mould index (mi)

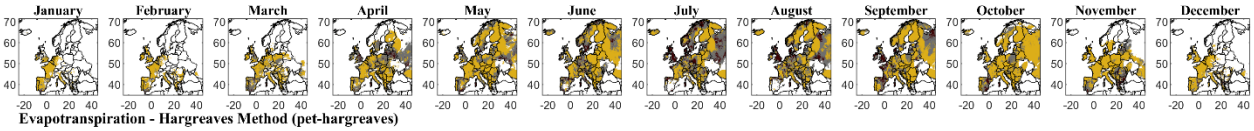

Evapotranspiration - Hargreaves Method (pet-hargreaves)

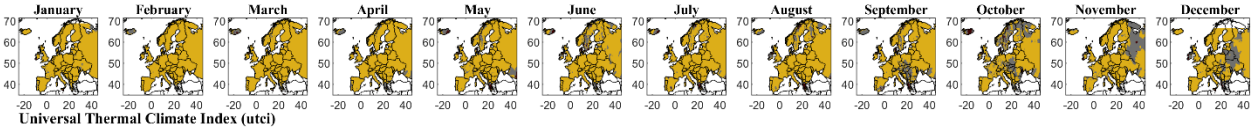

Universal Thermal Climate Index (utci)

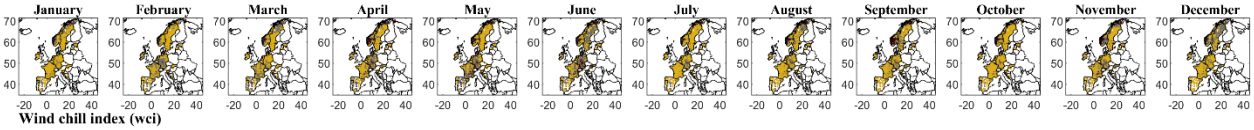

Wind chill index (wci)

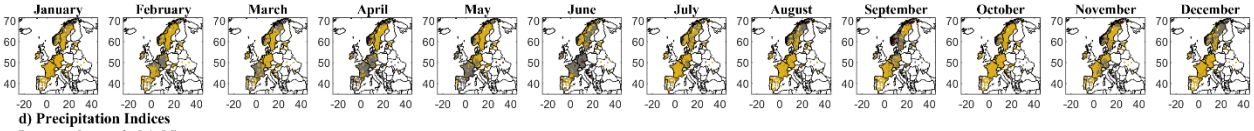

d) Precipitation Indices

Longest dry period (cdd)

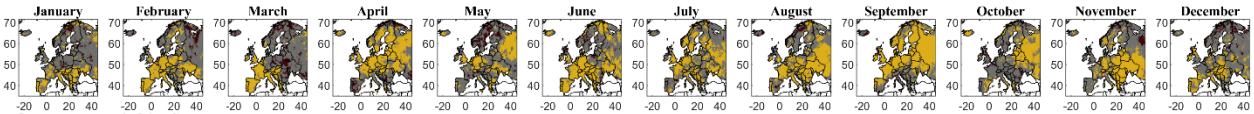

Longest wet period (cwd)

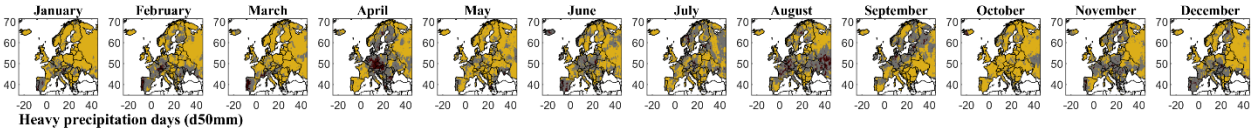

Heavy precipitation days (d50mm)

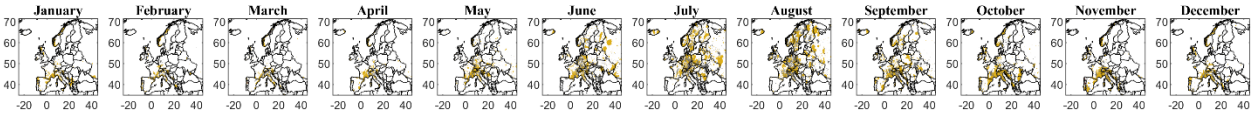


Very wet days (d95p)
Dry days (dd)
Wet days 1mm (dr1mm)
Wet days 3mm (dr3mm)
Total precipitation wet days (prcptot)
Days precipitation >= R10mm (r10mm)
Days precipitation >= R20mm (r20mm)
Percentage precipitation of very wet days (r95tot)
Precipitation fraction extremely wet days (r99tot)
Total precipitation (rti)
Maximum precipitation (rx1day)
Maximum 5 days R (rx5d)
January February March April May June July August September October November December

Simple precipitation intensity index (sdii)

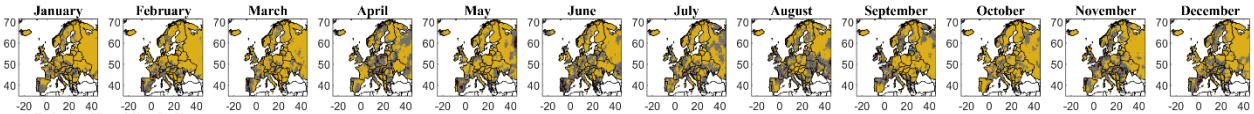

e) Relative Humidity Indices

Mean Relative Humidity (rh)

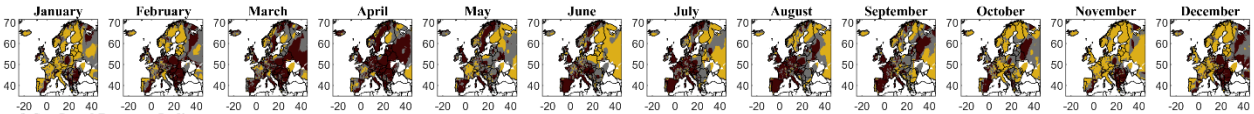

f) Sea Level Pressure Indices

Mean Sea Level Pressure (slp)

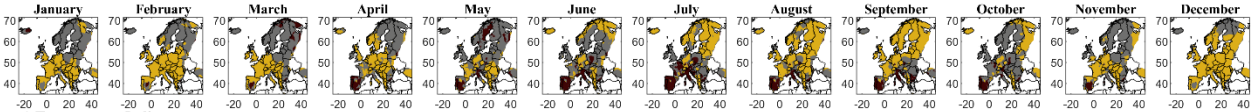

g) Temperature Indices

Maximum consecutive frost days (cfd)

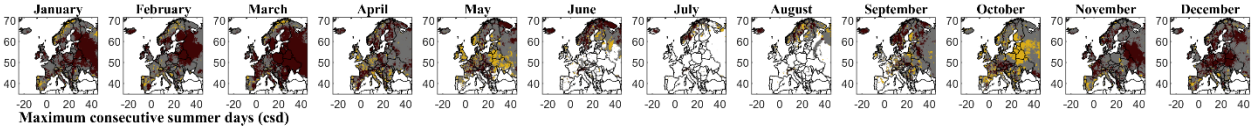

Maximum consecutive summer days (csd)

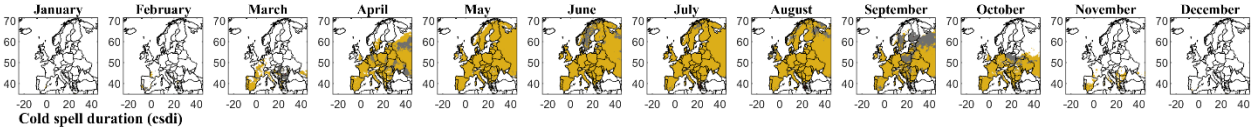

Cold spell duration (csdi)

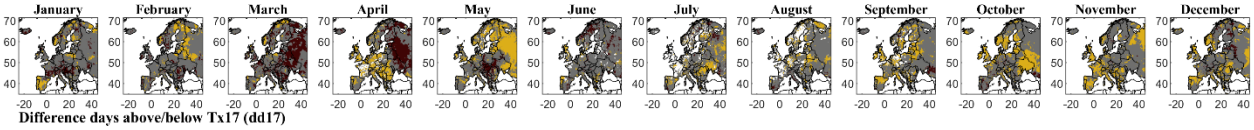

Difference days above/below Tx17 (dd17)

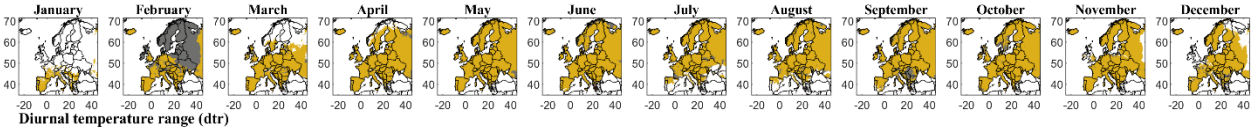

Diurnal temperature range (dtr)

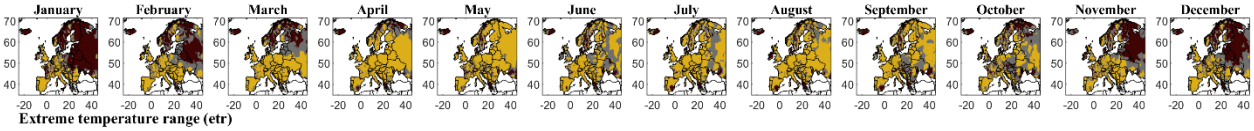

Extreme temperature range (etr)

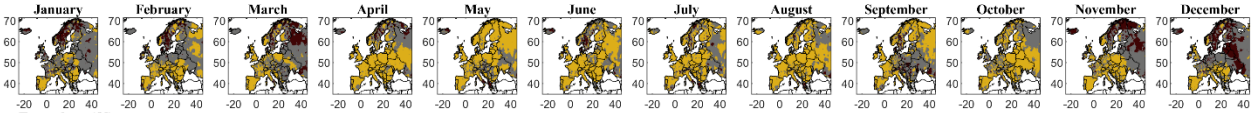

Frost days (fd)

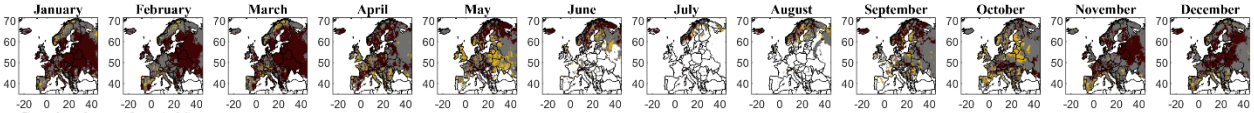

Growing degree days (gd4)

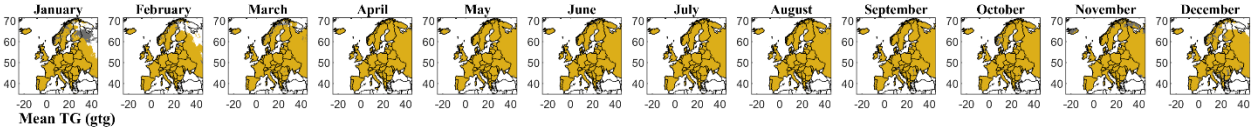

Mean TG (gtg)

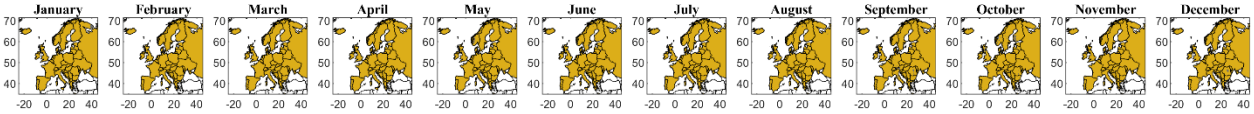


Mean TN (gtn)
Mean TX (gtx)
Heating degree days (hd17)
Ice days (id)
Minimum TG (ntg)
Onset of growing season 6 days (ogs6)
Onset of growing season 10 days (ogs10)
Summer days (su)
Percentage of cold nights (tn10p)
Warm nights (tn90p)
Minimum TN (tnn)
Maximum TN (tnx)
January
February
March
April
May
June
July
August
September
October
November
December

Tropical nights (tr)

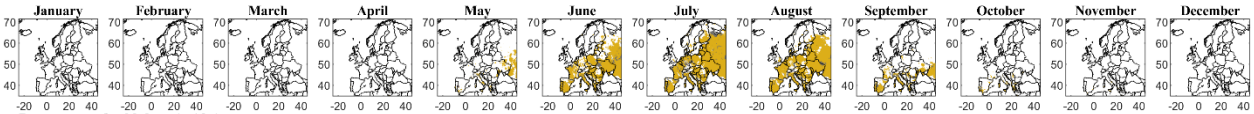

Percentage of cold days (tx10p)

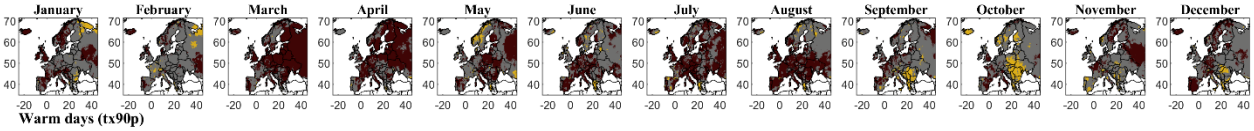

Warm days (tx90p)

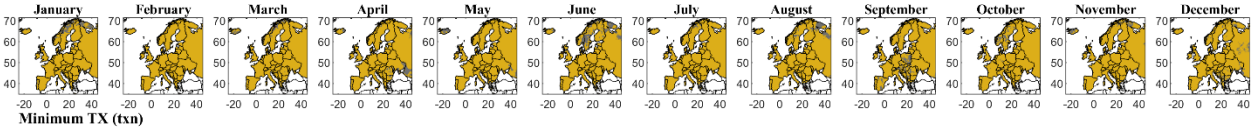

Minimum TX (txn)

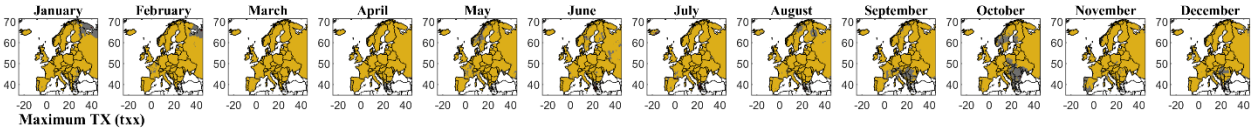

Maximum TX (txx)

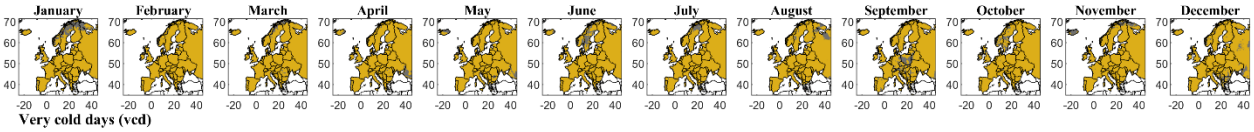

Very cold days (vcd)

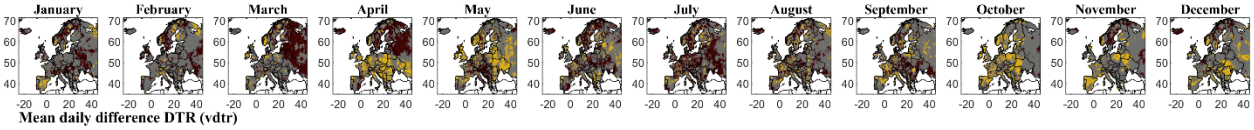

Mean daily difference DTR (vdtr)

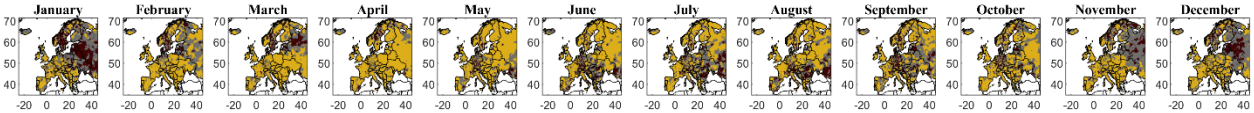

Very warm days (vwd)

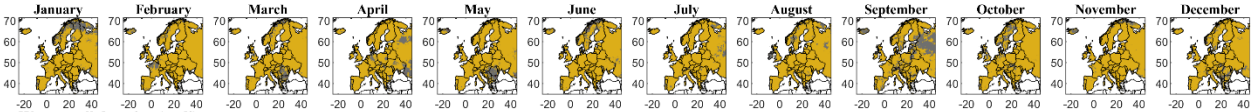

Warm spell duration (wsdi)

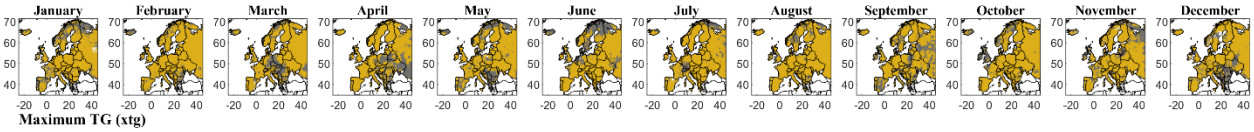

Maximum TG (xtg)

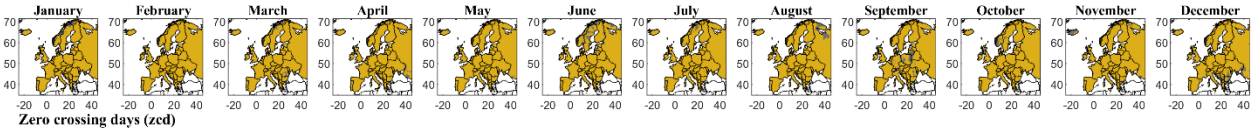

Zero crossing days (zcd)

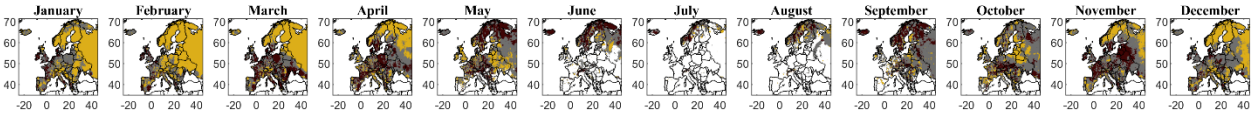

h) Wind Speed Indices

Mean of daily mean wind strength (fg)

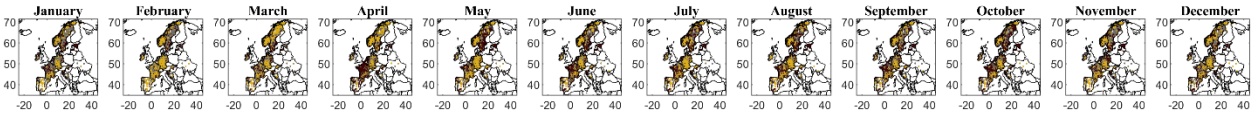

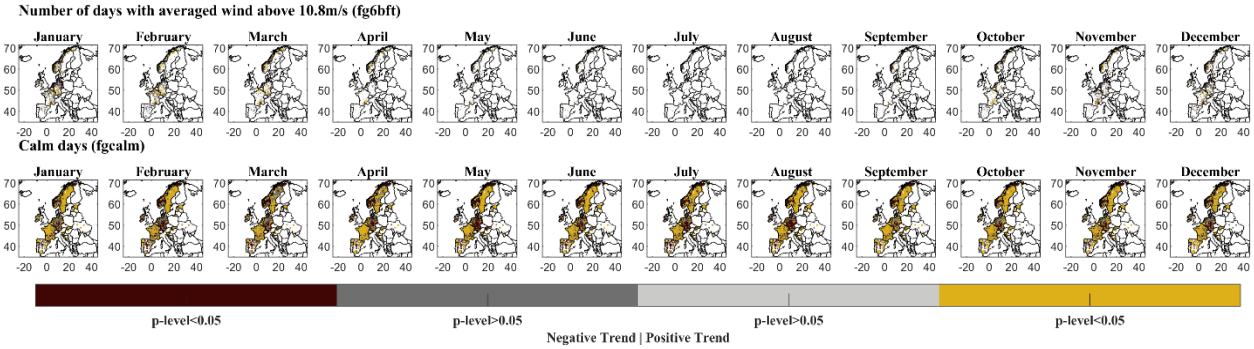

Figure S3: Spatial trend using Mann-Kendall test across Europe

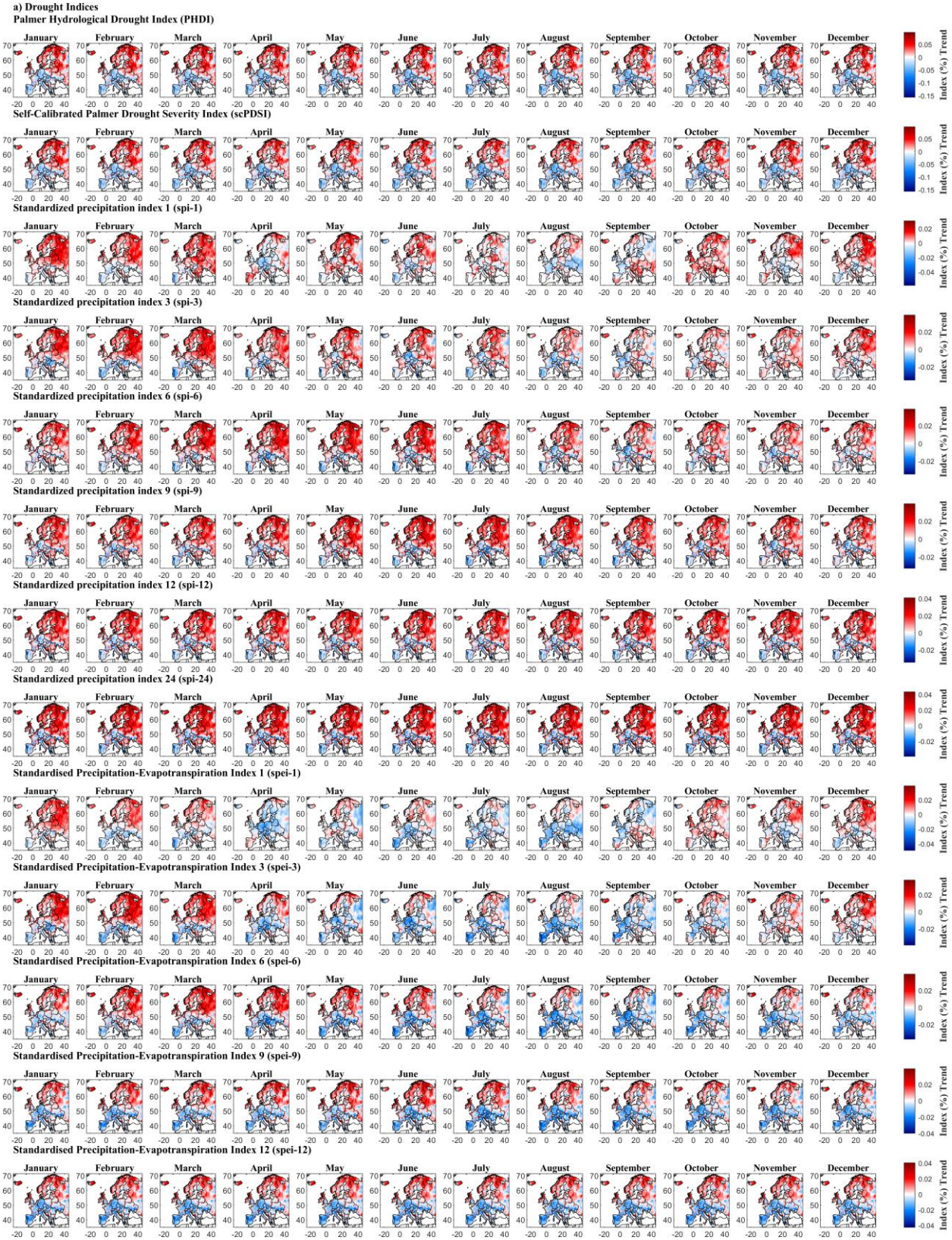
a) Drought Indices
Palmer Hydrological Drought Index (PHDI)
Self-Calibrated Palmer Drought Severity Index (scPDSI)
Standardized precipitation index 1 (spi-1)
Standardized precipitation index 3 (spi-3)
Standardized precipitation index 6 (spi-6)
Standardized precipitation index 9 (spi-9)
Standardized precipitation index 12 (spi-12)
Standardized precipitation index 24 (spi-24)
Standardized Precipitation-Evapotranspiration Index 1 (spei-1)
Standardised Precipitation-Evapotranspiration Index 3 (spei-3)
Standardised Precipitation-Evapotranspiration Index 6 (spei-6)
Standardised Precipitation-Evapotranspiration Index 9 (spei-9)
Standardised Precipitation-Evapotranspiration Index 12 (spei-12)
January
February
March
April
May
June
July
August
September
October
November
December
Index (%) Trend


Standardised Precipitation-Evapotranspiration Index 24 (spei-24)
Weighted Palmer Drought Severity Index (WPLM)
b) Global Radiation Indices
Mean radiation (bio20)
c) Multi-element Indices
Heat Index (hi)
Mould index (mi)
Evapotranspiration - Hargreaves Method (pet-hargreaves)
Universal Thermal Climate Index (utci)
Wind chill index (wci)
d) Precipitation Indices
Longest dry period (cdd)
Longest wet period (cwd)
Heavy precipitation days (d50mm)
Very wet days (d95p)
January
February
March
April
May
June
July
August
September
October
November
December
Index (%) Trend
Watt/square meter (%) Trend
Degree celsius (%) Trend
Millimeter/month (%) Trend
Days (%) Trend

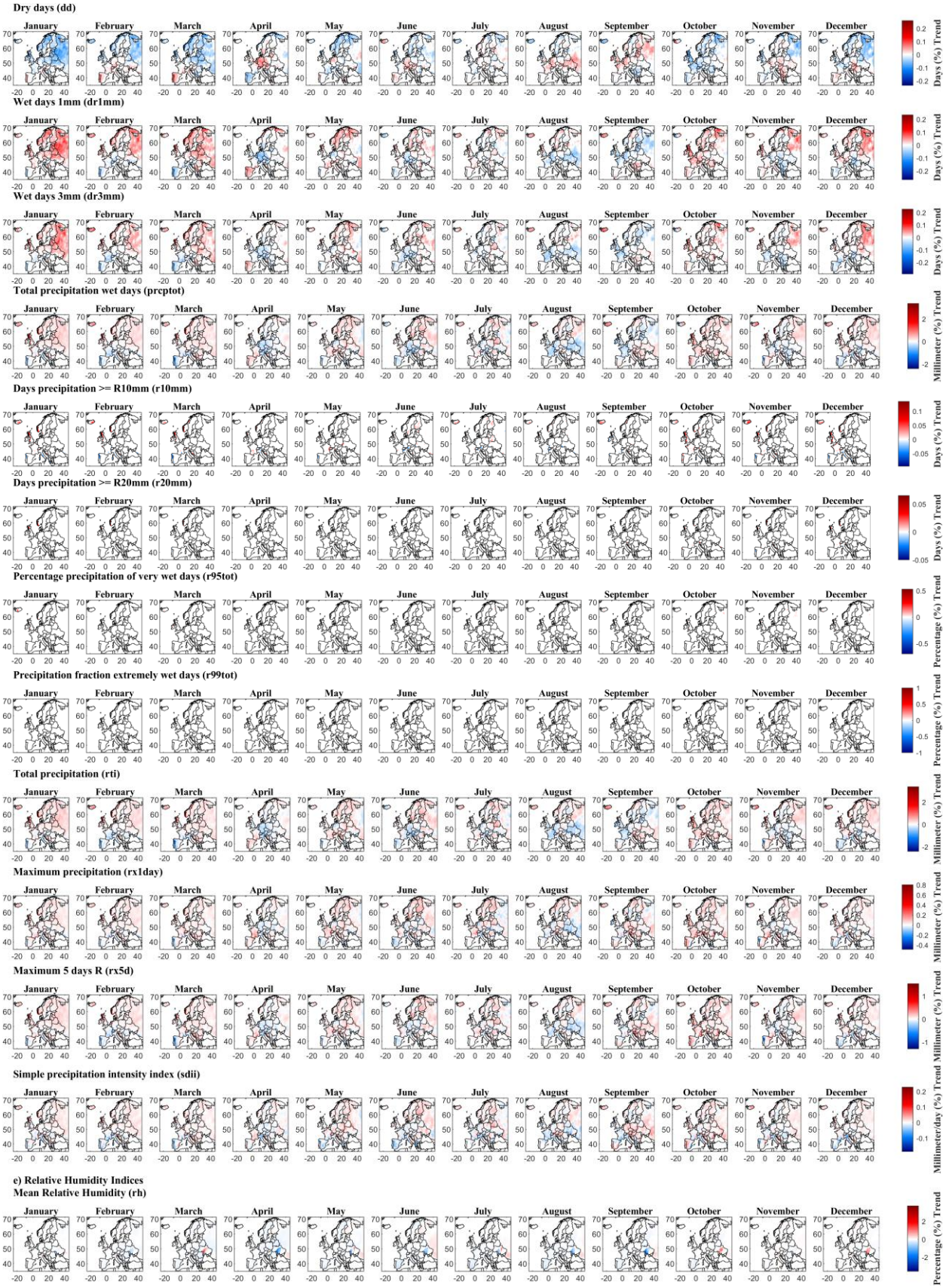
Dry days (dd)
Wet days 1mm (dr1mm)
Wet days 3mm (dr3mm)
Total precipitation wet days (prcptot)
Days precipitation >= R10mm (r10mm)
Days precipitation >= R20mm (r20mm)
Percentage precipitation of very wet days (r95tot)
Precipitation fraction extremely wet days (r99tot)
Total precipitation (rti)
Maximum precipitation (rx1day)
Maximum 5 days R (rx5d)
Simple precipitation intensity index (sdii)
e) Relative Humidity Indices
Mean Relative Humidity (rh)
January February March April May June July August September October November December
Days (%) Trend
Millimeter (%) Trend
Percentage (%) Trend
Millimeter/day (%) Trend

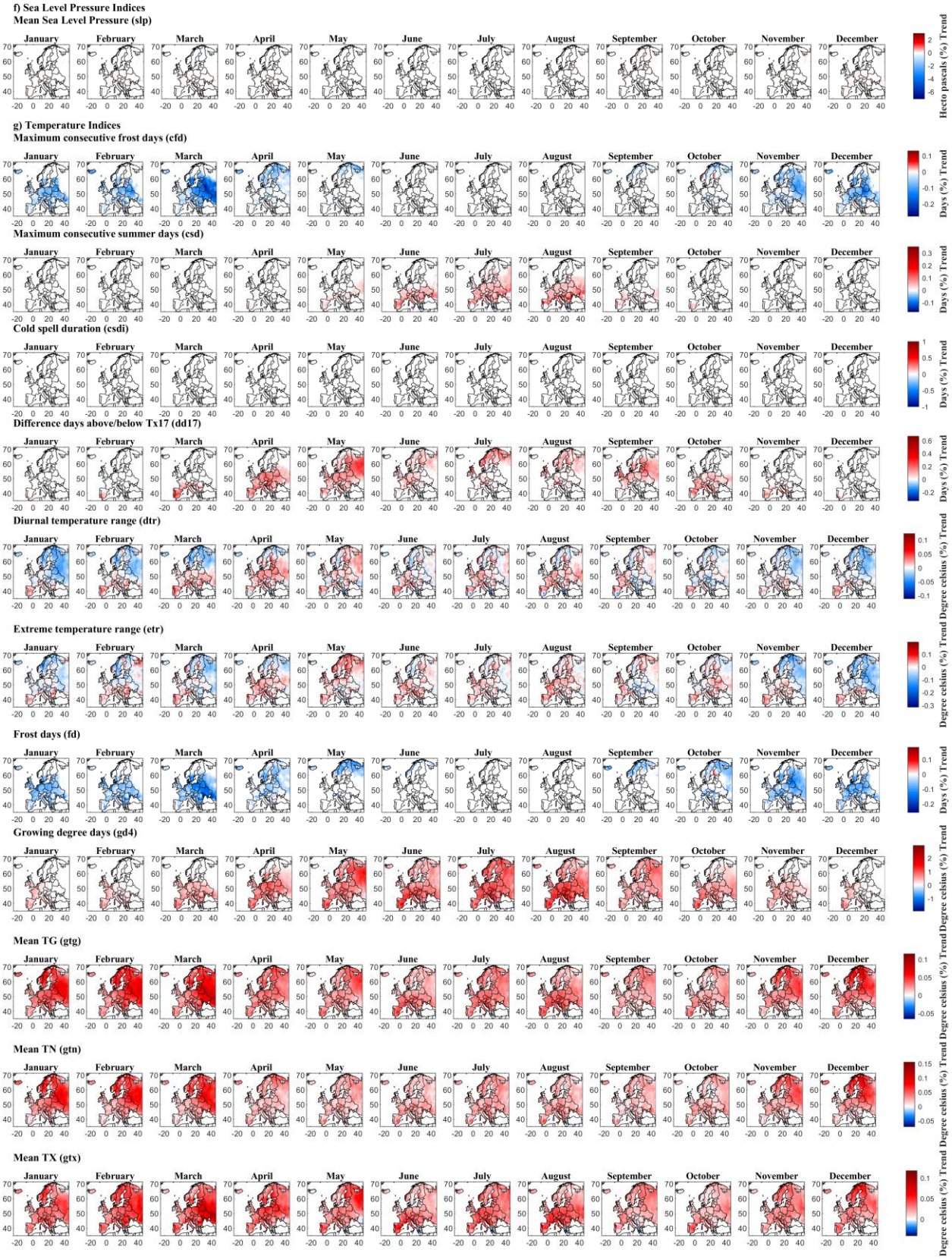
f) Sea Level Pressure Indices
Mean Sea Level Pressure (slp)
January February March April May June July August September October November December
Hecto pascals (%) Trend
g) Temperature Indices
Maximum consecutive frost days (cfd)
Maximum consecutive summer days (csd)
Cold spell duration (csdi)
Difference days above/below Tx17 (dd17)
Days (%) Trend
Diurnal temperature range (dtr)
Extreme temperature range (etr)
Degree celsius (%) Trend
Frost days (fd)
Growing degree days (gd4)
Mean TG (gtg)
Mean TN (gtn)
Mean TX (gtx)

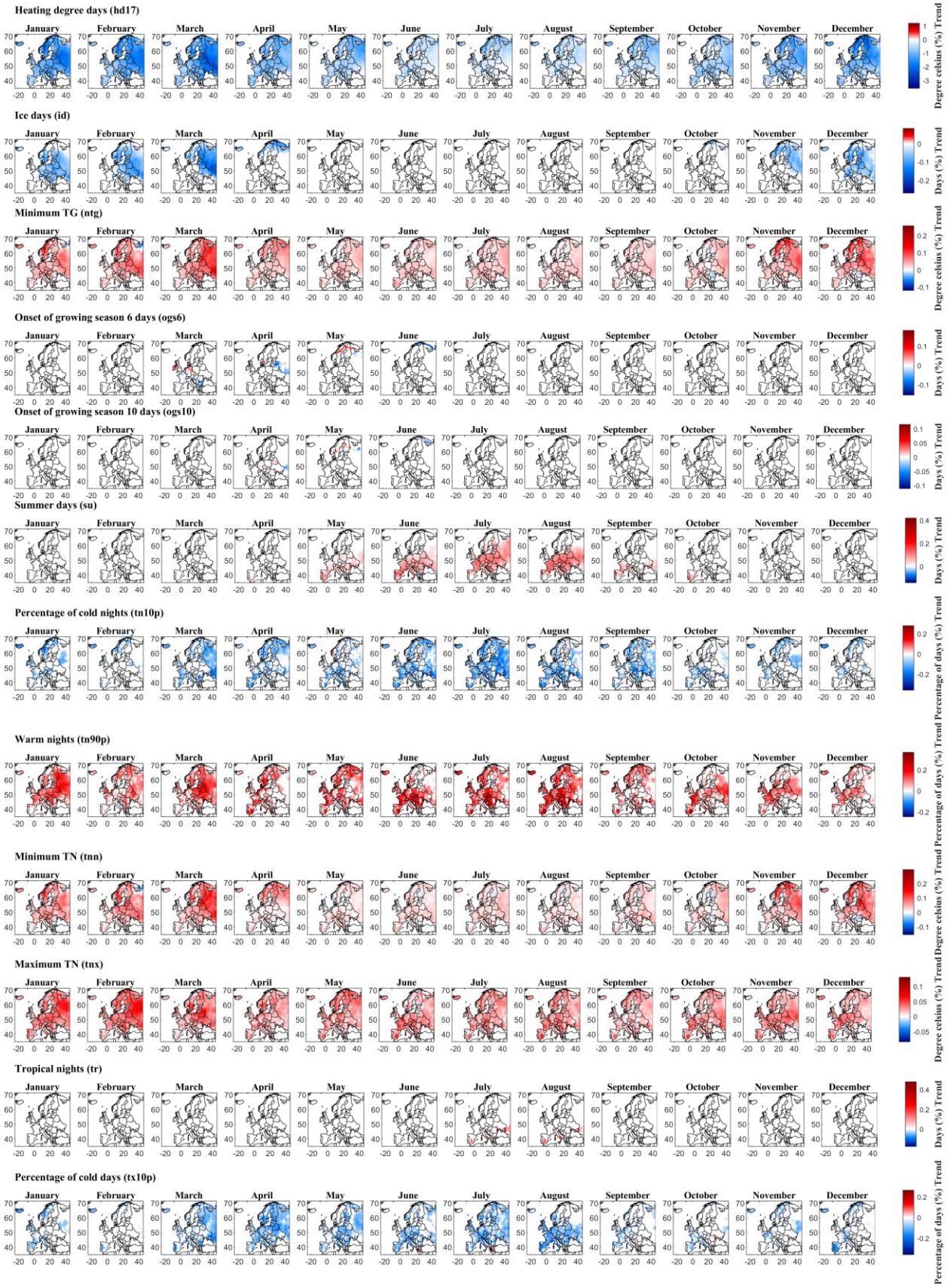
Heating degree days (hd17)
Degree celsius (%) Trend
Ice days (id)
Days (%) Trend
Minimum TG (ntg)
Degree celsius (%) Trend
Onset of growing season 6 days (ogs6)
Days (%) Trend
Onset of growing season 10 days (ogs10)
Days (%) Trend
Summer days (su)
Days (%) Trend
Percentage of cold nights (tn10p)
Percentage of days (%) Trend
Warm nights (tn90p)
Percentage of days (%) Trend
Minimum TN (tnn)
Degree celsius (%) Trend
Maximum TN (tnx)
Degree celsius (%) Trend
Tropical nights (tr)
Days (%) Trend
Percentage of cold days (tx10p)
Percentage of days (%) Trend
January
February
March
April
May
June
July
August
September
October
November
December

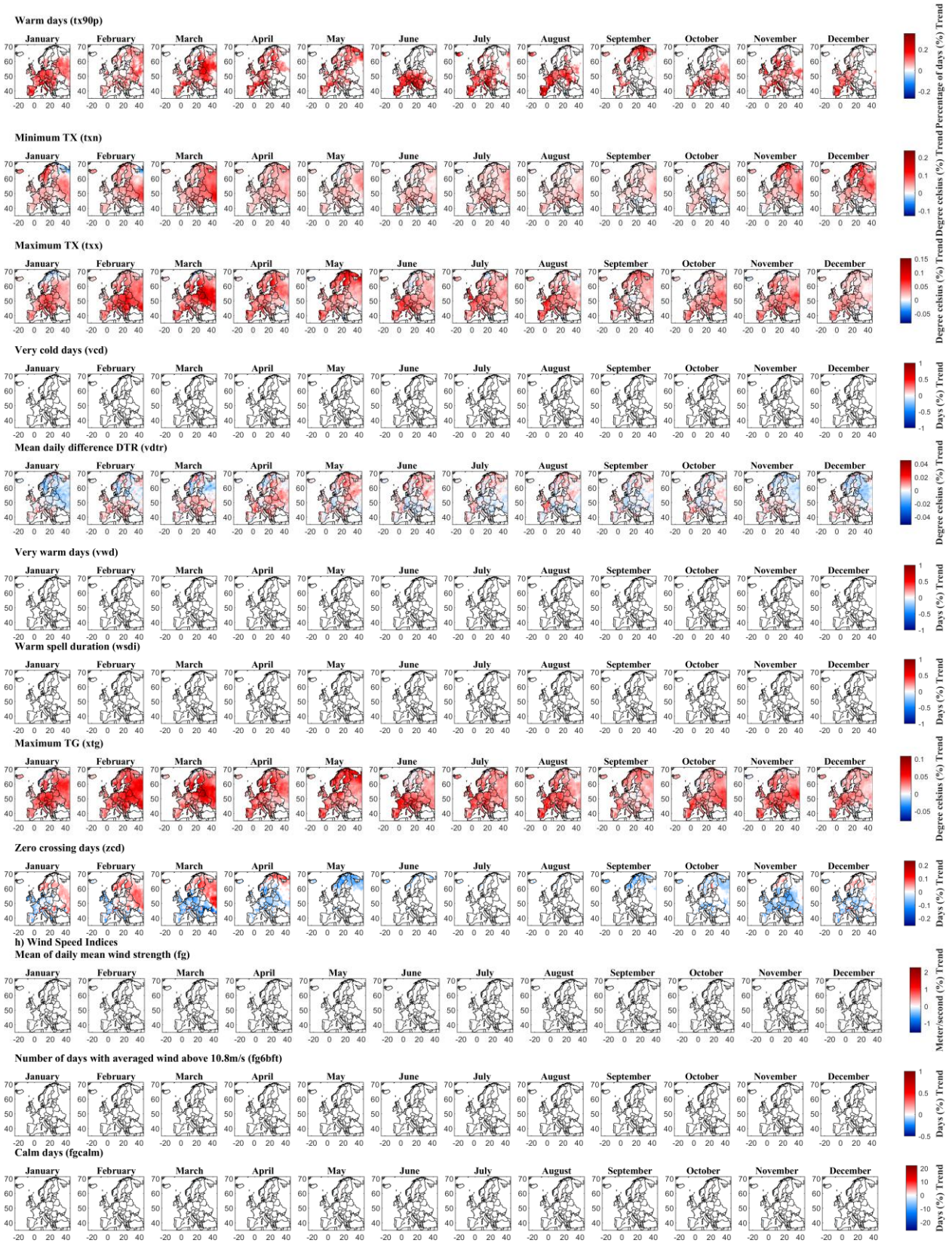

Figure S4: Spatial trend using Sen's slope estimator across Europe

Table S1: List of climate indices computed for Europe (1950-2021). Remark section indicates yellow and green which represents the 17 (39) climate indices that have high probabilities for the specific month at certain (many) zones of Europe. (Chapter 5 – Table S1)

ID	Indices Name	Definitions	Units	Remark
a) Drought Indices				
PHDI	Palmer hydrological drought index	Time series of palmer hydrological drought index		
scPDSI	Self-calibrated palmer drought severity index	Time series of self-calibrated palmer drought severity index		
spi-1	Standardized precipitation index 1	Standardized precipitation index calculated at 1-month time scale		
spi-3	Standardized precipitation index 3	Standardized precipitation index calculated at 3-month time scale		
spi-6	Standardized precipitation index 6	Standardized precipitation index calculated at 6-month time scale		
spi-9	Standardized precipitation index 9	Standardized precipitation index calculated at 9-month time scale		
spi-12	Standardized precipitation index 12	Standardized precipitation index calculated at 12-month time scale		
spi-24	Standardized precipitation index 24	Standardized precipitation index calculated at 24-month time scale		
spei-1	Standardized precipitation-evapotranspiration index 1	Standardized precipitation-evapotranspiration index calculated at 1-month time scale		
spei-3	Standardized precipitation-evapotranspiration index 3	Standardized precipitation-evapotranspiration index calculated at 3-month time scale		
spei-6	Standardized precipitation-evapotranspiration index 6	Standardized precipitation-evapotranspiration index calculated at 6-month time scale		
spei-9	Standardized precipitation-evapotranspiration index 9	Standardized precipitation-evapotranspiration index calculated at 9-month time scale		
spei-12	Standardized precipitation-evapotranspiration index 12	Standardized precipitation-evapotranspiration index calculated at 12-month time scale		
spei-24	Standardized precipitation-evapotranspiration index 24	Standardized precipitation-evapotranspiration index calculated at 24-month time scale		
WPLM	Weighted palmer drought severity index	Time series of weighted palmer drought severity index		
b) Global Radiation				
bio20	Mean radiation	Average daily global radiation	W/m^2	
c) Multi-element Indices				

hi	Heat index	Combines air temperature and relative humidity to determine the human-perceived equivalent temperature		
mi	Mould index	Combined air temperature and relative humidity affecting growth rate of mould. Number of days with a relative humidity over 90% and temperature falls over 10°C.		
pet	Reference evapotranspiration	Using Hargreaves Method	mm/day	
utci	Universal thermal climate index	Air temperature of reference condition causing the same model response as actual conditions		
wci	Wind chill index	Combines air temperature and wind speed; lowering of body temperature due to the passing-flow of lower-temperature air.		
d) Precipitation Indices				
cdd	Longest dry period	Maximum length of consecutive dry days	days	
cwd	Longest wet period	Maximum length of consecutive wet days	days	
d50mm	Heavy precipitation days	Number of days with precipitation above 50mm	days	
d95p	Very wet days	Days with precipitation > 95th percentile	days	
dd	Dry days	Number of days with precipitation less than 1 mm	days	
dr1mm	Wet days 1 mm	Total number of wet days ≥ 1 mm	days	
dr3mm	Wet days 3 mm	Total number of Wet days ≥ 3mm	days	
prcptot	Total precipitation wet days	Precipitation amount on days ≥ 1 mm	mm	
r10mm	Days precipitation ≥ 10mm	Days with daily precipitation amount ≥ 10mm	days	
r20mm	Days precipitation ≥ 20mm	Days with daily precipitation amount ≥ 20mm	days	
r95tot	Percentage precipitation of very wet days	Precipitation at days exceeding the 95th percentile divided by total precipitation	%	
r99tot	Precipitation fraction extremely wet days	Precipitation at days exceeding the 99th percentile divided by total precipitation	%	
rti	Total precipitation	Total amounts of precipitation	mm	
rx1day	Maximum precipitation	Highest amount of daily precipitation	mm	
rx5d	Maximum 5 days precipitation	Maximum consecutive 5-day precipitation	mm	
sdii	Simple precipitation intensity index	Sum of precipitation in wet days (>1mm) divided by	mm/day	

		number of wet days in the period.		
e) Relative Humidity Indices				
rh	Mean relative humidity	Average daily relative humidity	%	
f) Sea Level Pressure Indices				
slp	Mean sea level pressure	Average daily sea level pressure	hPa	
g) Temperature Indices				
cfd	Maximum consecutive frost days	Maximum number of consecutive days with TN < 0°C	days	
csd	Maximum consecutive summer days	Maximum number of consecutive summer days with TX > 25°C	days	
csdi	Cold spell duration	Count of days with at least 6 consecutive days when daily minimum temperature < 10th percentile	days	
dd17	Difference days above/below TX-17°C	days TX > 17°C - days TX < 17°C	days	
dtr	Diurnal temperature range	Mean difference between TX and TN	°C	
etr	Extreme temperature range	Difference between the maximum TX and the minimum TN	°C	
fd	Frost days	Number of days with TN < 0°C	days	
gd4	Growing degree days	Sum of degree days of TG over 4°C	°C	
gtg	Mean TG	Mean of daily mean air temperature (TG)	°C	
gtn	Mean TN	Mean of daily minimum air temperature (TN)	°C	
gtx	Mean TX	Mean of daily maximum air temperature (TX)	°C	
hd17	Heating degree days	Accumulated degree when TG is below 17°C	°C	
id	Ice days	Number of days with TX < 0°C	days	
ntg	Minimum TG	Minimum value of daily mean air temperature	°C	
ogs6	Onset of growing season 6 days	Date of the start of the first span with at least 6 days with TG >5°C	days	
ogs10	Onset of growing season 10 days	Date of the start of the first span with at least 10 days with TG >5°C	days	
su	Summer days	Number of days with daily maximum temperature > 25°C	days	
tn10p	Percentage of cold nights	Percentages of days with TN < 10th percentile	%	
tn90p	Percentage of warm nights	Percentages of days with TN > 90th percentile	%	
tnn	Minimum TN	Minimum of daily minimum air temperature	°C	
tnx	Maximum TN	Maximum of daily minimum air temperature	°C	

tr	Tropical nights	Number of days with TN > 20°C	days	
tx10p	Percentage of cold days	Percentages of days with TX < 10th percentile	%	
tx90p	Percentage of warm days	Percentages of days with TX > 90th percentile	%	
txn	Minimum TX	Minimum of daily maximum air temperature	°C	
txx	Maximum TX	Maximum of daily maximum air temperature	°C	
vcd	Very cold days	Days with TN <1st percentile	days	
vdtr	Mean daily difference dtr	Mean absolute day-to-day difference in dtr	°C	
vwd	Very warm days	Days with TX >99th percentile	days	
wsdi	Warm spell duration	Number of days which are part of groups of at least 6 consecutive days when TX > 90th percentile	days	
xtg	Maximum TG	Maximum of daily mean air temperature	°C	
zcd	Zero crossing days	Number of days with TX > 0°C and TN < 0°C	days	
h) Wind Speed Indices				
fg	Mean of daily FG	Mean of daily mean wind strength	m/s	
fg6bft	Number of days with FG ≥10.8m/s	Number of days with averaged wind ≥ 10.8m/s	days	
fgcalm	Calm days	Number of days with averaged wind ≤ 2m/s	days	

Table S2: Country specific trend analysis of climate indices

Climate Indices	Highest decreasing trend (- ↓)			Highest increasing trend (+ ↑)		
	Country	**Month**	**% / month**	**Country**	**Month**	**% / month**
bio20	Russia	May	1.9	Russia	Jun	0.6
cdd	Andorra	Jul	0.1	Portugal	Mar	0.1
cfd	Estonia	Mar	0.2	Latvia	Oct	0.0
csd	Greece	Jul	0.0	San Marino	Jun	0.1
csdi	-	-	-	-	-	-
cwd	Portugal	Mar	0.0	Ireland	Jan	0.0
d50mm	-	-	-	Slovenia	Oct	0.0
d95p	Portugal	May	0.0	Montenegro	Mar	0.0
dd	Estonia	Jan	0.1	Portugal	Mar	0.1
dd17	Greece	Dec	0.0	San Marino	Apr	0.3
dr1mm	Portugal	Mar	0.1	Estonia	Jan	0.1
dr3mm	Portugal	Mar	0.1	Iceland	Sep	0.1
dtr	Belarus	Jan	0.0	Lithuania	Apr	0.0
etr	Latvia	Dec	0.1	San Marino	Apr	0.1
fd	Denmark	Mar	0.2	Estonia	Oct	0.0
fg	Liechtenstein	Jun	0.3	Liechtenstein	Jul	0.5
fg6bft	United Kingdom	Jan	0.0	United Kingdom	Jul	0.0
fgcalm	Liechtenstein	Jul	21.0	Liechtenstein	Jun	7.0
gd4	Greece	Dec	0.1	San Marino	Jun	1.4
gtg	Greece	Dec	0.0	Belarus	Mar	0.1
gtn	Lithuania	Oct	0.0	Finland	Dec	0.1
gtx	Greece	Dec	0.0	Ukraine	Mar	0.1
hd17	Belarus	Mar	2.1	-	-	-

hi	Ukraine	Feb	0.2	Ukraine	Oct	0.3
id	Estonia	Mar	0.1	Sweden	May	0.0
mi	Moldova	Oct	0.1	Luxembourg	Oct	0.0
ntg	Romania	Oct	0.0	Estonia	Dec	0.1
ogs10	Andorra	Jun	0.0	Denmark	Apr	0.0
ogs6	Bulgaria	Mar	0.0	Ireland	Mar	0.0
pet	Denmark	Jun	0.1	Bosnia and Herzegovina	Jul	0.3
PHDI	San Marino	Jul	0.1	Estonia	Mar	0.0
prcptot	Portugal	Mar	0.9	Iceland	Sep	0.6
r10mm	Andorra	Dec	0.0	Iceland	Nov	0.0
r20mm	Portugal	Nov	0.0	Slovenia	Oct	0.0
r95tot	Ireland	Sep	0.0	Iceland	Jan	0.0
r99tot	-	-	-	-	-	-
rh	Moldova	Sep	1.1	Ukraine	Oct	0.4
rti	Portugal	Mar	0.9	Iceland	Sep	0.6
rx1day	San Marino	Jul	0.1	Slovenia	Oct	0.2
rx5d	Portugal	Mar	0.4	Montenegro	Mar	0.4
scPDSI	San Marino	Jun	0.0	Montenegro	Mar	0.0
sdii	San Marino	Jul	0.1	Malta	Sep	0.1
slp	Greece	Jan	0.1	Moldova	Jan	0.2
spei-1	Malta	Jul	0.0	Estonia	Jan	0.0
spei-3	Portugal	Aug	0.0	Estonia	Mar	0.0
spei-6	Portugal	Jul	0.0	Estonia	Mar	0.0
spei-9	Portugal	Sep	0.0	Estonia	Jun	0.0
spei-12	San Marino	Aug	0.0	Iceland	Jan	0.0
spei-24	San Marino	Aug	0.0	Iceland	Jan	0.0

spi-1	Portugal	Mar	0.0	Estonia	Jan	0.0
spi-3	Portugal	Mar	0.0	Lithuania	Jan	0.1
spi-6	Portugal	Jul	0.0	Estonia	Mar	0.0
spi-9	Portugal	Sep	0.0	Estonia	Nov	0.0
spi-12	Albania	Nov	0.0	Estonia	Jul	0.0
spi-24	Albania	Apr	0.0	Estonia	Jul	0.0
su	Greece	Sep	0.0	San Marino	Jun	0.2
tn10p	Malta	Apr	0.2	Greece	Dec	0.0
tn90p	Greece	Dec	0.0	Sweden	May	0.5
tnn	Romania	Dec	0.0	Latvia	Mar	0.1
tnx	Andorra	Nov	0.0	Belarus	Mar	0.1
tr	Slovenia	Jul	0.0	San Marino	Jul	0.2
tx10p	Malta	May	0.2	Greece	Jul	0.1
tx90p	Greece	Dec	0.0	San Marino	Jun	0.2
txn	Liechtenstein	Sep	0.0	Finland	Dec	0.1
txx	Malta	Feb	0.0	Belarus	Mar	0.1
utci	Russia	Dec	0.5	Liechtenstein	Jul	3.9
vcd	-	-	-	-	-	-
vdtr	Andorra	Sep	0.0	Bosnia and Herzegovina	Apr	0.0
vwd	-	-	-	-	-	-
wci	Ukraine	May	0.5	Portugal	May	0.7
WPLM	France	Aug	0.1	Estonia	Mar	0.0
wsdi	-	-	-	-	-	-
xtg	Iceland	Nov	0.0	Belarus	Mar	0.1
zcd	Denmark	Mar	0.1	Finland	Mar	0.1

Appendix B

Supplementary materials for chapter 4

Figure S1: Correlation of extreme climate indices

A) Method 1: Pearson

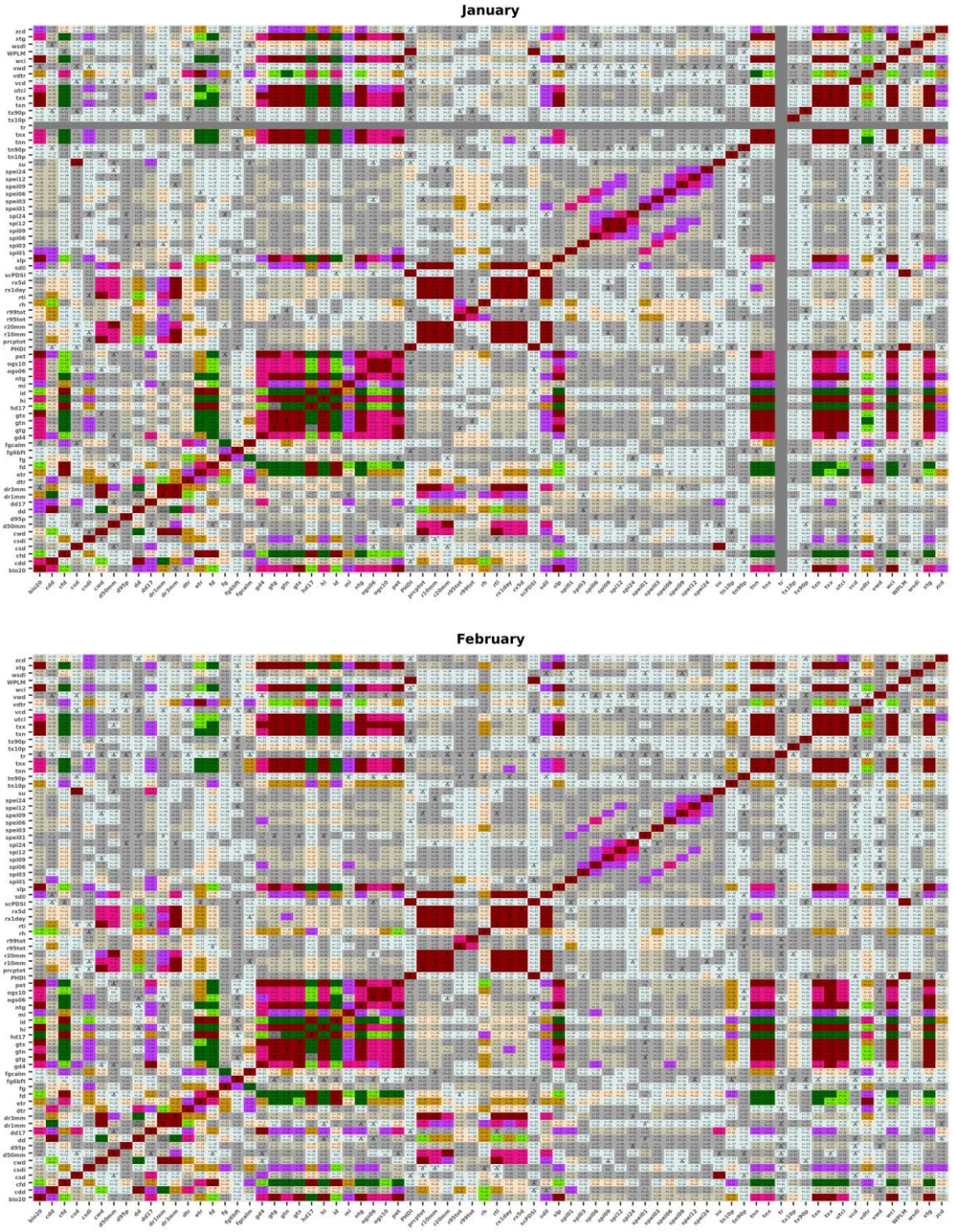

March

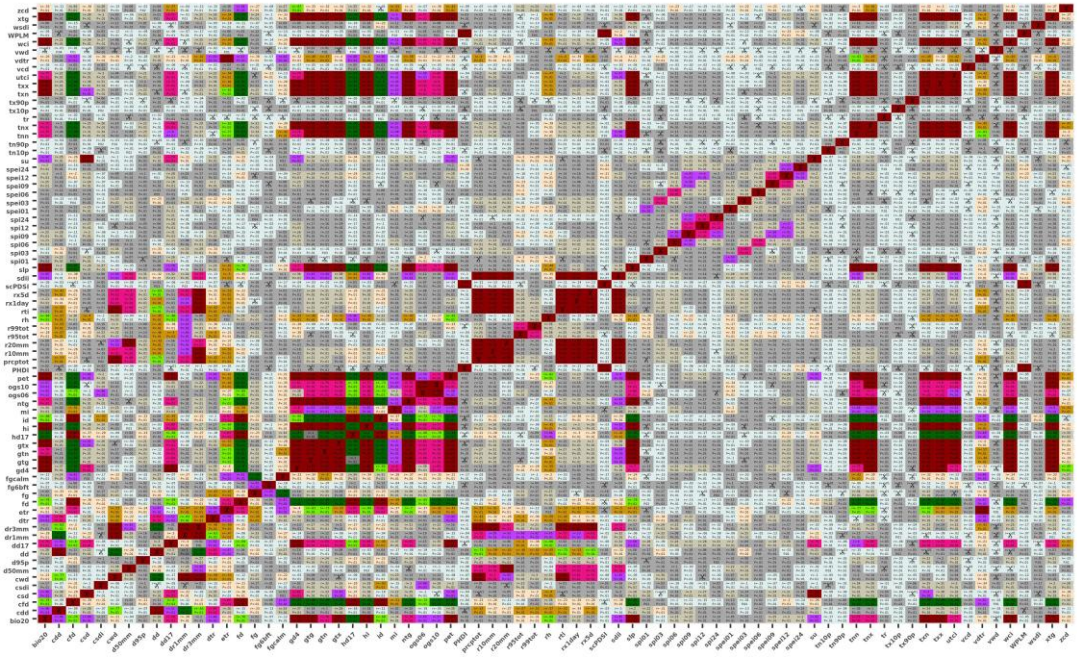

April

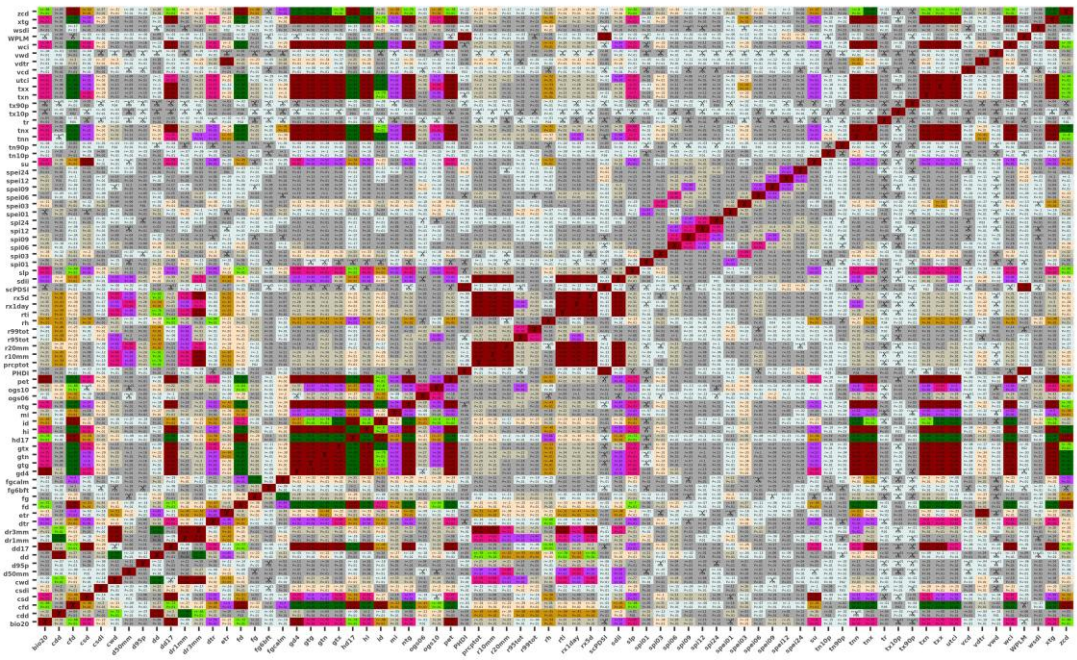

May

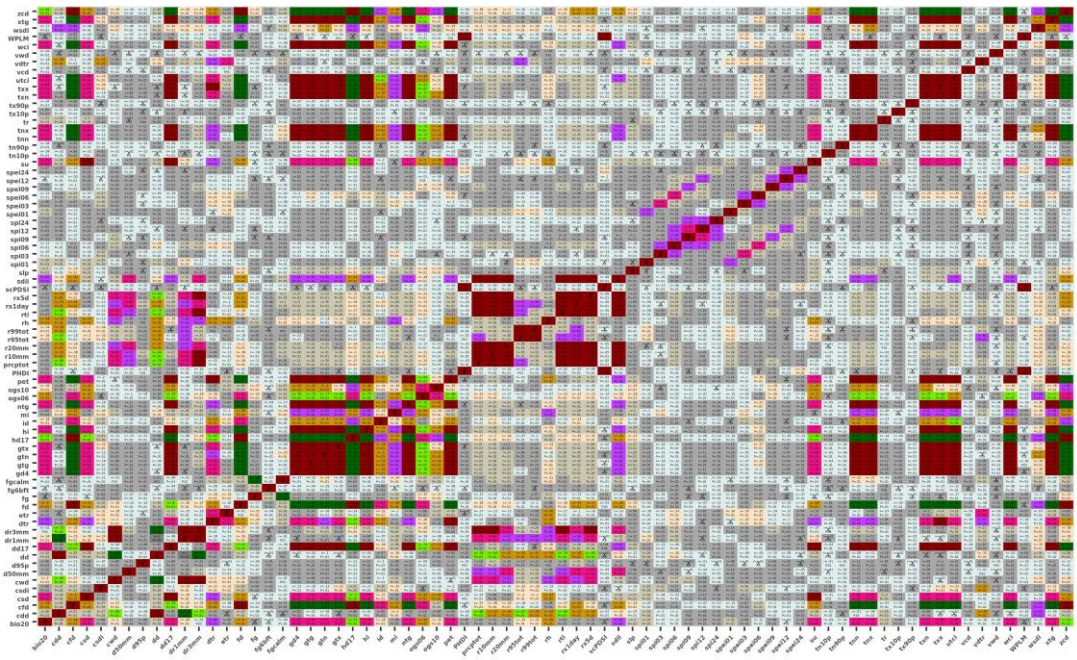

June

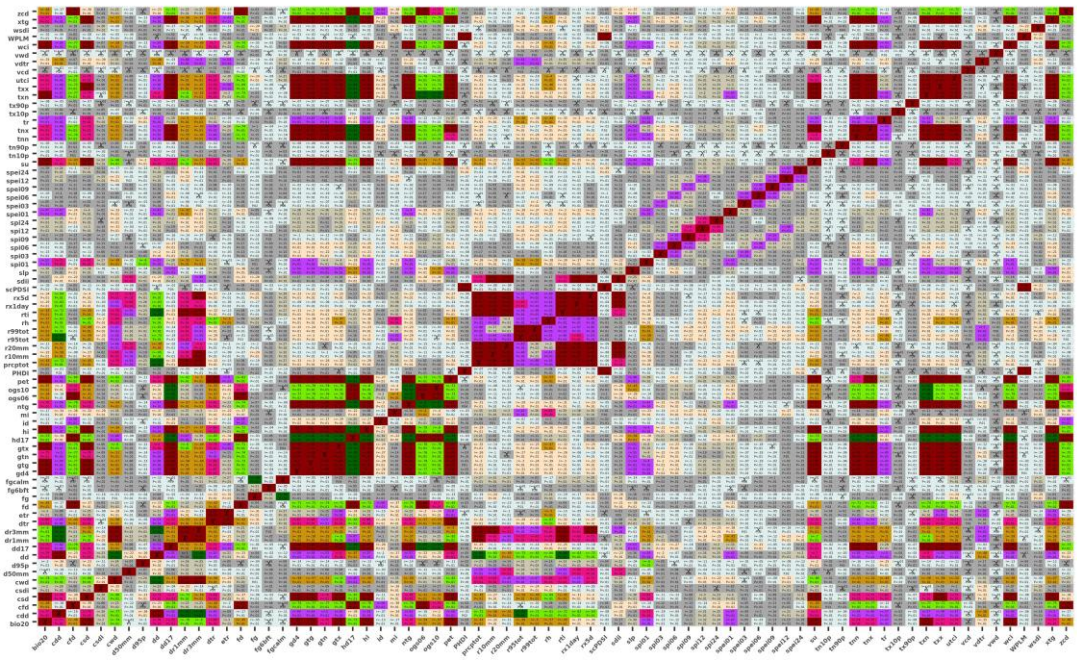

July

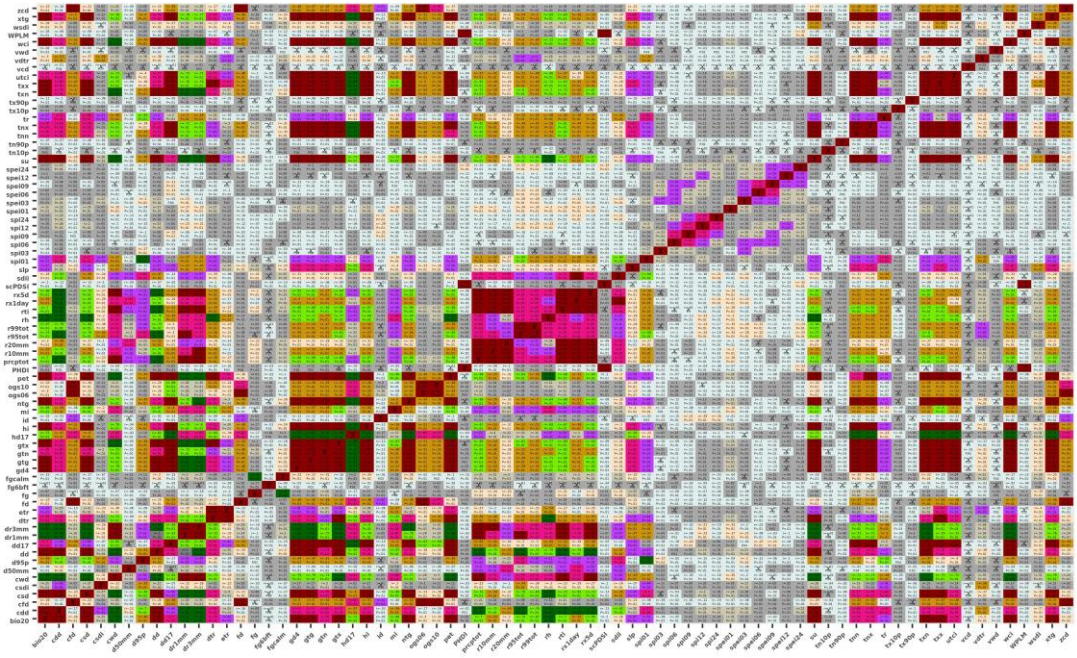

August

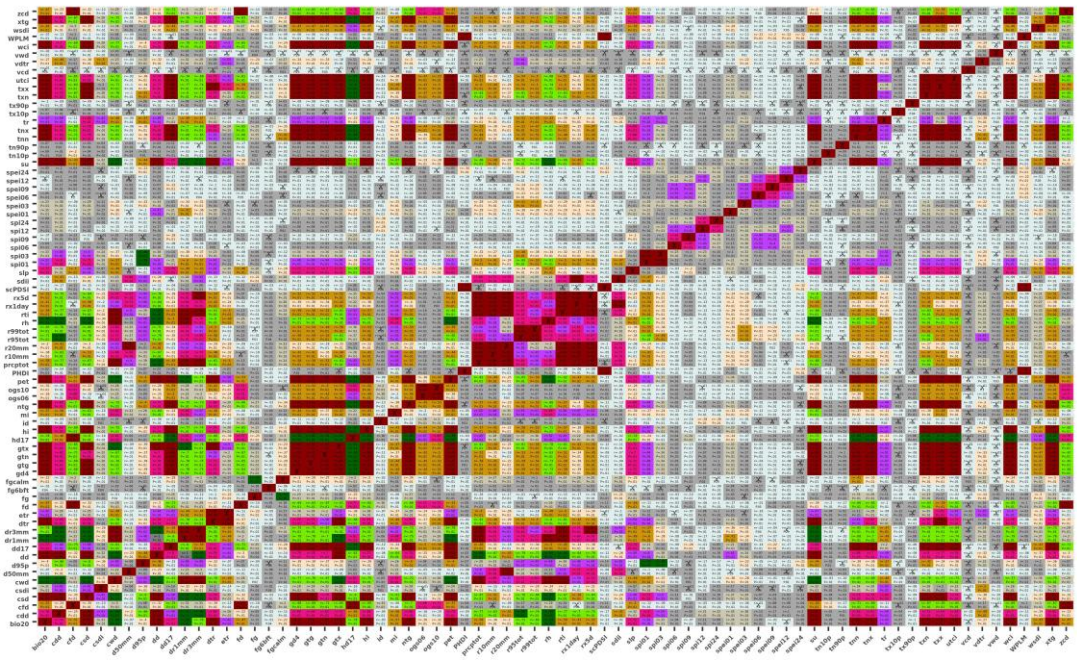

September

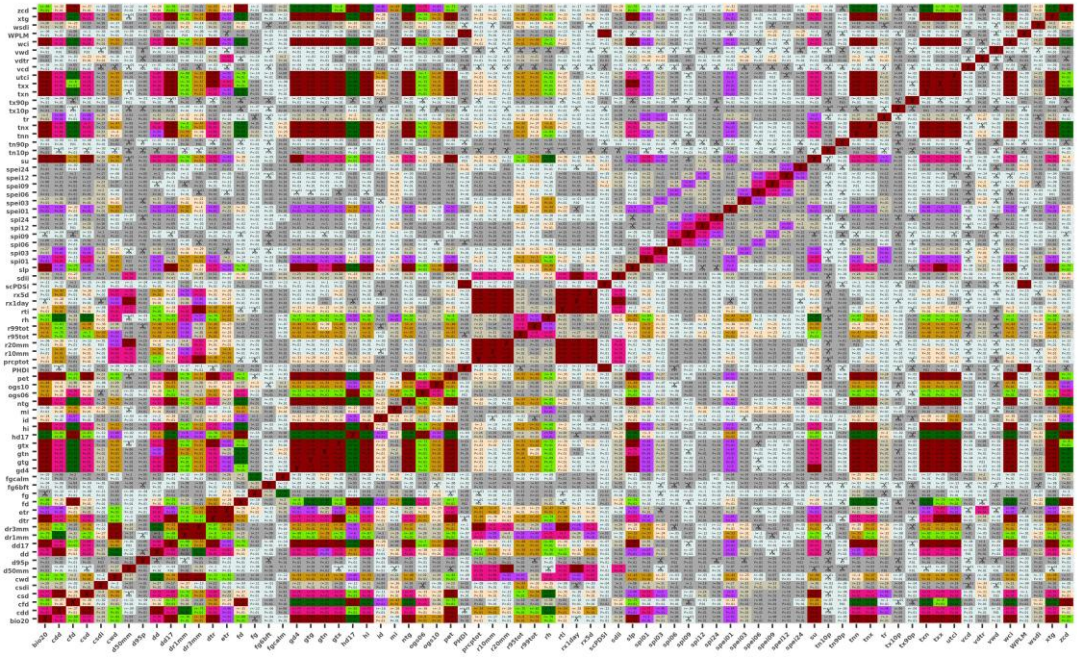

October

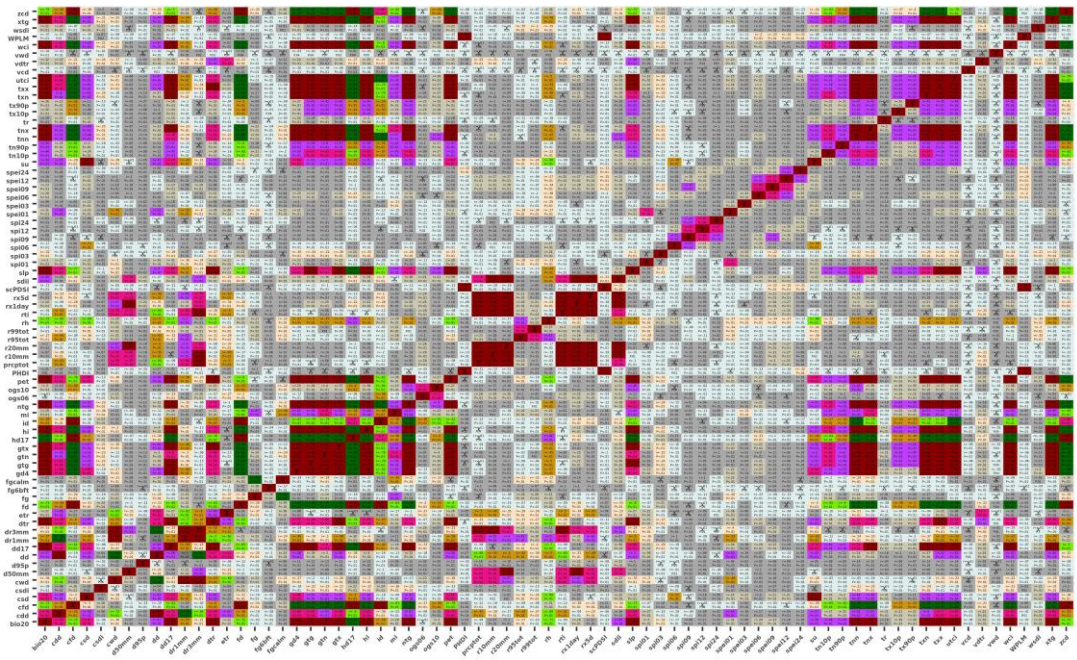

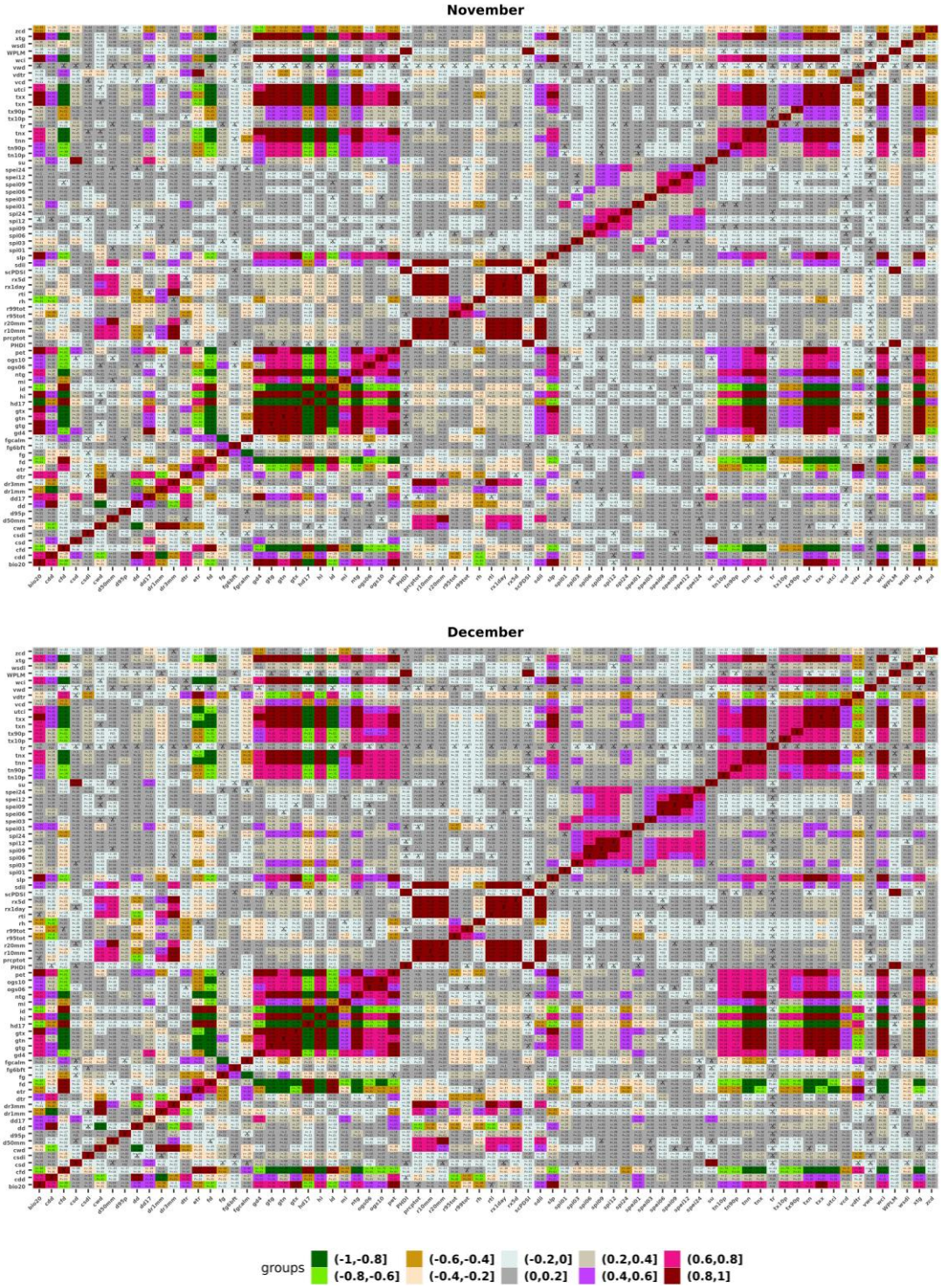
November
December
groups
(-1,-0.8]
(-0.8,-0.6]
(-0.6,-0.4]
(-0.4,-0.2]
(-0.2,0]
(0,0.2]
(0.2,0.4]
(0.4,0.6]
(0.6,0.8]
(0.8,1]

B) Method 2: Kendall

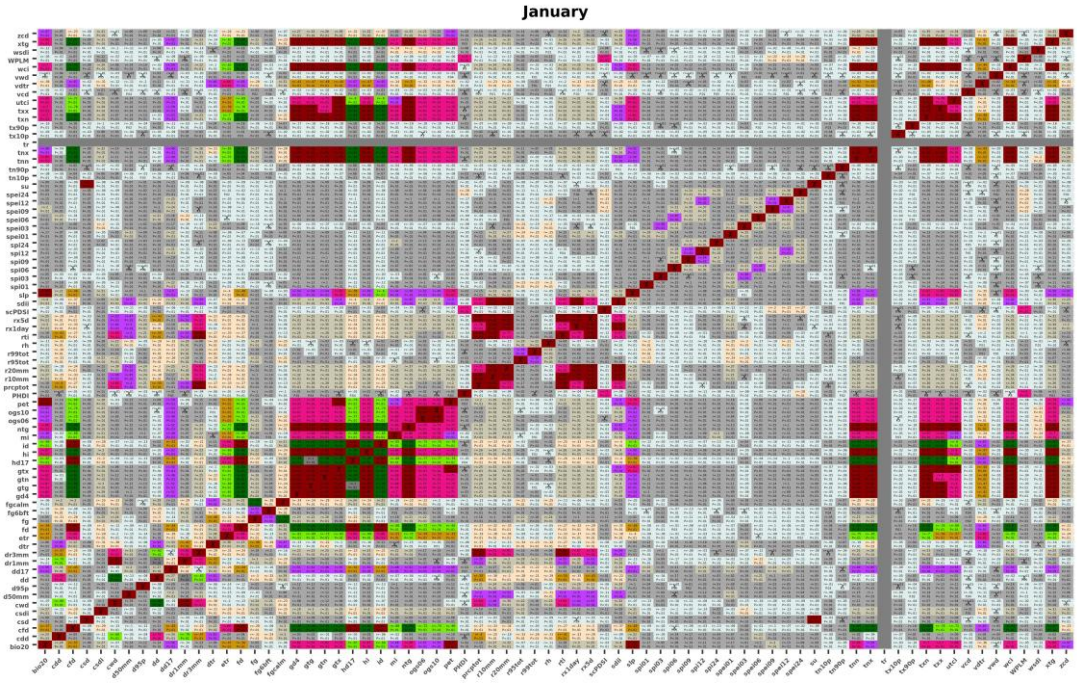

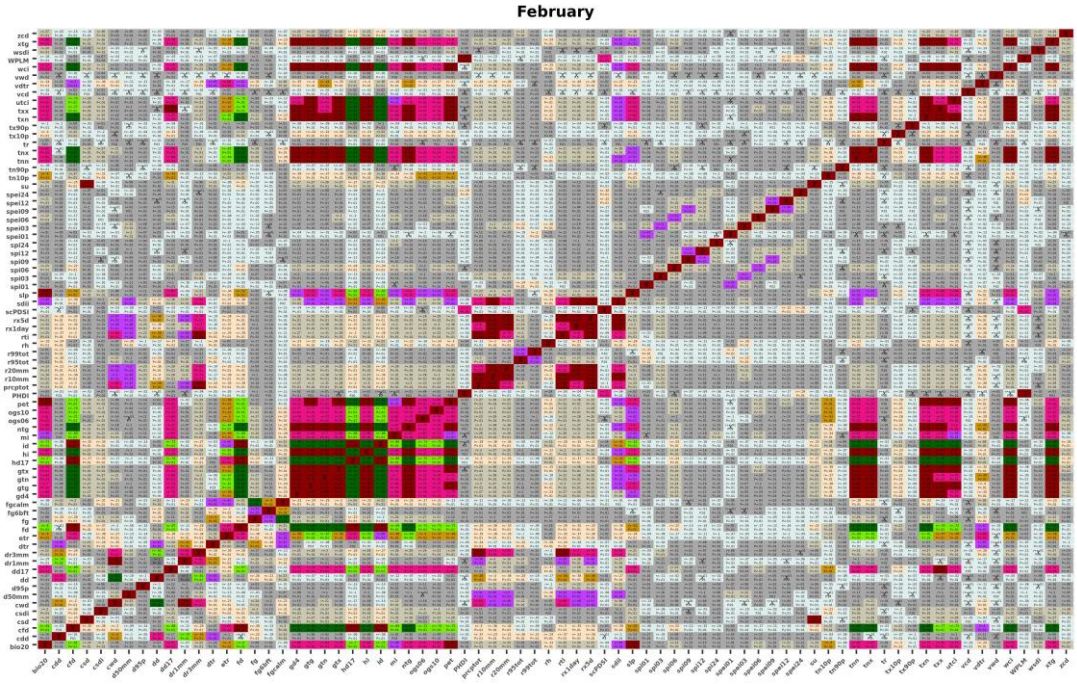

March

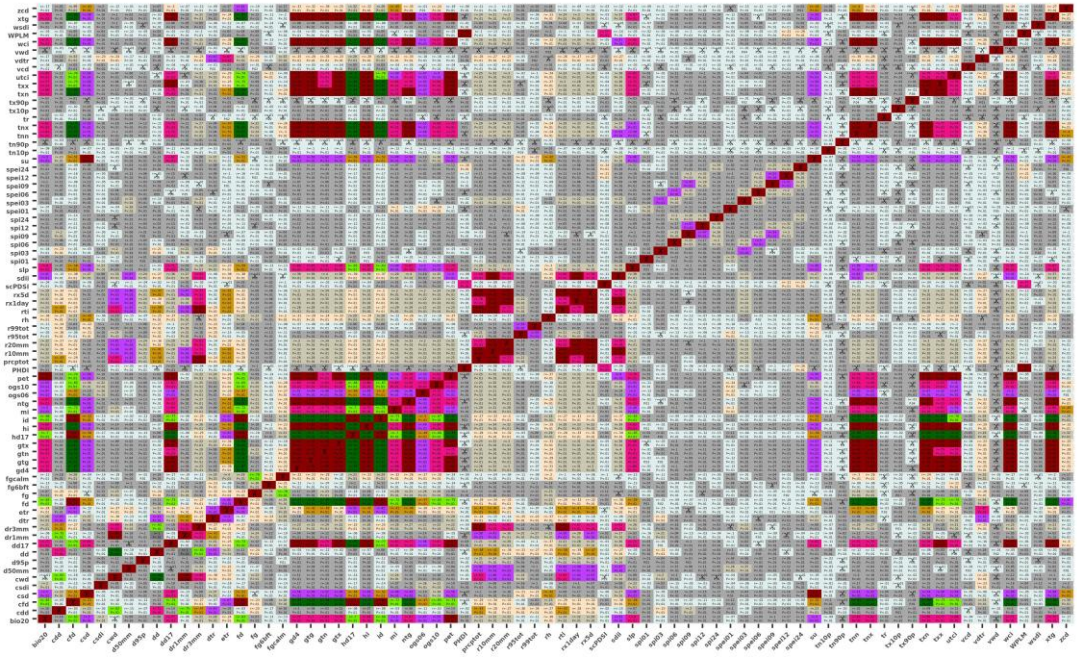

April

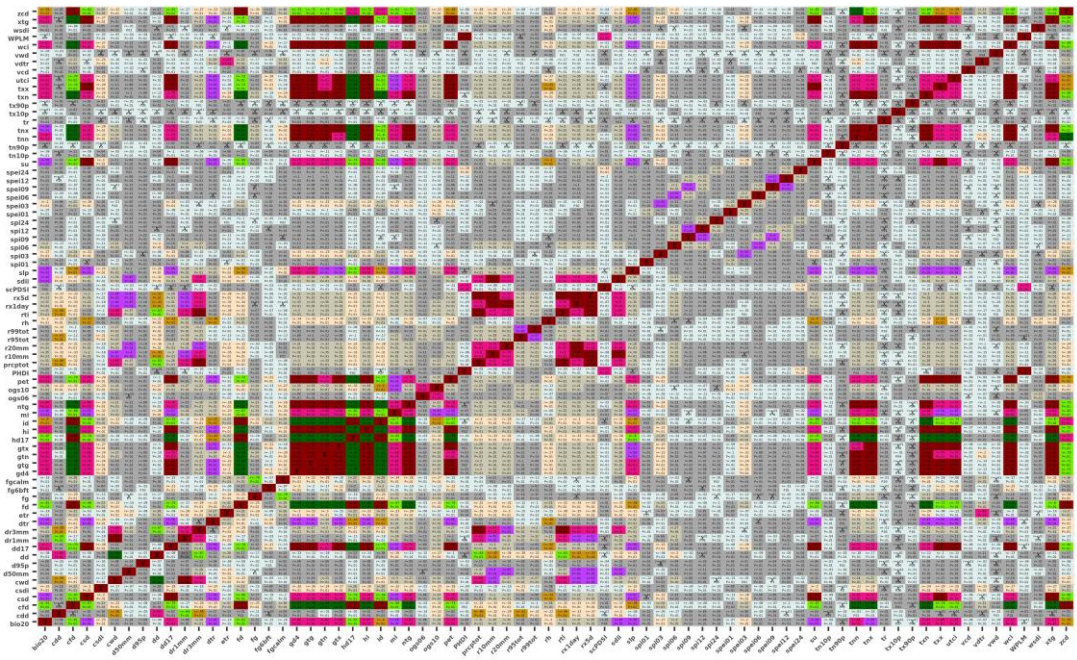

May

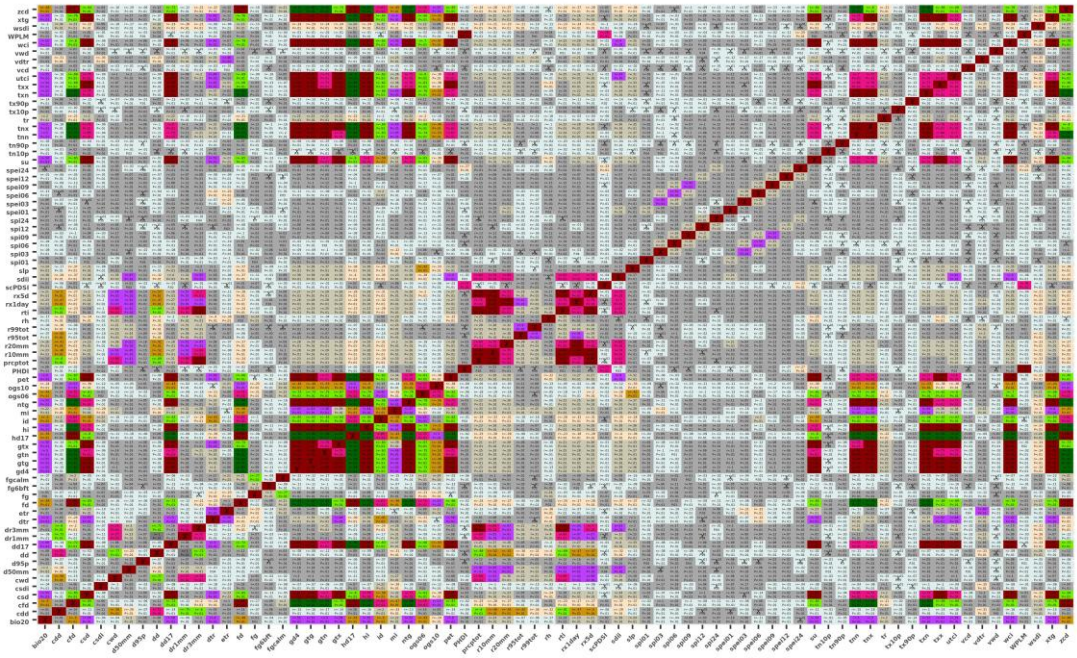

June

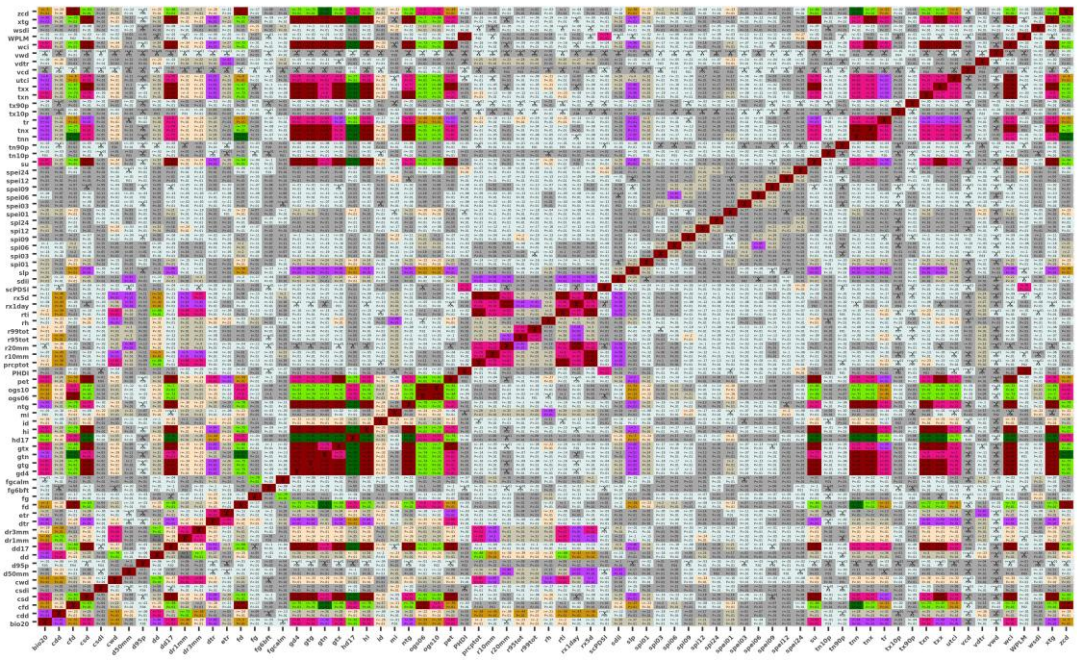

July

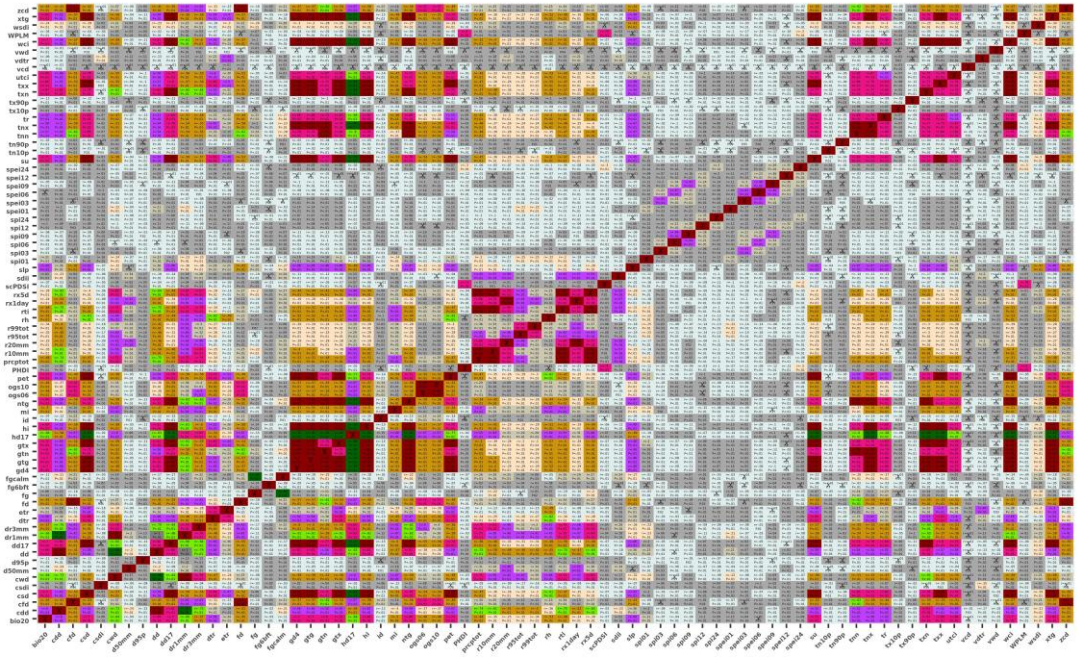

August

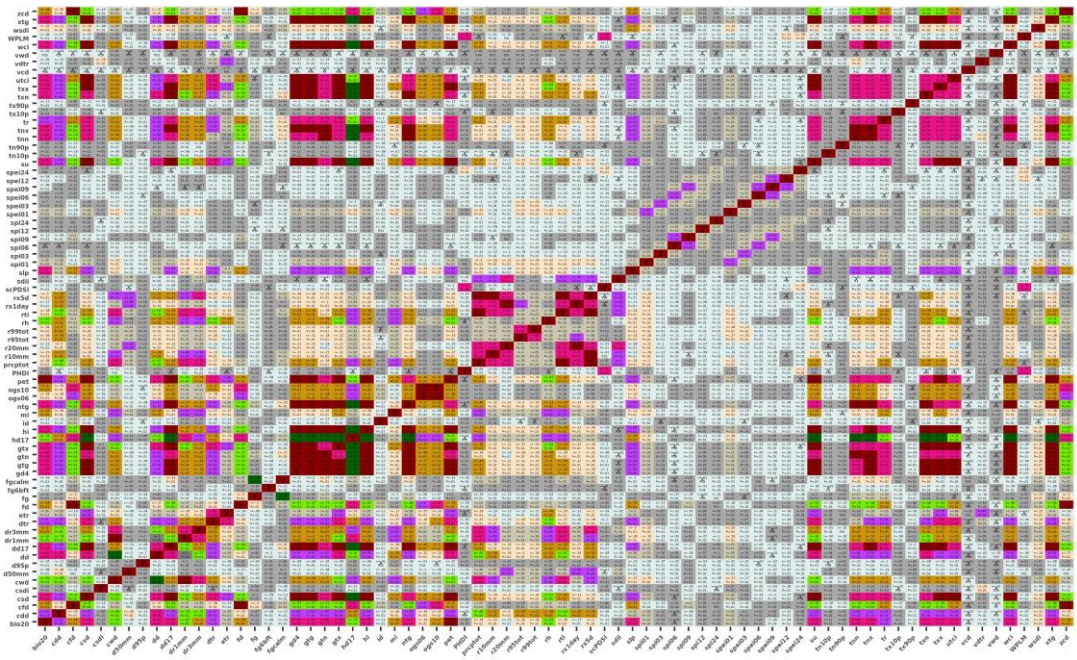

September

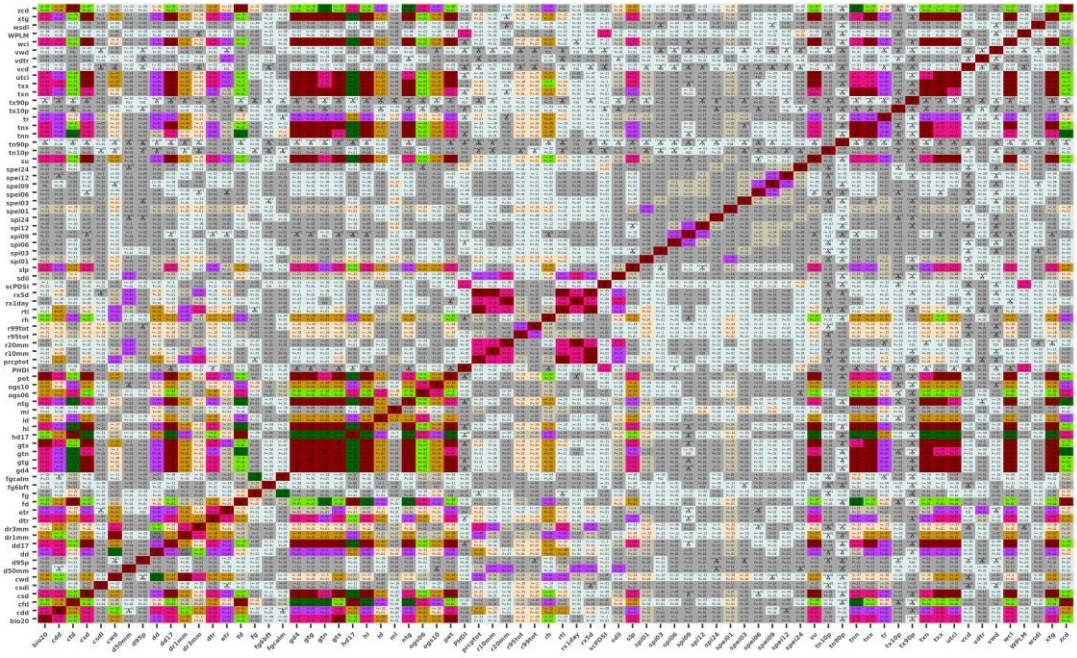

October

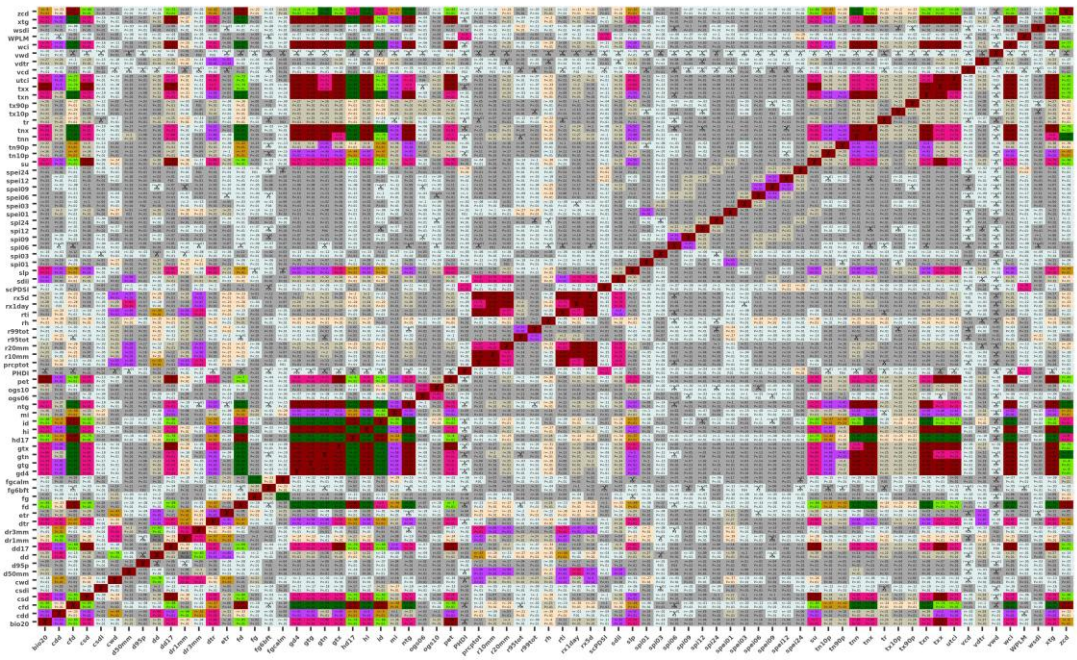

November

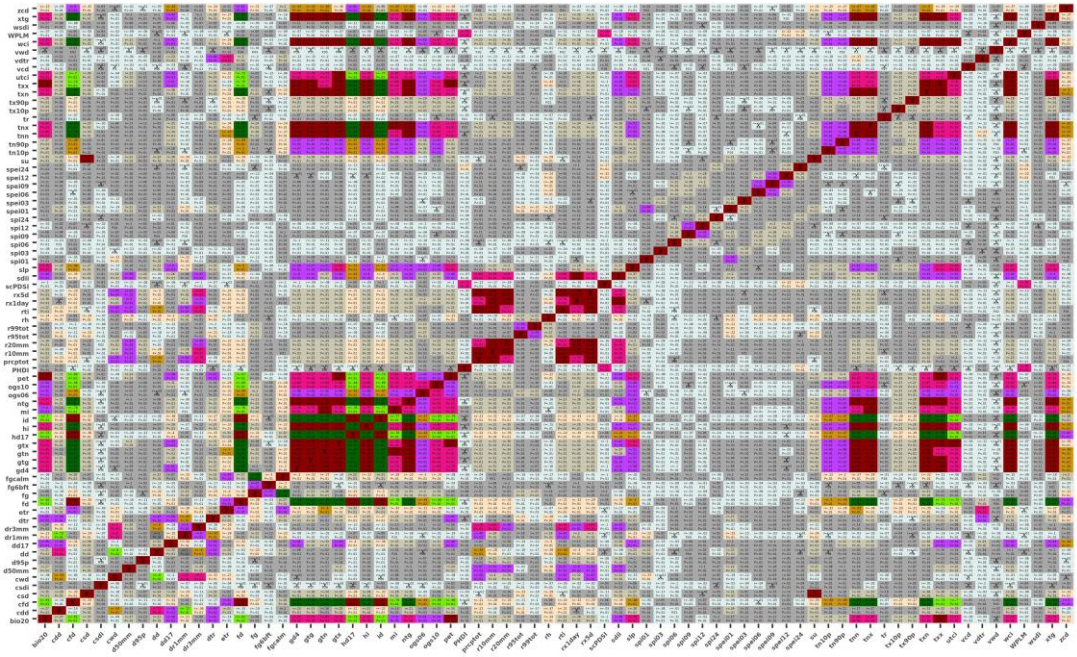

December

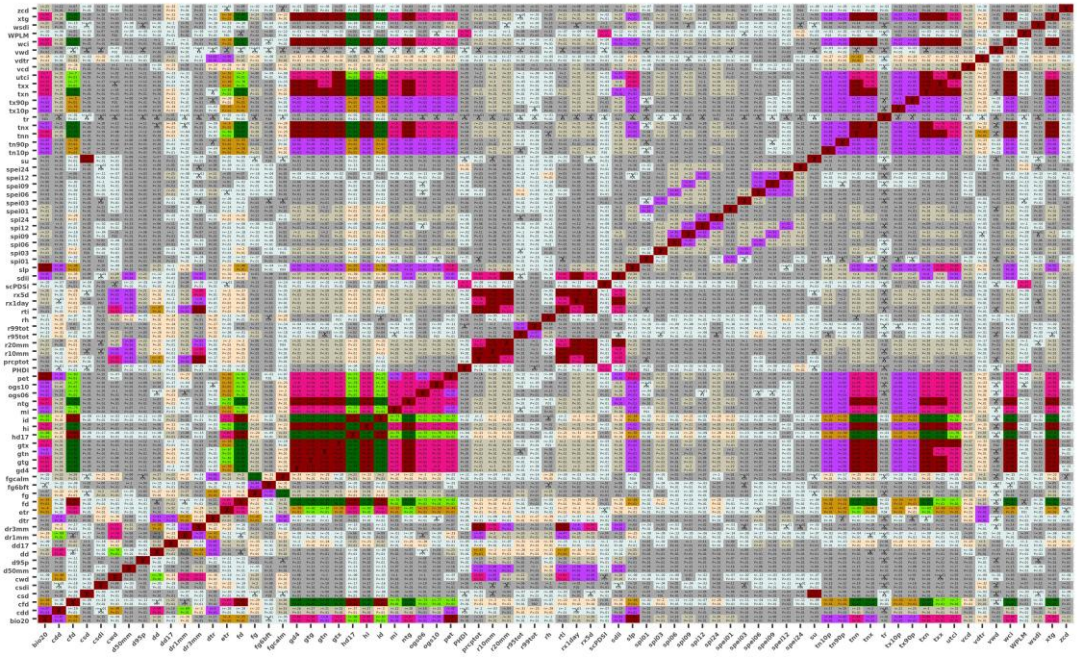



C) Method 3: Spearman

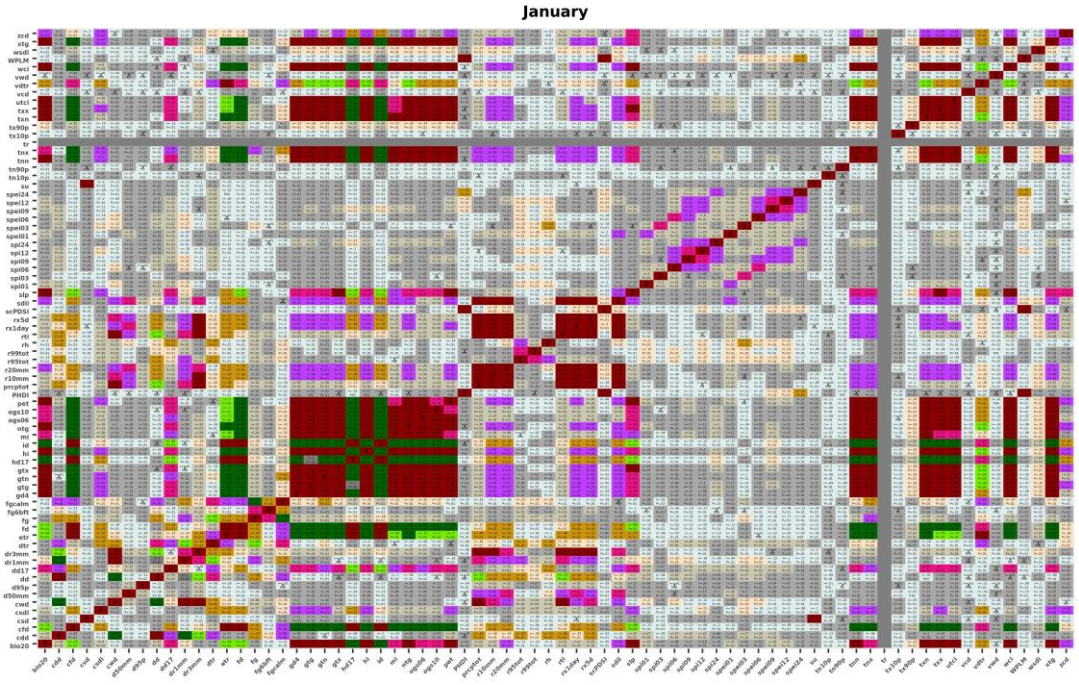

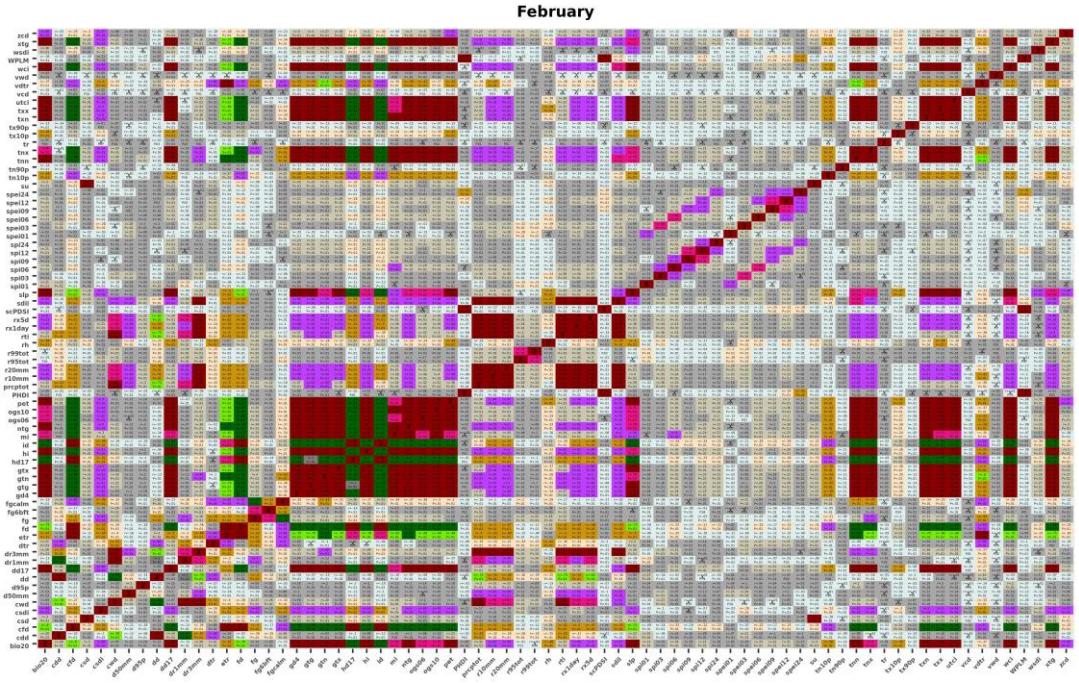

March

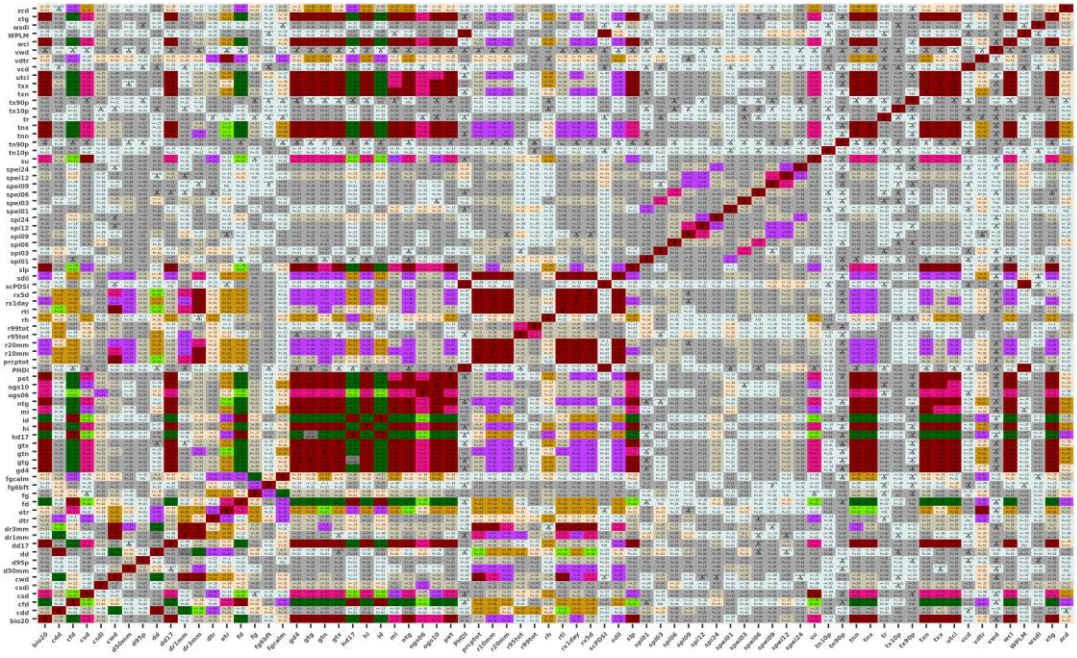

April

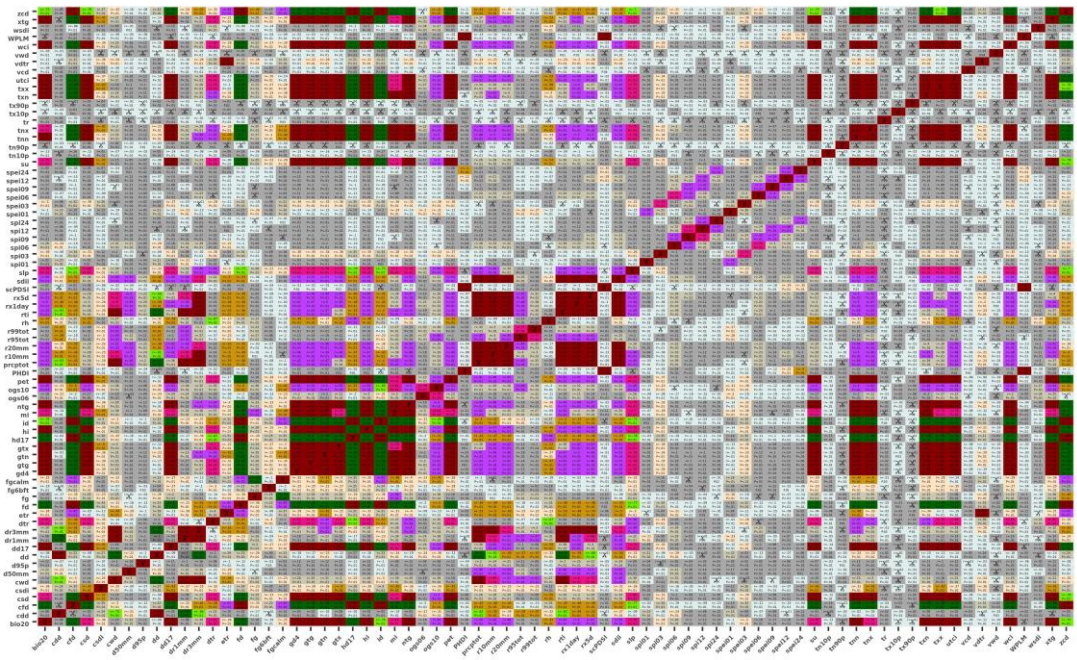

May

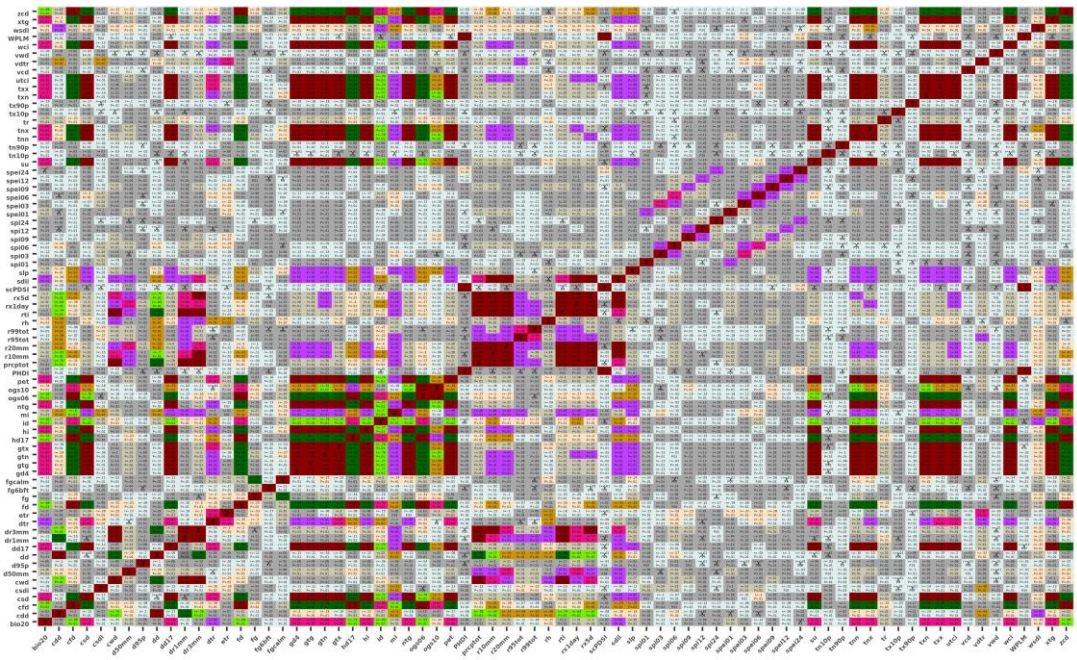

June

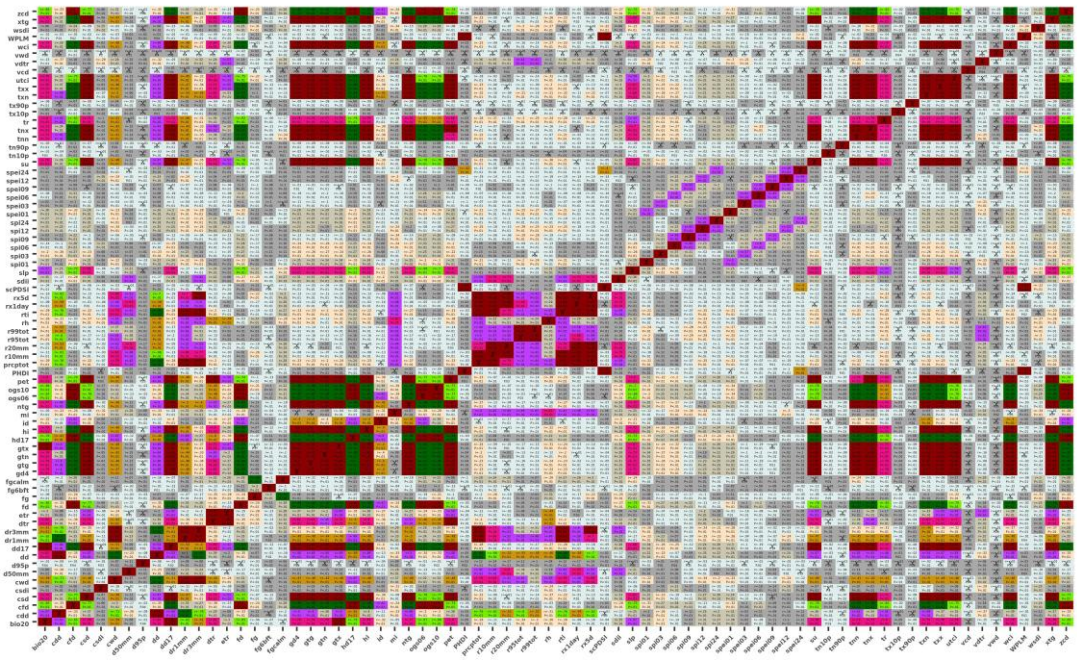

July

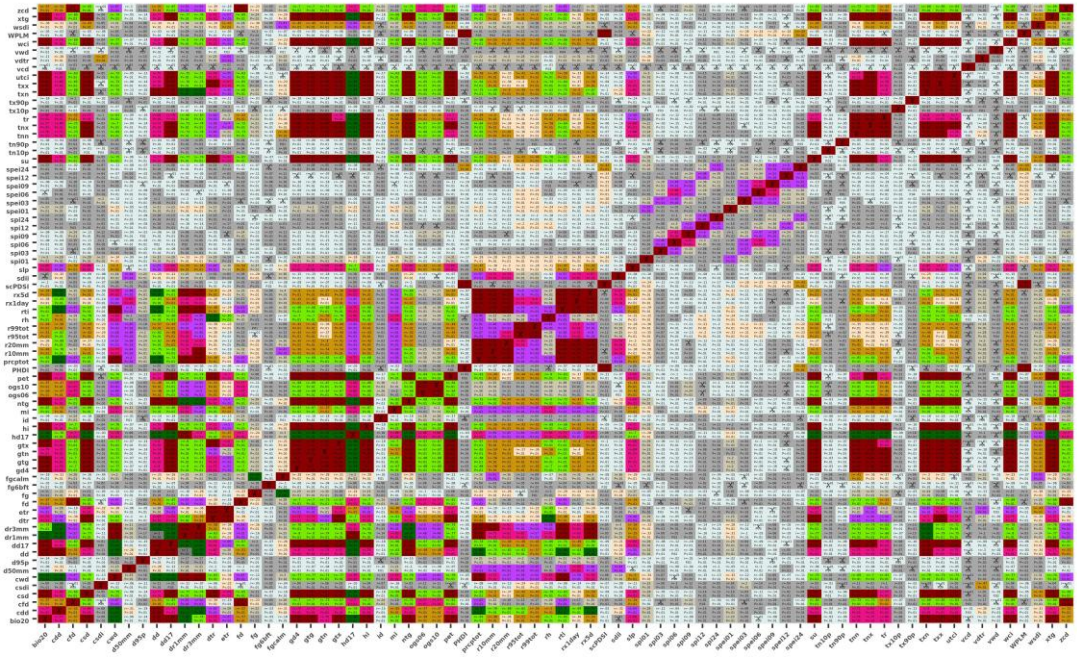

August

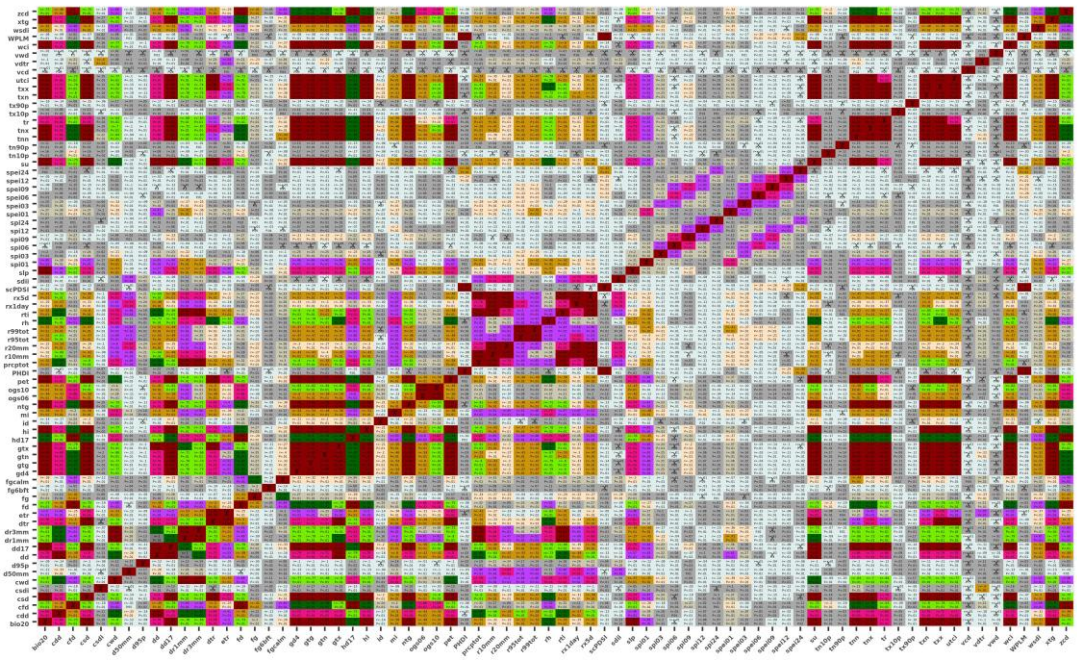

September

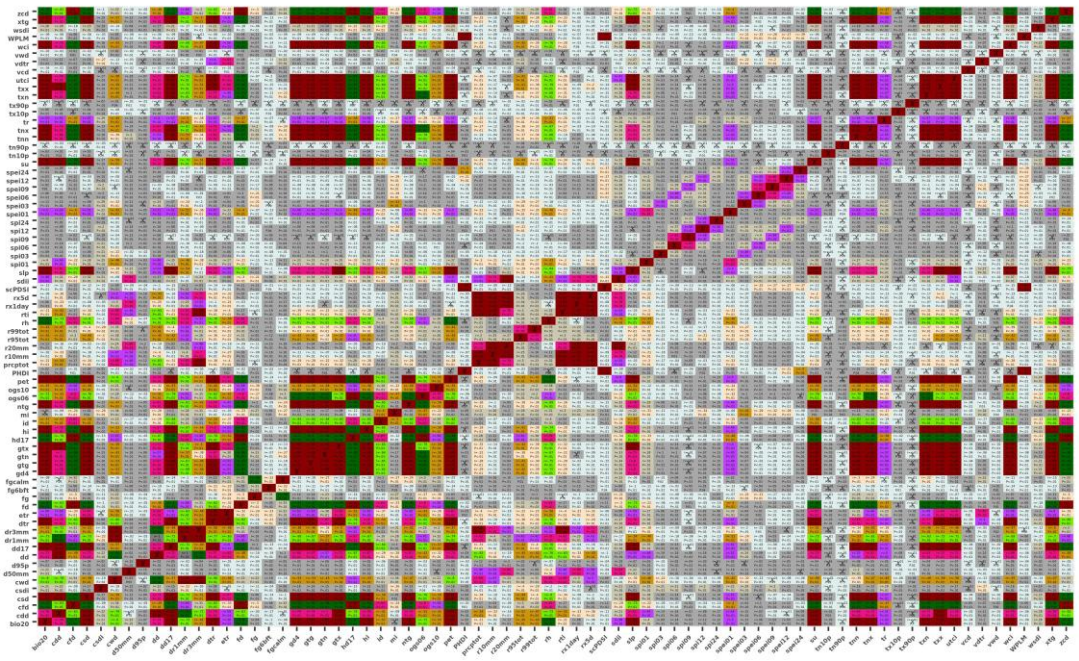

October

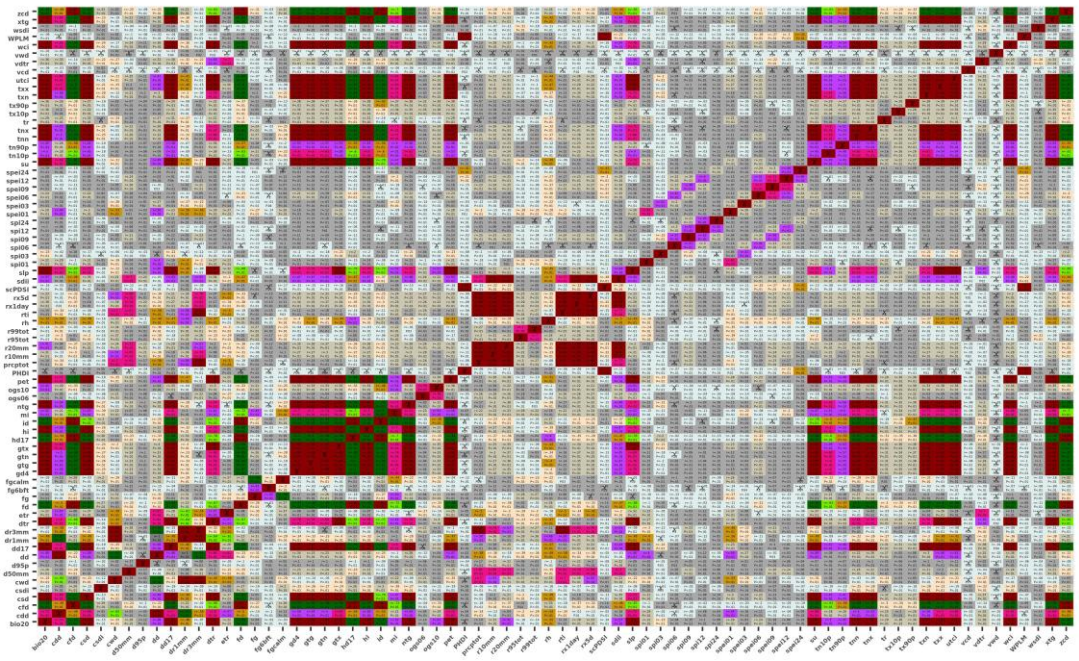

November

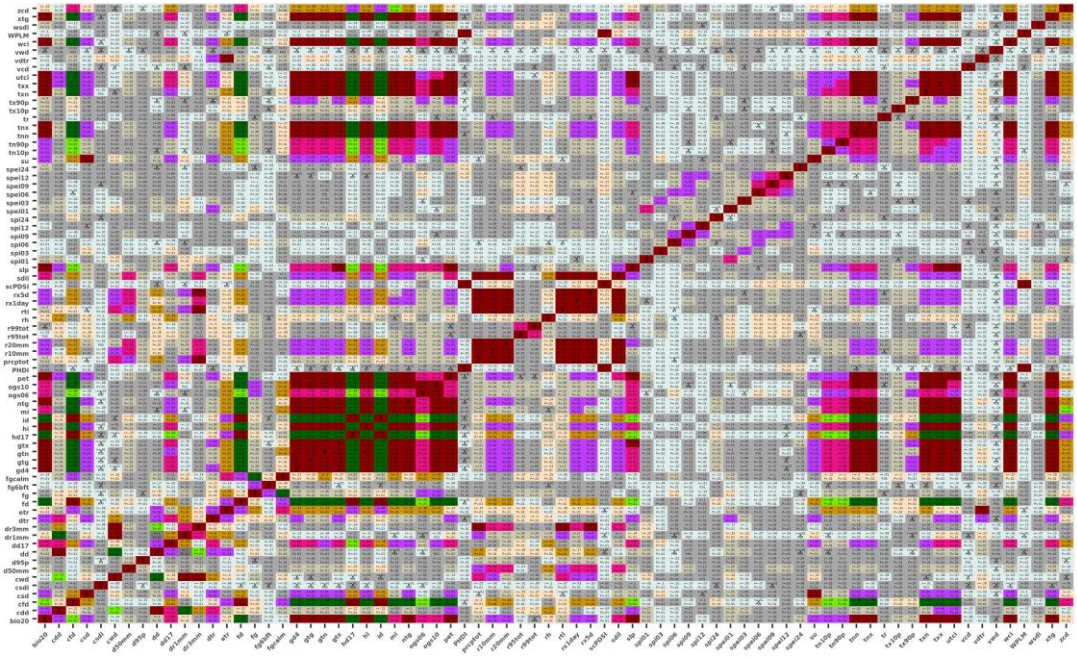

December

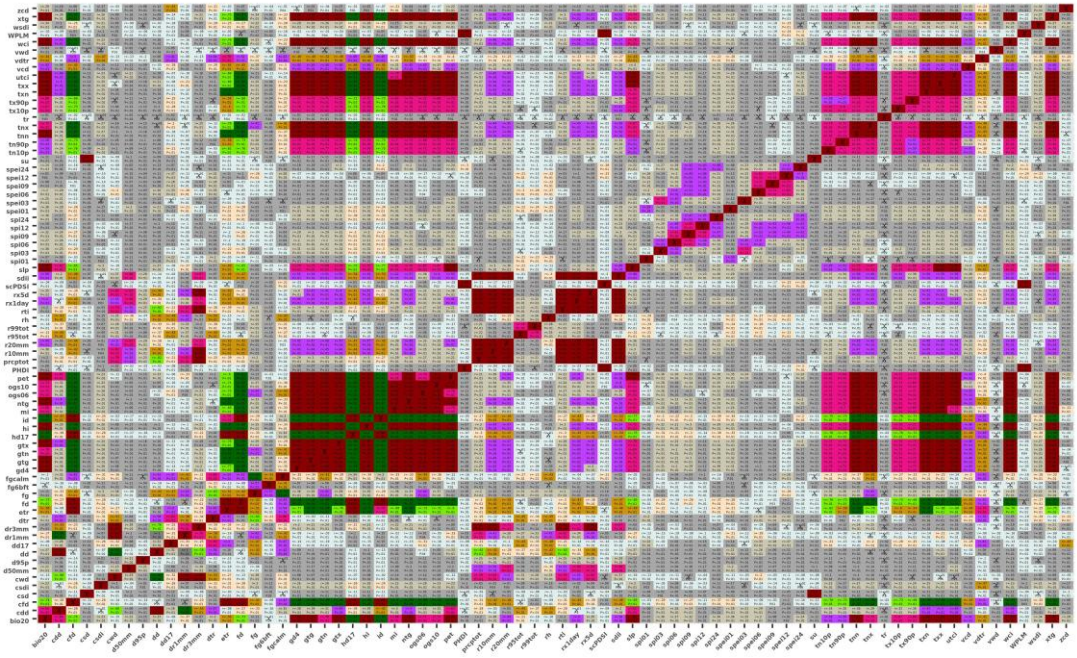



D) Maximum of Pearson, Kendall and Spearman

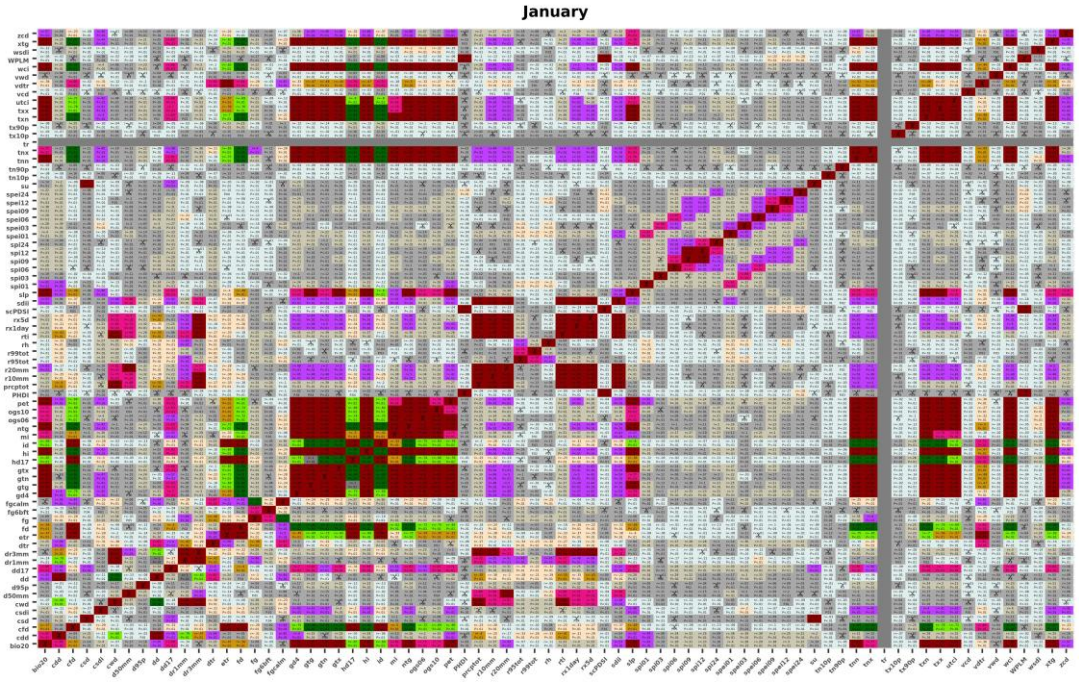

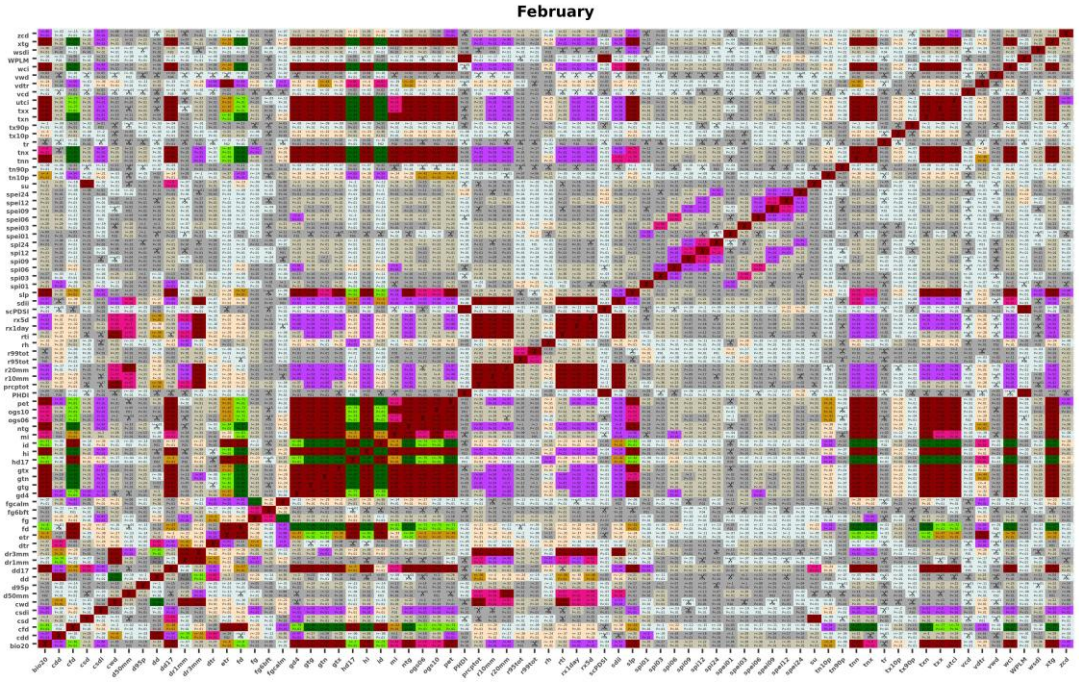

March

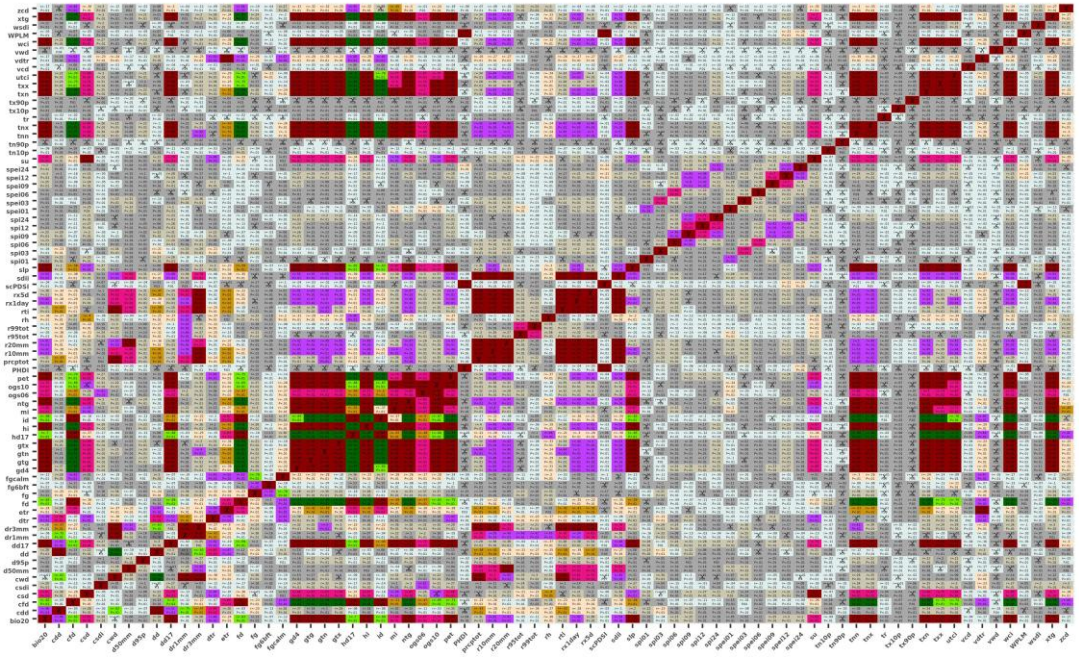

April

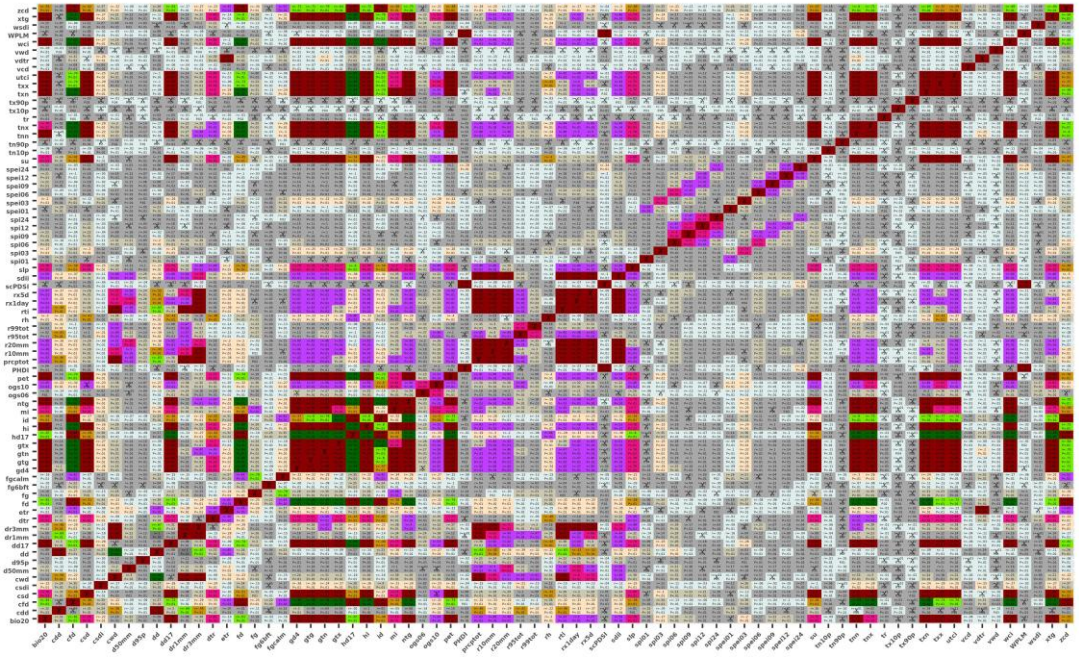

May

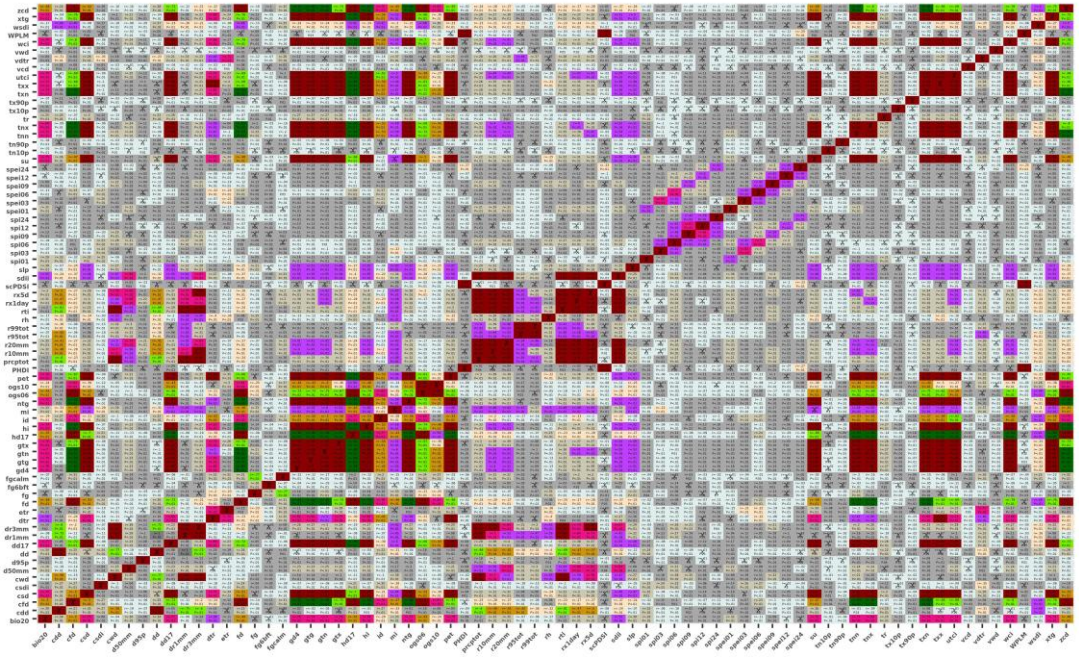

June

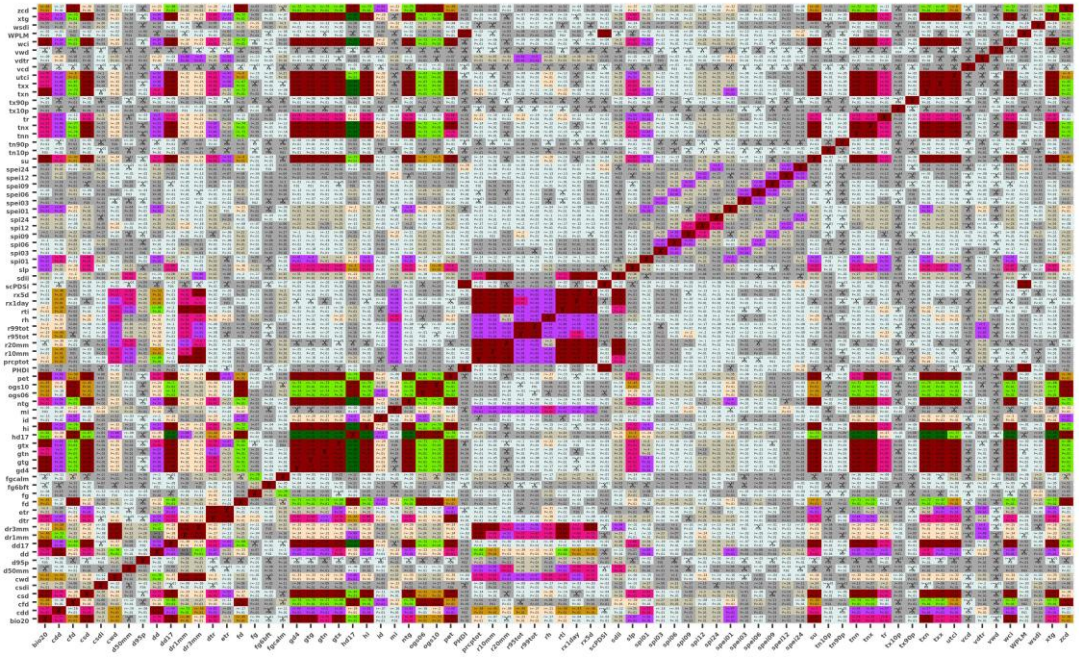

July

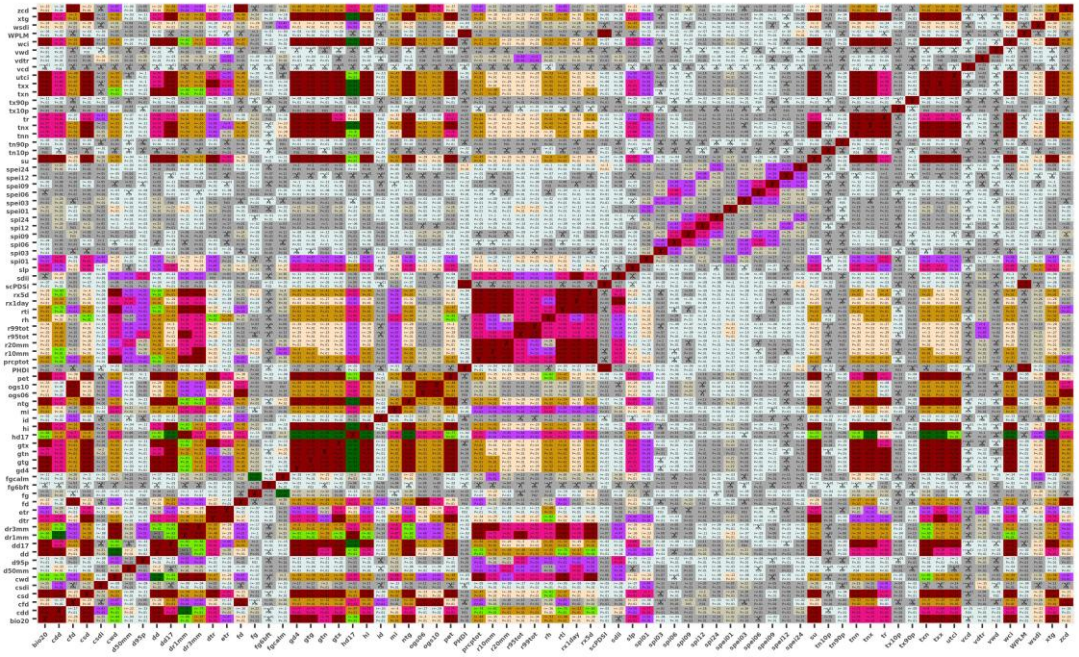

August

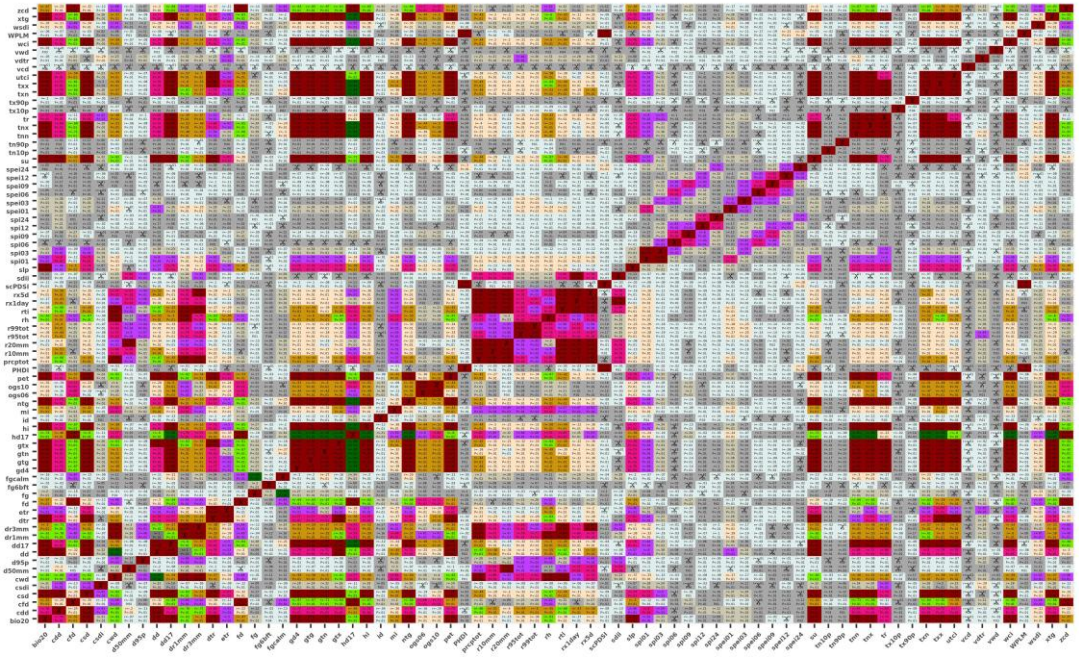

September

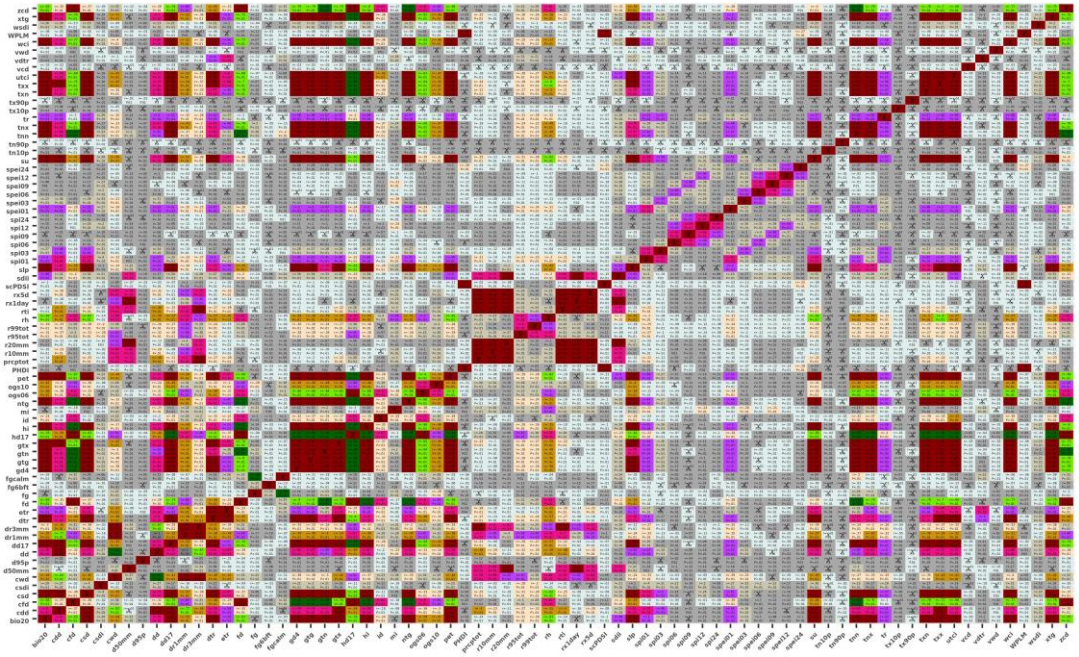

October

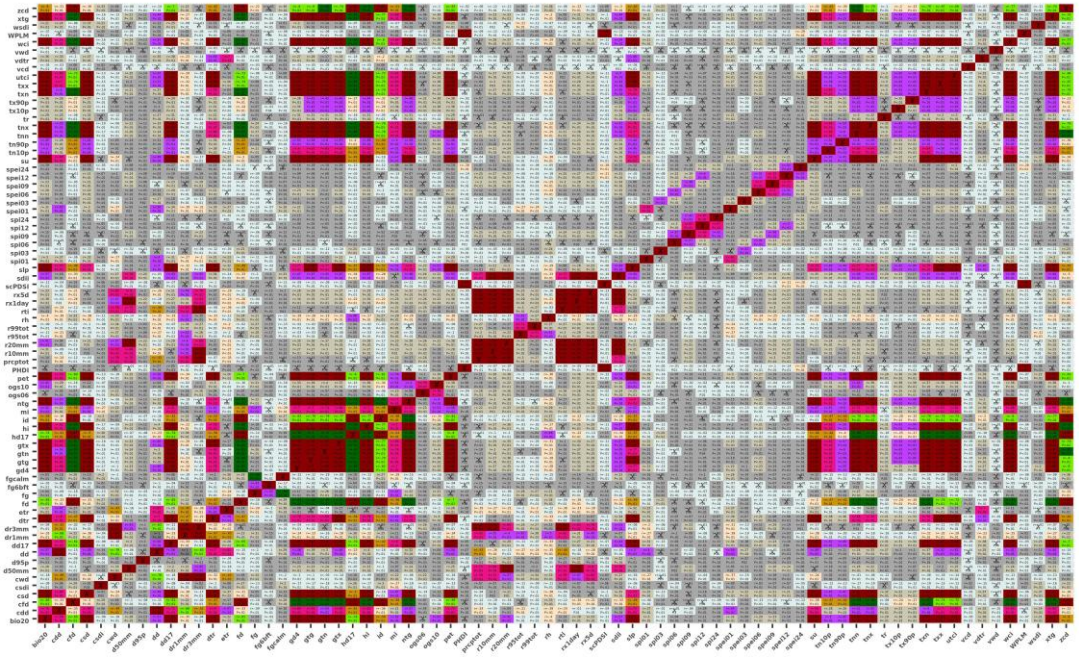

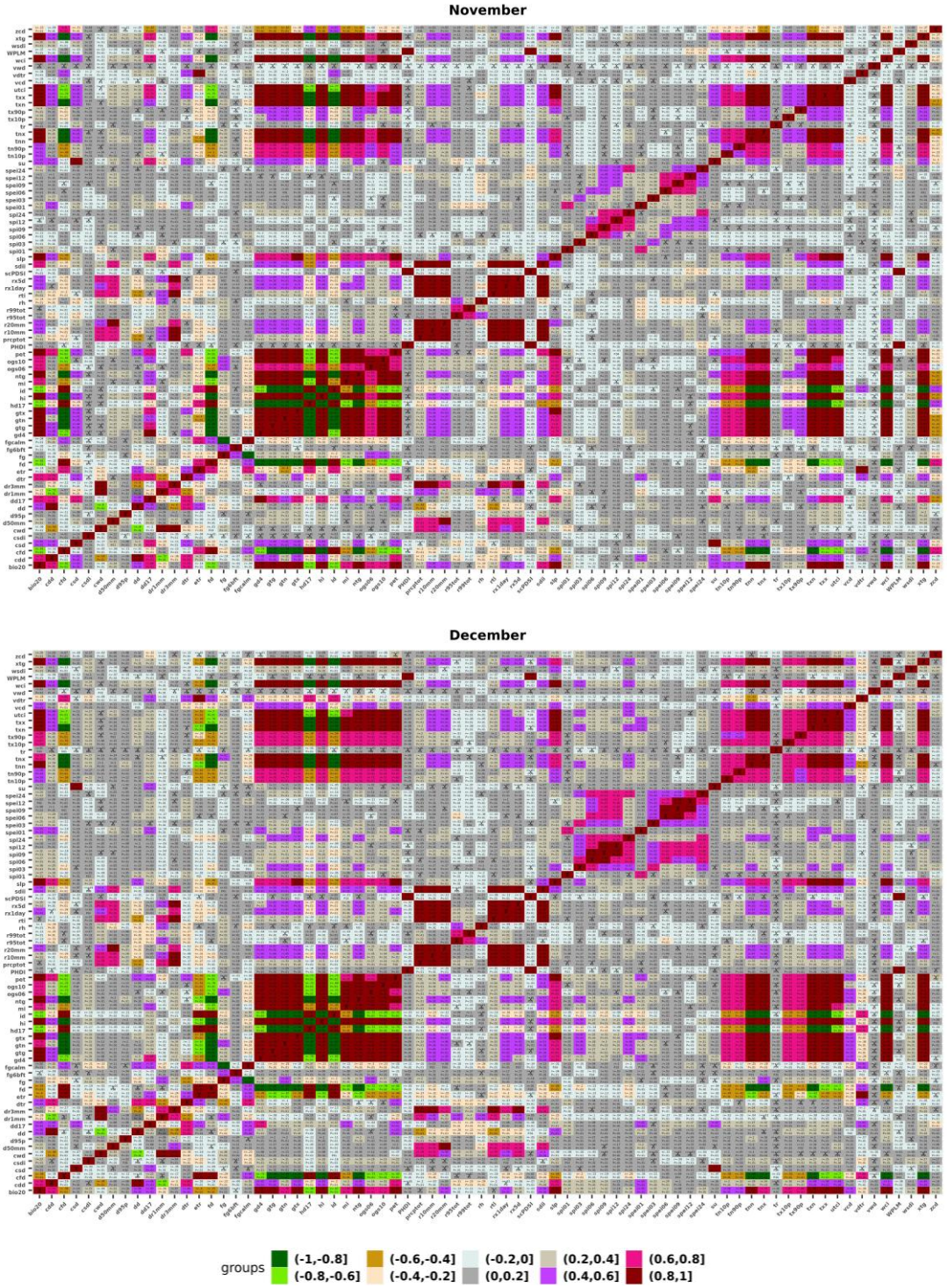

Figure S1: Comparison of various correlation methods to indicate the relation between different pairs of climate indices. A) Pearson B) Kendall C) Spearman and D) Maximum of Pearson, Kendall and Spearman. Dark brown and dark pink indicates strong positive correlation and shades of green indicate strong negative correlation between indices.

Figure S2: Risk maps of compound event

A) Bivariate pairs

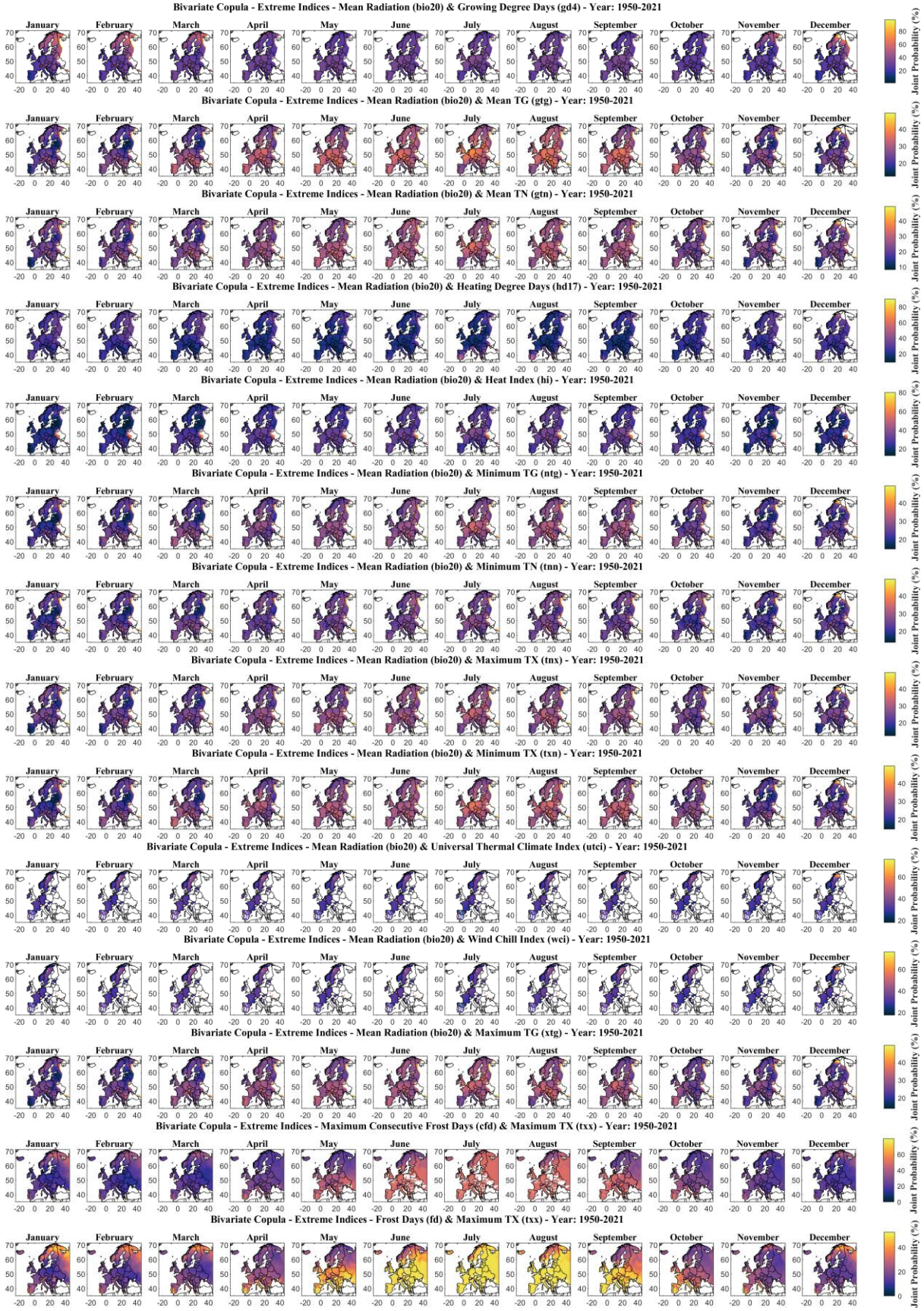

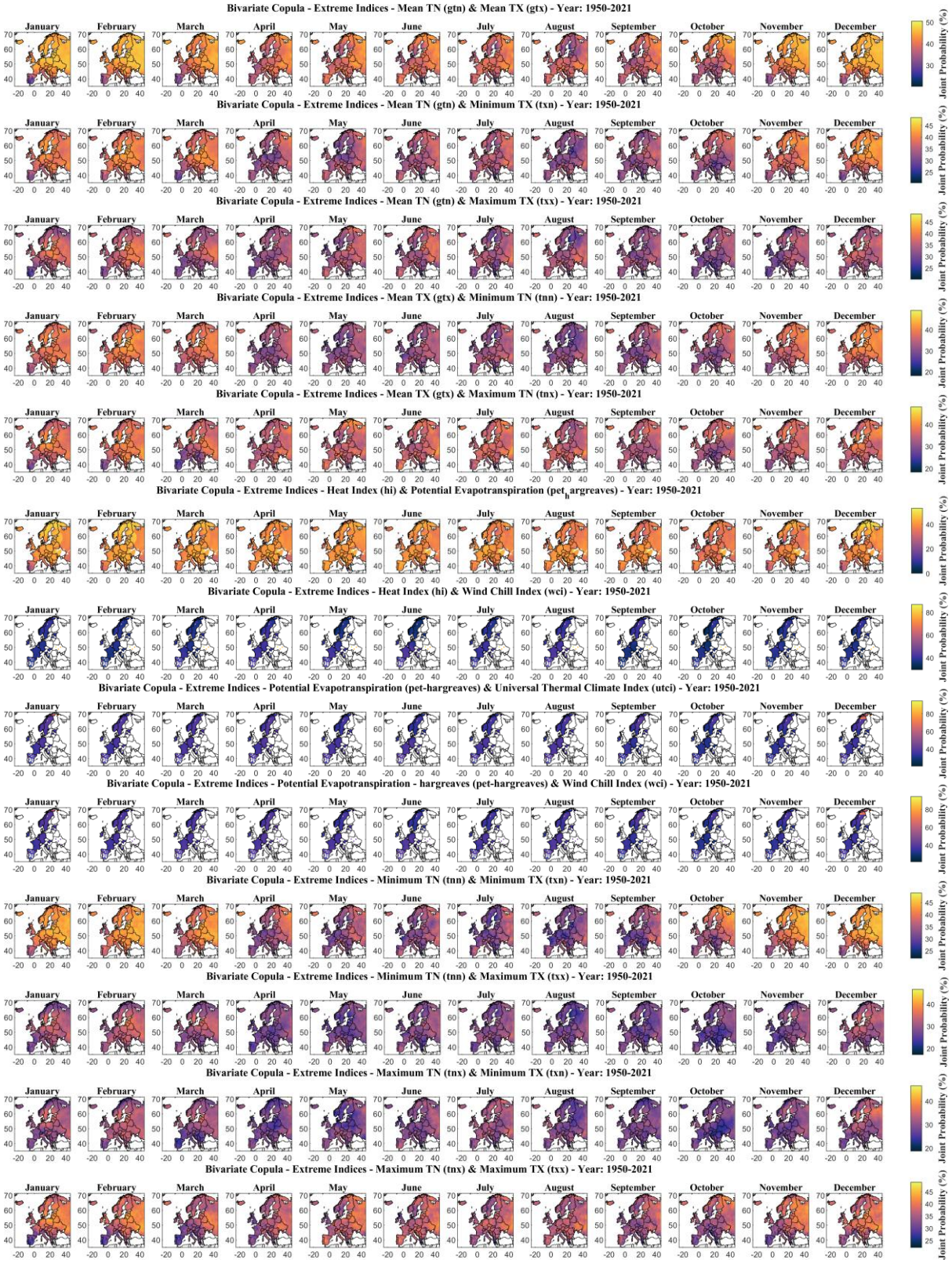
Bivariate Copula - Extreme Indices - Mean TN (gtn) & Mean TX (gtx) - Year: 1950-2021
Bivariate Copula - Extreme Indices - Mean TN (gtn) & Minimum TX (txn) - Year: 1950-2021
Bivariate Copula - Extreme Indices - Mean TN (gtn) & Maximum TX (txx) - Year: 1950-2021
Bivariate Copula - Extreme Indices - Mean TX (gtx) & Minimum TN (tnn) - Year: 1950-2021
Bivariate Copula - Extreme Indices - Mean TX (gtx) & Maximum TN (tnx) - Year: 1950-2021
Bivariate Copula - Extreme Indices - Heat Index (hi) & Potential Evapotranspiration (pet_h argreaves) - Year: 1950-2021
Bivariate Copula - Extreme Indices - Heat Index (hi) & Wind Chill Index (wci) - Year: 1950-2021
Bivariate Copula - Extreme Indices - Potential Evapotranspiration (pet-hargreaves) & Universal Thermal Climate Index (utci) - Year: 1950-2021
Bivariate Copula - Extreme Indices - Potential Evapotranspiration - hargreaves (pet-hargreaves) & Wind Chill Index (wci) - Year: 1950-2021
Bivariate Copula - Extreme Indices - Minimum TN (tnn) & Minimum TX (txn) - Year: 1950-2021
Bivariate Copula - Extreme Indices - Minimum TN (tnn) & Maximum TX (txx) - Year: 1950-2021
Bivariate Copula - Extreme Indices - Maximum TN (tnx) & Minimum TX (txn) - Year: 1950-2021
Bivariate Copula - Extreme Indices - Maximum TN (tnx) & Maximum TX (txx) - Year: 1950-2021
January
February
March
April
May
June
July
August
September
October
November
December
Joint Probability (%)

B) Trivariate pairs

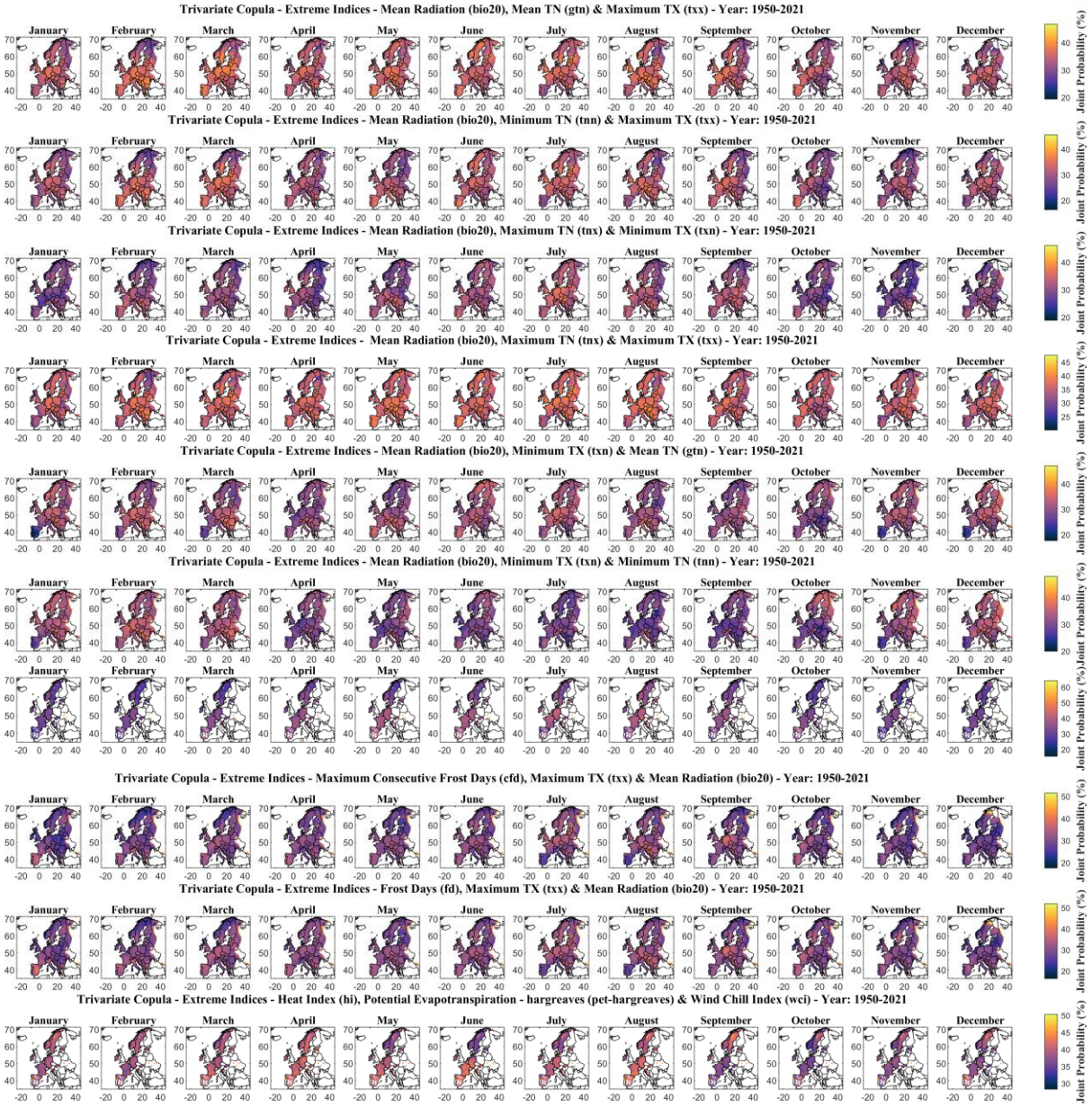

Figure S2: Risk maps of compound events of A) bivariate B) trivariate pairs obtained using best-fit copula approach. Risk maps depicts joint probability distribution of A) two B) three different climate indices. Yellow indicates the highest joint probability and dark blue indicates lowest joint probability of that compound event.

Figure S3: Box plot for comparison of various copula methods

A) Bivariate Analysis

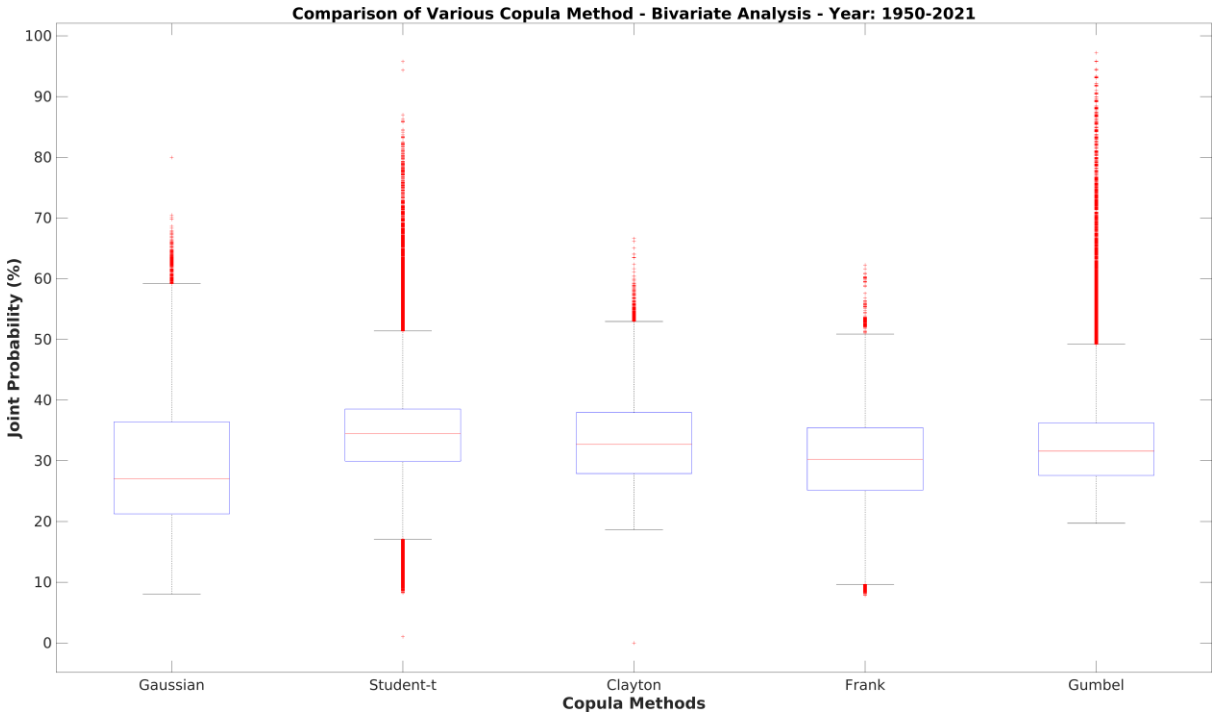

B) Trivariate Analysis

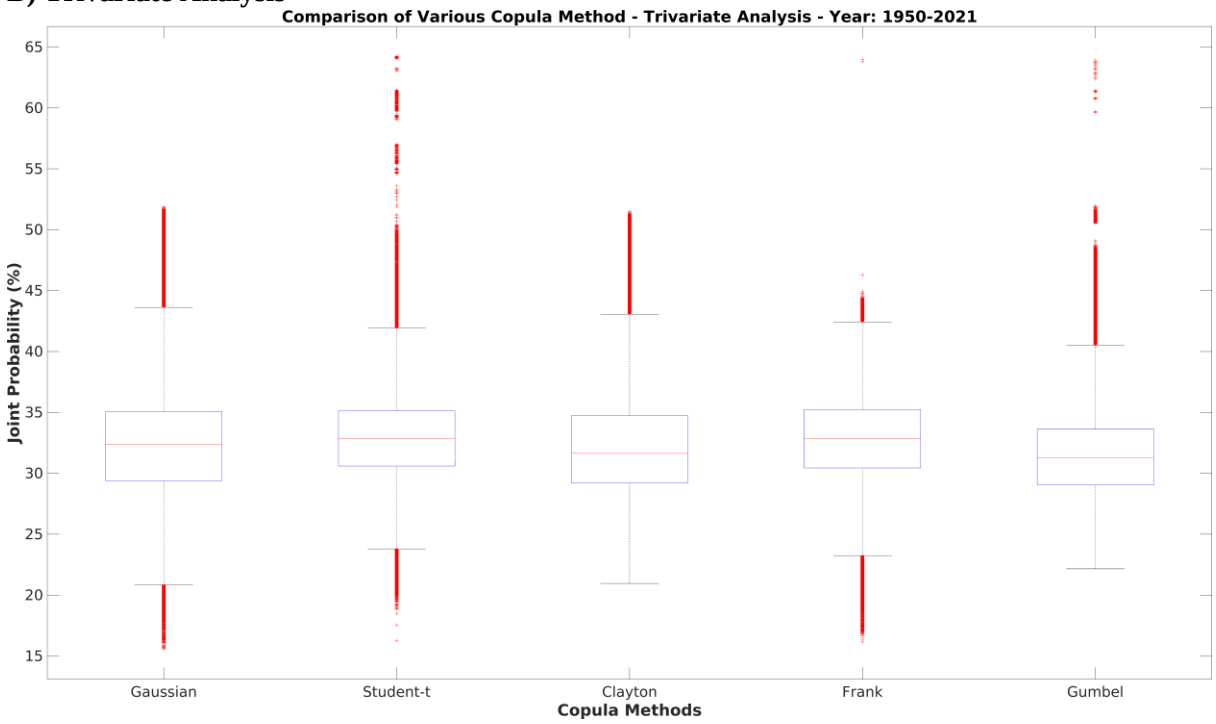

Figure S3: Box plot comparing the performance of various copula methods used in the study to determine the joint probabilities for each grid A) Bivariate B) Trivariate. Minimum, maximum, quantiles, median and outliers could be visualized in each of the approach.

Figure S4: Spatial trend analysis using Mann-Kendall and Sen's slope for compound events

A) Mann-Kendall test - bivariate pairs




Mean radiation (bio20) & Universal thermal climate index (utci)
Mean radiation (bio20) & Wind chill index (wci)
Mean radiation (bio20) & Maximum TG (xtg)
Maximum consecutive frost days (cfd) & Maximum TX (txx)
Frost days (fd) & Maximum TX (txx)
Mean TN (gtn) & Mean TX (gtx)
Mean radiation (bio20) & Mean TG (gtg)
Mean TN (gtn) & Minimum TX (txn)
Mean TN (gtn) & Maximum TX (txx)
Trend Analysis: Mann-Kendall - Year: 1950-2021
Mean TX (gtx) & Minimum TN (tnn)
Mean TX (gtx) & Maximum TN (tnx)
January
February
March
April
May
June
July
August
September
October
November
December


Heat index (hi) & Evapotranspiration - Hargreaves Method (pet-hargreaves)
Heat index (hi) & Wind chill index (wci)
Trend Analysis: Mann-Kendall - Year: 1950-2021
Trend Analysis: Mann-Kendall - Year: 1950-2021
Trend Analysis: Mann-Kendall - Year: 1950-2021
Trend Analysis: Mann-Kendall - Year: 1950-2021
Trend Analysis: Mann-Kendall - Year: 1950-2021
Evapotranspiration - Hargreaves Method (pet-hargreaves) & Universal thermal climate index (utci)
Evapotranspiration - Hargreaves Method (pet-hargreaves) & Wind chill index (wci)
Minimum TN (tnn) & Minimum TX (txn)
Minimum TN (tnn) & Maximum TX (txx)
Maximum TN (tnx) & Minimum TX (txn)
January
February
March
April
May
June
July
August
September
October
November
December

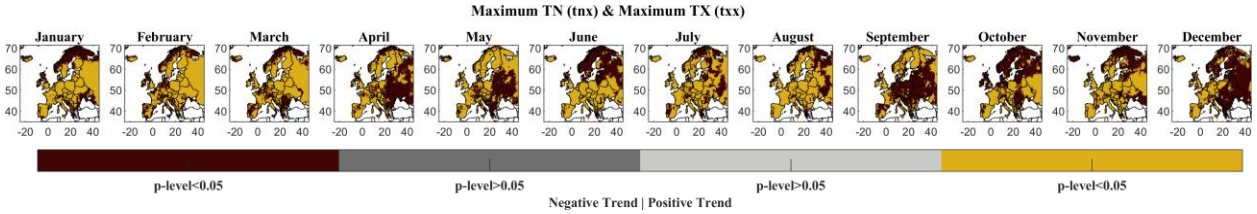

B) Sen's slope estimator - bivariate pairs

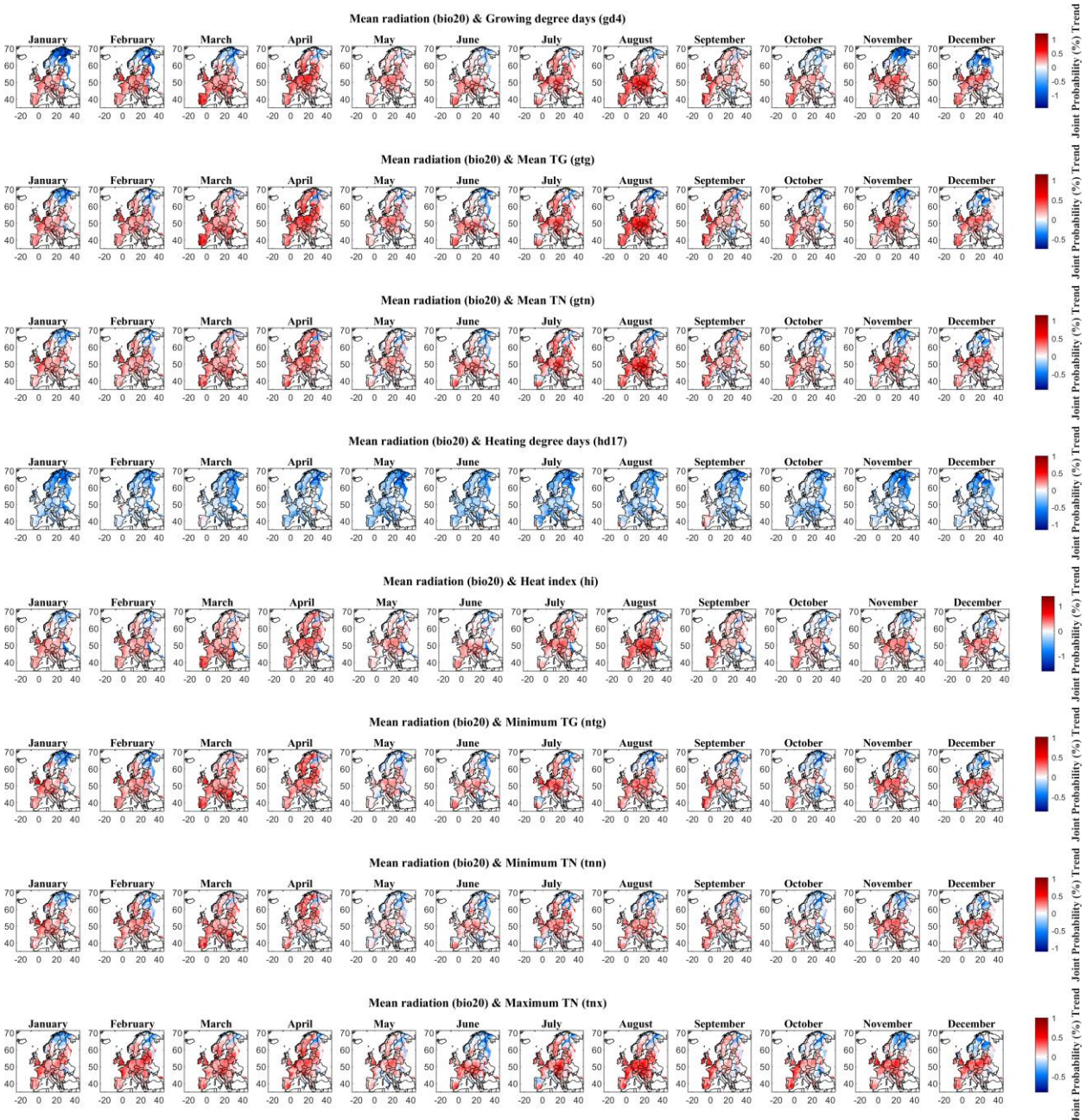

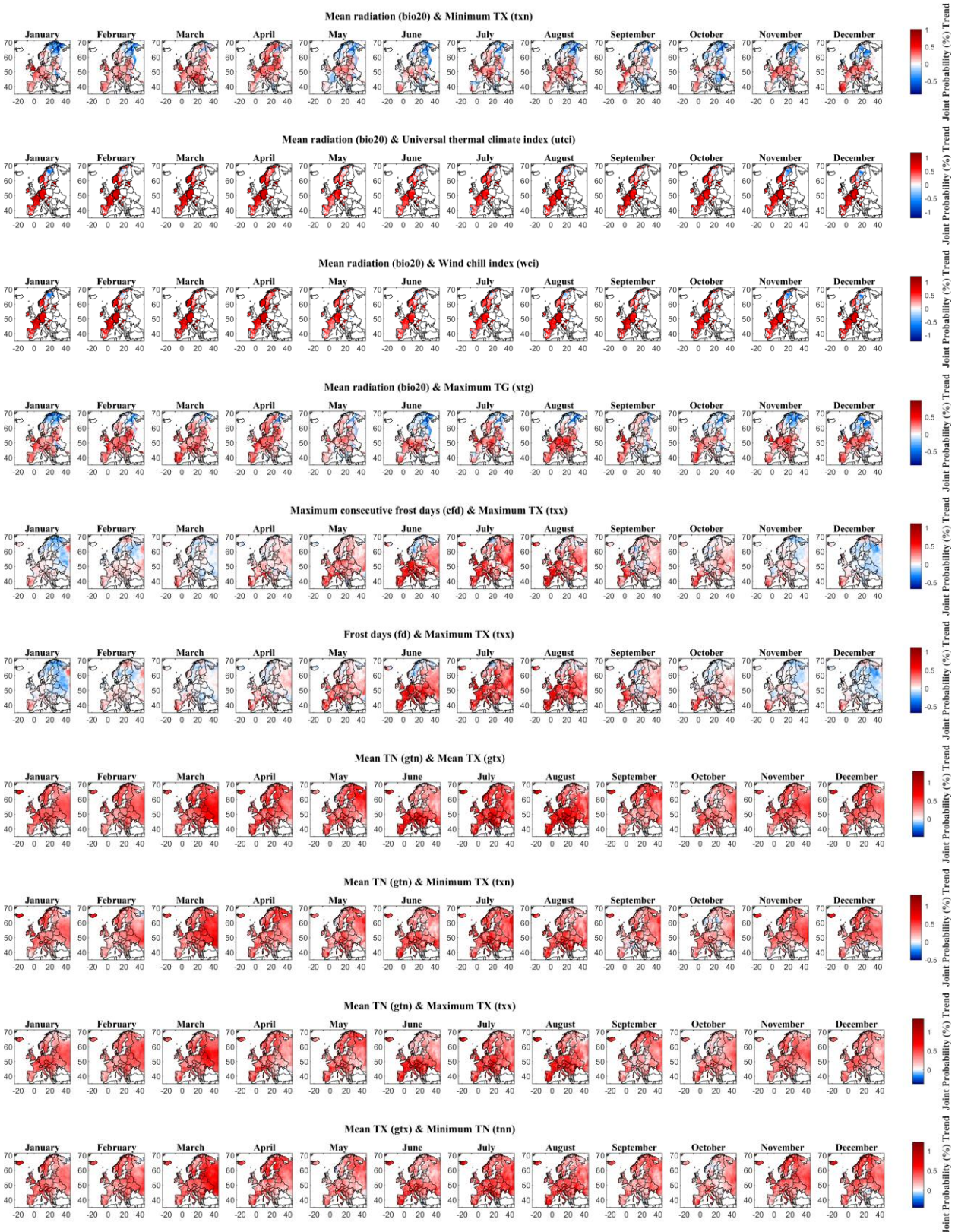
Mean radiation (bio20) & Minimum TX (txn)
Mean radiation (bio20) & Universal thermal climate index (utci)
Mean radiation (bio20) & Wind chill index (wci)
Mean radiation (bio20) & Maximum TG (xtg)
Maximum consecutive frost days (cfd) & Maximum TX (txx)
Frost days (fd) & Maximum TX (txx)
Mean TN (gtn) & Mean TX (gtx)
Mean TN (gtn) & Minimum TX (txn)
Mean TN (gtn) & Maximum TX (txx)
Mean TX (gtx) & Minimum TN (tnn)
January
February
March
April
May
June
July
August
September
October
November
December
Joint Probability (%) Trend

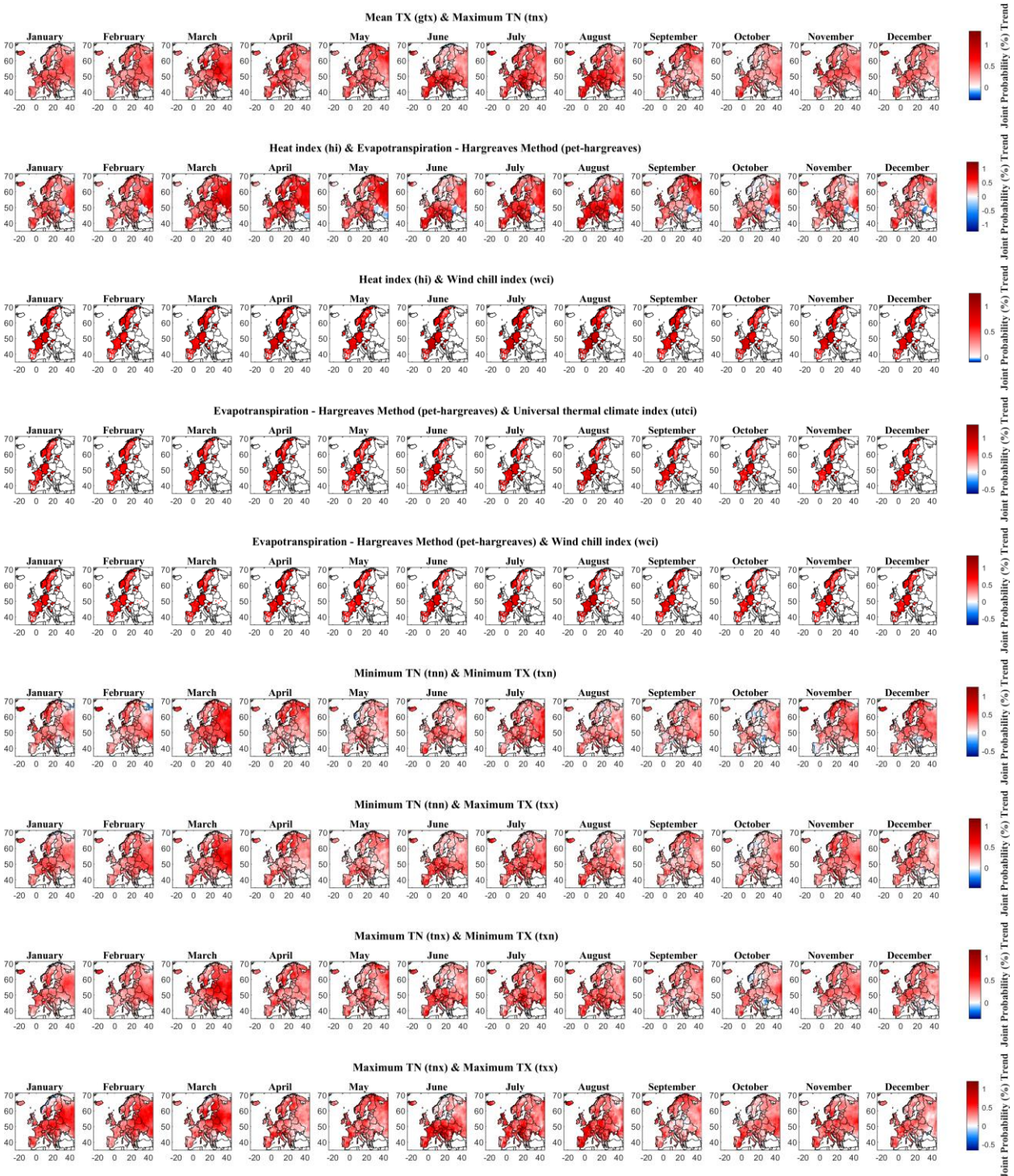
Mean TX (gtx) & Maximum TN (tnx)
Heat index (hi) & Evapotranspiration - Hargreaves Method (pet-hargreaves)
Heat index (hi) & Wind chill index (wci)
Evapotranspiration - Hargreaves Method (pet-hargreaves) & Universal thermal climate index (utci)
Evapotranspiration - Hargreaves Method (pet-hargreaves) & Wind chill index (wci)
Minimum TN (tnn) & Minimum TX (txn)
Minimum TN (tnn) & Maximum TX (txx)
Maximum TN (tnx) & Minimum TX (txn)
Maximum TN (tnx) & Maximum TX (txx)
January
February
March
April
May
June
July
August
September
October
November
December
Joint Probability (%) Trend

C) Mann-Kendall test - trivariate pairs



D) Sen's slope estimator - trivariate pairs

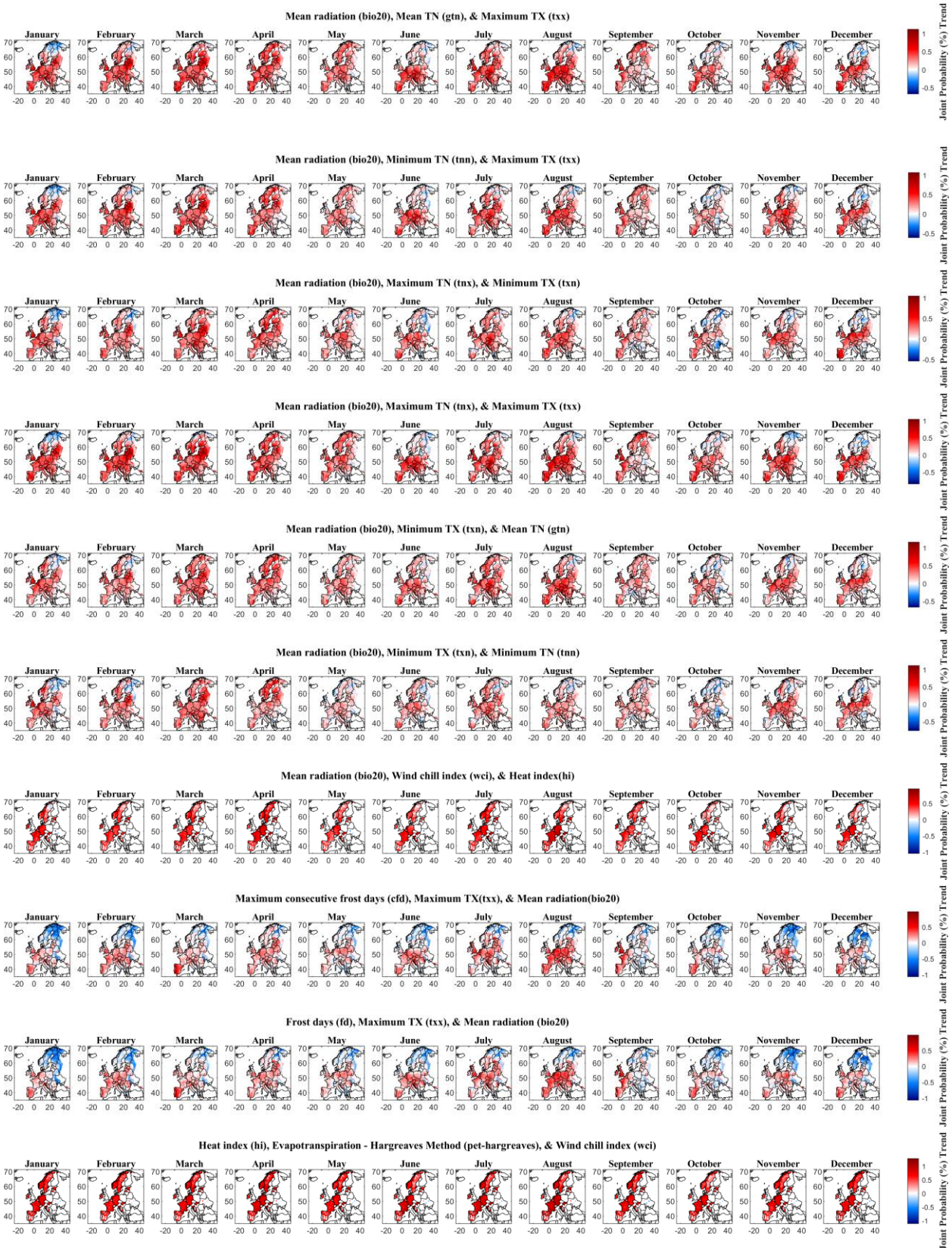

Figure S4: Mann-Kendall and Sen's slope for A)/B) Bivariate and C)/D) Trivariate: spatial distribution across Europe. Direction of trend from Mann-Kendall with significance level <0.05 (Dark yellow for positive and Maroon for negative trend). Magnitude of change from Sen's slope estimator (Red increasing percentage and blue is decreasing percentage of joint probability; white there is no change in the joint probability). Positive trend and increasing magnitude of change indicates European regions, which are more likely to be in risk for future.

Table S1-: A) Very high positive correlation > 0.8 extreme climate indices (I – seasonal II – monthly) B) Very high negative correlation < -0.8 extreme climate indices (I – seasonal II – monthly:

A)

I) Seasonal:

Dec, Jan, Feb (DJF)	Mar, Apr, May (MAM)	Jun, Jul, Aug (JJA)	Sep, Oct, Nov (SON)
pet_hargreaves, gtx, txn, txx, wci with slp	gtn, tnn, tnx with dd17	csd, dd17, gd4, gtg, gtx, hi, pet_hargreaves, su, txn, wci with bio20	gd4, gtg, gtn, gtx, hi, ntg, pet_hargreaves, slp, tnn, tnx, txn, txx, utci, wci, xtg with bio20
gd4, gtx, gtg, hi, ntg, tnn, txn, txx, utci, wci, pet_hargreaves, slp, xtg with bio20		gtn, tnn, tnx with dd17	gtx, pet_hargreaves, txx, utci, wci, xtg with slp
cfd, fd with id		gtn, tnn, tnx with su	
mi with wci		gtn, tnn, tnx with csd	

II) Monthly:

Jan	Feb	Mar	Apr	May	Jun	Jul	Aug	Sep	Oct	Nov	Dec
gtg, hi, ntg with slp	gd4, gtg, hi, ntg, utci, xtg with slp	cfd, fd with id	cfd, fd with id	gtn, tnn, tnx with csd		cdd, dd, ntg, txx, utci, xtg with bio20	csd, dd17 gtx, su with dd	cdd, gtn, tnn, tnx with dd17	cfd, fd with id	cfd, fd with id	utci with slp
gtn with bio20	dd17, gtn with bio20	dd17, gd4, gtg, gtn, gtx, hi, ntg, pet, slp, tnn, tnx, txn, txx, utci, wci, xtg with bio20	dd17, gd4, gtg, gtn, gtx, hi, ntg, pet, tnn, tnx, txn, txx, utci, wci, xtg	gtn, tnn, tnx, with su		csd, su with cdd	csd, su with cdd	csd, dd17, dtr, su with bio20	csd, dd17, dtr, su with bio20	pet , wci with mi	

			with bio20								
	gtn, slp, tnn, tnx with dd17	dd17, gd4, gtg, gtn, gtx, hi, ntg, pet, tnn, tnx, txn, txx, utci, wci, xtg with slp	gtn, tnn, tnx with su			csd, dd17 gd4, gtg, gtx, ntg, su, txn, wci with dd	cwd, dr1mm with rh	csd, gtx, txx, su with cdd	gtn, tnn, tnx with dd17		
		mi with wci	mi with wci			dr1mm with hd17	dd, dtr, gtn, ntg, slp, tnn, tnx, txx, utci, xtg with bio20	csd, dd17, gd4, gtg1 hi, ntg, su with slp	dd17, dtr, gtg, hi with slp		
							dd17, gtx, txn, txx with tr	gtn, tnn, tnx with csd	gtn, tnn, tnx with csd		
								gtn, tnn, tnx with su	gtn, tnn, tnx with su		

B)

I) Seasonal:

Dec, Jan, Feb (DJF)	**Mar, Apr, May (MAM)**	**Jun, Jul, Aug (JJA)**	**Sep, Oct, Nov (SON)**
hd17, id with bio20	dd17, gtx, txn, txx with cfd		fd, hd17 with bio20
gtx, txn, txx with cfd	dd17, gtx, txn, txx with fd		gtx, txn, txx with cfd
gtx, txn, txx with fd			gtx, txn, txx with fd
gtn, tnn, tnx with id			

II) Monthly:

Jan	Feb	Mar	Apr	May	Jun	Jul	Aug	Sep	Oct	Nov	Dec
hd17, id with slp	cfd, fd with dd17	cfd, fd, hd17, id with bio20	cfd, fd, hd17 with bio20	cfd, fd with csd	dd17, gtx, txn, txx with cfd	cwd, dr1mm, dr3mm, hd17, rh with bio20	cwd, dr1mm, hd17, rh with bio20	cfd, rh, zcd with bio20	cfd, id, zcd with bio20	bio20, gtn, tnn, tnx with id	
	hd17, id with slp	cfd, hd17, id with slp	cfd, fd with csd	cfd, fd with su	dd17, gtx, txn, txx with fd	cdd with rh	cdd with rh	cdd with rh	csd, dd17, su with cfd		
		gtn, tnn, tnx with id	cfd, fd with su			cwd, dr1mm, dr3mm, rh with csd	cwd, dr1mm, dr3mm, rh with csd	csd, dd17, su with cfd	csd, dd17, su with fd		
			gtn, tnn, tnx with id			dd17, gtx, su, txn, wci with cwd	gtx, su with cwd	csd, pet, su with rh	gtn, tnn, tnx with id		
						dd with hd17	dd, dtr, gtx, pet, su, txx, xtg with rh	csd, dd17, su with fd	hd17 with slp		
						dd17, gd4, gtg, gtx, ntg, su, txn, wci with dr1mm	dd17, gtx, su with dr1mm	hd17 with slp			
						dd17, gd4, gtg, gtx, ntg, su, txn, wci with dr3mm	su with dr3mm				

						dtr, pet, su with rh					

Table S2: Detailed description of hotspots of compound events

Figure 2 marked zone	Compound event	Location	Month	Best fit Copula Method	Joint Probability (%)
1	bio20 & gd4	Kiruna, Sweden	December	Gumbel	97
	bio20 & utci		December	Student-t	76
	bio20 & wci		December	Student-t	76
	pet & utci	Northern Lapland, Finland	January	Gumbel	94
	pet & wci		December	Gumbel	94
2	bio20 & tnn	Murmansk Oblast, Russia	October	Gaussian	49
	hi & pet		December	Gumbel	53
3	bio20 & gd4	Novgorod Oblast, Russia	January	Gumbel	97
	bio20 & gtg	Tver Oblast, Russia	July	Gaussian	49
	bio20 & gtn		July	Gaussian	49
	cfd, txx & bio20	Vologda Oblast, Russia	November	Gaussian	51
4	bio20 & hi	Zhytomyr Oblast, Ukraine	November	Student-t	87
	hi & wci		August-November	Student-t	87
	bio20, wci & hi	Cherkasy Oblast, Ukraine	November	Gumbel	64
5	bio20 & hd17	Krasnodar Krai, Russia	July	Gumbel	90
	bio20 & ntg		July	Gaussian	49
	bio20 & tnx		October	Gaussian	50
	bio20 & xtg		October	Gaussian	50
	bio20 & txn	Adygea Republic, Russia	July	Gaussian	50
	bio20 & xtg		August	Gaussian	50
	fd, txx & bio20	Krasnodar Krai, Russia	January	Gaussian	52
6	fd & txx	Mousoures, Greece	January	Gaussian	52
	gtn & gtx	Likongremos, Greece	August	Gumbel	51
	gtn & txn		August	Gumbel	48
	gtn & txx	Messiniakos Kolpos, Greece	October	Gumbel	48
	gtx & tnn	Likongremos, Greece	August	Gumbel	49
	gtx & tnx	Messiniakos Kolpos, Greece	August	Gumbel	48
	tnn & txn		January	Gumbel	49
	tnn & txx	Mousoures, Greece	October	Gumbel	47
	tnx & txn	Molai, Greece	August	Gumbel	47
	tnx & txx	Likongremos, Greece	May	Gumbel	49
	bio20, gtn & txx	Messiniakos Kolpos, Greece	December	Gumbel	47
	bio20, tnn & txx		August	Gumbel	46
	bio20, tnx & txn	Likongremos, Greece	August	Gumbel	46
	bio20, tnx & txx	Messiniakos Kolpos, Greece	December	Gumbel	48
	bio20, txn & gtn	Likongremos, Greece	August	Gumbel	47
	bio20, txn & tnn	Kythira, Greece	July	Gumbel	48
7	cfd & txx	Inverness, United Kingdom	June	Gaussian	80
	hi, pet & wci	Donegal, Ireland	September	Clayton	50

Table S3: Statistical indicators value for the determined compound events

Bivariate Pairs		bio20/gd4	bio20/gtg	bio20/gtn	bio20/hd17	bio20/hi	bio20/ntg	bio20/tnn	bio20/tnx	bio20/txn	bio20/utci	bio20/wci	bio20/xtg	cfd/txx	fd/txx	gtn/gtx	gtn/txn	gtn/txx	gtx/tnn	gtx/tnx	hi/pet-hargreaves	hi/wci	pet-hargreaves/utci	pet-hargreaves/wci	tnn/txn	tnn/txx	tnx/txn	tnx/txx
January	AIC	-608	-586	-587	-589	-590	-591	-589	-591	-593	-616	-612	-592	-578	-565	-649	-621	-605	-618	-598	-559	-445	-493	-482	-635	-602	-597	-609
	BIC	-608	-586	-587	-589	-590	-591	-589	-591	-593	-616	-612	-592	-578	-565	-649	-621	-605	-618	-598	-559	-445	-493	-482	-635	-602	-597	-609
	MAXL	304	293	294	295	295	296	294	295	297	308	306	296	289	283	325	311	302	309	299	280	222	246	241	317	301	298	305
	RMSE	0	0	0	0	0	0	0	0	0	0	0	0	0	0	0	0	0	0	0	0	0	0	0	0	0	0	0
	NSE	1	1	1	1	1	1	1	1	1	1	1	1	1	1	1	1	1	1	1	1	1	1	1	1	1	1	1
	p-value	0.001	-	-	-	0.001	-	-	-	-	0.001	0.001	-	0.101	0.101	0.106	0.104	0.096	0.104	0.106	-	0.001	0.001	0.001	0.099	0.101	0.096	0.104
	Method	Gaussian	Gaussian	Gaussian	Clayton	Gaussian	Gaussian	Gaussian	Gaussian	Gaussian	Gaussian	Gaussian	Frank	Gaussian	Gaussian	Student-t	Student-t	Student-t	Student-t	Student-t	Clayton	Clayton	Clayton	Clayton	Student-t	Student-t	Student-t	Student-t
February	AIC	-605	-579	-581	-570	-582	-593	-595	-588	-591	-622	-618	-590	-557	-556	-652	-613	-609	-616	-613	-572	-445	-490	-473	-634	-600	-600	-614
	BIC	-605	-579	-581	-570	-582	-593	-595	-588	-591	-622	-618	-590	-557	-556	-652	-613	-609	-616	-613	-572	-445	-490	-473	-634	-600	-600	-614
	MAXL	303	290	290	285	291	297	298	294	295	311	309	295	278	278	326	306	305	308	306	286	223	245	237	317	300	300	307
	RMSE	0	0	0	0	0	0	0	0	0	0	0	0	0	0	0	0	0	0	0	0	0	0	0	0	0	0	0
	NSE	1	1	1	1	1	1	1	1	1	1	1	1	1	1	1	1	1	1	1	1	1	1	1	1	1	1	1
	p-value	0.001	-	-	-	0.001	-	-	-	-	0.001	0.001	-	0.103	0.103	0.105	0.099	0.105	0.103	0.104	-	0.001	0.109	0.109	0.104	0.098	0.080	0.101
	Method	Gumbel	Gumbel	Frank	Gumbel	Frank	Frank	Gaussian	Frank	Gumbel	Gaussian	Gaussian	Frank	Frank	Frank	Student-t	Student-t	Student-t	Student-t	Student-t	Clayton	Clayton	Clayton	Clayton	Student-t	Student-t	Student-t	Student-t
March	AIC	-591	-590	-587	-582	-591	-598	-595	-578	-599	-591	-587	-583	-579	-575	-628	-604	-594	-615	-597	-586	-440	-493	-476	-614	-598	-592	-604
	BIC	-591	-590	-587	-582	-591	-598	-595	-578	-599	-591	-587	-583	-579	-575	-628	-604	-594	-615	-597	-586	-440	-493	-476	-614	-598	-592	-604
	MAXL	295	295	294	291	296	299	298	289	300	296	294	291	289	287	314	302	297	307	299	293	220	246	238	307	299	296	302
	RMSE	0	0	0	0	0	0	0	0	0	0	0	0	0	0	0	0	0	0	0	0	0	0	0	0	0	0	0
	NSE	1	1	1	1	1	1	1	1	1	1	1	1	1	1	1	1	1	1	1	1	1	1	1	1	1	1	1
	p-value	0.001	-	-	-	0.001	-	-	-	-	0.001	0.001	-	0.103	0.103	0.105	0.104	0.105	0.103	0.101	-	0.001	-	-	0.106	0.097	0.084	0.102
	Method	Frank	Frank	Frank	Gaussian	Frank	Gumbel	Gumbel	Frank	Gumbel	Gaussian	Gaussian	Frank	Gaussian	Gaussian	Student-t	Frank	Student-t	Student-t	Student-t	Clayton	Clayton	Clayton	Clayton	Student-t	Student-t	Student-t	Student-t
April	AIC	-599	-603	-598	-588	-606	-602	-600	-596	-602	-594	-586	-599	-580	-579	-619	-605	-608	-597	-610	-578	-442	-513	-487	-610	-597	-597	-612
	BIC	-599	-603	-598	-588	-606	-602	-600	-596	-602	-594	-586	-599	-580	-579	-619	-605	-608	-597	-610	-578	-442	-513	-487	-610	-597	-597	-612
	MAXL	300	301	299	294	303	301	300	298	301	297	293	300	290	289	310	303	304	299	305	289	221	257	243	305	299	298	306
	RMSE	0	0	0	0	0	0	0	0	0	0	0	0	0	0	0	0	0	0	0	0	0	0	0	0	0	0	0
	NSE	1	1	1	1	1	1	1	1	1	1	1	1	1	1	1	1	1	1	1	1	1	1	1	1	1	1	1
	p-value	0.001	-	-	-	0.001	-	-	-	-	0.001	0.001	-	-	0.102	0.106	0.094	0.103	0.089	0.101	-	0.000	-	-	0.097	0.120	0.101	0.105
	Method	Student-t	Student-t	Gumbel	Gaussian	Student-t	Student-t	Gumbel	Clayton	Student-t	Gaussian	Gaussian	Clayton	Gaussian	Gaussian	Student-t	Gumbel	Student-t	Gumbel	Student-t	Student-t	Clayton	Clayton	Clayton	Student-t	Gumbel	Student-t	Student-t
May	AIC	-598	-599	-598	-588	-601	-593	-597	-595	-597	-580	-564	-592	-600	-600	-621	-606	-606	-601	-607	-588	-440	-506	-479	-611	-588	-595	-619
	BIC	-598	-599	-598	-588	-601	-593	-597	-595	-597	-580	-564	-592	-600	-600	-621	-606	-606	-601	-607	-588	-440	-506	-479	-611	-588	-595	-619
	MAXL	299	299	299	294	300	296	298	297	299	290	282	296	300	300	311	303	303	300	304	294	220	253	239	305	294	298	310
	RMSE	0	0	0	0	0	0	0	0	0	0	0	0	0	0	0	0	0	0	0	0	0	0	0	0	0	0	0
	NSE	1	1	1	1	1	1	1	1	1	1	1	1	1	1	1	1	1	1	1	1	1	1	1	1	1	1	1
	p-value	0.001	-	-	-	0.001	-	-	-	-	0.001	0.001	-	-	-	0.105	0.098	0.101	0.101	0.104	0.106	0.001	-	-	0.105	0.085	0.086	0.106
	Method	Student-t	Student-t	Frank	Gaussian	Student-t	Gumbel	Gumbel	Clayton	Gumbel	Clayton	Clayton	Clayton	Gaussian	Gaussian	Student-t	Student-t	Student-t	Gumbel	Student-t	Student-t	Clayton	Clayton	Clayton	Student-t	Gumbel	Student-t	Student-t
June	AIC	-583	-583	-590	-582	-589	-592	-595	-592	-587	-564	-547	-588	-614	-610	-618	-602	-608	-598	-611	-583	-437	-509	-482	-604	-599	-596	-614
	BIC	-583	-583	-590	-582	-589	-592	-595	-592	-587	-564	-547	-588	-614	-610	-618	-602	-608	-598	-611	-583	-437	-509	-482	-604	-599	-596	-614
	MAXL	292	291	295	291	295	296	298	296	293	282	273	294	307	305	309	301	304	299	306	291	219	254	241	302	299	298	307
	RMSE	0	0	0	0	0	0	0	0	0	0	0	0	0	0	0	0	0	0	0	0	0	0	0	0	0	0	0
	NSE	1	1	1	1	1	1	1	1	1	1	1	1	1	1	1	1	1	1	1	1	1	1	1	1	1	1	1
	p-value	-	-	-	0.001	0.001	-	-	-	-	0.001	0.001	-	-	-	0.101	0.102	0.255	0.099	0.101	-	0.001	-	-	0.103	0.086	0.097	0.104
	Method	Frank	Frank	Frank	Gaussian	Frank	Gumbel	Gumbel	Clayton	Frank	Clayton	Clayton	Clayton	Clayton	Clayton	Student-t	Student-t	Student-t	Gumbel	Student-t	Student-t	Clayton	Clayton	Clayton	Student-t	Student-t	Student-t	Student-t
July	AIC	-588	-588	-590	-590	-594	-594	-598	-593	-589	-564	-553	-591	-601	-600	-618	-594	-602	-593	-611	-584	-441	-507	-490	-600	-593	-595	-609
	BIC	-588	-588	-590	-590	-594	-594	-598	-593	-589	-564	-553	-591	-601	-600	-618	-594	-602	-593	-611	-584	-441	-507	-490	-600	-593	-595	-609
	MAXL	294	294	295	295	297	297	299	297	295	282	277	295	300	300	309	297	301	297	305	292	220	254	245	300	297	298	305
	RMSE	0	0	0	0	0	0	0	0	0	0	0	0	0	0	0	0	0	0	0	0	0	0	0	0	0	0	0
	NSE	1	1	1	1	1	1	1	1	1	1	1	1	1	1	1	1	1	1	1	1	1	1	1	1	1	1	1
	p-value	-	-	-	0.001	0.001	-	-	-	-	0.001	0.001	-	-	-	0.103	0.101	0.094	0.104	0.105	-	0.001	-	-	0.106	0.105	0.101	0.103
	Method	Student-t	Student-t	Gumbel	Gaussian	Student-t	Gumbel	Gumbel	Clayton	Frank	Clayton	Clayton	Frank	Clayton	Clayton	Student-t	Gumbel	Student-t	Gumbel	Student-t	Gumbel	Clayton	Clayton	Clayton	Gumbel	Gumbel	Gumbel	Student-t
August	AIC	-590	-590	-595	-591	-596	-596	-595	-591	-594	-567	-552	-589	-616	-614	-613	-601	-601	-604	-607	-588	-433	-513	-493	-602	-594	-595	-608
	BIC	-590	-590	-595	-591	-596	-596	-595	-591	-594	-567	-552	-589	-616	-614	-613	-601	-601	-604	-607	-588	-433	-513	-493	-602	-594	-595	-608
	MAXL	295	295	298	295	298	298	296	297	297	283	276	295	308	307	306	300	301	302	304	294	216	257	247	301	297	297	304
	RMSE	0	0	0	0	0	0	0	0	0	0	0	0	0	0	0	0	0	0	0	0	0	0	0	0	0	0	0
	NSE	1	1	1	1	1	1	1	1	1	1	1	1	1	1	1	1	1	1	1	1	1	1	1	1	1	1	1
	p-value	-	-	-	0.001	0.001	-	-	-	-	0.001	0.001	-	-	-	0.106	0.103	0.101	0.106	0.099	0.105	0.001	-	-	0.106	0.103	0.140	0.105
	Method	Frank	Frank	Gumbel	Gaussian	Frank	Frank	Gumbel	Clayton	Frank	Clayton	Clayton	Clayton	Clayton	Clayton	Student-t	Gumbel	Student-t	Gumbel	Student-t	Student-t	Clayton	Clayton	Clayton	Gumbel	Student-t	Gumbel	Student-t
September	AIC	-600	-601	-598	-591	-607	-599	-598	-591	-598	-578	-566	-593	-612	-608	-617	-607	-601	-605	-605	-585	-443	-526	-506	-610	-593	-597	-607
	BIC	-600	-601	-598	-591	-607	-599	-598	-591	-598	-578	-566	-593	-612	-608	-617	-607	-601	-605	-605	-585	-443	-526	-506	-610	-593	-597	-607
	MAXL	300	301	299	296	304	300	299	296	299	289	283	296	306	304	309	303	300	302	302	293	221	263	253	305	297	298	303
	RMSE	0	0	0	0	0	0	0	0	0	0	0	0	0	0	0	0	0	0	0	0	0	0	0	0	0	0	0
	NSE	1	1	1	1	1	1	1	1	1	1	1	1	1	1	1	1	1	1	1	1	1	1	1	1	1	1	1
	p-value	-	-	-	0.001	0.001	-	-	-	-	0.001	0.001	-	-	-	0.100	0.094	0.093	0.105	0.096	-	0.001	-	-	0.104	0.091	0.095	0.104
	Method	Student-t	Clayton	Frank	Gaussian	Clayton	Clayton	Gumbel	Clayton	Gumbel	Gaussian	Clayton	Clayton	Student-t	Student-t	Student-t	Student-t	Student-t	Student-t	Student-t	Student-t	Clayton	Clayton	Clayton	Student-t	Clayton	Clayton	Student-t
October	AIC	-599	-599	-590	-590	-601	-601	-599	-594	-598	-608	-604	-599	-584	-582	-621	-607	-600	-607	-606	-579	-451	-558	-540	-614	-592	-592	-610
	BIC	-599	-599	-590	-590	-601	-601	-599	-594	-598	-608	-604	-599	-584	-582	-621	-607	-600	-607	-606	-579	-451	-558	-540	-614	-592	-592	-610
	MAXL	299	300	295	295	301	300	300	297	299	304	302	299	292	291	310	303	300	303	303	290	226	279	270	307	296	296	305
	RMSE	0	0	0	0	0	0	0	0	0	0	0	0	0	0	0	0	0	0	0	0	0	0	0	0	0	0	0
	NSE	1	1	1	1	1	1	1	1	1	1	1	1	1	1	1	1	1	1	1	1	1	1	1	1	1	1	1
	p-value	0.000	-	-	-	0.001	-	-	-	-	0.001	0.001	-	-	-	0.107	0.105	0.106	0.104	0.106	-	0.001	-	0.999	0.103	0.103	0.101	0.106
	Method	Clayton	Clayton	Gaussian	Gaussian	Clayton	Gumbel	Gaussian	Clayton	Gumbel	Clayton	Clayton	Clayton	Gaussian	Gaussian	Student-t	Student-t	Student-t	Student-t	Student-t	Student-t	Clayton	Clayton	Clayton	Student-t	Clayton	Gumbel	Student-t
November	AIC	-590	-589	-588	-584	-592	-591	-588	-590	-593	-615	-612	-592	-571	-566	-636	-608	-601	-609	-604	-582	-452	-536	-521	-624	-595	-592	-612
	BIC	-590	-589	-588	-584	-592	-591	-588	-590	-593	-615	-612	-592	-571	-566	-636	-608	-601	-609	-604	-582	-452	-536	-521	-624	-595	-592	-612
	MAXL	295	295	294	292	296	296	294	295	297	307	306	296	286	283	318	304	300	305	302	291	226	268	260	312	297	296	306
	RMSE	0	0	0	0	0	0	0	0	0	0	0	0	0	0	0	0	0	0	0	0	0	0	0	0	0	0	0
	NSE	1	1	1	1	1	1	1	1	1	1	1	1	1	1	1	1	1	1	1	1	1	1	1	1	1	1	1
	p-value	0.001	-	-	-	0.001	-	-	-	-	0.757	0.001	-	0.102	0.102	0.107	0.099	0.107	-	0.098	-	0.001	-	-	0.102	0.099	0.089	0.102
	Method	Gaussian	Gaussian	Gaussian	Gumbel	Gaussian	Gaussian	Frank	Frank	Frank	Gaussian	Gaussian	Gumbel	Frank	Gaussian	Student-t	Student-t	Student-t	Student-t	Student-t	Student-t	Clayton	Clayton	Clayton	Student-t	Gumbel	Gumbel	Student-t
December	AIC	-603	-592	-591	-590	-593	-590	-589	-598	-592	-628	-628	-597	-569	-562	-648	-611	-601	-615	-602	-565	-442	-525	-516	-632	-598	-597	-610
	BIC	-603	-592	-591	-590	-593	-590	-589	-598	-592	-628	-628	-597	-569	-562	-648	-611	-601	-615	-602	-565	-442	-525	-516	-632	-598	-597	-610
	MAXL	302	296	295	295	297	295	295	299	296	314	314	298	285	281	324	306	301	307	301	283	221	263	258	316	299	299	305
	RMSE	0	0	0	0	0	0	0	0	0	0	0	0	0	0	0	0	0	0	0	0	0	0	0	0	0	0	0
	NSE	1	1	1	1	1	1	1	1	1	1	1	1	1	1	1	1	1	1	1	1	1	1	1	1	1	1	1
	p-value	0.001	-	-	-	0.001	-	-	-	-	0.001	0.001	-	0.103	0.103	0.105	0.100	0.103	0.097	0.097	-	0.001	0.001	0.001	0.098	0.103	0.094	0.104
	Method	Gaussian	Gaussian	Gaussian	Clayton	Gaussian	Gumbel	Gaussian	Gaussian	Gumbel	Frank	Frank	Gumbel	Gaussian	Gaussian	Student-t	Student-t	Student-t	Student-t	Student-t	Clayton	Clayton	Clayton	Clayton	Student-t	Student-t	Student-t	Student-t

Trivariate Pairs		bio20/gtn/txx	bio20/tnn/txx	bio20/tnx/txn	bio20/tnx/txx	bio20/txn/gtn	bio20/txn/tnn	bio20/wci/hi	cfd/txx/bio20	fd/txx/bio20	hi/pet-hargreaves/wci
January	AIC	-601	-601	-599	-600	-596	-586	-563	-599	-601	-452
	BIC	-601	-601	-599	-600	-596	-586	-563	-599	-601	-452
	MAXL	300	301	299	300	298	293	281	300	300	226
	RMSE	0	0	0	0	0	0	0	0	0	0
	NSE	1	1	1	1	1	1	1	1	1	1
	p-value	0.091	0.090	0.084	0.096	0.092	0.089	0.001	0.767	0.608	-
	Method	Student-t	Student-t	Clayton	Student-t	Student-t	Student-t	Clayton	Clayton	Clayton	Clayton
February	AIC	-602	-601	-595	-604	-595	-594	-567	-594	-593	-450
	BIC	-602	-601	-595	-604	-595	-594	-567	-594	-593	-450
	MAXL	301	301	297	302	298	297	283	297	297	225
	RMSE	0	0	0	0	0	0	0	0	0	0
	NSE	1	1	1	1	1	1	1	1	1	1
	p-value	0.095	0.124	0.098	0.089	0.092	0.101	0.001	0.894	0.266	-
	Method	Student-t	Student-t	Gumbel	Student-t	Student-t	Student-t	Clayton	Clayton	Clayton	Clayton
March	AIC	-597	-602	-598	-601	-598	-598	-563	-599	-600	-447
	BIC	-597	-602	-598	-601	-598	-598	-563	-599	-600	-447
	MAXL	298	301	299	300	299	299	282	299	300	223
	RMSE	0	0	0	0	0	0	0	0	0	0
	NSE	1	1	1	1	1	1	1	1	1	1
	p-value	0.096	0.118	0.094	0.099	0.102	0.099	0.001	0.693	0.779	-
	Method	Student-t	Student-t	Student-t	Student-t	Student-t	Student-t	Clayton	Clayton	Clayton	Clayton
April	AIC	-602	-599	-594	-607	-601	-602	-598	-597	-599	-450
	BIC	-602	-599	-594	-607	-601	-602	-598	-597	-599	-450
	MAXL	301	299	297	303	300	301	299	299	299	225
	RMSE	0	0	0	0	0	0	0	0	0	0
	NSE	1	1	1	1	1	1	1	1	1	1
	p-value	0.091	0.096	0.087	0.103	0.095	0.090	0.001	0.957	0.829	-
	Method	Student-t	Student-t	Student-t	Student-t	Student-t	Student-t	Student-t	Clayton	Clayton	Clayton
May	AIC	-601	-593	-596	-606	-604	-602	-584	-591	-590	-445
	BIC	-601	-593	-596	-606	-604	-602	-584	-591	-590	-445
	MAXL	301	297	298	303	302	301	292	295	295	223
	RMSE	0	0	0	0	0	0	0	0	0	0
	NSE	1	1	1	1	1	1	1	1	1	1
	p-value	0.097	0.081	0.096	0.097	0.096	0.140	0.001	0.716	0.364	-
	Method	Student-t	Student-t	Gumbel	Student-t	Student-t	Student-t	Student-t	Clayton	Clayton	Clayton
June	AIC	-605	-602	-597	-608	-603	-601	-585	-586	-586	-444
	BIC	-605	-602	-597	-608	-603	-601	-585	-586	-586	-444
	MAXL	302	301	298	304	302	300	292	293	293	222
	RMSE	0	0	0	0	0	0	0	0	0	0
	NSE	1	1	1	1	1	1	1	1	1	1
	p-value	0.250	0.095	0.093	0.249	0.100	0.102	0.001	0.999	0.762	-
	Method	Student-t	Student-t	Gumbel	Student-t	Student-t	Gumbel	Clayton	Clayton	Clayton	Clayton
July	AIC	-603	-599	-597	-606	-599	-600	-609	-585	-585	-451
	BIC	-603	-599	-597	-606	-599	-600	-609	-585	-585	-451
	MAXL	302	299	298	303	300	300	304	293	293	225
	RMSE	0	0	0	0	0	0	0	0	0	0
	NSE	1	1	1	1	1	1	1	1	1	1
	p-value	0.089	0.089	0.103	0.087	0.103	0.103	0.001	0.998	0.998	-
	Method	Student-t	Student-t	Gumbel	Student-t	Gumbel	Gumbel	Student-t	Student-t	Student-t	Clayton
August	AIC	-606	-599	-599	-606	-596	-597	-602	-588	-588	-444
	BIC	-606	-599	-599	-606	-596	-597	-602	-588	-588	-444
	MAXL	303	300	299	303	298	298	301	294	294	222
	RMSE	0	0	0	0	0	0	0	0	0	0
	NSE	1	1	1	1	1	1	1	1	1	1
	p-value	0.090	0.090	0.085	0.096	0.086	0.096	0.001	0.999	0.999	-
	Method	Student-t	Student-t	Gumbel	Student-t	Gumbel	Gumbel	Frank	Clayton	Clayton	Clayton
September	AIC	-595	-594	-601	-600	-602	-600	-573	-591	-591	-458
	BIC	-595	-594	-601	-600	-602	-600	-573	-591	-591	-458
	MAXL	298	297	301	300	301	300	286	296	295	229
	RMSE	0	0	0	0	0	0	0	0	0	0
	NSE	1	1	1	1	1	1	1	1	1	1
	p-value	0.078	0.087	0.090	0.085	0.090	0.099	0.001	0.991	0.958	-
	Method	Clayton	Clayton	Student-t	Student-t	Student-t	Student-t	Clayton	Clayton	Clayton	Clayton
October	AIC	-599	-596	-592	-605	-598	-600	-567	-601	-597	-476
	BIC	-599	-596	-592	-605	-598	-600	-567	-601	-597	-476
	MAXL	299	298	296	303	299	300	284	300	299	238
	RMSE	0	0	0	0	0	0	0	0	0	0
	NSE	1	1	1	1	1	1	1	1	1	1
	p-value	0.096	0.091	0.100	0.095	0.073	0.100	0.001	0.878	0.428	-
	Method	Clayton	Clayton	Gumbel	Student-t	Student-t	Student-t	Clayton	Clayton	Clayton	Clayton
November	AIC	-601	-596	-596	-599	-595	-592	-584	-596	-596	-468
	BIC	-601	-596	-596	-599	-595	-592	-584	-596	-596	-468
	MAXL	300	298	298	300	297	296	292	298	298	234
	RMSE	0	0	0	0	0	0	0	0	0	0
	NSE	1	1	1	1	1	1	1	1	1	1
	p-value	0.103	0.103	0.092	0.104	0.101	0.098	0.001	0.578	0.481	-
	Method	Student-t	Student-t	Gumbel	Student-t	Student-t	Student-t	Clayton	Clayton	Clayton	Clayton
December	AIC	-594	-599	-601	-602	-584	-587	-567	-599	-599	-456
	BIC	-594	-599	-601	-602	-584	-587	-567	-599	-599	-456
	MAXL	297	300	300	301	292	294	284	299	299	228
	RMSE	0	0	0	0	0	0	0	0	0	0
	NSE	1	1	1	1	1	1	1	1	1	1
	p-value	0.096	0.085	0.104	0.104	0.124	0.096	0.001	0.724	0.461	-
	Method	Student-t	Student-t	Student-t	Student-t	Student-t	Student-t	Clayton	Clayton	Clayton	Clayton

Table S4: Detailed description of monthly shifts and trend analysis of hotspots of compound events

A) Bivariate Pairs

Compound event	January	February	March	April	May	June	July	August	September	October	November	December
bio20 & gd4	RU 0	RU 0	RU **0**	RU 0	RU 0	RU **0.56**	RU **0.41**	RU **0.67**	RU **0.47**	RU **0**	RU **0**	SE 0
Max Increasing Trend	GR **0.73**	GR **0.65**	BY **0.86**	UA **0.77**	GR **0.93**	GR **1.21**	GR **1.09**	GR **0.97**	GR **1.08**	GR **0.82**	BY **0.78**	UA **0.68**
bio20 & gtg	RU **0.43**	RU 0.34	RU **0.48**	BY **0.57**	RU **0.56**	UA **0.58**	RU **0.4**	RU **0.67**	RU **0.47**	RU 0.29	RU 0.17	UA 0.15
Max Increasing Trend	GR **0.71**	UA **0.65**	BY **0.91**	UA **0.82**	GR **0.93**	GR **1.15**	GR **1.02**	UA **0.94**	GR **1.08**	GR **0.8**	BY **0.73**	BY **0.68**
bio20 & gtn	RU **0.51**	RU 0.3	RU **0.45**	BY 0.32	RU 0.34	RU 0.23	RU **0.48**	RU **0.72**	RU **0.48**	RU 0.32	UA 0.17	UA 0.19
Max Increasing Trend	GR **0.86**	GR **0.75**	GR **0.91**	GR **0.84**	GR **0.99**	GR **1.02**	GR **1.02**	GR **1.02**	GR **1.05**	GR **0.94**	BY **0.72**	BY **0.73**
bio20 & hd17	RU 0.19	RU **0.39**	RU **0.57**	RU **0.38**	RU **0.62**	GR 0	RU **0**	RU **0**	GR 0	RU 0.32	RU **0.47**	SE **0.49**
Max Increasing Trend	GR **0.86**	GR **0.95**	GR **0.88**	GR **0.81**	GR **0.61**	GR **0.97**	GR **0.88**	GR **1.01**	GR **0.88**	GR **0.84**	GR **0.99**	GR **1**
bio20 & hi	UA **0**	UA **0**	UA **0**	UA **0**	UA **0**	UA **0**	UA **0**	UA **0**	UA **0**	UA **0**	UA **0**	IS **0**
Max Increasing Trend	BY **1.14**	BY **1.31**	BY **1.39**	BY **1.35**	BY **1.19**	BY **1.08**	BY **1.24**	BY **1.19**	BY **1.07**	BY **1.09**	BY **1.1**	BY **1.06**
bio20 & ntg	RU 0.16	RU 0.22	UA **0.45**	BY **0.37**	RU 0.17	UA **0.43**	RU **0.51**	RU **0.65**	RU 0.23	RU 0.22	UA 0.31	RU 0.24
Max Increasing Trend	GR **0.91**	GR **0.78**	RU **0.86**	UA **0.75**	GR **0.89**	UA **0.77**	GR **1.02**	GR **0.9**	GR **0.86**	GR **0.63**	GR **0.74**	BY **0.71**
bio20 & tnn	RU 0.13	RU 0.28	UA **0.43**	BY 0.05	RU 0.12	UA **0.56**	RU **0.47**	RU 0.22	RU 0.19	RU 0.19	RU 0.29	UA **0.36**
Max Increasing Trend	GR **1.02**	GR **0.78**	GR **0.88**	GR **0.78**	GR **0.95**	GR **0.77**	GR **1.03**	GR **0.95**	GR **0.96**	GR **0.76**	GR **0.82**	BY **0.73**
bio20 & tnx	RU **0.64**	RU **0.59**	RU **0.5**	RU 0.3	RU **0.44**	RU **0.42**	RU 0.18	RU **0.54**	RU **0.55**	RU **0.58**	UA 0.14	UA 0.22
Max Increasing Trend	GR **0.78**	BY **0.92**	BY **1**	GR **0.73**	GR **0.83**	GR **0.98**	GR **1**	GR **0.95**	GR **0.95**	GR **0.85**	BY **0.8**	GR **0.72**
bio20 & txn	RU 0.19	RU 0.18	UA **0.49**	BY **0.58**	RU 0.1	UA 0.15	RU **0.42**	RU 0.26	RU **0.43**	BY 0.34	UA 0.19	RU 0.03
Max Increasing Trend	GR **0.72**	RU **0.7**	BY **0.93**	BY **0.89**	GR **0.7**	GR **0.95**	GR **0.99**	GR **1.01**	GR **0.82**	GR **0.67**	GR **0.7**	BY **0.69**
bio20 & utci	FI **1.12**	FI **1.1**	FI **0.9**	FI **0.93**	FI **1.08**	FI **1.09**	FI **1.05**	FI **1.03**	FI **1.01**	FI **1.17**	SE **0.83**	SE 0
Max Increasing Trend	FR **1.11**	FR **1.17**	GB **1.08**	NL **1.06**	DE **0.93**	ES **0.92**	ES **1.01**	DE **1**	FR **1.15**	GB **1.13**	NL **1.04**	NL **1.19**
bio20 & wci	UA 0	UA 0	UA 0	UA 0	UA 0	UA 0	UA 0	UA 0	UA 0	UA 0	UA 0	SE 0
Max Increasing Trend	FR **1.13**	FR **1.17**	IIU **1.06**	NL **1.04**	NL **0.91**	ES **0.98**	ES **0.96**	DE **1.01**	FR **1.16**	GB **1.14**	NL **1.02**	SE **1.22**
bio20 & xtg	RU **0.58**	RU **0.56**	RU **0.49**	BY **0.37**	RU 0.2	RU **0.55**	RU **0.06**	RU **0.57**	UA 0.14	RU **0.36**	UA **0.4**	UA 0.23
Max Increasing Trend	GR **0.75**	BY **0.92**	BY **0.94**	GR **0.68**	RU **0.75**	GR **0.97**	GR **0.99**	GR **0.85**	GR **0.89**	GR **0.88**	BY **0.78**	UA **0.66**
cfd & txx	GR **0.71**	GR **0.69**	GR **0.6**	GR **0.73**	GR **0.85**	GB 0	GR **1.01**	GR **0.77**	GR **1.05**	GR **0.89**	GR **0.74**	GR **0.59**
Max Increasing Trend	GR **0.83**	GR **0.81**	FR **0.91**	FR **0.96**	GR **0.98**	GR **1**	GR **1.1**	FR **1.13**	GR **1.1**	FR **0.99**	FR **0.86**	GR **0.75**
fd & txx	GR **0.71**	GR **0.69**	GR **0.6**	GR **0.73**	GR **0.85**	GR **1.01**	GR **1.01**	GR **0.77**	GR **1.05**	GR **0.89**	GR **0.74**	GR **0.59**
Max Increasing Trend	GR **0.82**	GR **0.84**	FR **0.91**	FR **0.96**	GR **0.97**	GR **1.13**	FR **1.08**	FR **1.13**	GR **1.1**	FR **0.99**	FR **0.86**	GR **0.75**
gtn & gtx	GR **0.82**	GR **0.69**	GR **0.73**	GR **0.75**	GR **0.8**	GR **0.93**	GR **1.08**	GR **0.87**	GR **0.74**	GR **0.76**	GR **0.58**	GR **0.67**
Max Increasing Trend	GR **0.95**	SE **0.89**	GR **0.94**	GR **1.08**	GR **1.13**	GR **1.3**	GR **1.28**	GR **1.2**	GR **1.28**	GR **1.02**	FR **0.97**	FR **0.91**
gtn & txn	GR **0.97**	GR **0.77**	GR **0.81**	GR **0.61**	GR **0.78**	GR **0.81**	GR **1.08**	GR **0.88**	GR **1.05**	GR **0.81**	GR **0.6**	GR **0.58**
Max Increasing Trend	GR **1.09**	GR **0.97**	GR **0.94**	GR **1.01**	IT **0.96**	GR **1.2**	GR **1.31**	GR **1.2**	GR **1.2**	GR **0.89**	SE **0.96**	SE **0.98**
gtn & txx	GR **0.81**	GR **0.64**	GR **0.55**	GR **0.83**	GR **1.03**	GR **0.66**	GR **1.04**	GR **0.86**	GR **0.72**	GR **0.81**	GR **0.82**	GR **0.71**
Max Increasing Trend	IT **1.03**	GR **0.82**	GR **0.88**	GR **1.11**	GR **1.08**	GR **1.2**	GR **1.23**	GR **1.13**	GR **1.35**	GR **1.1**	FR **0.92**	FR **0.94**
gts & tnn	GR **0.8**	GR **0.64**	GR **0.78**	GR **0.86**	GR **0.94**	GR **0.82**	GR **1.17**	GR **0.87**	GR **0.72**	GR **0.91**	GR **0.64**	GR **0.59**
Max Increasing Trend	GR **1.03**	SE **0.91**	GR **0.93**	GR **1.01**	GR **1.04**	GR **1.18**	GR **1.23**	GR **1.19**	GR **1.12**	GR **0.93**	SE **0.97**	SE **0.96**
gtx & tnx	GR **0.79**	GR **0.65**	GR **0.73**	GR **0.77**	GR **0.71**	GR **0.95**	GR **0.94**	GR **0.79**	GR **0.69**	GR **0.9**	GR **0.67**	GR **0.53**
Max Increasing Trend	IT **0.91**	IT **0.87**	FR **0.96**	FR **1.05**	GR **1.06**	GR **1.32**	GR **1.14**	GR **1.11**	GR **1.09**	GR **0.97**	IT **0.91**	FR **0.81**
hi & pet	NO 0.1	SE **0.37**	UA **0.67**	UA **0.61**	GR **0.71**	UA 0.39	MD **0.47**	GR **0.81**	UA 0.08	UA 0.13	NO **0.45**	RU **0.84**
Max Increasing Trend	IT **0.9**	IT **0.83**	RU **1.01**	FR **1.16**	FR **1.05**	GR **1.23**	FR **1.22**	FR **1.21**	GR **1.07**	FR **0.98**	IT **0.91**	FR **0.89**
hi & wci	UA **0**	UA **0**	UA **0**	UA **0**	UA **0**	UA **0**	UA **0**	UA **0**	UA **0**	UA **0**	UA **0**	UA **0**
Max Increasing Trend	FR **1.15**	GB **0.99**	LV **1.07**	FR **1.23**	SE **1.13**	AT **1.25**	FR **1.15**	ES **1.2**	FI **1.11**	FR **1.14**	FR **1.09**	FR **1.16**
pet & utci	FI **0**	NO **0.31**	CH 0.2	AT **0.47**	FI **0.63**	BE 0.35	FI **0.37**	ES **0.84**	AT 0.08	AT 0.16	AT **0.36**	FI **0**
Max Increasing Trend	NO **1.28**	FR **1.21**	ES **1.3**	FR **1.36**	ES **1.26**	FR **1.35**	FR **1.38**	FR **1.37**	FR **1.32**	FR **1.37**	ES **1.3**	ES **1.33**
pet & wci	FI **0**	NO **0.31**	CH 0.2	AT **0.47**	FI **0.63**	BE 0.35	FI **0.38**	ES **0.84**	AT 0.08	AT 0.16	AT **0.36**	FI **0**
Max Increasing Trend	NO **1.29**	ES **1.16**	ES **1.25**	FR **1.33**	FR **1.21**	FR **1.32**	FR **1.36**	FR **1.36**	FR **1.32**	FR **1.36**	ES **1.29**	ES **1.31**
tnn & txn	GR **0.74**	GR **0.68**	GR **0.58**	GR **0.82**	GR **0.97**	GR **0.93**	GR **1.05**	GR **0.85**	GR **0.76**	GR **0.93**	GR **0.66**	GR **0.54**
Max Increasing Trend	GR **0.94**	IT **0.96**	FR **0.94**	GR **0.96**	GR **1.04**	GR **1.19**	GR **1.15**	GR **1.07**	GR **1.2**	GR **1.07**	IT **0.87**	CH **0.88**
tnn & txx	GR **0.86**	GR **0.67**	GR **0.91**	GR **0.53**	GR **0.87**	GR **0.94**	GR **1.09**	GR **0.87**	GR **0.78**	GR **0.75**	GR **0.9**	GR **0.54**
Max Increasing Trend	GR **1.06**	SE **0.96**	SE **0.97**	GR **0.96**	IT **0.97**	GR **1.12**	GR **1.26**	GR **1.19**	GR **1.09**	IT **0.87**	SE **0.99**	SE **1.03**
tnx & txn	GR **0.88**	GR **0.58**	GR **0.69**	GR **0.77**	GR **0.63**	GR **0.71**	GR **0.86**	GR **0.69**	GR **1.03**	GR **1.04**	GR **0.78**	GR **0.6**
Max Increasing Trend	GR **0.98**	GR **0.81**	GR **0.88**	FR **0.91**	GR **0.95**	GR **1.06**	GR **1.18**	GR **1.16**	GR **1.18**	GR **1.05**	GR **0.95**	FR **0.87**
tnx & txx	GR **0.77**	GR **0.88**	GR **0.75**	GR **0.79**	GR **0.66**	GR **1.08**	GR **0.86**	GR **0.8**	GR **0.83**	GR **0.81**	GR **0.71**	GR **0.63**
Max Increasing Trend	GR **0.95**	GR **0.92**	GR **0.86**	IT **0.88**	IT **0.89**	GR **1.15**	GR **1.17**	GR **1.1**	GR **1.02**	GR **0.86**	GR **0.78**	SE **0.73**

B) Trivariate Pairs

Compound event	January	February	March	April	May	June	July	August	September	October	November	December
bio20, gtn & txx	GR **0.54**	GR **0.52**	GR **0.38**	GR **0.7**	GR **0.92**	GR **0.56**	GR **0.8**	GR **0.62**	GR **0.66**	GR **0.82**	GR **0.56**	GR **0.48**
Max Increasing Trend	IT **0.89**	LT **0.8**	ES **0.81**	SE **0.83**	GR **0.93**	GR **1.1**	GR **1.1**	GR **1**	GR **1.1**	GR **0.88**	GR **0.79**	ES **0.76**
bio20, tnn & txx	GR **0.53**	GR 0.27	GR **0.52**	GR **0.63**	GR **0.81**	GR **0.64**	GR **0.77**	GR **0.58**	GR **0.57**	GR **0.81**	GR **0.75**	GR 0.31
Max Increasing Trend	IT **0.87**	RU **0.76**	ES **0.79**	SE **0.79**	ES **0.86**	GR **0.9**	GR **1.1**	GR **1**	GR **1**	GR **0.85**	GR **0.78**	IT **0.7**
bio20, tnx & txn	GR **0.72**	GR **0.52**	GR **0.66**	GR **0.52**	GR **0.47**	GR **0.77**	GR **0.79**	GR **0.67**	GR **0.84**	GR **0.67**	GR **0.45**	GR **0.53**
Max Increasing Trend	GR **0.79**	BY **0.74**	SE **0.78**	GR **0.75**	GR **1.03**	GR **1.1**	GR **1**	GR **1**	GR **0.9**	GR **0.7**	ES **0.7**	ES **0.8**
bio20, tnx & txx	GR **0.61**	GR **0.44**	GR **0.48**	GR **0.62**	GR **0.59**	GR **0.71**	GR **0.8**	GR **0.68**	GR **0.64**	GR **0.73**	GR **0.6**	GR **0.55**
Max Increasing Trend	IT **0.81**	LV **0.78**	BY **0.81**	SE **0.83**	GR **0.92**	GR **1.03**	GR **1**	GR **1**	GR **1**	GR **0.85**	GR **0.74**	PT **0.75**
bio20, txn & tnn	GR **0.78**	GR **0.6**	GR **0.69**	GR **0.68**	GR **0.63**	GR **0.52**	GR **0.93**	GR **0.75**	GR **0.92**	GR **0.58**	GR **0.61**	GR 0.35
Max Increasing Trend	GR **1.02**	GR **0.74**	FI **0.87**	FI **0.81**	GR **0.86**	GR **0.88**	GR **1.1**	GR **1**	GR **1**	GR **0.73**	GR **0.84**	SE **0.76**
bio20, wci & hi	DK **0.7**	UA **0**	UA **0**	UA **0**	UA **0**	UA **0**	UA **0**	UA **0**	UA **0**	UA **0**	UA **0**	UA **0**
Max Increasing Trend	FR **0.82**	SE **0.69**	ES **0.84**	FR **0.91**	FR **0.78**	ES **0.84**	ES **0.9**	FR **1**	IE **0.8**	ES **0.81**	BE **0.88**	NO **0.92**
cfd, txx & bio20	RU 0	RU **0.4**	RU 0.2	RU 0.11	RU 0.1	UA 0.32	RU 0	RU **0.46**	RU 0.2	RU **0.37**	RU 0.3	RU 0
Max Increasing Trend	IT **0.76**	GR **0.81**	GR **0.71**	GR **0.98**	GR **0.79**	GR **0.96**	GR **0.9**	GR **0.9**	GR **1**	GR **0.81**	GR **0.7**	RU **0.65**
fd, txx & bio20	RU 0	UA **0**	RU -0.0	RU **0.43**	RU **0.3**	RU **0.5**	UA **0.42**	RU **0.46**	RU 0.19	RU 0	RU 0.3	RU 0.16
Max Increasing Trend	IT **0.76**	GR **0.8**	GR **0.76**	GR **0.96**	GR **0.79**	GR **0.96**	GR **0.9**	GR **0.9**	GR **1**	GR **0.81**	GR **0.72**	RU **0.72**
hi, pet & wci	ES **0.9**	ES **0.65**	BE 0.24	AT **0.43**	NO **0.62**	LU **0.51**	FI **0.56**	ES **0.9**	IE **0.39**	ES **0.68**	AT 0.2	AT 0.26
Max Increasing Trend	ES **1.16**	NO **1.05**	LV **1.15**	ES **1.2**	RU **1.15**	AT **1.22**	HR **1.3**	FR **1.3**	RU **1.2**	FR **1.19**	HU **1.12**	ES **1.2**

Legend

Joint Probability (%) >90 & <=100 | >80 & <=90 | >70 & <=80 | >60 & <=70 | >50 & <=60 | <50

Direction of Trend Increasing Trend | Decreasing Trend

The circles and the colour represents the joint probability in %, arrows represents the direction of trend whether increasing or decreasing, and the values represent the magnitude of change in %/month. The country code is as per alpha-2 international standard ISO 3166. Bold value indicates that it is statistically significant (p-value is < 0.05).

Appendix C

Supplementary materials for Chapter 5

Figure S1: Box plot for comparison of various probability distribution fit

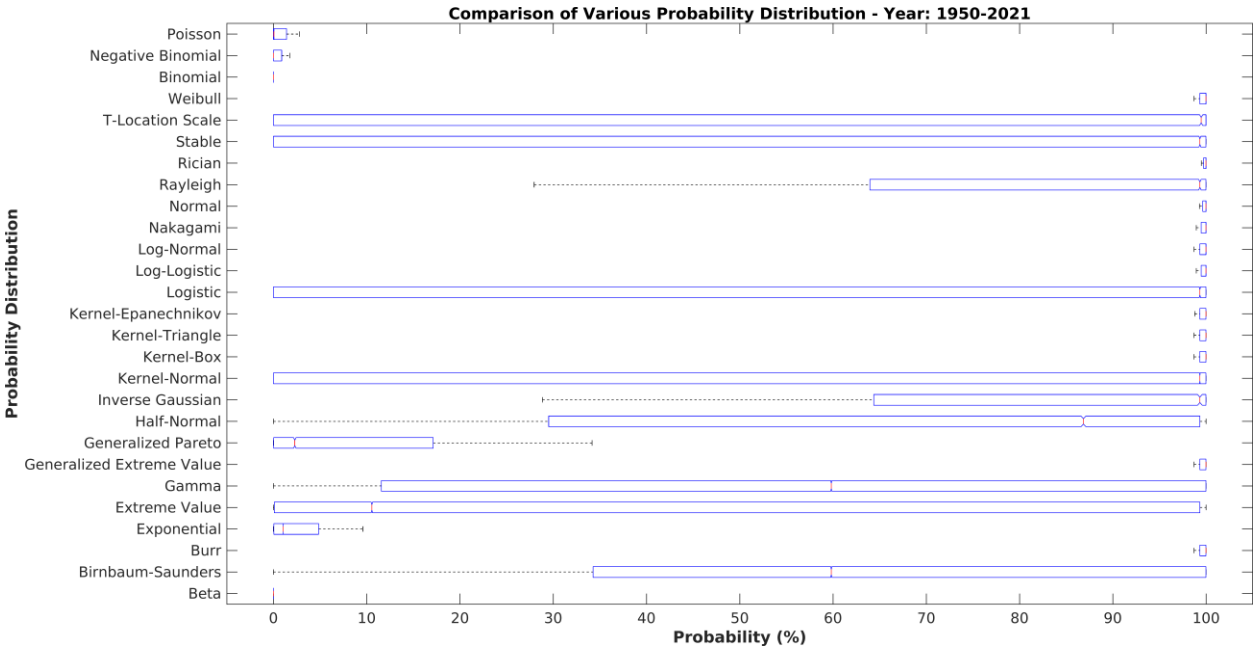

Box plot comparing the performance of various probability distribution fit used in the study to determine the probabilities for each grid.

Figure S2: Co-occurrences of climate indices

A) Number of co-occurrences: European continent

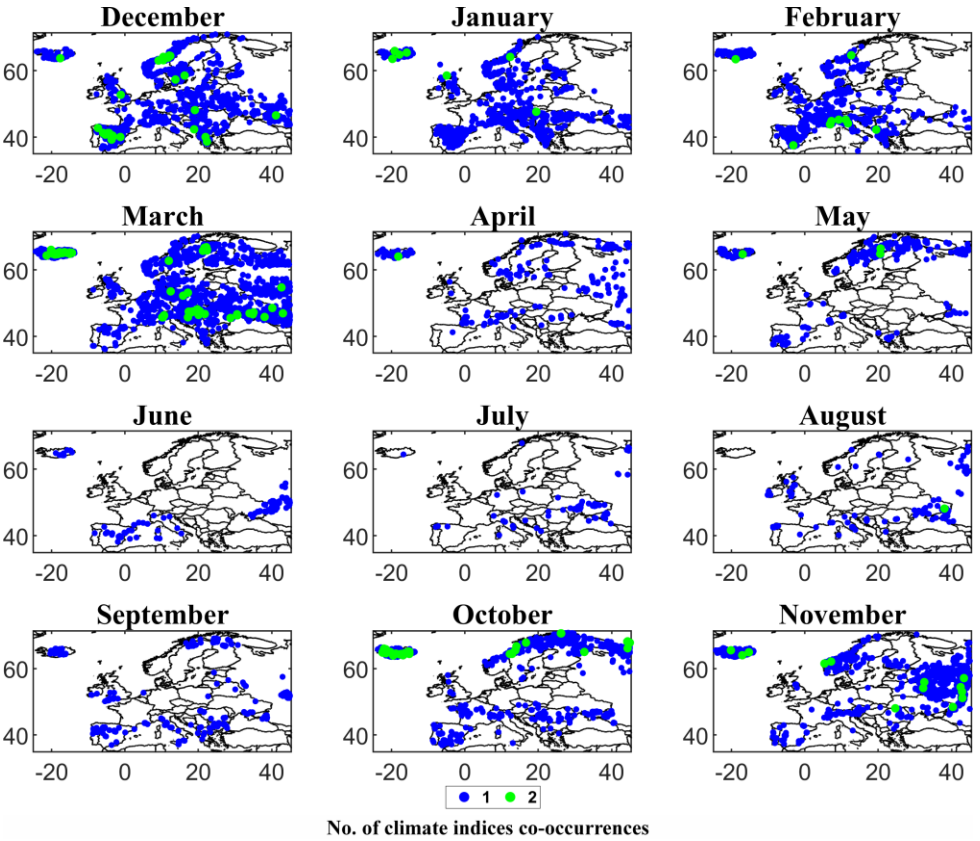

B) Variability of climate indices co-occurrences across different countries in Europe

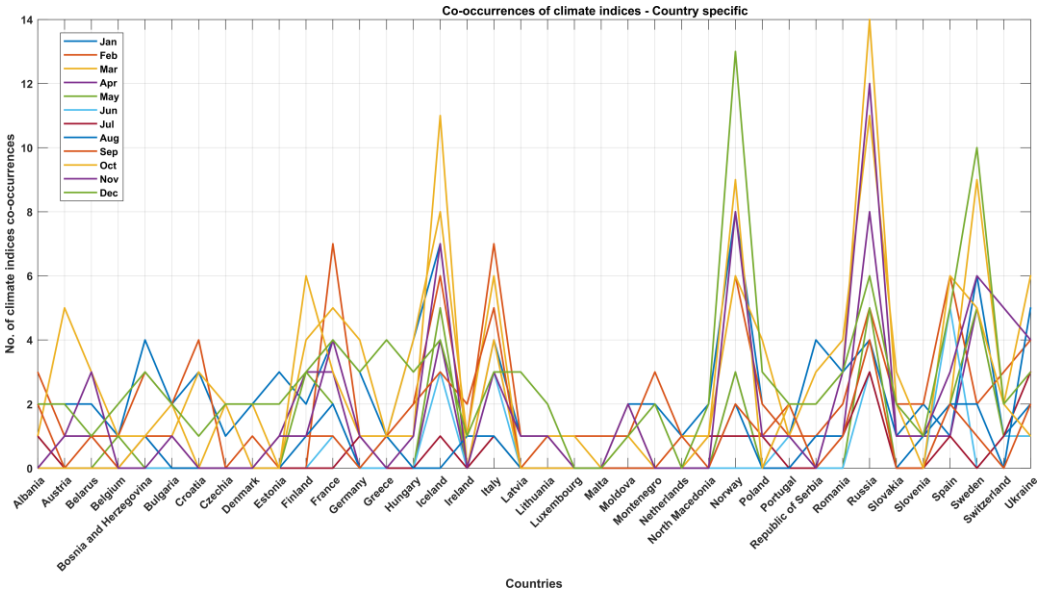

Highlights the number of co-occurrences of climate indices at a monthly scale across A) European continent and B) country specific.

Table S2: Detailed description of hotspots of climate indices (high risk – probability > 90%)

Sr. No.	Climate Indices	Location	Month	Best probability distribution fit
1	cdd	Krasnodar Krai, Russia	August	Negative Binomial
		Krasnodar Krai, Russia	September	Inverse Gaussian
2	cfd	Tver Oblast, Russia	November	Kernel Normal
		Stavropol Krai, Russia	December	Kernel Normal
3	csd	Odesa Oblast, Ukraine	August	Kernel Normal
		Toledo, Spain	September	Kernel Normal
4	cwd	Knockrour East, Ireland	December	Birnbaum-Saunders
		Galway, Ireland	December	Birnbaum-Saunders
5	dd	Grímsnes- og Grafningshreppur, Iceland	May	Generalized Extreme Value
6	dd17	Granada, Spain	February	Kernel Normal
		Stavropol Krai, Russia	April	Kernel Normal
		Murmansk Oblast, Russia	July	Kernel Normal
7	dr1mm	Eyjafjarðarsveit, Iceland	January	Normal
8	dr3mm	Skaftárhreppur, Iceland	January	Gamma
9	fd	Krasnodar Krai, Russia	March	Kernel Normal
		Odesa Oblast, Ukraine	March	Kernel Normal
		Teruel, Spain	November	Normal
10	id	Skaftárhreppur, Iceland	March	Normal
		Eyjafjarðarsveit, Iceland	March	Stable
		Múlaþing, Iceland	March	Kernel Box
		Vesturbyggð, Iceland	March	Kernel Normal
		Súðavíkurhreppur, Iceland	March	Kernel Normal
11	mi	Highland Council, UK	August	Kernel Normal
12	ogs6	Oryol Oblast, Russia	April	Kernel Normal
		Valle Municipality, Norway	May	Kernel Normal
		Lillehammer Municipality, Norway	May	Kernel Normal
		Orsa Municipality, Sweden	May	Kernel Normal
		Kalajoki, Finland	May	Kernel Normal
		Älvsbyn Municipality, Sweden	May	Kernel Normal
		Piteå Municipality, Sweden	May	Kernel Normal
		Simo, Finland	May	Kernel Normal, Kernel Box
		Tervola, Finland	May	Kernel Normal
		Ylitornio, Finland	May	Kernel Normal
		Övertorneå Municipality, Sweden	May	Kernel Normal
		Rovaniemi, Finland	May	Kernel Normal
		Korpilombolo, Sweden	May	Kernel Normal
13	ogs10	Risdal, Norway	May	Kernel Normal
		Färila, Sweden	May	Kernel Normal
14	r10mm	Inner Seas off the West Coast of Scotland	January	Negative Binomial
		Hyen, Norway	December	Kernel Normal
15	su	Volgograd Oblast, Russia	June	Normal
16	tr	Krasnodar Krai, Russia	July	Kernel Normal
17	zcd	Jaén, Spain	January	Kernel Normal

Appendix D

Supplementary materials for Chapter 7

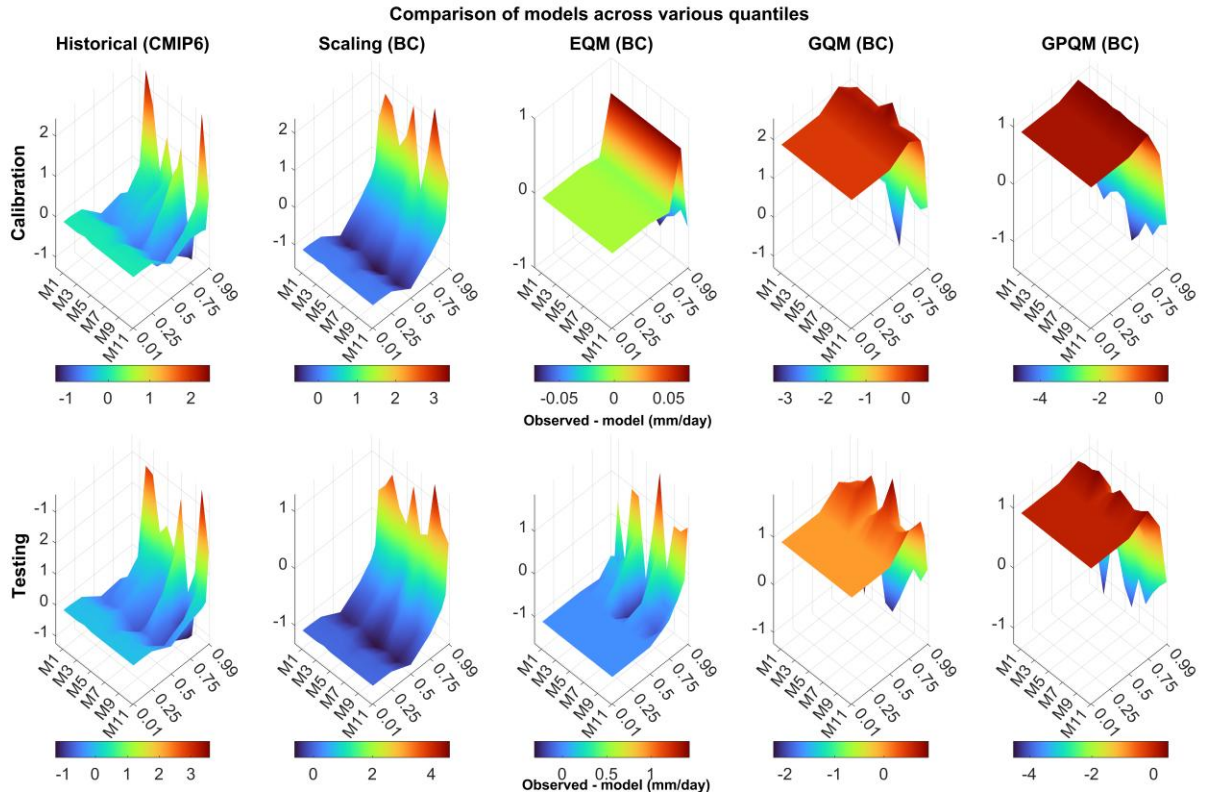

Supplementary Figure S1: Comparison of models across various precipitation quantiles. M1 to M11 are CMIP6 models (notations similar to Table 1).

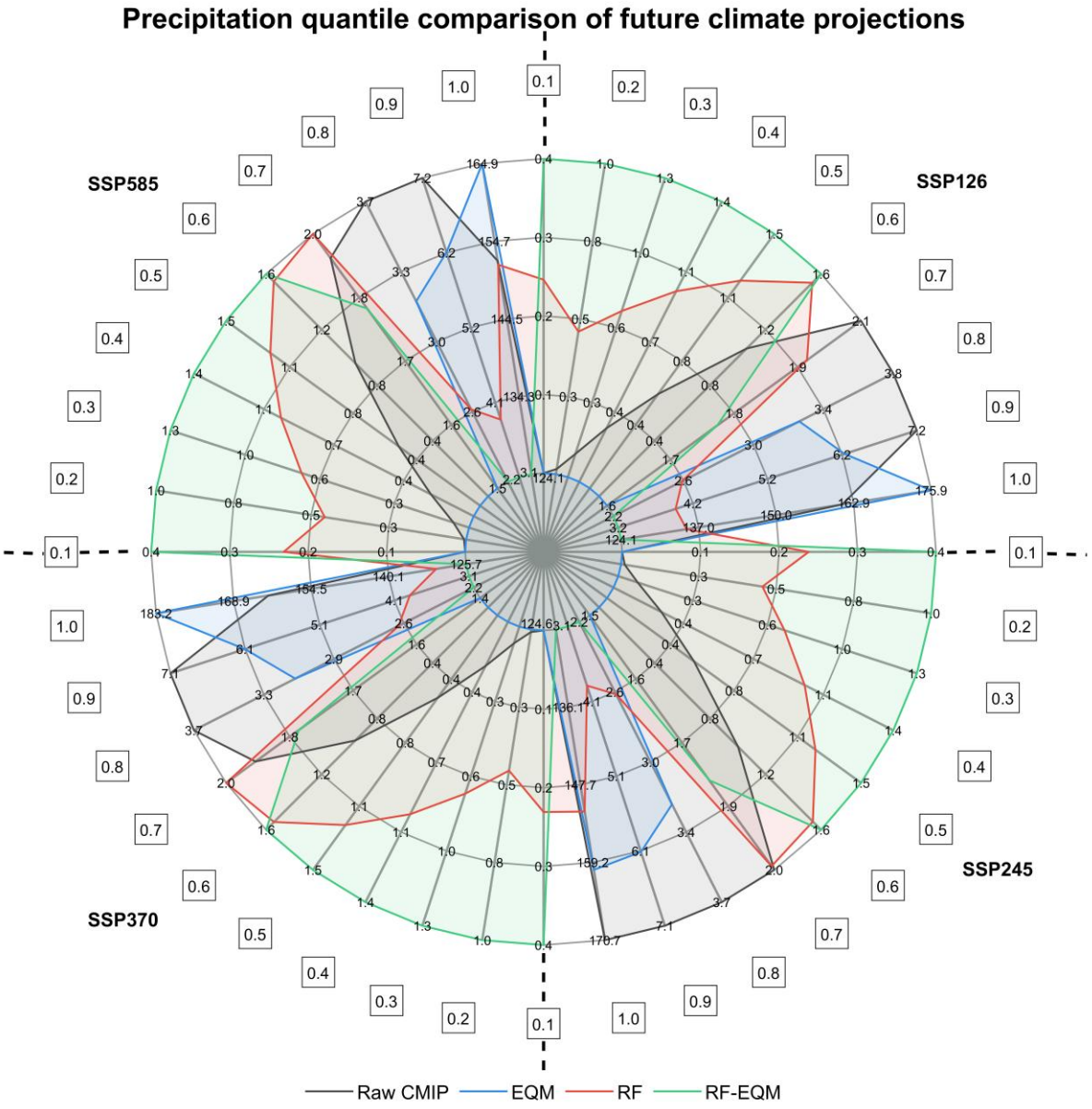

Supplementary Figure S2: Quantile comparison for future climate projections: Precipitation quantile plots for various SSP scenario.

References

Abdelmoaty, H.M., Rajulapati, C.R., Nerantzaki, S.D., Papalexiou, S.M., 2025. Bias-corrected high-resolution temperature and precipitation projections for Canada. Sci. Data 12, 191.

Adger, W.N., Arnell, N.W., Tompkins, E.L., 2005. Successful adaptation to climate change across scales. Glob. Environ. Chang. 15, 77–86.

AghaKouchak, A., Chiang, F., Huning, L.S., Love, C.A., Mallakpour, I., Mazdiyasni, O., Moftakhari, H., Papalexiou, S.M., Ragno, E., Sadegh, M., 2020. Climate extremes and compound hazards in a warming world. Annu. Rev. Earth Planet. Sci. 48, 519–548.

Atlas, D., Ulbrich, C.W., 1977. Path-and area-integrated rainfall measurement by microwave attenuation in the 1–3 cm band. J. Appl. Meteorol. Climatol. 16, 1322–1331.

Barriopedro, D., Fischer, E.M., Luterbacher, J., Trigo, R.M., García-Herrera, R., 2011. The hot summer of 2010: redrawing the temperature record map of Europe. Science (80-.). 332, 220–224.

Beniston, M., Goyette, S., 2007. Changes in variability and persistence of climate in Switzerland: exploring 20th century observations and 21st century simulations. Glob. Planet. Change 57, 1–15.

Bennett, J.C., Grose, M.R., Post, D.A., Ling, F.L.N., Corney, S.P., Bindoff, N.L., 2011. Performance of quantile-quantile bias-correction for use in hydroclimatological projections, in: MODSIM2011 International Congress on Modelling and Simulation, Perth. pp. 2668–2675.

Berényi, A., Bartholy, J., Pongrácz, R., 2023. Analysis of precipitation-related climatic conditions in European plain regions. Weather Clim. Extrem. 42, 100610.

Berg, P., Moseley, C., Haerter, J.O., 2013. Strong increase in convective precipitation in response to higher temperatures. Nat. Geosci. 6, 181–185.

Berghuijs, W.R., Harrigan, S., Molnar, P., Slater, L.J., Kirchner, J.W., 2019. The relative importance of different flood-generating mechanisms across Europe. Water Resour. Res. 55, 4582–4593.

Beritelli, F., Capizzi, G., Sciuto, G. Lo, Napoli, C., Scaglione, F., 2018. Rainfall estimation based on the intensity of the received signal in a LTE/4G mobile terminal by using a probabilistic neural network. IEEE Access 6, 30865–30873.

Bevacqua, E., Maraun, D., Vousdoukas, M.I., Voukouvalas, E., Vrac, M., Mentaschi, L., Widmann, M., 2019. Higher probability of compound flooding from precipitation and storm surge in Europe under anthropogenic climate change. Sci. Adv. 5, eaaw5531.

Bevacqua, E., Zappa, G., Lehner, F., Zscheischler, J., 2022. Precipitation trends determine future occurrences of compound hot–dry events. Nat. Clim. Chang. 12, 350–355.

Beyer, R., Krapp, M., Manica, A., 2020. An empirical evaluation of bias correction methods for palaeoclimate simulations. Clim. Past 16, 1493–1508.

Bhatti, H.A., Rientjes, T., Haile, A.T., Habib, E., Verhoef, W., 2016. Evaluation of bias correction method for satellite-based rainfall data. Sensors 16, 884.

Blettner, N., Chwala, C., Haese, B., Hörning, S., Kunstmann, H., 2022. Combining commercial microwave link and rain gauge observations to estimate countrywide precipitation: a stochastic reconstruction and pattern analysis approach. Water Resour. Res. 58, e2022WR032563.

Bocchi, S., La Rosa, D., Pileri, P., 2012. Agro-ecological analysis for the EU water framework directive: an applied case study for the river contract of the Seveso Basin (Italy). Environ. Manage. 50, 514–529.

Bourdeau-Goulet, S., Hassanzadeh, E., 2021. Comparisons between CMIP5 and CMIP6 models: Simulations of climate indices influencing food security, infrastructure resilience, and human health in Canada. Earth's Futur. 9, e2021EF001995.

Bowman, A.W., Azzalini, A., 1997. Applied smoothing techniques for data analysis: the kernel approach with S-Plus illustrations. OUP Oxford.

Breiman, L., 2001. Random forests. Mach. Learn. 45, 5–32.

Bull-Kamanga, L., Diagne, K., Lavell, A., Leon, E., Lerise, F., MacGregor, H., Maskrey, A., Meshack, M., Pelling, M., Reid, H., 2003. From everyday hazards to disasters: the accumulation of risk in urban areas. Environ. Urban. 15, 193–204.

Cannon, A.J., Sobie, S.R., Murdock, T.Q., 2015. Bias correction of GCM precipitation by quantile mapping: how well do methods preserve changes in quantiles and extremes? J. Clim. 28, 6938–6959.

Cardell, M.F., Amengual, A., Romero, R., Ramis, C., 2020. Future extremes of temperature and precipitation in Europe derived from a combination of dynamical and statistical approaches. Int. J. Climatol. 40, 4800–4827. https://doi.org/10.1002/joc.6490

Cheah, J.Y.C., 1993. Wet antenna effect on VSAT rain margin. IEEE Trans. Commun. 41, 1238–1244.

Chen, J., Brissette, F.P., Chaumont, D., Braun, M., 2013a. Finding appropriate bias correction methods in downscaling precipitation for hydrologic impact studies over North America. Water Resour. Res. 49, 4187–4205.

Chen, J., Brissette, F.P., Chaumont, D., Braun, M., 2013b. Performance and uncertainty evaluation of empirical downscaling methods in quantifying the climate change impacts on hydrology over two North American river basins. J. Hydrol. 479, 200–214.

Chen, J., Brissette, F.P., Leconte, R., 2011. Uncertainty of downscaling method in quantifying the

impact of climate change on hydrology. J. Hydrol. 401, 190–202.

Chen, J., Yang, Y., Tang, J., 2022. Bias correction of surface air temperature and precipitation in CORDEX East Asia simulation: What should we do when applying bias correction? Atmos. Res. 280, 106439.

Chervenkov, H., Slavov, K., 2021. ETCCDI climate indices for assessment of the recent climate over southeast Europe, in: Advances in High Performance Computing: Results of the International Conference on "High Performance Computing" Borovets, Bulgaria, 2019. Springer, pp. 398–412.

Cho, D., Yoo, C., Im, J., Cha, D., 2020. Comparative assessment of various machine learning-based bias correction methods for numerical weather prediction model forecasts of extreme air temperatures in urban areas. Earth Sp. Sci. 7, e2019EA000740.

Christensen, J.H., Boberg, F., Christensen, O.B., Lucas-Picher, P., 2008. On the need for bias correction of regional climate change projections of temperature and precipitation. Geophys. Res. Lett. 35.

Chwala, C., Keis, F., Kunstmann, H., 2016. Real-time data acquisition of commercial microwave link networks for hydrometeorological applications. Atmos. Meas. Tech. 9, 991–999.

Clarke, B., Otto, F., Stuart-Smith, R., Harrington, L., 2022. Extreme weather impacts of climate change: an attribution perspective. Environ. Res. Clim. 1, 12001.

Contzen, J., Dickhaus, T., Lohmann, G., 2022. Variability extremes: Statistical validation of the Alfred Wegener Institute Earth System Model (AWI-ESM). Geosci. Model Dev. 15, 1803–1820. https://doi.org/10.5194/gmd-15-1803-2022

Coppola, E., Nogherotto, R., Ciarlo', J.M., Giorgi, F., van Meijgaard, E., Kadygrov, N., Iles, C., Corre, L., Sandstad, M., Somot, S., Nabat, P., Vautard, R., Levavasseur, G., Schwingshackl, C., Sillmann, J., Kjellström, E., Nikulin, G., Aalbers, E., Lenderink, G., Christensen, O.B., Boberg, F., Sørland, S.L., Demory, M.E., Bülow, K., Teichmann, C., Warrach-Sagi, K., Wulfmeyer, V., 2021. Assessment of the European Climate Projections as Simulated by the Large EURO-CORDEX Regional and Global Climate Model Ensemble. J. Geophys. Res. Atmos. 126, 1–20. https://doi.org/10.1029/2019JD032356

Cornes, R.C., van der Schrier, G., van den Besselaar, E.J.M., Jones, P.D., 2018. An Ensemble Version of the E-OBS Temperature and Precipitation Data Sets. J. Geophys. Res. Atmos. 123, 9391–9409. https://doi.org/10.1029/2017JD028200

Crockett, J.L., Westerling, A.L., 2018. Greater temperature and precipitation extremes intensify Western US droughts, wildfire severity, and Sierra Nevada tree mortality. J. Clim. 31, 341–354.

da Silva Mello, L.A.R., Pontes, M.S., 2007. Prediction of rain attenuation in terrestrial links with the

full rainfall rate distribution.

Daher, A., Al Sakka, H., Chaaban, K., 2022. Low complexity single-layer neural network for enhanced rainfall estimation using microwave links. J. Hydroinformatics.

Daniel, H., 2023. Performance assessment of bias correction methods using observed and regional climate model data in different watersheds, Ethiopia. J. Water Clim. Chang. 14, 2007–2028.

De Vos, L.W., Droste, A.M., Zander, M.J., Overeem, A., Leijnse, H., Heusinkveld, B.G., Steeneveld, G.J., Uijlenhoet, R., 2020. Hydrometeorological monitoring using opportunistic sensing networks in the Amsterdam metropolitan area. Bull. Am. Meteorol. Soc. 101, E167–E185.

De Vos, L.W., Overeem, A., Leijnse, H., Uijlenhoet, R., 2019. Rainfall estimation accuracy of a nationwide instantaneously sampling commercial microwave link network: Error dependency on known characteristics. J. Atmos. Ocean. Technol. 36, 1267–1283.

Deen, T.A., Arain, M.A., Champagne, O., Chow-Fraser, P., Nagabhatla, N., Martin-Hill, D., 2021. Evaluation of observed and projected extreme climate trends for decision making in Six Nations of the Grand River, Canada. Clim. Serv. 24, 100263.

Dell, M., Jones, B.F., Olken, B.A., 2014. What do we learn from the weather? The new climate-economy literature. J. Econ. Lit. 52, 740–798.

Dey, A., Sahoo, D.P., Kumar, R., Remesan, R., 2022. A multimodel ensemble machine learning approach for CMIP6 climate model projections in an Indian River basin. Int. J. Climatol. 42, 9215–9236.

Di Napoli, C., Pappenberger, F., Cloke, H.L., 2018. Assessing heat-related health risk in Europe via the Universal Thermal Climate Index (UTCI). Int. J. Biometeorol. 62, 1155–1165.

Domínguez-Castro, F., Reig, F., Vicente-Serrano, S.M., Aguilar, E., Peña-Angulo, D., Noguera, I., Revuelto, J., van der Schrier, G., El Kenawy, A.M., 2020. A multidecadal assessment of climate indices over Europe. Sci. data 7, 125.

Dong, B., Sutton, R.T., Shaffrey, L., 2017. Understanding the rapid summer warming and changes in temperature extremes since the mid-1990s over Western Europe. Clim. Dyn. 48, 1537–1554. https://doi.org/10.1007/s00382-016-3158-8

Donnelly, C., Greuell, W., Andersson, J., Gerten, D., Pisacane, G., Roudier, P., Ludwig, F., 2017. Impacts of climate change on European hydrology at 1.5, 2 and 3 degrees mean global warming above preindustrial level. Clim. Change 143, 13–26.

Doshi, S.C., Gerrit, L., and Ionita, M., 2025. Probabilistic assessment of climate indices across Europe: analysing risk exposure in population density and land use types. Geomatics, Nat. Hazards Risk 16, 2484397. https://doi.org/10.1080/19475705.2025.2484397

Doshi, S.C., Lohmann, G., Ionita, M., 2023a. Hotspot movement of compound events on the Europe

continent. Sci. Rep. 13, 18100. https://doi.org/10.1038/s41598-023-45067-6

Doshi, S.C., Lohmann, G., Rimbu, N., Ionita, M., 2023b. Spatiotemporal trend analysis of climate indices for the European continent. J. Water Clim. Chang. 14, 3112–3130. https://doi.org/10.2166/wcc.2023.183

Doumounia, A., Gosset, M., Cazenave, F., Kacou, M., Zougmore, F., 2014. Rainfall monitoring based on microwave links from cellular telecommunication networks: First results from a West African test bed. Geophys. Res. Lett. 41, 6016–6022.

Dunn, R.J.H., Alexander, L. V, Donat, M.G., Zhang, X., Bador, M., Herold, N., Lippmann, T., Allan, R., Aguilar, E., Barry, A.A., 2020. Development of an updated global land in situ-based data set of temperature and precipitation extremes: HadEX3. J. Geophys. Res. Atmos. 125, e2019JD032263.

Easterling, D.R., Evans, J.L., Groisman, P.Y., Karl, T.R., Kunkel, K.E., Ambenje, P., 2000. Observed variability and trends in extreme climate events: a brief review. Bull. Am. Meteorol. Soc. 81, 417–426.

Ebi, K.L., Vanos, J., Baldwin, J.W., Bell, J.E., Hondula, D.M., Errett, N.A., Hayes, K., Reid, C.E., Saha, S., Spector, J., 2021. Extreme weather and climate change: population health and health system implications. Annu. Rev. Public Health 42, 293–315.

EEA, 2024. Economic losses from weather- and climate-related extremes in Europe [WWW Document]. URL https://www.eea.europa.eu/en/analysis/indicators/economic-losses-from-climate-related

Eyring, V., Bony, S., Meehl, G.A., Senior, C.A., Stevens, B., Stouffer, R.J., Taylor, K.E., 2016. Overview of the Coupled Model Intercomparison Project Phase 6 (CMIP6) experimental design and organization. Geosci. Model Dev. 9, 1937–1958.

Fan, X., Jiang, L., Gou, J., 2021. Statistical downscaling and projection of future temperatures across the Loess Plateau, China. Weather Clim. Extrem. 32, 100328.

Fang, G.H., Yang, J., Chen, Y.N., Zammit, C., 2015. Comparing bias correction methods in downscaling meteorological variables for a hydrologic impact study in an arid area in China. Hydrol. Earth Syst. Sci. 19, 2547–2559.

Fencl, M., Dohnal, M., Rieckermann, J., Bareš, V., 2017. Gauge-adjusted rainfall estimates from commercial microwave links. Hydrol. Earth Syst. Sci. 21, 617–634.

Fencl, M., Rieckermann, J., Sýkora, P., Stránský, D., Bareš, V., 2015. Commercial microwave links instead of rain gauges: Fiction or reality? Water Sci. Technol. 71, 31–37.

Fencl, M., Valtr, P., Kvičera, M., Bareš, V., 2018. Quantifying wet antenna attenuation in 38-GHz commercial microwave links of cellular backhaul. IEEE Geosci. Remote Sens. Lett. 16, 514–

518.

Fenicia, F., Pfister, L., Kavetski, D., Matgen, P., Iffly, J.-F., Hoffmann, L., Uijlenhoet, R., 2012. Microwave links for rainfall estimation in an urban environment: Insights from an experimental setup in Luxembourg-City. J. Hydrol. 464, 69–78.

Field, C.B., Barros, V., Stocker, T.F., Dahe, Q., 2012. Managing the risks of extreme events and disasters to advance climate change adaptation: special report of the intergovernmental panel on climate change. Cambridge University Press.

Field, C.B., Barros, V.R., 2014. Climate change 2014–Impacts, adaptation and vulnerability: Regional aspects. Cambridge University Press.

Fink, A.H., Brücher, T., Krüger, A., Leckebusch, G.C., Pinto, J.G., Ulbrich, U., 2004. The 2003 European summer heatwaves and drought-synoptic diagnosis and impacts. Weather 59, 209–216.

Francis, D., Temimi, M., Fonseca, R., Nelli, N.R., Abida, R., Weston, M., Whebe, Y., 2021. On the analysis of a summertime convective event in a hyperarid environment. Q. J. R. Meteorol. Soc. 147, 501–525.

Furtak, K., Wolińska, A., 2023. The impact of extreme weather events as a consequence of climate change on the soil moisture and on the quality of the soil environment and agriculture–A review. Catena 231, 107378.

Garcia-Rubia, J.M., Riera, J.M., Benarroch, A., Garcia-del-Pino, P., 2011. Estimation of rain attenuation from experimental drop size distributions. IEEE Antennas Wirel. Propag. Lett. 10, 839–842.

Gariano, S.L., Guzzetti, F., 2016. Landslides in a changing climate. Earth-science Rev. 162, 227–252.

Gasper, R., Blohm, A., Ruth, M., 2011. Social and economic impacts of climate change on the urban environment. Curr. Opin. Environ. Sustain. 3, 150–157.

Gazol, A., Camarero, J.J., 2022. Compound climate events increase tree drought mortality across European forests. Sci. Total Environ. 816, 151604.

Giorgi, F., Gutowski Jr, W.J., 2015. Regional dynamical downscaling and the CORDEX initiative. Annu. Rev. Environ. Resour. 40, 467–490.

Gocic, M., Trajkovic, S., 2013. Analysis of changes in meteorological variables using Mann-Kendall and Sen's slope estimator statistical tests in Serbia. Glob. Planet. Change 100, 172–182.

Goldshtein, O., Messer, H., Zinevich, A., 2009. Rain rate estimation using measurements from commercial telecommunications links. IEEE Trans. signal Process. 57, 1616–1625.

Gosset, M., Kunstmann, H., Zougmore, F., Cazenave, F., Leijnse, H., Uijlenhoet, R., Chwala, C., Keis, F., Doumounia, A., Boubacar, B., 2016. Improving rainfall measurement in gauge poor

regions thanks to mobile telecommunication networks. Bull. Am. Meteorol. Soc. 97, ES49–ES51.

Graf, M., Chwala, C., Polz, J., Kunstmann, H., 2020. Rainfall estimation from a German-wide commercial microwave link network: optimized processing and validation for 1 year of data. Hydrol. Earth Syst. Sci. 24, 2931–2950.

Graf, M., El Hachem, A., Eisele, M., Seidel, J., Chwala, C., Kunstmann, H., Bárdossy, A., 2021. Rainfall estimates from opportunistic sensors in Germany across spatio-temporal scales. J. Hydrol. Reg. Stud. 37, 100883.

Güçlü, Y.S., 2020. Improved visualization for trend analysis by comparing with classical Mann-Kendall test and ITA. J. Hydrol. 584, 124674.

Guerreiro, S.B., Dawson, R.J., Kilsby, C., Lewis, E., Ford, A., 2018. Future heat-waves, droughts and floods in 571 European cities. Environ. Res. Lett. 13, 34009.

Guthrie, R.H., Mitchell, S.J., Lanquaye-Opoku, N., Evans, S.G., 2010. Extreme weather and landslide initiation in coastal British Columbia. Geological Society of London.

Gutjahr, O., Heinemann, G., 2013. Comparing precipitation bias correction methods for high-resolution regional climate simulations using COSMO-CLM: Effects on extreme values and climate change signal. Theor. Appl. Climatol. 114, 511–529.

Hall, A., 2014. Projecting regional change. Science (80-.). 346, 1461–1462.

Hao, Z., AghaKouchak, A., 2013. Multivariate standardized drought index: a parametric multi-index model. Adv. Water Resour. 57, 12–18.

Hartmann, D.L., 2016. Chapter 11—Global climate models. Glob. Phys. Climatol. 2nd, ed.; Elsevier Boston, MA, USA 325–360.

Haylock, M.R., Goodess, C.M., 2004. Interannual variability of European extreme winter rainfall and links with mean large-scale circulation. Int. J. Climatol. A J. R. Meteorol. Soc. 24, 759–776.

He, X., Chaney, N.W., Schleiss, M., Sheffield, J., 2016. Spatial downscaling of precipitation using adaptable random forests. Water Resour. Res. 52, 8217–8237.

Heinlein, R.A., 1973. Time Enough for Love. 1973. New York: Berkley, 1974. Time Enough Love.

Heinrich, P., Hagemann, S., Weisse, R., Schrum, C., Daewel, U., Gaslikova, L., 2023. Compound flood events: analysing the joint occurrence of extreme river discharge events and storm surges in northern and central Europe. Nat. hazards earth Syst. Sci. 23, 1967–1985.

Hertig, E., Beck, C., Wanner, H., Jacobeit, J., 2015. A review of non-stationarities in climate variability of the last century with focus on the North Atlantic–European sector. Earth-science Rev. 147, 1–17.

Hess, P., Lange, S., Schötz, C., Boers, N., 2023. Deep learning for bias-correcting CMIP6-class earth

system models. Earth's Futur. 11, e2023EF004002.

Homsi, R., Shiru, M.S., Shahid, S., Ismail, T., Harun, S. Bin, Al-Ansari, N., Chau, K.-W., Yaseen, Z.M., 2020. Precipitation projection using a CMIP5 GCM ensemble model: a regional investigation of Syria. Eng. Appl. Comput. Fluid Mech. 14, 90–106.

Hong, E.S., Lane, S., Murrell, D., Tarasenko, N., Christodoulou, C., 2017. Mitigation of reflector dish wet antenna effect at 72 and 84 GHz. IEEE Antennas Wirel. Propag. Lett. 16, 3100–3103.

Hotovy, O., Nedelcev, O., Jenicek, M., 2023. Changes in rain-on-snow events in mountain catchments in the rain–snow transition zone. Hydrol. Sci. J. 68, 572–584.

Hou, A.Y., Kakar, R.K., Neeck, S., Azarbarzin, A.A., Kummerow, C.D., Kojima, M., Oki, R., Nakamura, K., Iguchi, T., 2014. The global precipitation measurement mission. Bull. Am. Meteorol. Soc. 95, 701–722.

Hu, T., Sun, Y., Zhang, X., Min, S.-K., Kim, Y.-H., 2020. Human influence on frequency of temperature extremes. Environ. Res. Lett. 15, 64014.

Huang, B., Liu, Z., Duan, Q., Rajib, A., Yin, J., 2024. Unsupervised deep learning bias correction of CMIP6 global ensemble precipitation predictions with cycle generative adversarial network. Environ. Res. Lett. 19, 94003.

Hurrell, J.W., 1995. Decadal trends in the North Atlantic Oscillation: Regional temperatures and precipitation. Science (80-.). 269, 676–679.

Imhoff, R.O., Overeem, A., Brauer, C.C., Leijnse, H., Weerts, A.H., Uijlenhoet, R., 2020. Rainfall nowcasting using commercial microwave links. Geophys. Res. Lett. 47, e2020GL089365.

Ionita, M., Caldarescu, D.E., Nagavciuc, V., 2021. Compound hot and dry events in Europe: variability and large-scale drivers. Front. Clim. 3, 688991.

Ionita, M., Dima, M., Lohmann, G., Scholz, P., Rimbu, N., 2015. Predicting the June 2013 European flooding based on precipitation, soil moisture, and sea level pressure. J. Hydrometeorol. 16, 598–614.

Ionita, M., Lohmann, G., Rimbu, N., Chelcea, S., Dima, M., 2012. Interannual to decadal summer drought variability over Europe and its relationship to global sea surface temperature. Clim. Dyn. 38, 363–377. https://doi.org/10.1007/s00382-011-1028-y

IPCC, 2025. History of the IPCC [WWW Document]. URL https://www.ipcc.ch/

IPCC, 2023. Climate Change 2023: Synthesis Report, Summary for Policymakers. Contribution of Working Groups I, II and III to the Sixth Assessment Report of the Intergovernmental Panel on Climate Change [Core Writing Team, H. Lee and J. Romero (eds.)]. IPC.

IPCC, 2013. Climate Change 2013 – The Physical Science Basis: Working Group I Contribution to the Fifth Assessment Report of the Intergovernmental Panel on Climate Change. Cambridge

University Press, Cambridge. https://doi.org/DOI: 10.1017/CBO9781107415324

ITU-R, 2005. Recommendation ITU-R P.838-3: Specific attenuation model for rain. Int. Telecommun. Union, Genevae 1–8.

Jaiswal, R., Mall, R.K., Singh, N., Lakshmi Kumar, T. V, Niyogi, D., 2022. Evaluation of bias correction methods for regional climate models: Downscaled rainfall analysis over diverse agroclimatic zones of India. Earth Sp. Sci. 9, e2021EA001981.

Jiang, S., Babovic, V., Zheng, Y., Xiong, J., 2019. Advancing opportunistic sensing in hydrology: A novel approach to measuring rainfall with ordinary surveillance cameras. Water Resour. Res. 55, 3004–3027.

Joe, H., 2014. Dependence modeling with copulas. CRC press.

Johnson, N.L., Kotz, S., Balakrishnan, N., 1995. Continuous univariate distributions, volume 2. John wiley & sons.

Jose, D.M., Vincent, A.M., Dwarakish, G.S., 2022. Improving multiple model ensemble predictions of daily precipitation and temperature through machine learning techniques. Sci. Rep. 12, 4678.

Kaur, L., Rishi, M.S., Sharma, S., Khosla, A., 2019. Impervious surfaces an indicator of hydrological changes in urban watershed: a review. Jour. Environ. Soil Sci 4, 469–473.

Kendall, M.G., 1975. Rank correlation methods.

Kesavavarthini, T., Rajesh, A.N., Venkata Srinivas, C., Kumar, T.V.L., 2023. Bias correction of CMIP6 simulations of precipitation over Indian monsoon core region using deep learning algorithms. Int. J. Climatol. 43, 3749–3767.

Kew, S.F., Selten, F.M., Lenderink, G., Hazeleger, W., 2013. The simultaneous occurrence of surge and discharge extremes for the Rhine delta. Nat. Hazards Earth Syst. Sci. 13, 2017–2029.

Kharadly, M.M.Z., Ross, R., 2001. Effect of wet antenna attenuation on propagation data statistics. IEEE Trans. Antennas Propag. 49, 1183–1191.

Khozani, Z.S., Precht, E., Ionita, M., 2024. Weekly streamflow forecasting of Rhine river based on machine learning approaches. Nat. Hazards 1–19.

Kidd, C., Becker, A., Huffman, G.J., Muller, C.L., Joe, P., Skofronick-Jackson, G., Kirschbaum, D.B., 2017. So, how much of the Earth's surface is covered by rain gauges? Bull. Am. Meteorol. Soc. 98, 69–78.

Kim, H., Ham, Y.G., Joo, Y.S., Son, S.W., 2021. Deep learning for bias correction of MJO prediction. Nat. Commun. 12, 3087.

Kornhuber, K., Osprey, S., Coumou, D., Petri, S., Petoukhov, V., Rahmstorf, S., Gray, L., 2019. Extreme weather events in early summer 2018 connected by a recurrent hemispheric wave-7 pattern. Environ. Res. Lett. 14, 54002.

Leal Filho, W., Azeiteiro, U.M., Balogun, A.-L., Setti, A.F.F., Mucova, S.A.R., Ayal, D., Totin, E., Lydia, A.M., Kalaba, F.K., Oguge, N.O., 2021. The influence of ecosystems services depletion to climate change adaptation efforts in Africa. Sci. Total Environ. 779, 146414.

Leeding, R., Riboldi, J., Messori, G., 2023. On Pan-Atlantic cold, wet and windy compound extremes. Weather Clim. Extrem. 39, 100524.

Leijnse, H., Uijlenhoet, R., Berne, A., 2010. Errors and uncertainties in microwave link rainfall estimation explored using drop size measurements and high-resolution radar data. J. Hydrometeorol. 11, 1330–1344.

Leijnse, H., Uijlenhoet, R., Stricker, J.N.M., 2008. Microwave link rainfall estimation: Effects of link length and frequency, temporal sampling, power resolution, and wet antenna attenuation. Adv. Water Resour. 31, 1481–1493.

Leijnse, H., Uijlenhoet, R., Stricker, J.N.M., 2007. Hydrometeorological application of a microwave link: 2. Precipitation. Water Resour. Res. 43.

Lenderink, G., Buishand, A., Van Deursen, W., 2007. Estimates of future discharges of the river Rhine using two scenario methodologies: direct versus delta approach. Hydrol. Earth Syst. Sci. 11, 1145–1159.

Leonard, M., Metcalfe, A., Lambert, M., 2008. Frequency analysis of rainfall and streamflow extremes accounting for seasonal and climatic partitions. J. Hydrol. 348, 135–147.

Leone, V., Elia, M., Lovreglio, R., Correia, F., Tedim, F., 2023. The 2017 extreme wildfires events in Portugal through the perceptions of volunteer and professional firefighters. Fire 6, 133.

Li, C., Zwiers, F., Zhang, X., Li, G., Sun, Y., Wehner, M., 2021. Changes in annual extremes of daily temperature and precipitation in CMIP6 models. J. Clim. 34, 3441–3460.

Li, J.L.F., Xu, K.-M., Richardson, M., Lee, W.-L., Jiang, J.H., Yu, J.-Y., Wang, Y.-H., Fetzer, E., Wang, L.-C., Stephens, G., 2020. Annual and seasonal mean tropical and subtropical precipitation bias in CMIP5 and CMIP6 models. Environ. Res. Lett. 15, 124068.

Li, Y., Li, Z., Zhang, Z., Chen, L., Kurkute, S., Scaff, L., Pan, X., 2019. High-resolution regional climate modeling and projection over western Canada using a weather research forecasting model with a pseudo-global warming approach. Hydrol. Earth Syst. Sci. 23, 4635–4659.

Li, Z., Deng, X., Zhang, Y., 2021. Evaluation and convergence analysis of socio-economic vulnerability to natural hazards of Belt and Road Initiative countries. J. Clean. Prod. 282, 125406.

Lian, B., Wei, Z., Sun, X., Li, Z., Zhao, J., 2022. A Review on Rainfall Measurement Based on Commercial Microwave Links in Wireless Cellular Networks. Sensors 22, 4395.

Lin, S.H., 1977. 11-GHz radio: nationwide long-term rain rate statistics and empirical calculation of

11-GHz microwave rain attenuation. Bell Syst. Tech. J. 56, 1581–1604.

Ling, F., Li, Y., Luo, J.-J., Zhong, X., Wang, Z., 2022. Two deep learning-based bias-correction pathways improve summer precipitation prediction over China. Environ. Res. Lett. 17, 124025.

Liu, R., Zhou, W., Yin, H., Ren, W., Feng, J., Deng, J., 2024. Prediction of rainfall-induced debris flow using Random Forests and Bayesian Optimization in Yingxiu Town, Wenchuan County, China. Bull. Eng. Geol. Environ. 83, 156.

Liu, T., Zhu, X., Tang, M., Guo, C., Lu, D., 2024. Multi-model ensemble bias-corrected precipitation dataset and its application in identification of drought-flood abrupt alternation in China. Atmos. Res. 307, 107481.

Lohmann, G., Pfeiffer, M., Laepple, T., Leduc, G., Kim, J.H., 2013. A model-data comparison of the Holocene global sea surface temperature evolution. Clim. Past 9, 1807–1839. https://doi.org/10.5194/cp-9-1807-2013

Lorenz, R., Stalhandske, Z., Fischer, E.M., 2019. Detection of a climate change signal in extreme heat, heat stress, and cold in Europe from observations. Geophys. Res. Lett. 46, 8363–8374.

Luo, M., Liu, T., Meng, F., Duan, Y., Frankl, A., Bao, A., De Maeyer, P., 2018. Comparing bias correction methods used in downscaling precipitation and temperature from regional climate models: a case study from the Kaidu River Basin in Western China. Water 10, 1046.

Madsen, H., Lawrence, D., Lang, M., Martinkova, M., Kjeldsen, T.R., 2014. Review of trend analysis and climate change projections of extreme precipitation and floods in Europe. J. Hydrol. 519, 3634–3650.

Mahmoud, M.T., Mohammed, S.A., Hamouda, M.A., Mohamed, M.M., 2020. Impact of topography and rainfall intensity on the accuracy of imerg precipitation estimates in an arid region. Remote Sens. 13, 13.

Mandeep, J.S., 2009. Analysis effect of water on a Ka-band antenna. Prog. Electromagn. Res. 9, 49–57.

Mann, H.B., 1945. Nonparametric tests against trend. Econom. J. Econom. Soc. 245–259.

Maraun, D., 2013a. When will trends in European mean and heavy daily precipitation emerge? Environ. Res. Lett. 8, 14004.

Maraun, D., 2013b. Bias correction, quantile mapping, and downscaling: Revisiting the inflation issue. J. Clim. 26, 2137–2143.

Maraun, D., Widmann, M., 2018. Statistical downscaling and bias correction for climate research. Cambridge University Press.

Maraun, D., Widmann, M., 2015. The representation of location by a regional climate model in complex terrain. Hydrol. Earth Syst. Sci. 19, 3449–3456.

Markantonis, I., Vlachogiannis, D., Sfetsos, A., Kioutsioukis, I., 2022. Investigation of the extreme wet–cold compound events changes between 2025–2049 and 1980–2004 using regional simulations in Greece. Earth Syst. Dyn. 13, 1491–1504.

Marshall, G.J., Jylhä, K., Kivinen, S., Laapas, M., Dyrrdal, A.V., 2020. The role of atmospheric circulation patterns in driving recent changes in indices of extreme seasonal precipitation across Arctic Fennoscandia. Clim. Change 162, 741–759.

Martius, O., Pfahl, S., Chevalier, C., 2016. A global quantification of compound precipitation and wind extremes. Geophys. Res. Lett. 43, 7709–7717.

Masseroni, D., Cislaghi, A., 2016. Green roof benefits for reducing flood risk at the catchment scale. Environ. Earth Sci. 75, 1–11.

Masseroni, D., Cislaghi, A., Camici, S., Massari, C., Brocca, L., 2017. A reliable rainfall–runoff model for flood forecasting: Review and application to a semi-urbanized watershed at high flood risk in Italy. Hydrol. Res. 48, 726–740.

Masson-Delmotte, V., Zhai, P., Pirani, A., Connors, S.L., Péan, C., Berger, S., Caud, N., Chen, Y., Goldfarb, L., Gomis, M.I., 2021. Climate change 2021: the physical science basis. Contrib. Work. Gr. I to sixth Assess. Rep. Intergov. panel Clim. Chang. 2, 2391.

Mazdiyasni, O., AghaKouchak, A., 2015. Substantial increase in concurrent droughts and heatwaves in the United States. Proc. Natl. Acad. Sci. 112, 11484–11489.

McCabe, M.F., Rodell, M., Alsdorf, D.E., Miralles, D.G., Uijlenhoet, R., Wagner, W., Lucieer, A., Houborg, R., Verhoest, N.E.C., Franz, T.E., 2017. The future of Earth observation in hydrology. Hydrol. earth Syst. Sci. 21, 3879–3914.

Menapace, A., Dhawan, P., Dalla Torre, D., Kaffas, K., Crespi, A., Larcher, M., Righetti, M., Cannon, A.J., 2025. Review of bias correction methods for climate model outputs in hydrology. J. Hydrol. 133213.

Mendez, M., Maathuis, B., Hein-Griggs, D., Alvarado-Gamboa, L.-F., 2020. Performance evaluation of bias correction methods for climate change monthly precipitation projections over Costa Rica. Water 12, 482.

Messer, H., Sendik, O., 2015. A new approach to precipitation monitoring: A critical survey of existing technologies and challenges. IEEE Signal Process. Mag. 32, 110–122.

Messer, H., Zinevich, A., Alpert, P., 2006. Environmental monitoring by wireless communication networks. Science (80-.). 312, 713.

Miao, C., Sun, Q., Duan, Q., Wang, Y., 2016. Joint analysis of changes in temperature and precipitation on the Loess Plateau during the period 1961–2011. Clim. Dyn. 47, 3221–3234.

Michaelides, S., Levizzani, V., Anagnostou, E., Bauer, P., Kasparis, T., Lane, J.E., 2009.

Precipitation: Measurement, remote sensing, climatology and modeling. Atmos. Res. 94, 512–533.

Minda, H., Nakamura, K., 2005. High temporal resolution path-average rain gauge with 50-GHz band microwave. J. Atmos. Ocean. Technol. 22, 165–179.

Miralles, D.G., Teuling, A.J., Van Heerwaarden, C.C., Vilà-Guerau de Arellano, J., 2014. Mega-heatwave temperatures due to combined soil desiccation and atmospheric heat accumulation. Nat. Geosci. 7, 345–349.

Montz, B.E., Tobin, G.A., Hagelman, R.R., 2017. Natural hazards: explanation and integration. Guilford Publications.

Moraga, J.S., Peleg, N., Fatichi, S., Molnar, P., Burlando, P., 2021. Revealing the impacts of climate change on mountainous catchments through high-resolution modelling. J. Hydrol. 603, 126806.

Morán-Tejeda, E., López-Moreno, J.I., Stoffel, M., Beniston, M., 2016. Rain-on-snow events in Switzerland: recent observations and projections for the 21st century. Clim. Res. 71, 111–125.

Moroder, C., Siart, U., Chwala, C., Kunstmann, H., 2019. Modeling of wet antenna attenuation for precipitation estimation from microwave links. IEEE Geosci. Remote Sens. Lett. 17, 386–390.

Myhre, G., Alterskjær, K., Stjern, C.W., Hodnebrog, Ø., Marelle, L., Samset, B.H., Sillmann, J., Schaller, N., Fischer, E., Schulz, M., 2019. Frequency of extreme precipitation increases extensively with event rareness under global warming. Sci. Rep. 9, 16063.

Nahar, J., Johnson, F., Sharma, A., 2017. Assessing the extent of non-stationary biases in GCMs. J. Hydrol. 549, 148–162.

Nebuloni, R., Cazzaniga, G., D'Amico, M., Deidda, C., De Michele, C., 2022. Comparison of CML rainfall data against rain gauges and disdrometers in a mountainous environment. Sensors 22, 3218.

Nešpor, V., Sevruk, B., 1999. Estimation of wind-induced error of rainfall gauge measurements using a numerical simulation. J. Atmos. Ocean. Technol. 16, 450–464.

Nourani, V., Razzaghzadeh, Z., Baghanam, A.H., Molajou, A., 2019. ANN-based statistical downscaling of climatic parameters using decision tree predictor screening method. Theor. Appl. Climatol. 137, 1729–1746.

Obada, E., Alamou, A.E., Zandagba, E.J., Biao, I.E., Chabi, A., Afouda, A., 2016. Comparative study of seven bias correction methods applied to three Regional Climate Models in Mekrou catchment (Benin, West Africa).

Olsen, R., Rogers, D., Hodge, D., 1978. The aR b relation in the calculation of rain attenuation. IEEE Trans. Antennas Propag. 26, 318–329.

Osso, A., Craig, P., Allan, R.P., 2023. An assessment of CMIP6 climate signals and biases in

temperature, precipitation and soil moisture over Europe. Int. J. Climatol. 43, 5698–5719.

Ostrometzky, J., Messer, H., 2017. Dynamic determination of the baseline level in microwave links for rain monitoring from minimum attenuation values. IEEE J. Sel. Top. Appl. Earth Obs. Remote Sens. 11, 24–33.

Ostrometzky, J., Raich, R., Bao, L., Hansryd, J., Messer, H., 2017. The wet-antenna effect—A factor to be considered in future communication networks. IEEE Trans. Antennas Propag. 66, 315–322.

Overeem, A., Leijnse, H., Uijlenhoet, R., 2016. Retrieval algorithm for rainfall mapping from microwave links in a cellular communication network. Atmos. Meas. Tech. 9, 2425–2444.

Overeem, A., Leijnse, H., Uijlenhoet, R., 2013. Country-wide rainfall maps from cellular communication networks. Proc. Natl. Acad. Sci. 110, 2741–2745.

Overeem, A., Leijnse, H., Uijlenhoet, R., 2011. Measuring urban rainfall using microwave links from commercial cellular communication networks. Water Resour. Res. 47.

Overeem, A., Leijnse, H., van Leth, T.C., Bogerd, L., Priebe, J., Tricarico, D., Droste, A., Uijlenhoet, R., 2021. Tropical rainfall monitoring with commercial microwave links in Sri Lanka. Environ. Res. Lett. 16, 74058.

Owen, L.E., Catto, J.L., Stephenson, D.B., Dunstone, N.J., 2021. Compound precipitation and wind extremes over Europe and their relationship to extratropical cyclones. Weather Clim. Extrem. 33, 100342. https://doi.org/https://doi.org/10.1016/j.wace.2021.100342

Pachauri, R.K., Reisinger, A., 2007. Climate change 2007: Synthesis report. Contribution of working groups I, II and III to the fourth assessment report of the Intergovernmental Panel on Climate Change. IPCC.

Pall, P., Tallaksen, L.M., Stordal, F., 2019. A climatology of rain-on-snow events for Norway. J. Clim. 32, 6995–7016.

Palmer, T.E., McSweeney, C.F., Booth, B.B.B., Priestley, M.D.K., Davini, P., Brunner, L., Borchert, L., Menary, M.B., 2023. Performance-based sub-selection of CMIP6 models for impact assessments in Europe. Earth Syst. Dyn. 14, 457–483.

Pariartha, I.P.G.S., Aggarwal, S., Rallapalli, S., Egodawatta, P., McGree, J., Goonetilleke, A., 2023. Compounding effects of urbanization, climate change and sea-level rise on monetary projections of flood damage. J. Hydrol. 620, 129535.

Pastorek, J., Fencl, M., Rieckermann, J., Bareš, V., 2021. Precipitation Estimates From Commercial Microwave Links: Practical Approaches to Wet-Antenna Correction. IEEE Trans. Geosci. Remote Sens. 60, 1–9.

Peña-Angulo, D., Reig-Gracia, F., Domínguez-Castro, F., Revuelto, J., Aguilar, E., van der Schrier,

G., Vicente-Serrano, S.M., 2020. ECTACI: European climatology and trend atlas of climate indices (1979–2017). J. Geophys. Res. Atmos. 125, e2020JD032798.

Persson, G., Bärring, L., Kjellström, E., Strandberg, G., Rummukainen, M., 2007. Climate indices for vulnerability assessments. SMHI.

Piani, C., Haerter, J.O., Coppola, E., 2010a. Statistical bias correction for daily precipitation in regional climate models over Europe. Theor. Appl. Climatol. 99, 187–192.

Piani, C., Weedon, G.P., Best, M., Gomes, S.M., Viterbo, P., Hagemann, S., Haerter, J.O., 2010b. Statistical bias correction of global simulated daily precipitation and temperature for the application of hydrological models. J. Hydrol. 395, 199–215.

Plavcová, E., Lhotka, O., Beranová, R., Dubrovský, M., Skalák, P., 2025. Precipitation variability in CMIP6 climate models across the North Atlantic–European region and their Links to Atmospheric Circulation. Clim. Dyn. 63, 98.

Pradhan, P., Seydewitz, T., Zhou, B., Lüdeke, M.K.B., Kropp, J.P., 2022. Climate extremes are becoming more frequent, co-occurring, and persistent in Europe. Anthr. Sci. 1, 264–277.

Pu, K., Liu, X., He, H., 2020. Wet antenna attenuation model of E-band microwave links based on the LSTM Algorithm. IEEE Antennas Wirel. Propag. Lett. 19, 1586–1590.

Pudashine, J., Guyot, A., Petitjean, F., Pauwels, V.R.N., Uijlenhoet, R., Seed, A., Prakash, M., Walker, J.P., 2020. Deep learning for an improved prediction of rainfall retrievals from commercial microwave links. Water Resour. Res. 56, e2019WR026255.

Raeesi, M., Zolfaghari, A.A., Kaboli, S.H., Rahimi, M., Vente, J. de, Eekhout, J.P.C., 2024. Using quantile mapping and random forest for bias-correction of high-resolution reanalysis precipitation data and CMIP6 climate projections over Iran. Int. J. Climatol. 44, 4495–4514.

Räty, O., Räisänen, J., Ylhäisi, J.S., 2014. Evaluation of delta change and bias correction methods for future daily precipitation: intermodel cross-validation using ENSEMBLES simulations. Clim. Dyn. 42, 2287–2303.

Razavi, T., Switzman, H., Arain, A., Coulibaly, P., 2016. Regional climate change trends and uncertainty analysis using extreme indices: A case study of Hamilton, Canada. Clim. Risk Manag. 13, 43–63. https://doi.org/10.1016/j.crm.2016.06.002

Recommendation, I., 2017. Propagation data required for the design of earth-space land mobile telecommunication systems. Int. Telecommun. Union Geneva, Switz. 681–710.

Rhymee, H., Shams, S., Ratnayake, U., Rahman, E.K.A., 2022. Comparing statistical downscaling and arithmetic mean in simulating CMIP6 multi-model ensemble over Brunei. Hydrology 9, 161.

Ridder, N.N., Pitman, A.J., Ukkola, A.M., 2021. Do CMIP6 climate models simulate global or

regional compound events skillfully? Geophys. Res. Lett. 48, e2020GL091152.

Ridder, N.N., Pitman, A.J., Westra, S., Ukkola, A., Do, H.X., Bador, M., Hirsch, A.L., Evans, J.P., Di Luca, A., Zscheischler, J., 2020. Global hotspots for the occurrence of compound events. Nat. Commun. 11, 5956.

Ritchie, H., Rosado, P., Roser, M., 2022. Natural disasters. Our world data.

Roggenkamp, T., Herget, J., 2024. Flood reconstruction–The unexpected rather frequent event at River Ahr in July 2021. Glob. Planet. Change 240, 104541.

Roversi, G., Alberoni, P.P., Fornasiero, A., Porcù, F., 2020. Commercial microwave links as a tool for operational rainfall monitoring in Northern Italy. Atmos. Meas. Tech. 13, 5779–5797.

Rummukainen, M., 2010. State-of-the-art with regional climate models. Wiley Interdiscip. Rev. Clim. Chang. 1, 82–96.

Rutgersson, A., Kjellström, E., Haapala, J., Stendel, M., Danilovich, I., Drews, M., Jylhä, K., Kujala, P., Guo Larsén, X., Halsnæs, K., 2021. Natural hazards and extreme events in the Baltic Sea region. Earth Syst. Dyn. Discuss. 2021, 1–80.

Salman, S.A., Hamed, M.M., Shahid, S., Ahmed, K., Sharafati, A., Asaduzzaman, M., Ziarh, G.F., Ismail, T., WANG, X., Dewan, A., 2022. Projecting spatiotemporal changes of precipitation and temperature in Iraq for different shared socioeconomic pathways with selected Coupled Model Intercomparison Project Phase 6. Int. J. Climatol.

Schleiss, M., Rieckermann, J., Berne, A., 2013. Quantification and modeling of wet-antenna attenuation for commercial microwave links. IEEE Geosci. Remote Sens. Lett. 10, 1195–1199.

Sedlmeier, K., Feldmann, H., Schädler, G., 2018. Compound summer temperature and precipitation extremes over central Europe. Theor. Appl. Climatol. 131, 1493–1501.

Sen, P.K., 1968. Estimates of the Regression Coefficient Based on Kendall's Tau. J. Am. Stat. Assoc. 63, 1379–1389. https://doi.org/10.1080/01621459.1968.10480934

Seneviratne, S.I., Nicholls, N., Easterling, D., Goodess, C.M., Kanae, S., Kossin, J., Luo, Y., Marengo, J., Mc Innes, K., Rahimi, M., Reichstein, M., Sorteberg, A., Vera, C., Zhang, X., Rusticucci, M., Semenov, V., Alexander, L. V., Allen, S., Benito, G., Cavazos, T., Clague, J., Conway, D., Della-Marta, P.M., Gerber, M., Gong, S., Goswami, B.N., Hemer, M., Huggel, C., Van den Hurk, B., Kharin, V. V., Kitoh, A., Klein Tank, A.M.G., Li, G., Mason, S., Mc Guire, W., Van Oldenborgh, G.J., Orlowsky, B., Smith, S., Thiaw, W., Velegrakis, A., Yiou, P., Zhang, T., Zhou, T., Zwiers, F.W., 2012. Changes in climate extremes and their impacts on the natural physical environment. Manag. Risks Extrem. Events Disasters to Adv. Clim. Chang. Adapt. Spec. Rep. Intergov. Panel Clim. Chang. 9781107025, 109–230. https://doi.org/10.1017/CBO9781139177245.006

Seneviratne, S.I., Zhang, X., Adnan, M., Badi, W., Dereczynski, C., Di Luca, A., Vicente-Serrano, S.M., Wehner, M., Zhou, B., 2021. Chapter 11: Weather and climate extreme events in a changing climate.

Sengupta, A., King, A.D., Brown, J.R., 2025. Do CMIP6 Models Capture Seasonal and Regional Differences in the Asymmetry of ENSO-Precipitation Teleconnections? J. Geophys. Res. Atmos. 130, e2024JD041031.

Seo, G.-Y., Ahn, J.-B., 2023. Comparison of bias correction methods for summertime daily rainfall in South Korea using quantile mapping and machine learning model. Atmosphere (Basel). 14, 1057.

Series, R.P., 2015. Propagation data and prediction methods required for the design of terrestrial line-of-sight systems. Recomm. ITU-R 512–530.

Shanmugam, H., Lakshmanan, V.R., 2025. Development of stacking algorithm for bias-correcting the precipitation projections using a multi-model ensemble of CMIP6 GCMs in a semi-arid basin, India. Theor. Appl. Climatol. 156, 1–28.

Sharma, S., Mujumdar, P., 2017. Increasing frequency and spatial extent of concurrent meteorological droughts and heatwaves in India. Sci. Rep. 7, 15582.

Sheffield, J., Goteti, G., Wood, E.F., 2006. Development of a 50-year high-resolution global dataset of meteorological forcings for land surface modeling. J. Clim. 19, 3088–3111.

Shiru, M.S., Park, I., 2020. Comparison of ensembles projections of rainfall from four bias correction methods over Nigeria. Water 12, 3044.

Shiru, M.S., Shahid, S., Chung, E.-S., Alias, N., Scherer, L., 2019. A MCDM-based framework for selection of general circulation models and projection of spatio-temporal rainfall changes: a case study of Nigeria. Atmos. Res. 225, 1–16.

Shrestha, S.G., Pradhanang, S.M., 2022. Optimal selection of representative climate models and statistical downscaling for climate change impact studies: a case study of Rhode Island, USA. Theor. Appl. Climatol. 149, 695–708.

Sillmann, J., Kharin, V. V, Zhang, X., Zwiers, F.W., Bronaugh, D., 2013. Climate extremes indices in the CMIP5 multimodel ensemble: Part 1. Model evaluation in the present climate. J. Geophys. Res. Atmos. 118, 1716–1733.

Soares, P.M.M., Johannsen, F., Lima, D.C.A., Lemos, G., Bento, V.A., Bushenkova, A., 2024. High-resolution downscaling of CMIP6 Earth system and global climate models using deep learning for Iberia. Geosci. Model Dev. 17, 229–259.

Song, K., Liu, X., Gao, T., 2021. Real-time rainfall estimation using microwave links: A case study in east China during the plum rain season in 2020. Sensors 21, 858.

Sorooshian, S., AghaKouchak, A., Arkin, P., Eylander, J., Foufoula-Georgiou, E., Harmon, R., Hendrickx, J.M.H., Imam, B., Kuligowski, R., Skahill, B., 2011. Advancing the remote sensing of precipitation. Bull. Am. Meteorol. Soc. 92, 1271–1272.

Stenšin, A., Bloznelis, D., 2022. Copulas and Portfolios in the Electric Vehicle Sector. J. Risk Financ. Manag. 15, 132.

Stephens, C.M., Pham, H.T., Marshall, L.A., Johnson, F.M., 2022. Which rainfall errors can hydrologic models handle? Implications for using satellite-derived products in sparsely gauged catchments. Water Resour. Res. 58, e2020WR029331.

Stephens, G.L., L'Ecuyer, T., Forbes, R., Gettelmen, A., Golaz, J., Bodas-Salcedo, A., Suzuki, K., Gabriel, P., Haynes, J., 2010. Dreary state of precipitation in global models. J. Geophys. Res. Atmos. 115.

Sun, Q., Miao, C., Duan, Q., Ashouri, H., Sorooshian, S., Hsu, K., 2018. A review of global precipitation data sets: Data sources, estimation, and intercomparisons. Rev. Geophys. 56, 79–107.

Sun, Q., Zhang, X., Zwiers, F., Westra, S., Alexander, L. V, 2021. A global, continental, and regional analysis of changes in extreme precipitation. J. Clim. 34, 243–258.

Tabor, K., Williams, J.W., 2010. Globally downscaled climate projections for assessing the conservation impacts of climate change. Ecol. Appl. 20, 554–565.

Talchabhadel, R., Aryal, A., Kawaike, K., Yamanoi, K., Nakagawa, H., Bhatta, B., Karki, S., Thapa, B.R., 2021. Evaluation of precipitation elasticity using precipitation data from ground and satellite-based estimates and watershed modeling in Western Nepal. J. Hydrol. Reg. Stud. 33, 100768.

Tanimu, B., Bello, A.-A.D., Abdullahi, S.A., Ajibike, M.A., Yaseen, Z.M., Kamruzzaman, M., Muhammad, M.K.I. bin, Shahid, S., 2024. Comparison of conventional and machine learning methods for bias correcting CMIP6 rainfall and temperature in Nigeria. Theor. Appl. Climatol. 155, 4423–4452.

Tank, A.M.G.K., Zwiers, F.W., Zhang, X., 2009. Guidelines on analysis of extremes in a changing climate in support of informed decisions for adaptation. World Meteorol. Organ. 1500, 72.

Tavares, P. da S., Rodrigues, D.C., Chou, S.C., Laureanti, N.C., Medeiros, G.S., Gomes, J.L., Vergasta, L.A., Correia, F.W.S., 2025. Dynamical-statistical downscaling of seasonal hindcasts of temperature and precipitation over South America. RBRH 30, e7.

Terink, W., Hurkmans, R., Torfs, P., Uijlenhoet, R., 2009. Bias correction of temperature and precipitation data for regional climate model application to the Rhine basin. Hydrol. Earth Syst. Sci. Discuss. 6, 5377–5413.

Teutschbein, C., Seibert, J., 2012. Bias correction of regional climate model simulations for hydrological climate-change impact studies: Review and evaluation of different methods. J. Hydrol. 456, 12–29.

Themeßl, M.J., Gobiet, A., Heinrich, G., 2012. Empirical-statistical downscaling and error correction of regional climate models and its impact on the climate change signal. Clim. Change 112, 449–468.

Thrasher, B., Wang, W., Michaelis, A., Melton, F., Lee, T., Nemani, R., 2022. NASA global daily downscaled projections, CMIP6. Sci. data 9, 262.

Tian, B., Dong, X., 2020. The double-ITCZ bias in CMIP3, CMIP5, and CMIP6 models based on annual mean precipitation. Geophys. Res. Lett. 47, e2020GL087232.

Tian, Y., Giaquinto, D., Di Capua, G., Claassen, J.N., Ali, J., Li, H., De Michele, C., 2024. Historical changes in the Causal Effect Networks of compound hot and dry extremes in central Europe. Commun. Earth Environ. 5, 1–14.

Tiku, T.W., Tarekegn, G.B., Sahlu, D., Teshebo, G.B., Enyew, F.B., Umer, Y., Debele, S.E., 2025. Evaluating CMIP6 Precipitation Simulations Across Different Rainfall Regimes in the Amhara Region, Ethiopia. Nat. Hazards Res.

Tong, X., Yan, Z., Xia, J., Lou, X., 2019. Decisive atmospheric circulation indices for July–August precipitation in North China based on tree models. J. Hydrometeorol. 20, 1707–1720.

Tootoonchi, F., Sadegh, M., Haerter, J.O., Räty, O., Grabs, T., Teutschbein, C., 2022. Copulas for hydroclimatic analysis: A practice-oriented overview. Wiley Interdiscip. Rev. Water 9, e1579.

Trigo, R.M., Osborn, T.J., Corte-Real, J.M., 2002. The North Atlantic Oscillation influence on Europe: climate impacts and associated physical mechanisms. Clim. Res. 20, 9–17.

Tripathy, K.P., Mishra, A.K., 2023. How unusual is the 2022 European compound drought and heatwave event? Geophys. Res. Lett. 50, e2023GL105453.

Tripathy, K.P., Mukherjee, S., Mishra, A.K., Mann, M.E., Williams, A.P., 2023. Climate change will accelerate the high-end risk of compound drought and heatwave events. Proc. Natl. Acad. Sci. 120, e2219825120.

Tyfield, D., Willis, R., Yuille, A., 2022. Bringing Governance Back Home—Lessons for Local Government regarding Rapid Climate Action. MDPI-Multidisciplinary Digital Publishing Institute.

Uijlenhoet, R., Overeem, A., Leijnse, H., 2018. Opportunistic remote sensing of rainfall using microwave links from cellular communication networks. Wiley Interdiscip. Rev. Water 5, e1289.

Ulbrich, C.W., Lee, L.G., 1999. Rainfall measurement error by WSR-88D radars due to variations in

Z–R law parameters and the radar constant. J. Atmos. Ocean. Technol. 16, 1017–1024.

Upton, G.J.G., Holt, A.R., Cummings, R.J., Rahimi, A.R., Goddard, J.W.F., 2005. Microwave links: The future for urban rainfall measurement? Atmos. Res. 77, 300–312.

Valtr, P., Fencl, M., Bareš, V., 2019. Excess attenuation caused by antenna wetting of terrestrial microwave links at 32 GHz. IEEE Antennas Wirel. Propag. Lett. 18, 1636–1640.

van de Wal, R.S.W., Melet, A., Bellafiore, D., Vousdoukas, M., Camus, P., Ferrarin, C., Oude Essink, G., Haigh, I.D., Lionello, P., Luijendijk, A., 2023. Sea Level Rise in Europe: impacts and consequences. State Planet Discuss. 2023, 1–65.

Van den Besselaar, E.J.M., Klein Tank, A.M.G., Buishand, T.A., 2013. Trends in European precipitation extremes over 1951–2010. Int. J. Climatol. 33, 2682–2689.

van den Hurk, B., van Meijgaard, E., de Valk, P., van Heeringen, K.-J., Gooijer, J., 2015. Analysis of a compounding surge and precipitation event in the Netherlands. Environ. Res. Lett. 10, 35001.

Van Dijk, A.I.J.M., Beck, H.E., Crosbie, R.S., De Jeu, R.A.M., Liu, Y.Y., Podger, G.M., Timbal, B., Viney, N.R., 2013. The Millennium Drought in southeast Australia (2001–2009): Natural and human causes and implications for water resources, ecosystems, economy, and society. Water Resour. Res. 49, 1040–1057.

Van Leth, T.C., Overeem, A., Leijnse, H., Uijlenhoet, R., 2018. A measurement campaign to assess sources of error in microwave link rainfall estimation. Atmos. Meas. Tech. 11, 4645–4669.

Vautard, R., van Aalst, M., Boucher, O., Drouin, A., Haustein, K., Kreienkamp, F., Van Oldenborgh, G.J., Otto, F.E.L., Ribes, A., Robin, Y., 2020. Human contribution to the record-breaking June and July 2019 heatwaves in Western Europe. Environ. Res. Lett. 15, 94077.

Venkadesh, P., Divya, S. V, Marymariyal, P., Keerthana, S., 2024. Predicting Natural Disasters With AI and Machine Learning, in: Utilizing AI and Machine Learning for Natural Disaster Management. IGI Global, pp. 39–64.

Vikhamar-Schuler, D., Isaksen, K., Haugen, J.E., Tømmervik, H., Luks, B., Schuler, T.V., Bjerke, J.W., 2016. Changes in winter warming events in the Nordic Arctic Region. J. Clim. 29, 6223–6244.

Vogel, J., Paton, E., Aich, V., Bronstert, A., 2021. Increasing compound warm spells and droughts in the Mediterranean Basin. Weather Clim. Extrem. 32, 100312.

Vogel, M.M., Hauser, M., Seneviratne, S.I., 2020. Projected changes in hot, dry and wet extreme events' clusters in CMIP6 multi-model ensemble. Environ. Res. Lett. 15, 94021.

Volosciuk, C., Maraun, D., Vrac, M., Widmann, M., 2017. A combined statistical bias correction and stochastic downscaling method for precipitation. Hydrol. Earth Syst. Sci. 21, 1693–1719.

Vörösmarty, C.J., Green, P., Salisbury, J., Lammers, R.B., 2000. Global water resources:

Vulnerability from climate change and population growth. science, 289 (5477), 284–288.

Vrac, M., Noël, T., Vautard, R., 2016. Bias correction of precipitation through Singularity Stochastic Removal: Because occurrences matter. J. Geophys. Res. Atmos. 121, 5237–5258.

Vrac, M., Thao, S., Yiou, P., 2023. Changes in temperature–precipitation correlations over Europe: are climate models reliable? Clim. Dyn. 60, 2713–2733.

Vrac, M., Thao, S., Yiou, P., 2022. Should multivariate bias corrections of climate simulations account for changes of rank correlation over time? J. Geophys. Res. Atmos. 127, e2022JD036562.

Wada, I.M., Usman, H.S., Nwankwegu, A.S., Usman, M.N., Gebresellase, S.H., 2023. Selection and downscaling of CMIP6 climate models in Northern Nigeria. Theor. Appl. Climatol. 153, 1157–1175.

Wang, B., Zheng, L., Liu, D.L., Ji, F., Clark, A., Yu, Q., 2018. Using multi-model ensembles of CMIP5 global climate models to reproduce observed monthly rainfall and temperature with machine learning methods in Australia. Int. J. Climatol. 38, 4891–4902.

Wang, T., Tu, X., Singh, V.P., Chen, X., Lin, K., 2021. Global data assessment and analysis of drought characteristics based on CMIP6. J. Hydrol. 596, 126091.

Wilby, R.L., Charles, S.P., Zorita, E., Timbal, B., Whetton, P., Mearns, L.O., 2004. Guidelines for use of climate scenarios developed from statistical downscaling methods. Support. Mater. Intergov. Panel Clim. Chang. available from DDC IPCC TGCIA 27.

Williams, M., Eggleston, S., 2017. Using indicators to explain our changing climate to policymakers and the public. WMO Bull 66, 33–39.

WMO, 2002. Introduction to climate change: Lecture notes for meteorologists. Secretariat of the World Meteorological Organization Geneva, Switzerland.

Worako, A.W., Haile, A.T., Taye, M.T., 2022. Implication of bias correction on climate change impact projection of surface water resources in the Gidabo sub-basin, Southern Ethiopia. J. Water Clim. Chang. 13, 2070–2088.

Yang, J., Xiang, Y., Sun, J., Xu, X., 2022. Multi-model ensemble prediction of summer precipitation in China based on machine learning algorithms. Atmosphere (Basel). 13, 1424.

Yang, W., Andréasson, J., Phil Graham, L., Olsson, J., Rosberg, J., Wetterhall, F., 2010. Distribution-based scaling to improve usability of regional climate model projections for hydrological climate change impacts studies. Hydrol. Res. 41, 211–229.

Zarei, M., Najarchi, M., Mastouri, R., 2021. Bias correction of global ensemble precipitation forecasts by Random Forest method. Earth Sci. Informatics 14, 677–689.

Zhang, P., Liu, X., Pu, K., 2023. Precipitation monitoring using commercial microwave links: current

status, challenges and prospectives. Remote Sens. 15, 4821.

Zhang, Q., Li, Y.P., Huang, G.H., Wang, H., Li, Y.F., Liu, Y.R., Shen, Z.Y., 2022. A novel statistical downscaling approach for analyzing daily precipitation and extremes under the impact of climate change: Application to an arid region. J. Hydrol. 615, 128730.

Zheng, X., Messer, H., Wang, Q., Xu, T., Qin, Y., Yang, T., 2022. On the potential of commercial microwave link networks for high spatial resolution rainfall monitoring in urban areas. Atmos. Res. 277, 106289.

Zhou, B., Wen, Q.H., Xu, Y., Song, L., Zhang, X., 2014. Projected changes in temperature and precipitation extremes in China by the CMIP5 multimodel ensembles. J. Clim. 27, 6591–6611.

Zinevich, A., Messer, H., Alpert, P., 2010. Prediction of rainfall intensity measurement errors using commercial microwave communication links. Atmos. Meas. Tech. 3, 1385–1402.

Zscheischler, J., Fischer, E.M., 2020. The record-breaking compound hot and dry 2018 growing season in Germany. Weather Clim. Extrem. 29, 100270.

Zscheischler, J., Seneviratne, S.I., 2017. Dependence of drivers affects risks associated with compound events. Sci. Adv. 3, e1700263.

Zscheischler, J., Sillmann, J., Alexander, L., 2022. Introduction to the special issue: Compound weather and climate events. Weather Clim. Extrem.

Zscheischler, J., Westra, S., Van Den Hurk, B.J.J.M., Seneviratne, S.I., Ward, P.J., Pitman, A., Aghakouchak, A., Bresch, D.N., Leonard, M., Wahl, T., Zhang, X., 2018. Future climate risk from compound events. Nat. Clim. Chang. 8, 469–477. https://doi.org/10.1038/s41558-018-0156-3

Acknowledgments

This work was supported by multiple organizations and initiatives whose contributions are acknowledged. Funding was provided by the AWI Inspires Project—"Compound extreme events: a long-term perspective (LongCEX)" (Smit Chetan Doshi), the Helmholtz Climate Initiative—REKLIM (Monica Ionita), and Helmholtz Association through the joint program 'Changing Earth—Sustaining our Future' (PoF IV) of the Alfred Wegner Institute. We also acknowledge the support of the Open Access Publication Funds of Alfred Wegener Institute for Polar and Marine Research. We acknowledge the EU COST Action "OPENSENSE" (CA20136, Opportunistic Precipitation Sensing Network, https://opensenseaction.eu/) for funding the short-term scientific mission of Smit Chetan Doshi at Politecnico di Milano and Consiglio Nazionale delle Ricerche,Milan, Italy in 2023. Part of dissertation was supported by a fellowship of the German Academic Exchange Service (DAAD). Acknowledgment to E-OBS dataset from the EU-FP6 project UERRA (http://www.uerra.eu), the Copernicus Climate Change Service, data providers in the ECA&D project (https://www.ecad.eu), and World Climate Research Programme's Working Group on Coupled Modelling, responsible for CMIP data.

I would like to express my gratitude to both my supervisors, Prof. Dr. Gerrit Lohmann, and Dr. Monica Ionita, for granting me the invaluable opportunity to pursue the doctoral research under their expert guidance. Their trust, continuous support, and insightful advice enriched my academic journey. They patiently listened to all my questions and provided suggestions whenever needed. Their openness and willingness to assist created a supportive and inspiring environment, which greatly contributed to success of this work. Moreover, they consistently encouraged my career growth by allowing me to participate in conferences, summer schools, and training programs, which have been invaluable addition to my skills and communication abilities. I would extend my appreciation to supervisors in Milan for their support during research on commercial microwave links and statistical downscaling in Milan. I am grateful to Dr. Roberto Nubeloni, for introducing me to the concept of opportunistic sensing and fundamental principles underlying this field. Also thank Prof. Dr. Carlo De Michele, who consistently supported, trusted, and guided throughout the research process. His mentorship and encouragement were vital in advancing my work.

The majority of this work was made possible thanks to the high-performance computing (HPC) resources and continuous support provided by Alfred Wegner Institute. Thanks to the helpdesk team, especially Natalja Rakowsky, Sebastian Hinck, and Sven Harig for their patience and support – their willingness to listen and helping me understand use of the HPC resources were greatly appreciated.

The excellent workplace facilities and supporting working environment greatly contributed to the successful progress of this research.

Thanks to the entire team of paleoclimate dynamics and POLMAR at the Alfred Wegner Institute, Bremerhaven, Germany. A special thanks goes to: Diana Elena Caldarescu, Fernanda Matos, Norel Rimbu, Zohreh Sheikh Khozani who have been much more than work colleagues to me; their support, suggestions, and friendship made this journey rewarding.

Finally, a heartfelt thank you to my family – my mother, father, and sister; without your love and guidance in helping me navigate stressful situations, it would have been never possible for me to come this far. Your belief in me has been my greatest strength throughout this journey.